ISSN 1580-3155 Pages 505–752 ■ Year 2021, Vol. 68, No. 3

Slovensko kemijsko društvo
Slovenian Chemical Society

Acta Chimica Slovenica

3

68/2021

http://acta.chem-soc.si

Acta Chimica Slovenica is indexed in: *Academic Search Complete, Central & Eastern European Academic Source, Chemical Abstracts Plus, Chemical Engineering Collection (India), Chemistry Citation Index Expanded, Current Contents (Physical, Chemical and Earth Sciences), Digitalna knjižnica Slovenije (dLib.si), DOAJ, ISI Alerting Services, PubMed, Science Citation Index Expanded, SciFinder (CAS), Scopus and Web of Science.* Impact factor for 2020 is IF = 1.735.

Izdaja – Published by:
SLOVENSKO KEMIJSKO DRUŠTVO – SLOVENIAN CHEMICAL SOCIETY
Naslov redakcije in uprave – Address of the Editorial Board and Administration
Hajdrihova 19, SI-1000 Ljubljana, Slovenija
Tel.: (+386)-1-476-0252; Fax: (+386)-1-476-0300; E-mail: chem.soc@ki.si

Slovensko kemijsko društvo
Slovenian Chemical Society

Izdajanje sofinancirajo – Financially supported by:
National Institute of Chemistry, Ljubljana, Slovenia
Jožef Stefan Institute, Ljubljana, Slovenia
Faculty of Chemistry and Chemical Technology, University of Ljubljana, Slovenia
Faculty of Chemistry and Chemical Engineering, University of Maribor, Slovenia

Acta Chimica Slovenica izhaja štirikrat letno v elektronski obliki na spletni strani http://*acta.chem-soc.si*. V primeru posvečenih številk izhaja revija tudi v tiskani obliki v omejenem številu izvodov.

Acta Chimica Slovenica appears quarterly in electronic form on the web site *http://acta.chem-soc.si*. In case of dedicated issues, a limited number of printed copies are issued as well.

Transakcijski račun: 02053-0013322846 Bank Account No.: SI56020530013322846-Nova Ljubljanska banka d. d., Trg republike 2, SI-1520 Ljubljana, Slovenia, SWIFT Code: LJBA SI 2X

Oblikovanje ovitka – Design cover: KULT, oblikovalski studio, Simon KAJTNA, s. p. Grafična priprava za tisk: OSITO, Laura Jankovič, s.p.

Graphical Contents

Acta Chimica Slovenica

Year 2021, Vol. 68, No. 3

FEATURE ARTICLE

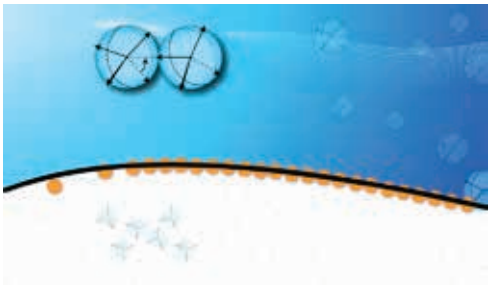

SCIENTIFIC PAPER

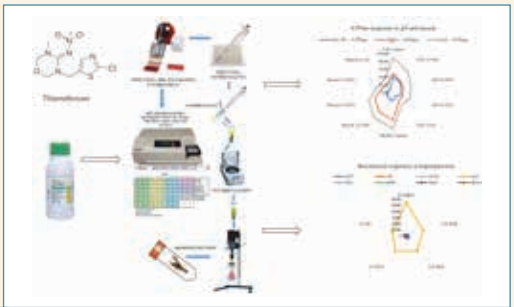

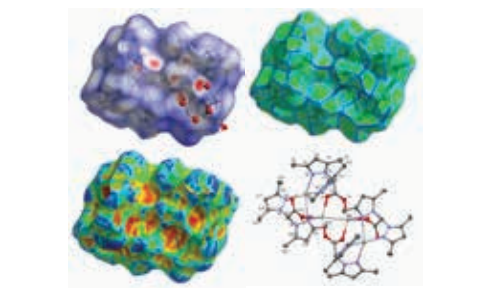

Graphical Contents

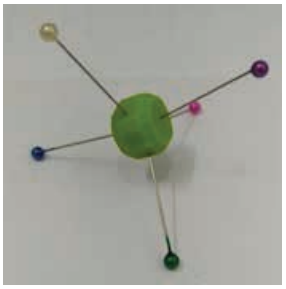

TECHNICAL PAPERS

DRUŠTVENE VESTI

Feature article

Analytical Modeling of Thermodynamic and Transport Anomalies of Water

Tomaz Urbic*

University of Ljubljana, Faculty of Chemistry and Chemical Technology, Chair of Physical Chemistry, Večna pot 113, SI-1000 Ljubljana, Slovenia

** Corresponding author: E-mail: tomaz.urbic@fkkt.uni-lj.si*

Received: 07-12-2021

Abstract

The structures and properties of biomolecules like proteins, nucleic acids, and membranes depend on water. Water is also very important in industry. Overall, water is an unusual substance with more than 70 anomalous properties. The understanding of water is advancing significantly due to the theoretical and computational modeling. There are different kinds of models, models with fine-scale properties and increasing structural detail with increasing computational expense, and simple models, which focus on global properties of water like thermodynamics, phase diagram and are less computationally expensive. Simplified models give a better understanding of water in ways that complement more complex models. Here, we review analytical modelling of properties of water on different levels, the two- and three-dimensional Mercedes– Benz (MB) models of water and experimental water.

Keywords: Water, statistical model, anomalies, transport properties, analytical model

1. Introduction

The Earth is a watery place by water being the most important fluid in nature for life and for humans in the industry.[1–4] About 71 percent of the Earth's surface is water-covered, and the oceans hold about 96.5 percent of all Earth's water. Water also exists in the air as water vapor, in rivers and lakes, in icecaps and glaciers, in the ground as soil moisture etc. Water controls the planets geochemical cycles; is a dominant driver of biomolecules, drug interactions, and biological actions; and central to green chemistry and many industrial processes.[5,6] Water is essential for our bodies. Every major system in our body depends on water to function since approximately two thirds of your body is water. Due to all these facts the structure and thermodynamics of water and aqueous solutions is of great importance for all sciences, especially chemistry and biology. Water exhibits many anomalous properties that affect life at a larger scale. Many animals benefit from the large latent heat of water to cool them down through sweating. The large heat capacity of water prevents local temperature fluctuations, facilitating thermal regulation of organisms. The density anomaly and lower ice (hexagonal ice I_h) density have a huge effect on surviving of organisms in frozen seas and lakes. Water is an almost universal solvent.[7] Nearly all known chemical substances will dissolve in water at least to a small extent. In comparison to other liquids, it has the most puzzling behavior.[7,8] It is said that water is an anomalous liquid. Anomalous liquids are liquids that exhibit unexpected behavior upon variations of the thermodynamic conditions in comparison to normal (argon-like) liquids. Water is the classic example of such anomalous liquids. Water's density maximum at 4 °C, the lower density of the solid phase compared to the liquid phase, high and nearly constant heat capacity in the liquid phase, negative expansion coefficient below the temperature of the density maximum, as well as high surface tension and viscosity are the most known examples of anomalous properties. If we continue, we have an anomalous increase in the compressibility and specific heat by cooling, unusually high boiling, freezing and critical points. The reason for water's complexity is due to its strong orientation-dependent hydrogen bonding and strong intermolecular associations.

An understanding of the hydrogen bonding is therefore crucial to understand the behavior and properties of water and aqueous solutions. Yet, despite extensive theory and simulations, the fact how water's properties come from its molecular structure remains poorly understood. Many models of varying complexity have been developed and analyzed to model water's extraordinary properties,

for review see literature.[7–19] The rigid models are considered the simplest water models and rely on non-bonded interactions. The electrostatic interaction is modeled using Coulomb's law, and the dispersion and repulsion forces using the Lennard-Jones potential. Examples of such models are SPC (simple point-charge)[20], TIP3P (transferable intermolecular potential with 3 points)[20] and TIP4P (transferable intermolecular potential with 4 points)[21] etc. In polarizable models we consider many-body energies which can be effectively accounted for by a single term representing classical many-body polarization. Several polarizable water models, with different degrees of sophistication, have been developed and used in molecular dynamics and Monte Carlo simulations of aqueous systems.[22] A key goal of the liquid-state statistical thermodynamics is to develop a quantitative theory for water and aqueous solutions. Theory and simulations have not yet been able to explain how water's molecular structure leads to its density, compressibility, expansion coefficient and heat capacity as functions of temperature and pressure, including its well-known anomalies. The properties of water can be determined with quantum-mechanical calculations.[22,23] These methods offer the highest degree of exactness, but a high computational cost of these approaches limits their use to small water systems, even though these insights allow the development and fine-tuning of simplified water models.[24–26] There have been two main approaches to modeling liquids. One approach is to perform computer simulations of atomically detailed models. Another way captures many properties of water and aqueous solutions by simpler models.

One of the simplest models for water is the so-called Mercedes-Benz (MB) model,[27] which is a 2-dimensional model that was originally proposed by Ben-Naim in 1971.[28,29] Each MB water particle is modeled as a disk that interacts with other particles through: (1) a Lennard-Jones (LJ) interaction and (2) an orientation-dependent hydrogen bonding interaction through three radial arms arranged as in the MB logo. Interest in simplified models is due to insights that are not obtainable from all-atom computer simulations. Simpler models are more flexible in providing insights and illuminating concepts, and they do not require big computer resources. The analytical models can also provide functional relationships for engineering applications and lead to improved models of greater computational efficiency. For the MB model, the NPT Monte Carlo simulations have shown that it predicts qualitatively the density anomaly, the minimum in the isothermal compressibility as a function of temperature, the large heat capacity, as well as the experimental trends for the thermodynamic properties of solvation of nonpolar solutes[27] and cold denaturation of proteins.[30] The MB model was also extensively studied with analytical methods like integral equation and thermodynamic perturbation theory[31–36] and statistical mechanic modeling[37–39]. Recently also phase diagram of liquid part and percolation curve of the model was calculated and reported.[40] The MB model has also been used to study systems with water molecules confined in partially quenched disordered matrix[41–43] and within small geometric spaces.[44,45] Nonequilibrium Monte Carlo and molecular dynamics simulations were used to study the effect of translational and rotational degrees of freedom on the structural and thermodynamic properties of this MB model.[46–48] By holding one of the temperatures constant and varying the other one, the effect of faster motion in the corresponding degrees of freedom on the properties of the simple water model was investigated. The situation where the rotational temperature exceeded the translational one is mimicking the effects of microwaves on the water model. A decrease of rotational temperature leads to the higher structural order while an increase causes the structure to be more Lennard-Jones fluid like. The 2D MB model was also extended to 3D by Dias et al.[49] and Bizjak et al.[50,51]

Even though computer simulations play an important role in understanding the properties of liquids, they can be quite time consuming, even for simple two-dimensional 2D models. Due to this it is equally important to develop simplified, more analytical approaches. One such model is a statistical mechanical model, developed by Urbic and Dill[33]. The model is directly descendant from a treatment of Truskett and Dill, who developed a nearly analytical version of the 2D MB model.[52,53] In the model, each water particle interacts with its neighboring particle through a van der Waals interaction and an orientation-dependent interaction that models hydrogen bonds. Recently this theory was extended to 3D MB model[38] and later parametrized to describe properties of experimental water.[54]

In this paper, we made review of analytical modeling for MB model of water, its properties in bulk which are starting point to develop the theory for solvation of polar and nonpolar solutes, important for example in self-association of surface-active compounds such as ionic liquids,[55] protein folding, etc. The outline of the paper is as follows. We present the 2D and 3D MB model in Sec. 2, and the details of the statistical mechanical methods are done in Sec. 3. In Sec. 4 we show and discuss the results and summarize everything in Sec. 5.

2. The Model

2. 1. 2D MB Model

In 2D, the water particles are modelled as a two-dimensional disk with three bonding arms separated by an angle of 120°, which is fixed as in Mercedes-Benz logo (See Figure 1).[27] These arms mimic formation of hydrogen bonds. The interaction potential between particles i and j is a sum of a Lennard-Jones (LJ) and a hydrogen-bonding (HB) term

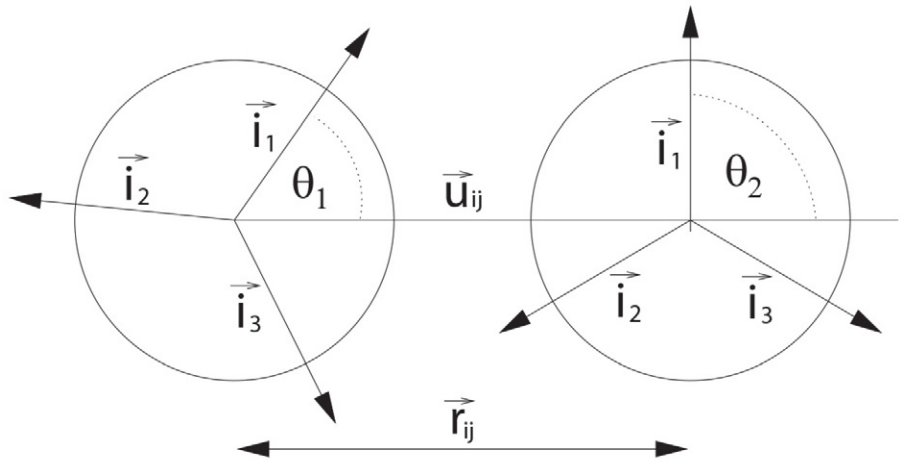

Figure 1: The MB particles in 2D.

$$U(\vec{X_\iota}, \vec{X_j}) = U_{LJ}(r_{ij}) + U_{HB}(\vec{X_\iota}, \vec{X_j}) \tag{1}$$

Where r_{ij} is the distance between centers of particles i and j. $\vec{X_i}$, $\vec{X_j}$ are the vectors representing the coordinates and the orientation of the particles i and j. The Lennard-Jones part has a standard form

$$U_{LJ}(r_{ij}) = 4\varepsilon_{LJ}\left(\left(\frac{r_{ij}}{\sigma_{LJ}}\right)^{12} - \left(\frac{r_{ij}}{\sigma_{LJ}}\right)^{6}\right). \tag{2}$$

σ_{LJ} and $\varepsilon_{\mathrm{LJ}}$ are the depth and the contact value of the LJ potential. The hydrogen bonding part is the sum of interactions between all pairs of the arms of different molecules

$$U_{HB}(\vec{X_\iota}, \vec{X_j}) = \sum_{l,k=1}^{3} U_{HB}^{kl}(r_{ij}, \theta_i, \theta_j) \tag{3}$$

and is described by Gaussian function in distance and both angles

$$U_{HB}^{kl}(r_{ij}, \theta_i, \theta_j) = \varepsilon_{HB} G(r_{ij} - r_{HB}) G(\vec{\imath_k}\vec{u_{\iota j}} - 1) G(\vec{j_l}\vec{u_{\iota j}} + 1) =$$
$$\varepsilon_{HB} G(r_{ij} - r_{HB}) G\left(\cos\left(\theta_i + \tfrac{2\pi(k-1)}{3}\right) - 1\right) \tag{4}$$
$$G\left(\cos\left(\theta_j + \tfrac{2\pi(l-1)}{3}\right) + 1\right).$$

Here, $\varepsilon_{\mathrm{HB}} = -1$ is a HB energy parameter and $\mathrm{r_{HB}} = \mathrm{i}$ is a characteristic length of HB, $\vec{u_{ij}}$ is the unit vector along $\vec{r_{ij}}$ and $\vec{\imath_k}$ is the unit vector of the k^{th} arm of the particle I, and θ_i is the unit vector of the $\mathrm{i^{th}}$ arm of the particle j. θ_i, θ_j are the orientations of the particle with respect to x axes. G(x) is the unnormalized Gaussian function

$$G(x) = e^{-\frac{x}{2\sigma^2}}. \tag{5}$$

The strongest hydrogen bond occurs when an arm of one particle is co-linear with the arm of another particle and the two arms point in opposing directions. The LJ well-depth ε_{LJ} is 0.1 times the HB interaction energy $|\varepsilon_{\mathrm{HB}}|$ and the Lennard-Jones contact parameter σ_{LJ} is 0.7 r_{HB}. The width of the Gaussian function for distances and angles ($\sigma = 0.085\ r_{\mathrm{HB}}$) is small enough that a direct hydrogen bond is more favorable than a bifurcated one.

2. 2. 3D MB Model

In 3D, each water molecule is represented as a Lennard-Jones sphere (LJ) with four arms oriented tetrahedrally.[50] The angle between neighboring arms in a molecule is 109.47° (see Figure 2). Like in 2D, in 3D the inter-

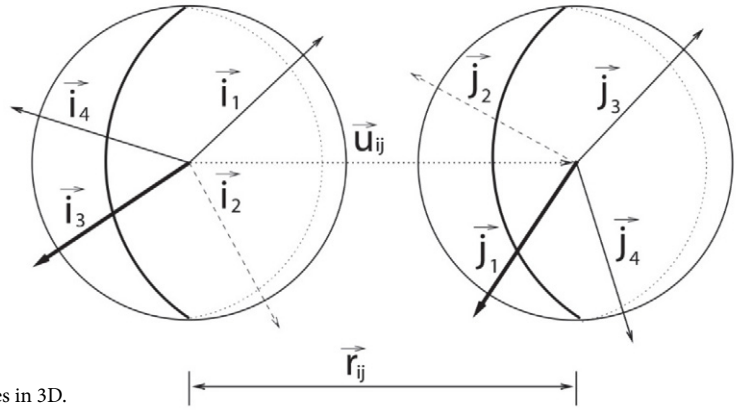

Figure 2: The MB particles in 3D.

action potential between two water molecules is a sum of the Lennard-Jones potential and the hydrogen bond term

$$U(\vec{X_\iota}, \vec{X_J}) = U_{LJ}(r_{ij}) + U_{HB}(\vec{X_\iota}, \vec{X_J}) \quad (6)$$

The Lennard-Jones part of the potential is the same as in 2D. The hydrogen bonding part of the interaction potential is

$$U_{HB}(\vec{X_\iota}, \vec{X_J}) = \sum_{l,k=1}^{4} U_{HB}^{kl}(r_{ij}, \vec{\Omega_\iota}, \vec{\Omega_J}) \quad (7)$$

Where $\vec{\Omega_i}$. $\vec{\Omega_j}$ are the orientational vectors of both particles and U^{kl}_{HB} $(r_{ij}, \vec{\Omega_i}, \vec{\Omega_j})$ describes the interaction between two HB arms of different molecules

$$U_{HB}^{kl}(r_{ij}, \vec{\Omega_\iota}, \vec{\Omega_J}) = \varepsilon_{HB} G(r_{ij} - r_{HB}) G(\vec{l_k u_{ij}} - 1) G(\vec{j_l u_{ij}} + 1) \quad (8)$$

Like in 2D, the strongest hydrogen bond occurs when an arm of one particle is colinear with the arm of another particle pointed towards each other. The model does not make a distinction between hydrogen bond donors and acceptors. Apart from the dimensionality, we want to keep the 3D MB model as similar as possible to the original 2D MB model. Hence, the parameters of our 3D model are the same as used in the 2D MB model calculations, except for the depth of the Lennard-Jones potential well ε_{LJ}. This change was made to maintain the same ratio between strength of the Lennard-Jones interaction and hydrogen bond interaction due to the different geometries; ε_{LJ}=1/35 ε_{HB}. These model parameters were not chosen or optimized to compare with experiments and can undoubtedly be improved for those purposes.

3. The Statistical Mechanics Theory

3.1. 2D MB Model

In the theory, the system consists of N water molecules.[37] To keep track of the state of interaction of each possible hydrogen bonding arm of each water molecule we are using an underlying ice lattice as a bookkeeping tool. For the 2D water model, the underlying lattice is hexagonal (See Figure 3). We focus on a single water molecule in the hexagon and the relationship of that water to its clockwise neighbor. Figure 4 shows the three possible relationships: the test water can either form a hydrogen bond, a van der Waals contact, or no interaction at all. We compute the isothermal-isobaric statistical weights, Δ_{HB} of the hydrogen-bonded molecules, Δ_{LJ} of the van der Waals contacts, and Δ_0 of the unbonded population as functions of temperature, pressure, and interaction energies.

The hydrogen-bonded state. If the test water molecule points one of its three hydrogen bonding arms at an angle θ to within $\pi/3$ of the center of its clockwise neighbor water, it forms a hydrogen bond. The energy of interaction of the test water is

$$u_{HB}(\vartheta) = -\varepsilon_{HB} - \varepsilon_{LJ} + k\vartheta^2, -\pi/3 \le \vartheta \le \pi/3 \quad (9)$$

k is the angular spring constant that describes the weakening of the hydrogen bond as it becomes increasingly off-angle, and ε_{HB} and ε_{LJ} are the potential energy parameters. We regard this type of hydrogen bond as weak insofar as it is not cooperative with neighboring hydrogen bonds. We consider a more cooperative type of hydrogen bonding below. To compute the isothermal-isobaric partition func-

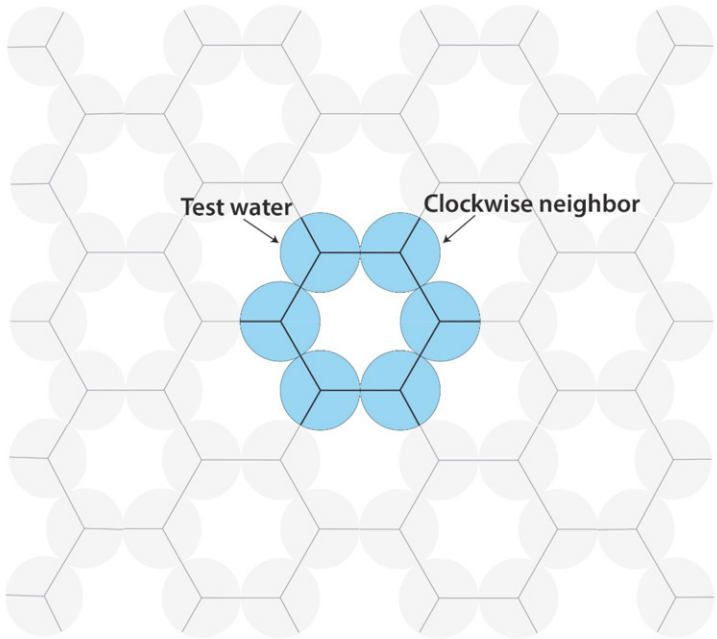

Figure 3: The lattice of the model showing both the hexagon of the icelike structure and illustrating a pair interaction used for bookkeeping to avoid triple counting.

tion, Δ_{HB}, of this HB state, we integrate this Boltzmann factor over all the allowable angles and over all the allowable separations x and y of the test molecule relative to its clockwise neighbor,

$$\Delta_{HB} = c(T) \iint dxdy \int_{-\pi/3}^{\pi/3} e^{-\beta(u_{HB}+2pv_{HB}/3)} d\vartheta \quad (10)$$

Where $\beta = 1/k_BT$ is inverse temperature, c(T) is the 2D version of the kinetic energy contribution to the partition function and v_{HB} is volume per molecule in this state. $\iint dxdy$ represents the volume over which the second molecule has translational freedom to form a hydrogen bond with the first water and is equal to the effective volume $v_{HB}^{eff} = \sqrt{\frac{k_BT\pi}{4k}}$. The volume v_{HB} of the hydrogen-bonded state is determined in the following way. First, we estimate an upper bound on the volume, from a simple geometric calculation. For the perfect hexagon crystal, representing low-pressure ice, the volume of the solid if the center of the hexagon is unoccupied is

$$v_s = \frac{3\sqrt{3}r_{HB}^2}{4}. \quad (11)$$

Second, since liquid water is denser than ice, we estimate a lower bound on the volume using high-pressure ice, where another MB water occupies the center of each hexagonal cage[52,53]

$$v_{s2} = \frac{\sqrt{3}r_{HB}^2}{2}. \quad (12)$$

Since the density of liquid water must lie between these limits, we estimate its volume as

$$v_{HB} = \frac{\sqrt{3}r_{HB}^2 x_v}{2}. \quad (13)$$

Where $x_v = 1.01$ is chosen empirically by fitting the density dependence vs. temperature. Using these definitions and performing the integration in Equation (10) gives

$$\Delta_{HB} = c(T) v_{HB}^{eff} e^{\beta(\varepsilon_{HB}+\varepsilon_{LJ}-2pv_{HB}/3)} \sqrt{\frac{k_BT\pi}{k}} erf\left(\sqrt{\frac{k\pi^2}{9k_BT}}\right) \quad (14)$$

The van der Waals (vdW) state. Here, the test water molecule forms only a van der Waals contact with its clockwise neighboring water. The water molecule has an energy

$$u_{LJ}(\vartheta) = -\varepsilon_{LJ}, -\pi/3 \le \vartheta \le \pi/3. \quad (15)$$

The isothermal-isobaric partition function, Δ_{LJ} of this state is given by integrating over angles and positions of the test particle relative to its clockwise neighbor as in case of the HB state

$$\Delta_{LJ} = c(T) \iint dxdy \int_{-\pi/3}^{\pi/3} e^{-\beta(u_{LJ}+2pv_{LJ}/3)} d\vartheta. \quad (16)$$

The integral $\iint dxfy$ represents the translation volume over which the second molecule forms a van der Waals contact with the first water and is equal to the effective volume $v^{eff}_{LJ} = 0.104$. The volume occupied by molecule in this state, v_{LJ}, is volume of packed LJ disks

$$v_{LJ} = \frac{\sqrt[3]{2}\sqrt{3}\sigma_{LJ}^2}{2}. \quad (17)$$

Integrating the partition function gives

$$\Delta_{LJ} = \frac{2\pi}{3} c(T) v_{LJ}^{eff} e^{\beta(\varepsilon_{LJ}-2pv_{LJ}/3)} \quad (18)$$

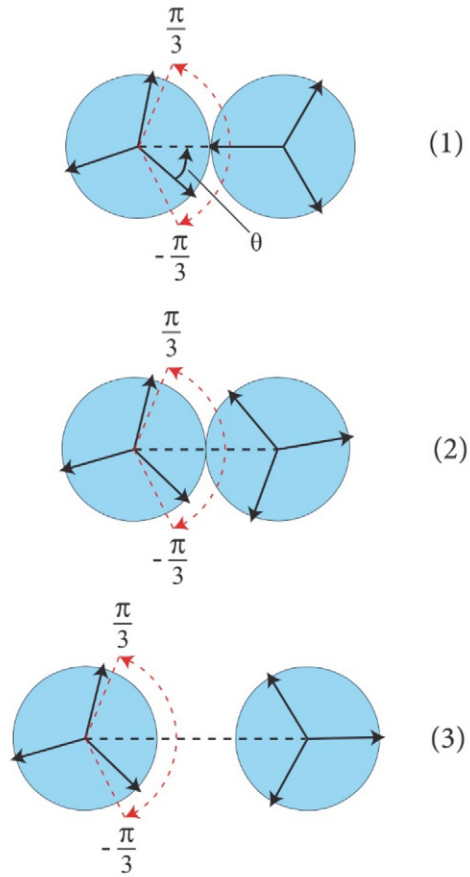

Figure 4: The three model states: (1) hydrogen bonded, (2) vdW bonded, and (3) nonbonded in 2D.

The non-interacting state. In this third possible state, the test water has no interaction with its clockwise neighbor

$$u_0(\vartheta) = 0, -\pi/3 \le \vartheta \le \pi/3. \quad (19)$$

The same way as for the other two states, the isothermal-isobaric partition function is obtained by integrating over translational degrees of freedom

$$\Delta_0 = c(T) \iint dxdy \int_{-\pi/3}^{\pi/3} e^{-\beta(u_0+2pv_0/3)} d\vartheta, \quad (20)$$

where v_0 is the volume available to the test molecule in this state and is calculated as the van der Waals gas approximation

$$v_0 = \frac{k_B T}{p} + v_d. \quad (21)$$

Where $v_d = v_s$ for MB water. Integrating of the partition function gives

$$\Delta_0 = \frac{2\pi}{3} c(T) \frac{k_B T}{p} e^{\beta(-2pv_0/3)} \quad (22)$$

These three expressions, Equations (14), (18) and (22), give the isobaric-isothermal ensemble Boltzmann weights of the three possible states of each water molecule. We assume a mean-field attractive energy, $-Na/v$,[52,53] among cages, where a is the van der Waals dispersion parameter (0.02, here) and v is the average molar volume, which we will define below. The partition function for a single full hexagon of 6 waters would be given by

$$Q_1 = \left(\Delta_{HB} + \Delta_{LJ} + \Delta_0\right)^6 - \Delta_{HB}^6 + \delta\Delta_s^6 \quad (23)$$

Here, we treat hexagons a little differently instead. We define cooperative HB state or solid state that involves a higher degree of HB cooperativity than the hydrogen bonding that is just formed pairwise among nearest neighbor waters in the liquid state. So, the partition function for each hexagon will be given by

$$Q_1 = \left(\Delta_{HB} + \Delta_{LJ} + \Delta_0\right)^6 - \Delta_{HB}^6 + \delta\Delta_s^6 \quad (24)$$

where $\delta = e^{-\beta\varepsilon_c}$ is the Boltzmann factor for the cooperativity energy, ε_c, that applies only when 6 water molecules all connected into a full hexagonal cage. The terms on the right-side of this expression simply replace the statistical weight for each weakly hydrogen-bonded full hexagonal cage with the statistical weight for a cooperative strongly hydrogen-bonded hexagonal cage. Δ_s is the Boltzmann factor for a cooperative HB or solid state. It differs from Δ_{HB} only in that the former uses the hexagonal cage volume per molecule, v_s, while the HB state uses the liquid water hydrogen bonding volume per molecule, v_{HB}. Now we combine the Boltzmann factors for the individual water molecules to get the partition function Q for the whole system of N particles,

$$Q = Q_1^{N/6}. \quad (25)$$

The factor N/6 accounts for the 3 possible interaction sites per water molecule and corrects for double counting the hydrogen bonds. We compute the populations of the states i = 1 (HB), 2 (LJ), 3(o), 4(solid) using

$$f_i = \frac{d\log Q_1}{d\log \Delta_i^6} \quad (26)$$

The chemical potential is given by

$$\mu = -\frac{k_B T}{N} \log Q \quad (27)$$

The molar volume is

$$v = \frac{V}{N} = \left(\frac{\partial \mu}{\partial p}\right)_T = \sum_{i=1}^{4} f_i v_i \quad (28)$$

and all the other thermodynamic properties below are obtained as described previously.[52,53] For all the model calculations, we used the parameters from potential function ε_{HB}, ε_{LJ}, r_{HB} and σ_{LJ}. The parameter $k = 10$ was determined from the shape of the MB potential while $\varepsilon_c = 0.03$ was determined empirically.

3. 2. 3D MB Model

Here, we will point out only the differences between the theory in 3D in comparison to 2D.[38] We consider a system of 3D MB model water molecules, modeled as three-dimensional spheres, and suppose that the structure of the liquid state of 3D model water is a perturbation from an underlying hexagonal (ice) lattice; (See Figure 5). Each molecule can be in one of the three possible orientational states like in 2D. These states are graphically presented in Fig. 6.

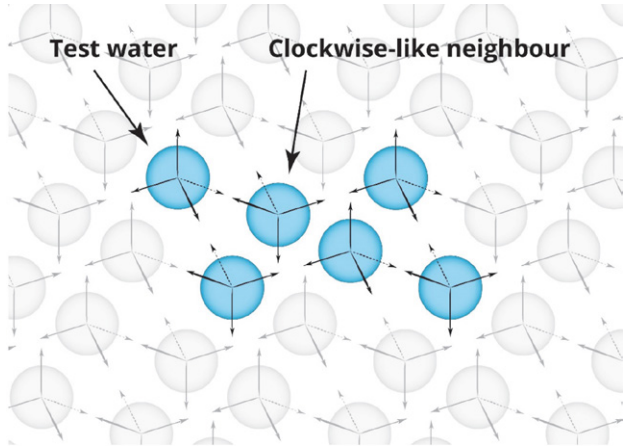

Figure 5: Lattice of the model showing both the hexagon of the ice-like structure and a pair interaction used for bookkeeping to avoid triple counting. Presented is only one layer.

The hydrogen-bonded state. If the test water molecule points one of its four hydrogen bonding arms at an angle θ to within π/3 of the center of its clockwise neighbor water, it forms a hydrogen bond. This is equivalent to about one fourth of the full solid angle. The energy of interaction of the test water is

$$u_{HB}(\vartheta) = -\varepsilon_{HB} - \varepsilon_{LJ} + k(1 - \cos\vartheta)^2, 0 \le \vartheta \le \pi/3 \quad (29)$$

k is the angular spring constant that describes the weakening of the hydrogen bond as it becomes increasingly off angle. To compute the isothermal-isobaric partition func-

tion, Δ_{HB}, of this HB state, we integrate this Boltzmann factor over all the allowable angles and over all the allowable separations of the test molecule relative to its clockwise neighbor,

$$\Delta_{HB} = c(T) \iint \iiint dxdydzd\varphi d\psi \int_0^{\pi/3} e^{-\beta(u_{HB}+pv_{HB}/2)} sin\vartheta d\vartheta \quad (30)$$

Where $c(T)$ is here the 3D version of the kinetic energy contribution to the partition function. $\iiint dxfydz$ represents the volume over which the second molecule has translational freedom to form a hydrogen bond with the first water and is equal to effective volume $v^{eff}_{HB} = 0.242$. The double integral $\iint d\alpha f\psi$ sums the orientations over which the test molecule has orientational freedom and is equal to $4\pi^2$. The volume v_{HB} of the hydrogen-bonded state we determine similarly as for the 2D model. For the perfect hexagon crystal representing low-pressure ice, the volume of the solid is

$$v_s = \frac{8\sqrt{3}r_{HB}^3}{9}. \quad (31)$$

We estimate volume v_{HB} as perturbation of this state as

$$x_v v_{HB} = v_s. \quad (32)$$

where $x_v = 1.12$ is chosen empirically because density of the liquid state at room temperature is about 12% more dense than ice. Using these definitions and performing the integration in Equation (30) gives

$$\Delta_{HB} = 4\pi^2 c(T) v_{HB}^{eff} e^{\beta(\varepsilon_{HB}+\varepsilon_{LJ}-pv_{HB}/2)} \sqrt{\frac{k_B T\pi}{4k}} erf\left(\sqrt{\frac{k}{4k_B T}}\right) \quad (33)$$

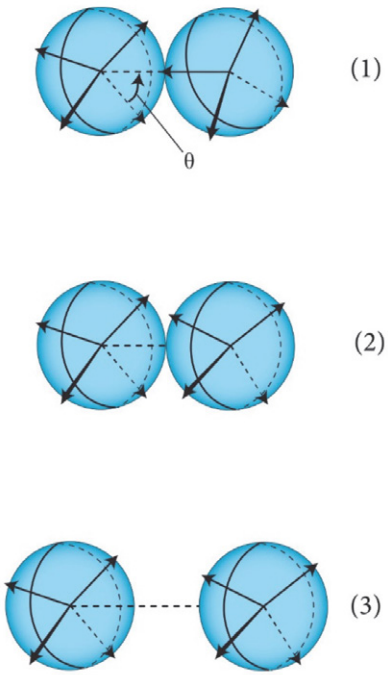

Figure 6: The three model states: (1) hydrogen bonded, (2) vdW bonded, and (3) nonbonded in 3D.

The van der Waals (vdW) state. Here, the test water molecule forms only a van der Waals contact with its clockwise neighboring water. The water molecule has an energy

$$u_{LJ}(\vartheta) = -\varepsilon_{LJ}, 0 \le \vartheta \le \pi/3. \quad (34)$$

The isothermal-isobaric partition function, Δ_{LJ} is

$$\Delta_{LJ} = c(T) \iint \iiint dxdydzd\varphi d\psi \int_0^{\pi/3} e^{-\beta(u_{LJ}+pv_{LJ}/2)} sin\vartheta d\vartheta \quad (35)$$

The triple integral $\iiint dxfydz$ represents the translation volume over which the second molecule forms a van der Waals contact with the first water and is equal to effective volume $v^{eff}_{LJ} = 0.086$. The integrals over angles are equal to $8\pi^2$. The volume v_{LJ} of this state is approximated as a volume of cubic close-packed crystal where the closest molecules are at distance $\sigma_{LJ}\sqrt[6]{2}$

$$v_{LJ} = \sigma_{LJ}^3. \quad (36)$$

we also tried other symmetries, but the results did not change much. Integrating of the partition function gives

$$\Delta_{LJ} = 2\pi^2 c(T) v_{LJ}^{eff} e^{\beta(\varepsilon_{LJ}-pv_{LJ}/4)} \quad (37)$$

The non-interacting state. In this third possible state, the test water has no interaction with its clockwise neighbor and the isothermal-isobaric partition function is equal to

$$\Delta_0 = 2\pi^2 c(T) \frac{k_B T}{p} e^{\beta(-pv_0/2)} \quad (38)$$

Here, we also assume a mean-field attractive energy, $-Na/v$,[52,53] among cages, where a is the van der Waals dispersion parameter (0.045, here). The partition function for a single full hexagon of 6 waters and other properties are calculated in the same way as in 2D. For all the model calculations, we used the parameters from potential function ε_{HB}, ε_{LJ}, r_{HB} and σ_{LJ}. The parameter $k = 80$ was determined from the shape of the 3D MB potential while $\varepsilon_c = 0.18$ was determined empirically.

3.3. The Real Water – CageWater

Here we made slight modification in comparison with 3D MB.[54] Two water molecules can interact through a hydrogen bond (which depends on their relative orientations), interact through a contact (which is orientation independent and occurs when they are close in space and no HB is present), or be noninteracting (when they are far apart, as in van der Waals gas). Hydrogen bonds are further parsed into two types: an HB can occur between 2 adjacent waters that have no higher order structure or can occur within a 12-water hexagonal unit cell (cage) forming 15 HBs. Parameters needed for calculations were obtained by getting good agreement with tempera-

Table 1: To obtain the parameters, the intrinsic HB energy and HB distance are fixed while all other parameters were optimized.

Parameter	Value	Description
ε_{HB}	4.106 *kcal/mol*	intrinsic HB energy between two molecules
r_{HB}	2.767 *Å*	intrinsic HB distance between two molecules
k	225.83 *kcal/mol*	angle flexibility of HB
ε_{LJ}	0.8212 *kcal/mol*	intrinsic LJ energy between two molecules
σ_{LJ}	3.293 *Å*	intrinsic LJ distance between two molecules
v_d	16.85 $Å^3$	hard core of water molecule
ε_c	–0.252 *kcal/mol*	correlation energy per bond in 12-mer
x_v	1.133	ratio between volumes of strong and weak HB states
v^{eff}_{HB}	42369.9 $Å^3$	effective volume of HB state
v^{eff}_{s}	48089.8 $Å^3$	effective volume of s state
v^{eff}_{LJ}	74147.3 $Å^3$	effective volume of LJ state

ture dependence of density at normal pressure and of boiling point position and are presented in Table 1.

4. Results

We present our results below in dimensionless or reduced units for both MB models, normalized to the strength of the optimal hydrogen bond $\varepsilon_{\mathrm{HB}}$ and hydrogen bond separation r_{HB} ($T^* = \frac{k_B T}{\varepsilon_{HB}}$, $U^* = \frac{U}{\varepsilon_{HB}}$, $V^* = \frac{V}{{r_{HB}}^2}$, $p^* = \frac{p{r_{HB}}^2}{\varepsilon_{HB}}$ for 2D MB model and $V^* = \frac{V}{{r_{HB}}^3}$, $p^* = \frac{p{r_{HB}}^3}{\varepsilon_{HB}}$ for 3D MB model).

4. 1. 2D MB Model

Analytical theory has additional approximations compared to computer simulations, which is why we first

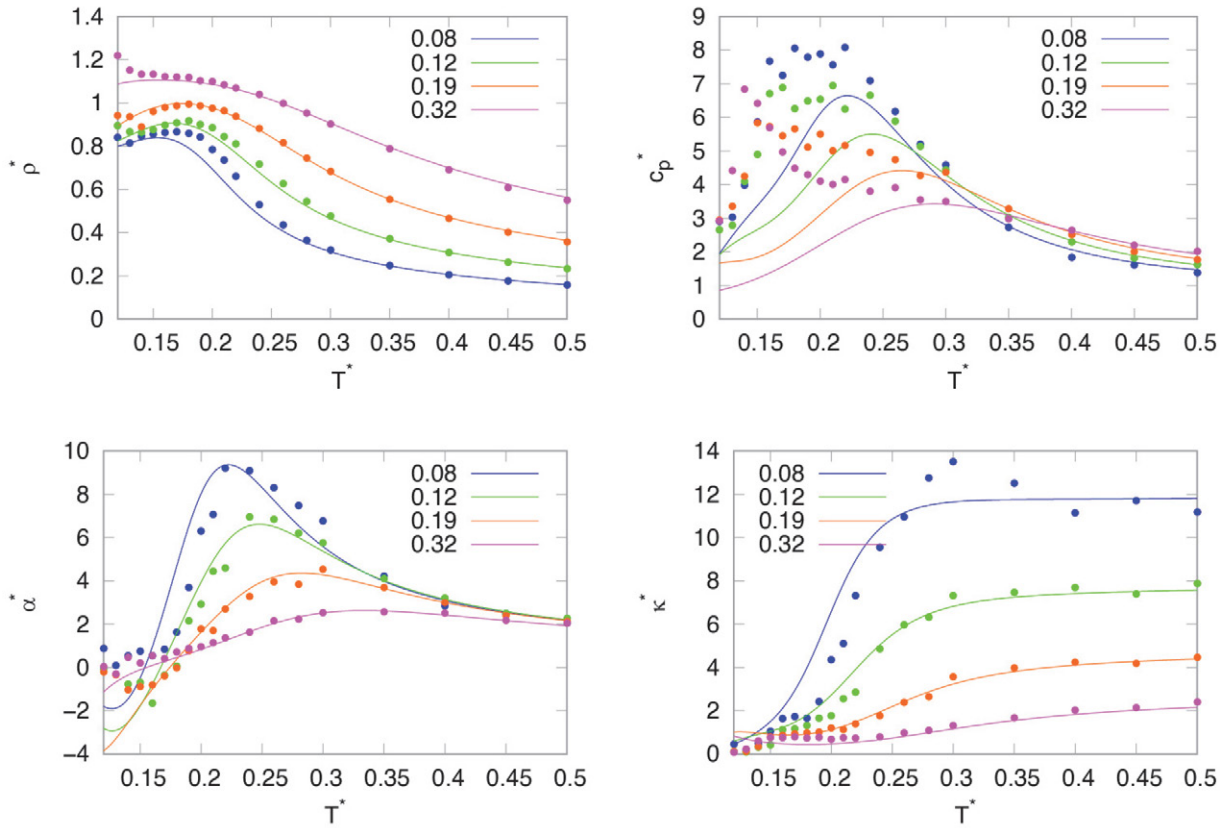

Figure 7: Temperature dependence of the density (ρ^*), heat capacity (c_p^*), thermal expansion coefficient (α^*), and isothermal compressibility (κ^*) for 2D MB water for different pressures. Results from the theory are plotted with lines and from the computer simulations[40] by points.

checked the quality of the predictions of the analytical theory. We calculated the temperature dependence of the density (ρ^*), heat capacity (c_p^*), thermal expansion coefficient (α^*), and isothermal compressibility (κ^*) for different pressures. For a 2D MB model it was previously shown that the Mercedes-Benz water qualitatively correctly reproduces the anomalies of water[27,31,32] for these quantities. In Fig. 7 a comparison of predictions of the present theory (lines) for the density, the thermal expansion coefficient, the isothermal compressibility, and the heat capacity vs temperature to NPT Monte Carlo simulations (symbols) of the 2D MB model with the same parameters is shown. The calculations of the theory were performed at reduced pressure of 0.08, 0.12, 0.19 and 0.32. The theory is in good general agreement with the simulations, including the density maximum (minima in molar volume). The thermal expansion coefficient is negative at low temperatures, which is consistent with computer simulations and with experiments for water. The Monte Carlo simulations of MB water do not show an experimentally observed minimum in the isothermal compressibility versus temperature. On the other hand, the present theory predicts a minimum for higher pressures. At low temperatures, our present model shows a drop in heat capacity as the temperature is reduced. Being satisfied with the prediction of the model, we calculated non crystalline part of the phase diagram, shown in Fig. 8. The 2D MB model exhibits two critical points: the liquid-gas critical point (C_1) at temperature $T^* = 0.118$ and pressure $p^* = 0.00035$ which is slightly lower than obtained from computer simulations,[40] and the liquid-liquid critical point (C_2) at temperature 0.0212 and pressure 0.42. There exists also a region of pressures between both critical points where we have only one fluid phase, at higher pressures we have two liquid phases, and at lower pressures the liquid and the gas phases.

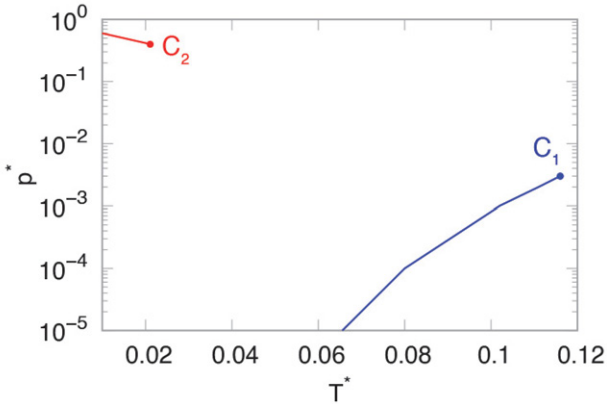

Figure 8: Phase diagram of the noncrystalline phases of water. Red line is liquid-liquid and blue line liquid-gas coexistence line.

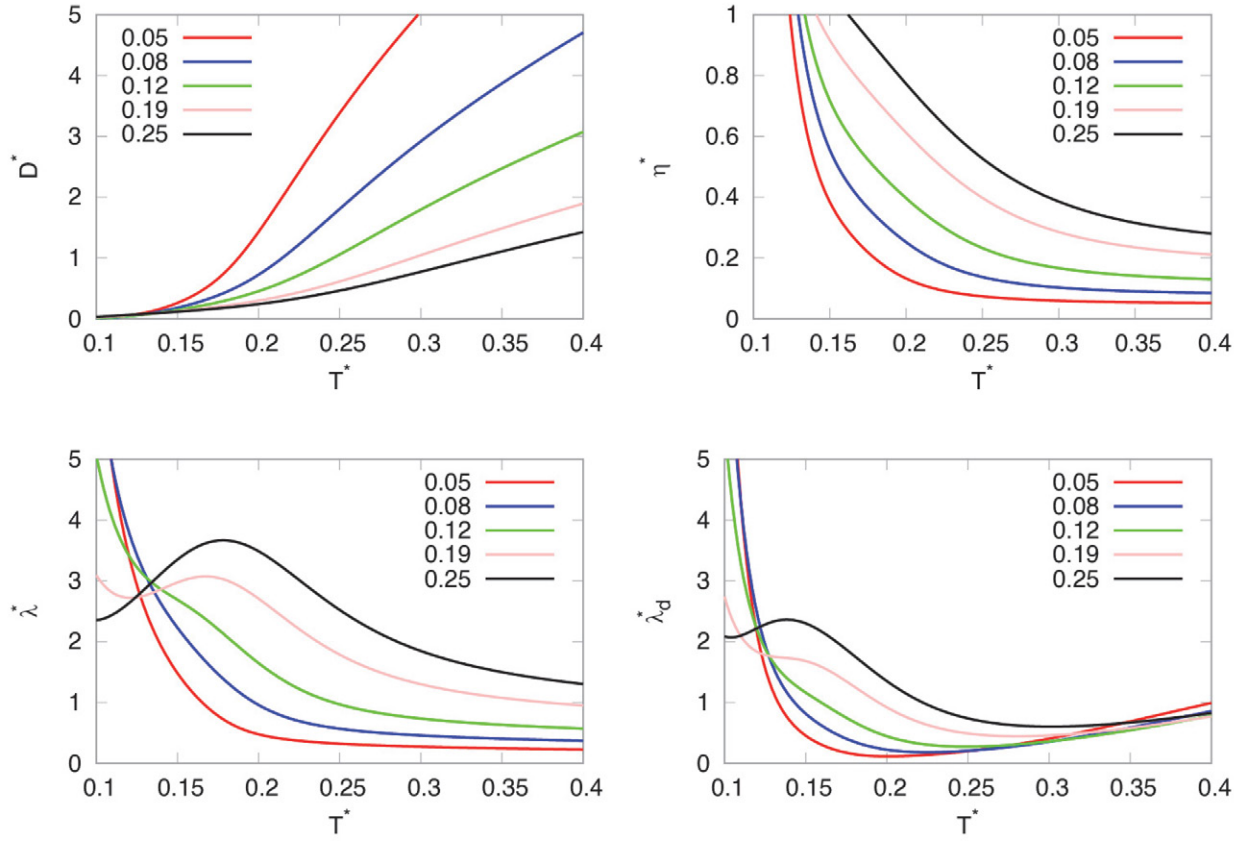

Figure 9: Temperature dependence of the diffusion (D^*), viscosity (η^*), thermal conductivity (λ^*) and thermal diffusivity (λ_d^*) for 2D MB water for different pressures calculated by the theory.

We have also developed the theory for dynamical properties. The diffusion processes occur in fluid or gas whenever a property is transported in a manner resembling a random walk. If we assume that the water molecules are doing random walk, we can say, for our 2D molecules in each state, that the diffusion is proportional to the step size, λ, and a step frequency, ν. The step frequency is proportional to the Boltzmann factor for the change of energy from bonded to free state. This means that the energy of interaction is negative of bonding energy of molecule. We assumed that the step size is equal to the characteristic length of interaction in each state ($\lambda_{HB} = \lambda_s = r_{HB}$ for HB and s state, $\lambda_{LJ} = \sigma_{LJ}$ for LJ state and for 0 state for 0 state the average distance between molecules in this state $\lambda_0 = \sqrt{v_0}$). For our model, we calculated the diffusion constant as a sum of all states of individual contributions

$$D = \sum_i f_i D_i \tag{39}$$

Where $D_i = \lambda_I \nu_i$ for HB, s, LJ and 0 state of water. The step frequency is equal to Boltzmann factor of negative average bonding energy (u_i)

$$\nu_i = e^{\beta \langle u_i \rangle} \tag{40}$$

To model viscosity, η, we start from Stokes-Einstein relation between viscosity and diffusion coefficient, D,

$$D = \frac{kT}{6\pi d\eta} \tag{41}$$

We can express viscosity from this equation as

$$\eta = \frac{kT}{6\pi dD} \tag{42}$$

We see that we can calculate viscosity from diffusion coefficient, temperature and diameter, d, of particle. In our case, we use averaged particle diameter which we calculated as a sum over all possible states of water

$$d = \sum_i f_i d_i \tag{43}$$

For water molecules in states HB, LJ and 0 we used diameter of molecule equal to r_{HB} while for state s waters form hexagons and we use the diameter of water in hexagon state as equal to $2r_{HB}$. Next, we calculated the speed of sound c_s as

$$c_s = \sqrt{\frac{v}{\chi}} \tag{44}$$

and thermal conductivity λ using modified Eyring's formula as

$$\lambda = \frac{2.8kc_s}{\sqrt{v}} \tag{45}$$

and thermal diffusivity λ_d as

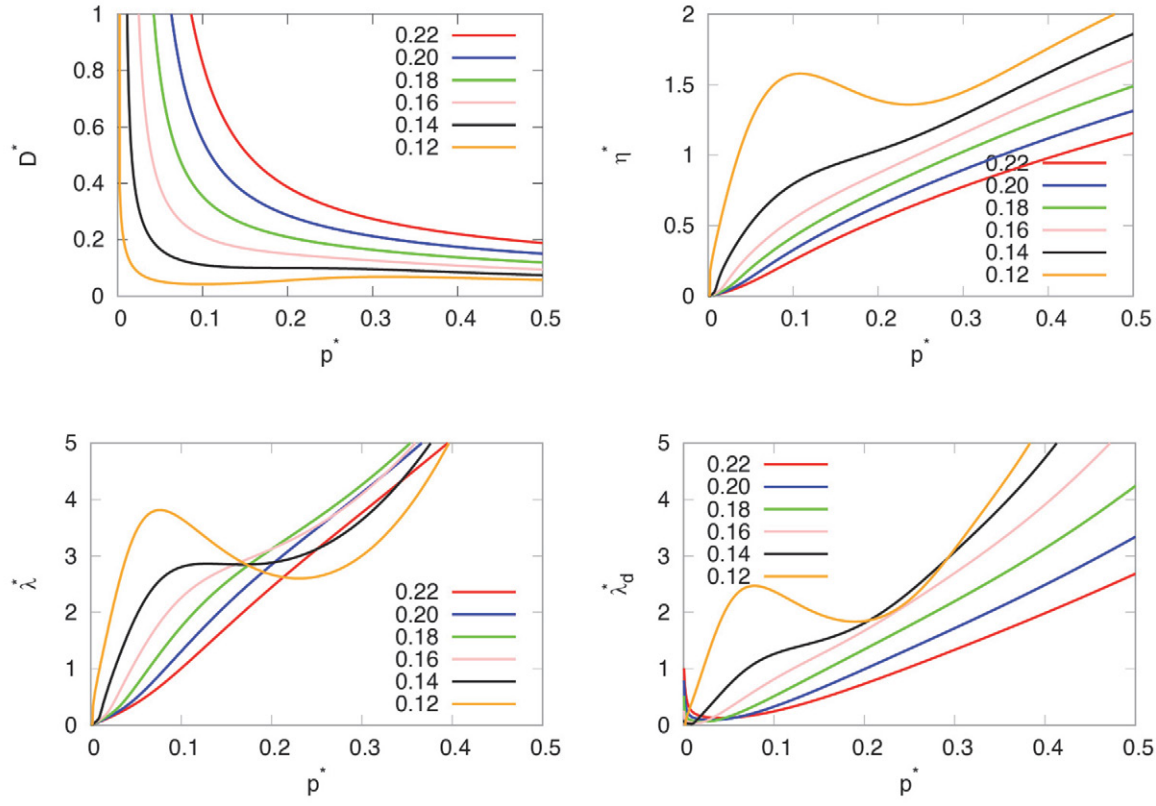

Figure 10: Pressure dependence of the diffusion (D^*), viscosity (η^*), thermal conductivity (λ^*) and thermal diffusivity (λ_d^*) for 2D MB water for different temperatures calculated by the theory.

$$\lambda_d = \frac{\lambda v}{c_p}. \quad (46)$$

In Fig. 9 and 10, we have plotted temperature and pressure dependence of the dynamical properties (diffusivity, viscosity, thermal conductivity, and thermal diffusivity). All the quantities have similar anomalous non-monotonic behavior as for experimental water.

4. 2. 3D MB Model

As for 2D MB we first checked the quality of the predictions of the analytical theory also for 3D MB. We also calculated the temperature dependence of the molar volume, heat capacity, isothermal compressibility, and thermal expansion coefficient for different pressures. For a 3D MB model, it was previously shown that the Mercedes-Benz water qualitatively correctly reproduces the anomalies of water[49,50,51] for these quantities. In Fig. 11, a comparison of predictions of the present theory (lines) for the molar volume (V^*/N), heat capacity (c_p^*), thermal expansion coefficient (α^*), and isothermal compressibility (κ^*), vs temperature to NPT Monte Carlo simulations (symbols) of the 3D MB model with the same parameters is shown. The calculations of the theory were performed at reduced pressure of 0.12 and 0.19. The theory is in good general agreement with the simulations, including the minima in molar volume (density maximum). The thermal expansion coefficient is negative at low temperatures, which is consistent with computer simulations and with experiments for water. The Monte Carlo simulations of MB water do not show an experimentally observed minimum in the isothermal compressibility versus temperature. On the other hand, the present theory predicts a minimum for higher pressures. At low temperatures, our present model shows a drop in heat capacity as the temperature is reduced. Being satisfied with the prediction of the model, we continued our research by calculating the density of 3D MB water as a function of temperature along isobars (up to $p^* = 0.25$) and determine critical points of the model. Results are shown in Fig. 12. In this pressure range, upon increase of temperature density increases, reaches a maximum, and then decreases. We determined non crystalline part of the phase diagram, shown in Fig. 13. The 3D MB model exhibits two critical points: the liquid-gas critical point (C_1) at temperature $T^*= 0.117$ and pressure $p^* = 0.0115$, and the liquid-liquid critical point (C_2) at temperature 0.0779 and pressure 0.167. There exists also a region of pressures between both critical points where we have only one fluid phase, at higher pressures we have two liquid phases, and at lower pressures the liquid and the gas phases.

4. 3. The Real Water – CageWater

Here, we compare the measured properties over water's liquid range to those predicted by parametrization for

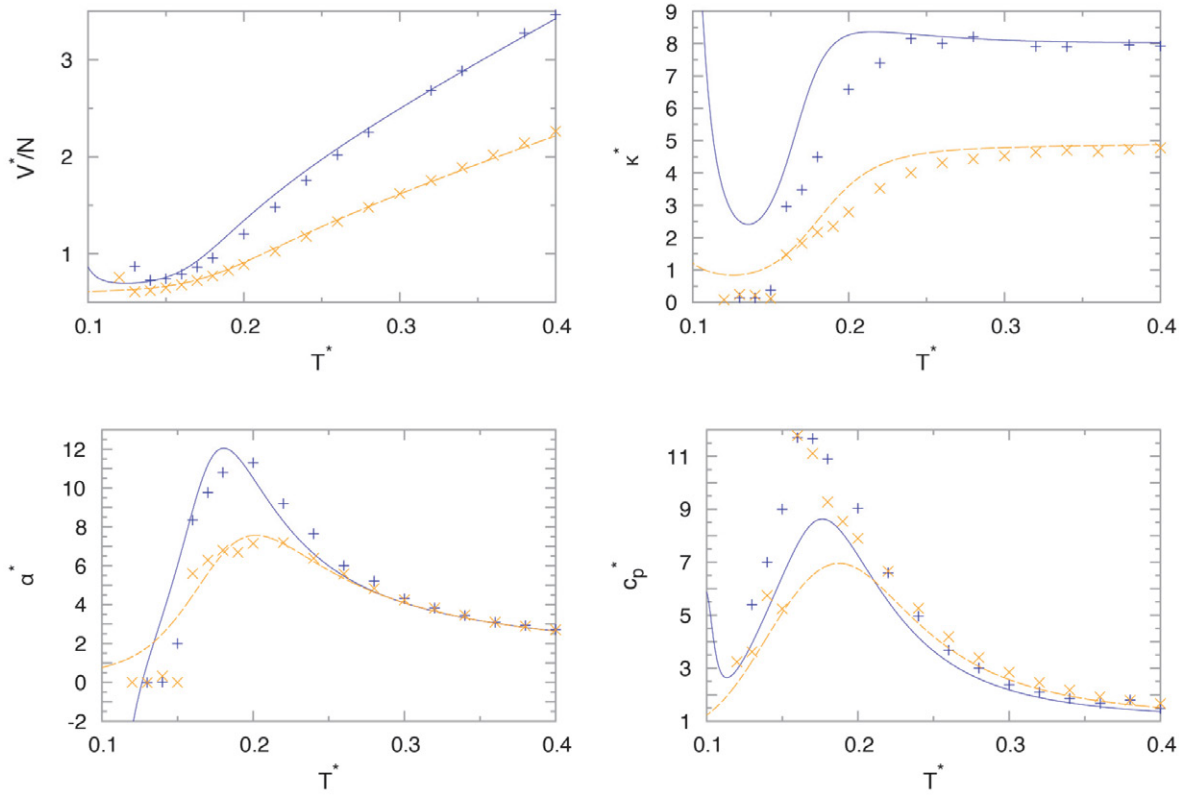

Figure 11: Temperature dependence of the molar volume (V^*/N), heat capacity (c_p^*), thermal expansion coefficient (α^*), and isothermal compressibility (κ^*), for 3D MB water for pressures $p^* = 0.19$ (orange) and $p^* = 0.12$ (blue). Results from the theory are plotted with lines and from the computer simulations by symbols.[50,51]

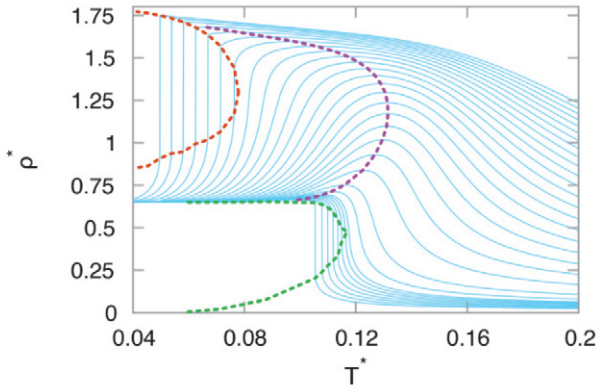

Figure 12: Temperature dependence of the density for various pressures (blue solid lines), high-density liquid–low-density liquid coexistence line (red dashed line), liquid-gas density coexistence line (green dashed line), and maximum densities (pink dashed line).

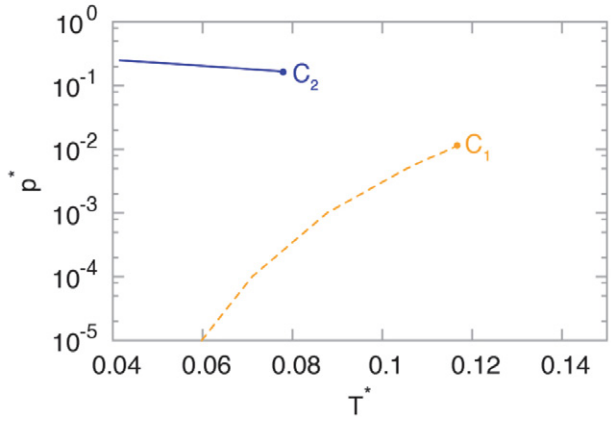

Figure 13: Phase diagram of the noncrystalline phases of water. Blue solid line is liquid-liquid and orange dashed line liquid-gas coexistence line.

experimental data, called CageWater.[54] In Fig. 14a we have plotted experimental data[8] and data by best practices water simulation models TIP4P/2005,[21] TIP3P,[20] SPC,[20] and mW[56] of the four main thermal and volumetric properties of water: the density, the thermal expansion coefficient, the isothermal compressibility, and the heat capacity. The comparison to experiments shows that the present model gives equal or better agreement than the simulation models over the normal and supercooled liquid temperature range and does not have the fluctuation errors that simulations have, but the theoretical model has more parameters The model allows us to parse the experimental observables into hydrogen-bonding, caging, van der Waals, and non-interacting molecular components. Water is known to have a high heat capacity (ability to absorb thermal energy upon heating) among liquids of similar molecular size. The main conclusions from Figure 14b. are the following. In the normal liquid range, the high heat capacity comes from the breaking of two types of bonds: pairwise H bonds and Lennard–Jones-like contacts. Heating hot water near the boiling point leads to lower density, as it would for any LJ fluid, because heating hot water changes the contact interactions more than the H bonds. Figure 14c shows the same bulk properties as in Figure 14a except now computed as a function of pressure, not temperature. As increasing pressure squeezes water to become more compact (density increases and compressibility decreases), it crumples the hexagonal water cages breaking them into component pieces that just have pairwise water–water hydrogen bonding with little change to LJ and noninteracting water populations. Pressure decreases the heat capacity (bond-breaking capability) because although it melts out some cages it is also "freezing in" some pairwise H bonds. The thermal expansion coefficient increases with pressure because pressure melts out the rigid cages into fragmented H-bond pairs, which can be more readily squeezed together by pressure. Figure 15 shows that CageWater accurately reproduces the anomalous hallmark thermal and volumetric signatures of the LLPT, namely, the divergent increasing heat capacity and compressibility with lowered temperature. Moreover, this model gives the microscopic components of those observables. We find that the large diverging heat capacity is due to the water cages, which have dominant populations in cold and supercooled water. The heat capacity is the sum of two contributions for each state: the population of that state multiplied by the individual heat capacity. We also find that the negative thermal expansion of supercooled water is dominated by the cage term. Heating supercooled water shrinks the average volume by melting the cages, which are voluminous, and converts them to smaller H-bonded fragments, like breaking a glass jar into shards that pack more compactly. This same physics is reflected in the peak of the compressibility at the supercooling peak temperature. Our model indicates that the two liquids that are in equilibrium around −50 °C are cage structures and broken H-bonded pieces.

5. Conclusion and Future Perspectives

We developed an analytical theory of water and applied it to 2D MB, 3D MB water models and parametrized it for experimental data. We used it for explaining how the pVT properties of liquid water arise from water's hydrogen bonding and contacts. The theory predicts volumetric and energetic properties rather well, for experimental data it is more accurate than explicit simulation models yet is much faster to compute. Its simplicity and predictive power come from representing water using only four factors in the partition function, hydrogen bonds, Lennard-Jones contacts, noninteracting terms and cooperative cages, rather than as a more extensive density expansion. The analytical theory advances our understanding of water's structure–property relations in showing that water's long-known 2-density behavior is encoded in relatively infrequent cages which melt out strongly with temperature and pressure. This un-

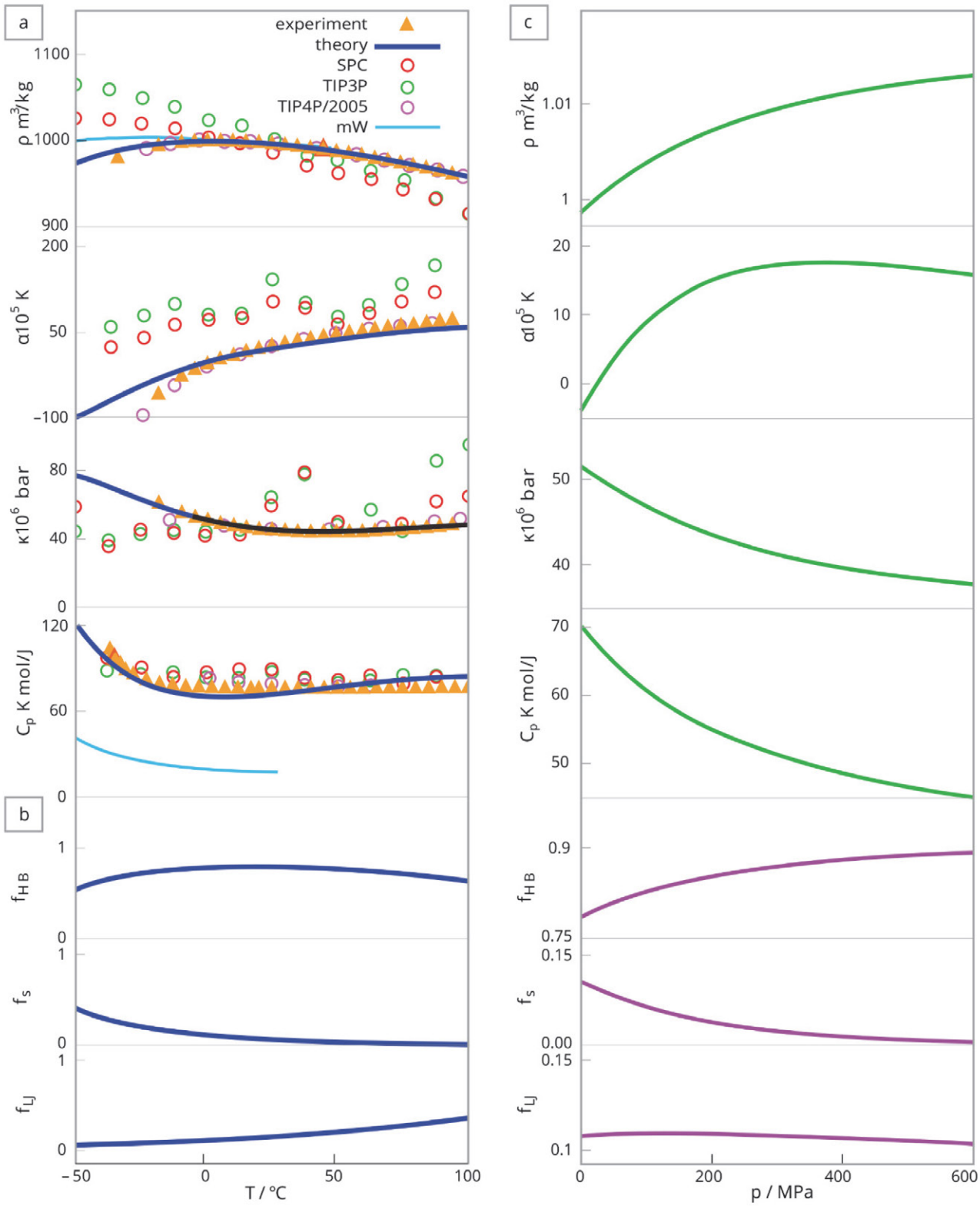

Figure 14: Experimental liquid water properties (yellow full triangles) vs model predictions (dark blue solid line) and computer simulations. (a) Temperature dependence of liquid water's density, thermal expansion coefficient, isothermal compressibility, and heat capacity at 1 bar pressure. Experiments are from Eisenberg and Kauzmann.[8] Computer simulations are from Abascal and Vega for TIP4P/2005[21] and Jorgensen and Jenson for TIP3P[20] and SPC[20], and mW model predictions from Molinero and Moore[56]. (b) Molecular constituents of water at different temperatures: HB (hydrogen-bonded waters), s (12-mer hexagons), and LJ (waters in contact but not hydrogen bonded). (c) Pressure dependences of the same properties and their constituents at a temperature of 273 K.

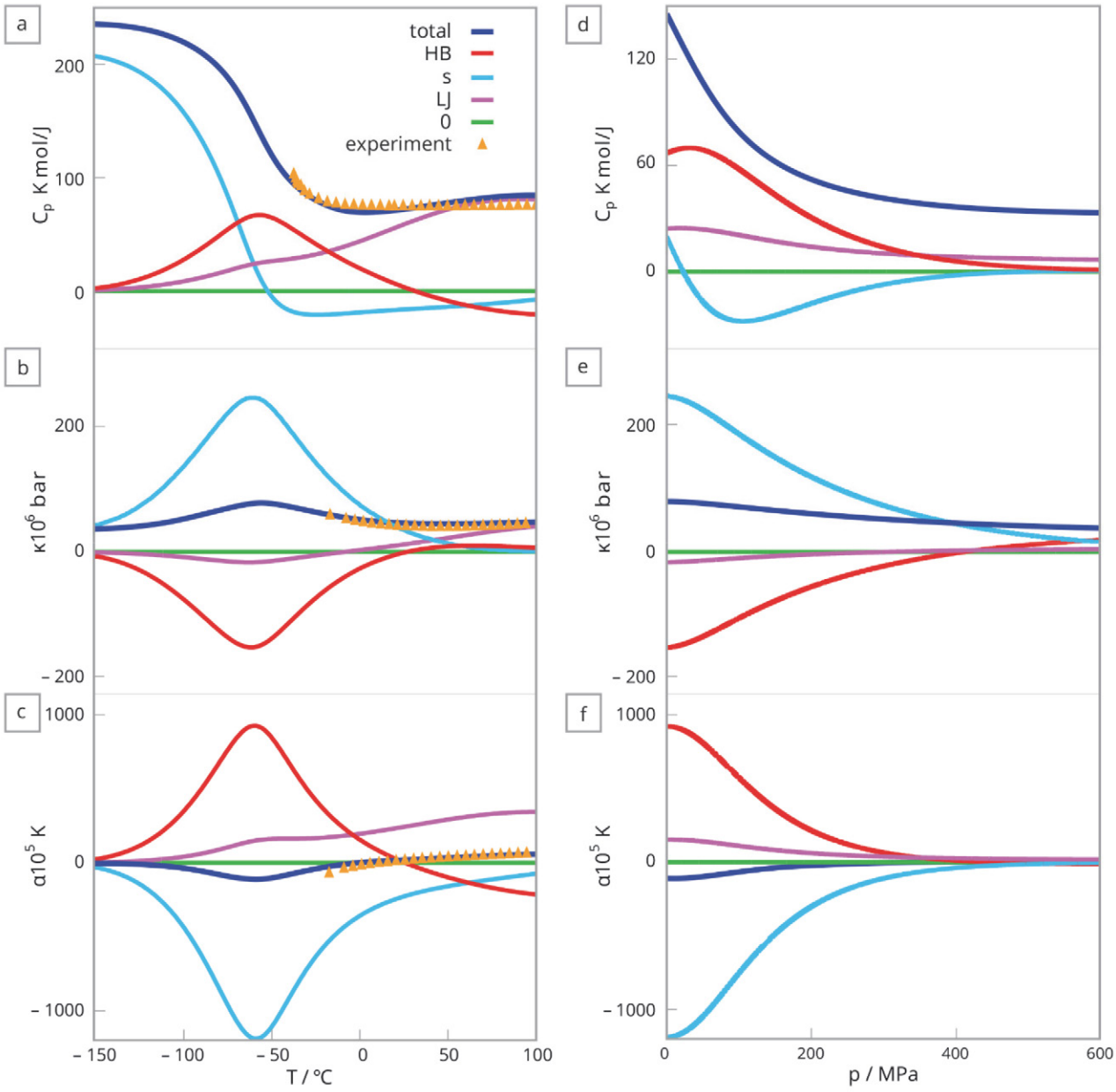

Figure 15: Molecular components of supercooled water vary with temperature and pressure. Colored lines show the components HB (pairwise H bonded), s (12-mer cages), LJ (waters in pairwise contact), and 0 (waters separated and noncontacting). Dark blue line is the sum of all components. Pressure dependence is calculated at –35 °C and temperature dependence at 0.1 MPa (1 atm). Most definitive features are the strong variations of the balance of molecular components with T and p and how strongly the caging behaviors are opposed by the pairwise hydrogen-bonded waters.

derstanding of water structure–property relations may aid in engineering filtration, osmosis, and desalination materials, in better solvation models for drugs and biomolecule actions, and for interpreting planetary geochemistry and hydrological cycles. The challenge of the current model is in calculating dielectric permittivity[57,58] and solvation of polar molecules and ions. To be able to do this the model will have to be upgraded to version to include also charges on the water test particles, but this will add new parameters. Another challenge in theoretical modelling lies in developing the same kind of theory for other compounds like ionic liquids[55], alcohols etc. We are expecting that all this can be done.

6. Acknowledgments

The financial support of the Slovenian Research Agency through Grant P1-0201 as well as to projects J7-1816, J1-1708, N1-0186 and N2-0067 is acknowledged as well as National Institutes for Health RM1 award RM1GM135136.

7. References

1 M. Chaplin, *Nat. Rev. Mol. Cell Biol.* **2006,** *7,* 861. **DOI:**10.1038/nrm2021
2. M. J. Tait, F. Franks, *Nature* **1971,** *230,* 91. **DOI:**10.1038/230091a0
3. P. Gallo, K. Amann-Winkel, C. A. Angell, M. A. Anisimov, F. Caupin, C. Chakravarty, E. Lascaris, T. Loerting, A. Z. Panagiotopoulos, J. Russo, J. A. Sellberg, H. E. Stanley, H. Tanaka, C. Vega, L. Xu and L. G. M. Pettersson, *Chem. Rev.* **2016,** *116,* 7463. **DOI:**10.1021/acs.chemrev.5b00750
4. E. Brini, C. J. Fennell, M. Fernandez-Serra, B. Hribar-Lee, M. Luksic, and K. A. Dill, *Chem. Rev.* **2017,** *117,* 12385. **DOI:**10.1021/acs.chemrev.7b00259
5. P. Žnidaršič-Plazl, *Acta Chim. Slov.* **2021,** *68,* 1. **DOI:**10.17344/acsi.2020.6488
6. J. Vladić, N. Nastić, T. Stanojković, Ž. Žižak, J. Čakarević, L. Popović and S. Vidovic, *Acta Chim. Slov.* **2019,** *66,* 473. **DOI:**10.17344/acsi.2019.5011
7. F. Franks., Ed. Water, a Comprehensive Treatise, (Plenum Press, New York, 1972–1980) Vol. 1–7.
8. D. Eisenberg and W. Kauzmann, The structure and properties of water (Oxford University Press, Oxford, 1969).
9. W. L. Jorgensen, J. Chandrasekhar, J. D. Madura, R. W. Impey, and M. L. Klein, *J. Chem. Phys.* **1983,** *79,* 926. **DOI:**10.1063/1.445869
10 .I. Nezbeda, *J. Mol. Liq*. **1997,** *73/74,* 317. **DOI:**10.1016/S0167-7322(97)00076-7
11 .B. Guillot, *J. Mol. Liq.* **2002,** *101,* 219. **DOI:**10.1016/S0167-7322(02)00094-6
12. C. Vega, J. L. F. Abascal, M. M. Conde, and J. L. Aragones, *Faraday Discuss.* **2009,** *141,* 251. **DOI:**10.1039/B805531A
13. F. H. Stillinger, *Science* **1980,** *209,* 451. **DOI:**10.1126/science.209.4455.451
14. C. Tanford, The hydrophobic effect: formation of micelles and biological membranes, 2nd ed. (Wiley, New York, 1980,.
15. W. Blokzijl and J. B. F. N. Engberts, *Angew. Chem. Int. Ed. Engl.* **1993,** *32,* 1545. **DOI:**10.1002/anie.199315451
16. G. Robinson, S.–B. Zhu, S.Singh and M. Evans, Water in Biology, Chemistry and Physics: Experimental Overviews and Computational Methodologies (World Scientific, Singapore, 1996). **DOI:**10.1142/2923
17. R. Schmidt, M*onatshefte fu¨r Chemie* **1993,** *132,* 1295.
18. A. Ben-Naim, *Biophys. Chem.* **2003,** *105,* 183. **DOI:**10.1016/S0301-4622(03)00088-7
19. L. R. Pratt, Annu. *Rev. Phys. Chem.* **2002,** *53,* 409.
20. L. W. Jorgensen and C. Jenson, *J. Comput. Chem.* **1998,** *19,* 1179.
21 .J. L. F. Abascal and C. Vega, *J. Chem. Phys.* **2005,** *123,* 234505. **DOI:**10.1063/1.2121687
22. E. Lambros and F. Paesani, *J. Chem. Phys.* **2020,** *153,* 060901. **DOI:**10.1063/5.0017590
23. K. B. Lipkowitz, D. B. Boyd, S. J. Smith, and B. T. Sutcliffe, *Rev. Comput. Chem.* **2007,** *10,* 271.
24. E. J. Baerends and O. V. Gritsenko, *J. Phys. Chem.* **1997,** *A 101,* 5383. **DOI:**10.1021/jp9703768
24. D. van der Spoel, P. J. van Maaren, and H. J. C. Berendsen, J. *Chem. Phys.* **1998,** *108,* 10220. **DOI:**10.1063/1.476482
25. H. W. Horn, W. C. Swope, J. W. Pitera, J. D. Madura, T. J. Dick, G. L. Hura, and T. Head- Gordon, *J. Chem. Phys.* **2004,** *120,* 9665. **DOI:**10.1063/1.1683075
26. J. L.F. Abascal and C. Vega, *J. Chem. Phys.* **2005,** *123,* 234505. **DOI:**10.1063/1.2121687
27. K. A. T. Silverstein, A. D. J. Haymet and K. A. Dill, *J. Am. Chem. Soc.* **1998,** *120,* 3166. **DOI:**10.1021/ja973029k
28 .A. Ben–Naim, *J. Chem. Phys.* **1971,** *54,* 3682. **DOI:**10.1063/1.1675414
29 .A. Ben–Naim, *Mol. Phys.* **1972,** *24,* 705. **DOI:**10.1080/00268972001010851
30 .C. L. Dias, *Phys. Rev. Lett.* **2012,** *109,* 048104. **DOI:**10.1103/PhysRevLett.109.048104
31. T. Urbic, V. Vlachy, Yu. V. Kalyuzhnyi, N. T. Southall and K. A. Dill, *J. Chem. Phys.* **2000,** *112,* 2843. **DOI:**10.1063/1.480928
32. T. Urbic, V. Vlachy, Yu. V. Kalyuzhnyi, N. T. Southall and K. A. Dill, *J. Chem. Phys.* **2002,** *116,* 723. **DOI:**10.1063/1.1427307
33. T. Urbic, V. Vlachy, Yu. V. Kalyuzhnyi and K. A. Dill, *J. Chem. Phys.* **2003,** *118,* 5516. **DOI:**10.1063/1.1556754
34. T. Urbic, V. Vlachy, O. Pizio, K. A. Dill, *J. Mol. Liq.* **2004,** *112,* 71. **DOI:**10.1016/j.molliq.2003.12.001
35. T. Urbic, V. Vlachy, Yu. V. Kalyuzhnyi and K. A. Dill, *J. Chem. Phys.* **2007,** *127,* 174511. **DOI:**10.1063/1.2784124
36. T. Urbic and M. F. Holovko, *J. Chem. Phys.* **2011,** *135,* 134706. **DOI:**10.1063/1.3644934
37. T. Urbic and K. A. Dill, *J. Chem. Phys.* **2010,** *132,* 224507. **DOI:**10.1063/1.3454193
38 .T. Urbic, *Phys. Rev. E* **2012,** *85,* 061503. **DOI:**10.1103/PhysRevE.85.061503
39 .T. Urbic, *Phys. Rev. E* **2016,** *94,* 042126. **DOI:**10.1103/PhysRevE.94.042126
40 .T. Urbic, *Phys. Rev. E* **2017,** *96,* 032122. **DOI:**10.1103/PhysRevE.96.032101
41. T. Urbic, V. Vlachy, O. Pizio, K. A. Dill, *J. Mol. Liq.* **2004,** 112, 7180. **DOI:**10.1016/j.molliq.2003.12.001
42. M. Kurtjak, T. Urbic, *Mol. Phys. 112,* **2014,** 1132–1148. **DOI:**10.1080/00268976.2013.836608
43. M. Kurtjak, T. Urbic, *Mol. Phys.* **2015,** *113,* 727–738. **DOI:**10.1080/00268976.2014.973919
44. T. Urbic, V. Vlachy, K. A. Dill, *J. Phys. Chem.* **2006,** *B 110,* 49634970. **DOI:**10.1021/jp055543f
45. T. Urbic, M. F. Holovko, *J. Chem. Phys.* **2011,** *135,* 19. **DOI:**10.1063/1.4967807
46 .T. Urbic, T. Mohoric, *J. Chem. Phys.* **2017,** *146* 094505. **DOI:**10.1063/1.4977214
47 .P. Ogrin, T. Urbic, *J. Mol. Liq.* **2020,** *114880*. **DOI:**10.1016/j.molliq.2020.114880
48 .P. Ogrin, T. Urbic, *J. Mol. Liq.* **2021**.
49. C. L. Dias, T. Hynninen, T. Ala–Nissila, A. S. Foster and M. Karttunen, *J. Chem. Phys.* **2011,** *134,* 065106. **DOI:**10.1063/1.3537734
50. A. Bizjak, T. Urbic, V. Vlachy, and K. A. Dill, *Acta Chim. Slov.* **2007,** *54,* 532.
51. A. Bizjak, T. Urbic, V. Vlachy and K. A. Dill, *J. Chem. Phys.*

2009, *131,* 194504. **DOI:**10.1063/1.3259970
52. T. M. Truskett and K. A. Dill, *J. Chem. Phys.* **2002,** *117,* 5101. **DOI:**10.1063/1.1505438
53. T. M. Truskett and K. A. Dill, *J. Phys. Chem.* **2002,** *B 106,* 11829. **DOI:**10.1021/jp021418h
54. T. Urbic and K. A. Dill, *J. Am. Chem. Soc.* **2018,** *140,* 17106. **DOI:**10.1021/jacs.8b08856
55. M. Bešter-Rogač, *Acta Chim. Slov.* **2009,** *67,* 1. **DOI:**10.17344/acsi.2020.5870
56. V. Molinero and E. B. Moore, *J. Phys. Chem.* **2009,** *B 113,* 4008. **DOI:**10.1021/jp805227c
57. A. V. Dubtsov, S. V. Pasechnik, D. V. Shmeliova, A. Sh. Saidgaziev, E. Gongadze, A. Iglič, S. Kralj, *Electrostatic Effects, Soft Matter,* **2018,** *14,* 9619–9630. **DOI:**10.1039/C8SM01529E
58. A. Iglič, E. Gongadze, V. Kralj-Iglič, *Acta Chim. Slov.* **2019,** *66,* 534. **DOI:**10.17344/acsi.2019.5495

Povzetek

Struktura in lastnosti biomolekul, kot so proteini, nukleinske kisline in membrane, so odvisne od vode. Voda je zelo pomembna tudi v industriji. Na splošno je nenavadna snov z več kot 70 anomalnimi lastnostmi. Zaradi teoretičnega in računalniškega modeliranja vode jo vse bolje razumemo. Obstajajo različni tipi modelov vode. Prvi so kompleksi, ki upoštevajo veliko podrobnosti, in njihova računska zahtevnost narašča z detelji. Drugi pa so enostavni, ki se osredotočajo na razlago osnovnih zakonitosti kot so termodinamika, fazni diagram. Ti modeli so računsko manj potratni. Enostavni modeli omogočajo boljše razumevanje vode na način, ki dopolnjuje kompleksne modele. Tu predstavljamo analitično modeliranje lastnosti vode na različnih nivojih, dve- in tridimenzionalnega Mercedes Benz modela vode ter eksperimentalne vode.

Scientific paper

Acute Toxicity of Insecticide Thiamethoxam to Crayfish (*Astacus leptodactylus*): Alterations in Oxidative Stress Markers, ATPases and Cholinesterase

Miraç Uçkun,[1] Ertan Yoloğlu,[2] Aysel Alkan Uçkun[3*] and Özden Barım Öz[4]

[1] *Department of Food Engineering, Faculty of Engineering, Adıyaman University, Adıyaman, Turkey*

[2] *Department of Mathematics and Science Education, Faculty of Education, Adıyaman, Turkey*

[3] *Department of Environmental Engineering, Faculty of Engineering, Adıyaman University, Adıyaman, Turkey*

[4] *Department of Physiology, Faculty of Aquaculture, Fırat University, Elazığ, Turkey*

** Corresponding author: E-mail: ayseluckun@gmail.com*
Phone: [+90] 4162233800/4539

Received: 06-03-2021

Abstract

Thiamethoxam (Thmx) is a globally used neonicotinoid pesticide contaminated in freshwater ecosystems with residues detected in fishery products. *Astacus leptodactylus* is a popular freshwater crustacean that is cultivated and exported in many countries. In this study, we investigated the acute toxic effects of Thmx on *A. leptodactylus* using various biomarkers (acetylcholinesterase, carboxylesterase, glutathione S-transferase, glutathione, superoxide dismutase, glutathione peroxidase, glutathione reductase, and adenosinetriphosphatases). The 96-h LC_{50} value of Thmx was calculated as 8.95 mg active ingredient L^{-1}. As the dose of Thmx increased, oxidative stress was induced by the inhibition/activation of antioxidant enzymes, while the activities of acetylcholinesterase, carboxylesterase and adenosinetriphosphatases were inhibited. As a result, it can be said that Thmx has highly toxic effects on crayfish, therefore they are under threat in the areas where this pesticide is used.

Keywords: Acetylcholinesterase; Antioxidant enzymes; Crustacean; Insecticide; Metabolic enzymes; Toxicity

1. Introduction

Among the insecticides widely used in agriculture, it is necessary to focus on neonicotinoids, which are chemically similar to nicotine.[1] Neonicotinoid insecticides have been the fastest growing insecticide class due to their safe use of biochemical properties, broad spectrum activities, and systemic distribution mechanism in plants.[2,3] Thiamethoxam (Thmx) 3-(2-chloro-1,3-thiazol-5-ylmethyl)-5-methyl-1,3,5-oxadiazinan-4-ylidene (nitro) amine is one of the second generation neonicotinoid insecticides and is used against a wide target population of insects.[4] Thmx is a potential pollutant that is mixed with surface and ground water due to its low absorption from the soil, high leakage capacity and high water solubility.[5] Thmx, like other neonicotinoid insecticides, bind agonistically with high affinity to nicotinic acetylcholine receptors, which are target sites in insects.[6] There is much information in the literature specific to the exposure profiles of neonicotinoids in aquatic ecosystems, but there is little information about second-generation neonicotinoids such as Thmx in published studies on the effects of neonicotinoids on non-target aquatic organisms. Knowing the effect of neonicotinoids on aquatic invertebrates provides important data for aquatic risk assessment.[7] Although low-risk for some non-target organisms, Thmx is a potential pollutant for surface and groundwater due to its low absorption, low infiltration, high water solubility and resistance to biological treatment, therefore it poses a danger to aquatic organisms.[8,9] Thmx has been found to be generally around 0.001–225 ppb in surface waters.[10] The persistence in the soil (229 days) and high-water solubility (4100 mg L^{-1}) of Thmx mean there is high potential to be transported into surface waters.[11] The results of a comprehensive review of laboratory and semi-field microcosm studies show that aquatic invertebrates are highly susceptible to neonicoti-

noids.[12] However, the most studied of neonicotinoids in aquatic ecosystems is imidacloprid, the effects of a newer neonicotinoid, Thmx, on aquatic organisms have been less studied.[13]

Turkey's natural freshwater crayfish species, *A. leptodactylus*, one of the most popular species in Europe is due to the presence of a wide range of areas outside of Anatolia and economic importance.[14] Crayfish are part of the ecological balance in their natural freshwater areas. Due to the important role they play in the processing of all kinds of organic materials, they are active on energy balances in the ecosystem, therefore they are seen as key species for still and fluvial habitats.[15,16] Indicator species in aquatic ecosystems are considered to be a suitable way of demonstrating environmental quality.[17] Not all organisms are suitable for use as an indicator. Crayfish are benthic, solitary, constantly in contact with objects, omnivorous, long-lived, slow-moving, narrow habitat, large enough to easily sample from different body tissues, and can accumulate pollutants increases its value as an indicator species.[18]

Many xenobiotics, including pesticides, can trigger the production of reactive oxygen species by various biochemical mechanisms, such as disruption of electron transport across the cell membrane, facilitation of the Fenton reaction, inactivation of antioxidant enzymes, and depletion of free radical scavengers.[19] Antioxidant defense systems have been developed in organisms to scavenge these reactive oxygen species, and by evaluating the activation / inhibition level of these antioxidant systems, the oxidative damage caused by xenobiotics to the organism is estimated.[20] The aim of this study was to investigate the acute toxic effects of Thmx on *A. leptodactylus*. For this, we tested the effect of different doses of Thmx on the enzymes responsible for ion homeostasis in the cell (Na^+/K^+ -ATPase, Mg^{2+} -ATPase, Ca^{2+} -ATPase), neurotoxicity biomarker acetylcholinesterase (AChE), antioxidant defense system parameters [superoxide dismutase (SOD), glutathione (GSH), glutathione peroxidase (GPx), glutathione reductase (GR)], an oxidative damage marker [malondialdehyde (MDA)], phase II biotransformation enzymes [glutathione S-transferase (GST), carboxylesterase (CaE)] of aquatic invertebrate crayfish *A. leptodactylus*.

2. Materials and Methods

2. 1. Test Animals and Experimental Design

Crayfish used in this study were obtained from the Crayfish Breeding Unit at the Firat University Fisheries Faculty, Elazığ, Turkey. During the study, glass aquariums with a capacity of 30 liters with tubular shelters were used. Studies were done at room temperature (23 ± 1 °C) and in natural daylight (12 h dark /12 h light). Adequate ventilation was provided with the air pump. Rested tap water was placed in the aquariums. Before applying the pesticide, the crayfish were adapted to the laboratory environment for 15 days. Matured crayfish were used regardless of their gender. In order to achieve standardization, crayfish weighing around 20 ± 5 g were preferred. Crayfish were not given food during the applications. The pesticide sold under the trade name Actara 25 WG was obtained from Syngenta. The Active Ingredient (AI) of Thmx is 240 g L^{-1}. Water prepared according to ASTM standards was used in the study.[21] Stock solution of 5000 mg L^{-1} was prepared freshly by dissolving Thmx in tap water. Test waters containing Thmx solution were left in the containers with static renewal every 24 hours and the pH values of these waters were recorded daily. A total of five groups were formed, four of which were the pesticide-treated groups and one was the non-pesticide-applied group (control). Four crayfish were placed in each aquarium and the study was done in three replicates, so fifteen aquariums and sixty animals were used in total.

2. 2. Determination of LC_{50} Values and Application Concentrations of Thiamethoxam

Dose ranges of 0.50–400 mg L^{-1} of the commercial stock solution were used to determine the 96-h LC_{50} value of Thmx. Among live animals, those who were immobilized over time and showed signs of death were considered dead.[22] The number of dead animals was recorded at 24, 48, 72 and 96 hours and accordingly 96h-LC_{50} was determined as 8.95 mg AI L^{-1} using SPSS 24 probit. This determined LC_{50} dose and its three sub-doses of Thmx ($LC_{50}/2$, $LC_{50}/4$, $LC_{50}/8$) were administered to the crayfish. No Thmx application was applied to the control group. The experiment was repeated three times for each group of four animals (N = 12). After applying solutions containing Thmx at its own concentration to each group for 96 hours, the animals were sacrificed and the hepatopancreas, muscle and gill tissues were removed and stored at –80°C until analyzed. An ice bath was used for anesthesia of the animals, and the abdominal areas of the animals between the thorax and tail were dissected.[23]

2. 3. Biochemical Assays

Analysis of biochemical markers was performed in tissues of surviving animals after a 96-h acute toxicity test. The numbers of animals by groups are as follows: Control: 12, $LC_{50}/8$: 12, $LC_{50}/4$: 12, $LC_{50}/2$: 9, LC_{50}: 8. Homogenisation of the tissues was carried out in homogenization buffer (0.1 M, pH 7.4 in potassium phosphate buffer; 0.15 M KCl, 1 mM EDTA, 1 mM DTT) and on ice using a polytron homogenizer (Heidolph RZ 2021 Germany). The homogenates were centrifuged at 16,000 × g for 20 min at 4 °C (Hettich 460 R). Total protein and all enzyme readings were done in triplicate on a microplate reader (Thermo Varioscan Flash 2000). The total protein level was meas-

ured according to Bradford method (1976).[24] The protein levels of the samples were determined using the standard curve constructed from measurements of the following bovine serum albumin standard solutions. In hepatopancreas tissue, GST, GR, AChE, CarE, GPx, SOD, GSH and MDA analyses were performed. ATPases analyses were done in gill and muscle tissues. All enzyme activities were expressed as specific activity (nmol min^{-1} mg $protein^{-1}$).

2. 3. 1. Cellular Redox Status

The GST activity was determined by a spectrophotometric method according to protocol described by Habig et al. (1974)[25] using CDNB as substrate. The change in absorbance was measured at 344 nm for 2 min. The GR activity was detected according to Cribb et al., (1989)[26] by microplate assay with modifications. The reaction was initiated by the addition of GSSG into the reaction solution. Due to formation of GSH from GSSG, the decrease in the amount of DTNB was monitored at 405 nm for 3 min. The CarE activity was determined according to a modified procedure of Santhoshkumar and Shivanandappa (1999)[27] for a microplate reader. The reaction was initiated by the addition of PNPA as substrate to the reaction solution. The liberated *p*-nitrophenol was monitored at 405 nm for 2 min. In the determination of GPx activity, the method developed by Bell et al. (1985),[28] Based on using hydrogen peroxide (H_2O_2) as substrate and sodium azide (NaN_3) as catalase inhibitor, was used. The specific activity value of the enzyme was calculated based on the change in absorbance at 340 nm based on the oxidation of NADPH in a microplate reader. Superoxide dismutase (SOD) activity was determined by the method (Sun et al., 1988)[29] based on the production of superoxide radicals by interacting xanthine with xanthine oxidase. The absorbance value was measured according to the color change created by the interaction of superoxide radicals with nitrobluetetrazolium. The reduced GSH level was determined according to Moron et al. (1979)[30] with some modifications adapted to microplate reader system. The absorbance was read at 412 nm against the GSH standard curve. GSH level of samples was expressed as nmol GSH mg^{-1} protein. The MDA concentration was measured based on thiobarbituric acid reactive substance assay as described by Placer et al. (1966)[31] with some modifications. The absorbance was read at 532 nm. MDA contents were determined using malondialdehyde bis (diethyl acetal) as a standard. The MDA concentration was expressed as nmol MDA mg^{-1} protein.

2. 3. 2. Neurotoxicity (AChE)

The AChE activity was determined following the Ellman and Andres (1961)[32] method using ACTI as a substrate, modified for the microplate reader by Ozmen et al. (1998).[33] Enzyme activity was monitored at 412 nm for 1 min.

2. 3. 3. Ion Transport

The methods of Atlı and Canlı (2011)[34] were used to determine ATPase activities (Na^+/K^+ -ATPase, Mg^{2+}-ATPase, Ca^{2+} -ATPase) in gill and muscle. Analyzes were performed in a microplate reader in triplicate. 5 µL of sample and 60 µL of incubation medium consisting of 1 mM ouabain, 40 mM Tris-HCl, 4 mM $MgCl_2$, 20 mM KCl and 100 mM NaCl were pipetted into each microplate well and incubated at 37 ° C for 5 minutes. 10 µL of 3 mM ATP was added to the top of the mixture in these wells and incubated at 37 ° C for 30 minutes, so the reaction was initiated. After incubation, 35 µL of cold distilled water (+4 ° C) was added to these wells to stop the reaction. The value of the inorganic phosphate (Pi) released from ATP at the end of the reaction was calculated by measuring the absorbance at 390 nm of the yellow compound formed by the main reagent consisting of polyoxyethylene 10 lauryl ether and ammonium molybdate (Atkinson *et al.* 1973).[35] 190 µL of main reagent was added to microplate wells containing 60 µL of incubation medium, 5 µL of supernatant and 35 µL of cold distilled water, and after incubating at room temperature for 10 minutes, absorbance values were measured at 390 nm. The results were evaluated based on the standard curve obtained using different concentrations of KH_2PO_4 solution. Enzyme activities were expressed as specific activity (µmol P_i min^{-1} mg $protein^{-1}$). Na^+/K^+ ATPase activity was calculated by subtracting the Mg^{2+} ATPase (containing Ouabain) activity from the total ATPase (without Ouabain) activity. The Mg^{2+} ATPase activity arises from the inhibition of Ouabain's activity by binding to Na^+/K^+ ATPase. Ca^{2+} ATPase activity was calculated by subtracting the enzyme activity measured in the absence of enzyme activity in the presence of $CaCl_2$.

2. 4. LC-MS/MS Analysis of Thiamethoxam in the Test Water

The actual Thmx concentrations in the test waters were determined using a liquid chromotgraphy tandem mass spectrometry (LC-MS/MS) in Adiyaman University Central Research Laboratory. The retention time of Thmx was aproximately 3.84 min. The calibration curve constructed from the standards for the calculation of Thmx concentrations was in the range of 1–100 µg L^{-1}. The limits of detection, quantification, and coefficient of determination (r^2) were determined as 0.07 µg L^{-1}, 0.32 µg L^{-1}, and 0.999, respectively. Thmx was detected through the transitions 292.1 → 211.0 mass-to-charge ratio (*m/z*) (collision energy (CE); –12 V) and 292.1 → 181.0 *m/z*, CE; –24 V. The Thmx standard was purchased from Dr. Ehrenstorfer GmbH with 99.8% purity. Each water sample was analyzed in triplicate.

2. 5. Data Analyses

In the statistical analysis of the data, computer software package SPSS 22 was used. Data normality was evaluated using Shapiro-Wilk test ($p < 0.05$). Kruskal Wallis

test was used to determine the comparison of data between groups. Mann Whitney U test was used to determine whether there was a significant difference within the groups. The statistical significance level was based on $p < 0.05$.

The integrated biomarker response (IBR) was used to incorporate all the biochemical marker reactions assessed into a single overall stress index to determine the risk potential of thiamethoxam. The IBR indexes were calculated according to the method defined by Arzate-Cárdenas and Martínez-Jerónimo (2012).[36] The IBR index was calculated based on the mean and standard deviation for each biomarker. The average value for each response was standardized separately using the formula Y = (Xm) / SD; where Y is the standardized value, X is the average value, and m is the average of the biochemical markers. Depending on the biochemical responses, Z values were calculated as Z = Y (inhibition) or Z = –Y (activation). Score (S) was evaluated with the formula S = |min|+Z; where |min| is the absolute value of the minimum of all biochemical markers. The scores were utilized were [(S1 × S2) / 2 + (S2 × S3) / 2 +… (Sn – 1 × Sn) / 2] to give a normalized IBR, and estimated values were divided by the number of biochemical markers calculated.

3. Results and Discussion

3. 1. The Actual Thiamethoxam Concentrations in the Test Waters

Data on the actual concentrations of Thmx in solutions applied to crayfish as determined by LCMSMS are shown in Table 1. A difference of approximately 15%, 12%, 10% and 11% was found between the nominal and actual concentrations, respectively. These differences may be because Thmx is not sufficiently soluble in water due to surfactants, solvents, and preservatives found in this commercial form (Korkmaz et al. 2018).[37]

Table 1. Concentrations measured by LCMSMS in test waters (Actual concentrations expressed as mean±standart error)

Nominal Dose	N	Mean		SE
1.12	3	0.95	±	0.03
2.24	3	1.97	±	0.04
4.48	3	4.01	±	0.06
8.95	3	7.98	±	0.04

3. 2. Acute Toxicity Assay

In our search, and to the best of our knowledge, no peerreviewed studies examining Thmx toxicity to *A. leptodactylus* have been published. In our study, the 96-hour acute lethal concentration value (96 h-LC_{50}) of Thmx for *A. leptodactylus* was determined as 8.95 mg AI L^{-1}. The 96 h LC_{50} value for crayfish, *Procambarus clarkii* was determined as 0.967 mg AI L^{-1} by Barbee and Stout (2009)[38] and 10 mg AI L^{-1} by Maloney et al. (2018)[39] in two separate studies. In a study, 48-h LC_{50} value of Thmx for water louse *Asellus aquaticus* was found as 2.3 mg L^{-1}.[39] For crustacean *Gammarus kischineffensis*, the 96-h LC_{50} value of Thmx determined as 8.985 mg L^{-1} and 3.751 mg L^{-1}.[40,41] The reason that these acute LC_{50} values of Thmx determined for crustaceans differ from each other may be due to the differences in the experimental conditions and the parameters such as application period, physiological status, life stage, age and body weight of the animals used in the experiment.[42]

3. 3. Mortality Rates of Crayfish Determined During 96-h of Study

The mortality rates of crayfish exposed to Thmx at different concentrations for 24, 48, 72 and 96-h are shown in Table 2. No death was observed at any Thmx concentration at 24th hour. At 48th hour, only 1 death was observed for each of the LC_{50}/2 and LC_{50} doses. At 72th hour, 1 animal died at the LC_{50}/2 dose and 2 animals died at the LC_{50} dose. At 96th hour, 1 animal died at both the LC_{50}/2 and LC_{50} doses. Mortality rates were 25% and 33% at the LC_{50}/2 and LC_{50} doses, respectively and the difference between these groups from control was statistically significant ($p < 0.05$).

Comparison of mortality rates were made by Dunnett's t-test. Results showed statistical importance compared with control (*: $p < 0.05$). LC_{50}/8: 1.12 mg AI L^{-1}. LC_{50}/4: 2.24 mg AI L^{-1}. LC_{50}/2: 4.48 mg AI L^{-1}. LC_{50}: 8.95 mg AI L^{-1}. N: The number of the animals used.

3. 4. Biochemical Responses

The data of the biomarkers evaluated in the hepatopancreas are given in Table 3, those in the gill in Table 4, and those in the muscle in Table 5.

Table 2. The mortality of crayfish exposed to Thmx at different concentrations for 24, 48, 72 and 96-h.

Concentration (mg AI L^{-1})	N	Mortality 24 h	48 h	72 h	96 h	Total death	Mortality rate (%)
Control	12	0	0	0	0	0	0
LC_{50}/8	12	0	0	0	0	0	0
LC_{50}/4	12	0	0	0	0	0	0
LC_{50}/2	12	0	1	1	1	3	25*
LC_{50}	12	0	1	2	1	4	33*

3. 4. 1. Cellular Redox Status

In GST activity, there were significant increases in all Thmx concentrations, not dependent on Thmx concentration increase compared to the control group. The highest increase in GST activity was seen in the group in which the $LC_{50}/4$ dose was applied. The GST activity value at the LC_{50} concentration was close to that of the $LC_{50}/4$ concentration. Contrary to uor study, Han et al. (2016)[43] observed a significant increase in GST activity in the liver of zebra fish treated with azoxystrobin for 4 weeks and attributed this increase to the free radical scavenging effect of GST. Husak et al. (2017)[44] found that when they applied penconazole to goldfish, the GST activity in their livers was significantly higher than the control group. Similarly, Korkmaz et al. (2018)[37] observed GST was induced by phosalone-based (PBP) and cypermethrin-based (CBP) pesticides in zebrafish (*Danio rerio*) after 96 h exposure. Liu et al. (2015)[45] suggested that when azoxystrobin was applied to green algae *Chlorella vulgaris*, GSH level decreased and GST activity increased due to excessive ROS production, thus scavenging free radicals. GST catalyzes the conjugation of xenobiotics with GSH, allowing them to be removed from the organism[46] thus, GST induction is used as a biomarker of cellular damage caused by xenobiotics.[47] There are many studies in the literature revealing that GST activity increases in aquatic organisms treated with pesticide.[48–52]

GR activity decreased significantly in the Thmx applied groups compared to the control. The greatest increase in inhibition was seen at the LC_{50} dose, with a rate of approximately 84% compared to the control. Although all inhibitions were statistically significant, the least inhibition was seen at $LC_{50}/8$ dose with 76% difference from the control. GR is an enzyme that indirectly acts as an antioxidant by converting oxidized glutathione (GSSG) formed during reactions catalyzed by glutathione peroxidase (GPx) and glutathione S-transferase (GST) into reduced glutathione (GSH).[53] In this study, observation of significant decreases in GR activity in all groups may be due to extracellular transport of GSSG rather than GSH to inhibit the cytotoxic effects of Thmx.[54]

CarE activity was significantly inhibited in all Thmx concentrations compared to the control. At the highest Thmx concentration (LC_{50}) the greatest inhibition (approximately 55% increase over control) was observed. CarEs are members of the esterase family that catalyze the hydrolysis of substrates such as carboxylic esters, thioesters, amides and carbamates, and various xenobiotics.[55] CarEs are involved in important physiological processes such as lipid metabolism,[56] pro-drug activation,[57] pesticide metabolism,[58] and hydrolysis of phthalates.[59] In agreement with our results, Denton et al. (2003)[60] reported that CarE activity was inhibited by 50% in fathead minnows compared to the unexposed group due to diazinon exposure. Wheelock et al. (2005)[61] observed that after applying chlorpyrifos to Chinook salmon (*Oncorhynchus tshawytscha*) for 96 hour, CarE activity decreased significantly compared to control. Uçkun and Öz (2020a),[51] who first demonstrated that CarE was inhibited as a result of acute application (96 h) of pesticide penconazole to crayfish, suggested that CarE is a sensitive biomarker of pesticide toxicity in crayfish hepatopancreas. In our study, data on CarE inhibition due to Thmx administration also support this view.

In GPx activity, there were significant increases in all Thmx concentrations. These increases in GPx activity were not dependent on dose increase. The greatest increase was seen at the $LC_{50}/8$ dose, approximately 44% difference from the control. The main function of GPx is to reduce the lipid hydroperoxides formed in the cell due to xenobiotic exposure to their end product alcohols and to reduce free hydrogen peroxide.[62,63] Inhibition in the GPx enzyme may reflect the failure of the antioxidant system to prevent the destructive effect of the pesticide,[64] or it may be related to the direct effect of reactive oxygen species formed in cells on the synthesis of this enzyme.[65] From this perspective, the GPx increase observed in this study may reflect the protective role of GPx against the oxidative damage induced by Thmx in the cell. In parallel with our findings, Blahova et al.[66] found that when they subchronically applied atrazine to zebrafish, GPx activity was significantly increased.

There was a decrease in SOD activity at the $LC_{50}/8$ dose, and an increase in the other doses compared to the control depending on the dose. Only the increase in the LC_{50} administration dose was statistically significant from the control ($p < 0.05$). SOD is an important antioxidant enzyme that catalyzes the conversion of superoxide radicals to H_2O_2 and $O_2^{\cdot -}$ in organisms and forms the first defense against free oxygen radicals formed in cells.[67] When an organism is exposed to a xenobiotic, a decrease in the antioxidant system may be followed by an increase, which may reflect that the organism is adapting.[68,69] The increase in SOD activity at high Thmx concentrations indicates that SOD scavenges the overproduction of superoxide ions under the oxidative stress created by Thmx. Many studies have shown that SOD activity is increased in organisms exposed to pesticides.[66,70,71]

GSH level decreased significantly in all groups treated with Thmx compared to control. The greatest reduction was seen at the LC_{50} dose, with a rate of 45%. GSH is an essential endogenous tripeptide, which prevents the cell from oxidative injury. GSH acts as a cofactor for GST,[72] which is responsible for detoxification of xenobiotics, so an increase or decrease in GSH level can be an important indicator of the detoxification ability of the organism.[73] Our findings are in line with many studies in the literature that GSH level decreased as a result of pesticide application to aquatic organisms.[74–78] A decrease in GSH may mean that the antioxidant defense system is activated against the oxidative damage caused by ROS in the cell, as this reduction is an indication that GSH is spent converting to oxidized glutathione or regenerating GSH.[79] Also, a

Table 3. Biochemical responses of 96-h Thmx exposure in hepatopancreas. Total protein amount expressed as mg ml^{-1}, and enzyme activities expressed as nmol min^{-1} mg $protein^{-1}$ ± ***mean standard error. GSH and MDA levels expressed as nmol GSH mg protein***$^{-1}$ ± mean standard error and nmol MDA mg $protein^{-1}$ ± mean standard error, respectively.

Dose	N	Total Protein	GST	GR	AChE	CarE	GPx	SOD	GSH	MDA
Control	12	5.74	160.86 ± 7.03	36.91 ± 1.70	6.42 ± 0.36	5442.60 ± 278.80	8.01 ± 0.33	4.47 ± 0.21	0.20 ± 0.02	3.00 ± 0.17
LC_{50}/8	12	9.87	282.77 ± 3.72*	8.98 ± 0.20*	2.91 ± 0.10*	2884.40 ± 39.03 *	14.24 ± 0.51*	4.04 ± 0.11	0.13 ± 0.01*	3.07 ± 0.04
LC_{50}/4	12	7.62	395.32 ± 9.74*	8.49 ± 0.27*	3.23 ± 0.11*	2968.20 ± 88.25 *	14.23 ± 0.51*	4.61 ± 0.15	0.14 ± 0.03*	4.23 ± 0.21*
LC_{50}/2	9	8.72	277.38 ± 10.3*	8.84 ± 0.31*	1.50 ± 0.10*	3075.10 ± 110.50*	11.22 ± 0.17*	6.77 ± 0.22	0.14 ± 0.01*	4.58 ± 0.12*
LC_{50}	8	11.43	385.33 ± 5.01*	6.09 ± 0.33*	1.84 ± 0.07*	2455.50 ± 61.82 *	13.48 ± 1.13*	7.92 ± 0.28*	0.11 ± 0.01*	5.29 ± 0.30*

N: Number of animals that survived after the 96-h acute toxicity test.
*: $p < 0.05$ showed statistical importance compared with control group.

decrease in GSH level indicates a disrupt in phase II biotransformation, which increases the risk of oxidative stress due to decreased cell protection activity.[80]

There was an increase in the MDA level at all Thmx concentrations and these increases were in a dose-dependent fashion. Differences in all concentrations were statistically significant except for the LC_{50}/8 concentration. The highest increase in MDA level was at the LC_{50} concentration, approximately 43% compared to the control. Lipid peroxidation is the first indicator of cell membrane damage caused by exposure of organisms to pesticides, metals and various xenobiotics.[81] The reason for the high level of MDA in our study may be the peroxidation of unsaturated fatty acids in the cell membranes, as Thmx exposure causes oxidative damage in the cell and increases ROS production. It has been reported that the level of MDA increased significantly in various aquatic organisms exposed to different pesticides compared to the groups not treated with pesticides.[44,66,78,82,83,84]

3. 4. 2. Neurotoxicity (AChE)

There was a significant decrease in AChE activity in the Thmx applied groups compared to the control. The reductions in all Thmx concentrations relative to control were not dose dependent. The highest AChE inhibition was observed in the LC_{50}/2 group with an approximately 77% difference from the control. The inhibition in the LC_{50} application was approximately 71% compared to the control. When AChE is inhibited by xenobiotics, acetylcholine accumulates in the synaptic space and the receptors are highly stimulated. Activation of muscarinic ACh receptors is relatively slow (milliseconds to seconds) and, depending on the subtypes present, they directly alter cellular homeostasis. Unlike muscarinic receptors, the nicotinic receptors are inactivated due to sustained increase in ACh concentrations, which ultimately results in paralysis. Therefore, AChE is used as a biomarker of pesticides that target it directly or indirectly by altering the cholinergic neurotransmission.[85] In our study, significant AChE inhibition due to Thmx administration indicates that Thmx has neurotoxic effects in crayfish at the doses applied. Similar to our findings, AChE inhibition was observed after 96 hours of Thmx application to the midge *Chironomus riparius*.[86] Many researches reported that AChE is inhibited by neonicotinoid pesticides in various aquatic organisms.[87–89]

3. 4. 3. Ion Transport

ATPases are responsible for ion homeostasis in cell membranes, play a central role in the physiological functions of the cell by providing energy conversion in chemical reactions,[90] so they are considered a good indicator in toxicological studies. In our study, significant inhibitions of all ATPases (Na^+K^+ATPase, Mg^{2+}ATPase, Ca^{2+}ATPase) were noticed in Thmx treated groups in both gill and muscle compared to control (Table 3 and Table 4).

Na^+K^+ATPase was inhibited at the highest Thmx concentration (LC_{50}) in both gill and muscle. In gill tissue, inhibitions at all Thmx doses were significant ($p<0.05$). Na^+K^+ATPase inhibition rates in the gill were 25%, 49%, 50% and 71%, respectively, based on the applied Thmx concentrations. In muscle tissue, all Na^+K^+ATPase inhibitions were statistically significant except for LC_{50}/8 ($p<0.05$). Na^+K^+ATPase inhibition rates relative to control in muscle were 6%, 17%, 38% and 42%, respectively. Na^+K^+ATPase has a vital function in maintaining the cell membrane potential difference by keeping Na^+ outside the cell and K^+ inside the cell.[91] Inhibitions in Na^+K^+ATPase activity indicates the destruction of cellular ion regulation in the tissues of fish.[92] The researcher reported that this degradation may also be due to the effect of pesticide on the passive movement of ions, namely its permeability properties. *Cirrhinus mrigala*, which is exposed to the lethal and subletal effects of deltamethrin, has been found to decrease Na^+K^+ATPase activity in gill, liver and muscle tissue.[93] It has been determined that the gill tissue Na^+K^+ATPase activity of *Cyprinus carpio*, which is exposed to cypermethrin sub-lethal effect for different periods, shows a decrease depending on the time.[94] Similar observations were reported by Begum (2011)[92] in the fish *C. batrachus* exposed to carbofuran. In a study conducted by Temiz et al. (2018),[95] it was determined that under the effect of chlorantraniliprole (CHL), the decrease in

Table 4. Biochemical responses of 96-h Thmx exposure in gill. Total protein amount expresses as mg ml^{-1}, and enzyme activities expressed as μmol P_i min^{-1}mg $protein^{-1}$ ± mean standard error.

Dose	N	Total protein	Na^+/K^+ -ATPase	Mg^{2+} -ATPase	Ca^{2+} -ATPase
Control	12	12.26	40.74 ± 1.58	48.72 ± 0.95	89.46±2.11
LC_{50}/8	12	9.31	30.58 ± 0.91 *	34.37 ± 0.39 *	64.94±1.12 *
LC_{50}/4	12	11.49	20.82 ± 0.62 *	27.09 ± 0.51 *	48.01±0.62 *
LC_{50}/2	9	10.77	20.17 ± 1.03 *	25.80 ± 0.60 *	45.97±0.55 *
LC_{50}	8	11.91	11.97 ± 0.37 *	26.07 ± 0.40 *	38.03±0.29 *

N: Number of animals that survived after the 96-h acute toxicity test.
*: $p < 0.05$ showed statistical importance compared with control group

Table 5. Biochemical responses of 96-h Thmx exposure in muscle. Total protein amount expressed as mg ml^{-1}, and enzyme activities expressed as μmol P_i min^{-1}mg $protein^{-1}$ ± mean standard error.

Dose	N	Total protein	Na^+/K^+ -ATPase	Mg^{2+} -ATPase	Ca^{2+} -ATPase
Control	12	15.13	21.18 ± 0.91	72.03 ± 1.32	93.21±1.32
LC_{50}/8	12	11.40	19.97 ± 0.44	61.51 ± 0.98 *	81.48±1.13 *
LC_{50}/4	12	12.19	17.55 ± 0.66 *	49.15 ± 1.04 *	66.70±0.69 *
LC_{50}/2	9	12.02	13.18 ± 0.17 *	31.15 ± 0.06 *	44.33±0.18 *
LC_{50}	8	11.37	12.32 ± 0.23 *	26.60 ± 1.25 *	38.92±1.25 *

N: Number of animals that survived after the 96-h acute toxicity test.
*: $p < 0.05$ showed statistical importance compared with control group

Na^+K^+ATPase activity of *O. niloticus* gill tissue increased due to the prolongation of the time. The observed decrease in the activities of Na^+K^+ATPase may be due to the change in ionic homeostasis and may also be due to ATP depletion.[92]

In both gill and muscle tissues, Mg^{2+}ATPase activity decreased as the applied Thmx concentration increased. The highest reduction was observed in the groups where the highest Thmx concentration (LC_{50}) was applied. Mg^{2+}ATPase inhibition rates in the gill were 29%, 44%, 47%, 47%; in muscle, it was 15%, 32%, 57% and 63% compared to control depending on the increase in Thmx concentration. Mg^{2+}ATPase is an enzyme that ensures the integrity of the cell membrane by transepithelial regulation of Mg^{2+} ions and is associated with the synthesis of ATP through oxidative phosphorylation in mitochondria.[91] Inhibition of Mg^{2+}ATPase in the present study may have caused a disruption in the transport of ions across the cell membrane and a decrease in ATP production.[92,96]

Ca^{2+}ATPase was inhibited increasingly as Thmx concentration increased in both gill and muscle tissues. The highest inhibitions in the gill and muscle were seen at the LC_{50} dose with rates of 57% and 58%, and the lowest were at the LC_{50}/8 dose with rates of 27% and 13%, respectively. All of these inhibition of Ca^{2+}ATPase activity were statistically significant ($p < 0.05$). Ca^{2+}ATPase is an enzyme that serves to remove calcium (Ca^{2+}) from the cell and is vital in regulating the amount of Ca^{2+} within cells.[97] Inhibition of Ca^{2+}ATPase activity in gill and muscle tissues may be associated with the disruption of the osmoregulation mechanism due to the blockage of the active transport system by Thmx.[98] Additionally, Thmx may have caused inhibition of membrane bound enzymes due to degradation products of lipid peroxidation in the cell membrane by inducing oxidative stress.[99] This may result in disruption of the active transport mechanism due to altered membrane permeability and impaired Ca^{2+}ATPase homeostasis.[98] Similar to our findings, Uçkun and Öz (2020a, 2020b)[51,52] observed that ATPase activities (Na^+K^+ATPase, Mg^{2+}ATPase, Ca^{2+}ATPase) in gill and muscle tissues decreased significantly in a dose-dependent manner in two separate studies in which *A. leptodactylus* applied the fungicides penconazole and azoxystrobin for 96 hours. In our study, the ATPase inhibition rates in the gill were found to be higher than those in the muscle. This decrease is thought to be the result of impairment of ion balance and gill permeability, since it is the first tissue in contact with the pesticide in the aquatic environment. In fish, various toxic substances and ions enter the body by absorption and adsorption by the gill surface, followed by diffusion. Interaction with the membrane may impair the osmotic and ionic regulation of gill tissue by affecting membrane permeability.[93] The reason that responses to biomarkers vary according to the organ is related to the defense capacities of the organs as well as their anatomical location that determines the path and distribution of xenobiotic exposure.[92]

When evaluating the responses of biomarkers, we used IBR analysis to allow combining all parameters into one general stress index (Figure 1). IBR analysis is a useful method that provides a brief information in comparing multiple biomarkers.[100] The IBR index expressing the toxicity caused by Thmx in the hepatopancreas was determined to be the highest at the LC_{50} dose. At the $LC_{50}/2$ and $LC_{50}/4$ doses, the IBR index was found to be close to each other and lower than the LC_{50} dose. Compared to other doses, the lowest IBR index was determined at the $LC_{50}/8$ dose. As can be seen, although hepatopancreas IBR index rised with increasing Thmx dose, it was suppressed compared to control. This may be because the hepatopancreas plays a role in detoxification. In gill and muscle tissues, IBR index was inhibited compared to the control due to increasing Thmx dose. The IBR index was completely suppressed at the LC_{50} dose in both tissues because ATPase inhibitions were highest at this dose. The findings of our study are in line with various studies using the IBR index in the assessment of the effects of environmental pollutants on macroinvertebrate[40], mussel[101] and fish.[102,103]

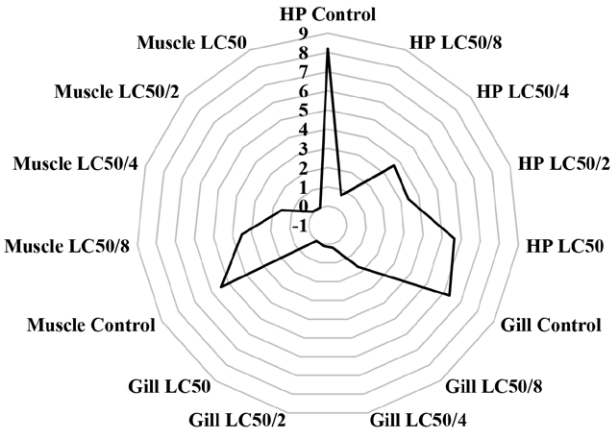

Figure 1. IBR analysis of biomarkers in the hepatopancreas, gill, and muscle.

4. Conclussion

Information on the potential ecotoxicological effects of Thmx with respect to freshwater crustaceans is still limited. In this context, our study has made an important contribution to the literature on the toxic effects of Thmx on non-target organisms. Our study shows that Thmx has significant toxic effects on *A. leptodactylus* even at low concentrations. Therefore we can say that *A. leptodactylus* living in fresh waters close to the agricultural areas where Thmx is used may be under threat. Since almost all of the biomarkers used in our study respond to Thmx administration, we would like to state that these markers are useful in reflecting the acute toxicity of Thmx in crayfish.

Compliance with Ethical Standards

All applicable international, national, and/or institutional guidelines for the care and use of animals were followed. All procedures performed in studies involving animals were in accordance with the ethical standards of the institution or practice at which the studies were conducted.

Conflict of Interest

The authors declare that they have no conflict of interest.

5. References

1. D. Pietrzak, J. Kania, E. Kmiecik, G. Malina, *Chemosphere*. **2020**, 126981. **DOI:**10.1016/j.chemosphere.2020.126981.
2. P. Maienfisch, M, Angst, F. Brandl, W. Fischer, D. Hofer, H. Kayser, W. Kobel, A. Rindlisbacher, R. Senn, A. Steinemann, H. Widmer, *Pest Manag Sci*. **2001a**, *57*, 906–913. **DOI**:10.1002/ps.365.
3. P. Maienfisch, H. Huerlimann, A. Rindlisbacher, L. Gsell, H. Dettwiler, J. Haettenschwiler, E. Sieger, M. Walti, *Pest Manag Sci,* **2001b**, *57*, 165–176. **DOI:**10.1002/1526-4998(200102)57:2<165::AID-PS289>3.0.CO;2-G.
4. C. I. Rumbos, A. C. Dutton, C. G. Athanassiou, *J Stored Prod Res.* **2018**, *75*, 56–63. **DOI:**10.1016/j.jspr.2017.10.004.
5. X. P. Zhao, C. X. Wu, Y. Wang, T. Cang, L. Chen, R. Yu, Q. Wang, *J Econ Entomol*. **2012**, *105*, 92–101. **DOI**:10.1603/EC11259.
6. J. E. Casida, K.A. Durkin. *Chem Biol Interact*. **2013**, *203*, 221–225. **DOI:**10.1016/j.cbi.2012.08.002.
7. M. C. Finnegan, L. R. Baxter, J. D. Maul, M. L. Hanson, *Environ Toxicol Chem*. **2017**, *36*, 2838–2848. **DOI:**10.1002/etc.3846.
8. P. Jeschke, R. Nauen, M, Schindler, A. Elbert, *J Agric Food Chem*. **2011**, *59*, 2897–2908. **DOI:**10.1021/jf101303g.
9. W. J. Zhang, W. Liu, J. Zhang, H. Zhao, Y. Zhang, X. Quan, Y. Jin, *J Environ Sci*. **2012**, *24*, 2019–2027. **DOI:**10.1016/S1001-0742(11)61030-9.
10. C. A. Morrissey, P. Mineau, J. H. Devries, F. Sanchez-Bayo, M. Liess, M. C. Cavallaro, K. Liber, *Environ Int*. **2015**, *74*, 291–303. **DOI:**10.1016/j.envint.2014.10.024.
11. A. R. Main, J. V. Headley, K. M. Peru, N. L. Michel, A. J. Cessna, C. A. Morrissey, *PLoS One* **2014**, *9*, 92821. **DOI:**10.1371/journal.pone.0092821.
12. L. W. Pisa, V. Amaral-Rogers, L. P. Belzunces et al., *Environ Sci Pollut Res Int*. **2015**, *22*, 68–102. **DOI:**10.1007/s11356-014-3471-x.
13. Defra, **2014**. https://secure.fera.defra.gov.uk/pusstats. Accessed 07 Feb 2014.
14. G. Köksal, *Astacus leptodactylus* in Europe. Freshwater Crayfish: Biology, Management and Exploitation, Croom Helm, London. **1988**, 365–400.
15. P. Nyström, Biology of freshwater crayfish. Blackwell Science,

Oxford, UK. **2002,** 192–235.
16. S. P. Zhang, H. Jin, Y. Feng, L. Zhang, J. Lu, *Acta Hydrobiol Sinica*. **2003**, *27*, 496–501
17. P. Alcorlo, M. Otero, M. Crehuet, A. Baltanás, C. Montes, *Sci Total Environ*. **2006**, *366*, 380–390. **DOI:**10.1016/j.scitotenv.2006.02.023.
18. E. Tunca, S. Atasagun, A. Y. Saygı, *Ecology*. **2012,** *21*, 68–76. **DOI:**10.5053/ekoloji.2012.838.
19. G. W. Winston, R. T. Di Giulio, *Aquat Toxicol*. **1991**, *19*, 137–161. **DOI**:10.1016/0166-445X(91)90033-6.
20. R. T. Di Giulio, J. N. Meyer, Reactive oxygen species and oxidative stress. In: Di Giulio RT, Hinton DE, editors. The Toxicology of Fishes. Boca Raton: CRC Press, Taylor and Francis Group. **2008**, 273–324.
21. ASTM E729-96. Standard Guide for Conducting Acute Toxicity Tests on Test Materials with Fishes, Macroinvertebrates, and Amphibians. **2014**.
22. R. L. Anderson. *Environ Entomol*. **1982**, *11*, 1251–1257. **DOI:**10.1093/ee/11.6.1251.
23. B. Leksrisawat, A. S. Cooper, A. B. Gilberts, R. L. Cooper, *J Vis Exp*. **2010**, *45*, 2323. **DOI**:10.3791/2323.
24. M. M. Bradford, *Anal Biochem*. **1976**, *72*, 248–254. **DOI**:10.1016/0003-2697(76)90527-3.
25. W. H. Habig, M. J. Pabst, W. B. Jakoby, *J Biol Chem*. **1974**, *249*, 7130–7139. **DOI**:10.1016/S0021-9258(19)42083-8.
26. E. Cribb, J. S. Leeder, S.P. Spielberg, *Anal Biochem*. **1989**, *183*, 195–196. **DOI**:10.1016/0003-2697(89)90188-7.
27. P. Santhoshkumar, T. Shivanandappa, *Chem-Biol Interact*. **1999**, *119*, 277–282. **DOI**:10.1016/S0009-2797(99)00037-X.
28. J. G. Bell, C. B. Cowey, J. W. Adron, A. M. Shanks, *Br J Nutr*. **1985**, *53*, 149–157. **DOI**:10.1079/bjn19850019.
29. Y. Sun, L. W. Oberley, Y. Li, *Clin Chem*. **1988,** *34*, 497–500. **DOI**:10.1093/clinchem/34.3.497
30. M. S. Moron, J. W. Depierre, B. Mannervik, *Biochim Biophys Acta*. **1979**, *582*, 67–78. **DOI**:10.1016/0304-4165(79)90289-7.
31. Z. A. Placer, L. L. Cushman, B. C. Johnson, *Anal Biochem*. **1966**, *16*, 359–364. **DOI:**10.1016/0003-2697(66)90167-9.
32. G. L. Ellman, D. C. Andres, *Biochem Pharmacol*. **1961**, *7*, 88–95. **DOI**:10.1016/0006-2952(61)90145-9.
33. M. Ozmen, S, E, Dominguez, A, Fairbrother, *Bull Environ Contam Toxicol*. **1998**, *60*, 194–201. **DOI:**10.1007/s001289900610.
34. G. Atlı, M. Canlı, *Ecotoxicology*. **2011**, *20*, 1861–1869. **DOI:**10.1007/s10646-011-0724-z.
35. Atkinson, A. O. Gatemby, A. G. Lowe, *Biochim. Biophys. Acta*. **1973**, *320*, 195–204. **DOI:**10.1016/0304-4165(73)90178-5.
36. M. A. Arzate-Cárdenas, F. Martínez-Jerónimo, *Environmental Toxicology and Pharmacology*, **2012**, *34*, 106–116. **DOI:** https://dx.doi.org/10.1016/j.etap.2012.03.003.
37. V. Korkmaz, A. Güngördü, M. Ozmen, *Ecotoxicol Environ Saf*. **2018**, *160*, 265–272. **DOI:**10.1016/j.ecoenv.2018.05.055.
38. G. C. Barbee, M. J. Stout, *Pest Manag Sci*. **2009**, *65*, 1250–1256. **DOI:**10.1002/ps.1817.
39. E. M. Maloney, C. A. Morrissey, J. V. Headley, K.M. Peru, K. Liber, *Ecotoxicol Environ Safe*. **2018**, *156*, 354–365. **DOI**:10.1016/j.ecoenv.2018.03.003.
40. *Ö. Demirci, K. Güven, D. Asma, S. Öğüt, P. Uğurlu, Ecotoxicol Environ Safe*. **2018,** *147*, 749–758. **DOI:**10.1016/j.ecoenv.2017.09.038.
41. P. Uğurlu, E. Ünlü, E. I. Satar, *Ecotox Environ Safe*. **2015**, *39*, 720–726. **DOI:**10.1016/j.etap.2015.01.013.
42. S. S. Mahnaz, P. Sadegh, *Oceanogr Fish Open Access J*. **2018**, *7*, 555–722. **DOI**:10.19080/OFOAJ.2018.07.555722.
43. Y. Han, T. Liu, J. Wang. C. Zhang, L. Zhu, *Pestic Biochem Phys*. **2016**, *133*, 13–19. **DOI:**10.1016/j.pestbp.2016.03.011.
44. V. V. Husak, N. M. Mosiichuk, J. M. Storey, K. B. Storey, V. I. Lushchak, *Comp Biochem Phys C*. **2017**, *193*, 1–8. **DOI**:10.1016/j.cbpc.2016.12.003.
45. L. Liu, B. Zhu, G. X. Wang. *Environ Sci Pollut Res Int.* **2015**, *22*, 7766–7775. **DOI**:10.1007/s11356-015-4121-7.
46. S. Mukanganyama, C. Figueroa, J. Hasler, H. Niemeyer, *J Insect Physiol*. **2003**, *49*, 223–229. **DOI**:10.1016/s0022-1910(02)00269-x.
47. C. Wang, G. Lu, J. Cui, P. Wang, *Environ Toxicol Pharmacol*. **2009**, *28*, 414–419. **DOI**:10.1016/j.etap.2009.07.005.
48. Sayeed, S. Parvez, S. Pandey, B. Bin-Hafeez, R. Haque, S. Raisuddin, *Ecotoxicol Environ Safe.* **2003**, *56*, 295–301. **DOI**:10.1016/s0147-6513(03)00009-5.
49. E. O. Oruç, *Pestic Biochem Physiol*. **2010**, *96*, 160–166. **DOI**:10.1016/j.pestbp.2009.11.005.
50. S. Moreira, M. Moreira-Santos, J. Rendón-von Osten, E. M. Silva, R. Ribeiro, L. Guilhermino, A.M.V.N. Soares, *Ecotoxicol Environ Safe*. **2010**, *73*, 893–899. **DOI**:10.1016/j.ecoenv.2010.04.007.
51. A. Uçkun, Ö. B. Öz, *Environ Sci Pollut Res.* **2020a**, *27*, 35626–35637. **DOI**:10.1007/s11356-020-09595.
52. A. Uçkun, Ö. B. Öz, *Drug Chem Toxicol.* **2020b**. **DOI**:10.1080/01480545.2020.1774604.
53. R. Van der Oost, J. Beyer, N. P. Vermeulen, *Environ Toxicol Phar*. **2003**, *13*, 57–149. **DOI**:10.1016/S1382-6689(02)00126-6.
54. T. Szkudelski, *Physiol Res*. **2001**, *50*, 537–546. **DOI**:10.1177/014833101050003101
55. N. Lenfant, T. Hotelier, E. Velluet, Y. Bourne, P. Marchot, A. Chatonnet, *Nucleic Acids Res*. **2013**, *41*, D423–9. **DOI:**10.1093/nar/gks1154.
56. J. Lian, R. Nelson, R. Lehner. *Protein Cell*. **2018**, *9*, 178–195. **DOI**:10.1007/s13238-017-0437-z.
57. T. Satoh, M. Hosokawa, *Chem-Biol Interact*. **2006**, *162*, 195–211. **DOI:**10.1016/B978-012088523-7/50017-X.
58. M. K. Ross, J. A. Crow, *J Biochem Mol Toxicol*. **2007,** *21*,187–96. **DOI:**10:1002/jbt.20178.
59. H. Ozaki, K. Sugihara, Y. Watanabe, K. Moriguchi, N. Uramaru, T. Sone, S. Ohta, S. Kitamura, *Food Chem Toxicol*. **2017**, *100*, 217–224. **DOI**:10.1016/j.fct.2016.12.019.
60. D. L. Denton, C. E. Wheelock, S. Murray, L. A. Deanovic, B. D. Hammock, D. E. Hinton, *Environ Toxicol Chem*. **2003**, *22*, 336–341. **DOI**:10.1002/etc.5620220214.
61. C. E. Wheelock, K. J. Eder, I. Werner, H. Huang, *Aquat Toxicol*. **2005,** *74*, 172–192. **DOI**:10.1016/j.aquatox.2005.05.009.
62. Moreno, S. Pichardo, L. Góomez-Amores, A. Mate, C. M. Vazquez, A. M. Cameán, *Toxicon*. **2005**, *45*, 395–402.

DOI:10.1016/j.toxicon.2004.11.001.
63. K. S. El-Gendy, N. M. Aly, F. H. Mahmoud, A. Kenawy, A. K. H. El-Sebae, *Food Chem Toxicol*. **2010**, *48*, 215–221. **DOI**:10.1016/j.fct.2009.10.003.
64. M. L. Ballesteros, D. A. Wunderlin, M. A. Bistoni, *Ecotoxicol Environ Saf*. **2009**, *72*, 199–205. **DOI**:10.1016/j.ecoenv.2008.01.008.
65. S. M. Yonar, M. Ş. Ural, S. Silici, M. E. Yonar, *Ecotoxicol Environ Safe*. **2014**, *102*, 202–209. **DOI**:10.1016/j.ecoenv.2014.01.007.
66. J. Blahova, L. Plhalova, M. Hostovsky, L. Divišová, R. Dobšíková, I. Mikulíková, S. Šteˇpánová, Z. Svobodová, *Food Chem Toxicol*. **2013**, *61*, 82–85. **DOI**:10.1016/j.fct.2013.02.041.
67. H. Kappus, Lipid peroxidation: Mechanisms, analysis, enzymology and biological relevance. In: Oxidative Stress, London: Academic Press. **1985**, 273–310. **DOI**:10.1016/B978-0-12-642760-8.50016-8
68. A. Doyotte, C. Cossu, M. C. Jacquin, M. Babut, P. Vasseur, *Aquat Toxicol*. **1997**, *39*, 93–110.
69. E. Ö. Oruç, D. Usta, *Environ Toxicol Pharmacol*. **2007**, *23*, 48–55. **DOI**:10.1016/j.etap.2006.06.005.
70. İ. Celik, H. Suzek, *Ecotoxicol Environ Saf*. **2009**, *72*, 905–908. **DOI**:10.1016/j.ecoenv.2008.04.007.
71. L. Zhu, X. Dong, H. Xie, J. Wang, J. Wang, J. Su, C. Yu, *Environ Toxicol.* **2011**, *26*, 480–488. **DOI:**10.1002/tox.20575.
72. L. Gate, J. Paul, G. N. Ba, K. D. Tew, H. Tapiero, *Biomed Pharmacother*. **1999**, *53*, 169–180. **DOI:**10.1016/S0753-3322(99)80086-9.
73. C. C. C. Cheung, G. J. Zheng, A. M. Y. Li, B. J. Richardson, P. K. Lam, *Aquat Toxicol*. **2001**, *52*, 189–203. **DOI:**10.1016/s0166-445x(00)00145-4.
74. Venturino, O. L. Anguiano, L. Gauna, C. Cocca, R. M. Bergoc, A. M. P. D'Angelo, *Comp Biochem Physiol C Toxicol Pharmacol*. **2001**, *130*, 191–198. **DOI:**10.1016/S1532-0456(01)00241-1.
75. A. Ferrari, A. Venturino, A. M. P. de D'Angelo, *Pestic Biochem Physiol*. **2007**, *88*, 134–142. **DOI**:10.1016/j.pestbp.2006.10.005.
76. O. Serdar, N. C. Yildirim, S. Tatar, N. Yildirim, A. Ogedey, *Environ Sci Pollut Res*. **2018**, 1–7. **DOI**:10.1007/s11356-018-1491-7.
77. N. C. Yildirim, M. Tanyol, N. Yildirim, O. Serdar, S. Tatar, *Ecotoxicol Environ Safe*. **2018**, *156*, 41–47. **DOI**:10.1016/j.ecoenv.2018.02.059.
78. O. Serdar, *Environ Sci Pollut Res.* **2019**, *26*, 1905–1914. **DOI:**10.1007/s11356-019-04629-w.
79. E. O. Oruç, Y. Sevgiler, N. Uner, *Comp Biochem Physiol C*. **2004**, *137*, 43–51. **DOI**:10.1016/j.cca.2003.11.006.
80. D. A. Monteiro, J. A. Almeida, F. T. Rantin, A. L. Kalinin, *Comp Biochem Physiol Part C*. **2006**, *143*, 141–149. **DOI:**10.1016/j.cbpc.2006.01.004.
81. F. Regoli, M. Nigro, E. Orlando. *Aquat Toxicol*. **1998**, *40*, 375–392. **DOI:**10.1016/S0166-445X(97)00059-3.
82. J. Wang, W. Ge, S. Yan, L. Zhu, A. Chen, J. Wang, *J Agric Food Chem*. **2015,** *63*, 1856–1862. **DOI**:10.1021/jf504895h.
83. S. Shukla, R. C. Jhamtani, M. S. Dahiya, R. Agarwal, *Toxicol Rep*. **2017**, *4*, 240–244. **DOI**:10.1016/j.toxrep.2017.05.002.
84. M. Kaur, R. Jindal, *MOJ Biol Med*. **2017**, *1*, 103–112. **DOI**:10.15406/mojbm.2017.01.00021
85. M. B. Colovic, D. Z. Krsti, T. D. Lazarevic-Pasti, A. M. Bondzic, V. M. Vasi, *Curr. Neuropharmacol*. **2013**, *11*, 315–335. **DOI**:10.2174/1570159X11311030006.
86. S. Saraiva, R. A. Sarmento, A. C. M. Rodrigues, D. Campos, G. Fedorovac, V. Žlábek, C. Gravato. J. L. T. Pestana, A. M. V. M. Soares *Ecotoxicol Environ Safe.* **2017**, *137*, 240–246. **DOI**:10.1016/j.ecoenv.2016.12.009.
87. F. Dondero, A. Negri, L. Boatti, F. Marsano, F. Mignone, A. Viarengo, 2010. *Sci Total Environ*. **2010**, *408*, 3775–3786. **DOI**:10.1016/j.scitotenv.2010.03.040.
88. H. M. V. S. Azevedo-Pereira, M. F. L. Lemos, A. M. V. M. Soares, 2011. *Water Air Soil Pollut*. **2011**, *219*, 215–224. **DOI**:10.1007/s11270-010-0700-x.
89. M. Mörtl, A. Vehovszky, S. Klátyik, E. Takács, J. Győri, A. Székács, *Int J Environ Res Public Health*. **2020**, *17*, 2006. **DOI**:10.3390/ijerph17062006.
90. K. Takao, *Physiol Rev*. **1985,** *65*, 467. **DOI**:10.1152/physrev.1985.65.2.467.
91. T. Clausen, *Physiol Rev*. **2003**, *83*, 1269–1324. **DOI:**10.1152/physrev.00011.2003.
92. G. Begum, *Fish Physiol Biochem*. **2011**, *37*, 61–69. **DOI**:10.1007/s10695-010-9417-4.
93. M. David, J. Sangeetha, E. R. Harish, J. Shrinivas, V. R. Naik, *Int J Pure Appl Zool*. **2014**, *2*, 175–181.
94. G. Balaji, M. Nachiyappan, R. Venugopal. *World J Zool*. **2015**, *10*, 168–174. **DOI**:10.5829/idosi.wjz.2015.10.3.9581.
95. Ö. Temiz, H. Y. Çoğun, F. Kargın, *Fresen Environ Bull.* **2018**, *27*, 5027–5032.
96. T. A. Kumosani, *JKAU Sci*. **2005**, *17*, 143–152. **DOI**:10.4197/Sci.17-1.15.
97. P. Gmaj, H. Murer, *Physiol Rev*. **1986**, *66*, 36–70. **DOI:**10.1152/physrev.1986.66.1.36.
98. N. P. Okolie, K. Audu, *J Biomed Scien*. **2004**, *3*, 37–44. **DOI**:10.4314/jmbr.v3i1.10654.
99. S. Daya, R. B. Walker, S. Anoopkumar-Dukie, *Metab Brain Dis*. **2000**, *15*, 203–210. **DOI**:10.1007/BF02674529.
100. Venturino, E. Rosenbaum, A. Caballero, O. Anguiano, Biomarkers. **2003**, *8*, 167–186. **DOI:**10.1080/1354700031000120116.
101. S. J. Brooks, C. Harman, M. T. Hultman, J. A. Berge, *Science and Total Environment,* **2015**, *524*, 104–114. **DOI**:10.1016/j.scitotenv.2015.03.135.
102. Z. H. Li, J. Velisek, V. Zlabek, R. Grabic, J. Machova, J. Kolarova, P. Li, T. Randak, *J. Hazard. Mater.* **2011**, *185*, 870–880. **DOI:**10. 1016/j.jhazmat.2010.09.102.
103. T. Suman, S. R. R. Rasajree, R. Kirubagaran, *Ecotoxicol. Environ. Saf.* **2015**, *113*, 23–30. **DOI**:10.1016/j.ecoenv.2014.11. 015.

Povzetek

Tiametoksam (Thmx) je globalno razširjen neonikotinoidni pesticid, ki onesnažuje sladkovodne ekosisteme in katerega ostanke so zaznali v ribiških proizvodih. *Astacus leptodactylus* je priljubljen sladkovodni rak, ki ga gojijo in izvažajo v mnogih državah. V okviru raziskave smo preučevali akutne toksične učinke Thmx na *A. leptodactylus* z uporabo različnih biomarkerjev (acetilholinesteraza, karboksilesteraza, glutation S-transferaza, glutation, superoksidna dismutaza, glutation peroksidaza, glutation reduktaza in adenozintrifosfataze). 96-urna vrednost LC_{50} Thmx je bila izračunana kot 8.95 mg aktivne učinkovine L^{-1}. Ko se je odmerek Thx povečeval, je oksidativni stres povzročil inhibicijo/ aktivacijo antioksidativnih encimov, medtem ko so bile aktivnosti acetilholinesteraze, karboksilesteraze in adenozintrifosfataz inhibirane. Posledično lahko rečemo, da Thmx izkazuje močno toksične učinke na rake, zato so ti na območjih, kjer se ta pesticid uporablja, ogroženi.

DOI: 10.17344/acsi.2021.6961 *Acta Chim. Slov.* **2018,** *65,* 532–540

Scientific paper

A Novel Tetranuclear Silver Compound with bis(3,5-dimethylpyrazol-1-yl)acetate: a Simple Synthesis Yielding Complex Crystal Structure

Marta Počkaj and Nives Kitanovski*

Faculty of Chemistry and Chemical Technology, University of Ljubljana, Večna pot 113, SI-1000 Ljubljana, Slovenia.

** Corresponding author: E-mail: nives.kitanovski@fkkt.uni-lj.si.*

Received: 05-21-2021

Abstract

A novel tetranuclear silver coordination compound with the formula $[Ag_4(bdmpza)_4]\cdot 10H_2O$ (bdmpza = bis(3,5-dimethylpyrazol-1-yl)acetate) was synthesized by a reaction between an aqueous solution of silver nitrate and an aqueous solution prepared by bis(3,5-dimethylpyrazol-1-yl)acetic acid and potassium hydroxide (1:1 molar ratio). The obtained compound was characterized by elemental analysis, coupled thermogravimetric–mass spectrometry analysis, vibrational IR spectroscopy, and its crystal structure was determined by single-crystal X-ray diffraction method. Furthermore, the obtained crystal structure was additionally evaluated by Hirshfeld surface analysis.

Keywords: coordination chemistry; silver; bis(3,5-dimethylpyrazol-1-yl)acetate; crystal structure; Hirshfeld surface analysis.

1. Introduction

Due to the modelling of active sites of some zinc enzymes, and of active sites of the non-heme iron enzymes, which are required in oxygen activation, diverse tripodal heteroscorpionate *N*,*N*,O ligands have been prepared in last decades. Such type of compounds can serve as suitable structural mimics for the facial 2-His-1-carboxylate triad, since they express high binding affinity to occupy a trigonal face of coordination polyhedron.[1-4] Numerous compounds based on bis(pyrazol-1-yl)acetate with pyrazolyl rings substituted at 3 and 5 positions are reported.[5]

The scarcity of suitable *N*,*N*,O-triple ligands initially led to model compounds with *N*,*N*,*N*-binding sites. First *N*,*N*,*N*-tris(pyrazolyl)borate-complexes were reported by Trofimenko in the late 1970s.[6] In 1999, the first two compounds, lithium and niobium, with bis(3,5-dimethylpyrazol-1-yl)acetate (bdmpza) were published.[7] Crystal structure of bis(pyrazol-1-yl)acetic acid (Hbpza) and its synthetic route, as well the synthesis of bis(3,5-dimethylpyrazol-1-yl)acetic acid (Hbdmpza), were reported two years later.[5,8] So far, variety of mono, di-, tetra- and hexanuclear metal complexes with bis(3,5-dimethylpyrazol-1-yl) acetate have been reported.[4,7,9–13] Among all the described compounds, formed by the routes with bis(3,5-dimethylpyrazol-1-yl)acetic acid, only two complexes are known in which the acetate group is not deprotonated, $[Cu(Hbdmpza)_2](HSO_4)_2$ and $[Cu(Hbdmpza)_2]Cl_2$. Two Cu(II) compounds with methyl ester acetate group were previously published as well.[14,15]

On the other hand, silver is known to be bioactive and this property is widely exploited in different everyday products as well as in medical devices, especially when in form of nano- or colloidal silver or different binary silver compounds. For this reason the research on the coordination chemistry of silver(I) has increased dramatically in last decades, and it became widely known that silver complexes with oxygen and nitrogen atoms exhibit different antimicrobial activities among others.[16, 17] Furthermore, the silver(I) complexes have found different applications in material science for their structural diversity originating from a d^{10} electron configuration which allows the formation of different coordination geometries and represent a foundation for construction of supramolecular frameworks.[18,19,20]

Herein we report the crystal structure of first silver coordination compound with bdmpza ligands. The compound was also characterized by Hirshfeld surface analysis, coupled thermogravimetric–mass spectrometry analysis and infrared spectroscopy.

2. Experimental

2. 1. Materials and Physical Measurements

All reagents and chemicals were purchased from commercial sources and used without further purification. Bis(3,5-dimethylpyrazol-1-yl)acetic acid was synthesized as reported previously.[5] An aqueous solution of bis(3,5-dimethylpyrazol-1-yl)acetate was prepared by bis(3,5-dimethylpyrazol-1-yl)acetic acid and sodium hydroxide in 1:1 molar ratio.

CHN elemental analyses were performed with a PerkinElmer 2400 CHN Elemental Analyzer. The infrared spectra were measured on solid samples using a Perkin-Elmer Spectrum 100 series FT-IR spectrometer equipped with an ATR sampling accessory.

Coupled thermogravimetric–mass spectrometry analysis (TG-MS) measurements were performed on a Mettler Toledo TGA/DSC1 instrument under dynamic flow of argon. Around 1.2 mg of the sample was put into 150 μL platinum crucible and heated from 25 °C to 700 °C with a heating rate of 10 K min^{-1}. Evolved gases were introduced into Balzers ThermoStar mass spectrometer via 75 cm long heated capillary. To lower the water content in the mass spectrometer, the sample was kept at 25 °C for 15 min at the beginning of the mesurement. Blank curve was subtracted.

2. 2. Synthesis

To the aqueous solution of silver nitrate, $AgNO_3$, (0.10 mmol, i.e. 1.0 mL of 0.10 M solution) 1.0 mL of the aqueous solution prepared of bis(3,5-dimethylpyrazol-1-yl)acetic acid (0.040 mmol) and potassium hydroxide (0.040 mmol) was added. The obtained precipitate was filtered off and colourless solution was left in a closed beaker, wrapped in aluminium foil, in the dark space, to prevent reduction of Ag(I) to elemental silver. The colourless prismatic crystals which are also light-sensitive appeared in 17 days. Yield: 3.68 mg (23%). Anal. Calcd. for $C_{48}H_{80}Ag_4N_{16}O_{18}$: C, 36.02%; H, 5.04 %; N, 14.00%. Found: C, 35.87%; H, 5.19 %; N, 14.21%. ν_{max}: 3180 (vw ν(OH), 1651(vs, ν_{as}(OCO)), 1614 (vs, ν_{as}(OCO)), 1556 (s, ν(CN), 1463 (m, ν(CN), 1443 (m), 1417 (s, ν(CC)), 1384 (m), 1345 (vs, ν_s(OCO)), 1327 (vs), 1299 (m), 1255 (v, ν_s(OCO)), 1146 (w), 1113 (w), 1034 (s), 896 (w), 875 (s), 801 (s), 768 (ws), 711 (s), 650 (w), 626 (w), 618 (w).

2.3. X-Ray Crystallography

For X-ray structural analysis, single crystal of the title compound was surrounded by silicon grease, mounted onto the tip of glass fibre and transferred to the goniometer head in the liquid nitrogen cryostream. Data were collected on a SuperNova diffractometer equipped with Atlas detector using *CrysAlis* software and monochromated Mo Kα radiation (0.71073 Å) at 150 K.[21] The initial structural model was obtained via direct methods using the *SIR*97 structure solution program.[22] A full-matrix least-squares refinement on F^2 magnitudes with anisotropic displacement parameters for all nonhydrogen atoms using *SHELXL*-2018/3 was employed.[23] All H atoms were initially located in difference Fourier maps; those residing on C-atoms were further treated as riding on their parent atoms with C(aromatic)–H distance and C(methyl)-H distances of 0.95 and 0.98 Å, respectively. On the other hand, the hydrogen atoms bonded to oxygen atoms were refined in the beginning and due to unstable refinement, they were treated using AFIX 3 command at the very last refinement cycles. Details on crystal data, data collection and structure refinement are given in Table 1. Figures depicting the structures were prepared with *Mercury*.[24]

Table 1. Crystal data, data collection and refinement.

Crystal data	
Formula	$C_{48}H_{80}Ag_4N_{16}O_{18}$
M_r	1600.76
Cell setting, space group	Triclinic, *P*–1
a (Å)	10.8581(4)
b (Å)	12.6003(6)
c (Å)	12.9796(5)
α (°)	72.307(4)
β (°)	89.235(3)
γ (°)	71.190(4)
V (Å^3)	1594.39(12)
Z	1
D_x (Mg m^{-3})	1.667
μ (mm^{-1})	1.288
F(000)	812
Crystal form, colour	Prism, colourless
Crystal size (mm^3)	0.4x0.3x0.3
Data collection	
T (K)	150(2)
No. of measured, independent and observed reflections	14694, 8314, 6539
R_{int}	0.0293
Refinement	
R (on F_{obs}), *wR* (on F_{obs}), *S*	0.0340, 0.0646, 1.060
No. of contributing reflections	8314
No. of parameters	406
No. of restraints	0
$\Delta\rho_{max}$, $\Delta\rho_{min}$ (eÅ^{-3})	0.754, −0.906

$R = \Sigma||F_o| - |F_c||/\Sigma|F_o|$; $wR_2 = \{\Sigma[w(F_o^2 - F_c^2)^2]/\Sigma[w(F_o^2)^2]\}^{1/2}$; $S = \{\Sigma[w(F_o^2 - F_c^2)^2]/(n - p)\}^{1/2}$ where *n* is the number of independent reflections and *p* is the total number of parameters refined.

2. 3. Hirshfeld Surface Analysis

To study intermolecular interactions in the title compound, the Hirshfeld surface analyses were performed using Crystal Explorer, both based on the results of previous single crystal X-ray diffraction study.[25,26] The Hirshfeld surfaces were plotted over three quantities: a) d_{norm},

plotted in red-white-blue colour code, representing shorter/close to the sum of van der Waals radii/longer contacts between the molecules, b) curvedness and c) shape index, in which red areas represent hollows and blue areas represents bumps. Additionally, the full and resolved 2D fingerprint plots that show distances from each point on the Hirshfeld surface to the nearest atom inside (d_i) and outside (d_e) of it were calculated.

3. Results and Discussion

3. 1. Crystal Structure

The tetranuclear molecule, $[Ag_4(bdmpza)_4]$ (Fig. 1), is surrounded by ten solvent water molecules. The asymmetric unit consists of half of the coordination moiety and five water molecules, while the other half is formed by an inversion centre. Two of symmetry independent bdmpza ligands are coordinated in different manners. The first bdmpza ligand acts as a tetradentate ligand and thus fulfils its binding potential coordinating *via* its both nitrogen atoms and both oxygen atoms from deprotonated carboxylate group. Such tetradentate coordination of bdmpza ligand is observed very rarely, only in four crystal structures where the bdmpza is coordinated to two different metal centres.[27,28] Contrary to the first bdmpza ligand, the second bdmpza ligand is bound tridentately *via* both of its N-atoms and additional O from deprotonated carboxylate group; such tridentate coordination of bdmpza is prevalent, it appears in more than 90% of crystal structures with bdmpza in a role of ligand.[9]

As a consequence of the described coordination modes of bdmpza ligands, both symmetry independent silver ions are coordinated differently (the relevant bonds and angles around the metal centres are given in Table 2). Ag1 is coordinated with four nitrogens, a pair from each of the two bdmpza ligands, possessing a seesaw geometry as indicated τ_4 value of 0.523.[29] In other words, the geometry around Ag1 is somewhere between the ideal tetrahedral and square planar geometries (the value of 0.497 for τ_4' does not completely confirm the intermediate seesaw geometry).[30] It is worth mentioning that the fourth nitrogen atom (N7) is further away than the previous three (N1, N3, N5) and thus close to the upper limit of such contacts. Therefore, such coordination environment of Ag1 might also be described as trigonal with additional contact (i.e. 3+1) but usually, despite of the significant difference in bondlegths, such coordination number is still considered to be four. The longest bond can be regarded as secondary and still important coordination interaction. Such situation often occurs when multidentate ligands with limited flexibility are present.[31–33]

On the other hand, Ag2 is coordinated with three oxygen atoms each from one of three different bdmpza ligands and one nitrogen atom further away. The relevant τ_4 and τ_4' values are 0.683 indicating severely distorted tetrahedral geometry around Ag2. The coordination sphere of Ag2 is accomplished by Ag2' obtained by inversion centre which is positioned in between them. Additionally, Ag2 and Ag2' are bridged by two carboxylate bridges, bringing both atoms to the distance of 2.9062(4) Å which represents very strong argentophilic interaction.[34,35]

Although the tetrasilver compounds are frequent in coordination chemistry of silver(I), such tetrasilver cluster $Ag_4O_6N_8$ as found in the title compound has not been observed yet.[9] The same holds true for the presence of tetradentately and tridentately coordinated bdmpza ligand: to the best of our knowledge, the title compound is the first that contains bdmpza ligands ligated in both manners to the metal centre.

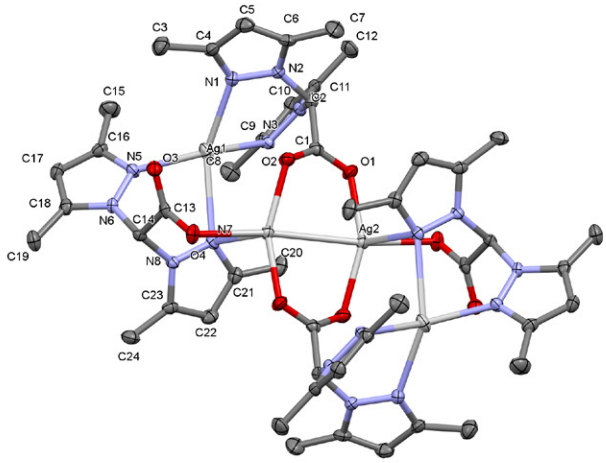

Figure 1. ORTEP representation of tetranuclear coordination molecules $[Ag_4(bdmpza)_4]$. Only the atoms in the asymmetric unit are labeled. The thermal ellipsoids are given at 30% probability level while hydrogens and water molecules are omitted for clarity. The strong argentophilic interaction between Ag2 and its symmetry equivalent is also shown.

Table 2. Selected bond lengths and angles (Å, °) for the title compound.

Ag1–N1	2.368(2)	N1–Ag1–N3	80.55(8)
Ag1–N3	2.311(2)	N1–Ag1–N5	122.41(8)
Ag1–N5	2.199(2)	N1–Ag1–N7	147.30(7)
Ag1–N7	2.622(2)	N3–Ag1–N5	139.02(8)
Ag2–O1^i	2.229(2)	N3–Ag1–N7	97.54(7)
Ag2–O2^i	2.245(2)	N5–Ag1–N7	80.02(7)
Ag2–O4^i	2.380(2)	O1–Ag2–O2^i	154.34(8)
Ag2–N7^i	2.582(2)	O1–Ag2–O4^i	88.75(7)
Ag2–Ag2^i	2.9062(4)	O1–Ag2–N7^i	106.73(7)
		O2^i–Ag2–O4^i	109.32(7)
		O2^i–Ag2–N7^i	95.48(7)
		O4^i–Ag2–N7^i	76.27(7)
		O1–Ag2–Ag2^i	82.51(5)
		O2^i–Ag2–Ag2^i	77.89(5)
		O4^i–Ag2–Ag2^i	170.51(4)
		N7^i–Ag2–Ag2^i	109.75(5)

Symmetry codes: (*i*) –*x*+1, –*y*, –*z* +1.

Molecular entities in the title crystal structure are intensely connected with hydrogen bonds (Table 3, Figs. 2 and 3). The O-H···O hydrogen bonds strongly dominate and connect either coordination clusters with water molecules or water molecules with adjacent water molecules. As shown in Fig. 2, the O-H···O interactions lead to the formation of characteristic five-membered ring defined by oxygen atoms which are further connected and as a consequence, parallel zig-zag chains of interchanging water and coordination molecules are formed as shown in Fig. 3. These are further connected by C-H···O interactions. Note that in Table 3 only the hydrogen bonds compliant with classical criteria, i.e. D–H···A angle > 110 °, O···O distance < 3.04 Å and C···O distance < 3.22 Å are given. Additional C-H···O interactions are present between the zig-zag chains, for which the C···O distances are significantly larger than the sum of van der Waals radii. Such bonds are between two neighbouring coordination molecules (C19···O4^{i}, 3.402(3) Å) and between coordination and water molecules (C2···O5w^{iv}, 3.258(4) Å; C24···O2w^{v}, 3.521(3) Å); the corresponding symmetry codes are as given under Table 3.

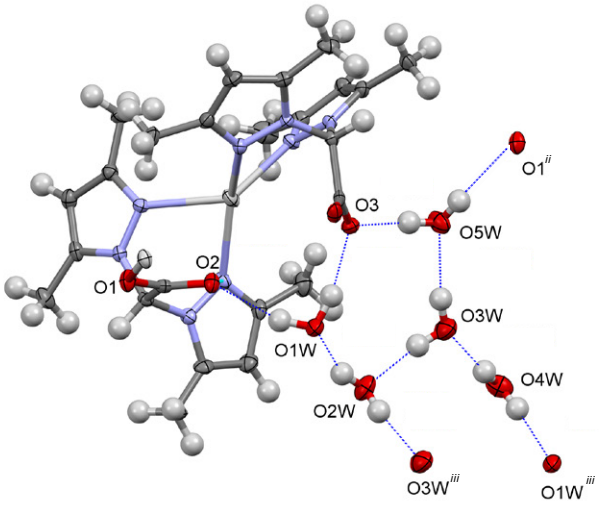

Figure 2. A branched hydrogen bond network around the asymmetric unit; for clarity, only H-bonds in an asymmetric unit are shown.

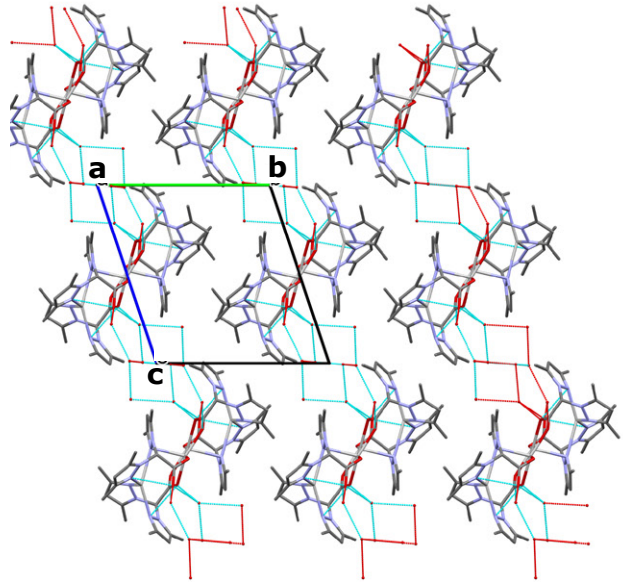

Figure 3. A view down *a* axis on crystal packing. O–H···O hydrogen bonds between water-water or water-coordination molecule lead to the formation of parallel zig-zag chains. Hydrogen atoms and C-H···O interactions are omitted for clarity.

3. 2. Hirshfeld Surface Analysis

To additionally evaluate the intermolecular interactions in the crystal structure, Hirshfeld surface (HS) analysis was used. Fig. 4a represents Hirshfeld surface of tetranuclear coordination molecule mapped over d_{norm} in a range from −0,6379 to +1.6617 arbitrary units. The intense red spots in the vicinity of oxygens and hydrogens indicate donors and acceptors of O–H···O interactions, i.e. hydrogen bonds between coordination molecule and adjacent water molecules. HS mapped over curvedness and shape index (Figs. 4b and 4c) indicate the absence of broad

Table 3. Hydrogen bond geometry in $C_{48}H_{80}Ag_4N_{16}O_{18}$.

D–H···A	D–H (Å)	H···A (Å)	D···A (Å)	D–H···A (°)	Symmetry code of A
C14–H14···O4	1.00	2.30	3.129(3)	139.7	*i*
O1W–H1WA···O2	0.92	2.06	2.903(3)	152.3	–
O1W–H1WB···O3	0.91	1.97	2.834(3)	156.6	–
O5W–H5WB···O1	0.86	2.13	2.953(3)	160.2	*ii*
O5W–H5WA···O3	0.86	1.91	2.750(3)	166.6	–
O2W–H2WB···O1W	0.89	1.98	2.822(3)	158.3	–
O2W–H2WA···O3W	0.89	1.98	2.857(3)	168.9	*iii*
O3W–H3WA···O2W	0.84	1.97	2.784(4)	161.1	–
O3W–H3WB···O5W	0.86	2.02	2.872(3)	167.4	–
O4W–H4WA···O3W	0.87	2.08	2.949(3)	173.2	–
O4W–H4WB···O1W	0.84	2.14	2.971(3)	170.0	–

iii Symmetry codes: (*i*) −*x*+2, −*y*, −*z* +1; (*ii*) *x*+1, *y*, *z*; (*iii*) −*x*+2, −*y*, −*z*; (*iv*) *x*−1, *y*, *z*; (*v*) *x*, *y*, *z*+1. Note that symmetry codes (*iv*) and (*v*) refer to the information in text.

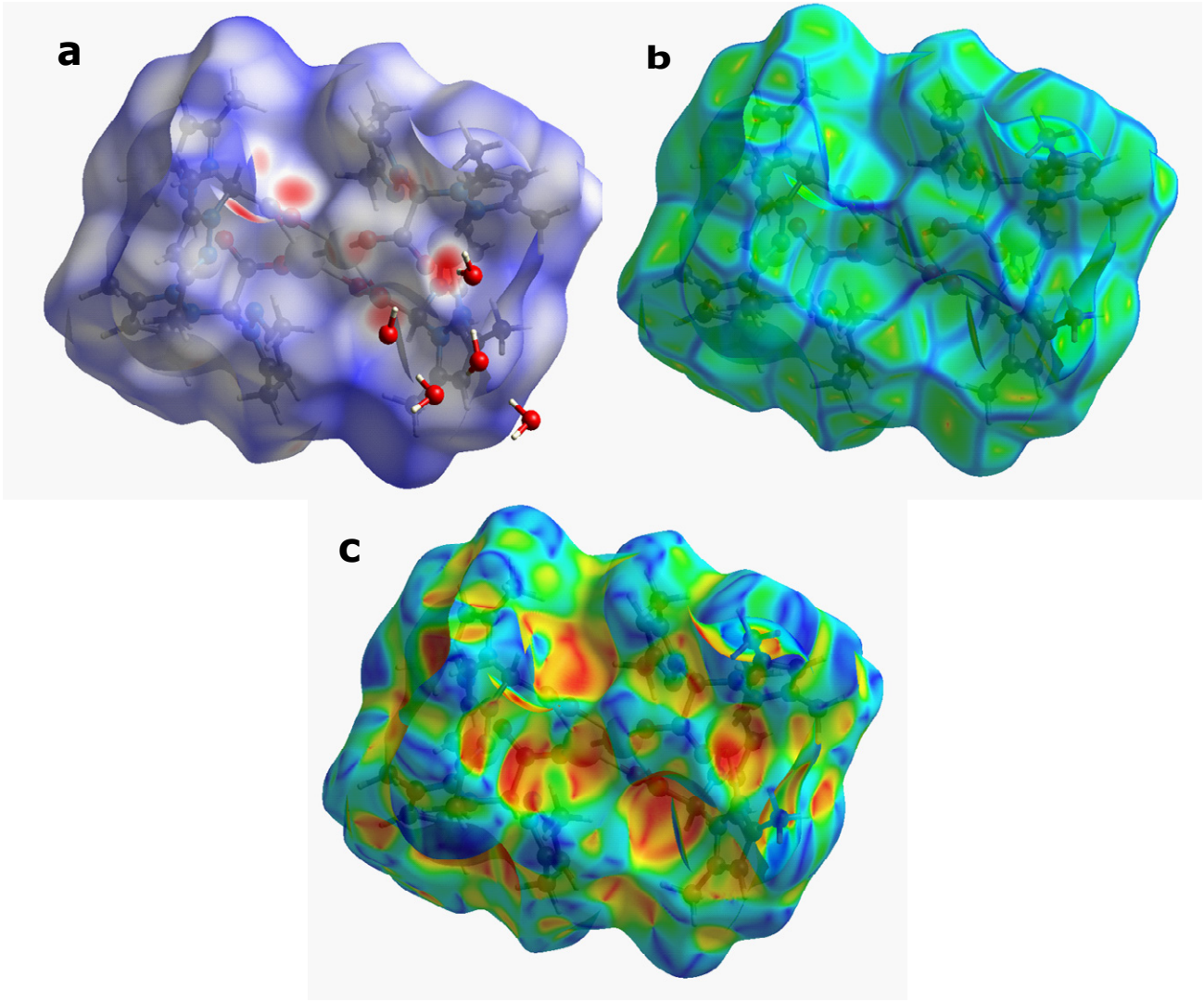

Figure 4. Hirshfeld surface of coordination molecule $[Ag_4(bdmpza)_4]$; a) plotted over d_{norm} in the range from −0,6379 to +1,6617 a. u., together with the adjacent water molecules, b) plotted over curvedness (range from −4.000 to 0.4000), and c) plotted over shape-index (range from −1.000 to 1.000).

flat regions that disable planar stacking of the coordination molecules, and also show the bumps and hollows to represent the touching of the molecules.

Additionally, selected 2D fingerprint plots for the coordination molecules are shown in Fig. 5, i.e. for all contacts as well as for individual H···H, O···H / H···O, C···H / H···C and N···H / H···N contacts, whose percentage to the total Hirshfeld surface area is also given. These contacts comprise more than 99% of the HS area; the other two minor contributions are from C···O / O···C and Ag···H / H···Ag contacts. The H···H interactions are in the middle of the scattered points in the 2D fingerprint plots with an overall contribution of 60.8% (Fig. 5b). Two sharp spikes at $d_i + d_e$ at ~1.8 and 2.1 Å, respectively, represent the reciprocal O···H / H···O interactions (Fig. 5c) contributing 18.4% to the total HS. C…H/H…C and N…H/H…N interactions appear as broad shoulders at $d_i + d_e$ around 2.6 Å (Figs. 5d and 5e).

3. 3. Coupled Thermogravimetric–Mass Spectrometry Analysis

The TG curve of the title compound in argon flow shows two-step thermal degradation and a total mass loss of 68.58%. The mass loss starts at room temperature and ends at about 400 °C and proceeds in two distinctive steps as observed in Fig. 6. The first step starts already at the beginnig of isothermal measurement at 25 °C and ends at around 80 °C with 10.49% mass loss. The observed mass loss correpsonds to the dehydration (calc. 11.25%). At the end of this step small signal m/z = 18 was detected in mass spectrometer, confirming dehydration. Since at the beginnig of the measureument there is high water content in the system, signals due to water evolution are relatively low. The second mass loss step of 58.09% from 150–400 °C represents the thermal decomposition of four bdmpza ligands; during this step evolution of CO_2 (m/z = 44) and

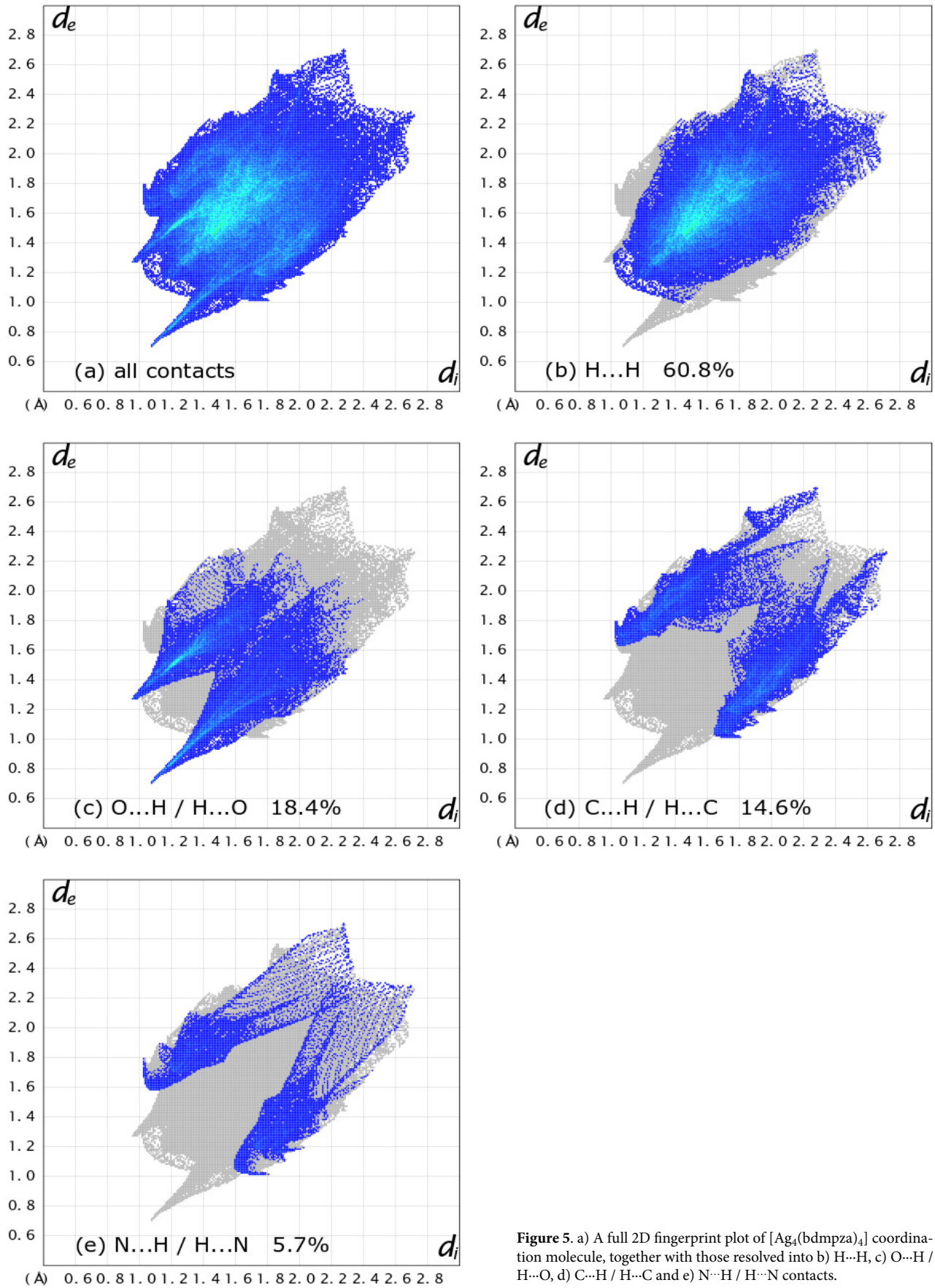

Figure 5. a) A full 2D fingerprint plot of $[Ag_4(bdmpza)_4]$ coordination molecule, together with those resolved into b) H···H, c) O···H / H···O, d) C···H / H···C and e) N···H / H···N contacts.

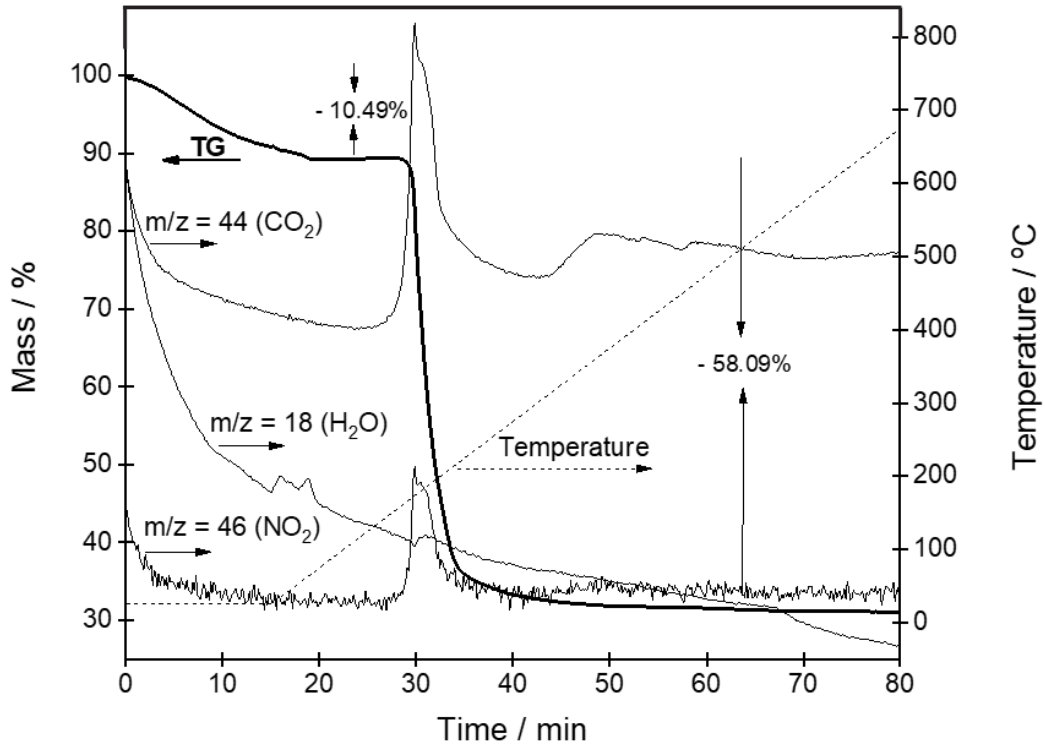

Figure 6. Coupled TG-MS curves of the title compound.

NO_2 (m/z = 46) was detected. For complete removal of bdmpza during this step the theoretical mass loss would be 61.79% of the initial mass. However, as different oxidizing products are formed during this step, the residue after the thermal treatment is Ag_2O. The mass of solid residue represents 31.42% of the starting mass which is in accordance with the theoretically expected (28.96%).

3. 4. Infrared Spectroscopy

In the infrared spectrum (Fig. 7) bands belonging to the vibrations of water molecules and bdmpza ligand can be assigned. The weak broad band at approx. 3200 cm^{-1} can be attributed to the O–H stretching in water molecules. The broadness of the band confirms the intense participation of such bonds in the hydrogen bond

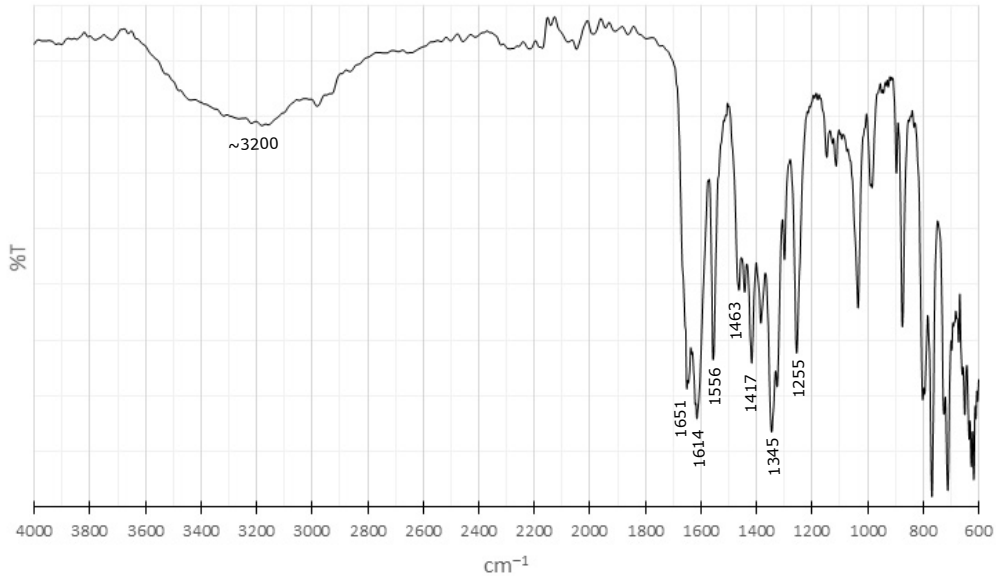

Figure 7. Vibrational IR spectrum of the title compound.

network. Since carboxylate groups of bdmpza ligand are coordinated to metal centers in two different modes, two pairs of bands belonging to the (OOC) stretching vibrations can be observed: (a) asymmetric longitudinal valence oscillations of carboxylate groups appear as two strong bands at 1651 and 1614 cm^{-1}, while (b) symmetric OOC stretching is also observed in a shape of two separated strong bands at 1345 and 1255 cm^{-1}, respectively. Bands at 1556 and 1463 cm^{-1} can be attributed to the stretches of the C=N and C–N bonds of pyrazole rings. A band that appears in the spectra at 1417 cm^{-1} is probably the band of longitudinal oscillation of the C–C bonds in rings.[4,36]

4. Conclusions

A new coordination compound $[Ag_4(bdmpza)_4]\cdot 10H_2O$ (bdmpza = bis(pyrazol-1-yl)acetate) was prepared by the reaction between an aqueous solution of silver nitrate and an aqueous solution of bis(3,5-dimethylpyrazol-1-yl)acetic acid and potassium hydroxide (1:1 molar ratio). The structure represents the first silver(I) coordination compound with bdmpza ligands in which the first bdmpza is tetra- and the second bdmpza is tridentately coordinated. The tetrasilver cluster $Ag_4O_6N_8$ forms which has not been observed till now. The coordination molecule $[Ag_4(bdmpza)_4]$ is surrounded by ten water molecules and an extense hydrogen bond network is formed. The TG-MS curve of the title compound in argon flow shows two-step of thermal degradation with a total mass loss of 68.58%, attributed to the dehydration (11.25%) and the thermal decomposition of four bdmpza ligands (58.09%). In the infrared spectrum, the vibrations of water molecules and bdmpza ligand can be assigned. The broadness of the weak O–H stretching band indicates the presence of intense hydrogen bond network in the compound. Unidentate and bidentate bonding of carboxylate groups of ligands reflects in two pairs of bands belonging to the (OOC) stretching vibrations, asymmetric and symmetric.

5. Supplementary Information

CCDC 2053074 contains the supplementary crystallographic data. These data can be obtained free of charge from The Cambridge Crystallographic Data Centre via www.ccdc.cam.ac.uk/data_request/cif.

Acknowledgments

This work was financially supported by Slovenian research agency (grant P1-0175). The authors thank Matej Jarc Rydzi for the synthesis of the ligand and EN-FIST Centre of Excellence for the use of SuperNova diffractometer.

6. References

1. S. Trofimenko, *Scorpionates, The Coordination Chemistry of Polypyrazolylborate Ligands*, Imperial College Press, London, **2005**.
2. C. Pettinari, R. Pettinari, *Coord. Chem. Rev.* **2005**, *249*, 663–691. **DOI:**10.1016/j.ccr.2004.08.017
3. N. Burzlaff, *Adv. Inorg. Chem.* **2008**, *60*, 101–165. **DOI:**10.1016/S0898-8838(08)00004-4
4. A. Beck, A. Barth, E. Hubner, N. Burzlaff, *Inorg. Chem.* **2003**, *42*, 7182–7188. **DOI:**10.1021/ic034097c
5. A. Beck, B. Weibert, N. Burzlaff , *Eur. J. Inorg. Chem.* **2001**, 521–527 **DOI:**10.1002/1099-0682(200102)2001:2<521::AID-EJIC521>3.0.CO;2-Q
6. S. Trofimenko, *J. Am. Chem. Soc.* **1967**, *89*, 3170. **DOI:**10.1021/ja00989a016
7. A. Otero, J. Fernandez-Baeza, J. Tejeda, A. Antinolo, F. Carrillo-Hermosilla, E. Diez Barra, A. Lara-Sanchez, M. Fernandez-Lopez, M. Lanfranchi, M. A Pellinghelli, *J. Chem. Soc., Dalton Trans.* **1999**, 3537–3539. **DOI:**10.1039/a907505d
8. N. Burzlaff, I. Hegelmann, B. Weibert, *J. Organomet. Chem.* **2001**, *626*, 16–23. **DOI:**10.1016/S0022-328X(01)00648-9
9. C. R. Groom, I. J. Bruno, M. P. Lightfoot, S. C. Ward, *Acta Crystallogr.* **2016**, B*72*, 171–179. **DOI:**10.1107/S2052520616003954
10. C. Pettinari, R. Pettinari, *Coord. Chem. Rev.* **2005**, *249*, 663–691. **DOI:**10.1016/j.ccr.2004.08.017
11. A. Otero, J. Fernandez-Baeza, A. Antinolo, J. Tejeda, A. Lara-Sanchez, L. Sanchez-Barba, M. Fernandez-Lopez, I. Lopez-Solera, *Inorg. Chem.* **2004**, *43*, 1350–1358. **DOI:**10.1021/ic035067c
12. B. Weibert, N. Burzlaff, *Eur. J. Inorg. Chem.* **2003**, 339–347. **DOI:**10.1002/ejic.200390046
13. A. Pevec, B. Kozlevčar, P. Gamez, J. Reedijk, *Acta Crystallogr.* **2007**, E*63*, m514–m516. **DOI:**10.1107/S1600536807001493
14. B. Kozlevčar, P. Gamez, Z. Jagličić, P. Strauch, N. Kitanovski, J. Reedijk, *Eur. J. Inorg. Chem.* **2011**, 3650–3655. **DOI:**10.1002/ejic.201100410
15. B. Kozlevčar, T, Pregelj, A. Pevec, N. Kitanovski, J, S, Costa, G, van Albada, P, Gamez, J. Reedijk, *Eur. J. Inorg. Chem*. **2008**, *31*, 4977–4982. **DOI:**10.1002/ejic.200800557
16. B. S. Fox, M. K. Beyer, V. E. Bondybey, *J. Am. Chem. Soc*. **2002**, *124*, 13613–13623. **DOI:**10.1021/ja0176604
17. N. D. Savić, B. Glišić, H. Wadepohl, A. Pavić, S. Lidija, J. Nikodinović-Runić, M. I. Djuran, *Med. Chem. Commun*. **2016**, *7*, 282–291. **DOI:**10.1039/C5MD00494B
18. C.-F. Liu, Z.-G. Ren, J.-P. Lang, *Eur. J. Inorg. Chem.* **2019**, 1816–1824. **DOI:**10.1002/ejic.201900026
19. F. R. Knight, R. R. M. Randall, L. Wakefield, A. M. Z. Slawin, J. D. Woollins, *Dalton Trans.* **2013**, *42*, 143–154. **DOI:**10.1039/C2DT31390A
20. L. Zhao, L.-Y. Xie, X.-L. Du, K. Zheng, T. Xie, R.-R. Huang, J. Qin, J.-P. Ma, L.-H. Ding, *Acta Chim. Slov.* **2020**, *67*, 822–829. **DOI:**10.17344/acsi.2019.5784
21. CrysAlisPRO, Oxford Diffraction /Agilent Technologies UK Ltd, Yarnton, England.

22. A. Altomare, M. C. Burla, M. Camalli, G. L. Cascarano, C. Giacovazzo, A. Guagliardi, A. G. G. Moliterni, G. Polidori, R. Spagna, *J. Appl. Cryst.* **1999**, *32*, 115–119. **DOI:**10.1107/S0021889898007717
23. G. M. Sheldrick, *Acta Crystallogr*. **2015**, C*71*, 3–8.
24. C. F. Macrae, P. R. Edgington, P. McCabe, E. Pidcock, G. P. Shields, R. Taylor, M. Towler, J. van de Streek, *J. Appl. Crystallogr*. **2006**, *39*, 453–457. **DOI:**10.1107/S002188980600731X
25. M. J. Turner, J. J. McKinnon, S. K. Wolff, D. J. Grimwood, P. R. Spackman, D. Jayatilaka, M. A. Spackman, CrystalExplorer17. University of Western Australia, 2017.
26. M. A. Spackman, D. Jayatilaka, *Cryst. Eng. Comm.* **2009**, *11*, 19–32. **DOI:**10.1039/B818330A
27. J. L. Rhinehart, K. A. Manbeck, S. K. Buzak, G. M. Lippa, W. W. Brennessel, K. I. Goldberg, W. D. Jones, *Organometallics* **2012**, *31*, 1943–1952. **DOI:**10.1021/om2012419
28. A. Beyer, M. S. von Gernler, S. Pflock, G. Turkoglu, L. Muller, A. Zahl, K. Gieb, P. Muller, T. Drewello, N. Burzlaff, *Eur. J. Inorg. Chem*. **2018**, 765–777. **DOI:**10.1002/ejic.201701400
29. A. Okuniewski, D. Rosiak, J. Chojnacki, B. Becker, *Polyhedron* **2015**, 90, 47–57. **DOI:**10.1016/j.poly.2015.01.035
30. D. Rosiak, A. Okuniewski, J. Chojnacki, *Polyhedron* **2018**, 146, 35–41. **DOI:**10.1016/j.poly.2018.02.016
31. M. Szymanska, M. Insinska-Rak, G. Dutkiewicz, G. N. Roviello, M. A. Fik-Jaskolka, V. Patroniak, *J. Mol. Liq.* **2020**, *319*, 114182 **DOI:**10.1016/j.molliq.2020.114182
32. M. H. H. Wurzenberger, V. Braun, M. Lommel, T. M. Klapotke, J. Stierstorfer, *Inorg. Chem*. **2020**, *59*, 10938 **DOI:**10.1021/acs.inorgchem.0c01403
33. S. Racioppi, M. Andrzejewski, V. Colombo, A. Sironi, P. Macchi, *Inorg. Chem*. **2020**, *59*, 2223 **DOI:**10.1021/acs.inorgchem.9b02852
34. H. Schmidbaur, A. Schier, *Angew. Chem. Int. Ed*. **2014**, *53*, 2–41. **DOI:**10.1002/anie.201490000
35. M. Drev, U. Grošelj, D. Kočar, F. Perdih, J. Svete, B. Štefane, F. Požgan, *Inorg. Chem*. **2020**, *59*, 3993–4001. **DOI:**10.1021/acs.inorgchem.9b03664
36. G. B. Deacon, R. J. Philips, *Coord. Chem. Rev.* **1980**, *33*, 227–250. **DOI:**10.1016/S0010-8545(00)80455-5

Povzetek

Pripravili smo novo štirijedrno spojino srebra s formulo $[Ag_4(bdmpza)_4]\cdot 10H_2O$ (bdmpza = bis(3,5-dimetilpirazol-1-il) acetat). Spojino smo sintetizirali z reakcijo med vodno raztopino, pripravljeno iz bis(3,5-dimetilpirazol-1-il)ocetne kisline in kalijevega hidroksida v množinskem razmerju 1:1 ter vodno raztopino srebrovega nitrata. Dobljen produkt smo analizirali z elementno analizo, termogravimetrično analizo sklopljeno z masno spektrometrijsko analizo, vibracijsko IR spektroskopijo, njeno kristalno strukturo pa smo določili z metodo rentgenske difrakcije na monokristalu. Kristalna struktura je bila dodatno ovrednotena z analizo Hirshfeldovih površin.

Scientific paper

Synthesis, Characterization and Crystal Structures of Fluoro-Substituted Aroylhydrazones with Antimicrobial Activity

Fu-Ming Wang,[1,*] Li-Jie Li,[2] Guo-Wei Zang,[2] Tong-Tong Deng[2] and Zhong-Lu You[3]

[1] *Key Laboratory of Coordination Chemistry and Functional Materials in Universities of Shandong, Department of Chemistry, Dezhou University, Dezhou 253023, P. R. China*

[2] *School of Chemistry and Chemical Engineering, Beijing Institute of Technology, Beijing 100081, P. R. China*

[3] *Department of Chemistry and Chemical Engineering, Liaoning Normal University, Dalian 116029, P. R. China*

* *Corresponding author: E-mail: wfm99999@126.com*

Received: 04-21-2020

Abstract

A series of five new fluoro-substituted aroylhydrazones were prepared and structurally characterized by elemental analysis, IR, UV-Vis and ^{1}H NMR spectroscopy, as well as single crystal X-ray diffraction. The compounds were evaluated for their antibacterial (*Bacillus subtilis*, *Staphylococcus aureus*, *Escherichia coli*, and *Pseudomonas fluorescence*) and antifungal (*Candida albicans* and *Aspergillus niger*) activities by MTT (3-(4,5-dimethylthiazol-2-yl)-2,5-diphenyl tetrazolium bromide) method. The biological assay indicated that the presence of the electron-withdrawing groups in the aroylhydrazones improved their antimicrobial activities.

Keywords: Aroylhydrazone; antimicrobial activity; organic synthesis; single crystal X-ray diffraction

1. Introduction

Aroylhydrazones are a kind of special Schiff bases, which can be obtained by the condensation reaction of carbonyl-containing compounds with aroylhydrazines. These compounds have attracted great attention for their wide range of biological activities, such as antibacterial,[1] antifungal,[2] antitumor,[3] anti-inflammatory,[4] and cytotoxic.[5] It was reported that the compounds bearing one or more halogen substituents in the aromatic rings can have improved biological activities especially for the antibacterial and antifungal activities.[6] Rai and co-workers reported a series of fluoro-, chloro-, bromo-, and iodo-substituted compounds, and found that they have significant antimicrobial activities.[7] Aroylhydrazones bearing C=N–NH-C(O) functional group are also a kind of interesting ligands in coordination chemistry. To date, a number of copper, zinc, nickel, vanadium, and molybdenum complexes with aroylhydrazone ligands have been reported.[8] As a continuation of work on the exploration of novel antimicrobial agents,[9] in the present paper, a series of new fluoro-substituted aroylhydrazones were prepared and evaluated for their antimicrobial activities. The structure–activity relationship was also investigated.

2. Experimental

2. 1. Materials and Measurements

2-Hydroxy-5-trifluoromethoxybenzaldehyde, 3-trifluoromethylbenzohydrazide, 4-methoxybenzohydrazide, picolinohydrazide, 2-chlorobenzohydrazide, 3-nitrobenzohydrazide with AR grade were purchased from Sigma-Aldrich Co. Ltd, and used as received. Elemental analyses were performed on a Perkin-Elmer 240C elemental analyzer. The IR spectra were recorded on a Jasco FT/IR-4000 spectrometer with KBr pellets. UV-Vis spectra were recorded on a Lambdar 35 spectrometer. ^{1}H NMR spectra were recorded on a Bruker instrument at 300 MHz. X-ray diffraction was carried out at a Bruker SMART 1000 CCD area diffractometer equipped with MoKα radiation.

2. 2. General Method for the Synthesis of the Compounds

Equimolar quantities (1.0 mmol each) of 2-hydroxy-5-trifluoromethoxybenzaldehyde and aroylhydrazines were dissolved in methanol (30 mL) and were stirred at room temperature for 30 min to give clear solution. X-ray quality single crystals were formed by slow evaporation of the solution in air for a few days.

_N_'-(2-Hydroxy-5-trifluoromethoxybenzylidene)-3-trifluoromethylbenzohydrazide (1)

Colorless crystals. Yield: 0.26 g (67%). M.p. 189.5–190.8 °C. Anal. calcd. for $C_{16}H_{10}F_6N_2O_3$: C, 48.99; H, 2.57; N, 7.14; found C, 48.78; H, 2.70; N, 7.23%. Characteristic IR data (cm^{-1}): 3445 (w), 3221 (w), 1651 (s), 1612 (m). UV-Vis data in methanol (λ, ε): 230 nm, 1.75×10^4 L mol^{-1} cm^{-1}; 285 nm, 1.93×10^4 L mol^{-1} cm^{-1}; 294 nm, 1.88×10^4 L $mol^{-1}cm^{-1}$; 330 nm, 1.70×10^4 L $mol^{-1}cm^{-1}$. ^{1}H NMR (300 MHz, DMSO-d_6): δ: 12.11 (s, 1H, OH), 11.26 (s, 1H, NH), 8.63 (s, 1H, CH=N), 8.16 (dd, 1H, ArH), 8.07 (d, 1H, ArH), 7.95 (d, 1H, ArH), 7.62 (s, 1H, ArH), 7.36 (t, 1H, ArH), 7.03–7.01 (m, 2H, ArH).

_N_'-(2-Hydroxy-5-trifluoromethoxybenzylidene)-4-methoxybenzohydrazide (2)

Colorless crystals. Yield: 0.27 g (75%). M.p. 172.3–173.5 °C. Anal. calcd. for $C_{16}H_{13}F_3N_2O_4$: C, 54.24; H, 3.70; N, 7.91; found C, 54.35; H, 3.81; N, 7.76%. Characteristic IR data (cm^{-1}): 3431 (w), 3259 (w), 1646 (s), 1610 (m). UV-Vis data in methanol (λ, ε): 215 nm, 1.87×10^4 L mol^{-1} cm^{-1}; 285 nm, 1.97×10^4 L mol^{-1} cm^{-1}; 297 nm, 2.12×10^4 L $mol^{-1}cm^{-1}$; 330 nm, 1.72×10^4 L $mol^{-1}cm^{-1}$. ^{1}H NMR (300 MHz, DMSO-d_6): δ: 12.08 (s, 1H, OH), 11.39 (s, 1H, NH), 8.65 (s, 1H, CH=N), 7.96 (d, 2H, ArH), 7.62 (s, 1H, ArH), 7.31 (dd, 1H, ArH), 7.10–7.01 (m, 3H, ArH), 3.85 (s, 3H, CH_3).

_N_'-(2-Hydroxy-5-trifluoromethoxybenzylidene)picolinohydrazide (3)

Colorless crystals. Yield: 0.20 g (63%). M.p. 134.0–135.5 °C. Anal. calcd. for $C_{14}H_{10}F_3N_3O_3$: C, 51.70; H, 3.10; N, 12.92; found C, 51.85; H, 3.16; N, 12.83%. Characteristic IR data (cm^{-1}): 3423 (w), 3277 (w), 1670 (s), 1615 (m). UV-Vis data in methanol (λ, ε): 213 nm, 2.03×10^4 L $mol^{-1}cm^{-1}$; 288 nm, 1.94×10^4 L $mol^{-1}cm^{-1}$; 297 nm, 1.91×10^4 L mol^{-1} cm^{-1}; 333 nm, 1.87×10^4 L mol^{-1} cm^{-1}. ^{1}H NMR (300 MHz, DMSO-d_6): δ: 12.58 (s, 1H, OH), 11.38 (s, 1H, NH), 8.86 (d, 1H, PyH), 8.75 (s, 1H, CH=N), 8.16 (d, 1H, PyH), 8.06 (t, 1H, PyH), 7.70 (t, 1H, PyH), 7.57 (s, 1H, ArH), 7.05 (m, 2H, ArH).

2-Chloro-_N_'-(2-hydroxy-5-trifluoromethoxybenzylidene)benzohydrazide (4)

Colorless crystals. Yield: 0.29 g (81%). M.p. 211.2–212.8 °C. Anal. calcd. for $C_{15}H_{10}ClF_3N_2O_3$: C, 50.23; H, 2.81; N, 7.81; found C, 50.37; H, 2.93; N, 7.76%. Characteristic IR data (cm^{-1}): 3432 (w), 3215 (w), 1645 (s), 1612 (m). UV-Vis data in methanol (λ, ε): 233 nm, 1.79×10^4 L mol^{-1} cm^{-1}; 285 nm, 2.11×10^4 L mol^{-1} cm^{-1}; 295 nm, 2.03×10^4 L mol^{-1} cm^{-1}; 333 nm, 1.75×10^4 L mol^{-1} cm^{-1}. ^{1}H NMR (300 MHz, DMSO-d_6): δ: 12.26 (s, 1H, OH), 11.23 (s, 1H, NH), 8.70 (s, 1H, CH=N), 8.01 (d, 1H, ArH), 7.94 (d, 1H, ArH), 7.72-7.58 (dt, 3H, ArH), 7.31 (t, 1H, ArH), 7.06 (d, 1H, ArH).

_N_'-(2-Hydroxy-5-trifluoromethoxybenzylidene)-3-nitrobenzohydrazide (5)

Yellow crystals. Yield: 0.26 g (70%). M.p. 238.5–240.0 °C. Anal. calcd. for $C_{15}H_{10}F_3N_3O_5$: C, 48.79; H, 2.73; N, 11.38; found C, 48.72; H, 2.82; N, 11.45%. Characteristic IR data (cm^{-1}): 3437 (w), 3215 (w), 1645 (s), 1613 (m), 1530 (s), 1354 (s). UV-Vis data in methanol (λ, ε): 215 nm, 2.23×10^4 L mol^{-1} cm^{-1}; 283 nm, 1.63×10^4 L mol^{-1} cm^{-1}; 330 nm, 1.51×10^4 L mol^{-1} cm^{-1}; 390 nm, 4.33×10^3 L mol^{-1} cm^{-1}. ^{1}H NMR (300 MHz, DMSO-d_6): δ: 12.47 (s, 1H, OH), 11.19 (s, 1H, NH), 8.81 (s, 1H, ArH), 8.75 (s, 1H, CH=N), 8.50 (dd, 1H, ArH), 8.39 (d, 1H, ArH), 7.88 (t, 1H, ArH), 7.68 (s, 1H, ArH), 7.05 (m, 2H, ArH).

2. 3. Antimicrobial Assay

The antibacterial activities of the compounds were tested against *B. subtilis*, *S. aureus*, *E. coli*, and *P. fluorescence* using MH (Mueller–Hinton) medium. The antifungal activities of the compounds were tested against *C. albicans* and *A. niger* using RPMI-1640 medium. The MIC values of the tested compounds were determined by a colorimetric method using the dye MTT.[10] A stock solution of the aroylhydrazone compound (150 μM) in DMSO was prepared and graded quantities (75 μM, 37.5 μM, 18.8 μM, 9.4 μM, 4.7 μM, 2.3 μM, 1.2 μM, 0.59 μM) of the tested compounds were incorporated in specified quantity of the corresponding sterilized liquid medium. A specified quantity of the medium containing the compound was poured into microtitration plates. Suspension of the microorganism was prepared to contain approximately 10^5 cfu/mL and applied to microtitration plates with serially diluted compounds in DMSO to be tested and incubated at 37 °C for 24 h and 48 h for bacteria and fungi, respectively. Then the MIC values were visually determined on each of the microtitration plates, 50 μL of PBS (phosphate buffered saline 0.01 M, pH = 7.4) containing 2 mg of MTT/mL was added to each well. Incubation was continued at room temperature for 4–5 h. The content of each well was removed, and 100 μL of isopropanol containing 5% 1 M HCl was added to extract the dye. After 12 h of incubation at room temperature, the optical density was measured with a microplate reader at 550 nm.

2. 4. Crystal Structure Determination

Diffraction intensities for the compounds were collected at 298(2) K using a Bruker SMART 1000 CCD

Table 1. Crystallographic and experimental data for the compounds **1**–**5**

Compound	**1**	**2**	**3**	**4**	**5**
Formula	$C_{16}H_{10}F_6N_2O_3$	$C_{16}H_{13}F_3N_2O_4$	$C_{14}H_{10}F_3N_3O_3$	$C_{15}H_{10}ClF_3N_2O_3$	$C_{15}H_{10}F_3N_3O_5$
Mr	392.3	354.3	325.2	363.2	369.3
Crystal system	Monoclinic	Monoclinic	Orthorhombic	Monoclinic	Monoclinic
Space group	$P2_1/c$	$P2_1/c$	*Pbca*	$P2_1/c$	$P2_1/c$
a (Å)	12.0732(9)	18.9700(11)	7.4144(8)	11.4106(5)	11.6290(7)
b (Å)	14.9373(10)	8.3470(10)	11.2352(10)	14.9261(7)	14.7428(8)
c (Å)	8.8606(7)	10.1475(11)	34.8550(13)	8.9011(4)	8.8921(5)
β (°)	95.045(2)	94.342(2)		94.5490(10)	96.192(1)
V (Å^3)	1591.7(2)	1602.2(3)	2903.5(4)	1511.22(12)	1515.60(15)
Z	4	4	8	4	4
D_c (g cm^{-3})	1.637	1.469	1.488	1.577	1.618
μ (Mo-Kα) (mm^{-1})	0.160	0.129	0.132	0.304	0.146
F(000)	792	728	1328	728	752
Reflections collected	7941	7607	11701	14025	14255
Unique reflections	2953	2931	2650	2770	2813
Observed reflections ($I \geq 2\sigma(I)$)	2182	1289	1537	2300	1972
Parameters	249	233	212	221	239
Restraints	1	2	1	1	1
Min. and max. transmission	0.9581 and 0.9642	0.9809 and 0.9835	0.9703 and 0.9741	0.9389 and 0.9502	0.9588 and 0.9671
Goodness-of-fit on F^2	1.032	1.028	0.965	1.042	1.030
R_1, wR_2 [$I \geq 2\sigma(I)$][a]	0.0442, 0.1060	0.0880, 0.2385	0.0813, 0.1858	0.0395, 0.0983	0.0426, 0.0955
R_1, wR_2 (all data)[a]	0.0656, 0.1212	0.1716, 0.3191	0.1278, 0.2241	0.0496, 0.1073	0.0704, 0.1088
Large diff. peak and hole (eÅ^{-3})	0.296 and –0.234	0.564 and –0.268	0.270 and –0.223	0.235 and –0.313	0.203 and –0.197

[a] $R_1 = \Sigma||F_o|-|F_c||/\Sigma|F_o|$, $wR_2 = [\Sigma w(F_o^2-F_c^2)^2/\Sigma w(F_o^2)^2]^{1/2}$.

area-detector diffractometer with Mo Kα radiation (λ = 0.71073 Å). The collected data were reduced with the SAINT program,[11] and multi-scan absorption correction was performed using the SADABS program.[12] The structures were solved by direct methods. The compounds were refined against F^2 by full-matrix least-squares method using the SHELXTL package.[13] All of the non-hydrogen atoms were refined anisotropically. The amino H atoms in the compounds were located from difference Fourier maps and refined isotropically, with N–H distances restrained to

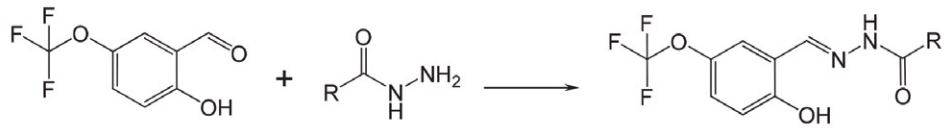

	R		R
1	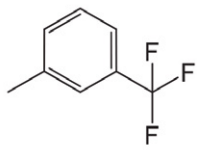	**2**	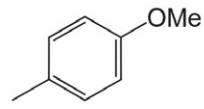
3	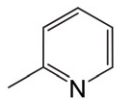	**4**	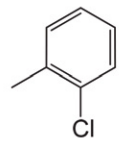
5	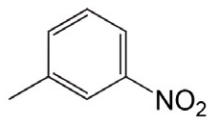		

Scheme 1. Synthesis of the compounds **1**–**5**.

0.90(1) Å. The remaining hydrogen atoms were placed in calculated positions and constrained to ride on their parent atoms. The crystallographic data for the compounds are summarized in Table 1.

3. Results and Discussion

3. 1. Synthesis and General Characterization

The aroylhydrazones were prepared by the condensation of equimolar quantities of 2-hydroxy-5-trifluoromethoxybenzaldehyde with various aroylhydrazines in methanol (Scheme 1). The compounds have been characterized by elemental analysis, IR, UV-Vis and ^{1}H NMR spectra. Structures of the compounds were further confirmed by single crystal X-ray determination. The compounds were crystallized as well-shaped single crystals, which are soluble in methanol, ethanol, acetonitrile, chloroform, DMF and DMSO, but insoluble in pure water.

3. 2. IR and Electronic Spectra

The characteristic intense bands in the range 1645–1670 cm^{-1} are generated by the ν(C=O) vibrations, whereas the bands in the range 1610–1615 cm^{-1} are assigned to the ν(C=N) vibrations.[14] In the spectra of the compounds, there are broad absorptions in the range 3420–3450 cm^{-1}, which can be attributed to the hydrogen-bonded phenol groups. The sharp bands in the range 3215–3277 cm^{-1} are assigned to the ν(N–H) vibrations. The bands indicative of the $\nu_{as}(NO_2)$ and $\nu_s(NO_2)$ vibrations are observed at 1530 and 1354 cm^{-1} for **5**.[13] In the electronic spectra of the compounds, there are four sets of bands in the UV regions. The first at 283–288 nm may be assigned to π–π^* transitions in the aromatic and intra-ligand π–π^* transitions.[15] The second set at 330–390 nm may be assigned to n–π^* transitions of the azomethine and carbonyl groups.[16] The C, H, N analyses were in accordance with the chemical formulae proposed by the single crystal X-ray analysis.

3. 3. ^{1}H NMR Spectra

The ^{1}H NMR data of the compounds show no signal of the amino group (NH_2) characteristic to the starting material (hydrazide). The spectra show singlet at 12–13 and 11–12 ppm ranges, which may be assigned to the hydroxyl proton (OH) and (NH) protons, respectively.[17] The singlet at 8.6–8.8 ppm range is assigned to the azomethine proton

Table 2. Selected bond lengths (Å) and angles (°) for the compounds **1**–**5**

	1	**2**	**3**	**4**	**5**
C8–N1	1.278(3)	1.277(6)	1.293(5)	1.278(2)	1.276(2)
N1–N2	1.382(2)	1.362(5)	1.364(5)	1.377(2)	1.380(2)
N2–C9	1.347(3)	1.365(6)	1.367(5)	1.347(2)	1.342(2)
C9–O2	1.227(2)	1.226(5)	1.230(5)	1.230(2)	1.227(2)
C8–N1–N2	116.01(17)	119.1(4)	120.8(3)	117.04(15)	117.39(16)
N1–N2–C9	119.56(16)	116.8(4)	116.3(4)	118.76(14)	117.96(15)
N2–C9–C10	115.08(17)	115.4(4)	114.2(4)	115.61(14)	115.96(16)
N2–C9–O2	122.98(19)	121.5(4)	122.4(4)	122.74(16)	123.06(17)

Table 3. Hydrogen bond distances (Å) and bond angles (°) for the compounds **1**–**5**

D–**H**···*A*	*d*(*D*–**H**)	*d*(**H**···*A*)	*d*(*D*···*A*)	**Angle** (*D*–**H**···*A*)
1				
N2–H2···O2^{i}	0.90(1)	2.035(12)	2.916(2)	165(3)
O1–H1···N1	0.82	1.92	2.644(2)	146(3)
2				
N2–H2···O2^{i}	0.90(1)	2.144(16)	3.021(4)	165(4)
O1–H1···N1	0.85(1)	1.79(3)	2.554(5)	149(5)
3				
N2–H2···O2^{ii}	0.90(1)	2.60(3)	3.396(5)	147(4)
O1–H1···N1	1.00	1.62	2.534(4)	149(4)
4				
N2–H2···O2^{iii}	0.90(1)	2.056(12)	2.929(2)	166(2)
O1–H1···N1	0.82	1.91	2.629(2)	146(2)
5				
N2–H2···O2^{i}	0.90(1)	2.058(12)	2.937(2)	166(2)
O1–H1···N1	0.82	1.91	2.622(2)	145(2)

Symmetry codes: (i) x, 1/2 – y, –1/2 + z; (ii) 1/2 – x, 1/2 + y, z; (iii) x, 3/2 – y, –1/2 + z.

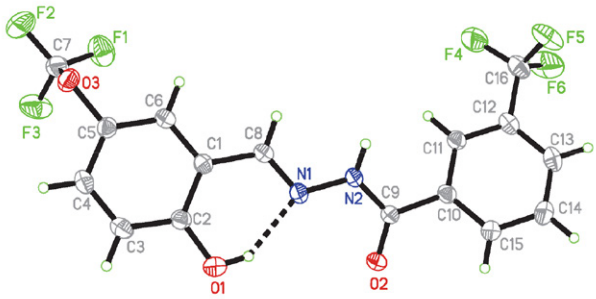

Figure 1. A perspective view of the molecular structure of **1** with the atom labeling scheme. Thermal ellipsoids are drawn at the 30% probability level. Hydrogen bond is shown as a dashed line.

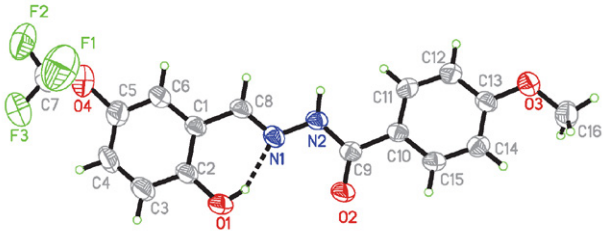

Figure 2. A perspective view of the molecular structure of **2** with the atom labeling scheme. Thermal ellipsoids are drawn at the 30% probability level. Hydrogen bond is shown as a dashed line.

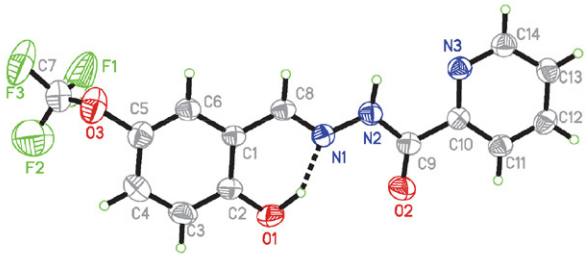

Figure 3. A perspective view of the molecular structure of **3** with the atom labeling scheme. Thermal ellipsoids are drawn at the 30% probability level. Hydrogen bonds are shown as dashed lines.

(CH=N).[18] The multiplets in the 8.05–7.00 ppm range are attributed to aromatic protons.[19] The triplet at 3.85 ppm for compound **2** is attributed to the methyl group.

3. 4. Crystal Structure Description

The molecular structures of the compounds **1**–**5** are shown in Figures 1–5, respectively. Selected bond lengths and angles are listed in Table 2. All the molecules of the compounds adopt *E* configuration with respect to the methylidene units. The distances of the methylidene bonds, ranging from 1.27 to 1.30 Å, confirm them as typical double bonds. The shorter distances of the C–N bonds and the longer distances of the C=O bonds for the –C(O)–NH– units than usual, suggest the presence of conjugation effects in the molecules. All the bond lengths in the compounds are comparable to each other, and are within normal values.[20] The aromatic rings of the

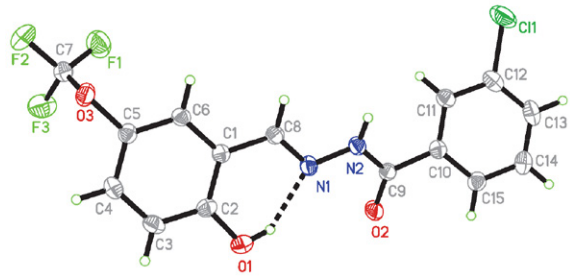

Figure 4. A perspective view of the molecular structure of **4** with the atom labeling scheme. Thermal ellipsoids are drawn at the 30% probability level. Hydrogen bond is shown as a dashed line.

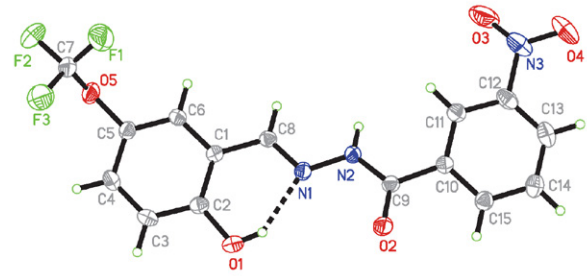

Figure 5. A perspective view of the molecular structure of **5** with the atom labeling scheme. Thermal ellipsoids are drawn at the 30% probability level. Hydrogen bond is shown as a dashed line.

compounds form dihedral angles of 10.9(2)° (**1**), 14.2(4)° (**2**), 9.7(4)° (**3**), 9.6(2)° (**4**), and 5.4(2)° (**5**). The crystal structures of the compounds are stabilized by intermolecular hydrogen bonds (Table 3).

3. 5. Antimicrobial Activity

The compounds were screened for antibacterial activity against two Gram positive bacterial strains (*B. subtilis* and *S. aureus*) and two Gram negative bacterial strains (*E. coli* and *P. fluorescence*) by MTT method. The MIC (minimum inhibitory concentration) values of the compounds against four bacteria are listed in Table 4. Kanamycin and Penicillin G were used as the standard materials. Compounds **1** and **4** showed the most effective activities against *B. subtilis*, and good activities against *S. aureus* and *E. coli*, while no or weak activity against *P. fluorescence*. Compounds **2** and **5** showed moderate activities against all the bacteria. Compound **3** showed weak activity agains *B. subtilis* and *E. coli*, while no activity against *E. coli* and *P. fluorescence*. After careful comparison we noticed that the presence of a trifluoromethyl group in **1** and a chloro group in **4** might play an important role in the antibacterial activities. In addition, the presence of an electron-withdrawing group (NO_2) in compound **5** made it more active than the compounds **2** and **3** which are bearing methoxybenzene and pyridine groups. The chloro substituents are known to be important constituents

Table 4. The MIC values (μM) of the compounds **1**–**5**

Tested material	*Bacillus subtilis*	*Staphylococcus aureus*	*Escherichia coli*	*Pseudomonas fluorescence*	*Candida albicans*	*Aspergillus niger*
1	0.62	9.4	18.7	>150	>150	75
2	9.4	37.5	75	>150	>150	>150
3	18.7	37.5	>150	>150	>150	>150
4	0.31	9.4	18.7	37.5	37.5	>150
5	3.13	18.7	75	>150	>150	>150
Kanamycin	0.59	2.3	4.7	4.7	>150	>150
Penicillin G	2.3	4.7	>150	>150	>150	>150
Ketoconazole	>150	>150	>150	>150	4.7	18.8

conferring the antibacterial activities.[21] It is interesting that compounds **1** and **4** have similar activities against *B. subtilis* as Kanamycin and Penicillin G. The results indicate that the electron-withdrawing groups on the aromatic rings may be important for the design of novel antibacterial materials.

The antifungal activities of the compounds were also evaluated against two fungal strains (*C. albicans* and *A. niger*) by MTT method. Ketoconazole was used as the reference mateiral. As a result, compound **4** has weak activity against *C. albicans*, and compound **1** has weak activity against *A. niger*.

4. Conclusions

In the present paper a series of five new fluoro-substituted aroylhydrazones were prepared and structurally characterized. The antimicrobial activities against the bacteria *B. subtilis*, *S. aureus*, *E. coli*, and *P. fluorescence*, and the fungi *C. albicans* and *A. niger* were evaluated by MTT methods. Among the compounds, *N*'-(2-hydroxy-5-trifluoromethoxybenzylidene)-3-trifluoromethylbenzohydrazide and 2-chloro-*N*'-(2-hydroxy-5-trifluoromethoxybenzylidene)benzohydrazide showed to be the most effective antimicrobial agents against *B. subtilis*. The electron-withdrawing groups, such as nitro, chloro, and fluoro, are important substituents for the design of novel effective antibacterial agents. The compounds presented here could be useful as a template for future development through modification to explore more effective antimicrobial materials.

5. Supplementary material

CCDC-1998070 for **1**, 1998075 for **2**, 1998076 for **3**, 1998077 for **4**, 1998079 for **5** contain the supplementary crystallographic data for this paper. These data can be obtained free of charge at http://www.ccdc.cam.ac.uk/const/retrieving.html or from the Cambridge Crystallographic Data Centre (CCDC), 12 Union Road, Cambridge CB2 1EZ, UK; fax: +44(0)1223-336033 or e-mail: deposit@ccdc.cam.ac.uk.

6. References

1. (a) M. V. Angelusiu, S. F. Barbuceanu, C. Draghici, G. L. Almajan, *Eur. J. Med. Chem.* **2010**, *45*, 2055–2062; **DOI:**10.1016/j.ejmech.2010.01.033
   (b) O. O. Ajani, C. A. Obafemi, O. C. Nwinyi, D. A. Akinpelu, *Bioorg. Med. Chem.* **2010**, *18*, 214–221. **DOI:**10.1016/j.bmc.2009.10.064
2. G. Visbal, G. San-Blas, A. Maldonado, A. Alvarez-Aular, M. V. Capparelli, J. Murgich, *Steroids* **2011**, *76*, 1069–1081. **DOI:**10.1016/j.steroids.2011.04.012
3. (a) Y. H. Zhang, L. Zhang, L. Liu, J. X. Guo, D. L. Wu, G. C. Xu, X. H. Wang, D. Z. Jia, *Inorg. Chim. Acta* **2010**, *363*, 289–293; **DOI:**10.1016/j.ica.2009.08.017
   (b) T. Horiuchi, J. Chiba, K. Uoto, T. Soga, *Bioorg. Med. Chem. Lett.* **2009**, *19*, 305–308. **DOI:**10.1016/j.bmcl.2008.11.090
4. (a) M. A. A. El-Sayed, N. I. Abdel-Aziz, A. A. M. Abdel-Aziz, A. S. El-Azab, Y. A. Asiri, K. E. H. ElTahir, *Bioorg. Med. Chem.* **2011**, *19*, 3416–3424; **DOI:**10.1016/j.bmc.2011.04.027
   (b) S. M. Sondhi, M. Dinodia, A. Kumar, *Bioorg. Med. Chem.* **2006**, *14*, 4657–4663. **DOI:**10.1016/j.bmc.2006.02.014
5. (a) P. Krishnamoorthy, P. Sathyadevi, A. H. Cowley, R. R. Butorac, N. Dharmaraj, *Eur. J. Med. Chem.* **2011**, *46*, 3376–3387; **DOI:**10.1016/j.ejmech.2011.05.001
   (b) P. G. Avaji, C. H. V. Kumar, S. A. Patil, K. N. Shivananda, C. Nagaraju, *Eur. J. Med. Chem.* **2009**, *44*, 3552–3559. **DOI:**10.1016/j.ejmech.2009.03.032
6. (a) L. C. Felton, J. H. Brewer, *Science* **1947**, *105*, 409–410; **DOI:**10.1126/science.105.2729.409
   (b) M. Gopalakrishnan, J. Thanusu, V. Kanagarajan, R. Govindaraju, *J. Enzyme Inhib. Med. Chem.* **2009**, *24*, 52–58; **DOI:**10.1080/14756360801906632
   (c) L. Shi, H.-M. Ge, S.-H. Tan, H.-Q. Li, Y.-C. Song, H.-L. Zhu, R.-X. Tan, *Eur. J. Med. Chem.* **2007**, *42*, 558–564. **DOI:**10.1016/j.ejmech.2006.11.010
7. (a) N. P. Rai, V. K. Narayanaswamy, T. Govender, B. K. Manuprasad, S. Shashikanth, P. N. Arunachalam, *Eur. J. Med. Chem.* **2010**, *45*, 2677–2682; **DOI:**10.1016/j.ejmech.2010.02.021
   (b) N. P. Rai, V. K. Narayanaswamy, S. Shashikanth, P. N. Arunachalam, *Eur. J. Med. Chem.* **2009**, *44*, 4522–4527.
8. (a) E.-C. Liu, W. Li, X.-S. Cheng, *Acta Chim. Slov.* **2019**, *66*, 971–977;

(b) H.-Y. Qian, *Acta Chim. Slov.* **2019**, *66*, 995–1001; **DOI:**10.4149/neo_2019_190112N36
(c) Y. Li, L. Xu, M. Duan, J. Wu, Y. Wang, K. Dong, M. Han, Z. You, *Inorg. Chem. Commun.* **2019**, *105*, 212–216; **DOI:**10.1016/j.inoche.2019.05.011
(d) X.-Q. Luo, Y.-J. Han, L.-W. Han, *Acta Chim. Slov.* **2020**, *67*, 853–859; **DOI:**10.17344/acsi.2020.5819
(e) Z. You, H. Yu, B. Zheng, C. Zhang, C. Lv, K. Li, L. Pan, *Inorg. Chim. Acta* **2018**, *469*, 44–50; **DOI:**10.1016/j.ica.2017.09.011
(f) Y.-L. Sang, X.-S. Lin, W.-D. Sun, *Acta Chim. Slov.* **2020**, *67*, 581–585; **DOI:**10.17344/acsi.2019.5595
(g) H. Zhao, X.-P. Tan, Q.-A. Peng, C.-Z. Shi, Y.-F. Zhao, Y. Cui, *Acta Chim. Slov.* **2020**, *67*, 638–643. **DOI:**10.17344/acsi.2019.5644

9. (a) R.-H. Hui, P. Zhou, Z.-L. You, *Indian J. Chem. A* **2009**, *48*, 1102–1106; **DOI:**10.1111/j.1755-3768.1970.tb06590.x
(b) Z.-L. You, H.-L. Zhu, *Z. Anorg. Allg. Chem.* **2006**, *632*, 140–146; **DOI:**10.1002/zaac.200500308
(c) Z.-L. You, Q.-Z. Jiao, *Synth. React. Inorg. Met.-Org. Nano-Met. Chem.* **2006**, *36*, 713–717. **DOI:**10.1080/15533170601028165
10. J. Meletiadis, J. F. Meis, J. W. Mouton, J. P. Donnelly, P. E. Verweij, *J. Clin. Microbiol.* **2000**, *38*, 2949–2954. **DOI:**10.1128/JCM.38.8.2949-2954.2000
11. Bruker, SMART (Version 5.625) and SAINT (Version 6.01). Bruker AXS Inc., Madison, Wisconsin, USA, 2007.
12. G. M. Sheldrick. *SADABS. Program for Empirical Absorption Correction of Area Detector*, University of Göttingen, Germany, 1996.
13. G. M. Sheldrick. *SHELXTL V5.1 Software Reference Manual*, Bruker AXS, Inc., Madison, Wisconsin, USA, 1997.
14. M. Zhang, D.-M. Xian, H.-H. Li, J.-C. Zhang, Z.-L. You, *Aust. J. Chem.* **2012**, *65*, 343–350. **DOI:**10.1071/CH11424
15. M. F. R. Fouda, M. M. Abd-Elzaher, M. M. Shakdofa, F. A. El-Saied, M. I. Ayad, A. S. El-Tabl, *J. Coord. Chem.* **2008**, *61*, 1983–1996. **DOI:**10.1080/00958970701795714
16. R. Gup, B. Kirkan, *Spectrochim. Acta A* **2005**, *62*, 1188–1195. **DOI:**10.1016/j.saa.2005.04.015
17. Ü. Ö. Özmen, G. Olgun, *Spectrochim. Acta A* **2008**, *70*, 641–645. **DOI:**10.1016/j.saa.2007.08.012
18. M. R. Maurya, S. Khurana, C. Schulzke, D. Rehder, *Eur. J. Inorg. Chem.* **2001**, *3*, 779–788. **DOI:**10.1002/1099-0682(200103)2001:3<779::AID-EJIC779>3.0.CO;2-#
19. P. N. Remya, C. H. Suresh, M. L. P. Reddy, *Polyhedron* **2007**, *26*, 5016–5022. **DOI:**10.1016/j.poly.2007.07.020
20. (a) S. N. Podyachev, I. A. Litvinov, R. R. Shagidullin, B. I. Buzykin, I. Bauer, D. V. Osyanina, L. V. Avvakumova, S. N. Sudakova, W. D. Habicher, A. I. Konovalov, *Spectrochim. Acta Part A* **2007**, *66*, 250–261; (b) S. M. S. V. Wardell, M. V. N. de Souza, J. L. Wardell, J. N. Low, C. Glidewell, *Acta Crystallogr.* **2005**, *C61*, o683–o689; (c) X.-L. Wang, Z.-L. You, C. Wang, *J. Chem. Crystallogr.* **2011**, *41*, 621–624. **DOI:**10.1016/j.saa.2006.02.049
21. Ö. Ö. Güven, T. Erdoğan, H. Göker, S. Yıldız, *Bioorg. Med. Chem.* **2007**, *17*, 2233–2236. **DOI:**10.1016/j.bmcl.2007.01.061

Povzetek

Opisujemo pripravo in strukturno karakterizacijo (elementna analiza, IR, UV-Vis in ^{1}H NMR spektroskopija ter rentgenska difrakcijska analiza monokristalov) petih novih fluorosubstituiranih aroilhidrazonov. Za vse spojine smo s pomočjo metode MTT (3-(4,5-dimetiltiazol-2-il)-2,5-difenil tetrazolijev bromid) določili tudi njihovo antibakterijsko delovanje (*Bacillus subtilis*, *Staphylococcus aureus*, *Escherichia coli* in *Pseudomonas fluorescence*) ter učinkovanje proti glivam (*Candida albicans* in *Aspergillus niger*), ki so pokazala, da prisotnost elektronakceptorskih skupin v aroilhidrazonih izboljša njihove antimikrobne aktivnosti.

DOI: 10.17344/acsi.2020.6248 *Acta Chim. Slov.* **2021,** *68,* 548–561

Scientific paper

Efficient Removal of Aqueous Manganese (II) Cations by Activated Opuntia Ficus Indica Powder: Adsorption Performance and Mechanism

Boutheina Djobbi,[1] Ghofrane Lassoued Ben Miled,[1] Hatem Raddadi[2] and Rached Ben Hassen[1,*]

[1] *Laboratory of Materials and Environment for Sustainable Development, LR18ES10, University of Tunis El Manar, ISSBAT, 9, Avenue Dr. Zoheir Safi, 1006 Tunis, Tunisia.*

[2] *National Sanitation Office of Tunis, Purification Department, Sidi Salah street, Chotrana, Ariana. Tunisia.*

* *Corresponding author: E-mail: rached.benhassen@issbat.utm.tn*

Received: 07-08-2020

Abstract

The adsorption of manganese ions from aqueous solutions by pure and acid-treated *Opuntia ficus indica* as natural low-cost and eco-friendly adsorbents was investigated. The adsorbents' structures were characterized by powder X-ray diffraction and infrared spectroscopy. Specific surface areas were determined using the Brunauer-Emmett-Tell equation. The study was carried out under various parameters influencing the manganese removal efficiency such as pH, temperature, contact time, adsorbent dose and initial concentration of manganese ion. The maximum adsorption capacity reached 42.02 mg/g for acid-treated *Opuntia ficus indica*, and only 20.8 mg /g for pure *Opuntia ficus indica*. The Langmuir, Freundlich and Temkin isotherms equations were tested, and the best fit was obtained by the Langmuir model for both adsorbents. The thermodynamic study shows that chemisorption is the main adsorption mechanism for the activated adsorbent while physisorption is the main adsorption mechanism for the pure adsorbent. The kinetics of the adsorption have been studied using four kinetics models of pseudo-first order, pseudo-second order, Elovich and intra-particle diffusion. Structural analyses indicate the appearance of MnO_x oxides on the cellulose fibers. The adsorption mechanisms consist of an electrostatic interaction followed by oxidation of the Mn (II) to higher degrees, then probably by binding to the surface of the adsorbent by different C-O-MnO_x bonds.

Keywords: Adsorption mechanism; manganese; removal efficiency; *Opuntia ficus indica*; environmental.

1. Introduction

Unlike organic pollutants, which are mostly affected by biological degradation, the hazards of heavy metals are related to their inability to degrade into non-harmful end products. It can cause acute and chronic damage to various organisms if present. Therefore, the removal of heavy metals from water and wastewater is crucial to protect the health of living organisms. Heavy metals are naturally present in the ecosystem, and their recent increase is attributed to the effluents of many industries, such as metal plating facilities, mining operations and tanneries. Manganese (Mn) is the third most abundant transition metal in nature, usually present in surface water and groundwater as a divalent ion (Mn^{2+}). It is considered as pollutant mainly because of its organoleptic properties.[1–6] Its removal from an aqueous solution is a serious problem in many countries as it is one of the most difficult elements to remove.[7] Contact of manganese-contaminated water with air enhances the oxidation of Mn (II) to Mn (IV). The Mn (IV) precipitate can stain utensils and clothing,[8] and gives water an unpleasant metallic taste and odor, an increased turbidity and a biofouling of pipelines.[2,9]

Manganese mainly affects on the brain and heart and can cause damage to the nervous system,[10] kidney, liver and cause mild anemia in low dose.[11] Several physicochemical methods for manganese elimination such as aeration, filtration , ion exchange, and settling techniques have evolved in search of efficiency, affordability, and ease of use.[12–14] During these last few years, the adsorption technique has been considered one of the most preferred methods for removing traces of heavy metals from water and wastewater due to its high efficiency, ease of handling and the availability of various adsorbents. This physicochemical process is a sustainable cost-effective alternative process in the environment.[15] A number of studies were carried out using differ-

ent adsorbents for manganese removal such as activated carbon,[1] moringa oleifera leaf, borassus flabellifer, mangifera indica,[16] pithecellobium dulce carbon,[7] palm fruit bunch, date stones or maize cobs.[17] Several parameters are important for comparing adsorbents such as local availability and the degree of treatment required, However, the cost parameter is rarely reported.[18] Plant materials, which are mainly composed of cellulosic materials, can adsorb micropollutants such as heavy metal cations in aqueous medium.[19,20] Several researches show that cellulose can be easily modified to obtain new adsorbent materials which are used for the adsorption of heavy metal ions and to improve its commercial value, making it eligible for new technological applications.[21] In the same context, Cactus cladodes from *Opuntia ficus indica* are primarily composed of water, carbohydrates (starch, cellulose, hemicellulose, pectin and chlorophyll), proteins, lignin, and lipids (carotene).[22,23] This composition allows *Opuntia ficus indica* to be used as an sorbent-coagulant. This study investigates heavy metals removal using cathodes powder. Preliminary results indicate low removal extents, less than 10 mg/g related to the very low specific surface area which is probably due to the covering of the majority of the surface by an excess of natural minerals, mainly $Ca(C_2O_4) \cdot H_2O$ (whewellite).[24] For performance improvement of this process, new by-products have been produced in the lab by modification of the surface of the natural *Opuntia ficus indica*.

The aim of this work is to develop a new adsorbent product following a valorization of a biomass, the activated *Opuntia ficus indica,* then to evaluate its properties of adsorption of manganese ions. The structures of the adsorbents as prepared (crude cactus and activated one) were identified by X-ray diffraction and infrared spectroscopy analysis. The influence of several parameters for manganese ions adsorption, such as pH, adsorbent dose, initial concentration, contact time and temperature were assessed. The adsorption equilibrium isotherm was fitted to Langmuir, Freundlich and Temkin models. The thermodynamic variables were calculated to verify the adsorption process. The adsorption kinetics process with the two adsorbents were analysed using the pseudo-first order, pseudo-second order, Elovich and intraparticle diffusion models. Different kinetic parameters, equilibrium adsorption capacities and correlation coefficients R^2 for each kinetic model were determined. The adsorption mechanism was elucidated for the activated adsorbent using IR spectroscopy and X-ray diffraction analysis.

2. Materials and Methods

2. 1. Materials and Reagents

The cladodes of *Opuntia ficus indica* were collected during July, in a plantation located in the region of Djebba in the north of Tunisia. All reagents were pure analytical grade and used as is without further purification. The chemicals used were hydrochloric acid, sodium hydroxide and $MnCl_2$, $4H_2O$ (Sigma-Aldrich, France).

2. 2. Methods

2. 2. 1. Preparation of *Opuntia Ficus Indica* Powder (OFIP)

Cladodes of *Opuntia ficus indica* were repeatedly washed with tap water to remove dust and extraneous material and then rinsed with distilled water. The pads were cut into small pieces of 1cm width to facilitate drying and followed by oven-drying at 333 K for 48 hours. The pads were then ground into a fine powder in the size range of 40 to 80 μm using a laboratory mill (Fisher Bioblock Scientific). Finally, the obtained adsorbent was stored in a clean and dry plastic vials for further use.

2. 2. 2. Synthesis of the Activated *Opuntia Ficus Indica* (Ac-OFIP)

The treatment of *Opuntia ficus indica* powder **OFIP** with a hydrochloric acid aqueous solution at a concentration of 1M was undertaken to ensure the removal of natural minerals excess such as whewellite and $CaCO_3$ from its surface. The suspension was stirred for about 4 hours until homogenized, after which the solution was filtered and washed with distilled water until the pH of the water became neutral. Finally, the chemically treated powder was dried overnight in an electric oven at 333 K, ground, stored in plastic containers. The adsorbents were named OFIP for the non-treated material and Ac-OFIP (activated *Opuntia ficus indica*) for the material treated with hydrochloric acid).

2. 2. 3. Characterization of OFIP and Ac-OFIP

All characterizations were carried out at the Materials and Environment Laboratory for Sustainable Development, LR18ES10. A powder X-ray diffractometer (Malvern PANalytical X'pert^3 Powder, Netherlands) was used to collect data, which works with a flat rotated sample holder and a 1 D-PIXcell detector.

The specific surface area of the materials based on the Brunauer–Emmett–Teller-theory (B.E.T measurements) were determined with a sorptometer (Micromeritics ASAP 2020, USA) using N_2 adsorption at 77 K.

The vibration properties as well as the chemical bonds present in the materials were analyzed by KBr pellet technique on a Bruker FT-IR spectrophotometer (Tensor 27, USA). Measurements were done within the range of 400–4000 cm^{-1}.

2. 2. 4. Chemical Analysis and Batch Adsorption Experiment

The manganese concentrations were determined by inductively coupled plasma optical emission spectrosco-

py ICP (ISO 11885: 2007) and results were expressed as mg/L. The solution pH was determined using a pH meter (BANTE Instruments). Batch adsorption experiments were carried out in conical flasks, with optimal values for adsorbent mass, pH, temperature and initial Mn (II) concentration. The flasks were then placed on an orbital laboratory shaker (Heidolph), at a constant speed of 100 rpm. Supernatant was collected and filtered through a Whatman filter paper before chemical analysis to remove the adsorbent materials particles that may be present in the supernatant.

2. 2. 5. Significance of Thermodynamic Parameters for the Adsorption Process

The adsorption capacity at equilibrium Qe (mg/g) of manganese by OFIP and Ac-OFIP was calculated using the following equation:

$$Qe = ((C_i - Ce) \times V/m) \quad (1)$$

where C_i and Ce are the solution manganese concentrations at the initial and at equilibrium (mg/L), V is the volume of the solution and m is the adsorbent mass added to the solutions (g).

The studies on the adsorption isotherm are of fundamental importance to determine the adsorption capacity of Mn (II) on the adsorbents and to develop an equation which accurately represents the results, and which could be used for the purposes of design. The models used in this process of fixing metal ions in solution on the two adsorbents are the Langmuir, the Freundlich and the Temkin equations.

The Langmuir isotherm involves adsorption on a single layer of the adsorbent and supposes three conditions: (a) the number of adsorption sites on the surface of the solid is fixed and the recovery of the surface of the solid in one molecular layer, (b) the enthalpy of adsorption is identical for each adsorption site and (c) no interaction between the adsorbed molecules.

The linear form of the Langmuir isotherm model can be expressed as:

$$\frac{Ce}{Qe} = \frac{1}{Q_{max} \times K_L} + \frac{Ce}{Q_{max}} \quad (2)$$

where Q_{max} (mg/g) is the monolayer saturation adsorption capacity and K_L (L/mg) is the Langmuir constant related to the adsorption capacity. The essential characteristics of the Langmuir isotherm can be expressed by a unitless constant called the separation factor (R_L) or equilibrium parameter, defined by Weber et al., as following:[25]

$$R_L = \frac{1}{1+K_L \times C_i} \quad (3)$$

with the K_L the Langmuir constant and C_i, initial concentration value. When $R_L > 1$, the isotherm is unfavorable and linear when equal to 1. It is favorable if $0 < R_L < 1$ and irreversible if it is equal to zero. Unlike Langmuir, who assumes that the enthalpy of adsorption of fluids on solids is a constant with respect to the recovery rate of the surface of the solid, Freundlich assumes a logarithmic variation of this enthalpy according to the rate of recovery. According to the logarithmic form of the Freundlich isotherm, when $R_L > 1$, the isotherm is unfavorable and when R_L is equal to 1, it is linear. It is favorable if $0 < R_L < 1$ and irreversible if R_L takes the value zero. The logarithmic form of the Freundlich isotherm is expressed as:

$$ln\, Qe = lnK_F + \frac{1}{n} ln\, Ce \quad (4)$$

K_F (mg/g) and n are Freundlich constants. The Temkin model is based on the fact that the heat of adsorption varies linearly with the degree of recovery; this variation can be related to the heterogeneity of the surface, or to lateral interactions between adsorbed molecules. The Temkin's relationship in linear form is expressed as follows:

$$Qe = B\, ln\, K_T + B\, ln\, Ce \quad (5)$$

B (J/mol), the Temkin constant relative to the heat of adsorption and K_T (L/g), the equilibrium adsorption constant corresponding to the maximum binding energy.

The variations of the standard enthalpy ΔH°, the standard entropy ΔS° and the Gibbs free energy ΔG° during the adsorption of manganese by OFIP and Ac-OFIP can be evaluated from the following equations:

$$\Delta G^\circ = -RT ln K_C \quad (6)$$

$$K_C = \frac{Qe}{Ce} \quad (7)$$

ΔG° is also linked to ΔH° and ΔS° by:

$$\Delta G^\circ = \Delta H^\circ - T\Delta S^\circ \quad (8)$$

R is the gas constant with a value of 8.314 J/mol K and T is the absolute temperature (K).

Substituting Eq. (6) into Eq. (8) gives:

$$ln\, K_C = -\frac{\Delta H^\circ}{RT} + \frac{\Delta S^\circ}{R} \quad (9)$$

The thermodynamic properties of an adsorption process are necessary to determine whether the process is favorable or not. They can also help to understand the binding mechanisms of metals on adsorbents and show whether the process follows physisorption or chemisorption.[26] In physisorption, the adsorbate (metal ion) is fixed to the surface of the solid (adsorbent) by weak Van der Waals attractions and by a low heat of adsorption of approximately 20 to 40 KJ/mol. Consequently, the process is rapid and reversible in nature.[27] However, the current study considers about chemisorption when chemical bonds form between the

surface of the solid (adsorbent) and the adsorbate (metal ion) and with high heat of adsorption (40–400 KJ/mol). In this case, it is difficult to remove the heavy metals adsorbed from the adsorbent; therefore, chemisorption is slow and irreversible in nature.[28]

Adsorption Kinetics Models

In order to investigate the mechanism of manganese adsorption on the two adsorbents (OFIP and Ac-OFIP), four kinetics models are studied: pseudo-first order, pseudo-second order, Elovich and intraparticle diffusion.

Pseudo-First Order

The Lagergren relation, based on the adsorbed quantity, is the first-rate equation established to describe the kinetics of sorption in a liquid – solid system. This pseudo-first order model is represented by the following relation:

$$ln(Qe - Q_t) = ln\,Qe - \frac{K_1\,t}{2.303} \quad (10)$$

where Qe (mg/g) is the quantity adsorbed at equilibrium, Q_t (mg/g) is the quantity adsorbed at the time of the adsorption process (t) and K_1 (min^{-1}) is the pseudo-first-order rate constant.

Pseudo-Second Order

The application of Blanchard's model, allows to describe the adsorption process as pseudo-second order reaction, represented by the following equation:

$$\frac{1}{Q_t} = \frac{1}{K_b \times Qe^2} + \frac{t}{Qe} \quad (11)$$

where Qe (mg/g) is the quantity adsorbed at equilibrium, Q_t (mg/g) is the quantity adsorbed at time t, t is the time of the adsorption process and k_b (mg/g.min) is the pseudo-second-order adsorption rate constant.

Elovich Equation

The Elovich model is one of the most useful for describing such activated chemical adsorption. It is often valid for systems in which the adsorption sites are heterogeneous. The Elovich equation is as follows:

$$Q_t = \frac{1}{b} ln(ab) + \frac{1}{b} ln\,t \quad (12$$

where Q_t (mg/g) is the quantity of adsorption at time t (min), a (mg/g) is an initial adsorption rate and b (g/mg) is the desorption constant.

Intraparticle Diffusion Model

The intraparticle diffusion model has widely been applied for the analysis of adsorption kinetics. This model is represented by the equation:

$$Q_t = k_i\,t^{0.5} + C \quad (13)$$

where Q_t is the quantity of adsorption (mg/g) at time t (min), k_i ($mg/g.min^{0.5}$) is an intraparticle diffusion rate constant and C is the intercept.

3. Results and Discussion

In this study, manganese adsorption onto OFIP and Ac-OFIP was investigated as a function of solution pH, adsorbent dosage, initial concentration of Mn (II) and temperature.

3. 1. Analysis of the biosorbents

3. 1. 1. XRD Characterization

The structure analysis of the *Opuntia ficus indica* powder by X-ray diffraction prior and after treatment (OFIP / Ac-OFIP) (Fig. 1) was performed to identify the crystalline and amorphous regions present in these samples. The X-ray pattern of OFIP powder shows strong crystalline peaks characteristic for calcium oxalate monohydrate (whewellite) at 14–15° and 24–25° (2θ), which was identified with the PDF # 20–0231 of ICDD-JCPDS database. This result is in agreement with that reported by Monje and Baran[29] and Contreras-Padilla et al.,[24] which identified the presence of calcium oxalate in different Cactaceae species belonging to the Opuntioideae subfamily, including *Opuntia ficus indica*. Furthermore, the results showed three Bragg reflections located at 29–30, 39–40 and 45–50° (2θ) in the pattern which are indicative of the presence of calcium carbonate $CaCO_3$ (PDF # 47-1743).

The x-ray pattern of Ac-OFIP powder (Fig. 1) is typical for cellulose I. The four well defined crystal peaks observed around 2θ = 15°, 16.5°, 22° and 35° are assigned to (1–10), (110), (200) and (004) respectively.[30] Unlike hemicellulose and lignin, which are amorphous in nature, cellulose has a crystal structure due to hydrogen bonding interactions and Van der Waals forces between adjacent molecules.[31] The crystallinity of the fibers of *Opuntia ficus indica* powder after treatment was well assessed. The treat-

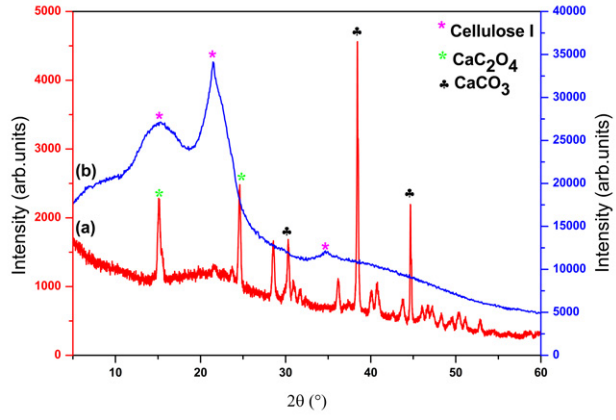

Fig. 1. XRD patterns of OFIP (a) and Ac-OFIP (b)

ment had effectively influenced the crystallinity of cellulose as reported by Mwaikambo and Ansell[32] stating that the alkaline chemical treatment on vegetable fibers increases their rigidity because the impurities present in them can be eliminated during this treatment. Therefore, the crystallinity of the Ac-OFIP powder can be determined and compared to the untreated OFIP powder to gain access to the effectiveness and importance of the activation process.

3. 1. 2. FT-IR Measurements

The spectra of OFIP and Ac-OFIP (Fig. 2) were investigated to obtain information on the nature of functional groups at the surface of the adsorbents. The infrared (IR) spectrum of OFIP showed broad, strong and superimposed bands in the 3600–3200 cm^{-1} region due to the elongation of the O-H bonds. The bands at 2928 cm^{-1}, 2858 cm^{-1} (different C-H vibrations), 1613.96 cm^{-1}, 1414.56 cm^{-1} and 780 cm^{-1} (different vibrations and deformation of the carboxylic groups) are characteristic of OFIP powder with the presence of calcium oxalate monohydrate (whewellite) and carbonates according to Contreras-Padilla et al.[24] Absorption peaks in the region of wavenumbers lower than 800 cm^{-1} could be attributed to N-containing bioligands as mentioned in the literature.[33] Due to OFIP's activation process with the acid treatment, a lot of FT-IR peaks have shifted in the Ac-OFIP spectrum. Thus, the intensity of the band linked to –OH (3600–3200 cm^{-1}) decreased after activation, which indicates that the treatment with acid leads to the breaking of weak bonds, and the band around between 1500–1750 cm^{-1} attributed to vibrations of carbonyl bonds C = O become more resolved and intense around 1740 cm^{-1}. The peaks at 1613.9 cm^{-1}, 1414.5 cm^{-1},780 cm^{-1} and near the region 800 cm^{-1} have completely disappeared in Ac-OFIP spectrum due to the elimination of calcium oxalate and carbonate and N-containing bioligands.

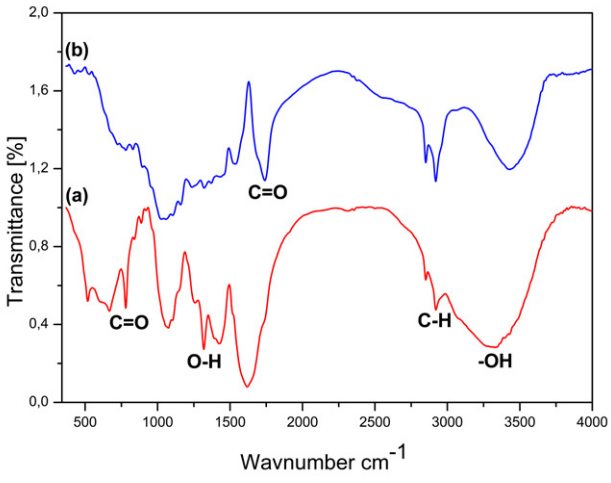

Fig. 2. FT-IR spectra of OFIP (a) and Ac-OFIP (b).

3. 1. 3. B.E.T Surface Areas

The specific surfaces of the two adsorbents Ac-OFIP and OFIP were determined by B.E.T and the values obtained indicate a very small specific surface for the untreated cactus powder. Barka et al. have already reported similar values in the range of 1.01 m^2/g in their study of the B.E.T surfaces of the Moroccan biosorbent *Opuntia ficus indica*.[33] They linked this result to the fact that the OFI can be considered as a non-porous material with no defined opening on their morphology and therefore without internal surface. The main reason could be the agglomeration of well-crystallized minerals ($CaCO_3$, CaC_2O_4 H_2O) on the surface of the cladodes, characterized by XRD measurement and IR spectroscopy[29] which contributes to the reduction of the porous surface and therefore to the specific surface. The OFIP product has a B.E.T surface area of 1.6 m^2/g and a porous volume equal to 0.002 cm^3/g, while Ac-OFIP has a significantly larger B.E.T surface area, 12.4 m^2/g and a porous volume equal to 0.090 cm^3/g. The increase in the B.E.T surface area of OFIP after treatment could be attributed to the removal of whewellite particles, carbonates and other impurities from OFIP. All these results confirmed the successful synthesis of Ac-OFIP.

3. 2. 1. Effect of pH

The pH of the aqueous solution is an important variable, which can have a significant effect on the extent of adsorption, because it influences on the surface properties of the adsorbent.[34–36] In addition, it influences the ionization degree of metals in the solution.[37–39] Manganese adsorption onto OFIP and Ac-OFIP was investigated at initial pH range of 4–8 and the results are shown in Fig. 3. All the other factors were kept constant that is: temperature at 298 K, adsorbent dosage at 0.4 g/L, contact time of 24 h, agitation speed kept at 100 rpm and Mn (II) initial concentration of 27.75 mg/L. As shown in Fig. 3 the percentage removal of Mn (II) greatly depends on pH for the Ac-OFIP powder. Firstly, the percentage removal was found to increase gradually with the increase of pH up to 5 for the OFIP with no considerable change after the pH 5. Secondly, for the adsorbent treated Ac-OFIP, the percentage removal of Mn (II) ion increased with an increase in the pH from 4 to 7 and it was almost constant up to pH 8. The results of the percentage of maximum elimination of the manganese ions were of the order of 35.5% and 91.6% for OFIP and Ac-OFIP, respectively. The small metal adsorption at low pH values could be attributed to the competition of hydrogen ions with the manganese for the occupancy of the adsorption sites. Indeed, at low pH values a protonation of functional groups was produced on the adsorbent surface which limited the interaction between the positively charged metal ions and the two adsorbents due to repulsive forces; this reduced the Mn (II) adsorption capacity.

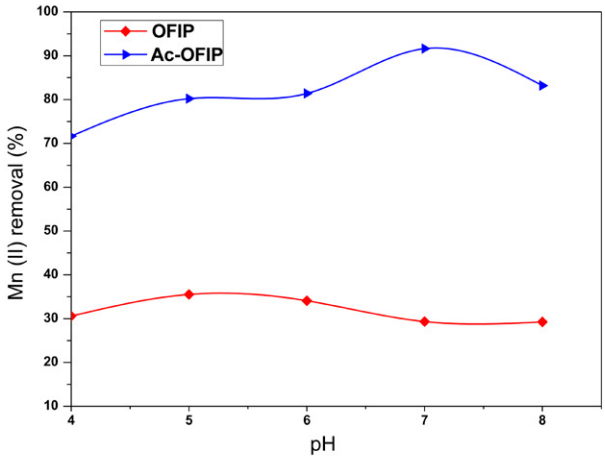

Fig. 3. Effect of pH on the adsorption of Mn (II) ions on OFIP and Ac-OFIP.

There was a significant increase in the removal of metal ions at pH 5 for OFIP and 7 for Ac-OFIP, this can be explained by the fact that the adsorption sites were no longer affected by the pH variation. At a higher pH, the removal efficiency of Mn (II) ions gradually decreased with the two adsorbents. A pH greater than 8 has been neglected due to the precipitation of $Mn(OH)_2$ which could be formed with the increasing amount of OH^- in the solution, which would be mistaken as adsorption due to the different powders. For subsequent investigations, pH 5 and 7 appeared as the optimal conditions for OFIP and Ac-OFIP respectively.

3. 2. 2. Effect of Adsorbents Dosage

The dependence of manganese adsorption on dose was studied at pH 5 for OFIP and pH 7 for Ac-OFIP. The initial concentration of Mn (II) was fixed at 27.75 mg/L and contact time at 24 h. All experiments were carried at ambient temperature with adsorbent concentrations from 0.2 g/L to 1.3 g/L. The relationship between the percentage removal of Mn (II) and the dose of OFIP and Ac-OFIP is shown in Fig. 4. The curves obtained show a great capacity of the Ac-OFIP material in the elimination of Mn (II) ions, which can reach approximately 99.6%, while it only reaches 52% for OFIP. The results obtained also indicate that the rate of removal of Mn (II) ions increases with the amounts of adsorbent in the solution to reach its maximum at optimal dosages of 0.7 g/L for Ac-OFIP and 1.1g/L for OFIP. This trend in uptake is attributed to the increasing number of negatively charged active sites and surface area for Mn (II) binding on the adsorbent. After the optimum dosage, the elimination rate does not change, which corresponds to the saturation of different types of adsorbent active sites by the adsorbate (ions of metals Mn (II) in the system).

3. 2. 3. Effect of Mn (II) Initial Concentration

In order to evaluate the effect of Mn (II) ion concentration on the adsorption behavior of the two adsorbents (OFIP and Ac-OFIP), adsorption experiments with varying manganese concentrations of 2 mg/L to 85 mg/L were studied in the best experimental conditions: pH 5.0 for OFIP, pH 7.0 for Ac-OFIP and adsorbent concentration of 0.7g/L for Ac-OFIP, and 1.1 g/ L for OFIP. Fig. 5 shows that the highest percentage removal of Mn (II) are observed for Ac-OFIP (99.99%) with a maximum adsorption capacity of 42.02 mg/g. However, pure OFIP exhibits a low adsorption capacity of only 20.8 mg/g. It can also be deduced from the results presented in Fig. 5 that for the two adsorbents, the maximum adsorption capacities are only reached for low initial concentrations of Mn (II), then the elimination values decrease with increasing initial concentration of the manganese solution. This is due to the fact that some manganese ions remained in the solution due to

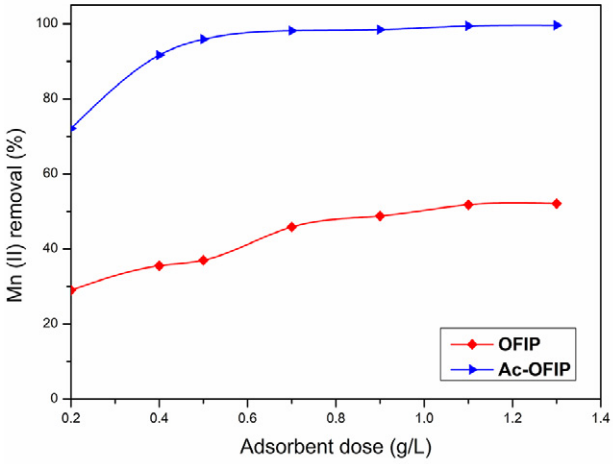

Fig. 4. Effect of adsorbent dose on the elimination of Mn (II) ions for OFIP and Ac-OFIP.

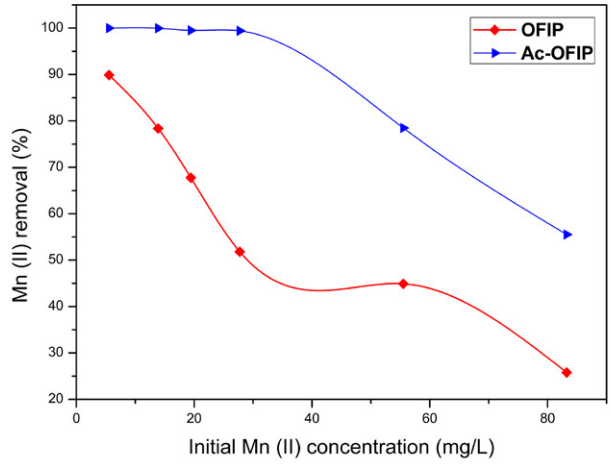

Fig. 5. Effect of Mn (II) concentration on removal rate for OFIP and Ac-OFIP.

Table 1. Fitting parameters and goodness of fit for three different isotherm models (Langmuir, Freundlich and Temkin) applied to experimental adsorption data.

Adsorbents	Langmuir			Freundlich			Temkin		
	Q_{max} (mg/g)	K_L	R^2	n	K_F	R^2	B	K_T	R^2
OFIP	20.8	0.245	0.99	3.244	6.157	0.95	3.306	6.36	0.96
Ac-OFIP	42.02	6.102	0.99	5.437	25.84	0.90	3.563	8.32	0.98

the saturation of the active sites on the adsorption surface of the adsorbent materials and thus sites with high affinity were the first to be saturated. Subsequently, the affinity of the metal cations for the remaining sites decreased.

3. 2. 4. Effect of Temperature

The temperature of the medium is a very important parameter in this process because it exerts a considerable influence on the adsorption rate.[40] The temperatures used in this experimental phase vary from 293 to 313 K with an interval of 5 K. The results of the tests carried out show that the temperature acts directly on this adsorption process with maximum fixation at 308 K for the two adsorbents. This is explained by the fact that the adsorption of manganese in aqueous medium by OFIP and Ac-OFIP is exothermic. The percentage removal of Mn (II) for this medium are 80% and 36% for Ac-OFIP and OFIP, respectively, (Fig. 6).

3. 2. 5 Effect of Contact Time

The effect of contact time on the percent removal of Mn (II) by OFIP and Ac-OFIP was studied in the range 10–120 min to find equilibrium time for adsorption (Fig. 7). The adsorption experiments were carried out at optimal experimental conditions: pH 5.0 in the case of OFIP as adsorbent with concentration of 1.1 g/L and pH 7.0 for the case of Ac-OFIP as adsorbent with concentration of 0.7 g/L. The initial concentration of manganese was 20 mg/L in both cases. As shown in Fig. 7 the percentage removal of Mn (II) with both adsorbents (OFIP and Ac-OFIP) is higher at the beginning. This is probably due to the fact that at the beginning a larger surface of adsorbent is available for the adsorption of Mn (II). The equilibrium was reached within the first 60 and 80 minutes of stirring with Ac-OFIP and OFIP, respectively. Beyond this time, we noticed it reached a saturation level. As the contact time increased the active surface adsorption sites on both adsorbents were filled.

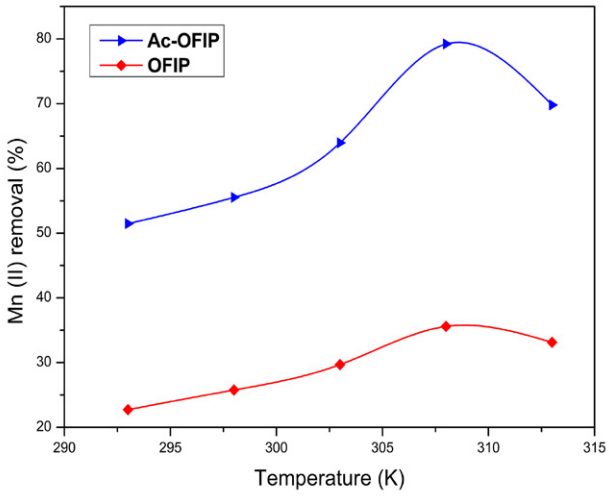

Fig. 6. Effect of temperature on removal rate for OFIP and Ac-OFIP.

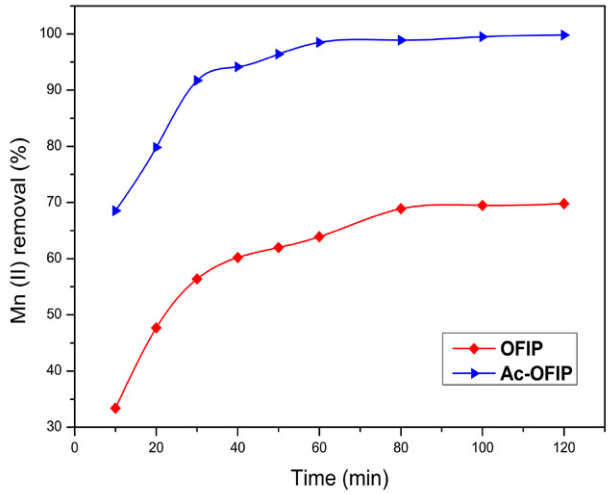

Fig. 7. Effect of contact on removal rate for OFIP and Ac-OFIP.

3. 3. Adsorption Isotherms

The application of Langmuir, Freundlich and of Temkin models on the results of the experiments was undertaken under the current study operating conditions (Vag: 100 rpm; T_{milieu}: 298 K; pH milieu: 5 with OFIP, 7 with Ac-OFIP; and $m_{(OFIPand\ Ac\text{-}OFIP)}$: 1.1g/L and 0.7 g/L). Fig. 8 (a) and Fig. 9 (a) demonstrate the linear plot of Ce/Qe as a function of Ce for OFIP and Ac-OFIP respectively. The values of Q_{max} and K_L were determined from slope and the ordinate at the origin of the linear regressions as shown in Table 1. The R_L values calculated for this study are illustrated in Table 2. Two plots of ln (Qe) as a function of ln (Ce) are shown in Fig. 8 (b) and Fig. 9 (b) for OFIP and Ac-OFIP, respectively, where the values of K_F, n and the correlation coefficient R^2 for the Freundlich model are given in Table 1.

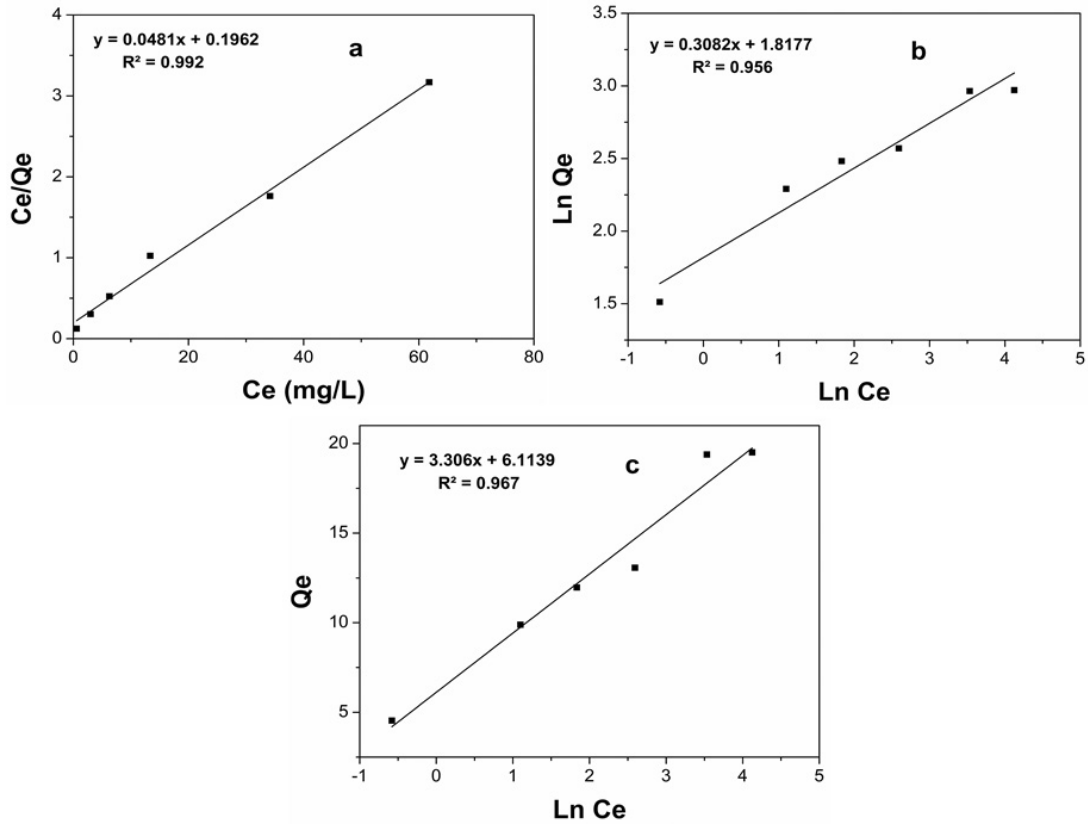

Fig. 8. Langmuir isotherm (a), Freundlich isotherm (b) and Temkin isotherm (c) for Mn (II) adsorption on OFIP adsorbent.

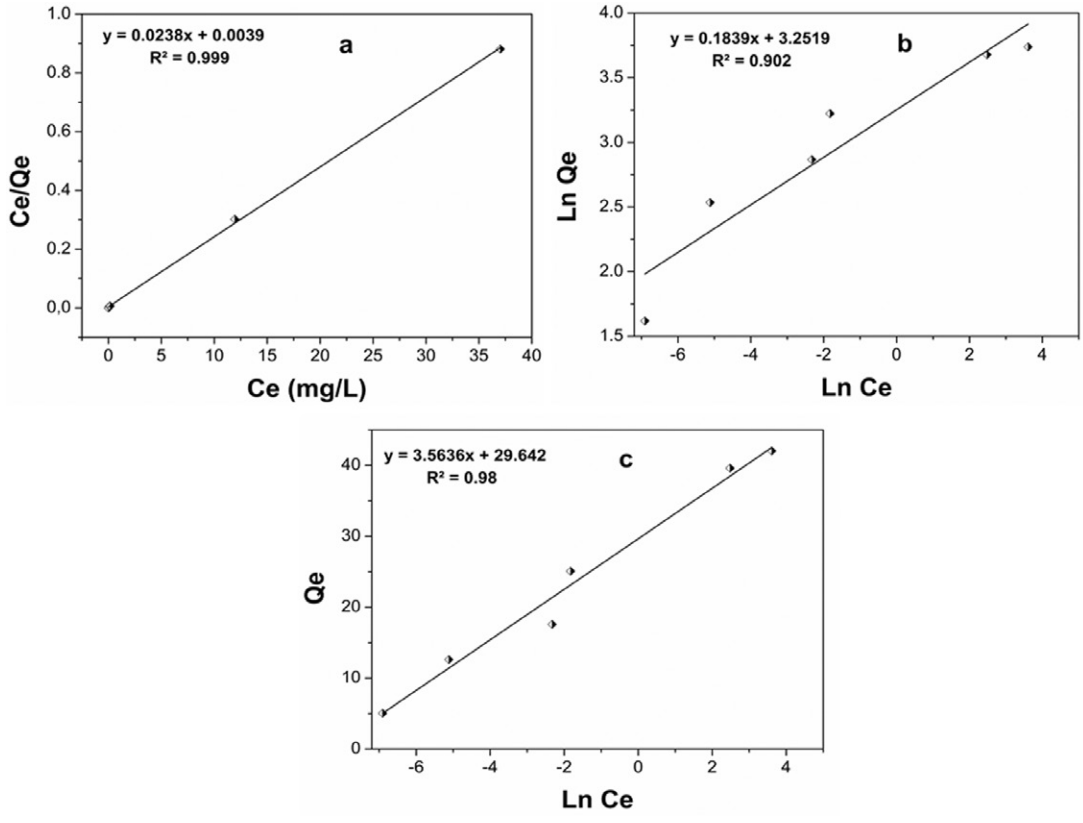

Fig. 9. Langmuir isotherm (a), Freundlich isotherm (b) and Temkin isotherm (c) for Mn (II) adsorption on Ac-OFIP adsorbent.

Table 2. R_L as a function of the initial concentration of manganese

C_i (mg/L)	5.55	13.87	19.42	27.75	55.50	83.25
R_L (OFIP)	0.424	0.227	0.173	0.128	0.068	0.046
R_L (Ac-OFIP)	0.028	0.011	0.008	0.005	0.002	0.001

Table 3. Values of thermodynamic parameters of manganese adsorption at different temperatures by OFIP and Ac-OFIP.

Adsorbent	Temperature K	K_F	ΔG° KJ/mol	ΔH° KJ/mol	ΔS° KJ/mol K
OFIP	293	0.2262	3.6210		
	298	0.2670	3.2717	26.30	0.077
	303	0.3248	2.8330		
	308	0.4248	2.1925		
	313	0.3807	2.5128		
Ac-OFIP	293	0.8158	0.4958		
	298	0.9605	0.0998	54.79	0.183
	303	1.3654	−0.7845		
	308	2.9303	−2.7530		
	313	1.7770	−1.4961		

Figures 8 (c) and 9 (c) show plots of Qe as a function of ln (Ce), which permitted to determine the isothermal constants K_T and B. The values of K_T, B and the correlation coefficient R^2 for Temkin model are given in Table 1.

The best data adjustments were obtained with the Langmuir isothermal model for the OFIP and Ac-OFIP. This observation is justified by the values of the regression coefficients which are better for the OFIP and Ac-OFIP with the Langmuir equation (R^2 Langmuir: 0.99). It is clear

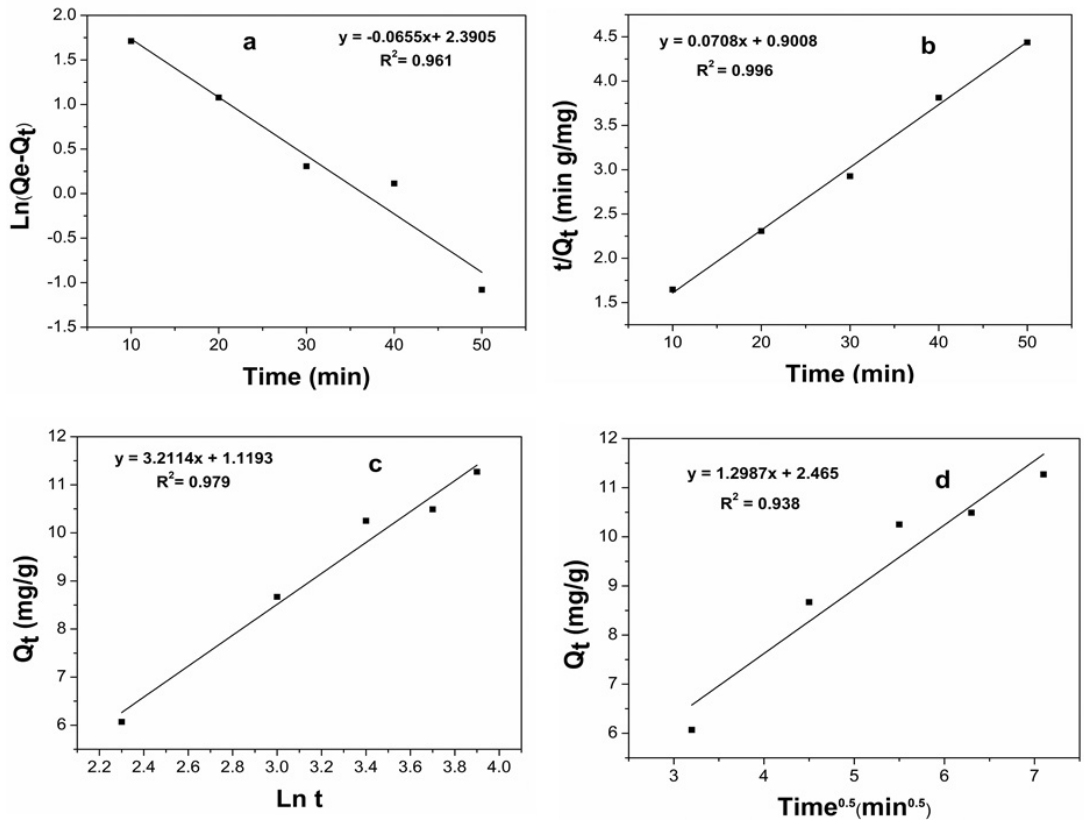

Fig. 10. Pseudo-first-order (a), pseudo-second-order (b), Elovich (c) and intraparticle diffusion (d) models for Mn (II) adsorption on OFIP adsorbent.

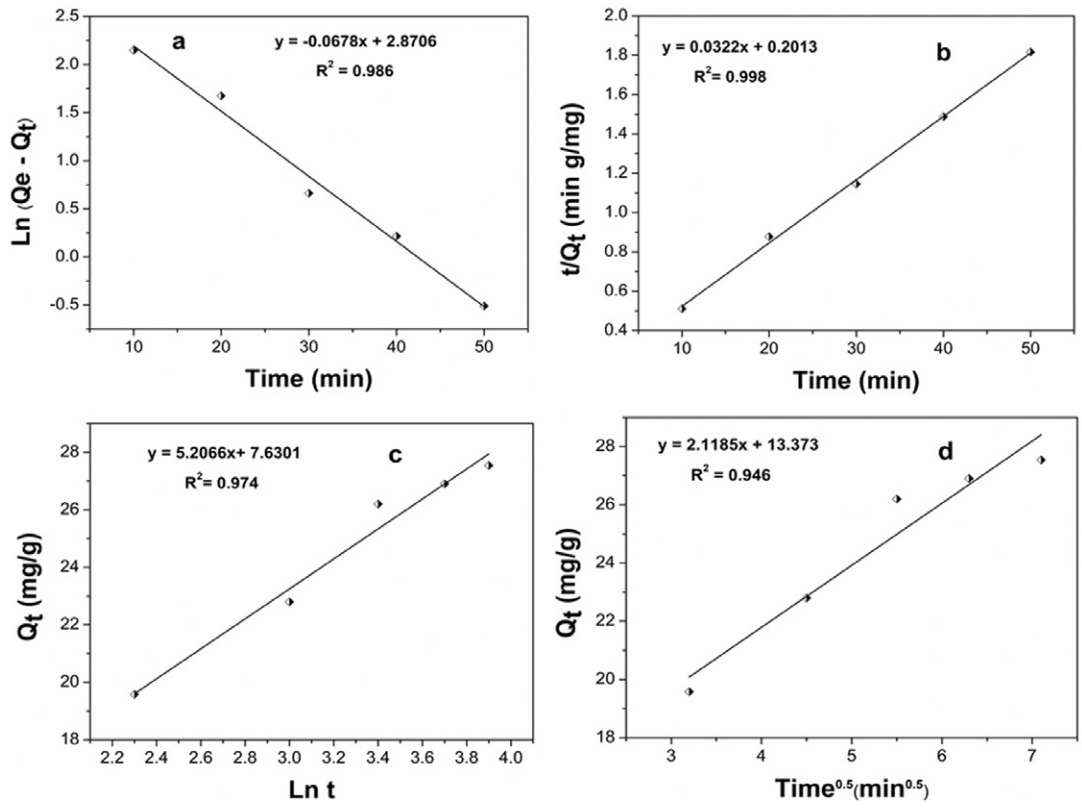

Fig. 11. Pseudo-first-order (a), pseudo-second-order (b), Elovich (c) and intraparticle diffusion (d) models for Mn (II) adsorption on Ac-OFIP adsorbent.

from Table 2 that the value of the R_L ratio decreases with the increase of the initial concentration for the two cases of adsorbents and remain between 0 and 1 suggesting a favorable significance for the Langmuir model.

3. 4. Thermodynamics Studies

The estimated thermodynamic parameters ΔH°, ΔS° and ΔG° of the effect of the temperature on the adsorption of Mn (II) by pure and modified *Opuntia ficus indica* (OFIP/Ac-OFIP) are given in the Table 3.

All the values of free energies for the chosen temperature range (ΔG° > 0) revealed that the adsorption of Mn (II) by OFIP was not a spontaneous process, whereas for the adsorption of Mn (II) by Ac-OFIP, the free energy values showed positive rates at low temperatures and tended towards the spontaneity of the adsorption process with increasing temperature. The adsorption of Mn (II) increased as the temperature increased in the range of 293 to 313 K, which implies that the process is more favorable at high temperatures.

A linear plot of ln K_F against 1/T in the temperature range of 293 to 308 K was established and ΔH° and ΔS° were determined.

The calculated enthalpy values are greater than zero (ΔH° > 0) and have been found to be 26.30 and 54.79 kJ/mol respectively for OFIP and Ac-OFIP, which shows that this adsorption process is endothermic in nature. The enthalpy value ΔH° is less than 40 kJ/mol for OFIP, which indicates that physisorption is the main adsorption mechanism, while it is greater than 40 kJ/mol for Ac-OFIP and this indicates in this case that chemisorption is the main mechanism of adsorption. The positive entropy values for the two adsorbents (ΔS° > 0) reflect a disorder in the system at the solid solution interface that occurred during adsorption.

3. 5. Adsorption Kinetics

Details of the application of the four kinetic models (pseudo-first order, pseudo-second order, Elovich and intraparticle diffusion). The results obtained from the experiments under optimum conditions are illustrated on Fig. 10 (a, b, c, d) and Fig. 11 (a, b, c, d). The linear plot of ln (Q_e-Q_t) versus of time t for OFIP and Ac-OFIP, respectively, is shown Fig. 10 (a) and Fig. 11 (b). The values of k_1, Q_e and R^2 were determined from slope and the ordinate at the origin of the linear regressions (Table 4).

Two plots of t/Q_t as a function of time t have been shown in Fig. 10 (b) and 11 (b) for OFIP and Ac-OFIP respectively, where the values of k_2, Q_e and the correlation coefficient R^2 for the pseudo-second order model are given in Table 4. Figures 10 (c) and 11 (c) show plots of Q_t as a function of ln t, which allowed to determine the constants

Table 4. Correlation coefficients R^2 and constant values of kinetics parameters of manganese adsorption by OFIP and Ac-OFIP.

Adsorbent	Pseudo-First-r Orde		Pseudo-Second-Order		Elovich Model		Intraparticle Diffusion	
OFIP	R^2	0.961	R^2	0.996	R^2	0.979	R^2	0.938
	$Q_{e\ (The)}$	11.61	$Q_{e\ (The)}$	11.61	a	4.553	k_i	1,298
	$Q_{e\ (Exp)}$	10.92	$Q_{e\ (Exp)}$	14.12	b	0.311	C	2,465
	K_1	0.150	K_2	0.006				
Ac-OFIP	R^2	0.986	R^2	0.998	R^2	0.974	R^2	0.946
	$Q_{e\ (The)}$	28.14	$Q_{e\ (The)}$	28.14	a	22.536	k_i	2.118
	$Q_{e\ (Exp)}$	17.65	$Q_{e\ (Exp)}$	31.06	b	0.192	C	13.373
	K_1	0.156	K_2	0.005				

a and b. The values of a, b and the correlation coefficient R^2 for Elovich model are given in Table 4. Figures 10 (d) and 11 (d) show the linear plot of Q_t as a function $t^{0.5}$ for OFIP and Ac-OFIP respectively, where the values of k_i and the correlation coefficient R^2 for the intraparticle diffusion model are given in Table 4.

As can be seen from the Fig. 10 and Fig. 11, the extremely high correlation coefficients R^2 for OFIP (0.996) and Ac-OFIP (0.998) were obtained for pseudo-second order model. Thus, adsorption of manganese onto adsorbents (OFIP and Ac- OFIP) followed the pseudo-second order kinetic process. In addition, equilibrium adsorption capacity values Qe calculated were in good agreement with experimental values for the two adsorbents.

3. 6. Adsorption Mechanisms of Mn (II)

3. 6. 1. XRD Analysis

Fig. 12 shows the XRD patterns of Ac-OFIP before and after the adsorption of Mn (II) ions. X-ray diffraction analysis was used to confirm the presence of Mn on the surface of the OFIP modified. Thanks to the appearance of new MnO_x peaks, it is possible to probe their presence. As mentioned in the previous sections, the adsorption of Mn (II) by Ac-OFIP is a chemisorption and a detailed inspection of the XRD diagram after the adsorption process could provide more information on the mechanism of adsorption. Compared to that of the pure Ac-OFIP pattern, new distinct peaks were observed on the Ac-OIFP diagram at 26.8°, 29.5° and 31.9° 2θ attributed to the typical peaks of MnO_x oxides according to references from PDF-4 database (ICDD). No strong evolution of the XRD diagram was noted, the Bragg angles of the cellulosic diagram (diffraction peaks) remained essentially unchanged following the adsorption process of the Mn (II) cations. These results suggest that the grafting of different MnO_x took place on the surface of the cellulose fibers, and the cellulose maintained its crystal structure. These results suggest that the Mn (II) adsorbed was first oxidized to higher degrees, and then, probably maintained on the surface of the adsorbent with different C-O-MnO_x bonds.

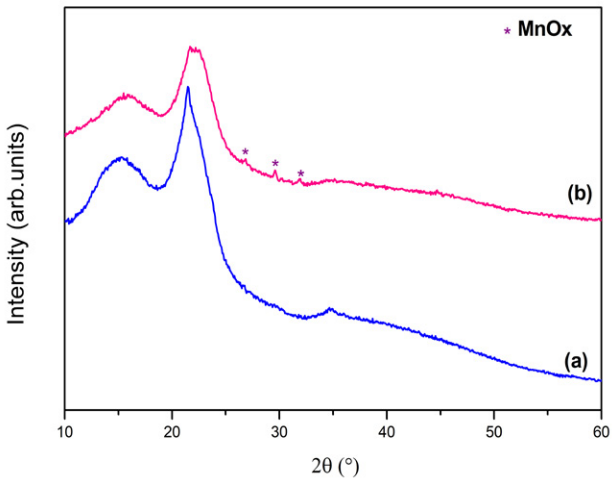

Fig. 12. Comparison in XRD patterns of Ac-OFIP (a) and Mn-Ac-OFIP (b).

3. 6. 2. Analysis of FT-IR Spectra

FT-IR spectra were also useful for judging the bonding states between functional groups of the adsorbent and the metal ion. The comparison of the IR spectra of pure Ac-OFIP and that after adsorption is well illustrated in Fig. 13. The appearance of an intense band at 620 cm^{-1} and three minor bands at 437cm^{-1}, 536 cm^{-1} and 474 cm^{-1} demonstrated the presence of different oxides of MnO_x on the adsorbent. In addition, the absorption bands of MnO_x, in the region of low frequencies were very broad; this was related to the crystalline and amorphous content and to the effect of the particle size on the spectral characteristics. Due to the interaction of the functional groups of the adsorbent with the Mn (II), FT-IR peaks can move towards lower or higher wavenumbers after the loading of Mn (II), depending on bond strength between metal ions and adsorbent.[41] It can be deduced from Figure 10 that after the adsorption of Mn (II), there was a change in the peak of the carbonyl group C = O from 1737 cm^{-1} to 1637 cm^{-1}, which may indicate that the carbonyl group is involved in the adsorption process.

Furthermore, the appearance of a broad band at 2130 cm^{-1} related to the carbonyl stretches for $Mn(CO)_n$ on the surface after adsorption, indicates the important role that it plays in the chemisorption of Mn (II) on ligands. On surfaces, the geometric arrangement of the CO bond can be determined from the vibration frequency.[42,43] The stretching of the free molecule C-O generally occurs at 2143 cm^{-1},[42,44] far from most other molecular vibrations, it provides a practical and sensitive indicator of binding interactions. In "classic" carbonyls, the stretching frequency C-O(ν_{CO}) is lowered compared to its value in the free CO molecule due to a marked decrease in bonding electron density and an increase in antibonding electron density in the π*.

The majority of the transition metal carbonyl complexes exhibit a red shift resulting in stretching of the carbonyl. In our case the charge-induced reduction in π back-bonding leads to a decreased red-shift in $Mn(CO)_n$ (υ_{CO} = 2130 cm^{-1}).

No change in the frequency of the cellulosic bands was noted following the adsorption process, suggesting that chemisorption took place on the surface of the cellulosic fiber, and also that Ac-OFIP continued to maintain its crystal structure.

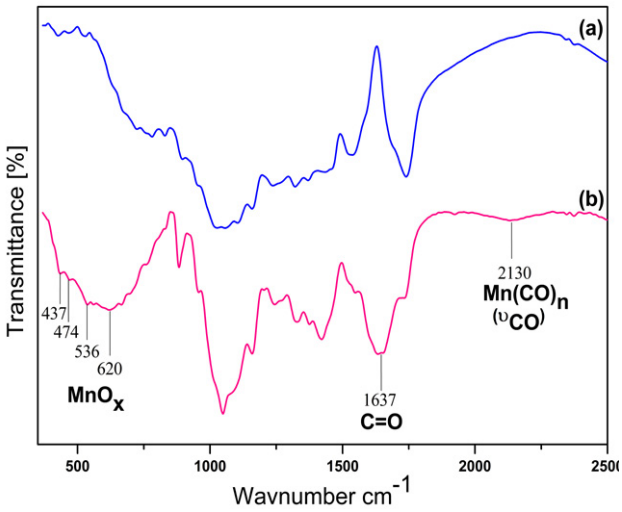

Fig. 13. Comparison in FT-IR spectra of Ac-OFIP (a) and Mn-Ac-OFIP (b).

3. 7. Comparison with the Other Adsorbents

Some adsorbents used for the removal of Mn (II) reported in the literature were compared with OFIP, and with Ac-OFIP as indicated in Table 5. The values obtained for the maximum adsorption capacity in this study are much higher compared to those obtained with other adsorbents (except the two studies 45 and 46). Therefore, it should be emphasized that OFIP and Ac-OFIP adsorbents can become a material of choice successfully compete with other absorbents.

Table 5. Comparison of maximum Mn (II) adsorption capacities with other adsorbents.

Adsorbents	Capacity (mg/g)	Reference
Ac-OFIP	42.0	This study
OFIP	19.5	This study
Pecan nutshell	103.8	45
Crab shell particles	69.9	46
Natural zeolitic tuff	10.0	47
Black carrot residues	5.2	48
Activated carbon immobilized Bytannic acid	1.7	49
Kaolinite	0.4	50
Pithacelobium dulce carbon	0.4	7

4. Conclusion

In this study, *Opuntia ficus indica* powder with and without activation treatment (OFIP, Ac-OFIP) have been used as an adsorbent in the removal of Mn (II) from aqueous solutions. The surface modifications of OFIP have been made to improve the selectivity of the by-products and thus have more affinity for the cations and improve the adsorption capacity. A very high percentage of manganese elimination has been observed in the case of Ac-OFIP. In the study of factors affecting the adsorption process, the percentage removal of Mn (II) increased with the pH and the dose of adsorbents up to the optimum values and there have been no considerable changes thereafter. The equilibrium absorption of the adsorbents has been found to decrease with the increase in the initial concentration of manganese ions in solution. The thermodynamic study has shown that this process is endothermic in nature and with a positive change in entropy for the two adsorbents, suggesting the affinity of the metal ion for the adsorbents. Chemisorption is the main adsorption mechanism for Ac-OFIP while it is physisorption for OFIP. A study of experimental isotherms such as Langmuir, Freundlich and Temkin revealed that the best fit has been obtained by the Langmuir model for OFIP and Ac-OFIP. The kinetic data is in good agreement with pseudo-second order kinetic model with high correlation coefficients for the two adsorbents. For Ac-OFIP, the XRD and infrared characterizations have confirmed that the process is chemisorption as suggested by the thermodynamic study. The adsorption mechanisms consisted of electrostatic interaction, oxidation of the Mn (II) adsorbed to higher degrees and then probably maintained on the surface of the adsorbent with different C-O-MnO_x bonds. The results have shown that Ac-OFIP is an effective adsorbent of Mn (II) which needs to be further explored.

Acknowledgements

Financial support from the Ministry of Higher Education and Scientific Research of Tunisia is gratefully ac-

knowledged. The authors appreciate Ms. Hajer REBAI for linguistic editing and proofreading of the manuscript.

Declaration of Interest Statement

We declare that we do not have any commercial or associative interest that represents a conflict of interest in connection with the work submitted.

5. References

1. A. Omri, M. Benzina, *Alex. Eng. J.* **2012**, *51*, 343–350. **DOI:**10.1016/j.aej.2012.06.003
2. H. A. Aziz, P. G. Smith, *Wat. Res.* **1996**, *30*, 489–492. **DOI:**10.1016/0043-1354(95)00178-6
3. D. L. Jensen, J. k. Boddum, S. Redemann, T. H. Christensen, *Environ. Sci. Technol.* **1998**, *32*, 2657–2664. **DOI:**10.1021/es9711270
4. G. R. Watzlaf, *Proceedings America Society of Mining and Reclamation*, **1987**, *17*, 83–90. **DOI:**10.21000/JASMR88010083
5. UNEP, North America's Environment, A thirty-years State of the Environment and Policy Retrospective, UNEP, New York, **2002.**
6. S. R. Taffarel, J. Rubio, *Miner. Eng.* **2010,** *23*, 1131–1138. **DOI:**10.1016/j.mineng.2010.07.007
7. K. A. Emmanuel, A. Veerabhadra Rao, *Rasayan J. Chem.* **2008**, *1*, 840–852.
8. B. Kwakye-Awuah, B. Sefa-Ntiri, E. Von-Kiti, I. Nkrumah, C. Williams, *Water J.* **2019**, *11*,1–19. **DOI:**10.3390/w11091912
9. K. Z. Al-Wakeel, H. A. Abd-El Monem, M. M. H. Khalil, *Chem. Eng. J.*, **2015**, *3*, 179–186. **DOI:**10.1016/j.jece.2014.11.022
10. M. Aschner, K. M. Erikson, E. H. Hernández, R. Tjalkens, *Neuromolecular Med.* **2009**, *11*, 252–266. **DOI:**10.1007/s12017-009-8083-0
11. A. Abdul kadir, N. Othman, N. A. Azmi, *IJSCET*. **2012**, *3*, 2180–3242.
12. WHO, Guidelines for drinking-water quality, 2nd ed. WHO Press Geneva Switzerland, **2011**, 1–21.
13. J. B. Awuah, N. Dzade, R. Tia, E. Adei, B. Kwakye-Awuah, R. R. A. Catlow, N. H. De Leeuw, *Phys. Chem. Chem. Phys.* **2016**, *18*, 11297–11305. **DOI:**10.1039/C6CP00190D
14. M. Ahmad, Iron and Manganese removal from ground water: geochemical modeling of the vyredox method. Master Thesis, University of Oslo, Oslo, Norway, **2012**.
15. P. Marzal, A. Seco, C. Gabaldo, J. Ferrer, *J. Chem. Technol. Biotechnol.*, **1996**, *66*, 279–285. **DOI:**10.1002/(SICI)1097-4660(199607)66:3<279::AID-JCTB506>3.0.CO;2-K
16. A. Saranya, S. Sasikala, G. Muthuraman, *Int. J. Recent Sci. Res.* **2017**, *8*, 17867–17876.
17. M. M. Nassar, K. T. Ewida, E.E. Ebrahiem, Y. Magdy, M. H. Mheaedi, *Adsorpt. Sci. Technol.* **2004**, *22*, 25–37. **DOI:**10.1260/026361704323150971
18. S. E. Bailey, T. J. Olin, R.M. Bricka, D. D. Adrian, *Water Res.* **1999**, 33, 2469–2479. **DOI:**10.1016/S0043-1354(98)00475-8
19. G. Sun, W. Shi, *Ind. Eng. Chem. Res.***1998**, *37*, 1324–1328. **DOI:**10.1021/ie970468j
20. W. Zhang, H. Duo, S. Li, Y. An, Z. Chen, Z. Liu, Y. Ren, S. Wang, X. Zhang, X. Wang, *Colloids Interface Sci. Commun.* **2020,** *38,* 1–13. **DOI:**10.1016/j.colcom.2020.100308
21. A. Negrea, A. Gabor, C. M. Davidescu, M. Ciopec, P. Negrea, N. Duteanu, A. Barbulescu, *Sci. Rep.* **2018**, *8*, 1–11. **DOI:**10.1038/s41598-017-18623-0
22. M. A. Ayadi, W. Abdel maksoud, M. Ennouri, H. Attia, *Ind. Crop. Prod.* **2009**, *30*, 40–47. **DOI:**10.1016/j.indcrop.2009.01.003
23. G. Lassoued Ben Miled, B. Djobbi, R. Ben Hassen, *J. Water Chem. Techno.* **2018**, *40*, 285–290. **DOI:**10.3103/S1063455X18050065
24. M. Contreras-Padilla, E.M. Rivera-Muñoz, E. Gutiérrez-Cortez, A. Del Real, M.E. Rodríguez-García, *J. Biol. Phys.* **2015**, *41*, 99 –112. **DOI:**10.1007/s10867-014-9368-6
25. T. W. Weber, R. K. Chakravorti, *AIChE J.* **1974**, *20*, 228–238. **DOI:**10.1002/aic.690200204
26. M. N. Sahmoune, *Chem. Eng. Technol.* **2016**, *39***,** 1617–1628. **DOI:**10.1002/ceat.201500541
27. M. T. Yagub, T. K. Sen, S. Afroze, H. M. Ang, *Adv. Colloid. Interfac.*, **2014**, *209*, 172–184. **DOI:**10.1016/j.cis.2014.04.002
28. O. Aksakal, H. Ucun, *J. Hazard. Mater.* **2010**, *181*, 666–672. **DOI:**10.1016/j.jhazmat.2010.05.064
29. P. Monje, E. Baran, *J. Plant Physiol.*, **2004**, *161*, 121–123. **DOI:**10.1078/0176-1617-01049
30. D. Klemm, B. Heublein, H. P. Fink, A. Bohn, *Angew. Chem. Int. Ed.* **2005**, *44*, 3358–3393. **DOI:**10.1002/anie.200460587
31. Y. H. Zhang, L. R. Lynd, *Biotechnol. Bioeng.* **2004**, *88*, 797–824. **DOI:**10.1002/bit.20282
32. L. Y. Mwaikambo, M. P. Ansell, *J. Mater. Sci.* **2006**, *41*, 2483–2496. **DOI:**10.1007/s10853-006-5098-x
33. N. Barka, K. Ouzaouit, M. Abdennouri, M. El Makhfouk, *J. Taiwan Inst. Chem. E.* **2013**, *44***,** 52–60. **DOI:**10.1016/j.jtice.2012.09.007
34. A. F. Baybars, M. Korkmaz, C. Özmetin, *J. Disper. Sci. Technol.* **2016,** *37*, 991–1001. **DOI:**10.1080/01932691.2015.1077455
35. D. P. Tiwari, D. K. Singh, D. N. Saksena, *J. Environ. Eng.* **1995**, *121*, 479 – 481. **DOI:**10.1061/(ASCE)0733-9372(1995)121:6(479)
36. H. A. Elliot, C. P. Huang, *Water Res.*, **1981**, *15*, 849 – 855. **DOI:**10.1016/0043-1354(81)90139-1
37. Q. Du, Z. Sun, W. Forsling, H. Tang, *J. Colloid. Interf. Sci.* **1997**, *187*, 232–242. **DOI:**10.1006/jcis.1996.4676
38. K. S. Hui, C. Y. H. Chao, S. C. Kot, *J. Hazard. Mater.* **2005**, *127*, 89–101. **DOI:**10.1016/j.jhazmat.2005.06.027
39. M. Fadel, M. N. Hassanein, M. M. Elshafei, A. H. Mostafa, M. A. Ahmed, H. M. Khater, *HBRC.* **2017**, *13*, 106–113. **DOI:**10.1016/j.hbrcj.2014.12.006
40. K. P Yadava, B. S. Tyagi, V.N. Singh, *Environ. Technol. Lett.* **1988,** *9*, 1233–1244. **DOI:**10.1080/09593338809384686
41. Y. Gutha, V. S. Munagapati, M. Naushad, K. Abburi, *Desalin.*

Water Treat. 2014, 1–9.
42. Z. D. Reed, M. A. Duncan, *J. Am. Soc. Mass. Spectr.* **2010**, *21*, 739–749. **DOI:**10.1016/j.jasms.2010.01.022
43. G. A. Somorjai, Introduction to Surface Chemistry and Catalysis, Department of Chemistry University of California Berkeley. New York, **1994**.
44. K. P. Huber, G. Herzberg, Molecular Spectra and Molecular Structure IV. Constants of Diatomic Molecules, National Research Council of Canada. Canada, **1978**. **DOI:**10.1007/978-1-4757-0961-2_2
45. J. C. P. Vaghetti, E. C. Lima, B. Royer, B. M. da Cunha, N. F. Cardoso, J. L. Brasil, S. L. P. Dias, *J. Hazard. Mater.* **2009**, *162*, 270–280. **DOI:**10.1016/j.jhazmat.2008.05.039
46. K. Vijayaraghavan, H. Y. N. Winnie, R. Balasubramanian, *Desalinat.* **2011**, *266*, 195–200. **DOI:**10.1016/j.desal.2010.08.026
47. N. Rajic, D. Stojakovic, S. Jevtic, N. Zabukovec, J. Kovac, V. Kaucic, *J. Hazard. Mater.* **2009**, *172*, 1450–1457. **DOI:**10.1016/j.jhazmat.2009.08.011
48. F. Güzel, H. Yakut, G. Topal, *J. Hazard. Mater.* **2008**, *153*, 1275–1287. **DOI:**10.1016/j.jhazmat.2007.09.087
49. A. Uçer, A. Uyanik, S. F. Aygun, *Sep. Purif. Technol.* **2006**, *47*, 113–118. **DOI:**10.1016/j.seppur.2005.06.012
50. Ö. Yavuz, Y. Altunkaynak, F. Güzel, *Water Res.* **2003**, *37*, 948–952. **DOI:**10.1016/S0043-1354(02)00409-8

Povzetek

The adsorption of manganese ions from aqueous solutions by pure and acid-treated *Opuntia ficus indica* as natural low-cost and eco-friendly adsorbents was investigated. The adsorbents' structures were characterized by powder X-ray diffraction and infrared spectroscopy. Specific surface areas were determined using the Brunauer-Emmett-Tell equation. The study was carried out under various parameters influencing the manganese removal efficiency such as pH, temperature, contact time, adsorbent dose and initial concentration of manganese ion. The maximum adsorption capacity reached 42.02 mg/g for acid-treated *Opuntia ficus indica*, and only 20.8 mg/g for pure *Opuntia ficus indica*. The Langmuir, Freundlich and Temkin isotherms equations were tested, and the best fit was obtained by the Langmuir model for both adsorbents. The thermodynamic study shows that chemisorption is the main adsorption mechanism for the activated adsorbent while physisorption is the main adsorption mechanism for the pure adsorbent. The kinetics of the adsorption have been studied using four kinetics models of pseudo-first order, pseudo-second order, Elovich and intra-particle diffusion. Structural analyses indicate the appearance of MnO_x oxides on the cellulose fibers. The adsorption mechanisms consist of an electrostatic interaction followed by oxidation of the Mn (II) to higher degrees, then probably by binding to the surface of the adsorbent by different C-O-MnO_x bonds.

DOI: 10.17344/acsi.2020.6324 *Acta Chim. Slov.* **2021,** *68,* 562–566

Scientific paper

Benzothiazolylhydrazone-Based Turn-on Fluorescent Probe for Detecting Cu^{2+}: S-donor as a Cu^{2+}-induced Fluorescence Quenching Inhibitor

Qiao Li, Yang Zhao and Enju Wang*

Key Laboratory of Tropical Medicinal Resource Chemistry of Ministry of Education, Key Laboratory of Tropical Medicinal Plant Chemistry of Hainan Province, College of Chemistry & Chemical Engineering, Hainan Normal University, Haikou, 571158, China

** Corresponding author: E-mail: enjuwang@163.com*

Received: 08-07-2020

Abstract

The fluorescent turn-on detection of metal ions is highly desirable for public health and environmental security. Herein, we report a rationally designed fluorescent probe (**1**) for the detection of Cu^{2+} synthesized by integrating 2-hydrazinylbenzothiazole with 3-acetyl-7-hydroxycoumarin. The probe alone is non-fluorescent due to the isomerization of C=N in the excited state. The addition of Cu^{2+} can cause a delayed fluorescence enhancement. A comparative study of **1** and its analogues indicated that the turn-on fluorescence response was thanks to the sulfur atom coordinating to Cu^{2+}. The response delay of **1** in sensing Cu^{2+} was ascribed to the gradual transition from N-coordination to S-coordination (N and S in thiazole moiety). The proposed new function of S-donor would provide a new approach for the turn-on fluorescence sensation of Cu^{2+}.

Keywords: Fluorescent probe; Coumarin; Benzothiazole; Cupric ion; S-donor

1. Introduction

Copper is an essential trace element important for the function of enzymes. It plays a pivotal role in cell physiology as a catalytic cofactor in the cellular redox reactions. Nevertheless, excess copper is implicated in various neurodegenerative disorders, such as Wilson's and Alzheimer's diseases.[1] In addition, Copper is an environmental pollutant having highly toxic effect on aquatic organisms, especially on algaes.[2] Thus, the convenient and fast methods for the detection of trace amounts of cupric ion are significant not only for public health, but also for environmental security. Fluorescent probes are a powerful tool for the detection of metal ions, especially for biomonitoring owing to their non-invasiveness, visualization and real-time.

The turn-on fluorescence probes allow detection with less false positives, providing a better opportunity to accurately monitor the target object than the turn-off flu-

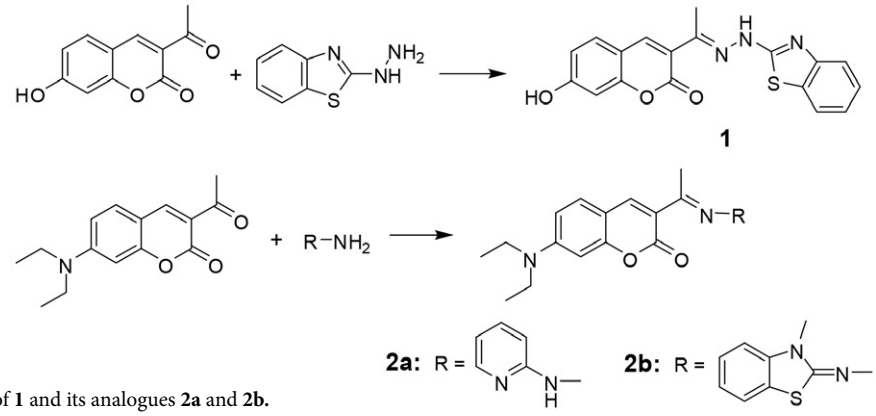

Scheme 1. Synthesis of **1** and its analogues **2a** and **2b.**

orescence probe. However, it is difficult to achieve turn-on fluorescent sensing of cupric ion due to its paramagnetic nature which leads to vigorous fluorescence quenching.[3–8] During the course of our ongoing efforts to develop fluorescent probes for mental ions[9–11], we have firstly found that some probes containing S-donor show turn on fluorescence responses to Cu^{2+}, and so the S-donor may play an important role in protecting from Cu^{2+}-induced fluorescence quenching.[12–14] Following this idea, a rationally designed fluorescent probe containing S-donor (**1**) was synthesized by incorporating 3-acetyl-7-hydroxycoumarin and 2-hydrazinylbenzo[d]thiazole for the fluorescence turn-on detection of cupric ion in the present work (Scheme 1). The binding mode between **1** and Cu^{2+} was determined by ESI-MS. The function of S-donor in protecting from fluorescence quenching was affirmed by control experiments using the analogues of **1** (**2a** and **2b** in Scheme 1). Besides preventing from fluorescence quenching, S-donor should be helpful for the improvement of Cu^{2+}-selective binding.[15]

2. Experimental

All chemicals were purchased from Aladdin Bio-Chem Technology Co., Ltd. (Shanghai, China) and used without further purification. Analytical grade acetonitrile and deionised water were used as solvents for all spectral measurements. The metal nitrates were used for the fluorescence sensing of metal ions. ^{1}H NMR and ^{13}C NMR spectra were recorded on a Bruker Av400 NMR spectrometer (Bruker Co., Ltd., Karlsruhe, Germany). ESI-MS spectra were performed on a Bruker Esquire HCT mass spectrometer (Bruker Technologies, Bremen, Germany) equipped with an electrospray ion source. Fluorescence spectra were taken on a Hitachi F-7000 fluorescence spectrometer (Hitachi, Tokyo, Japan). The synthetic routes of **1**, **2a** and **2b** were illustrated in Scheme 1. ^{1}H NMR, ^{13}C NMR and ESI-MS spectra of them were provided in the supporting information (Fig. S1-9).

3-(1-(2-(benzo[d]thiazol-2-yl)hydrazono)ethyl)-7-hydroxycoumarin (1):
3-acetyl-7-hydroxycoumarin (408 mg, 2.0 mmol), 2-hydrazinylbenzo[*d*]thiazole (330 mg, 2.0 mmol) and a catalytic amount of formic acid were added into 20 mL absolute ethanol and then refluxed for 3 h. A yellow solid precipitated out. The precipitate was collected by filtration and washed several times with ethanol to afford **1** (550 mg, 78 %). ^{1}H NMR (400 MHz, DMSO-d_6) δ 11.73 (s, 1H), 10.75 (s, 1H), 8.11 (s, 1H), 7.70 (s, 1H), 6.69 (d, 1H, J = 8.4 Hz), 7.35 (s, 1H), 7.29 (t, 1H, J = 7.6 Hz), 7.09 (t, 1H, J = 7.6 Hz), 6.84 (d, 1H, J = 8.4 Hz). 6.78 (s, 1H), 2.31 (s, 1H). ^{13}C NMR (100 MHz, DMSO-d_6) δ 168.4, 162.3, 160.1, 155.9, 141.6, 131.0, 126.5, 122.3, 122.2, 122.0, 114.1, 111.9, 102.3, 17.1. ESI-MS m/z calculated for $[M+H]^+$ 352.08, found 351.9; calculated for $[M-H]^-$ 350.06, found 349.8.

3-(1-(2-(pyridin-2-yl)hydrazono)ethyl)-7-diethylaminocoumarin (2a):
2a was synthesized according to the reported procedure[16]. Yield, 82%. ESI-MS m/z calculated for $[M+H]^+$ 351.18, found 351.0; calculated for $[M-H]^-$ 349.17, found 348.9.

3-(1-(3-methylbenzo[d]thiazol-2(3H)-ylidene)hydrazono)ethyl)-7-diethylaminocoumarin (2b):
3-acetyl-7-diethylaminocoumarin (519 mg, 2.0 mmol), 3-methyl-2-benzothiazolinone hydrazone hydrochloride (431 mg, 2.0 mmol) and triethylamine (274 μL, 2.0 mmol) were added into 20 mL absolute ethanol and then refluxed for 3 h. The resulting precipitation was collected by filtration to afford **2b** (603 mg, 72 %). ^{1}H NMR (400 MHz, DMSO-d_6) δ 8.06 (s, 1H), 7.56–7.60 (m, 2H), 7.27–7.36 (m, 2H), 7.08 (t, 1H, J = 7.2 Hz), 6.74 (d, 1H, J = 7.2 Hz), 6.57 (s, 1H), 3.59 (s, 3H), 3.46 (q, 4H, J = 6.8 Hz), 2.51 (s, 1H). 1.14 (t, 6H, J = 6.8 Hz). ^{13}C NMR (100 MHz, DMSO-d_6) δ 166.0, 160.6, 156.9, 156.4, 151.4, 141.9, 141.4, 130.7, 126.9, 124.1, 122.8, 122.1, 119.0, 110.4, 109.9, 108.3, 96.6, 44.6, 31.4, 17.4, 12.8. ESI-MS m/z calculated for $[M+H]^+$ 421.17, found 421.0.

3. Results and Discussion

3.1. Fluorescence Sensing of Cu^{2+}

With the compound **1** in hand, its fluorescence responds to various metal ions, including Ba^{2+}, Ca^{2+}, Mg^{2+}, K^+, Al^{3+}, Na^+, Zn^{2+}, Ag^+, Fe^{3+}, Mn^{2+}, Cd^{2+}, Ni^{2+}, Pb^{2+}, Co^{2+}, Cr^{3+}, Hg^{2+} and Cu^+, were examined. As shown in Fig. 1, Probe **1** alone in CH_3CN/H_2O (1/1) is nearly non-fluorescent due to the C=N isomerization which is a radiationless decay process of the excited states.[16,17] When adding Cu^{2+} into the solution and allowing it to sit for

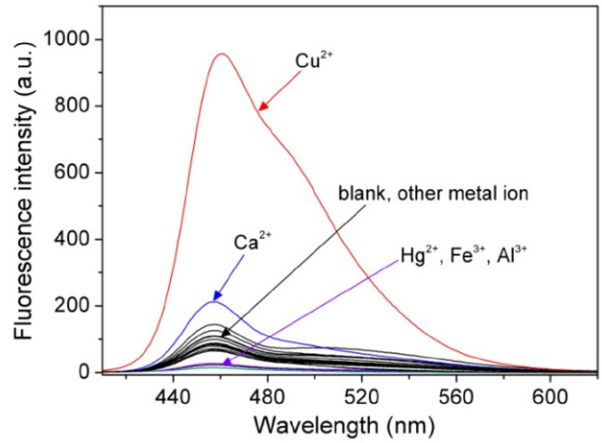

Figure 1. Fluorescence spectra of **1** (10 μM) in CH_3CN/H_2O (1/1) upon adding different metal ions (10 μM) and then allowing to sit for 2 hour at 30 °C when excited at 390 nm.

some time, an enhancement of fluorescence at 460 nm was observed under ultraviolet excitation at 360nm, which gives bright cyan luminescence. Ca^{2+} can also cause an slight enhancement of fluorescence at about 460 nm, but which is too negligible to cause visible fluorescence. Besides, Hg^{2+}, Fe^{3+} and Al^{3+} can induce a degree of fluorescence quenching. Other ions did not cause obvious fluorescence changes.

It is uncommon that the probe can not give an immediate fluorescence turn-on response to Cu^{2+}. For the determination of the optimum incubation time, time-dependent fluorescence spectra were carried out (Fig. 2). It was found that the rate of the fluorescence enhancement correlates with temperature. The fluorescence intensities of the mixture of **1** and Cu^{2+} reached a plateau in 100 minutes at 30 °C. When the temperature is 40 °C, the fluorescence emission maximum was found in 40 minutes.

The fluorescence titration of **1** with Cu^{2+} shows that the fluorescence emission maximum was observed when the Cu^{2+} reached 10 μmol/L (1 equiv), which suggested a high-affinity binding of Cu^{2+} to **1** with 1:1 stoichiometry (Fig. 3). The "turn-on" fluorescence response of **1** to Cu^{2+} should be ascribed to the coordination between them and the consequent restriction of the C=N isomerisation.[16] For demonstrating the binding between **1** and Cu^{2+}, ESI-MS spectrum of **1** in the presence of Cu^{2+} were scanned. The positive ion mode ESI-MS spectrum of the mixture of **1** and $Cu(NO_3)_2$ (1/1) in CH_3CN exhibits the base peak at m/z 412.8, which was assigned to [**1**-H+Cu]$^+$. The observed and calculated isotopic patterns (calcd 413.0) agree well with each other (Fig. 4). This indicated the deprotonation of the secondary amino group (NH) upon coordination with Cu^{2+}.

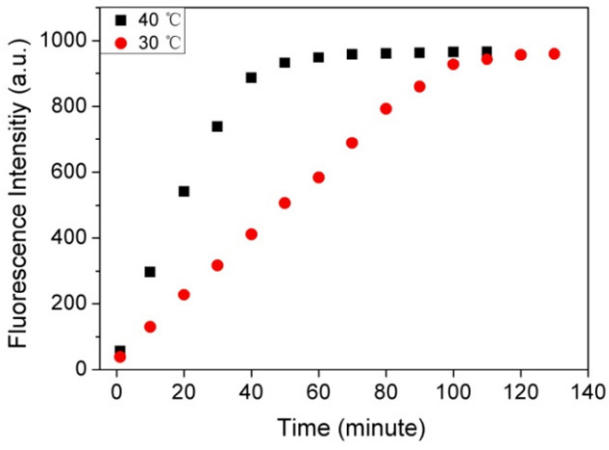

Figure 2. *Time-dependent* fluorescence responses of **1** (10 μM) to Cu^{2+} (10 μM).

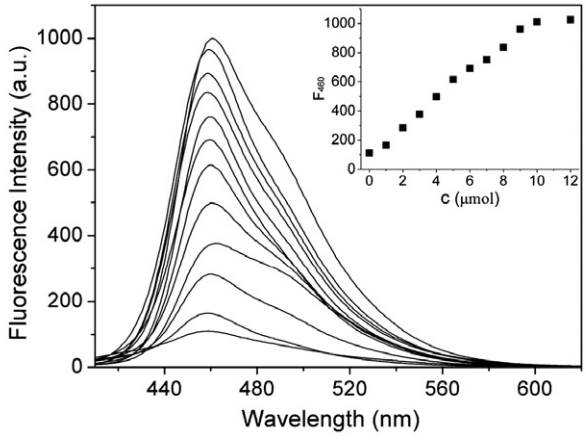

Figure 3. Fluorescence spectra of **1** (10 μM) in CH_3CN /H_2O (1/1) upon adding different concentrations of Cu^{2+} and then allowing to sit for 2 hour. The inset shows the emission intensities of **1** (10 μM) at 460 nm as a function of Cu^{2+} concentration.

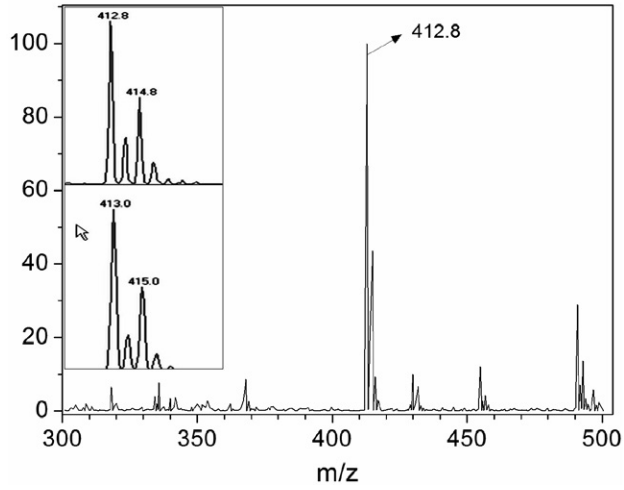

Figure 4. ESI-MS spectra of **1** in the presence of Cu^{2+}. The inset shows the observed (upper) and calculated (under) isotopic patterns.

For further evaluating the effects of common metal ions on the selectivity of **1** for Cu^{2+}, competition experiments were carried out by measuring the fluorescence res-

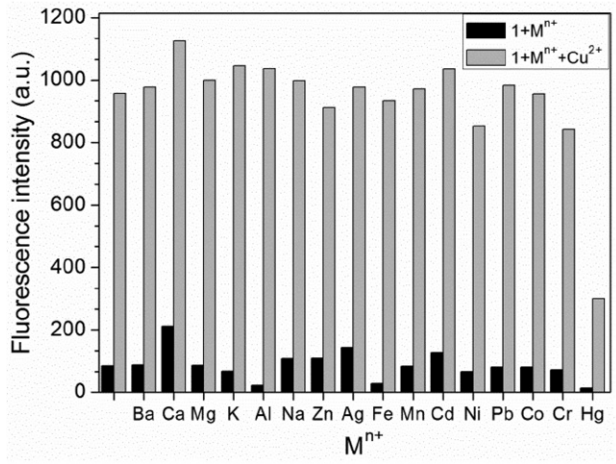

Figure 5. Selective fluorescence responses of **1** (10 μM) to Cu^{2+} (10 μM) in the presence of various foreign ions (10 μM).

ponse of **1** to Cu^{2+} in the presence of various foreign metal ions including Co^{2+}, Ni^{2+}, Zn^{2+}, Cd^{2+}, Fe^{3+}, Hg^{2+} and so on. As illustrated in Fig. 5, when adding the mixtures of Cu^{2+} and various foreign metal ions to the solution of **1** and then allowing it to sit for 2 h, the fluorescence intensity at 460 nm is similar to that upon the addition of only Cu^{2+} except for Hg^{2+}, which can partly quench the Cu^{2+}-induced fluorescence. These results suggested the high selectivity of **1** as an efficient probe for the detection of Cu^{2+}.

3. 2. Sensing Mechanism

It is well-known that Cu^{2+} is the most vigorous quencher among transition metal ions, which has been found for some reported probes with similar structures.[16,17] To explore the reason for the unusual fluorescence turn-on response of **1** to Cu^{2+}, the sensing reversibility was checked by the addition of a competing ligand (EDTA) to the fluorescence solution. As seen in Fig. 6, the Cu^{2+}-induced fluorescence was suppressed by the addition of EDTA, and then recovered by further addition of Cu^{2+}, which suggested the reversible coordination interaction between **1** and Cu^{2+}. The complex between **1** and Cu^{2+} has been further confirmed by ESI-MS (Fig. 4). The thiazole moiety of the probe molecule has two potential coordination atoms (S and N atom), which results in two possible binding models in which N or S of thiazole moiety serves as donor atom respectively. In order to determine the binding model, two analogues of **1** (**2a** and **2b)** were synthesized for the control

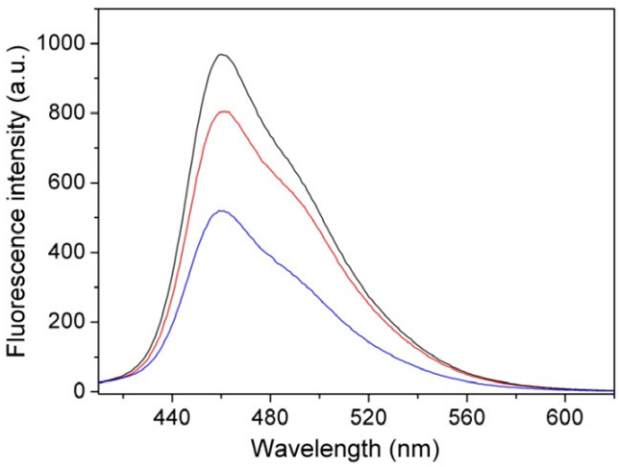

Figure 6. Fluorescence spectra of **1** (10 μM) upon successive addition of Cu^{2+} (blank), EDTA (blue) and then Cu^{2+} (red).

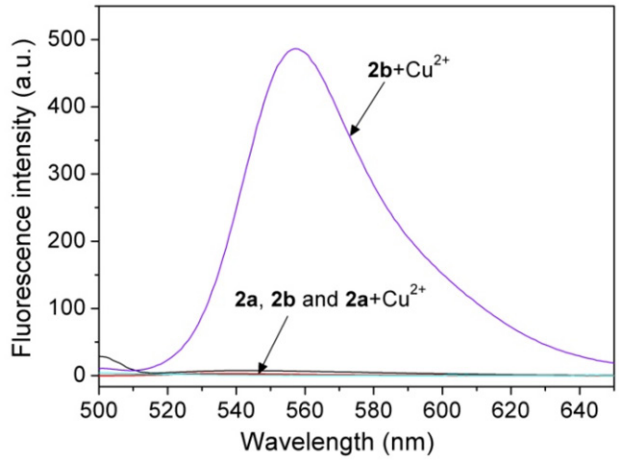

Figure 7. Fluorescence spectra of **2a** and **2b** (10 μM) in the absence and presence of Cu^{2+} (10 μM)

experiments. Sulfur-free **2a** provides a NNO donor set, but **2b** can only provides a NOS donor set, which correspond to the two possible binding models between **1** and Cu^{2+}. The fluorescence properties of **2a** and **2b** were illustrated in Fig 7. **2a** is non-fluorescent both in the presence and absence of Cu^{2+}. In contrast, **2b** gives an immediate turn-on fluorescence response to Cu^{2+}, which should be thanks to the S-donor. The similar phenomenon can been found in the other S-containing probe developed by Lee.[15] With this in mind, we can reasonably expect that the S-donor should be responsible for the fluorescence turn-on response of **1** to Cu^{2+}. The delayed fluorescence of **1** in sensing Cu^{2+} might be ascribed to the gradual formation of the **1**-Cu^{2+} complex with S-donor, that is, Cu(II) complex with NNO donor sites formed first, then gradually changed to the complex with NOS donor sites. On the basis of above discussion and the MS analysis (Fig. 4), the schematic diagram was proposed for illustrating the delayed fluorescence response of **1** to Cu^{2+} and the possible interaction between them as shown in Scheme 2.

4. Conclusion

A rationally designed turn-on fluorescent probe has been developed for the detection of Cu^{2+} which is the most vigorous fluorescence quencher among transition metal ions. The S-donor in the **1**-Cu^{2+}complex plays a crucial

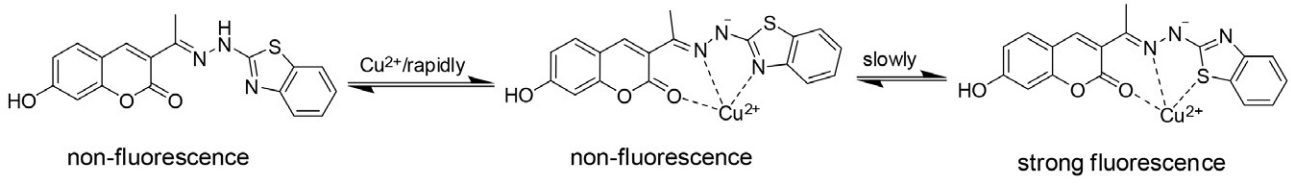

Scheme 2. Delayed fluorescence response of 1 to Cu^{2+} resulting from slowly transition from the NNO coordination to the NOS coordination

role for the turn-on fluorescence. The delay of the fluorescence response should be ascribed to the transition from the complex with NNO donor sites to the complex with NOS donor sites. We believe that the new proposed fluorescence turn-on mechanism would show great potential in fluorescence sensing of Cu^{2+}.

5. References

1. H. Tapiero, D. M. Townsend and K. D. Tew, *Biomed. Pharmacother*. **2003**, *57*, 386–398. **DOI:**10.1016/S0753-3322(03)00012-X
2. C. Barranguet, F. P. Van den Ende, M. Rutgers, A. M. Breure, M. Greijdanus, J. J. Sinke and W. Admiraal, *Environ. Toxicol. Chem.* **2003**, *22*, 1340–1349. **DOI:**10.1002/etc.5620220622
3. T. S. Reddy and A. R. Reddy, *Spectrochim. Acta A* **2014**, *128*, 880–886. **DOI:**10.1016/j.saa.2014.02.120
4. J. H. Jang, S. Bhuniya, J. Kang, A. Yeom, K. S. Hong and J. S. Kim, *Org. Lett*. **2013**, *15*, 4702–4705. **DOI:**10.1021/ol4025293
5. X. Tian, Z. Dong, J. Hou, R. Wang and J. Ma, *J. Lumin.* 2014, 145, 459–465. **DOI:**10.1016/j.jlumin.2013.07.006
6. J. Yang, N. Song, X. Lv and Q. Jia, *Sens. Actuators B* **2018**, *259*, 226–232. **DOI:**10.1016/j.snb.2017.12.045
7. S. Anbu, R. Ravishankaran, M. F. C. Guedes da Silva, A. A. Karande and A. J. L. Pombeiro, *Inorg. Chem*. **2014**, *53*, 6655–6664. **DOI:**10.1021/ic500313m
8. N. Wang, Y. Liu, Y. Li, Q. Liu and M. Xie, Sens. Actuators B 2018, 55, 78–86. **DOI:**10.1016/j.snb.2017.08.035
9. J. Chen, W. Su and E. Wang, *Chem. Res. Chin. Univ*. **2016**, *32*, 742–745. **DOI:**10.1007/s40242-016-6001-1
10. W. Su, S. Yuan and E. Wang, *J. Fluoresc.* **2017**, *27*, 1871–1875. **DOI:**10.1007/s10895-017-2124-0
11. S. Yuan, W. Su and E. Wang, *Acta Chim. Slov*. **2017**, *64*, 638–643. **DOI:**10.17344/acsi.2017.3442
12. J. Chen, W. Su and E. Wang, Y. Liu, *J. Lumin*. **2016**, *180*, 301–305. **DOI:**10.1016/j.jlumin.2016.08.040
13. Z. Zhang, S. Yuan and E. Wang, *J. Fluoresc.* **2018**, *28*, 1115–1119. **DOI:**10.1007/s10895-018-2274-8
14. Z. Zhang, Y Liu and E. Wang, *Dyes Pigments* **2019**, *163*, 533–537. **DOI:**10.1016/j.dyepig.2018.12.039
15. K. C. Ko, J. S. Wu, H. J. Kim, P. S. Kwon, J. W. Kim, P. A. Bartsch, J. Y. Lee and J. S. Kim, *Chem. Commun*. **2011**, *47*, 3165–3167. **DOI:**10.1039/c0cc05421f
16. J. Wu, R. Sheng, W. Liu, P. Wang, H. Zhang and J. Ma, *Tetrahedron* **2012**, *68*, 5458–5463. **DOI:**10.1016/j.tet.2012.04.090
17. J. S. Wu, W. M. Liu, X. Q. Zhuang, F. Wang, P. F. Wang, S. L. Tao, X. H. Zhang, S. K. Wu and S. T. Lee, *Org. Lett*., **2007**, *9*, 33–36. **DOI:**10.1021/ol062518z

Povzetek

Detekcija kovinskih ionov z uporabo fluorescence je zelo zaželena za zagotavljanje javnega zdravja in varnosti okolja. V tem članku poročamo o racionalno zasnovani fluorescenčni sondi (**1**) za detekcijo Cu^{2+}, ki smo jo sintetizirali z uporabo 2-hidrazinilbenzotiazola s 3-acetil-7-hidroksikumarinom. Zaradi izomerizacije C = N v vzbujenem stanju sama sonda ne fluorescira. Dodatek Cu^{2+} lahko povzroči zakasnitev povečanje fluorescence. Primerjalna študija sonde **1** in njenih analogov je pokazala, da je odziv fluorescence na vklop zaradi koordinacije atoma žvepla in Cu^{2+}. Zakasnitev odziva sonde **1** pri zaznavanju Cu^{2+} je bila pripisana postopnemu prehodu iz N-koordinacije v S-koordinacijo (N in S v tiazolnem delu). Predlagana nova funkcija S-donorja omogoča nov pristop k detekciji Cu^{2+} z vklapljanjem fluorescence.

Scientific paper

Synthesis, Structures, and Antibacterial Activities of Hydrazone Compounds Derived from 4-Dimethylaminobenzohydrazide

Guo-Xu He and Ling-Wei Xue*

School of Chemical and Environmental Engineering, Pingdingshan University, Pingdingshan Henan 467000, P. R. China

** Corresponding author: E-mail: pdsuchemistry@163.com*

Received: 08-13-2020

Abstract

A series of three new hydrazone compounds derived from the condensation reactions of 4-dimethylaminobenzohydrazide with 4-dimethylaminobenzaldehyde, 2-chloro-5-nitrobenzaldehyde and 3-methoxybenzaldehyde, respectively, were prepared. The compounds were characterized by elemental analysis, infrared and UV-vis spectra, HRMS, ^{1}H NMR and ^{13}C NMR spectra, and single crystal X-ray diffraction. Crystals of the compounds are stabilized by hydrogen bonds. The compounds were assayed for antibacterial (*Bacillus subtilis*, *Escherichia coli*, *Pseudomonas fluorescence* and *Staphylococcus aureus*) and antifungal (*Aspergillus niger* and *Candida albicans*) activities by MTT method. The results indicated that compound **2** is an effective antibacterial material.

Keywords: Hydrazone compound; crystal structure; hydrogen bonds; X-ray crystallography; antimicrobial activity

1. Introduction

Hydrazone compounds have been reported to possess interesting biological activities. Some of the compounds are found to be useful for the treatment of inflammatory diseases and tumors,[1] and some of the compounds have antibacterial, antifungal, antiviral, and many other activities.[2] The emphasis on structural studies of hydrazone compounds is a consequence of our interests in compounds having potential biological activity. In addition, hydrazone compounds have also been used as preferred ligands in construction of versatile structures of complexes with various metal salts like manganese, copper, vanadium and zinc.[3] The complexes displayed interesting biological and catalytic activities. It was reported that the compounds bearing one or more halo-substituents on the aromatic ring have improved biological activities, especially for the antibacterial and antifungal activities.[4] However, the structure-activity relationship was not clear until now. As an extension of our work on the structures and antibacterial activities of such compounds, in the present paper, three new hydrazone compounds, *N*'-(4-dimethylaminobenzylidene)-4-dimethylaminobenzohydrazide (**1**), *N*'-(2-chloro-5-nitrobenzylidene)-4-dimethylaminobenzohydrazide (**2**), and *N*'-(3-methoxybenzylidene)-4-dimethylaminobenzohydrazide (**3**) (Scheme 1), are reported.

2. Experimental

2. 1. Materials and Methods

4-Dimethylaminobenzohydrazide, 4-dimethylaminobenzaldehyde, 2-chloro-5-nitrobenzaldehyde and

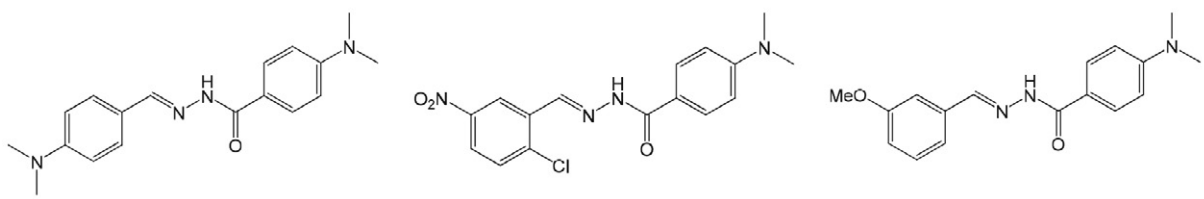

1 **2** **3**

Scheme 1. The hydrazone compounds.

3-methoxybenzaldehyde with AR grade were purchased from Fluka and used as received. All other chemicals with AR grade were obtained commercially and used without purification. Elemental analyses were carried out on a Perkin-Elmer model 240 analyzer. HRMS data was obtained with ESI (electrospray ionization) mode. ^{1}H NMR spectra were measured with a Bruker AVANCE 300 MHz spectrometer. ^{13}C NMR spectra were measured with an Oxford NMR spectrometer. FT-IR spectra were recorded on a Nicolet 55XC spectrometer. UV-vis spectra were recorded on a Lambda 900 spectrophotometer in methanol.

2. 2. Synthesis of N'-(4-Dimethylaminobenzylidene)-4-dimethylaminobenzohydrazide (1)

4-Dimethylaminobenzohydrazide (1.0 mmol, 0.18 g) was added with stirring to 4-dimethylaminobenzaldehyde (1.0 mmol, 0.15 g) in methanol. The mixture was heated under reflux for 1 h, and cooled to room temperature. After filtration and slow evaporation at room temperature for a few days, colorless needle-shaped single crystals were formed. The crystals were collected by filtration, washed three times with methanol. Yield, 0.21 g (69 %). Anal. Calcd. (%) for $C_{18}H_{22}N_4O$: C, 69.65; H, 7.14; N, 18.05. Found (%): C, 69.53; H, 7.27; N, 17.97. HRMS (ESI): *m/z* calcd for $C_{18}H_{23}N_4O$ $[M + H]^+$ 311.1866; found: 311.1869. Characteristic IR data (KBr, cm^{-1}): 1608 (s) ($\nu_{C=N}$). UV-vis data in methanol [λ_{max} (nm), ε (L mol^{-1} cm^{-1})]: 230, 9360; 361, 25900. ^{1}H NMR (300 MHz, DMSO-d_6, ppm): δ 11.23 (s, 1H), 8.28 (s, 1H), 7.80 (d, 2H), 7.50 (d, 2H), 6.75 (dd, J_1 = 9.0 Hz, J_2 = 7 Hz, 2H), 2.99 (s, 6H), 2.97 (s, 6H). ^{13}C NMR (75 MHz, DMSO-d_6, ppm): δ 164.5, 152.3, 151.3, 147.1, 128.9, 128.1, 122.1, 120.0, 111.8, 110.8, 40.4, 40.1, 39.8, 39.7, 39.3, 39.0.

2. 3. Synthesis of N'-(2-Chloro-5-nitrobenzylidene)-4-dimethylaminobenzohydrazide (2) and N'-(3-Methoxybenzylidene)-4-dimethylaminobenzohydrazide (3)

Compounds **2** and **3** were synthesized by the same method as that described for **1**, with 4-dimethylaminobenzaldehyde replaced by 2-chloro-5-nitrobenzaldehyde (1.0 mmol, 0.19 g) for **2** and 3-methoxybenzaldehyde (1.0 mmol, 0.14 g) for **3**. The filtrates for the two compounds were left still at room temperature to enable slow evaporation of the solvent to yield yellow block (for **2**) and colorless needle (for **3**) single crystals. For **2**: Yield, 0.26 g (76 %). Anal. Calcd. (%) for $C_{16}H_{15}ClN_4O_3$: C, 55.42; H, 4.36; N, 16.16. Found (%): C, 55.53; H, 4.28; N, 16.02. HRMS (ESI): *m/z* calcd for $C_{16}H_{15}ClN_4O_3$ [M] 347.0905; found: 347.0901. Characteristic IR data (KBr, cm^{-1}): 1610 (s) ($\nu_{C=N}$). UV-vis data in methanol [λ_{max} (nm), ε (L mol^{-1} cm^{-1})]: 280, 10500; 350, 12450. ^{1}H NMR (300 MHz, DMSO-d_6, ppm): δ 12.00 (s, 1H), 8.85 (s, 1H), 8.71 (d, 1H), 8.22 (dd, J_1 = 8.9 Hz, J_2 = 2.9 Hz, 1H), 7.84 (dd, J_1 = 8.9 Hz, J_2 = 3.7 Hz, 3H), 6.78 (d, 2H), 3.01 (s, 6H). ^{13}C NMR (75 MHz, DMSO-d_6, ppm): δ 163.7, 153.2, 145.8, 141.2, 138.3, 133.7, 131.6, 129.0, 127.9, 123.7, 121.5, 112.3, 40.7, 40.6. For **3**: Yield, 0.237 g (80 %). Anal. Calcd. (%) for $C_{17}H_{19}N_3O_2$: C, 68.67; H, 6.44; N, 14.13. Found (%): C, 68.54; H, 6.57; N, 14.24. HRMS (ESI): *m/z* calcd for $C_{17}H_{20}N_3O_2$ $[M + H]^+$ 298.1207; found: 298.1213. Characteristic IR data (KBr, cm^{-1}): 1616 (s) ($\nu_{C=N}$). UV-vis data in methanol [λ_{max} (nm), ε (L mol^{-1} cm^{-1})]: 275, 5389; 338, 11300. ^{1}H NMR (300 MHz, DMSO-d_6, ppm): δ 11.63 (s, 1H), 8.39 (s, 1H), 7.82 (d, 2H), 7.37 (t, 1H), 7.24 (m, 2H), 7.00 (d, 1H), 6.75 (d, 2H), 3.81 (s, 3H), 3.00 (s, 6H). ^{13}C NMR (75 MHz, DMSO-d_6, ppm): δ 162.6, 159.1, 152.5, 147.3, 137.6, 131.4, 128.7, 123.6, 120.0, 114.9, 112.2, 110.8, 54.5, 40.6, 40.5.

2. 4. X-Ray Crystallography

Single-crystal X-ray diffraction measurements for the compounds were carried out on a CrysAlis CCD diffractometer equipped with a graphite crystal monochromator for data collection at 298(2) K. The determinations of unit cell parameters and data collections were performed with Mo *Kα* radiation (λ = 0.71073 Å) and unit cell dimensions were obtained with least-squares refinements. Structures of the compounds were solved by direct methods using SHELXTL.[5] Non-hydrogen atoms were located in successive difference Fourier syntheses. The final refinement was performed by full-matrix least-squares methods with anisotropic thermal parameters for non-hydrogen atoms on F^2. The hydrogen atoms were treated by a mixture of independent and constrained refinement. The amino H atoms in the compounds were located from difference Fourier maps and refined isotropically, with N–H distances restrained to 0.90(1) Å. The remaining hydrogen atoms were located at their calculated positions. The observed/unique ratio for compound **1** is low, which is due to the weak diffraction of the crystal determined. Crystallographic data and experimental details for structural analyses are summarized in Table 1.

2. 5. Antimicrobial Test

The antibacterial activity of the compounds was tested against *B. subtilis*, *E. coli*, *P. fluorescence* and *S. aureus* using MH medium (Mueller–Hinton medium: casein hydrolysate 17.5 g, soluble starch 1.5 g, beef extract 1000 mL), the antifungal activity of the compounds was tested against *A. niger* and *C. albicans* using RPMI-1640 medium (RPMI-1640 (GIBCO BRL) 10 g, $NaHCO_3$ 2.0 g, 0.165 mol/L morpholinepropanesulfonic acid (MOPS) (Sigma) 34.5 g, triple distilled water 900 mL, buffered to pH 7.0

Table 1. Crystallographic data and refinement parameters for the compounds

Compound	**1**	**2**	**3**
Empirical formula	$C_{18}H_{22}N_4O$	$C_{16}H_{15}ClN_4O_3$	$C_{17}H_{19}N_3O_2$
Molecular weight	310.4	346.8	297.4
Crystal color, habit	Colorless, needle	Yellow, block	Colorless, needle
Crystal system	Orthorhombic	Monoclinic	Orthorhombic
Space group	*Pbca*	*Pc*	*Pbca*
Unit cell dimensions			
a (Å)	11.194(2)	9.608(2)	13.259(2)
b (Å)	8.029(1)	14.631(2)	8.389(1)
c (Å)	37.164(2)	14.092(2)	29.226(2)
β (°)	90	124.370(2)	90
V (Å^3)	3340.1(8)	1635.1(5)	3239.0(7)
Z	8	4	8
D_{calc} (g cm^{-3})	1.235	1.409	1.220
Absorption coefficient (μ, mm^{-1})	0.079	0.256	0.082
Reflections collected/unique	21612/2904	11559/5689	28475/2863
Data/restraints/parameters	2904/1/215	5689/4/443	2863/1/206
Observed reflections [$I \geq 2\sigma(I)$]	1084	3421	1239
R_1, wR_2 [$I \geq 2\sigma(I)$]	0.0698, 0.1021	0.0883, 0.2226	0.0861, 0.1752
R_1, wR_2 (all data)	0.2534, 0.1460	0.1349, 0.2752	0.2126, 0.2324
Goodness of fit (GOF) on F^2	1.007	1.022	1.029
Largest differences in peak/hole (e/Å^3)	0.169 and –0.148	1.315 and –0.275	0.553 and –0.172

with 1 mol/L NaOH (25 °C), metered volume to 1000 mL, filtered sterilization, conservation at 4 °C). The MICs of the test compounds were determined by a colorimetric method using the dye MTT.[6] A stock solution of the synthesized compound (50 μg/mL) in DMSO was prepared and graded quantities of the test compounds were incorporated in specified quantity of sterilized liquid medium (MH medium for antibacterial activity and RPMI-1640 medium for antifungal activity). A specified quantity of the medium containing the compound was poured into microtitration plates. Suspension of the microorganism was prepared to contain approximately 10^5 cfu/mL and applied to microtitration plates with serially diluted compounds in DMSO to be tested and incubated at 37 °C for 24 h and 48 h for bacterial and fungi, respectively. After the MICs were visually determined on each of the microtitration plates, 50 μL of PBS (phosphate buffered saline 0.01 mol/L, pH 7.4, $Na_2HPO_4{\cdot}12H_2O$ 2.9 g, KH_2PO_4 0.2 g, NaCl 8.0 g, KCl 0.2 g, distilled water 1000 mL) containing 2 mg of MTT/mL was added to each well. Incubation was continued at room temperature for 4–5 h. The content of each well was removed, and 100 μL of isopropanol containing 5% 1 mol/L HCl was added to extract the dye. After 12 h of incubation at room temperature, the optical density (OD) was measured with a microplate reader at 550 nm.

3. Results and Discussion

3. 1. Chemistry

The synthesis of the compounds was carried out as outlined in Scheme 2. Single crystals of the compounds were obtained by slow evaporation of the methanolic solutions of the compounds.

3. 2. Structure Description of the Compounds

The solid state structures of compounds **1**, **2** and **3** determined by X-ray diffraction are shown in Figures 1, 2

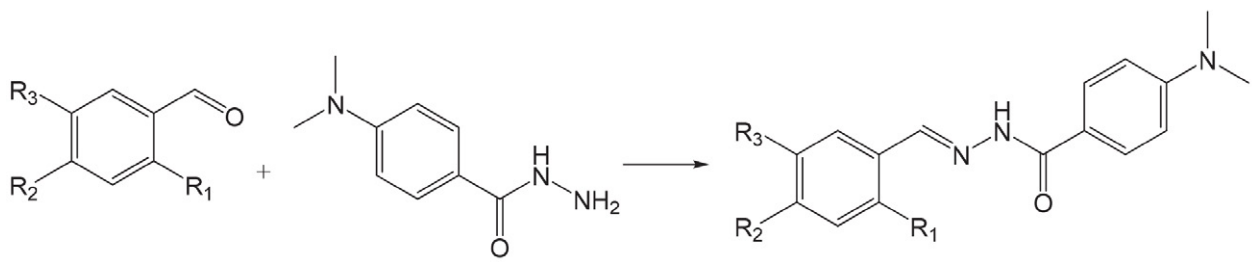

Scheme 2. The synthesis of the compounds. **1**: $R_1 = R_3 = H$, $R_2 = NMe_2$; **2**: $R_1 = Cl$, $R_2 = H$, $R_3 = NO_2$; **3**: $R_1 = R_2 = H$, $R_3 = OMe$.

and 3, respectively. The hydrazone molecules in the compounds adopt *E* configuration with respect to the C=N double bonds. The distances between C9 and N1 [1.296(4) Å] in **1**, C7 and N2 [1.269(8) Å] and C26 and N7 [1.256(8) Å] in **2**, and C8 and N1 [1.276(5) Å] in **3**, confirm them as typical double bonds. The distances between C10 and N2 [1.361(4) Å] in **1**, C8 and N3 [1.356(8) Å] and C25 and N6 [1.351(8) Å] in **2**, and C9 and N2 [1.351(5) Å] in **3**, are intermediate between single and double bonds, due to the conjugation effects of the molecules. The order of the distances of the C=N bonds is **1** > **3** > **2**, which is caused by the electron-donating or electron-withdrawing effects of the substituent groups. The remaining bond lengths in the three compounds are comparable to each other, and also similar to those in the literature.[7] In the molecules of the three compounds, the dihedral angles between the two benzene rings are 10.9(5)° for **1**, 5.7(4)° and 2.5(4)° for **2**, and 25.3(5)° for **3**.

In the crystal structure of **1**, molecules are linked through intermolecular N–H···O and C–H···O hydrogen bonds (Table 2), to form 1D chains along the *b* axis (Figure 4). In the crystal structure of **2**, molecules are linked through intermolecular N–H···O hydrogen bonds (Table 2), to form 1D chains along the *a* axis (Figure 5). In the crystal structure of **3**, molecules are linked through intermolecular N–H···O and C–H···O hydrogen bonds (Table 2), to form 1D chains along the *b* axis (Figure 6).

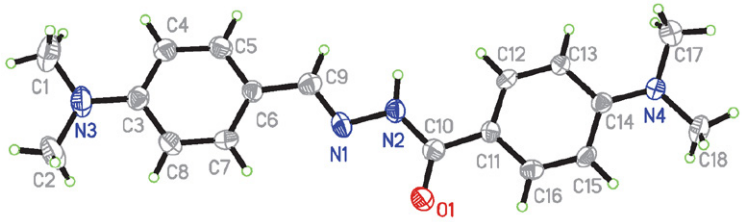

Figure 1. The molecular structure of **1**. The ellipsoids are shown with 30% probability.

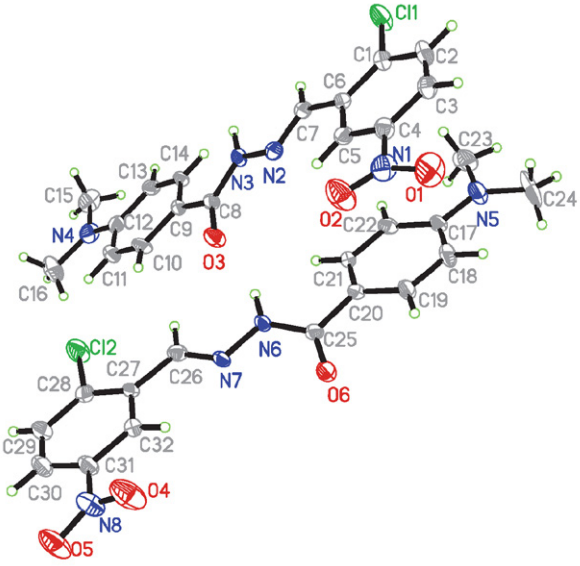

Figure 2. The asymmetric unit of **2**. The ellipsoids are shown with 30% probability.

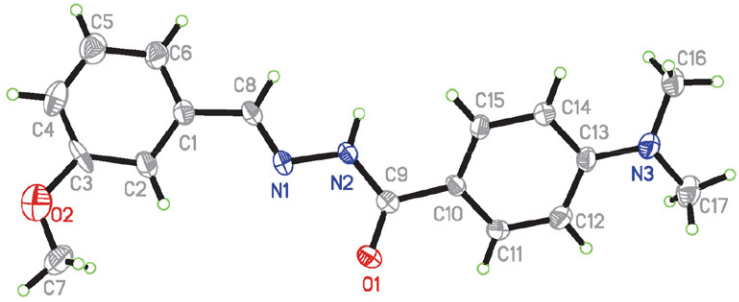

Figure 3. The molecular structure of **3**. The ellipsoids are shown with 30% probability.

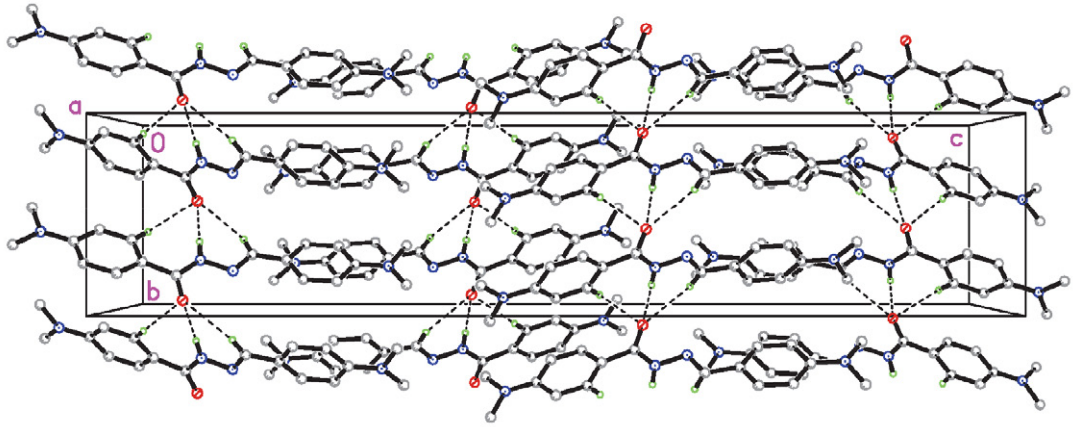

Figure 4. The packing diagram of **1**. Hydrogen bonding interactions are shown as dashed lines.

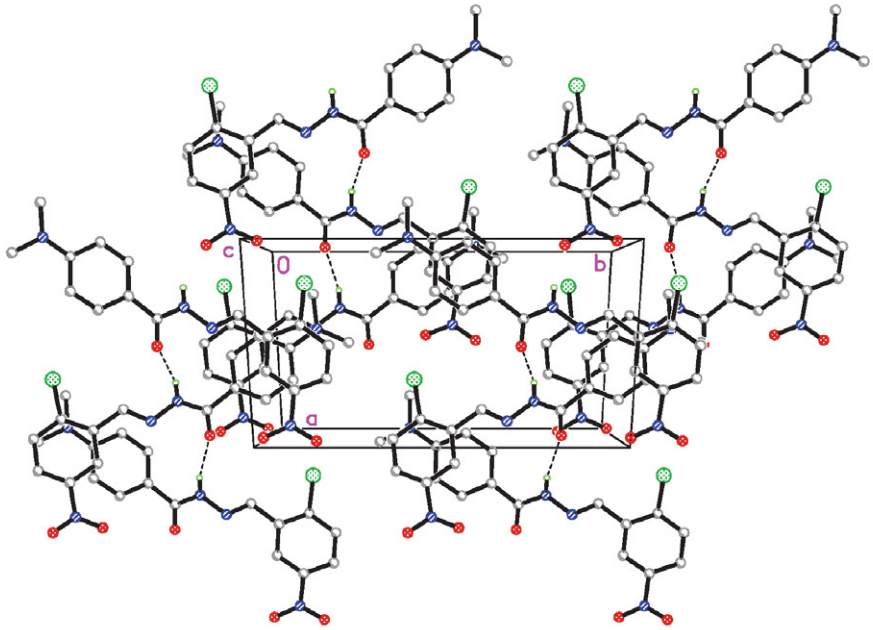

Figure 5. The packing diagram of **2**. Hydrogen bonding interactions are shown as dashed lines.

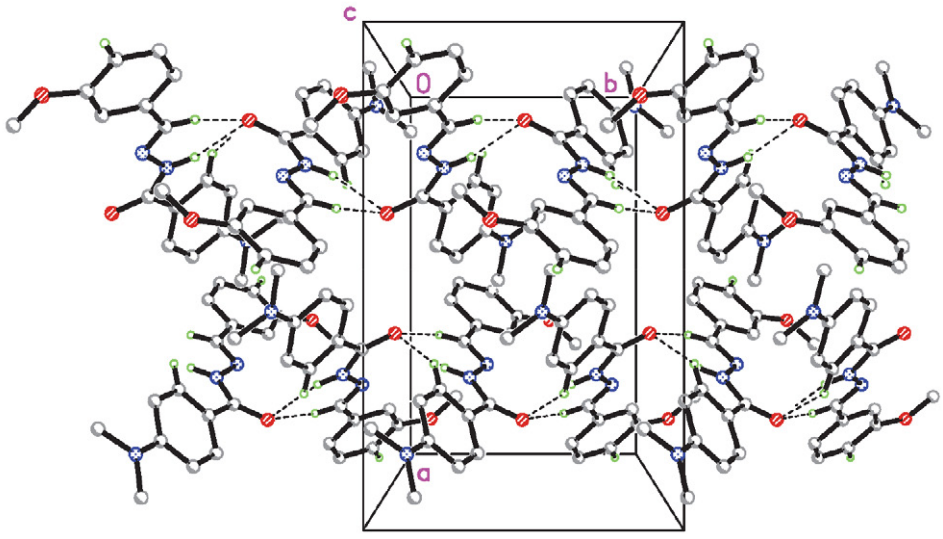

Figure 6. The packing diagram of **3**. Hydrogen bonding interactions are shown as dashed lines.

Table 2. Distances (Å) and angles (°) involving hydrogen bonding of the compounds

D–H···*A*	d(*D*–H)	d(H···*A*)	d(*D*···*A*)	Angle(*D*–H···*A*)
		1		
N2–H2···O1^{i}	0.90(1)	2.17(1)	3.061(4)	177(3)
C9–H9···O1^{i}	0.93	2.55(1)	3.360(5)	146(3)
C12–H12···O1^{i}	0.93	2.55(1)	3.431(5)	158(3)
		2		
N3–H3···O6^{ii}	0.90(1)	2.11(3)	2.985(7)	165(8)
N6–H6···O3	0.90(1)	2.07(3)	2.937(7)	162(8)
		3		
N2–H2···O1^{iii}	0.90(1)	2.01(3)	2.891(6)	166(7)
C4–H4···O1^{iv}	0.93	2.52(3)	3.303(7)	143(6)
C8–H8···O1^{iii}	0.93	2.49(3)	3.298(7)	145(6)
C15–H15···O1^{iii}	0.93	2.45(3)	3.226(7)	141(6)

Symmetry codes: (i) 3/2 – *x*, –1/2 + *y*, *z*; (ii) –1 + *x*, *y*, *z*; (iii) 3/2 – *x*, –1/2 + *y*, *z*; (iv) 1/2 + *x*, *y*, 1/2 – *z*.

3. 3. Infrared and UV-vis Spectra

The sharp and medium stretching vibrations in the range 3200–3270 cm^{-1} in the spectra of the compounds indicate the presence of amino groups, ν_{N-H}.[8] Compounds **1**, **2** and **3** exhibit strong stretching vibration frequencies of imino bonds formed by condensation of aldehyde and hydrazide at 1608, 1610 and 1616 cm^{-1}, respectively.[9] The Ar–O stretching vibration frequencies of hydroxyl groups substituted on the benzene rings are observed in the range 1250–1270 cm^{-1} for the three compounds.

The compounds have two sets of bands in the UV region. The first centered at 230 nm for **1**, 280 nm for **2**, and 275 nm for **3**, may be assigned to the π→π* transitions. The second set centered at 360 nm for **1**, 350 nm for **2**, and 340 nm for **3**, may be assigned to the *n*→π* transitions.

3. 4. Antimicrobial Activities

The MICs (minimum inhibitory concentrations) of the compounds against four bacteria strains are presented in Table 3. The activities of reference compounds kanamycin and penicillin were included. Compound **1** was found to be inactive against *B. subtilis* and *P. fluorescence*, and has strong activity against *E. coli*, and medium activity against *S. aureus*. Compound **2** was found to be active against all the bacteria, especially *E. coli* and *S. aureus*. Compound **3** was found to be inactive against *B. subtilis*, *E. coli* and *P. fluorescence*, and has weak activity against *S. aureus*. It is obvious that compound **2** showed stronger activities against the bacteria than compounds **1** and **3**, which might be due to the presence of chloro and nitro substituent groups. It is notable that compound **2** has stronger activity against *E. coli* than the reference drug kanamycin. Chloro substituent is known as an important group for antibacterial activities.[10] The results in this work are in accordance with those reported in the literature that the electron-withdrawing groups such as chloro and nitro can enhance the biological properties.[4]

The antifungal activity of the compounds was studied with two fungal strains by MTT method. The results are summarized in Table 3. Ketoconazole was used as the reference. The results indicate that the compounds have no activity against *A. niger* and *C. albicans*.

Table 3. MIC values of the compounds (μg/mL)

Compound	*Bacillus subtilis*	*Escherichia coli*	*Pseudomonas fluorescence*	*Staphylococcus aureus*	*Aspergillus niger*	*Candida albicans*
1	> 50	6.25	> 50	12.5	> 50	> 50
2	25	1.56	25	3.12	> 50	> 50
3	> 50	> 50	> 50	25	> 50	> 50
Ketoconazole	> 50	> 50	> 50	> 50	7.8	3.9
Kanamycin	0.39	3.9	3.9	1	> 50	> 50
Penicillin	0.78	> 50	> 50	2	> 50	> 50

4. Conclusion

Three new hydrazone compounds were synthesized and structurally characterized. Crystals of the compounds are stabilized by hydrogen bonds. The biological assay indicated that the presence of electron-withdrawing groups such as chloro and nitro can improve the antibacterial activities of the studied compounds. Among the three compounds, the one bearing chloro and nitro substituent dislayed the strongest activities against *E. coli* and *S. aureus*, therefore deserving further study to explore new antibacterial materials.

5. Supplementary Material

CCDC – 1035481 for **1**, 1035482 for **2**, and 1035483 for **3** contain the supplementary crystallographic data for this paper. These data can be obtained free of charge at http://www.ccdc.cam.ac.uk/const/retrieving.html or from the Cambridge Crystallographic Data Centre (CCDC), 12 Union Road, Cambridge CB2 1EZ, UK; fax: +44(0)1223-336033 or e-mail: deposit@ccdc.cam.ac.uk.

6. References

1. (a) M. X. Song, B. Liu, S. W. Yu, S. H. He, Y. Q. Liang, S. F. Li, Q. Y. Chen, X. Q. Deng, *Lett. Drug Des. Discov.* **2020**, *17*, 502–511; **DOI:**10.2174/1570180816666190731113441
(b) U. Debnath, S. Mukherjee, N. Joardar, S. P. S. Babu, K. Jana, A. K. Misra, *Eur. J. Pharm. Sci.* **2019**, *134*, 102–115; **DOI:**10.1016/j.ejps.2019.04.016
(c) E. M. Becker, D. B. Lovejoy, J. M. Greer, R. Watts, D. R. Richardson, *British J. Pharm.* **2003**, *138*, 819–830. **DOI:**10.1038/sj.bjp.0705089
2. (a) R. Fekri, M. Salehi, A. Asadi, M. Kubicki, *Inorg. Chim. Acta* **2019**, *484*, 245–254; **DOI:**10.1016/j.ica.2018.09.022
(b) Y. C. Wu, X. D. Ding, L. Ding, Y. S. Zhang, L. Cui, L. Sun, W. Li, D. Wang, Y. F. Zhao, *Eur. J. Med. Chem.* **2018**, *158*, 247–258; **DOI:**10.1016/j.ejmech.2018.09.004
(c) N. R. Appna, R. K. Nagiri, R. B. Korupolu, S. Kanugala, G. K. Chityal, G. Thipparapu, N. Banda, *Med. Chem. Res.* **2019**, *28*, 1509–1528; **DOI:**10.1007/s00044-019-02390-w
(d) K. Pyta, A. Janas, M. Szukowska, P. Pecyna, M. Jaworska, M. Gajecka, F. Bartl, P. Przybylski, *Eur. J. Med. Chem.* **2019**, *167*, 96–104; **DOI:**10.1016/j.ejmech.2019.02.009
(e) A. Erguc, M. D. Altintop, O. Atli, B. Sever, G. Iscan, G. Gormus, A. Ozdemir, *Lett. Drug Des. Discov.* **2018**, *15*, 193–202; **DOI:**10.2174/1570180814666171003145227
(f) A. A. El-Tombary, S. A. M. El-Hawash, *Med. Chem.* **2014**, *10*, 521–532. **DOI:**10.2174/1573406411309666006 9
3. (a) Y.-L. Sang, X.-S. Lin, W.-D. Sun, *Acta Chim. Slov.* **2020**, *67*, 581–585; **DOI:**10.17344/acsi.2019.5595
(b) N. Biswas, S. Bera, N. Sepay, A. Pal, T. Halder, S. Ray, S. Acharyya, A. K. Biswas, M. G. B. Drew, T. Ghosh, *New J. Chem.* **2020**, *44*, 3700–3716; **DOI:**10.1039/C9NJ06114B
(c) S. Dasgupta, S. Karim, S. Banerjee, M. Saha, K. D. Saha, D. Das, *Dalton Trans.* **2020**, *49*, 1232–1240; **DOI:**10.1039/C9DT04636D
(d) A. A. Khandar, Z. M. Azar, M. Eskandani, C. B. Hubschle, S. Van Smaalen, B. Shaabani, Y. Omidi, *Polyhedron* **2019**, *171*, 237–248; **DOI:**10.1016/j.poly.2019.06.026
(e) L.-W. Xue, H.-J. Zhang, P.-P. Wang, *Acta Chim. Slov.* **2019**, *66*, 190–195;
(f) L.-W. Xue, Y.-J. Han, X.-Q. Luo, *Acta Chim. Slov.* **2019**, *66*, 622–628; **DOI:**10.17344/acsi.2019.5039
(g) C.-L. Zhang, X.-Y. Qiu, S.-J. Liu, *Acta Chim. Slov.* **2019**, *66*, 719–725; **DOI:**10.17344/acsi.2019.5241
(h) F.-M. Wang, L.-J. Li, G.-W. Zang, T.-T. Deng, Z.-L. You, *Acta Chim. Slov.* **2020**, *67*, 1155–1162; **DOI:**10.17344/acsi.2020.6056
(i) Y. Tan, *Acta Chim. Slov.* **2020**, *67*, 1233–1238. **DOI:**10.17344/acsi.2020.6136
4. M. Zhang, D.-M. Xian, H.-H. Li, J.-C. Zhang, Z.-L. You, *Aust. J. Chem.* **2012**, *65*, 343–350. **DOI:**10.1071/CH11424
5. G. M. Sheldrick, *Acta Crystallogr.* **2008**, *A64*, 112–122. **DOI:**10.1107/S0108767307043930
6. J. Meletiadis, J. F. Meis, J. W. Mouton, J. P. Donnelly, P. E. Verweij, *J. Clin. Microbiol.* **2000**, *38*, 2949–2954. **DOI:**10.1128/JCM.38.8.2949-2954.2000
7. (a) Y.-J. Wei, F.-W. Wang, *J. Struct. Chem.* **2011**, *52*, 755–759;
(b) Y.-M. Cui, Y.-J. Cai, W. Chen, *J. Coord. Chem.* **2011**, *64*, 1385–1392; **DOI:**10.1080/00958972.2011.571680
(c) Q.-Y. Zhu, Y.-J. Wei, F.-W. Wang, *Polish J. Chem.* **2009**, *83*, 1233–1240;
(d) H.-K. Fun, Z.-L. Lu, C.-Y. Duan, Y.-P. Tian, X.-Z. You, X.-Y. Gong, Y.-M. Guo, *Acta Crystallogr.* **1997**, *C53*, 1454–1455; **DOI:**10.1107/S0108270197008147
(e) S. S. S. Raj, H.-K. Fun, Z.-L. Lu, W. Xiao, X.-Y. Gong, C.-M. Gen, *Acta Crystallogr.* **2000**, *C56*, 1013–1014; **DOI:**10.1107/S010827010000799X
(f) D. Qu, F. Niu, X. Zhao, K.-X. Yan, Y.-T. Ye, J. Wang, M. Zhang, Z. You, *Bioorg. Med. Chem.* **2015**, *23*, 1944–1949; **DOI:**10.1016/j.bmc.2015.03.036
(g) M. Taha, N. Ismail, M. Baharudin, S. Yousuf, S. Siddiqui, K. Khan, S. Lalani, S. Mehboob, M. Choudhary, *Med. Chem. Res.* **2015**, *24*, 1310–1324. **DOI:**10.1007/s00044-014-1213-8
8. Y. G. Atovmyan, L. A. Nikonova, I. I. Chuev, A. N. Utenyshv, M. Z. Aldoshina, S. M. Aldoshin, *J. Mol. Struct.* **1999**, *474*, 167–175. **DOI:**10.1016/S0022-2860(98)00570-5
9. (a) S. N. Podyachev, I. A. Litvinov, R. R. Shagidullin, B. I. Buzykin, I. Bauer, D. V. Osyanina, L. V. Avvakumova, S. N. Sudakova, W. D. Habicher, A. I. Konovalov, *Spectrochim. Acta A* **2007**, *66*, 250–261; **DOI:**10.1016/j.saa.2006.02.049
(b) N. Galić, B. Perić, B. Kojić-Prodić, Z. Cimerman, *J. Mol. Struct.* **2001**, *559*, 187–194. **DOI:**10.1016/S0022-2860(00)00703-1
10. (a) O. O. Güven, T. Erdogan, H. Goker, S. Yildiz, *Bioorg. Med. Chem. Lett.* **2007**, *17*, 2233–2236; **DOI:**10.1016/j.bmcl.2007.01.061

(b) Z.-Q. Sun, S.-F. Yu, X.-L. Xu, X.-Y. Qiu, S.-J. Liu, *Acta Chim. Slov.* **2020**, *67*, 1281–1289;
DOI:10.17344/acsi.2020.6236

(c) E.-C. Liu, W. Li, X.-S. Cheng, *Acta Chim. Slov.* **2019**, *66*, 971–977.

Povzetek

S pomočjo kondenzacije med 4-dimetilaminobenzohidrazidom kot prvim reaktantom in 4-dimetilaminobenzaldehidom, 2-kloro-5-nitrobenzaldehidom oz. 3-metoksibenzaldehidom kot drugim smo pripravili serijo treh novih hidrazonskih spojin. Spojine smo karakterizirali s pomočjo elementne analize, infrardeče in UV-vis spektroskopije, HRMS, ^{1}H NMR in ^{13}C NMR spektrov ter z rentgensko difrakcijsko analizo monokristalov. V kristalni strukturi so prisotne vodikove vezi. Spojinam smo s pomočjo MTT metode določili antibakterijsko delovanje (*Bacillus subtilis*, *Escherichia coli*, *Pseudomonas fluorescence* in *Staphylococcus aureus*) ter učinkovanje proti glivam (*Aspergillus niger* in *Candida albicans*). Rezultati kažejo, da je spojina **2** obetavno antibakterijsko sredstvo.

Scientific paper

Artificial Neural Networks and Response Surface Methodology Approach for Optimization of an Eco-Friendly and Detergent-Stable Lipase Production from *Actinomadura Keratinilytica* Strain Cpt29

Noura Semache,[1] Fatiha Benamia,[1,*] Bilal Kerouaz,[2] Inès Belhaj,[3] Selma Bounour,[1] Hafedh Belghith,[3] Ali Gargouri,[3] Ali Ladjama[2] and Zeineddine Djeghaba[1]

[1] *Laboratory of Applied Organic Chemistry, Chemistry Department, Faculty of Sciences, Badji Mokhtar University, P.O. Box 12, 23000 Annaba, Algeria*

[2] *Laboratory of Applied Biochemistry and Microbiology, Biochemistry Department, Faculty of Sciences, Badji Mokhtar University, P.O. Box 12, 23000, Annaba, Algeria*

[3] *Laboratory of Molecular Biotechnology of Eukaryotes, Centre of Biotechnology of Sfax, University of Sfax, Road of Sidi Mansour Km 6, P.O. Box 1177, Sfax 3018, Tunisia*

* *Corresponding author: E-mail: fatiha.benamia@univ-annaba.org*

Received: 09-21-2020

Abstract

This work mainly focused on the production of an efficient, economical, and eco-friendly lipase (AKL29) from *Actinomadura keratinilytica* strain Cpt29 isolated from poultry compost in north east of Algeria, for use in detergent industries. AKL29 shows a significant lipase activity (45 U/mL) towards hydrolyzed triacylglycerols, indicating that it is a true lipase. For maximum lipase production the modeling and optimization of potential culture parameters such as incubation temperature, cultivation time, and Tween 80 (v/v) were built using RSM and ANN approaches. The results show that both the two models provided good quality predictions, yet the ANN showed a clear superiority over RSM for both data fitting and estimation capabilities. A 4.1-fold increase in lipase production was recorded under the following optimal condition: incubation temperature (37.9 °C), cultivation time (111 h), and Tween 80 (3.27%, v/v). Furthermore, the partially purified lipase showed good stability, high compatibility, and significant wash performance with various commercial laundry detergents, making this novel lipase a promising potential candidate for detergent industries.

Keywords: Lipase; *Actinomadura keratinilytica*; Optimization; RSM; ANN; Detergent.

1. Introduction

Lipases are glycerol ester hydrolases that catalyzes the hydrolysis of triacylglycerols to release diacylglyceride, monoacylglycerol, long-chain fatty acids and glycerol at the interface of oil and water.[1] It has been reported that the first lipases were obtained from *Penicillium oxalicum* and *Aspergillus flavus*.[2] Since, the lipases were considered as a great biotechnological and industrial catalyst after carbohydrases and proteases.[3] Lipases are prevalent in nature and are produced by plants, animals, and microorganisms including fungi, bacteria, and actinomycetes.[4] Recently, it has been reported that several actinomycete isolates are able to hydrolyze fats and oils.[5] Microbial lipases are mainly extracellular and their production is significantly influenced by the culture medium parameters. Generally, the major factor influencing the lipase activity was the carbon source. The production of these lipases is generally conducted in the presence of oil, triacylglycerols, fatty acids, esters, glycerol, or Tweens.[6,7] Microbial lipases play a major role in various fields such as the synthesis of organic chemicals and industrial applications. Development of lipase-based technologies for the synthesis of novel compounds increased their use.[8] The main commercial

application for hydrolytic lipases is their use in laundry detergents. Detergent enzymes make up nearly 32% of the total lipase sales.[7] Approximately, sixty percent of industrial enzymes are hydrolytic in nature and are used by the detergent, dairy and leather industries.[9]

The main objective of this work is the production of an efficient, natural, and economical lipase for use in industrial applications and in particular the laundry detergent industry. For this purpose a novel lipase (AKL29) from *Actinomadura keratinilytica* strain Cpt29 isolated from poultry compost in local farm north east of Algeria, was produced. To our knowledge, the lipase cultivation from this strain has never been described. This study mainly focuses on the optimization of the parameters of culture medium to increase the production of AKL29. For this purpose artificial neural networks (ANN) and response surface methodology (RSM) have been investigated to build a predicted effects model and optimization of culture parameters of lipase production.

The last decade has seen a multitude of data analysis tools based on biological phenomena develop into well-established modeling techniques, such as artificial intelligence and evolutionary computing. Artificial neural network (ANN) is now the most popular machine learning tool in biotechnology.[10] On the other hand, the statistical optimization of processes has advantages compared to the classical one.[11] Numerous researchers have reported the use of statistical methods for the production of lipases by microorganisms.[12]

The classical method of optimization involves varying one parameter at time and ignoring the combined interactions between experimental conditions of the process. In recent years, the artificial neural network (ANN) has been used as a highly powerful and flexible method in various processes. It is expected to reveal functions representing phenomena but it cannot clarify the interaction among variables and the significance of each variable. Response surface methodology (RSM) is an effective statistical technique for developing, improving, and optimizing complex process.[11]

For an exhaustive study on the improvement of lipase production from *Actinomadura keratinilytica* strain Cpt29, both ANN and RSM as statistical approaches have been performed in the present work. After finding the most influential factors (incubation temperature, cultivation time, and Tween 80, v/v), for composition of production medium among several parameters of culture medium screened in our previous study, the optimization of these three significant parameters for maximum lipase production was carried out using RSM and ANN. In this work, also a partial purification was investigated to improve the lipolytic activity efficiency of the produced lipase. Furthermore, the stability, compatibility, and wash performance of the partially purified AKL29 with various laundry detergents were carried out to evaluate its potential as bio-additive in various detergents formulations.

2. Experimental

2. 1. Materials

Candida rugosa lipase (CRL, Type VII, 760 U/mg), Bradford reagent, bovine serum albumin (99%) were purchased from Sigma-Aldrich Chemie GmbH (Munich, Germany). Benzamidine were from Fluka (Buchs, Switzerland); Gum Arabic was from Merck (D-6100 Darmstadt, Germany), pH-stat was from Metrohm (Switzerland). Unless specified otherwise, all substrates, chemicals, and reagents were of the analytical grade or highest available purity purchased from Sigma Chemical Co. (St. Louis, MO, USA). Sephacryl S-75 was from Pharmacia (Pharmacia, Uppsala, Sweden).

2. 2. Microorganism Source

The organism required for the lipase production is a thermophilic actinomycetes *Actinomadura keratinilytica* strain Cpt29 [GenBank accession no. KC447297]. The strain Cpt29 was isolated from poultry compost collected from a local farm in north-east region of Annaba, Algeria as previously described elsewhere.[13] Stock culture of *Actinomadura keratinilytica* strain Cpt29 [C.p.t: Compost poultry thermophilic] was maintained by periodic subculture and stored at 4 °C.

2. 3. Lipase Production

The lipase production from *Actinomadura keratinilytica* strain Cpt29 was carried out as follows. Firstly, the bacterial isolate strain Cpt29 was subjected to a qualitative screening for lipase activity, using agar plates containing a slightly modified basal medium (g/L): K_2HPO_4, 0.8; KH_2PO_4, 6; $(NH_4)_2SO_4$, 1; $MgSO_4.7H_2O$, 0.2; $CaCl_2$, 0.5; NaCl, 3; $FeSO_4$, 0.001, supplemented with 3% (v/v) Tween 80; and bacteriological agar, 20.[14] The medium was adjusted to different pH (4-10) in order to set the optimum pH of the culture medium, and the plates were incubated at 35 °C for three days. Lipase producing strain Cpt29 was identified by monitoring clear zone formation around the bacterial colony. Halo zones seen were considered as positive for lipase production.

Lipase production was carried out using a method similar to that described in previous work.[15] 10mL of inoculums culture was added in 100 mL of culture medium in 500 mL Erlenmeyer flasks and incubated at 35 °C on a rotary shaker at 150 rpm for three days. The culture broths were centrifuged at 4830 xg for 20 min to remove mycelia and medium debris, and the cell-free supernatant was used as a crude enzyme solution for determination of the lipolytic activity.

2. 4. Lipase Activity Assay

Lipase activity was measured titrimetrically using olive oil hydrolysis. According to previous works[15-17] the

experiments were performed using olive oil emulsion obtained by mixing 5 mL of olive oil with 45 mL of 10% (w/v) of gum arabic (GA) in 30 mL of 25 mM Tris–HCl buffer (pH 8) in the presence of 2 mM $CaCl_2$, and 200 µl of enzyme solution. The quantity of free fatty acids (FFAs) released was titrated adding 0.1N sodium hydroxide to the reaction medium. Hydrolysis of olive oil emulsion was monitored by pH-stat (718 Stat Titrino, Metrohm, Switzerland). One unit (1U) of lipase activity corresponds to 1 µmol of fatty acid released per minute under the assay conditions used. All determinations were performed in triplicate.

2. 5. Estimation of Total Extracellular Protein

The total extracellular protein content was measured by Bradford method using Coomassie blue assay procedure and bovine serum albumin (BSA) as standard. Samples were analyzed in spectrophotometer (Jenway 6405 UV/Vis) at 595 nm and the protein concentration was determined using the calibration curve of BSA.[18]

2. 6. Partial Purification of AKL29

The partial purification of lipase from the isolate strain Cpt29 was carried out by two steps including acetone precipitation strategy and gel filtration on Sephacryl S-75. The experiments were performed at 4 °C using a method similar to that described in previous work.[19]

2. 6. 1. Acetone Precipitation

After the incubation period, the culture of strain Cpt29 (200 mL) grown on Tween 80 under optimal cultivation conditions was centrifuged for 20 min at 4830 xg to remove the microbial cells. The crude enzyme solution (188 U/mL) was submitted to the partial purification using acetone precipitation as important step. Four volumes of ice-cold acetone (–20 °C) were added to one volume of cell-free culture supernatant to remove most of the other proteins. To minimize the impurities as much as possible, the experiment was repeated with gradual increments of 3% acetone saturation under a gentle stirring. The precipitate was then recovered by centrifugation at 12000 xg for 25 min, and then was suspended in a minimal volume of 20 mM Tris-HCl buffer (pH 8) containing 1mM benzamidine, and the protein content was estimated.

2. 6. 2. Filtration on Sephacryl S-75

After the acetone precipitation step, the obtained supernatant was applied onto a column (3 cm × 160 cm) of gel filtration Sephacryl S-75 equilibrated with 20 mM Tris-HCl buffer (pH 8) containing 1mM benzamidine. The elution of lipase was performed with the same buffer solution at a rate of 45 mL/h. All the elute fractions (2mL each) were collected, and then were checked for lipase activity by titrimetric method. The fractions containing the lipase activity were pooled and the protein content was measured spectrophotomerically at 280 nm.[15]

2. 7. Optimization of Lipase Production

The optimization of lipase production from strain Cpt29 was carried out using two steps including the choice of the best carbon source and the culture medium optimization for maximum lipase production. The optimization of culture medium was investigated using RSM and ANN methodologies.

2. 7. 1. Selection of Carbon Source

To select the significant substrate for AKL29 production, a screening study was performed using four different sources of carbon (Tween 80, Tween 20, olive oil and wheat bran). Each substrate was added to the basal medium at various concentrations to evaluate its effect on the lipase production. Kinetics of the lipase production were monitored by inoculation of 10^6 spores/mL in basal medium followed by incubation at 35 °C, under shaking condition. Samples were taken aseptically every day and enzyme activity was measured using a pH-stat.

2. 7. 2. Statistical Analysis

In order to study the effects of culture conditions on the lipase production, two different statistical approaches were performed for the modeling and the optimization of the lipase activity which is the response (Y) of the experimental design and function of independent variables in RSM and training of the artificial neuron in ANN.

For this purpose a Box-Behnken design was performed to evaluate the effects of culture conditions on the activity of the produced lipase (U/mL), which is the response (Y) of experimental design. A total of fifteen runs with different combination of the significant experimental factors were performed (Table 1). The culture medium conditions are expressed by the following factors (Xi): incubation temperature X_1 (20–50 °C), cultivation time X_2 (2–5 days), and Tween 80 (v/v) as carbon source X_3 (2–4%). A quadratic polynomial regression model (Eq. 1) was assumed to predict the optimal response (Y). The proposed model for response (Y) was:

$$Y = \beta_0 + \sum_{i=1}^{k} \beta_i X_i + \sum_{i=1}^{k} \beta_{ii} X_i^2 + \sum_{j=1}^{k} \beta_{ij} X_i X_j \qquad (1)$$

Where β_0, β_i, β_{ii}, and β_{ij} are the regression coefficients (β_0 is the intercept term, β_i is the linear effect term, β_{ii} is the quadratic effect term, β_{ij} is the interaction effect term, and Y is the predicted response value); X_1, X_2,..., X_k are the input variables that explain the response Y.[11]

2. 8. Influence of Laundry Detergents on Partially Purified Lipase Activity

In this work, the enzymatic performance of partially purified AKL29 towards laundry detergents was verified by studying the effect of various brand commercial detergents on the stability and compatibility of lipase using the commercial *Candida rugosa* lipase (CRL) for comparison. Furthermore, wash performance of the partially purified AKL29 as a green additive for detergent, was evaluated. Effect of laundry detergents on the lipase activity was carried out using a method similar to that described in previous work.[20]

2. 8. 1. Influence of Detergents on the Lipase Stability and Compatibility

The enzyme compatibility and stability of the partially purified AKL29 with laundry detergents were assessed using a variety of commercial detergents including, ARIEL (Procter and Gamble, Switzerland), ISIS (Henkel, Algeria), OMO (Unilever, Algeria), LE CHAT (Henkel, Algeria), and NICE (Sarl Nice Plus, Algeria). All experiments were assessed using CRL as commercial lipase for comparative evaluation. In order to simulate the washing conditions, the selected commercial detergents were diluted in tap water to give a final concentration of 7 mg / mL. All pre-existing endogenous lipases contained in these detergents were inactivated by heating the diluted detergents for 60 min at 70 °C before addition of the enzyme. The effect of lipase stability as well as its compatibility with commercial laundry detergents were studied by incubating each of the two lipases tested (AKL29 or CRL) with the various modified detergents at 40 °C for 60 min. The residual activities were determined at pH 8 and 45 °C and the enzymatic activity in the absence of any detergent was taken as 100%.

2. 8. 2. Wash Performance Analysis of Partially Purified Lipase

The wash performance evaluation of partially purified AKL29 as eco-friendly additive in laundry detergent was investigated using small white cotton cloth pieces

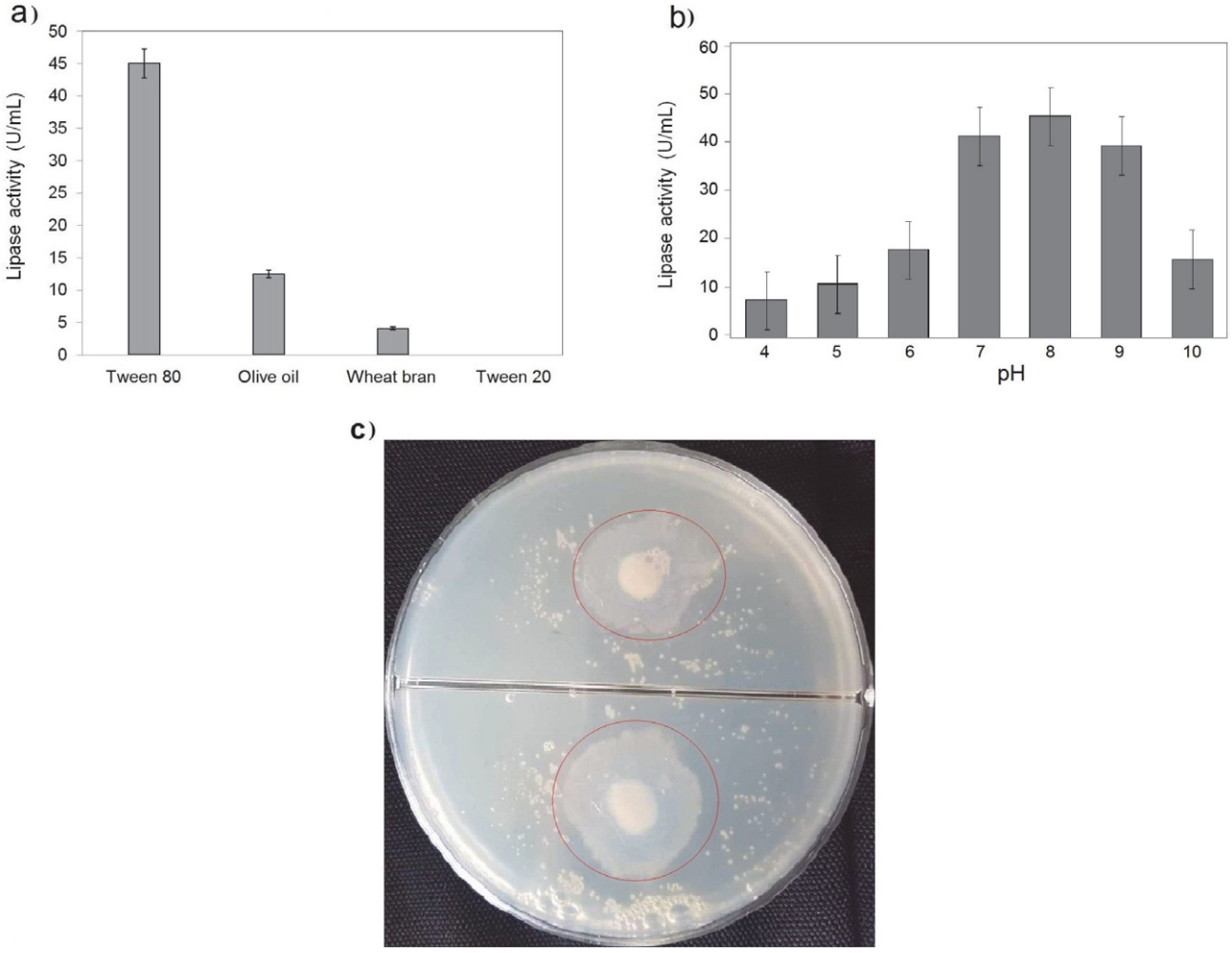

Figure 1. Influence of various carbon sources on the AKL29 activity (a). Effect of pH on the AKL29 activity (b). The lipase activities were measured at 35 °C, pH 8, after three days using different carbon sources, and different pH. The experiments were conducted three times and the error bars represent standard deviation. Hydrolysis zone formed by the lipolytic strain Cpt29 (c).

stained with a mixture of sauce sample and fat/greasy material. The cloth pieces were then incubated in different wash treatments at 40 °C and stirred at 100 rpm for 30 min. Incubation process was carried out using 100 mL of modified detergent at final concentration of 7 mg / mL (heat inactivated). After incubation the modified detergent was added to the lipase solution (50 U/mL). After that, the cloth pieces were removed, rinsed with distilled water, dried and submitted to visual observation to examine the stain removal effects of the lipase. Olive oil was extracted with petroleum ether for 6h using a Soxhlet extractor after complete evaporation of petroleum ether from the extract. The percentage of the removed olive oil was calculated by the following formula:[20]

$$Removal\,(\%) = \frac{W_1 - W_2}{W_2} \; X\; 100 \qquad (2)$$

Where, W_1 and W_2 denoted the weights of total olive oil before and after washing (mg), respectively.

3. Results and Discussion

3. 1. Selection of Carbon Sources

To select the appropriate carbon source that maximizes the activity of lipase produced by strain Cpt29, various carbon sources such as Tween 80, Tween 20, Olive oil, and Wheat bran were tested. The screened carbon sources were supplemented at 3%, v/v to the basal Mendel's medium. The effects of carbon sources on the lipase activity are illustrated by Figure 1a.

Figure 1a shows that the highest level of lipase activity (45 ± 2 U/mL) was produced in presence of Tween 80 emulsion as substrate after three days of growth. The lower lipase activity of 4 ± 1.5 U/mL was observed on media supplemented with oil olive as carbon source. Only Tween 20, present in the medium as carbon source, permits to decline significantly the lipase activity. Based on these results, Tween 80 was selected as the best carbon source for lipase production by isolate Cpt29. The produced lipase was assayed for its ability to hydrolyze Tween 80 as an exclusive carbon source, in agar plates incubated at 35 °C for three days. Lipase produced by strain Cpt29 was found more active over a range of pH from 7 to 9, with an optimum at pH 8 (Figure 1b). Colonies with a large clear zone formed by the hydrolysis of Tween 80 indicated the presence of lipolytic activity (Figure 1c).

3. 2. Optimization of AKL29 Activity

Response surface methodology (RSM) using Box-Behnken design was applied to determine the optimal levels of the activity of lipase produced by strain Cpt29. RSM allows the analysis of the effects of significant culture parameters and also generates a mathematical model which makes it possible to predict the optimal response (Y).[11] The evaluation of the resulting model (Table 2) was conducted by the statistical theory and analyzing data in Table 1 using Minitab 16 as statistical software.

The results of the analysis of variance (ANOVA, Table 2) show that the interaction terms are not significant (P-value > 0.05). So to improve data fit, these terms were excluded from this analysis. The final model is expressed in terms of linear terms (X_i) and quadratic terms (X_i^2) (Eq.3):

$$Y = 765 + 13.95\,X_1 + 124.10\,X_2 + 216.54\,X_3 - 0.197\,X_1^2 - 14.69\,X_2^2 - 34.54\,X_3^2 \qquad (3)$$

Table 1. Experimental design used in RSM and ANN studies with the values of selected independent variables and the corresponding observed and predicted responses (Y).

X_1 (°C)	X_2 (days)	X_3 (%)	Observed values	Y[a] (U/mL) RSM predicted values	ANN predicted values
50	5.0	3	147	142.63	146.71
35	5.0	4	157	155.50	157.44
20	3.5	2	51	49.88	51.25
35	5.0	2	122	121.75	122.33
35	2.0	4	57	61.75	57.13
35	3.5	3	158	159.33	159.05
50	3.5	2	73	77.38	73.44
35	3.5	3	156	159.33	159.05
35	2.0	2	31	28.00	30.74
20	2.0	3	24	21.38	24.25
50	2.0	3	48	48.88	48.05
20	3.5	4	86	83.63	85.88
35	3.5	3	164	159.33	159.05
50	3.5	4	112	111.13	111.99
20	5.0	3	109	115.13	108.60

[a]: values represent means of three replicates. Y: lipase activity (U/mL)

Table 2. All estimated regression coefficients for response (Y).

Term	Coefficient	*P*-value
X_1	13.95	0.000
X_2	124.10	0.000
X_3	216.54	0.000
X_1^2	–0.197	0.000
X_2^2	–14.69	0.000
X_3^2	–34.54	0.000
$X_1 X_2$	0.156	0.153
$X_1 X_3$	0.067	0.651
$X_2 X_3$	1.500	0.328

The coefficient of determination (R^2) of the model adjusted to 99.21% tested the fit of the model and indicates the real relationship among the selected parameters. These values showed that the best model that fits our data is the quadratic one. The results (Table 2) show that the carbon source (Tween 80) and the culture time exhibite high influence on the production of lipase. This significance was evaluated by the high values of their effect compared to that of incubation temperature. Also the very meaningful Fisher's coefficient ($F_{0.95}$ = 3.58 <<< 292.42) with the high coefficient of determination (R^2 = 99.6%), and the study of the linear regression between the observed values of response (Y_{obs}) and the predicted ones (Y_{pred}) confirm the validity of this model (Figure 2).

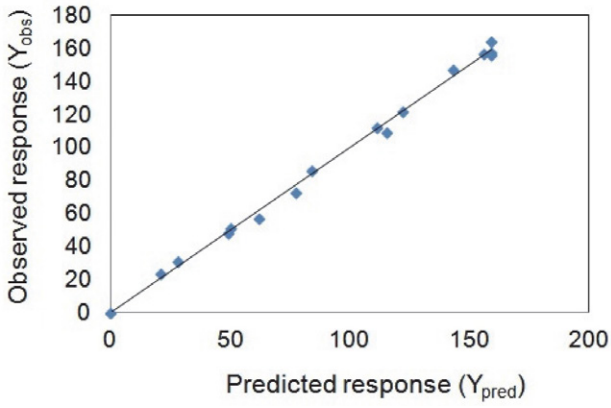

Figure 2. Parity plot showing the goodness-of-fit for RSM model (R^2 = 99.5%).

The fitting quality of RSM model is also shown by the results of analysis of variance (ANOVA, Table 3) which indicate that the model is adequate to represent the actual relationship between response (Y) and the significant variables.[11] The low values of residual errors and the no significance of the lack of fit, show that the quadratic model obtained by the RSM approach using Box-Behnken design can be accepted to describe the studied phenomenon (Table 3).

The best way to predict the relationship between response and parameters of the interactions is to analyze the contour plots and the response surface graphs that give a detailed presentation of the optimum value predicted from the results.[21,22] Each plot and graph that gives the variation of the lipase activity (Y) with independent variables represent an infinite number of combinations of two test variables with the other two fixed at their respective zero level (Figure 3). The contour plots and 3D response surface graphs represented in Figure 3 show that the lipase activity (U/mL) was enhanced by the values near the middle of the input variables.

3. 3. Artificial Neural Network (ANN) Analysis

The ANN architectures used in this purpose was a multilayer forward neural network trained with a Multi Layer Perceptron (MLP) incremental back propagation network with linear transfer function for output and TanH transfer function for hidden neurons. The input layer consists of incubation temperature (X_1), cultivation time (X_2), and Tween 80 (v/v) as carbon source (X_3). The output is represented by the activity of lipase produced by strain Cpt29. In order to select the optimal neural network architecture, which is an important test for a successful application, several ANN architectures (the number of hidden layers and the type of transfer functions), the top three ANN models are summarized in Table 4.

According to the values of coefficient of determination (R^2) and absolute average deviation (AAD) which indicate the significance of the model, we have used the three hidden layers to evaluate the ANN performance analysis compared with RSM one (Figure 4a). ANN analysis was

Table 3. ANOVA for the obtained model of RSM (Eq. 3).

Source	DF	Sum of squares	Least square mean	F	*P*-value
Regression	6	35018	5896	292.42	0.000
Linear	3	21369	5766	289.00	0.000
Square	3	13649	4550	228.00	0.000
Residual Error	8	160	20	221.00	0.000
Lack of fit	6	125	21	1.20	0.520 >> α = 0.05
Pure Error	2	35	17		
Total	14	35177			

DF: degree of freedom. *P* significant if value less than 0.05. R^2 = 99.6 %

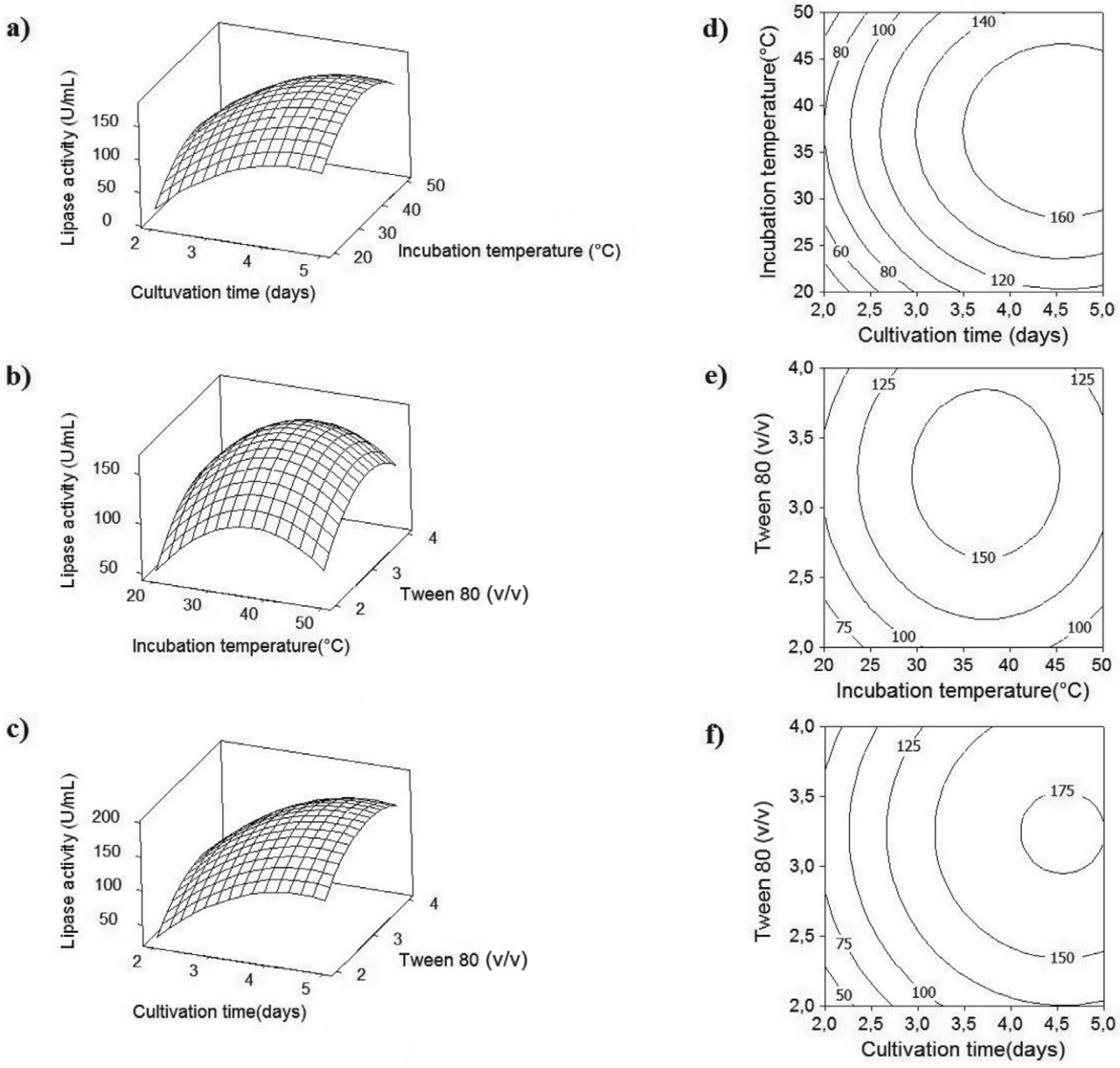

Figure 3. Response surface graphs with contour plots for the effects of independent variables on lipase activity (U/mL), and their mutual interactions, respectively: incubation temperature and cultivation time (a) and (d), incubation temperature and Tween 80 (v/v) (b) and (e), cultivation time and Tween 80 (v/v) (c) and (f).

conducted using SAS software (SAS software, version 9.0, SAS Institute, Inc., Cary, NC). The validity of the ANN (3-3-1) model for testing data is confirmed by the goodness of fit between predicted and experimental response values (Figure 4b, R^2 = 99.9%).

3. 4. Comparison of RSM and ANN Models

The observed values of the lipase activity (Y) along with the predicted ones calculated by ANN and RSM (Table 1) show the goodness of fit for the corresponding

Table 4. Significant ANN architectures and their effects on the estimation and prediction of lipase activity (Y).

Model	Learning Algorithm	Transfer function, output	Transfer function, hidden neurons	Training set, R^2 (%)	Validation set, R^2 (%)	Training set, AAD	Validation set, AAD
3-3-1	MLP	Linear	Tanh	99.73	99.80	0.013	0.0002
3-2-1	MLP	Linear	Tanh	95.12	95.10	0.055	0.0007
3-1-1	MLP	Linear	Tanh	79.24	76.60	0.114	0.0021

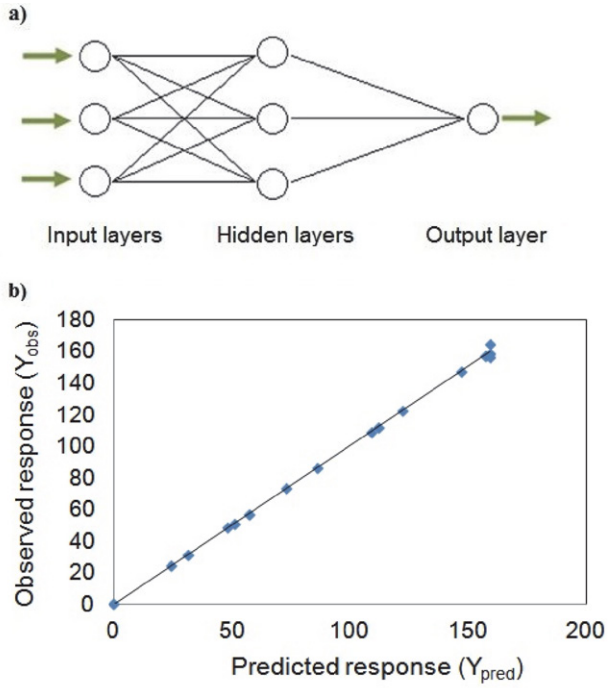

Figure 4. Neural network architecture used for the prediction of lipase activity (a). Parity plot showing the goodness-of-fit for RSM model (R^2 = 99.9%) (b).

models (R^2 = 99.9% and 99.5%, for ANN and RSM, respectively). Both performed models provided good quality predictions, yet the ANN showed a clear superiority over RSM for both data fitting and estimation capabilities (Figures 2 and 4b).

3. 5. Optimization of the Response (Y)

The optimal point of culture parameters for maximum lipase production was determined by the desirability function of Minitab software. The optimal lipase production expressed by lipase activity (U/mL) corresponds relatively to the middle values of the three powerful factors (Figure 5). Experimental validation of enzyme activity was performed using optimal operating variables which were set to incubation temperature of 37.9 °C, 111 h of cultivation time, and 3.27% (v/v) Tween 80.The experimental obtained value of the lipase activity (188 U/mL) is upper than the theoretical value (179.9 U/mL).

Furthermore, the lipase activity from *Actinomadura keratinilytica* strain Cpt29 as a thermophilic actinomycete, was found to be significantly superior than several ones reported previously for the most of the other actinomycetes (Table 5).

3. 6. Partial Purification of AKL29

Extracellular lipase was partially purified to homogeneity from the culture filtrates of *Actinomadura keratinilytica* strain Cpt29 grown on Tween 80 under optimal culture conditions. The crude enzyme was precipitated using acetone to yield as an active pellet. Next the obtained supernatant was applied onto a column (3 cm × 160 cm) of gel filtration Sephacryl S-75 equilibrated with buffer solution of Tris–HCl (20 mM; pH 8) containing 1mM benzamidine. Figure 6 presents the proteine elution profile

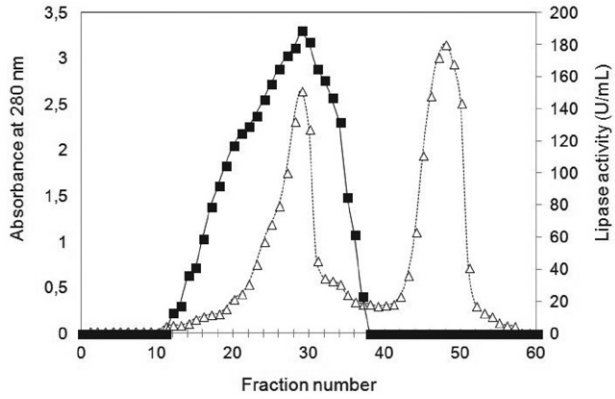

Figure 6. Elution profile of AKL29 obtained by gel filtration using chromatography on Sephacryl S-75. The column (3 cm × 160 cm) was equilibrated with buffer: 20 mM Tris–HCl, pH 8, and 1 mM benzamidine. The elution of lipase (2 mL) was performed at a rate of 45 ml/h. Lipase activity (▪) was measured as described in materials and methods section, and the protein (Δ) was monitored by absorbance at 280 nm.

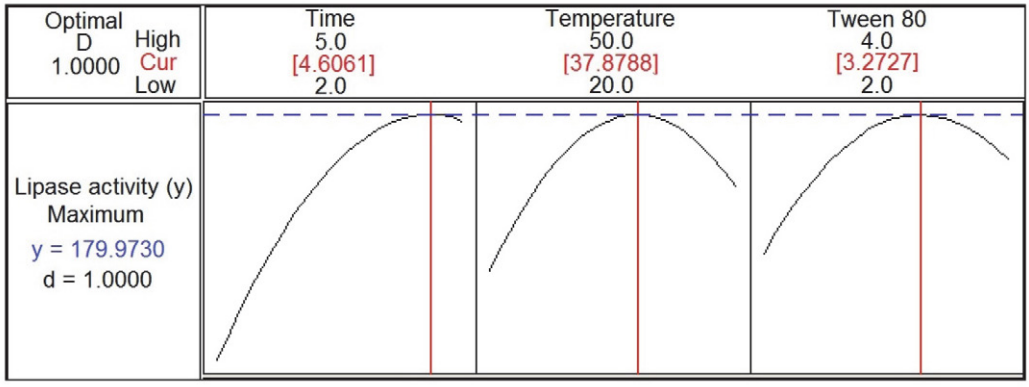

Figure 5. Composite desirability and optimization plot for maximum lipase activity.

Table 5. Lipase activity recorded in some Actinomycetes.

Organism	Substrate	Optimum pH and temperature	Cultivation time (h)	Lipase activity (U/mL)	Reference
Actinomadura keratinilytica strain Cpt29	Tween 80	8 and 37.9 °C	111	188	This work
Streptomyces sp. Al-Dhabi-49	Glucose	8 and 35 °C	120	162	[5]
Streptomyces variabilis NGP 3	Lactose	8.5 and 45 °C	168	39.4	[23]
Streptomyces exfoliates	Triacylglycerides	6 and 37 °C	72	6.9	[24]
Streptomyces sp. TEM 33 strain	*p*-nitrophenyl palmitate	9 and 37 °C	36	3	[25]

Table 6. Flow sheet of the AKL29 partial purification.

Purification step	Total activity[a] (U)	Protein amount[b] (mg)	Specific activity (U/mg)	Activity recovery (%)	Purification factor
Culture supernatant	31800 ± 1200	450 ± 36	70 ± 1.5	100	1
Acetone precipitation	30000 ± 700	89 ± 4	337 ± 2.7	94	5
S-75 chromatography	7800 ± 165	4 ± 0.4	1880 ± 79	24.5	27

[a] 1U corresponds to 1µmol of fatty acid released per minute using olive oil emulsion as substrate. [b] Protein amounts were estimated using Bradford's method.

recorded at the final step of the lipase patial purification. The specific activity of the pure lipase increased 27-fold compared to the crude extract (Table 6).

3. 7. Kinetic Study of AKL29

The ability of our partially purified lipase to hydrolyse its substrate without any surfactant, was also tested using the linear kinetic of FAAs release up on olive oil emulsion hydrolysis biocatalyzed by the partially purified lipase (AKL29) for 12 min. The results (Figure 7a) indicate that the lipase was efficient and seems to be resistant to interfacial denaturation at lipids-water interfaces. The presence of interfacial activation phenomenon of AKL29 was assessed by studying the rate of hydrolysis of TC3 emulsified in 0.33% gum arabic and 0.15 M NaCl by AKL29 as a function of the concentration of the substrate. As shown in Figure 7b, when TC3 was in the water-soluble state, AKL29 hydrolyzed slowly his substrate. However, the lipase activity increased rapidly above the solubility limit of TC3 to reach 100% (300 U/mg) at 34 mM. This result indicates that the AKL29 presents the interfacial activation phenomenon. AKL29 which hydrolyses olive oil emulsion, can be considered as a true lipase.[26]

3. 8. Compatability and Stabilty of Partially Purified AKL29 with Laundry Detrgents

On the basis of the lipase kinetic study, the stability and compatibility of AKL29 with various commercial laundry detergents have been investigated. Both the compatibility and the stability of AKL29 as a bio-additive in laundry detergents were evaluated by comparison with commercial *Candida rugosa* lipase (CRL). The results (Figure 8) show

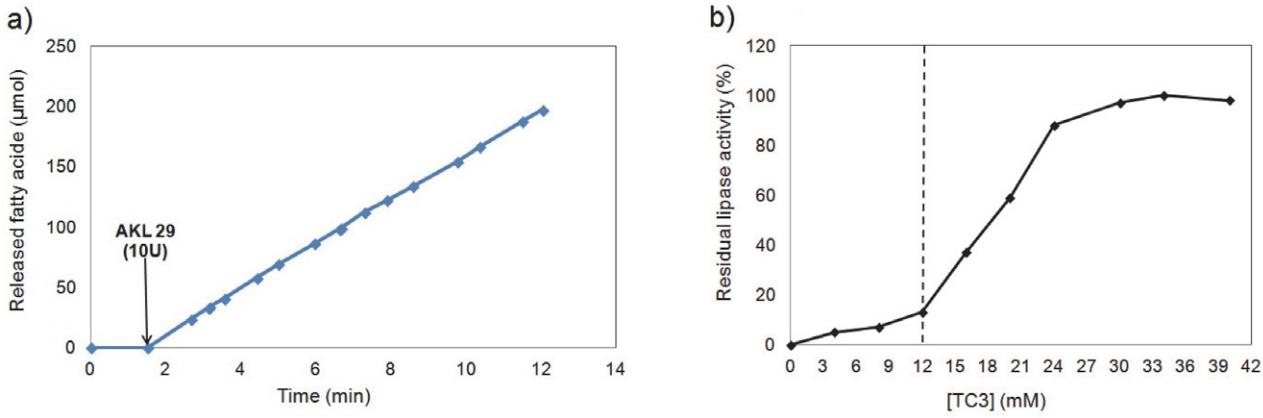

Figure 7. Parity plot showing kinetic study of lipase using olive oil emulsions as substrate (a). Hydrolysis rate of TC3 by AKL29 as function of substrate concentration. The TC3 solutions were systematically prepared by mixing (3 × 30 s) in a warring blender agiven amount of TC3 in 30 ml of 0.33% GA and 0.15 M NaCl. The release of propionic acid was recorded continuously at pH 8 and 45 °C using a pH-stat. The solubility limit of TC3 (12 mM) is indicated by a vertical dotted line (b).

that the lipase exhibited high stability and significant compatibility at 40 °C after 60 min of incubation in various laundry detergents compared to CRL. In fact, 100% of residual activity of AKL29 was recorded in the presence of NICE and ISIS. However, the results show a decrease in the residual activity of AKL29 with the other detergents tested. About 91%, 85% and 73% of residual activity was retained in the presence of OMO, ARIEL, and LE CHAT respectively. On the other hand, a slightly better compatibility and stability of commercial CRL were observed with OMO compared with AKL29 (Figure 8). According to these results, the lipolytic activity of AKL29 could be a potential candidate as a bio-additive for laundry detergent formulations.

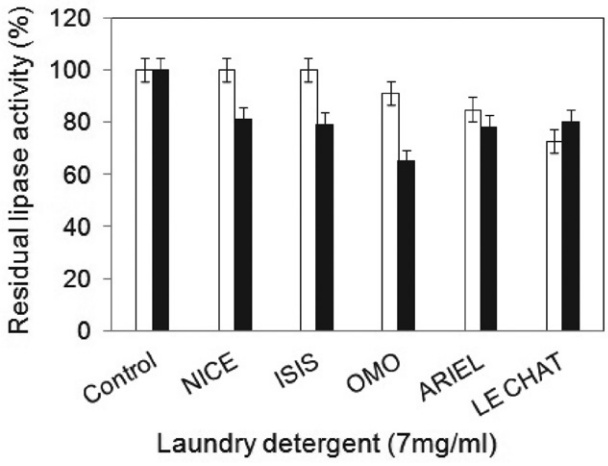

Figure 8. Residual activities of AKL29 (□) and CRL (▪) in the presence of various commercial laundry detergents: enzymes were incubated for 60 min at 40 °C in the presence of detergents at a final concentration of 7 mg/mL. The residual activities were determined at pH 8 and 45 °C using olive oil emulsion as a substrate. Enzymes activities determined without any detergent and incubated under the similar conditions, were taken as 100% (control). The experiments were conducted three times and standard errors are reported. Vertical bars indicate standard error of the mean.

3. 9. Wash Performance Test of Partially Purified AKL29

Partially purified lipase AKL29 was added in various laundry detergents to verify its effect on cleaning grease stains (Table 7). AKL29 showed high rates of olive oil removal compared with detergent alone which gives this novel lipase the advantage of its inclusion in some of laundry detergent formulation.

Table 7. Effect of partially purified AKL29 on removing sample stains from fat / fat (olive oil) sauce from cotton fabric with various commercial laundry detergents.

Laundry detergent (7mg/mL)	Oil removal (%)	
	Detergent	Detergent + AKL29
ISIS	40 ± 0.7	98 ± 1.4
ARIEL	28 ± 1.2	81 ± 1,3
LE CHAT	35 ± 1.9	79 ± 1.7
OMO	32 ± 0.6	70 ± 0.8
NICE	30 ± 1.3	62 ± 0.7

The washing performance of the partially purified AKL29 was evaluated using visual examination of the removal of fat/greasy material stains on cotton fabrics. The washing performance of AKL29 as a bio-additive in several brand laundry detergents was evaluated compared to the control (Figure 9).

4. Conclusion

This work describes the optimization process of a new lipase produced from a thermophilic Actinomycete *Actinomadura keratinilytica* strain Cpt29 isolated from poultry compost in north-east of Algeria. The optimization

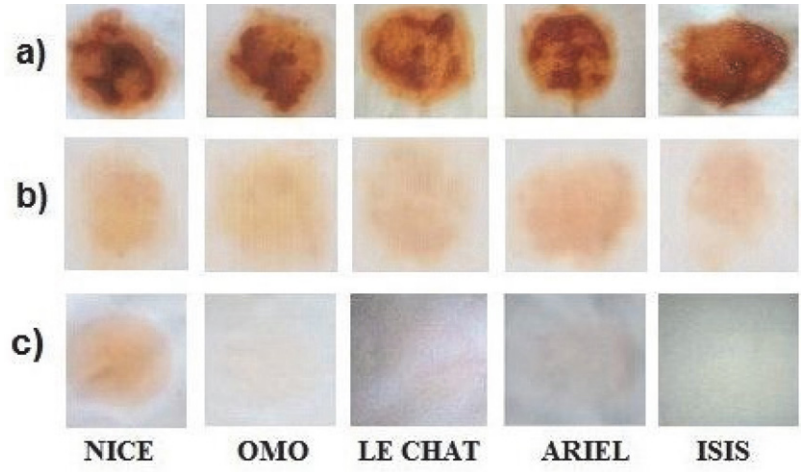

Figure 9. Cloth pieces stained with mixture of sauce sample and fat/greasy material, were washed with commercial laundry detergent (7 mg/mL) added with AKL29 (50 U/mL). Untreated cloth pieces taken as control (a), and treated cloth pieces by detergent alone (b), and treated cloth pieces by detergent with lipase (c).

study using artificial neural network (ANN) and response surface methodology (RSM) approaches, revealed significant improvement in lipase activity with optimal culture conditions. Maximum lipase production of 188 ± 3 U/ml was obtained in Tween 80 (3.27%, v/v), at 37.9 °C, and after 111 h of cultivation. An overall 4.1-fold increase in lipase production was recorded under optimized culture medium. Partial purification using acetone precipitation, and gel filtration on Sephacryl S-75, increased significantly the specific activity of AKL29. Finally, as commercial application, AKL29 exhibited good stability, high compatibility, and significant wash performance with various brand laundry detergents that make this novel lipase a suitable bio-additive for various detergents and a potential biocatalyst for subsequent industrial applications. According to these results, additional studies are underway by the laboratory team to better assess the lipase efficiency.

Acknowledgements

This work was generously supported by The General Directorate for Scientific Research and Technological Development (DG-RSDT), Algerian Ministry of Scientific Research.

5. References

1. O. Ilesanmi, A. E. Adekunle, J. A. Omolaiye, E. M. Olorode, A. L. Ogunkanmi, *Scientific African*, **2020**, *8*, e00279. **DOI:**10.1016/j.sciaf.2020.e00279
2. D. Kirsh, *Bot Gaz*, **1935**, *97*, 321–333. **DOI:**10.1086/334555
3. F. Hasan, A. A. Shah, A. Hameed, *Enzym Microb Technol*, **2006**, *39*, 235–251. **DOI:**10.1016/j.enzmictec.2005.10.016
4. N. A. Al-Dhabi, A. K. M. Ghilan, G. A. Esmail, M. V. Arasu, V. Duraipandiyan, K. Ponmurugan, *J Infect Public Health*, **2019**, *12*, 549–556. **DOI:**10.1016/j.jiph.2019.01.065
5. N .A. Al-Dhabi, G. A. Esmail, A. K. M. Ghilan, M. V. Arasu, *Saudi J Biol Sci*, **2020**, *27*, 474–479. **DOI:**10.1016/j.sjbs.2019.11.011
6. R. Gupta, N. Gupta, P. Rathi, *Appl Microbiol Biot*, **2004**, *64*, 763–781. **DOI:**10.1007/s00253-004-1568-8
7. R. Sharma, Y. Chisti, U. Banerjee, *Biotechnol Adv*, **2001**, *19*, 627–662. **DOI:**10.1016/S0734-9750(01)00086-6
8. B. Andualema, A. Gessesse, *Biotechnol*, **2012**, *11*, 100–118. **DOI:**10.3923/biotech.2012.100.118
9. R. Malathu, S. Chowdhury, M. Mishra, S. Das, P. Moharana, J. Mitra, U.K. Mukhopadhyay, A. R. Thakur, S.R, *Am J Appl Sci*, **2008**, *5*, 1650–1661. **DOI:**10.3844/ajassp.2008.1650.1661
10. M. Basri, R. N. Zaliha Raja Abd Rahman, A. Ebrahimpour, A. B. Salleh, E. R. Gunawan, M.B. Abd Rahman, *BMC Biotechnol*, **2007**, *7*, 1472. **DOI:**10.1186/1472-6750-7-53
11. F. Benamia, S. Bouchagra, Y. Saihi, Z. Djeghaba, N. Rebbani, *Prep Biochem Biotechnol*, **2013**, *43*, 33–47. **DOI:**10.1007/s11696-016-0080-9
12. L. M. Colla, A. L. Primaz, S. Benedetti, R. A. Loss, M. De Lima, C.O. Reinehr, T.E. Bertolin, J.A.V. Costa, *Braz J Microbiol*, **2016**, *47*, 461–467. **DOI:**10.1016/j.bjm.2016.01.028
13. A. Habbeche, B. Saoudi, B. Jaouadi, S. Haberra, B. Kerouaz, M. Boudelaa, A. Badis, A. Ladjama, *J Biosci Bioeng*, **2014**, *117*, 413–421. **DOI:**10.1016/j.jbiosc.2013.09.006
14. M. Mandels, J. Weber, *Advances in Chemistry*, **1969**, *95*, 391–413. **DOI:**10.1021/ba-1969-0095.ch023
15. I. Belhaj-Ben Romdhane, A. Fendri, Y. Gargouri, A. Gargouri, H. Belghith, *Biochem Eng J*, **2010**, *53*, 112–120. **DOI:**10.1016/j.bej.2010.10.002
16. A. Tiss, F. Carriere, R. Verger, *Anal Biochem*, **2001**, *294*, 36–43. **DOI:**10.1006/abio.2001.5095
17. J. Rathelot, R. Julien, P. Canioni, C. Coeroli, L. Sarda, *Biochimie*, **1975**, *57*, 1117–1122. **DOI:**10.1016/S0300-9084(76)80572-X
18. M. M. Bradford, *Anal Biochem*, **1976**, *72*, 248–254. **DOI:**10.1016/0003-2697(76)90527-3
19. E. Fic, S. Kedracka-Krok, U. Jankowska, A. Pirog, M. Dziedzicka-Wasylewska, *Electrophoresis*, **2010**, *31*, 3573–3579. **DOI:**10.1002/elps.201000197
20. S. Akmoussi-Toumi, S. Khemili-Talbi, I. Ferioune, S. Kebbouche-Gana, *Int J Biol Macromol*, **2018**, *116*, 817–830. **DOI:**10.1016/j.ijbiomac.2018.05.087
21. A. Guvenc, N. Kapucu, H. Kapucu, O. Aydogan, U. Mehmetoglu, *Enzym Microb Technol*, **2007**, *40*, 778–785. **DOI:**10.1016/j.enzmictec.2006.06.010
22. J. C. Santos, H. F. De Castro, *World J Microbiol Biotechnol*, **2006**, *22*, 1007–1011. **DOI:**10.1007/s11274-005-2818-3
23. K. Selvam, B. Vishnupriya, *IJPSR*, **2013**, *4*, 4281–4289. **DOI**:10.13040/IJPSR.0975-8232.4(11)
24. M. M. Aly, S. Tork, S. M. Al-Garni, L. Nawar, *Afr J Microbiol Res*, **2012**, *6*, 1125-1137. **DOI:**10.5897/AJMR11.1123
25. J. B. C. Dos Santos, R. G. Da Silva Cruz, P. W. Tardioli, *Appl Biochem Biotechnol*, **2017**, *183*, 218–240. **DOI:**10.1007/s12010-017-2440-5
26. F. Ferrato, F. Carriere, L. Sarda, R. Verger, *Methods in Enzymol*, **1997**, *286*, 327–347. **DOI:**10.1016/S0076-6879(97)86018-1

Povzetek

V tem delu smo se osredotočili na učinkovito, ekonomično ter okolju prijazno pridobivanje lipaze (AKL29), potencialno uporabne v pralni industriji, iz *Actinomadura keratinilytica* sev Cpt29, ki je bil izoliran iz perutninskega komposta severovzhodne Alžirije. AKL29 kaže visoko lipazno aktivnost (45 U/mL) pri hidrolizi triacilglicerolov, kar potrjuje, da gre za pravo lipazo. Da bi dosegli maksimalno proizvodnjo lipaze smo s pomočjo RSM in ANN modelov optimirali kultivacijske parametre kot so temperatura inkubacije, čas kultivacije in koncentracijo Tween 80 (v/v). Rezultati so pokazali, da oba modela dajeta dobre kvalitativne napovedi, da pa kaže ANN model znatno boljše napovedi in ujemanje z eksperimentalnimi podatki. Pod optimalnimi pogoji (temperatura inkubacije 37.9 °C, čas kultivacije 111 h, koncentracija Tween 80 3.27 % v/v) smo dosegli 4.1-kratni porast proizvodnje lipaze. Delno očiščena lipaza kaže dobro stabilnost in visoko kompatibilnost ter zmožnost spiranja v kombinaciji s pralnimi detergent, zaradi česar je obetaven kandidat za uporabo v pralni industriji.

Scientific paper

Biosorption of Hexavalent Chromium Metal Ions by *Lentinula Edodes* Biomass: Kinetic, Isothermal, and Thermodynamic Parameters

Aslı Göçenoğlu Sarıkaya*

** Bursa Uludag University, Faculty of Art and Science, Department of Chemistry, Görükle Campus, Turkey,*

** Corresponding author: E-mail: agocenoglu@uludag.edu.tr*
+90 224 294 28 67

Received: 09-23-2020

Abstract

Lentinula edodes was investigated as a biosorbent for hexavalent chromium biosorption in this study. To examine the optimum conditions of biosorption, the pH of the hexavalent chromium solution, biosorbent dosage, temperature, contact time, and initial hexavalent chromium concentration were identified. Further, to clarify the biosorption mechanism process, the isothermal, kinetic, and thermodynamic parameters were determined. The functional groups and surface morphology of the biosorbent were identified using Fourier transform infrared spectrometry and scanning electron microscopy in the absence and presence of hexavalent chromium, respectively. Based on the results, the maximum biosorption capacity was determined as 194.57 mg g^{-1} under acidic conditions at 45 °C. From the kinetics studies, the biosorption process was observed to follow the Freundlich isotherm and pseudo-second-order kinetic models well. Thus, *L. edodes* as a biosorbent has potential usage for wastewater treatment owing to its effective biosorption capacity.

Keywords: Biosorption, fungal biosorbent, hexavalent chromium, *Lentinula edodes*.

1. Introduction

Pollution by heavy metal impurities is one of the major problems of increasing industrial development.[1,2] Chromium is one of the common pollutants in nature and exists in different oxidation states (–2 to +6) in the environment; however, trivalent chromium (Cr^{3+}) and hexavalent chromium (Cr^{6+}) forms tend to be the most available and stable oxidation states in water.[3] The hexavalent form of chromium is more toxic than the trivalent form and is known as a carcinogenic that causes liver damage, congestion in the lungs, changes to the genetic code, and skin irritation.[4–6] The most common sources of hexavalent chromium wastes are industrial sectors such as textiles, metal finishing, leather tanning, electroplating, cement, and steel.[7,8]

The traditional processes used to remove hexavalent chromium are electrochemical reduction, solvent extraction, electro dialysis, ion exchange, reverse osmosis, and chemical precipitation. Owing to disadvantages such as high cost and increased time consumption of these methods, new procedures have been developed. Biosorption is one of the alternative methods for wastewater treatment and is widely used in batch and continuous studies because of its advantages such as low cost, reusability, and easy operation, which are attractive benefits.[9,10] Shells,[11] leaves,[12] fungi,[9] bacteria,[13] and yeast[14] have been previously reported as biosorbents for hexavalent chromium biosorption.

Lentinula edodes ranks second in the global mushroom market and is commonly known as ' 'shiitake mushroom"[15] it is- the most popular edible mushroom in Japan and China-, and its nutritional components enable *L. edodes* to be used as traditional medicinal mushrooms in eastern Asia. It grows in the deciduous forests of Asia under warm and humid climatic conditions. The goal of this study is to verify removal of hexavalent chromium from water using *L. edodes* as a biosorbent. The effects of different parameters on the biosorption process, reusability of the biosorbent, and some physicochemical parameters are optimized in this study.

2. Materials and Methods

2. 1. *L. edodes* Biosorbent Preparation

L. edodes was obtained from a commercial market in Izmir (Turkey), washed twice with deionized water, and

dehydrated at 30 °C. The dried fungus was then crushed with a grinder after cutting into small pieces. The biosorbent powder (90–120 μm size) was subsequently stored in a glass jar for biosorption studies.

2. 2. Batch Biosorption Experiments

The stock solution of hexavalent chromium (1000 mg L^{-1}) was prepared by dissolving $K_2Cr_2O_7$ (Sigma-Aldrich) in pure water and diluting in the range of 10–1000 mg L^{-1}. Approximately 0.01 g of the *L. edodes* biosorbent was used in the biosorption processes with 25 mL total volume of known hexavalent chromium solutions. To obtain the optimum pH in the range of 2–6, the solution was maintained using 0.1 mol L^{-1} NaOH and 0.1 mol L^{-1} HCl. The impact of temperature was examined via experiments performed at 4, 25, and 45 °C. To optimize the contact time, the biosorption process was conducted for 10–180 min. The biosorbent was removed from the solution before analyzing the remaining hexavalent chromium solution via centrifugation for 10 min at 5000 rpm, and the supernatant was analyzed according to the 1,5-diphenylcarbazide spectrophotometric method at 540 nm (Perkin Elmer Lambda 35 UV/Vis Spectrometer).

The hexavalent chromium concentration at equilibrium can be determined according to Eq. 1 as follows:

$$q_e = \frac{(C_0 - C_e)}{m} V \quad (1)$$

where q_e is the amount of absorbed hexavalent chromium ions (mg g^{-1}), C_o and C_e are the initial and final concentrations of hexavalent chromium (mg L^{-1}), V is the total solution volume (mL), and m is the mass of the biosorbent (g).

Desorption percentages were calculated with 0.1 mol L^{-1} HNO_3 and 0.1 mol L^{-1} HCl using the following equation:

$$\%\ Desorption = \frac{C_{des}}{C_{ads}} \times 100 \quad (2)$$

where C_{des} is the amount of hexavalent chromium ions desorbed on the desorption medium and C_{ads} is the amount of hexavalent chromium ions adsorbed onto the biosorbent. The adsorbed biosorbents were shaken at 200 rpm on a magnetic shaker at 25 °C for 24 h.

2. 3. Characterization of Biomass

Fourier transform infrared (FTIR) spectroscopy (Perkin Elmer Spectrum BX FTIR System) and scanning electron microscopy (SEM, ZEISS EVO 40) were used to identify the binding sites and functional groups on the fungal biosorbent surface as weel as the surface morphology of the biosorbent in the absence and presence of hexavalent chromium, respectively.

3. Results and Discussion

3. 1. Effects of pH

The pH of an aqueous solution is a crucial factor for the biosorption process and affects the ion sorption efficiency. The charges of the functional groups of the biosorbent and distribution of the hexavalent chromium species are affected by changes in the solution pH. Therefore, the biosorption and reduction processes have different affinities.[16] The maximum biosorption capacity (q_e) of hexavalent chromium on the *L. edodes* biosorbent was determined as 6.12 mg g^{-1} at a pH of 2.0 (Figure 1).

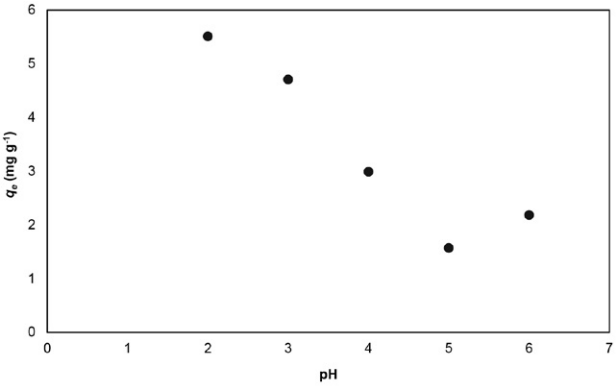

Figure 1. Effect of pH on hexavalent chromium biosorption capacity (q_e) onto *L. edodes* biosorbent.

The experiments were performed for 120 min at 25 °C with 10 mg L^{-1} as the initial hexavalent chromium concentration, hence, the suitable pH was chosen as 2.0 for biosorption. Generally, in aqueous hexavalent chromium solutions, $HCrO_4^-$, $Cr_2O_7^{2-}$, CrO_4^{2-}, and H_2CrO_4 are the dominant species.[17] Under acidic condition (pH ≤ 4.0) $HCrO_4^-$, $Cr_2O_7^{2-}$, and H_2CrO_4 are the main forms of hexavalent chromium. $HCrO_4^-$ is the dominant form of hexavalent chromium at a pH of 2.0.[18] Owing to protonation of the amino functional groups, the cell surface become positively charged, hence, the acid chromate can perfectly interact with the protonated biomass surface.[3,19]

3. 2. Effects of Biosorbent Dosage

To examine the effects of biosorbent dosage on hexavalent chromium biosorption, different amounts of the biosorbent were tested in the range of 0.025–0.200 g. Approximately 100 mg mL^{-1} of the initial hexavalent chromium concentration and 25 mL of total volume of the ion solutions were used at 25 °C. As the biosorbent dosage increased from 0.025 g to 0.200 g, the q_e value decreased from 24.46 mg g^{-1} to 3.94 mg g^{-1} (Figure 2). As the total amount of hexavalent chromium biosorbed on the biosorbent increases, the q_e per unit of biomass reduces because of the fixed concentration.[20]

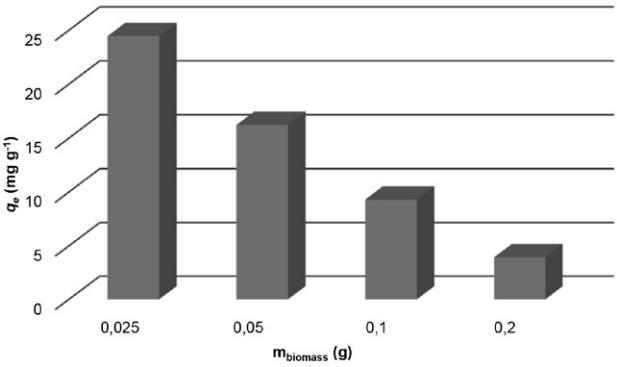

Figure 2. Effect of biosorbent dosage on hexavalent chromium biosorption capacity (q_e) onto the *L. edodes* biosorbent.

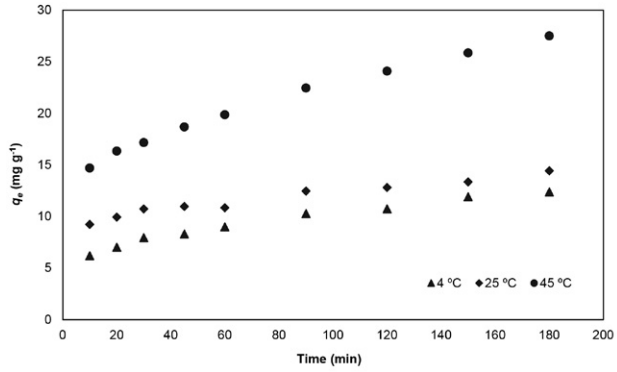

Figure 4. Effect of contact time on hexavalent chromium biosorption capacity (q_e) onto the *L. edodes* biosorbent.

3. 3. Effects of Initial Concentration of Hexavalent Chromium and Contact Time

To understand the effects of initial concentration of the hexavalent chromium, 10–1000 mg L^{-1} initial concentrations were tested for the 25 mL total solution volume and 0.025 g of the biosorbent. The q_e increased from 4.56 to 110.96 mg g^{-1} with increase in the initial hexavalent chromium concentration from 10 to 1000 mg L^{-1} at 25 °C. To identify the impact of temperature on the biosorption process, three different temperature values of 4, 25, and 45 °C were studied at both initial concentrations. The total volume of the hexavalent chromium solution and amount of biosorbent were 25 mL and 0.01 g, respectively. As seen in Figure 3, when the temperature increases from 4 to 45 °C, the q_e increases from 1.33 to 11.26 mg g^{-1} at 10 mg L^{-1} initial hexavalent chromium concentration. Figure 3 also depicts that the q_e values at 4, 25, and 45 °C are 87.67, 110.96 and 194.57 mg g^{-1}, respectively.

To examine the effects of contact time, about 0.025 g of the biosorbent in 25 mL of the total solution volume with 100 mg L^{-1} hexavalent chromium solution was tested at 4, 25, and 45 °C for 10–180 min. At 4 °C, q_e increased from 6.19 to 12.38 mg g^{-1}, with temperature increase from 25 to 45 °C, q_e increased from 14.42 to 27.48 mg g^{-1}. These results are illustrated in Figure 4.

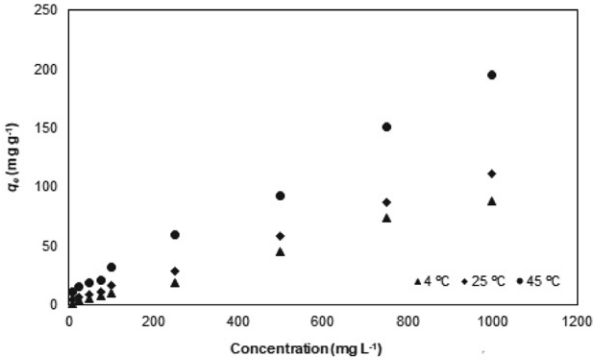

Figure 3. Effect of initial concentration of hexavalent chromium on its biosorption capacity (q_e) onto the *L. edodes* biosorbent.

3. 4. Biosorption Isotherms

To identify the interactions between the sorbate (liquid or gas) and sorbent, sorption isotherms were used. The Langmuir, Freundlich, and Sips isotherm models were investigated in this study. In the Langmuir isotherm model, the sorbate molecules interact with the sorbent molecules to form a monolayer, uniform and homogenous surface. In this model, all sorption sites are unique and morphologically homogeneous. The Langmuir equation can be expressed as follows:

$$\frac{C_e}{q_e} = \frac{1}{Q_L K_L} + \frac{C_e}{Q_L} \quad (3)$$

where K_L is the Langmuir constant (L mg^{-1}), C_e is the hexavalent chromium concentration under equilibrium (mg L^{-1}), q_e is the amount of biosorbed hexavalent chromium (mg g^{-1}) and Q_L is the maximum Langmuir monolayer coverage capacity (L mg^{-1}).[21]

The Freundlich isotherm model is suitable for heterogeneous surfaces and a reversible sorption process for multilayer sorbents. The Freundlich isotherm equality is given as follows:

$$\ln q_e = \ln K_F + \frac{1}{n} \ln C_e \quad (4)$$

Here, K_F represents the Freundlich isotherm and n is the biosorption intensity. The value of $1/n$ characterizes the feasibility of the isotherm.[22] To investigate the applicability of the isotherm, a linear graph of ln q_e versus ln C_e was plotted, and the K_F and n values were calculated from the intercept and slope of the plot, respectively.[23]

The Sips isotherm equality is given as follows:

$$\frac{1}{q_e} = \frac{1}{Q_{max} K_S} \left(\frac{1}{C_e}\right)^{1/n} + \frac{1}{Q_{max}} \quad (5)$$

where, Q_{max} is the maximum biosorption capacity (mg g^{-1}) and K_S is the Sips constant (L mg^{-1}).

The calculated data are given in Table 1. As seen, the *L. edodes* fits better with the Freundlich model than the Langmuir or Sips models. The K_F values were determined as 0.69, 0.20, and 0.19 L mg^{-1} at 4, 25, and 45 °C, respectively. The $1/n$ value gives the heterogeneity of the surface,[24] so the n values were calculated as 0.90, 0.75, and 0.65 at 4, 25, and 45 °C, respectively.

Table 1. Biosorption isotherm constants for hexavalent chromium biosorption onto the *L. edodes* biosorbent.

	Langmuir Isotherm Constants			Freundlich Isotherm Constants			Sips Isotherm Constants		
T (K)	$K_L \times 10^2$ (L mg^{-1})	Q_L (mg g^{-1})	R^2	K_F (L mg^{-1})	N	R^2	$K_S \times 10^2$ (L mg^{-1})	Q_{max} (mg g^{-1})	R^2
277	0.35	39.06	0.88	0.69	0.90	0.99	0.30	36.10	0.99
298	3.43	14.68	0.95	0.20	0.75	0.97	2.84	11.55	0.83
318	7.41	24.33	0.99	0.19	0.65	0.96	3.72	19.84	0.95

3. 5. Biosorption Kinetics

Kinetic analysis is important to clarify the transport mechanisms of biosorption, which have to be identified. Langergeren's first order (LFO), pseudo-second order (PSO), intraparticular diffusion (IPD), and Ritchie's second-order (RSO) kinetic models were thus calculated to identify the biosorption processes.

The LFO and PSO models are expressed as follows:[25,26]

$$\ln(q_e - q_t) = \ln q_e - k_1 t \quad (9)$$

$$\frac{t}{q_t} = \frac{1}{k_2 q_e^2} + \frac{t}{q_e} \quad (10)$$

Here, q_e is the amount of biosorbed hexavalent chromium at equilibrium time (mg g^{-1}), q_t is the amount of biosorbed hexavalent chromium at time t (min), and k_1 (min^{-1}) and k_2 (mol kg min^{-1}) are the LFO and PSO rate constants, respectively.

The IPD model represents the rate-limiting steps and is given as follows:[27]

$$q_t = k_{id} t^{1/2} \quad (11)$$

where q_t is the amount of biosorbed hexavalent chromium at time t (mol kg^{-1}), k_{id} is the IPD rate constant (mg g^{-1} $min^{-1/2}$), and $t^{1/2}$ is the half-life time (s). Plots of the biosorbate uptake q_t versus $t^{1/2}$ show a linear relationship when the IPD is rate limited.

The RSO model is expressed as follows:[28]

$$\frac{1}{q_t} = \frac{1}{k_R q_e t} + \frac{1}{q_e} \quad (12)$$

Here, k_R is the RSO rate constant (min^{-1}), q_e and q_t are the amounts of biosorbed hexavalent chromium at equilibrium time (mg g^{-1}) and at time t (min), respectively. In this model, the number of surface sites, n, are bounded by each biosorbate. The kinetic models are summarized at Table 2. According to the calculated values, the PSO kinetic model is suitable for the biosorption process. The R^2 values were 0.99 for all three temperatures (4, 25, and 45 °C), and the calculated q_e values, which are similar to the experimental q_e (Eq. 1) values, are 1.63, 4.27, and 12.05 mg g^{-1}, respectively. Comparative results of the biosorption of Cr(VI) by various sorbents are given in Table 3.

3. 6. Biosorption Thermodynamics

The van't Hoff equation was used to calculate the thermodynamic parameters at different temperatures. The free energy change (ΔG^o), entropy change (ΔS^o), and enthalpy change (ΔH^o) values were determined as follows:

$$lnK_L = -\frac{\Delta H^\circ}{RT} + \frac{\Delta S^\circ}{R} \quad (13)$$

$$\Delta G^\circ = \Delta H^\circ - T\Delta S^\circ \quad (14)$$

where T represents the absolute temperature (K), R is the universal gas constant (8.314 J mol^{-1} K^{-1}), and K_L is the Langmuir equilibrium constant.

Table 2. Biosorption kinetic models and parameters for hexavalent chromium biosorption onto the *L. edodes* biosorbent.

	LFO				PSO			IPD		RSO		
T (K)	q_e exp (mg g^{-1})	$k_1 \times 10^2$ (min^{-1})	q_e (mg g^{-1})	R^2	$k_2 \times 10^2$ (mol kg min^{-1})	q_e (mg g^{-1})	R^2	k_{id} (mg g^{-1} $min^{-1/2}$)	R^2	k_R (min^{-1})	q_{eq} (mg g^{-1})	R^2
277	1.32	1.60	2.08	0.93	7.49	1.63	0.99	0.60	0.99	4.37	6.02	0.85
298	4.56	1.72	2.07	0.66	7.01	4.27	0.99	0.42	0.88	8.06	4.23	0.55
318	11.26	1.38	2.76	0.98	3.42	12.05	0.99	1.25	0.99	10.49	12.50	0.79

Table 3. Biosorption of Cr(VI) by different sorbents.

Sorbent	Sorption capacity	pH	Time	T (K)	Isotherm model	Kinetic model	Reference
Arthrobacter viscosus	14.4 mg/g	2	144 h	299	Langmuir	–	29
Spirulina sp.	59.57 mg/g	5	60 min	298	Langmuir and Freundlich	PSO	30
Agaricus campestris	56.21 mg/g	2	60 min	318	Langmuir	PSO	9
Multi-shell hollow micro-meso-macroporous silica	257.67 mg/g	4	90 min	293	Langmuir	–	31
Activated carbon	54.8 mg/g	3.5	72 h	333	Langmuir	PSO	32
Cellulose hydrogel coating with Fe^0	98.2 %	5	4 h	313	–	LFO	33
Sugarcane bagasse	87 %	6.7	100 min	319	Redlich-Peterson and Temkin	LFO	34
Lentinula edodes	194,57 mg g^{-1}	2	3 ure	318,	Freundlich	PSO	This study

Positive or negative values of ΔG^o indicate the spontaneity or non-spontaneity of the biosorption process, ΔH^o supplies information about the process and whether it is exothermic or endothermic. [35] Finally, another thermodynamic parameter, ΔS^o, gives information about the randomness of the biosorption process. The thermodynamic parameters were calculated using Eq. 14, and these data are given in Table 4. It is observed that biosorption is an exothermic process (ΔH^o = –4.587 kJ mol^{-1}) and that the randomness decreases during the process (ΔS^o = –0.738 J mol^{-1} K^{-1}). The calculated ΔG^o values were 3.61, 3.36, and 3.14 kJ mol^{-1} at 4, 25, and 45 °C, respectively. These results indicate that ΔG^o decreases with increasing temperature and that the biosorption process is suitable for high temperatures.

Table 4. Thermodynamic parameters for hexavalent chromium biosorption onto the *L. edodes* biosorbent.

ΔH^o (kJ mol^{-1})		–4.587	
ΔS^o (J mol^{-1} K^{-1})		–0.738	
	277 K	**298 K**	**318 K**
ΔG^o (kJ mol^{-1})	3.61	3.36	3.14

3. 7. Desorption and Reusability of the Biosorbent

Approximately 0.1 mol L^{-1} HCl and 0.1 mol L^{-1} of HNO_3 were used as the desorption agents, and based on the results, the 0.1 mol L^{-1} concentration of HNO_3 (96.37%) was more effective than 0.1 mol L^{-1} of HCl (35.89%). To determine the reusability of the *L. edodes* as a biosorbent, the biosorption–desorption cycles were repeated five times, during which the biosorption capacity decreased by 7%.

3. 8. Characterization of the Biosorbent

The effective functional groups of the *L. edodes* biosorbent for hexavalent chromium biosorption were examined using FTIR spectroscopy. The FTIR spectra of the biosorbent before and after biosorption in the range of 4000–600 cm^{-1} are given in Figure 5. The strong and broad bands at 3267 and 3260 cm^{-1} are attributed to the -OH and -NH groups before and after biosorption, respectively. The peak at 2922 cm^{-1} are attributed to C-H stretching, and the peaks observed at 1628–1634 cm^{-1} correspond to carboxylate functional groups and carboxyl groups of the biosorbent. Stretching of the -COO group is represented at 1371–1364 cm^{-1}, and the peaks at 1017–1019 cm^{-1} are assigned to N-H or C-O band absorption.

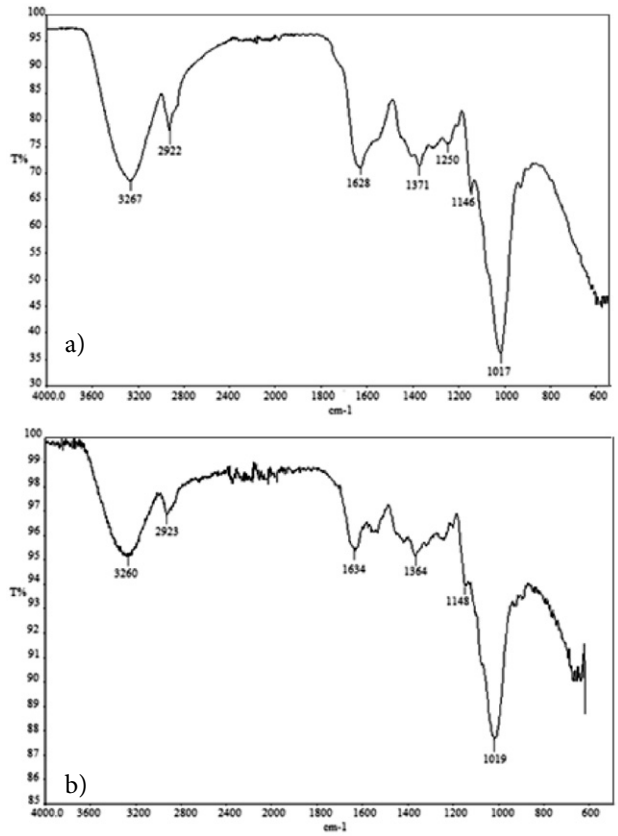

Figure 5. FTIR spectra of the *L. edodes* biosorbent **(a)** before and **(b)** after biosorption of hexavalent chromium.

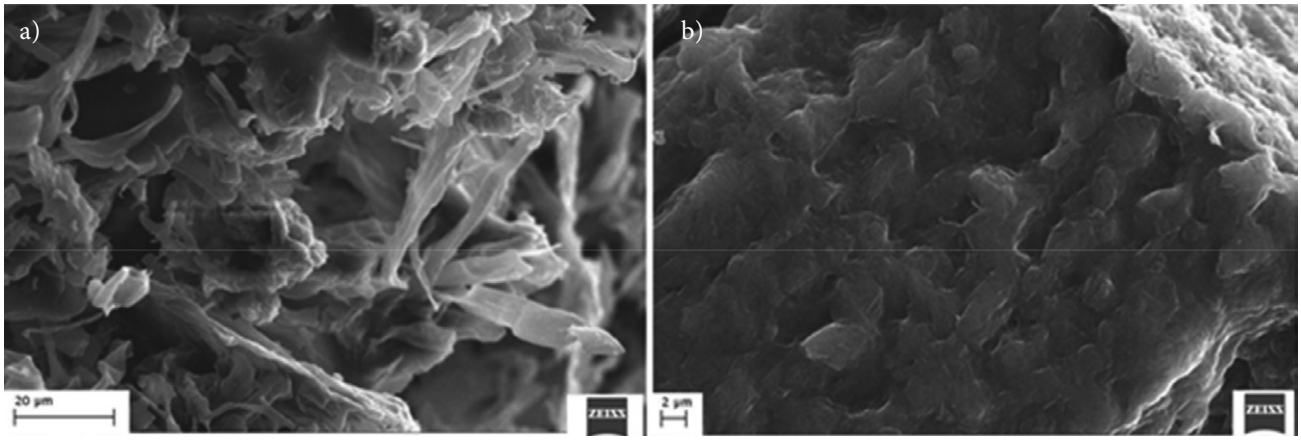

Figure 6. SEM images of the *L. edodes* biosorbent **(a)** before and **(b)** after biosorption of hexavalent chromium.

To identify the surface morphology of the biosorbent SEM was used. As seen in Figure 6, the surface of the biomass has some heterogeneity and becomes smoother after biosorption owing to binding of the hexavalent chromium ions to the functional sites of the biosorbent.

4. Conclusion

The main aim of this study was to examine the viability of *L. edodes* as a biosorbent for hexavalent chromium biosorption. In this assessment, the optimum biosorption parameters such as pH, temperature, biosorbent dosage, and contact time, were determined. The optimum process parameters were detected as pH of 2.0, total biosorbent dosage of 0.025 g, and maximum biosorption capacity of 194.57 mg g^{-1} during 3 h of biosorption at 45 °C. The obtained data were applied to certain physicochemical parameters, such as isotherm, thermodynamic, and kinetic models, to identify the biosorption process. The Freundlich isotherm and PSO kinetic models were found to be suitable for the biosorption process and observed to fit well with the experimental data. The standard enthalpy and standard entropy were calculated as –4.587 kJ mol^{-1} and –0.738 J mol^{-1} K^{-1}, respectively. In addition, the *L. edodes* biosorbent was determined to be an effective and a renewable biomaterial that was suitable for hexavalent chromium biosorption from aqueous solutions, this biosorbent showed high sorption capacity for treatment of wastewater contaminated with hexavalent chromium.

5. References

1. J. R. M. B. Smily, P. A. Sumithra, *HAYATI J. Biosci.* **2017**, *24(2)*, 65–71. **DOI:**10.1016/j.hjb.2017.08.005
2. J. Wang, Q. Xie, A. Li, X. Liu, F. Yu, J. Ji, *Water Sci. Technol.* **2020**, *81(6)*, 1114–1129. **DOI:**10.2166/wst.2020.167
3. N. K. Mondal, A. Samanta, S. Dutta, S. Chattoraj, *J. Genet. Eng. Biotechnol.* **2017**, *15(1)*, 151–160. **DOI:**10.1016/j.jgeb.2017.01.006
4. J. J. Pan, J. Jiang, R. K. Xu, *Chemosphere,* **2014**, *101*, 71–76. **DOI:**10.1016/j.chemosphere.2013.12.026
5. Y. Li, Y. Wei, S. Huang, X. Liu, Z. Jin, M. Zhang, J. Qu, Y. Jin, *J. Mol. Liq.* **2018**, *269*, 824–832. **DOI:**10.1016/j.molliq.2018.08.060
6. Z. Shi, S. Peng, X. Lin, Y. Liang, S. -Z. Lee, H. E. Allen, *Environ. Sci. Process. Impacts.* **2020**, *22*, 95–104. **DOI:**10.1039/C9EM00477G
7. E. Nakkeeran, C. Patra, T. Shahnaz, S. Rangabhashiyam, N. Selvaraju, *Bioresour. Technol. Reports.* **2018**, *3*, 256–260. **DOI:**10.1016/j.biteb.2018.09.001
8. R. Xiao, J. J. Wang, R. Li, J. Park, Y. Meng, B. Zhou, S. Pensky, Z. Zhang, *Chemosphere.,* **2018**, *208*, 408–416. **DOI:**10.1016/j.chemosphere.2018.05.175
9. A. Göçenoğlu Sarıkaya, *Environ. Technol.* **2021**, *42(1)*, 72–80. **DOI:**10.1080/09593330.2019.1620867
10. S. H. Abbas, Y. M. Younis, M. K. Hussain, F. H. Kamar, G. Nechifor, B. Pasca, *Rev. Chim.* **2020**, *71(1)*, 1–12. **DOI:**10.37358/RC.20.1.7804
11. C. Patra, T. Shahnaz, S. Subbiah, S. Narayanasamy, *Environ. Sci. Pollut. Res.* **2020**, *27*, 14836–14851. **DOI:**10.1007/s11356-020-07979-y
12. A. K. Prajapati, S. Das, M. K. Mondal, *J. Mol. Liq.* **2020**, *307*, 112956. **DOI:**10.1016/j.molliq.2020.112956
13. V. Kalola, C. Desai, *Environ. Sci. Pollut. Res.* 2019 **DOI:**10.1007/s11356-019-05942-0
14. A. De Rossi, M. R. Rigon, M. Zaparoli, R. D. Braido, L. M. Colla, G. L. Dotto, J. S. Piccin, *Environ. Sci. Pollut. Res.* **2018**, *25(19)*, 19179–19186. **DOI:**10.1007/s11356-018-2377-4
15. P. S. Bisen, R. K. Baghel, B. S. Sanodiya, G. S. Thakur, G. B. Prasad, *Curr. Med. Chem.* **2010**, *17(22)*, 2419–2430. **DOI:**10.2174/092986710791698495
16. T. Chen, Z. Zhou, S. Xu, H. Wang, W. Lu, *Bioresour. Technol.* **2015**, *190*, 388–394. **DOI:**10.1016/j.biortech.2015.04.115
17. P. Miretzky, A. Cirelli, *J. Hazard. Mater.* **2010**, *180(1–3)*, 1–19. **DOI:**10.1016/j.jhazmat.2010.04.060
18. S. Sugashini, K. M. M. S. Begum, *Clean. Technol. Environ. Policy.* **2013**, *15*, 293–302. **DOI:**10.1007/s10098-012-0512-3
19. Z. Aksu, U. Açikel, E. Kabasakal, S. Tezer, *Water Res.* **2002**,

36(12), 3063–3073. **DOI:**10.1016/S0043-1354(01)00530-9
20. Z. K. Wang, C. L. Ye, X. Y. Wang, J. Li, *Appl. Surf. Sci.* **2013**, *287*, 232–241. **DOI:**10.1016/j.apsusc.2013.09.133
21. I. Langmuir, *J. Am. Chem. Soc.* **1918**, *40(9)*, 1361–143. **DOI:**10.1021/ja02242a004
22. E. Radu, E. E. Oprescu, C. E. Enascuta, C. Calin, R. Stoica, G. V. Scaeteanu, G. Vasilievici, L. Capra, G. Ivan, A. C. Ion, *Rev. Chim.* **2018**, *69(1)*, 191–195. **DOI:**10.37358/RC.18.1.6072
23. H. Freundlich, *J. Phys. Chem. A.* **1906**, *57*, 385–471.
24. Y. Özüdoğru, M. Merdivan, *Trak. Univ. J. Nat. Sci.* **2017**, *18(2)*, 81–87. **DOI:**10.23902/trkjnat.300344
25. S. Lagergren, *Sven. Vetenskapsakad Handingarl,* **1898**, *24*, 1–39.
26. S. K. Srivastava, V. K. Gupta, S. Anurpam, D. Mohan, *Indian J. Chem.* **1995**, *34A*, 342–350.
27. T. Furusawa, J. M. Smith, *AlChE Journal,* **1974**, *20*, 88. **DOI:**10.1002/aic.690200111
28. A. G. Ritchie, *J. Chem. Soc. Faraday Trans.* **1977**, *73*, 1650. **DOI:**10.1039/f19777301650
29. R. M. Hlihor, H. Figueiredo, T. Tavares, M. Gavrilescu, *Process. Saf. Environ.* **2017**, *108*, 44–56. **DOI:**10.1016/j.psep.2016.06.016
30. H. Rezaei, *Arab. J. Chem.* **2016**, *9*, 846–853. **DOI:**10.1016/j.arabjc.2013.11.008
31. R. Soltani, A. Marjani, R. Soltani, S. Shirazian, *Sci. Rep.* **2020**,*10*, 9788. **DOI:**10.1038/s41598-020-66540-6
32. Y. Wang, C. Peng, E. Padilla-Ortega, A. Robledo-Cabrera, A. Lopez-Valdivieso, J. Environ. Chem. Eng. **2020**, *8(4)*, 104031. **DOI:**10.1016/j.jece.2020.104031
33. Y. Wang, L. Yu, R. Wang, Y. Wang, X Zhang, *Sci. Total Environ.* **2020**, *726*, 138625. **DOI:**10.1016/j.scitotenv.2020.138625
34. R. R. Karri, J. N. Sahu, B. C. Meikap, *Industrial Crops and Products,* **2020,** *143,* 111927. **DOI:**10.1016/j.indcrop.2019.111927
35. R. M. Senin, I. Ion, O. Oprea, R. Stoica, R. Ganea, A. C. Ion, *Rev. Chim.* **2018**, *69(5)*, 1233–1239. **DOI:**10.37358/RC.18.5.6297

Povzetek

Namen študije je bil preučitev sposobnosti adsorpcije kroma (VI) z glivo šitake (*Lentinula edodes*). Da bi določili optimalne pogoje smo spreminjali pH vrednost raztopine kroma (VI), količino *šitake*, temperaturo, kontaktni čas in koncentracijo kroma (VI). Adsorpcijski mehanizem smo opisali z izotermičnimi, kinetičnimi in termodinamskimi parametri. Funkcionalne skupine in morfologijo površine glive smo analizirali s FTIR in SEM v odsotnosti in prisotnosti kroma (VI). Maksimalna adsorpcijska kapaciteta je znašala 194.57 mg g^{-1}, pod kislimi pogoji pri temperaturi 45 °C. Na osnovi kinetičnih študij smo zaključili, da lahko ravnotežje opišemo s Freundlichovo izotermo, adsorpcijo pa s kinetičnim modelom psevdo-prvega reda. Visoka adsorpcijska sposobnost *L. edodes* kaže potencial njene uporabe za čiščenje odpadnih vod.

DOI: 10.17344/acsi.2020.6412 *Acta Chim. Slov.* **2021,** *68,* 594–603

Scientific paper

Ultrasmall Monodisperse NiO Nanocrystals as a Heterogeneous Catalyst for the A^3-Coupling Reaction Toward Propargylamines

Mohsen Moradian[1,*] and Masoomeh Nazarabi[2]

[1] *Department of Organic Chemistry, Faculty of Chemistry, University of Kashan, Kashan, 87317, I. R. Iran*

[2] *Nanostructures and Biopolymer Research Lab, Institute of Nanoscience and Nanotechnology, University of Kashan, 87317-53153, Kashan, Iran.*

** Corresponding author: E-mail: m.moradian@kashanu.ac.ir*
Fax: 03155912397; Tel:03155913055

Received: 09-24-2020

Abstract

Ultrasmall monodisperse NiO nanoparticles (7–9 nm) were synthesized through thermal decomposition of Ni-oleylamine complexes. Various measurement techniques involving Fourier-transform infrared spectroscopy (FT-IR), diffuse reflectance UV-Vis spectroscopy (DRS), X-ray diffractometer (XRD), energy dispersive X-ray analysis (EDX), scanning electron microscopy (SEM), dynamic light scattering technique (DLS), and vibrating sample magnetometer (VSM) were employed to characterize the synthesized catalyst. Propargylamine derivatives were synthesized with aldehydes, terminal alkynes and primary amines through a one-pot A^3-coupling reaction by using a 3 mol% amount of the NiO nanocrystals at 80 °C under solvent-free conditions with good to excellent yields. The structures of the products were confirmed by ^{1}H and ^{13}C NMR spectroscopy. The catalyst presents many advantages including being environmentally friendly, easy to recover, reusable, stable, and applicable to a wide variety of substrates, as well as having cost-effective preparation.

Keywords: Monodisperse, NiO nanocrystals, heterogeneous catalyst, A^3-cupling, propargylamine

1. Introduction

The expanding of environmentally benign, practical, economical and efficient synthetic procedures has been a major concern of many chemical researches.[1,2] Inasmuch as, one of the initial principles in green chemistry is to minimize the number of steps in chemical synthesis, being followed by some other rules, such as atom economy, elimination of hysteresis, eschewing the use of toxic or hazardous reagents and solvents.[3,4] Multicomponent reactions (MCRs) have been captivating academia and industry due to possessing a number of eminent conceptual and synthetic merits including sustainability, operational simplicity, cost-effectiveness, and high convergence which are all in accordance with green chemistry values.[5] Among all known MCRs, acetylene-Mannich reaction is an intriguing approach to synthesize propargylamines whose structural motifs have been found in different natural products and have been utilized as precursors of various biologically active components comprising β-lactams, isosteres, peptides, allylamines and oxazoles.[6,7] Classical method of propargylamines synthesis involves the nucleophilic addition of a metal acetylide to C=N electrophiles by exploiting highly active organometallic compounds combining organolitium, organozinc or Grignard reagents.[8–11] Hence, this method is less appealing owning to harsh reaction conditions, high moisture sensitivity of functional groups, and operational complexity.[12] Thus the efforts have been devoted to synthesize these nitrogen-containing compounds through three component reaction condition with various modified catalysts. Transition metals as heterogeneous catalysts have garnered a lot of attention since the first type of these catalysts was applied by Li *et al* in 2002 when they had performed lots of work with copper and ruthenium.[13] Afterwards, miscellaneous transition metal catalysts including different metals such as Cu, Ag, Au, Fe, Ni, Ir, In, and Zn were developed for synthesis of propargylamines; however the main disadvantage of these catalyst being their aggregation.[14–21]

Nanomaterials in the size range of 10–100 nm have attracted a lot of attention in the last few decades because

they show special physical and chemical properties compared to bulk materials. Accordingly, nanoparticles with a size of 3–10 nm also have unique properties and behavior different from nanoparticles with a larger size, which makes them to have a special function. The use of these ultrasmall (US) nanomaterials as catalysts in organic reactions is a new and effective approach in this field.[22,23] The nanoparticles properties capture them to become a connector between homogenous and heterogeneous catalytic systems.[24,25] Among all nanomaterials which have been investigated most of them involve copper, gold, silver, iron, and so on, while nickel nanoparticles studies are limited only to a few research papers, albeit this metal is cheaper than the others and requires mild reaction conditions for obtaining high yields.[26–31] All of the reported works using nickel as a catalyst have been limited to Ni(II) ion complexes such as $NiCl_2$,[32] MNPs@BimNiCl_2,[33] Ni-MOF,[34] and Ni^{II}-IL/SiO_2.[35] Also, nickel alongside copper as the metallic form has been used in such cases as Cu-Ni bimetallic[36] and Ni-Cu-Fe trimetallic nanoparticles.[37] In this study, propargylamines will be synthesized for the first time by utilizing ultrasmall monodisperse NiO nanocrystals as a heterogeneous catalyst. The monodisperse nanoparticles of NiO with particle size about 6 nm were synthesized using reported procedure by Hyeon and coworkers published in 2004.[38] Different aldehydes and amines will be applied to generalize the research. Herein, the questions posed with this research are that whether the catalyst is appropriate to synthesize different propoargylamine compounds or does the catalyst possesse high efficiency, stability, reusability and fulfils the other criteria which are important for a truly efficient catalyst.

2. Experimental Section

2. 1. Materials and Instrumentations

Nickel di(acetylacetonate) [Ni(acac)$_2$], oleylamine, triphenylphosphine (TPP), diphenyl ether (DE), and all other commercially available chemicals were purchased from Merck Chemical Company and were of high purity. The applied solvents were purified by standard procedures. Melting points were measured by a Yanagimoto Micro Melting Point apparatus in open capillary tubes. Fourier transform infrared (FT-IR) spectra were obtained (in KBr) by Nicolet FT-IR spectrophotometer. The ^{1}H and ^{13}C NMR spectra were recorded on Bruker DRX-400 spectrometer with $CDCl_3$ as the solvent at 25 °C and chemical shifts are given in ppm relative to Me_4Si. The mass spectra were recorded on a Shimadzu QP 1100-Ex mass spectrometer by direct inlet at 70 eV, and signals are given as *m/z* with relative intensity (%) in brackets. The XRD patterns were obtained by an X'PertPro (Philips) instrument with 1.54 Å wavelength of the X-ray beam and Cu anode material. Microscopic morphology of the nanoparticles was visualized by SEM (MIRA 3 TESCAN). Energy-dispersive X-ray spectroscopy (EDX) of the nanoparticles was imaged by a Sigma ZEISS, Oxford Instruments Field Emission. The purity determination of the substrates and reaction monitoring were accomplished by TLC on silicagel polygram SILG/UV 254 plates (from Merck Company).

2. 2. Synthesis of NiO Nanoparticles

The synthesis protocol for preparation of ultrasmall NiO nanoparticles is a modified method which was developed by Taeghwan and co-workers and employs the thermal decomposition of metal-surfactant complexes.[24,39] Initially, Ni(acac)$_2$ (0.32 g) and oleylamine (1.5 mL) were mixed under N_2 atmosphere at 100 °C. Afterwards, the freshly prepared Ni-oleylamine complex was added to a round-bottom flask containing a solution of TPP (1.8 g) in DE (2.5 mL) at 200 °C. After elapsing a short time the solution color changed from dark green to black due to the formation of colloidal Ni nanoparticles. The resultant solution was kept in 280 °C for 1 h and then the temperature was decreased to the ambient temperature. Thereafter, pure ethanol (200 mL) was added to the reaction chamber which caused Ni nanoparticles precipitation. In the following, the precipitate was centrifuged and washed with ethanol (3×50 mL) and then exposed to dry air for 24 h to form NiO nanoparticles and the resultant product was kept at 60 °C.

2. 3. Synthesis of Propargylamine Derivatives by NiO Nanoparticles Catalyst

All of the reactions were carried out at 80 °C in a 25 mL one-capped round-bottom flask equipped with a magnetic stirring bar in a paraffin bath. Generally, a mixture of the selected aldehyde (1.0 mmol), secondary amine (1.1 mmol) and alkyne (1.2 mmol) was added in the flask along with the catalytic amount of the NiO nanocrystals (3 mol %, 2.3 mg) as the catalyst. The reaction progress was examined by TLC, and after the completion of the reaction absolute ethanol (10 mL) was added and the resulting mixture was centrifuged. The catalyst was separated from the reaction mixture by centrifugation and washed with CH_2Cl_2 (3×5 mL) and methanol (3×5 mL) for recycling to be reused in the next run. The product was purified over silica gel by column chromatography (10% EtOAc in hexane) to give the desired propargylamines. All of the products are known compounds and have been reported already.

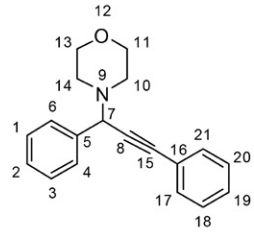

4-(1,3-Diphenylprop-2-yn-1-yl)morpholine (4a). Yield: 0.258 g (93%); light red oil; ^{1}H NMR ($CDCl_3$): δ 2.67–2.68 (m, 4H, 10-CH_2, 14-CH_2), 3.77–3.80 (m, 4H, 11-CH_2, 13-CH_2), 4.84 (s, 1H, 7-CH), 7.33–7.44 (m, 6H,

ArH), 7.56–7.58 (m, 2H, ArH), 7.68–7.70 (m, 2H, ArH); ^{13}C NMR ($CDCl_3$): δ 50.35 (C7), 57.21 (C10, C14), 68.54 (C11, C13), 84.08 (C8), 88.49 (C15), 115.17 (C16), 116.31 (C19), 121.96 (C21, C17), 123.67 (C2), 124.82 (C18, C20), 126.16 (C1, C3), 130.43 (C4), 131.87 (C6), 136.54 (C5); FT-IR (KBr disk): ν cm^{-1} 3059, 3014, 2984, 2957, 2950, 1598, 1489, 1449, 1318, 1280. MS *m/z* (%) 277 (M$^+$, 32), 246 (11), 191 (100), 189 (45), 165 (16), 86 (25), 77 (31), 56 (27).

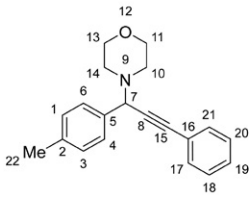

4-(3-Phenyl-1-(*para*-tolyl)prop-2-yn-1-yl)morpholine (4b). Yield: 0.268 g (92%); light orange oil; ^{1}H NMR ($CDCl_3$): δ 2.39 (s, 3H, Me), 2.65–2.67 (m, 4H, 10-CH_2, 14-CH_2), 3.75–3.76 (m, 4H, 11-CH_2, 13-CH_2), 4.78 (s, 1H, 7-CH), 7.20–7.22 (m, 2H, ArH), 7.34–7.36 (m, 3H, ArH), 7.53–7.55 (m, 4H, ArH); ^{13}C NMR ($CDCl_3$): δ 22.08 (C22), 49.14 (C7), 58.36 (C10, C14), 67.15 (C11, C13), 83.65 (C8), 87.91 (C15), 114.25 (C16), 117.55 (C19), 120.74 (C21, C17), 120.95 (C2), 122.33 (C18, C20), 123.85 (C1, C3), 126.80 (C4), 128.03 (C6), 132.17 (C5); FT-IR (KBr disk): ν cm^{-1} 3024, 2946, 2925, 2862, 2820, 2230, 1486, 1446, 1314, 1109. MS *m/z* (%) 291 (M$^+$, 37), 260 (22), 205 (100), 77 (42), 56 (28).

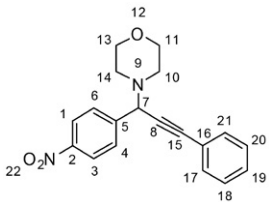

4-(1-(4-Nitrophenyl)-3-phenylprop-2-yn-1-yl)morpholine (4c). Yield: 0.306 g (95%); yellowish oil; ^{1}H NMR ($CDCl_3$): δ 2.63–2.66 (m, 4H, 10-CH_2, 14-CH_2), 3.75–3.76 (m, 4H, 11-CH_2, 13-CH_2), 4.89 (s, 1H, 7-CH), 7.38–7.39 (m, 3H, ArH), 7.53–7.55 (m, 2H, ArH), 7.87 (d, *J* = 8.1 Hz, 2H, ArH), 8.24 (d, *J* = 8.1 Hz, 2H, ArH); ^{13}C NMR ($CDCl_3$): δ 49.90 (C7), 61.45 (C10, C14), 67.04 (C11, C13), 83.16 (C8), 89.78 (C15), 122.31 (C16), 123.48 (C19), 128.45 (C21, C17), 128.72 (C2), 129.33 (C18, C20), 131.85 (C4, C6), 135.48 (C3, C1), 145.45 (C5), 149.23 (C2); FT-IR (KBr disk): ν cm^{-1} 3067, 2958, 2854, 2216, 1690, 1522, 1450, 1347, 1275, 1113, 1006. MS *m/z* (%) 322 (M$^+$, 10), 236 (41), 200 (57), 190 (37), 86 (18), 77 (30), 56 (100).

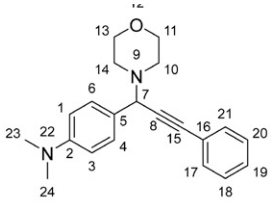

***N,N*-Dimethyl-4-(1-morpholino-3-phenylprop-2-yn-1-yl) aniline (4d).** Yield: 0.282 g (88%); yellowish oil; ^{1}H NMR ($CDCl_3$): δ 2.62–2.66 (m, 4H, 10-CH_2, 14-CH_2), 2.97 (s, 6H, NMe_2), 3.73–3.74 (m, 4H, 11-CH_2, 13-CH_2), 4.70 (s, 1H, 7-CH), 6.73 (d, *J* = 8.0 Hz, 2H, ArH), 7.32–7.33 (m, 3H, ArH), 7.45–7.51 (m, 4H, ArH); ^{13}C NMR ($CDCl_3$): δ 44.11 (C23), 49.25 (C24), 61.70 (C10, C14), 67.03 (C11, C13), 84.15 (C8), 87.54 (C15), 113.85 (C1, C3), 118.80 (C16), 120.41 (C19), 123.74 (C21, C17), 130.40 (C18, C20), 131.21 (C4), 134.38 (C6), 148.01 (C2), 149.21 (C5); FT-IR (KBr disk): ν cm^{-1} 3084, 2955, 2892, 2854, 1965, 1611, 1521, 1150. MS *m/z* (%) 320 (M$^+$, 40), 215 (100), 276 (62), 234 (12), 219 (27), 101 (17), 86 (20), 56 (65).

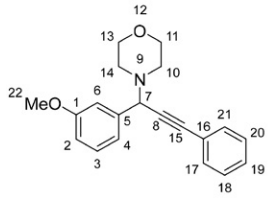

4-(1-(3-Methoxyphenyl)-3-phenylprop-2-yn-1-yl)morpholine (4e). Yield: 0.280 g (91%); yellowish oil; ^{1}H NMR ($CDCl_3$): δ 2.66–2.67 (m, 4H, 10-CH_2, 14-CH_2), 3.77–3.79 (m, 4H, 11-CH_2, 13-CH_2), 3.86 (s, 3H, OCH_3), 4.79 (s, 1H, 7-CH), 6.86 (s, 1H, 6-CH), 7.25–7.36 (m, 6H, ArH), 7.53–7.54 (m, 2H, ArH); ^{13}C NMR ($CDCl_3$): δ 49.99 (C7), 55.24 (C22), 62.01 (C10, C14), 67.20 (C11, C13), 85.15 (C8), 88.54 (C15), 113.10 (C2), 114.39 (C6), 120.99 (C4), 123.03 (C16), 128.36 (C21), 128.42 (C17), 129.28 (C18, C20), 131.88 (C19), 132.17 (C3), 139.57 (C5), 159.71 (C1); FT-IR (KBr disk): ν cm^{-1} 3057, 2995, 2851, 1965, 1599, 1486, 1449, 1317, 1150, 1048. MS *m/z* (%) 307 (M$^+$, 14), 221 (38), 178 (20), 135 (32), 87 (100), 77 (55), 43 (85).

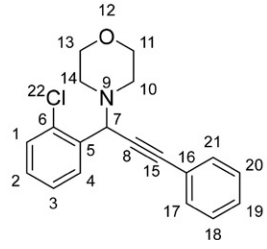

4-(1-(2-Chlorophenyl)-3-phenylprop-2-yn-1-yl)morpholine (4f). Yield: 0.290 g (93%); yellow oil; ^{1}H NMR ($CDCl_3$): δ 2.67–2.70 (m, 4H, 10-CH_2, 14-CH_2), 3.67–3.77 (m, 4H, 11-CH_2, 13-CH_2), 5.14 (s, 1H, 7-CH), 7.25–7.29 (m, 2H, 2-CH, 4-CH), 7.33–7.35 (m, 3H, 18-CH, 19-CH, 20-CH), 7.41–7.43 (m, 1H, 3-CH), 7.50–7.52 (m, 2H, 17-CH, 21-CH), 7.75–7.77 (m, 1H, 1-CH); ^{13}C NMR ($CDCl_3$): δ 49.87 (C7), 58.96 (C10, C14), 67.14 (C11, C13), 84.70 (C8), 88.40 (C15), 122.82 (C16), 125.58 (C3), 126.39 (C18, C20), 128.38 (C21), 128.41 (C17), 129.18 (C19), 130.58 (C2), 130.93 (C1), 131.85 (C4), 134.69 (C6), 135.56 (C5); FT-IR (KBr disk): ν cm^{-1} 3047, 2997, 2897, 2750, 1562, 1472, 1452, 1324, 1274, 1117, 1055. MS *m/z* (%) 313 (M+2$^+$, 8), 311 (M$^+$, 23), 280 (14), 225 (100), 189 (57), 86 (84), 56 (61).

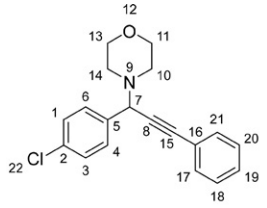

4-(1-(4-Chlorophenyl)-3-phenylprop-2-yn-1-yl)morpholine (4g). Yield: 0.293 g (94%); yellow oil; ^{1}H NMR ($CDCl_3$): δ 2.61–2.62 (m, 4H, 10-CH_2, 14-CH_2), 3.73–3.75 (m, 4H, 11-CH_2, 13-CH_2), 4.77 (s, 1H, 7-CH), 7.36–7.37 (m, 5H, ArH), 7.51–7.52 (m, 2H, ArH), 7.58–7.60 (m, 2H, ArH); ^{13}C NMR ($CDCl_3$): δ 49.85 (C7), 61.40 (C10, C14), 67.15 (C11, C13), 84.43 (C8), 88.98 (C15), 122.77 (C16), 128.43 (C1, C3), 128.48

(C18, C20), 129.70 (C19), 129.94 (C17, C21), 131.88 (C4, C6), 133.61 (C2), 136.53 (C5); FT-IR (KBr disk): ν cm^{-1} 3070, 3029, 2957, 2857, 1494, 1454, 1428, 1113, 1075, 1034. MS *m/z* (%) 313 ($M+2^+$, 11), 311 (M^+, 35), 280 (8), 225 (100), 189 (19), 135 (40), 86 (22), 77 (24), 56 (47).

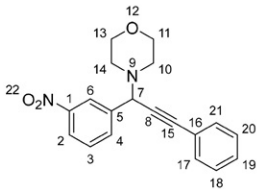

4-(1-(3-Nitrophenyl)-3-phenylprop-2-yn-1-yl)morpholine (4h). Yield: 0.293 g (91%); light yellow oil; ^{1}H NMR ($CDCl_3$): δ 2.63–2.69 (m, 4H, 10-CH_2, 14-CH_2), 3.76–3.78 (m, 4H, 11-CH_2, 13-CH_2), 4.90 (s, 1H, 7-CH), 7.34–7.38 (m, 3H, ArH), 7.54–7.62 (m, 3H, ArH), 8.02 (d, *J* = 7.6 Hz, 1H, 2-CH), 8.18 (d, *J* = 7.7 Hz, 1H, 4-CH), 8.56 (s, 1H, 6-CH); ^{13}C NMR ($CDCl_3$): δ 49.78 (C7), 61.24 (C10, C14), 66.95 (C11, C13), 83.17 (C8), 89.76 (C15), 122.36 (C16), 122.85 (C21, C17), 123.41 (C18, C20), 128.39 (C19), 128.71 (C6), 129.15 (C2), 131.83 (C3), 134.48 (C4), 140.36 (C5), 148.39 (C1); FT-IR (KBr disk): ν cm^{-1} 3085, 3028, 3002, 2986, 2882, 1506, 1473, 1419, 1263, 1208, 1168, 1121, 1045, 1014. MS *m/z* (%) 322 (M^+, 16), 236 (30), 200 (41), 190 (24), 86 (100), 56 (67).

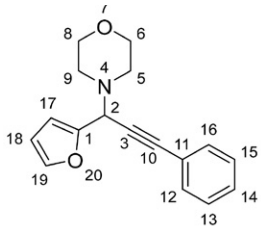

4-(1-(Furan-2-yl)-3-phenylprop-2-yn-1-yl)morpholine (4i). Yield: 0.235 g (88%); yellowish white oil; ^{1}H NMR ($CDCl_3$): δ 2.63–2.72 (m, 4H, 5-CH_2, 9-CH_2), 3.74–3.83 (m, 4H, 6-CH_2, 8-CH_2), 4.89 (s, 1H, 2-CH), 6.37 (t, *J* = 3 Hz, 1H, 18-CH), 6.52 (d, *J* = 2.8 Hz, 1H, 17-CH), 7.31–7.35 (m, 3H, ArH), 7.45–7.52 (m, 3H, ArH); ^{13}C NMR ($CDCl_3$): δ 49.61 (C2), 56.12 (C5, C9), 66.95 (C6, C8), 82.85 (C3), 87.02 (C10), 109.76 (C17), 110.13 (C18), 122.57 (C11), 128.35 (C13, C15), 128.50 (C12, C16), 131.87 (C14), 142.87 (C19), 150.76 (C1); FT-IR (KBr disk): ν cm^{-1} 3063, 3028, 2932, 1604, 1495, 1453, 1261, 1152, 1028. MS *m/z* (%) 267 (M^+, 11), 239 (18), 221 (17), 181 (100), 152 (34), 115 (9), 86 (25), 77 (47), 56 (28).

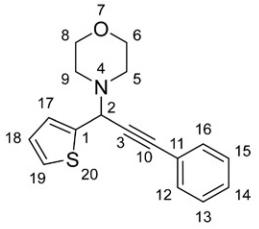

4-(3-Phenyl-1-(thiophen-2-yl)prop-2-yn-1-yl)morpholine (4j). Yield: 0.244 g (86%); white oil; ^{1}H NMR ($CDCl_3$): δ 2.66–2.74 (m, 4H, 5-CH_2, 9-CH_2), 3.73–3.82 (m, 4H, 6-CH_2, 8-CH_2), 5.01 (s, 1H, 2-CH), 6.97–6.99 (m, 1H, 18-CH), 7.25–7.27 (m, 1H, 17-CH), 7.30–7.31 (m, 1H, 19-CH), 7.34–7.36 (m, 3H, ArH), 7.51–7.54 (m, 2H, ArH); ^{13}C NMR ($CDCl_3$): δ 49.69 (C2), 57.83 (C5, C9), 67.15 (C6, C8), 84.29 (C3), 87.63 (C10), 122.69 (C11), 125.57 (C18), 125.87 (C17), 126.36 (C16), 126.44 (C12), 128.39 (C13), 128.48 (C15), 128.84 (C14), 131.89 (C19), 142.80 (C1); FT-IR (KBr disk): ν cm^{-1} 3062, 3028, 2955, 2934, 2248, 1607, 1490, 1454, 1125, 1109, 1065, 1016. MS *m/z* (%) 283 (M^+, 9), 197 (100), 86 (62), 83 (20), 77 (35), 56 (27).

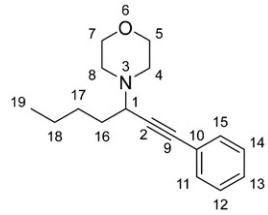

4-(1-Phenylhept-1-yn-3-yl) morpholine (4k). Yield: 0.221 g (86%); white oil; ^{1}H NMR ($CDCl_3$): δ 1.02 (t, *J* = 7.0 Hz, 3H, 19-CH_3), 1.38–1.39 (m, 4H, 17-CH_2, 18-CH_2), 1.60–1.62 (m, 2H, 16-CH_2), 2.95–2.96 (m, 4H, 4-CH_2, 8-CH_2), 3.63–3.68 (m, 4H, 5-CH_2, 7-CH_2), 3.81–3.82 (m, 1H, 1-CH), 7.45–7.48 (m, 3H, ArH), 7.69–7.72 (m, 2H, ArH); ^{13}C NMR ($CDCl_3$): δ 14.21 (C19), 21.70 (C18), 25.24 (C17), 34.47 (C16), 54.14 (C1), 57.30 (C4, C8), 67.79 (C5, C7), 87.45 (C2), 88.21 (C9), 123.64 (C10), 126.87 (C15, C11), 128.45 (C13), 129.70 (C12, C14); FT-IR (KBr disk): ν cm^{-1} 3035, 3020, 2964, 2874, 2234, 1568, 1479, 1439, 1328, 1263, 1184, 1120, 1064. MS *m/z* (%) 257 (M^+, 19), 242 (8), 200 (100), 184 (22), 128 (35), 115 (18), 77 (42), 56 (26).

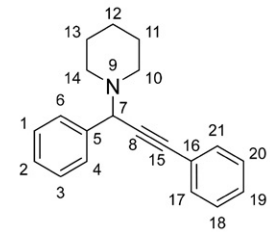

1-(1,3-Diphenylprop-2-yn-1-yl)piperidine (4l). Yield: 0.255 g (93%); red oil; ^{1}H NMR ($CDCl_3$): δ 1.45–1.58 (m, 6H, 11-CH_2, 12-CH_2, 13-CH_2), 2.38–2.41 (m, 4H, 10-CH_2, 14-CH_2), 4.94 (s, 1H, 7-CH), 7.33–7.94 (m, 10H, ArH); ^{13}C NMR ($CDCl_3$): δ 24.15 (C12), 26.07 (C11, C13), 52.47 (C7), 56.11 (C10, C14), 82.18 (C15), 87.19 (C8), 121.10 (C16), 126.01 (C19), 126.86 (C21, C17), 127.24 (C2), 127.60 (C18, C20), 128.74 (C1, C3), 129.03 (C4), 129.17 (C6), 138.41 (C5); FT-IR (KBr disk): ν cm^{-1} 3084, 3020, 2994, 2967, 1452, 1408, 1349, 1319, 1300. MS *m/z* (%) 275 (M^+, 15), 232 (7), 192 (14), 191 (100), 189 (50), 165 (18), 115 (24), 84 (37), 77 (30).

3. Results and Discussion

3.1. Characterization of the NiO Nanoparticles Catalyst

The properties, structure, size and size distribution of the synthesized NiO nanoparticles were measured by various techniques including FT-IR spectroscopy, TEM, SEM, DLS, DRS, XRD, EDX and VSM analysis. As shown in Figure 1 the FT-IR spectra of the catalyst delineates an absorption band at 443 cm^{-1} which is related to the vibration band of Ni–O stretching bond. As can be seen, no other peaks are observable in the spectra which confirms that the catalyst is without any impurity or any organic residues which would likely arise from organic components that consumed during the preparation process of nanoparticle.

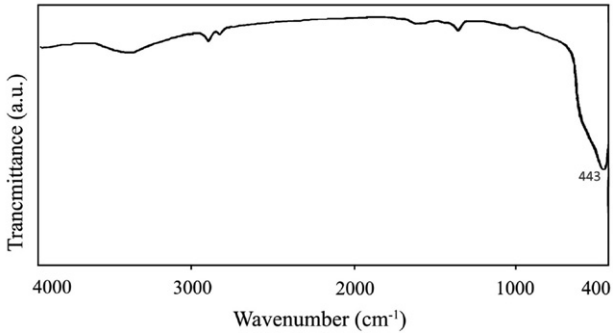

Figure 1. The FT-IR spectrum of the NiO nanoparticles

To observe the purity phase and local geometry of the crystalline scaffold of the synthesized NiO nanoparticles, X-ray diffraction analysis was carried out. As can be observed, the whole Ni nanoparticles are oxidized to the NiO nanoparticles without showing any impurities and all the peaks are in good agreement with the cubic structure of the catalyst according to the library patterns (JCPDS No. 71-1179). The estimated size of nanoparticles by Debye–Scherrer equation was measured to be around 8.4 nm (Figure 2).

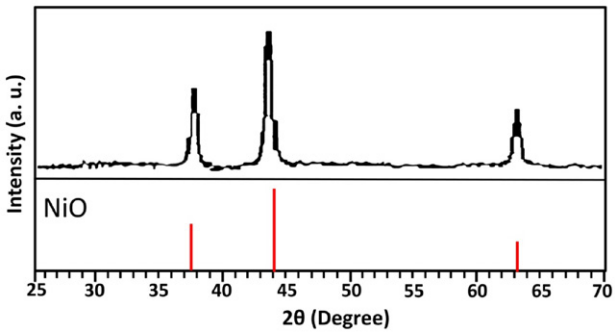

Figure 2. The XRD pattern of the NiO nanoparticles

To determine the size, size distribution, and morphology employing various measurement techniques is required due to basic differences in each represented method [39]. The SEM analysis of the synthesized catalyst exhibits that the size of the NiO nanocrystal is around 7–9 nm which confirms the XRD results (Figure 3a). The SEM image of the NiO ultrasmall nanoparticles was also determined. As can be seen, the NiO nanoparticles are spherical and possess high uniformity (Figure 3).

In accordance with the SEM image of the NiO nanoparticles, the particle size distribution histogram was provided by DLS technique and is shown in Figure 4, the dispersion nanoparticles size are not scattered and the mean value and standard deviation could be estimated to be 7.9 ± 1 nm according to the provided size distribution histogram.

The single point BET analysis was used to determine the specific surface area of the NiO nanoparticles. The surface area of nanoparticles was found to be 33.7 m^2/g and a mean particle size of 8.7 nm was calculated from the $d_{BET} = 6000/\tilde{n}S$ equation (S is specific surface area in m^2/g, d is the diameter in nanometer, and $\tilde{n}$ is the theoretical density in g/cm^3). This value is close to that obtained by SEM and XRD image and indicates that the powder consists of mono-dispersed solid crystals; also agglomeration and heaping of nanoparticles does not happen.

The EDX micrograph was also provided to prove the existence of nickel elements in the prepared nanoparticles (Figure 5). According to the graph, no other peaks in the spectrum from elements except Ni were observed thus confirming that the NiO nanoparticles are pure.

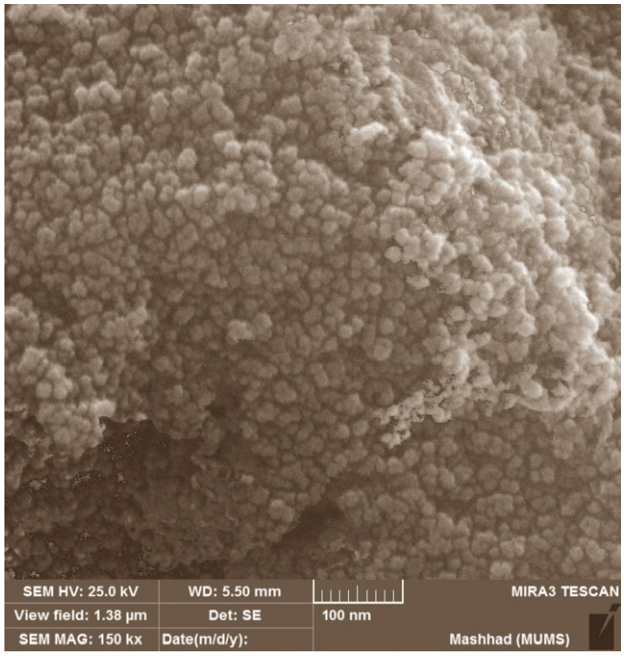

Figure 3. The SEM image of the NiO nanocrystals

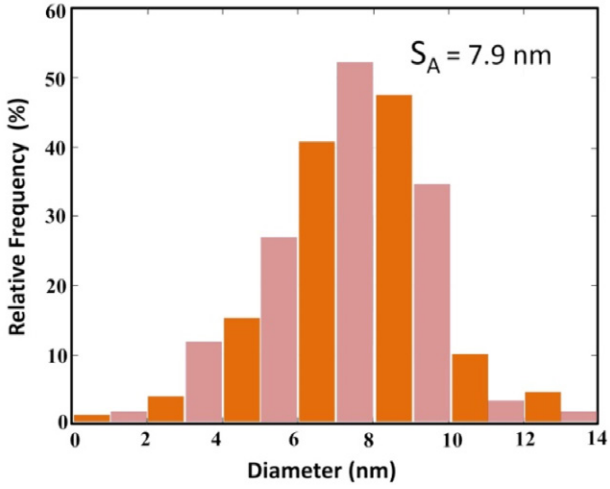

Figure 4. Histogram showing the particle size and size distribution of US-NiO nanocrystals

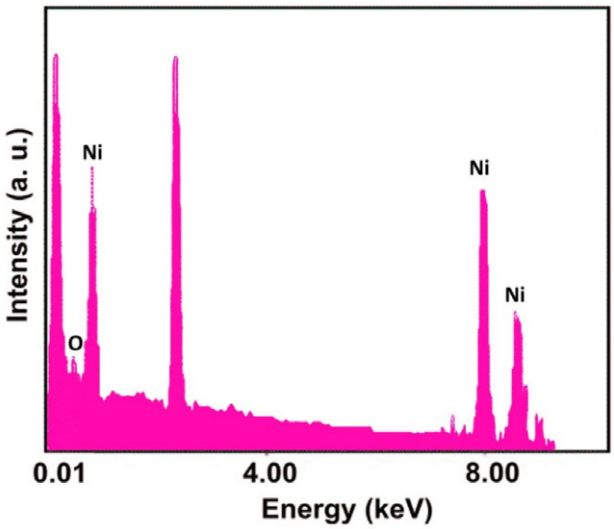

Figure 5. The energy dispersive X-ray analyzer of the NiO nanoparticles

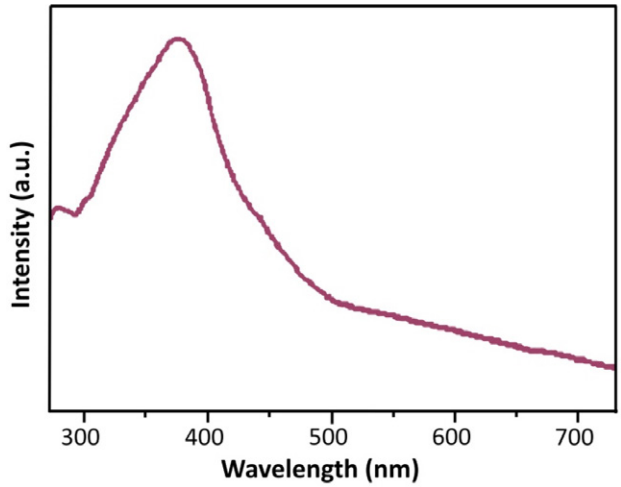

Figure 6. UV-Vis DRS of the US-NiO nanoparticles

The UV-Vis diffuse reflectance spectroscopy (DRS) measurement which is dispersed in ethanol was performed to achieve the optical property and consequently crystallinity of the nanoparticles (Figure 6). A strong absorption band has been observed in UV gamut (360 nm) which is attributed to the nanoparticles absorption in ratio of their crack bonds' absorption.

3.2. Reaction Optimization

The prepared ultrasmall nanocrystals of NiO were used as a catalyst in the A^3-coupling reaction of aromatic and aliphatic aldehydes, secondary amines, and phenylacetylene as the terminal alkyne (Scheme 1).

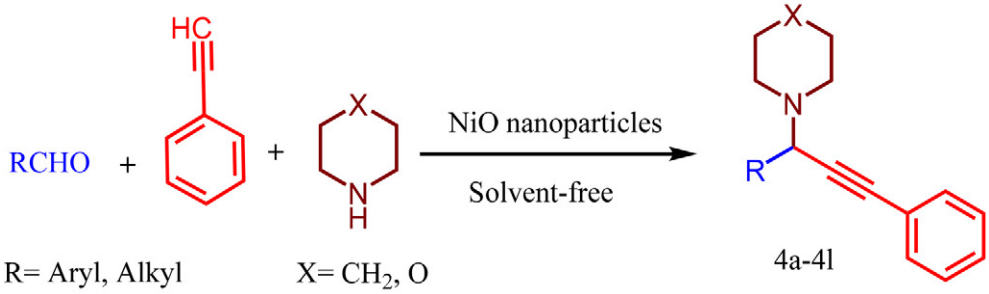

Scheme 1. General procedure of the A^3-coupling reaction

In continuation of our research, our first efforts were devoted to optimize reaction conditions. Therefore, the optimization was examined for solvent, temperature and catalyst. To put the purpose in action, the reaction among benzaldehyde (1 mmol), morpholine (1.1 mmol) and phenylacetylene (1.2 mmol) was selected as the model reaction carried out in the presence of the synthesized NiO nanoparticles as a reusable and heterogeneous catalyst. As depicted in Table 1, for solvent optimization, various protic and aprotic solvents including toluene, DMF, DMSO, THF, CH_2Cl_2, MeCN, H_2O, and MeOH under different temperatures, also reflux condition were investigated. It is obvious that the application of aprotic solvents with various conditions gave favorable results. Hence, utilizing protic solvents was not encouraged. According to the outputs, when dicholoromethane was employed (entry 10) propitious yield was obtained while using MeOH as a protic solvent represented good yield (entry 8). The highest yield was achieved under solvent-free conditions at 80 °C (bath of paraffin) with the shortest reaction time (entry 12).

According to Table 1, entries 11–14, temperature optimization for the solvent-free conditions was in demand. The best result for solvent-free temperature optimization was obtained at 80 °C (entries 11–14) which is evidence that further increase or decreases in the temperature did not lead to any distinguishable alteration.

The amount of catalyst is a crucial player factor in the yield of the reaction. A glance at Table 2 reveals that in the absence of the catalyst (entry 1) merely a negligible amount of product was obtained, this result demonstrating that using the catalyst is an obligatory factor for the progression of the reaction. Additionally, the best result was achieved

Table 1. The effects of various solvents and temperature on model reaction using NiO nanoparticles catalyst[a]

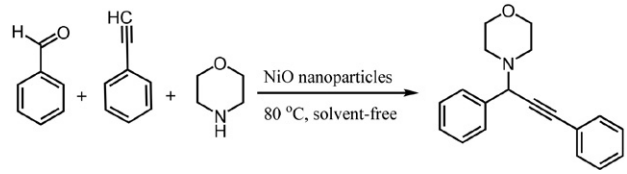

Entry	Solvent	Temperature [°C]	Time [h]	Yield[b] [%]
1	MeCN	Reflux	10	54
2	DMF	100	10	52
3	DMSO	100	10	65
4	Toluene	Reflux	10	69
5	H_2O	Reflux	10	18
6	H_2O	90	10	12
7	MeOH	Reflux	10	28
8	MeOH	40	10	20
9	THF	Reflux	10	38
10	CH_2Cl_2	38	6	44
11	Solvent-free	r.t.	10	54
12	Solvent-free	80	3	96
13	Solvent-free	60	5	80
14	Solvent-free	100	3	95

[a] Reaction conditions: benzaldehyde (1.0 mmol), phenylacetylene (1.2 mmol), morpholine (1.1 mmol), NiO nanoparticles (0.03 mmol, 2.3 mg). [b] Based on isolated yields. [c] The bold entry 12 represents the best conditions.

Table 2. Optimization of the catalyst amount of NiO nanoparticles on model reaction[a]

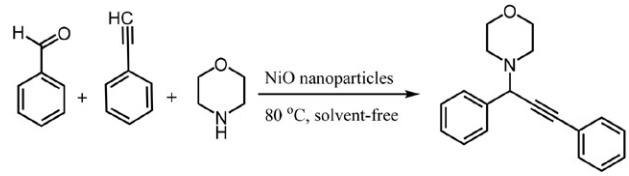

Entry	mass [mg] NiO	Time [h]	Yield[b] [%]
1	0 (0 mol %)	24	trace
2	0.7 (1 mol %)	8	48
3[c]	**2.3 (3 mol %)**	**3**	**96**
4	3.7 (5 mol %)	3	96
5	7.5 (10 mol %)	3	96

[a] Reaction condition: benzaldehyde (1.0 mmol), phenylacetylene (1.2 mmol), morpholine (1.1 mmol). [b] Based on isolated yields. [c] The bold entry 3 represents the best conditions.

when 2.3 mg of the catalyst were loaded into the reaction vessel (entry 3). It was observed that further increase of the catalyst amount did not affect the reaction yield.

After optimization of the reaction conditions, the next step of our study was based on determining the scope and limitation of the current protocol with the ultrasmall NiO nanoparticles as heterogeneous catalyst. Therefore, a number of different propargylamines were synthesized with applying various initial moieties including disparate aldehydes possessing electron withdrawing and electron donating functional groups, along with morpholine and pyridine as the secondary amines, also phenylacetylene as a fixed part of the reaction. The information regarding synthesized propargylamines is summarized in Table 3. Apparently, the reactions were accomplished successfully with good to high yields and in a short reaction time for all the prepared products. Furthermore, it is highly important to point out that the desired products involving benzaldehyde derivatives with an electron-withdrawing group were obtained in excellent yields (**4c**, **4g** and **4h**), whereas ben-

Table 3. NiO nanoparticles catalyzed three-component synthesis of propargylamines[a]

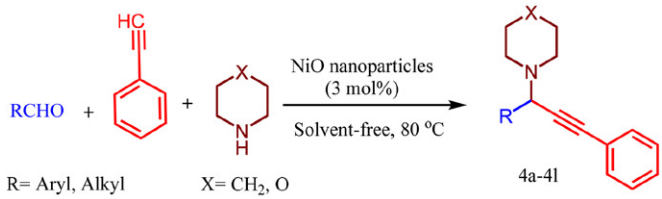

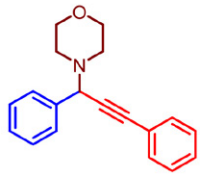

4a: 3 h, 96%
TON: 36
TOF (h^{-1}): 341
Ref: 40

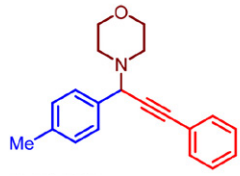

4b: 3 h, 96%
TON: 35
TOF (h^{-1}): 387
Ref: 41

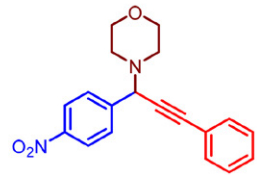

4c: 3 h, 96%
TON: 36
TOF (h^{-1}): 405
Ref: 41

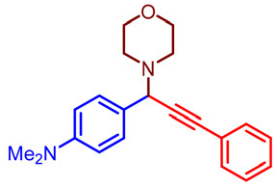

4d: 3 h, 96%
TON: 34
TOF (h^{-1}): 392
Ref: 42

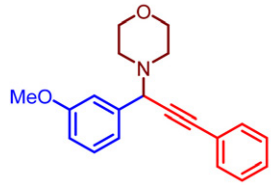

4e: 3 h, 96%
TON: 35
TOF (h^{-1}): 386
Ref: 43

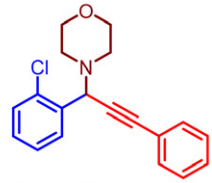

4f: 3 h, 96%
TON: 36
TOF (h^{-1}): 350
Ref: 43

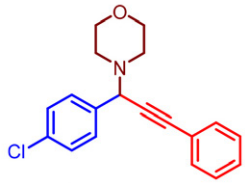

4g: 3 h, 96%
TON: 37
TOF (h^{-1}): 414
Ref: 44

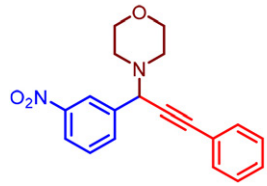

4h: 3 h, 96%
TON: 36
TOF (h^{-1}): 391
Ref: 44

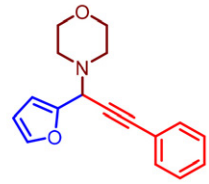

4i: 3 h, 96%
TON: 33
TOF (h^{-1}): 405
Ref: 45

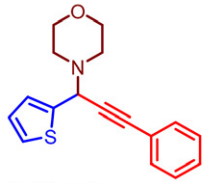

4j: 3 h, 96%
TON: 33
TOF (h^{-1}): 363
Ref: 45

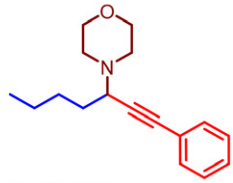

4k: 3 h, 96%
TON: 35
TOF (h^{-1}): 341
Ref: 46

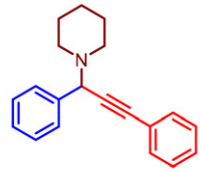

4l: 3 h, 96%
TON: 37
TOF (h^{-1}): 382
Ref: 47

[a] Reaction conditions: aldehyde (1.0 mmol), phenylacetylene (1.20 mmol), secondary amine (1.1 mmol), NiO nanoparticles as catalyst (2.3 mg) under solvent-free conditions at 80 °C. [b] Based on isolated yields.

zaldehyde having an electron-donating group gave the products in lower yields (**4b** and **4d**).

The proposed reaction mechanism for the catalytic reaction in the presence of US-NiO nanoparticles is shown in Scheme 2. The first step is the C–H activation of the alkyne moiety *via* adsorption on the surface of the catalyst and producing alkynyl–[NiO] complex. Then, the aromatic or aliphatic aldehydes are activated by the catalyst

through van der Waals interactions between ion pair of the oxygen atom from the carbonyl and the Ni atom of the catalyst. Nucleophilic attack of the alkynyl–[NiO] complex upon iminium ion formed from the reaction of aldehyde and amine produces the desired propargylamine and releases the NiO catalyst for the next catalytic cycle.

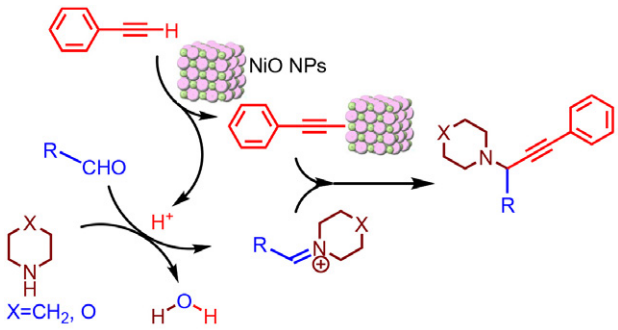

Scheme 2. Proposed reaction mechanism for the catalytic reaction

We also investigated the catalyst leaching study in this method. After the reaction was run, in half of the time of the reaction completion, the NiO catalyst was separated by centrifuge from the reaction media and the solution phase was subjected without any fresh catalyst added under the same reaction conditions. The reaction was monitored after 8 h and thus it was shown that there was no further conversion of substrates to desired propargylamine. This means that any solid nanoparticles or active metal leached from solid nanocatalyst remain in the filtrate.

In green chemistry, an essential matter to express environmentally friendly methods is recovery and reusability of the catalyst. Hence, after reaction completion, the NiO nanocatalyst was separated by centrifuge method. The recovered catalyst was thoroughly washed with CH_2Cl_2 (3×5 mL) and dried at 80 °C for 10 h, and then it was used for consecutive reaction without adding any fresh catalyst. As can be seen in Figure 7, the results show that NiO nanoparticles can be used at least for 12 sequential runs without important changes in their catalytic activity.

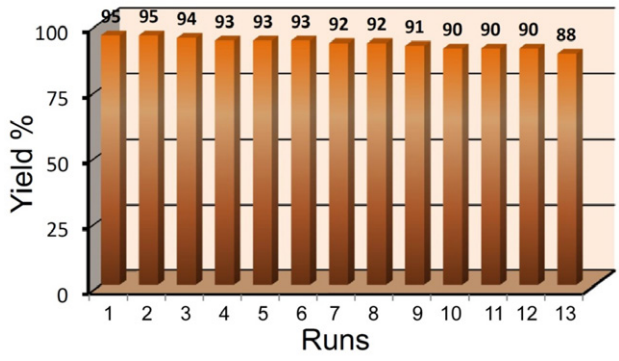

Figure 7. Reusability of ultrasmall NiO nanoparticles in the synthesis of compound **4a**.

4. Conclusion

To recapitulate, in this paper NiO nanoparticles were used for the first time as a green and efficient heterogeneous catalyst for successful preparation of propargylamines through A^3-coupling reaction under solvent-free conditions at 80 °C. Ease of preparation, reusability, facile work-up, high activity, stability, applicability to a wide variety of substrates, and being cheap are the advantages of this catalyst. The catalyst can be applied for seven successful runs of propargylamines preparation with high yields. Thereafter the aforementioned questions which were addressed by this papers were answered properly.

Acknowledgments

The authors are grateful to University of Kashan for supporting this work.

Conflict of Interest

The authors declare that there is no conflict of interests regarding the publication of this manuscript.

5. References

1. C. Wei, Z. Li, C.-J. Li, *Org. Lett.* **2003**, *5*, 4473–4475. **DOI:**10.1021/ol035781y
2. W.-W. Chen, R. V. Nguyen, C.-J. Li, *Tetrahedron Lett.* **2009**, *50*, 2895–2898. **DOI:**10.1016/j.tetlet.2009.03.182
3. M. K. Patil, M. Keller, B.M. Reddy, P. Pale, J. Sommer, *Eur. J. Org. Chem.* **2008**, 4440–4445. **DOI:**10.1002/ejoc.200800359
4. M. J. Aliaga, D. J. Ramon, M. Yus, *Org. Biomol. Chem.* **2010**, *8*, 43–46. **DOI:**10.1039/B917923B
5. J.-N. Mo, J. Su, J. Zhao, *Molecules* **2019**, *24*, 1216–1225. **DOI:**10.3390/molecules24071216
6. Z. Xu, H. Wu, H. Li, Z. Du, Y. Fu, *ChemistrySelect* **2018**, *3*, 13629–13631. **DOI:**10.1002/slct.201803313
7. E. Ramu, R. Varala, N. Sreelatha, S.R. Adapa, *Tetrahedron Lett.* **2007**, *48*, 7184–7190. **DOI:**10.1016/j.tetlet.2007.07.196
8. H.-B. Chen, Y. Zhaoa, Y. Liao, *RSC Adv.* **2015**, *5*, 37737–37741. **DOI:**10.1039/C5RA04729C
9. J. Clayden, (Ed.) Tetrahedron Organic Chemistry Series, Organolithiums: Selectivity for Synthesis, *Elsevier, Ltd.*, **2002**. 383 p.
10. B. J. Wakefield, Organomagnesium Methods in Organic Synthesis, *Academic Press*, London, **1988**, 249 p.
11. E. Erdik, Organozinc reagents in organic chemistry, *CRC Press*, London, **1996**, 432 p.
12. V. A. Peshkov, O. P. Pereshivko, E. V. Van der Eycken, *Chem. Soc. Rev.* **2012**, *41*, 3790–3807. **DOI:**10.1039/c2cs15356d

13. C. J. Li, C. M. Wei, *Chem. Commun.* **2002**, 268–269.
14. J. R. Cammarata, R. Rivera, F. Fuentes, Y. Otero, E. O-Mavárez, A. Arce, J. M. Garcia, *Tetrahedron Lett.* **2017**, *58*, 4078–4081. **DOI:**10.1016/j.tetlet.2017.09.031
15. P. Torabi, M. Moradian, *J. Nanostruct.* **2019**, *3*, 478–488.
16. J.-L. Huang, D. G. Gray, C.-J. Li, *Beilstein J. Org. Chem.* **2013**, *9*, 1388–1396. **DOI:**10.3762/bjoc.9.155
17. H. Alinezhad, K. Pakzad, M. Nasrollahzadeh, *Appl. Organomet. Chem*. **2020**, *34*, e5473. **DOI:**10.1002/aoc.5473
18. S. Sakaguchi, T. Mizuta, M. Furuwan, T. Kubo, *J. Org. Chem.* **2004**, *35*, 1638–1639. **DOI:**10.1039/b404430d
19. Y. Zhang, P. Li, M. Wang, L. Wang, *J. Org. Chem.* **2009**, *74*, 4364–4367. **DOI:**10.1021/jo900507v
20. M. L. Kantam, V. Balasubrahmanyam, K. B. S. Kumar, G. T. Venkanna, *Tetrahedron Lett.* **2007**, *48*, 7332–7334. **DOI:**10.1016/j.tetlet.2007.08.020
21. S. Chandra, A. Kumar, P. K. Tomar, *J. Saudi Chem. Soc.* **2014**, *18*, 149–153. **DOI:**10.1016/j.jscs.2011.06.009
22. S. Navalón H. García, *Nanomaterials* **2016**, *6*, 123–125. **DOI:**10.3390/nano6070123
23. B. H. Kim, M. J. Hackett, J. Park, T. Hyeon, *Chem. Mater.* **2014**, *26*, 59–71. **DOI:**10.1021/cm402225z
24. N. Narayan, A. Meiyazhagan, R. Vajtai, *Materials* **2019**, *12*, 3602–3609. **DOI:**10.3390/ma12213602
25. M. Kidwai, V. Bansal, N. K. Mishra, A. Kumar, S. Mozumdar, *Synlett* **2007**, *10*, 1581–1584. **DOI:**10.1055/s-2007-980365
26. M. Mirabedini, E. Motamedi, M. Z. Kassaee, *Chin. Chem. Lett.* **2015**, *26*, 1085–1090. **DOI:**10.1016/j.cclet.2015.05.021
27. H. Veisi, M. Farokhi, M. Hamelian, S. Hemmati, *RSC Adv.* **2018**, *8*, 38186–38195. **DOI:**10.1039/C8RA06819D
28. Y. Uozumi, K. Kim, *Synfacts* **2019**, *15*, 0408–0408. **DOI:**10.1055/s-0037-1612395
29. X. Y. Dong, Z. W. Gao, K. F. Yang, W. Q. Zhang, L. W. Xu, *Catal. Sci. Technol.* **2013**, *1*, 1–3.
30. W. Yan, R. Wang, Z. Xu, J. Xu, L, Lin, Z. Shen, Y. Zhou, *J. Mol. Catal. Chem.* **2006**, *255*, 81–85. **DOI:**10.1016/j.molcata.2006.03.055
31. B. Sreedhar, A. S. Kumar, P. S. Reddy, *Tetrahedron Lett.* **2010**, *51*, 1891–1895. **DOI:**10.1016/j.tetlet.2010.02.016
32. S. Samai, G. C. Nandi, M. S. Singh, *Tetrahedron Lett.* **2010**, *51*, 5555–5558. **DOI:**10.1016/j.tetlet.2010.08.043
33. M. Tajbakhsh, M. Farhang, S. M. Baghbanian, R. Hosseinzadeh, M. Tajbakhsh, *New J. Chem.*, **2015**, *39*, 1827–1839. **DOI:**10.1039/C4NJ01866D
34. G. H. Dang, D. T. Nguyen, D. T. Le, T. Truong, N. T.S. Phan, *J. Mol. Catal. A: Chem*., **2014**, *395*, 300–306. **DOI:**10.1016/j.molcata.2014.08.034
35. J. Safaei-Ghomi, S. H. Nazemzadeh, *Catal. Lett.* **2017**, *147*, 1696–1703. **DOI:**10.1007/s10562-017-2079-4
36. S. V. Katkar, R. V. Jayaram, *RSC Adv.* **2014**, *4*, 47958. **DOI:**10.1039/C4RA06275B
37. M. Daryanavard, A. Ataei, P. G. Sheykhabadi, E. Rafiee, M. Joshaghani, *ChemistrySelect*, **2020**, *5*, 18–27. **DOI:**10.1002/slct.201902617
38. J. Park, K. An, Y. Hwang, J. G. Park, H. J. Noh, J. Y. Kim, J. H. Park, N. M. Hwang, T. Hyeon, *Nature Mater*. **2004**, *3*, 891–895. **DOI:**10.1038/nmat1251
39. J. Park, E. Kang, S. U. Son, H. M. Park, J. Kim, K. W. Kim, H. J. Noh, J. H. Park, C. J. Bae, J. G. Park, T. Hyeon, *Adv. Mater.* **2005**, *17*, 429–434. **DOI:**10.1002/adma.200400611
40. H. Eshghi, G. H. Zohuri, S. Damavandi, *Eur. J. Chem.* **2011**, *2*, 100–103. **DOI:**10.5155/eurjchem.2.1.100-103.175
41. K. M. Reddy, N. S. Babu, I. Suryanarayana, P. S. S. Prasad, N. Lingaiah, *Tetrahedron Lett.* **2006**, *47*, 7563–7566. **DOI:**10.1016/j.tetlet.2006.08.094
42. P. Li, L. Wang, *Tetrahedron* **2007**, *63*, 5455–5459. **DOI:**10.1016/j.tet.2007.04.032
43. K. Namitharan, K. Pitchumani, *Eur. J. Org. Chem.* **2010**, *2010*, 411–415. **DOI:**10.1002/ejoc.200901084
44. M. L. Kantam, S. Laha, J. Yadav, S. Bhargava, *Tetrahedron Lett.* **2008**, *49*, 3083–3086. **DOI:**10.1016/j.tetlet.2008.03.053
45. M. Rahman, A. K. Bagdi, A. Majee, A. Hajra, *Tetrahedron Lett.* **2011**, *52*, 4437–4439. **DOI:**10.1016/j.tetlet.2011.06.067
46. A. Weissberg, B. Halak, M. Portnoy, *J. Org. Chem.* **2005**, *70*, 4556–4559. **DOI:**10.1021/jo050237j
47. B. Huang, X. Yao, C-J. Li, *Adv. Synth. Catal.* **2006**, *348*, 1528–1532. **DOI:**10.1002/adsc.200606118

Povzetek

S pomočjo termičnega razpada Ni-oleilaminskih kompleksov smo pripravili ultramajhne monodispergirane NiO nanodelce (7–9 nm). Za karakterizacijo tako dobljenega katalizatorskega materiala smo uporabili različne metode, vključno z infrardečo spektroskopijo s Fourierjevo transformacijo (FT-IR), difuzno-odbojno UV-Vis spektroskopijo (DRS), rentgensko difraktometrijo (XRD), rentgensko analizo z energijskim razklonom (EDX), vrstično elektronsko mikroskopijo (SEM), dinamično tehniko svetlobnega sipanja (DLS) in magnetometer na vibracije vzorca (VSM). Propargilaminske derivate smo z dobrimi do odličnimi izkoristki sintetizirali iz aldehidov, terminalnih alkinov in primarnih aminov z enolončnim A^3-pripajanjem, ob dodatku 3 mol% NiO nanokristalov pri 80 °C pod pogoji brez uporabe topil. Strukture produktov smo potrdili z ^{1}H in ^{13}C NMR spektroskopijo. Uporabljeni katalizator prinaša mnoge prednosti, saj je okolju prijazen, njegova ponovna uporaba je enostavna in učinkovita, je stabilen ter primeren za širok nabor substratov, poleg tega pa je njegova priprava tudi cenovno ugodna.

DOI: 10.17344/acsi.2020.6446 *Acta Chim. Slov.* **2021,** *68,* 604–616

Scientific paper

Synthesis and Anticancer Evaluations of Novel Thiazole Derivatives Derived from 4-Phenylthiazol-2-amine

Amira E. M. Abdallah,[1,*] Rafat M. Mohareb,[2] Maher H. E. Helal[1] and Germeen J. Mofeed[1]

[1] *Department of Chemistry, Faculty of Science, Helwan University, Ain Helwan, Cairo-11795, A. R. Egypt*

[2] *Department of Chemistry, Faculty of Science, Cairo University, Giza, A. R. Egypt*

* *Corresponding author: E-mail: amiraelsayed135@ yahoo.com*

Received: 10-12-2020

Abstract

Many novel thiazole derivatives were designed and synthesized using 4-phenylthiazol-2-amine. The reactivity of the latter compound toward different chemical reagents was studied. The structure of the newly synthesized compounds was established based on elemental analysis and spectral data. Furthermore, twenty compounds of the synthesized systems were selected and evaluated in (μM) as significant anticancer agents towards three human cancer cell lines [MCF-7 (breast adenocarcinoma), NCI-H460 (non-small cell lung cancer), and SF-268 (CNS cancer)] and normal fibroblasts human cell line (WI-38). The results showed that compounds **9** and **14a** displayed higher effeciency than the reference doxorubicin.

Keywords: Anticancer; chromene; 4-phenylthiazol-2-amine; pyridine; pyrimidine; thiophene

1. Introduction

Great concern has been recently focused on the development of heterocyclic compound bearing 1,3-thiazole ring system, which has been identified as a central structural element of several biologically active natural products such as thiamine vitamin B, and pharmacologically active substances in a large number of drugs as antibacterial,[1,2] antifungal,[3,4] antiviral,[5–7] anti-inflammatory,[8,9] anticancer,[10–14] anti-HIV,[15–17] anti-oxidant[18,19] and analgesic drugs.[20,21] Both classical and non-classical synthetic methods approaches were used to synthesize thiazole derivatives. Some of the examples of such organic synthesis methods were: the reaction between haloketones and thio-amides (Hantzsch thiazole synthesis, 1889),[22,23] 2-acylamino-ketones reacting with phosphorus pentasulfide (Robinson–Gabriel synthesis),[24–26] α-aminonitrile with carbon disulfide (Cook–Heilbron synthesis),[27] and the addition of a thiazole anion to an aromatic nitrile,[28] additionally certain thiazoles can be accessed through the application of the Herz reaction.[29] Also, various biosynthesis routes lead to the development of the thiazole ring system as required for the formation of thiamine.[30] Thiazole derivatives were widely used in dyeing, for example, anthroquinone dyes that contain benzothiazole moiety, such as Algol Yellow 8. Also, they were used as non-steroidal anti-inflammatory drugs (NSAID) like Meloxicam (Figure 1), antiretroviral drugs (Ritonavir), antineoplastic drugs (Tiazofurin), antifungal drugs (Abafungin), and antimicrobial drugs (Sulfathiazol). Moreover thiazole derivatives were used as fungicides, such as Thifluzamide, Tricyclazole, and Thiabendazole which were marketed to control various agricultural pests. So far, modifications of the thiazole ring have proven high effectiveness with improved potency and lesser toxicity.

In continuation of our previous work,[31–38] the current study reported synthesizing some novel thiazole de-

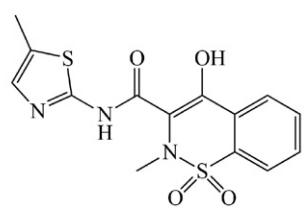

Fig. 1. Meloxicam Structure: 4-hydroxy-2-methyl-*N*-(5-methyl-2-thiazolyl)-2*H*-1,2-benzothiazine-3-carboxamide-1,1-dioxide.

rivatives based on 4-phenylthiazol-2-amine. The anticancer activity for all the synthesized compounds was evaluated. The latter products have a promising effect, as mentioned earlier by our research groups, in the preparation of a variety of close heterocyclic analogues compounds.[39–41]

2. Experimental

2. 1. General

All melting points were determined on an Electrothermal digital melting point apparatus and are uncorrected. IR spectra (KBr discs) were recorded on an FTIR plus 460 or Pye Unicam SP-1000 spectrophotometer (Pye Unicam, UK, Cambridge). ^{1}H NMR spectra were recorded with Varian EM-300 (300 MHz) (Cairo University) instrument in DMSO-d_6 as solvent using TMS as internal standard, and chemical shifts were expressed as δ ppm. The mass spectra were recorded with GCMS-QP 1000 Ex Shimadzu (EI, 70 eV) (Shimadzu, Japan) instrument. Analytical data were obtained from the Micro-analytical Data Unit at Cairo University and were performed on Vario EL III Elemental CHNS analyzer.

2. 2. Chemistry

2. 2. 1. Synthesis of Ethyl *N*-(4-Phenylthiazol-2-yl) formimidate (1)

To a solution of 4-phenylthiazol-2-amine (1.76 g, 0.01 mol) in ethanol (25 mL), triethyl orthoformate (1.48 g, 0.01 mol) was added. The reaction mixture was heated under reflux for three hours, then cooled and neutralized by pouring onto an ice/water mixture containing a few drops of hydrochloric acid. The solid product formed was collected by filtration and crystallized from ethanol.

Dark orange crystals, yield 78%. Mp 235–237 °C. IR (ν, cm^{-1}): 3065–3026 (CH aromatic), 2991, 2853 (CH, CH_2, CH_3), 1644, 1485 (C=C), 1579 (C=N). ^{1}H NMR (DMSO-d_6) δ 1.91 (t, J = 6.9 Hz, 3H, CH_3), 3.32 (q, J = 6.9 Hz, 2H, CH_2), 7.28 (s, 1H, thiazole H-5), 7.32–7.90 (s, 1H, CH; m, 5H, C_6H_5). ^{13}C NMR (DMSO-d_6) δ 22.5, 62.0, 107.8, 127.7 (2), 128.1, 128.7 (2), 134.3, 148.7, 157.9, 168.6. MS *m/z* (%): 234 [M$^+$+2] (0.31), 233 [M$^+$+1] (0.29), 232 [M$^+$] (0.18), 176 (100.00), 77 [C_6H_5]$^+$ (23.85). Anal. Calcd. for $C_{12}H_{12}N_2OS$ (232.30): C, 62.04; H, 5.21; N, 12.06; S, 13.80. Found: C, 61.71; H, 4.99; N, 11.66; S, 13.40.

2. 2. 2. General Procedure for the Synthesis of (4-Phenylthiazol-2-yl) formamidohydrazide Derivatives (2a,b)

Equimolar amounts of compound **1** (2.32 g, 0.01 mol) and hydrazine (0.50 g, 0.01 mol) or phenylhydrazine (1.08 g, 0.01 mol) in 1,4-dioxane (25 mL) were heated under reflux for three hours and cooled by pouring onto an ice/water mixture. The solid product formed in each case was collected by filtration, washed with water, and crystallized from 1,4-dioxane.

N"-(4-Phenylthiazol-2-yl)formimidohydrazide (2a)

Pale yellow crystals, yield 69%. Mp over 300 °C. IR (ν, cm^{-1}): 3413–3168 (NH, NH_2), 3066 (CH aromatic), 2990, 2852 (CH), 1644, 1490 (C=C), 1579 (C=N). ^{1}H NMR (DMSO-d_6) δ 7.32 (s, 1H, thiazole H-5), 7.34–7.90 (s, 1H, CH; m, 5H, C_6H_5), 7.58 (s, 2H, NH_2), 12.20 (s, 1H, NH). MS *m/z* (%): 220 [M$^+$+2] (2.06), 219 [M$^+$+1] (4.91), 218 [M$^+$] (32.03), 176 (100.00), 77 [C_6H_5]$^+$ (25.03). Anal. Calcd. for $C_{10}H_{10}N_4S$ (218.28): C, 55.02; H, 4.62; N, 25.67; S, 14.69. Found: C, 55.09; H, 4.39; N, 25.30; S, 14.30.

N'-Phenyl-N"-(4-phenylthiazol-2-yl)formimidohydrazide (2b)

Orange crystals, yield 71%. Mp 280–282 °C. IR (ν, cm^{-1}): 3426–3168 (2NH), 3066 (CH aromatic), 2991 (CH), 1643, 1442 (C=C), 1577 (C=N). ^{1}H NMR (DMSO-d_6) δ 7.32 (s, 1H, thiazole H-5), 7.34–7.90 (m, 10H, $2C_6H_5$), 7.57 (s, 1H, CH), 11.40, 12.18 (2s, 2H, 2NH). MS *m/z* (%): 293 [M$^+$–1] (0.24), 77 [C_6H_5]$^+$ (16.04), 69 (100.00). Anal. Calcd. for $C_{16}H_{14}N_4S$ (294.37): C, 65.28; H, 4.79; N, 19.03; S, 10.89. Found: C, 65.48; H, 4.43; N, 18.67; S, 10.53.

2. 2. 3. Synthesis of *N*-Phenyl-*N'*-(4-phenylthiazol-2-yl)formimidamide (3)

To a solution of compound **1** (2.32 g, 0.01 mol) in 1,4-dioxane (25 mL), aniline (0.93 g, 0.01 mol) was added. The reaction mixture was heated under reflux for three hours and then cooled by pouring onto an ice/water mixture. The solid product formed was collected by filtration and crystallized from 1,4-dioxane.

Paige crystals, yield 75%. Mp 280–282 °C. IR (ν, cm^{-1}): 3439–3168 (NH), 3066–3027 (CH aromatic), 2991, 2853 (CH), 1644, 1492 (C=C), 1579 (C=N). ^{1}H NMR (DMSO-d_6) δ 7.29 (s, 1H, thiazole H-5), 7.32–7.90 (m, 10H, $2C_6H_5$), 7.55 (s, 1H, CH), 12.14 (s, 1H, NH). MS *m/z* (%): 277 [M$^+$–2] (1.68), 77 [C_6H_5]$^+$ (37.99). Anal. Calcd. for $C_{16}H_{13}N_3S$ (279.36): C, 68.79; H, 4.69; N, 15.04; S, 11.48. Found: C, 68.48; H, 4.33; N, 15.40; S, 11.88.

2. 2. 4. Synthesis of 2-((4-Phenylthiazol-2-ylimino)methyl)malononitrile (4)[42,43]

To a solution of compound **1** (2.32 g, 0.01 mol) in 1,4-dioxane (25 mL) containing a catalytic amount of triethylamine (0.5 mL), malononitrile (0.66 g, 0.01 mol) was added. The reaction mixture was heated under reflux for three hours, then cooled and neutralized by pouring onto an ice/water mixture containing a few drops of hydrochloric acid. The formed solid product was collected by filtration and crystallized from 1,4-dioxane.

Paige crystals, yield 73%. Mp 203–205 °C. IR (ν, cm^{-1}): 3064 (CH aromatic), 2988, 2855 (2CH), 2202, 2200

(2CN), 1643, 1442 (C=C), 1577 (C=N). ^{1}H NMR (DMSO-d_6) δ 3.57 (s, 1H, CH), 7.29 (s, 1H, thiazole H-5), 7.31–7.90 (m, 5H, C_6H_5), 7.55 (s, 1H, CH). ^{13}C NMR (DMSO-d_6) δ 22.5, 107.8, 114.1 (2), 125.6, 127.7 (2), 128.7 (2), 134.3, 148.7, 157.9, 168.6. MS *m/z* (%): 254 [M^++2] (0.22), 253 [M^++1] (0.16), 252 [M^+] (0.13), 176 (100.00), 77 $[C_6H_5]^+$ (0.35). Anal. Calcd. for $C_{13}H_8N_4S$ (252.29): C, 61.89; H, 3.20; N, 22.21; S, 12.71. Found: C, 61.77; H, 3.60; N, 21.91; S, 12.53.

2. 2. 5. Synthesis of 1-Phenyl-3-(4-phenylthiazol-2-yl)thiourea (5)[44,45]

To a solution of 4-phenylthiazol-2-amine (1.76 g, 0.01 mol) in 1,4-dioxane (20 mL) containing a catalytic amount of triethylamine (0.5 mL), phenyl isothiocyanate (1.35 g, 0.01 mol) was added. The reaction mixture was heated under reflux for three hours then poured onto an ice/water mixture containing a few drops of hydrochloric acid. The formed solid product was collected by filtration, dried, and then crystallized from 1,4-dioxane.

Dark brown crystals, yield 64%. Mp 163–165 °C [Mp (lit.)[44] 225 °C]. IR (ν, cm^{-1}): 3440–3154 (2NH), 3060 (CH aromatic), 1600, 1443 (C=C), 1573 (C=N), 1379, 1288 (C=S). ^{1}H NMR (DMSO-d_6) δ 6.86–8.01 (m, 10H, $2C_6H_5$; s, 1H, thiazole H-5), 11.10, 11.86 (2s, 2H, 2NH). Anal. Calcd. for $C_{16}H_{13}N_3S_2$ (311.42): C, 61.71; H, 4.21; N, 13.49; S, 20.59. Found: C, 61.31; H, 4.06; N, 13.89; S, 20.20.

2. 2. 6. Synthesis of 2-Chloro-*N*-(4-phenylthiazol-2-yl)acetamide (6)[46–50]

To a solution of 4-phenylthiazol-2-amine (1.76 g, 0.01 mol) in 1,4-dioxane (20 mL), chloroacetylchloride (1.12 g, 0.01 mol) was added. The reaction mixture was heated under reflux for three hours and then poured onto a beaker containing an ice/water mixture. The formed solid product was collected by filtration, dried, and crystallized from 1,4-dioxane.

Light brown crystals, yield 71%. Mp 157–159 °C [Mp (lit.)[46] 171–173 °C]; IR (ν, cm^{-1}): 3444–3182 (NH), 3070 (CH aromatic), 2988, 2877 (CH_2), 1758 (C=O), 1654, 1487 (C=C), 1565 (C=N). ^{1}H NMR (DMSO-d_6) δ 4.42 (s, 2H, CH_2), 7.10–7.90 (m, 5H, C_6H_5), 7.91 (s, 1H, thiazole H-5), 12.66 (s, 1H, NH). Anal. Calcd. for $C_{11}H_9ClN_2OS$ (252.72): C, 52.28; H, 3.59; N, 11.08: S, 12.69. Found: C, 51.90; H, 3.97; N, 10.72; S, 12.30.

2. 2. 7. Synthesis of 2-Cyano-*N*-(4-phenylthiazol-2-yl)acetamide (7)

To a solution of 4-phenylthiazol-2-amine (1.76 g, 0.01 mol) in dimethylformamide (20 mL), ethyl cyanoacetate (1.13 g, 0.01 mol) was added. The reaction mixture was heated under reflux for three hours then poured onto an ice/water mixture. The solid product formed was collected by filtration and crystallized from ethanol.

Dark orange crystals, yield 75%. Mp 109–111 °C. IR (ν, cm^{-1}): 3444–3164 (NH), 3048 (CH aromatic), 2892 (CH, CH_2), 1687 (C=O), 1600, 1482 (C=C), 1564 (C=N). ^{1}H NMR (DMSO-d_6) δ 4.07 (s, 2H, CH_2), 7.30–7.90 (m, 5H, C_6H_5), 7.91 (s, 1H, thiazole H-5), 12.39 (s, 1H, NH). Anal. Calcd. for $C_{12}H_9N_3OS$ (243.28): C, 59.24; H, 3.73; N, 17.27; S, 13.18. Found: C, 59.64; H, 4.10; N, 16.88; S, 12.79.

2. 2. 8. Synthesis of 5-Imino-2-phenyl-6-(1-phenylethylidene)-5*H*-thiazolo[3,2-*a*]pyrimidin-7(6*H*)-one (8)

To a compound **7** (2.43 g, 0.01 mol) in ammonium acetate (1.00 g), acetophenone (1.20 g, 0.01 mol) was added. The reaction mixture was heated in an oil bath for two hours and then left to cool. The solid product formed when the product was triturated with ethanol was collected by filtration, then dried and crystallized from ethanol.

Dark yellow crystals, yield 73%. Mp 105–107 °C. IR (ν, cm^{-1}): 3431–3113 (NH), 3063 (CH aromatic), 2990 (CH_3), 1644 (C=O), 1590, 1490 (C=C), 1524 (C=N). ^{1}H NMR (DMSO-d_6) δ 2.17 (s, 3H, CH_3), 6.98–7.90 (m, 10H, $2C_6H_5$), 7.94 (s, 1H, thiazole H-5), 12.20 (s, 1H, NH). ^{13}C NMR (DMSO-d_6) δ 22.5, 108.4, 126.6 (2), 127.2, 127.7, 127.9, 128.1 (2), 128.4 (2), 128.7 (2), 129.1, 134.3, 148.7, 158.0, 159.7, 168.2, 168.6. Anal. Calcd. for $C_{20}H_{15}N_3OS$ (345.42): C, 69.54; H, 4.38; N, 12.17; S, 9.28. Found: C, 69.15; H, 4.39; N, 12.57; S, 9.60.

2. 2. 9. Synthesis of Ethyl 2,4-Diamino-5-((4-phenylthiazol-2-yl)carbamoyl)thiophene-3-carboxylate (9)

To a solution of compound **7** (2.43 g, 0.01 mol) in 1,4-dioxane (20 mL) containing a catalytic amount of triethylamine (0.50 ml) each of elemental sulfur (0.32 g, 0.01 mol) and ethyl cyanoacetate (1.13 g, 0.01 mol) were added. The reaction mixture was heated under reflux for three hours. The solid product formed upon pouring onto an acidified ice/water mixture was collected by filtration and crystallized from 1,4-dioxane.

Dark yellow crystals, yield 63%. Mp 156–158 °C. IR (ν, cm^{-1}): 3427–3164 (NH, $2NH_2$), 3104–3047 (CH aromatic), 2892 (CH_2, CH_3), 1756, 1687 (2C=O), 1565, 1478 (C=C), 1550 (C=N). ^{1}H NMR (DMSO-d_6) δ 1.20 (t, J = 7.2 Hz, 3H, CH_3), 4.05 (q, J = 7.2 Hz, 2H, CH_2), 7.30 (s, 1H, thiazole H-5), 7.32–7.91 (m, 5H, C_6H_5), 8.52 (s, 4H, $2NH_2$), 12.32 (s, 1H, NH). ^{13}C NMR (DMSO-d_6) δ 38.7, 66.0, 108.5, 125.7, 127.9 (2), 128.7 (2), 128.0, 130.1, 133.0, 134.1, 148.9, 156.3, 158.0, 159.7, 160.0. MS *m/z* (%): 388 [M^+] (0.80), 387 [M^+–1] (0.36), 386 [M^+–2] (0.28), 134 (100.00), 77 $[C_6H_5]^+$ (21.40). Anal. Calcd. for $C_{17}H_{16}N_4O_3S_2$ (388.46): C, 52.56; H, 4.15; N, 14.42; S, 16.51. Found: C, 52.96; H, 4.29; N, 14.79; S, 16.91.

2. 2. 10. Synthesis of 4,6-Diamino-2-oxo-1-(4-phenylthiazol-2-yl)-1,2-dihydropyridine-3-carbonitrile (10)

To a solution of compound **7** (2.43 g, 0.01 mol) in 1,4-dioxane (25 mL) containing a catalytic amount of triethylamine (0.50 mL), malononitrile (0.66 g, 0.01 mol) was added. The reaction mixture was heated under reflux for three hours. After cooling, the reaction mixture was acidified by a few drops of hydrochloric acid and the crude product was precipitated, collected by filtration and crystallized from 1,4-dioxane.

Dark brown crystals, yield 78%. Mp 150–152 °C. IR (ν, cm^{-1}): 3462–3164 ($2NH_2$), 3048 (CH aromatic), 2212 (CN), 1686 (C=O), 1563, 1482 (C=C), 1550 (C=N). ^{1}H NMR (DMSO-d_6) δ 4.26 (s, 1H, pyridinone H-5), 7.27 (s, 1H, thiazole H-5), 7.30–7.90 (m, 5H, C_6H_5), 7.91, 8.52 (2s, 4H, $2NH_2$). Anal. Calcd. for $C_{15}H_{11}N_5OS$ (309.35): C, 58.24; H, 3.58; N, 22.64; S, 10.37. Found: C, 58.64; H, 3.97; N, 22.24; S, 10.67.

2. 2. 11. Synthesis of 2-Oxo-*N*-(4-phenylthiazol-2-yl)-2*H*-chromene-3-carboxamide (11)[51,52]

To a solution of compound **7** (2.43 g, 0.01 mol) in 1,4-dioxane (20 mL) containing piperidine (0.5 mL), salicylaldehyde (1.22 g, 0.01 mol) was added. The reaction mixture was heated under reflux for three hours then poured onto an ice/water mixture containing a few drops of hydrochloric acid. The formed solid product was collected by filtration then crystallized from 1,4-dioxane.

Yellow crystals, yield 81%. Mp 180–182 °C. IR (ν, cm^{-1}): 3374–3263 (NH), 3107 (CH aromatic), 1711, 1627 (2C=O), 1600, 1490 (C=C), 1539 (C=N). ^{1}H NMR (DMSO-d_6) δ 7.24 (s, 1H, thiazole H-5), 6.84–8.05 (m, 9H, C_6H_4, C_6H_5), 8.34 (s, 1H, pyrane H-4), 12.09 (s, 1H, NH). MS *m/z* (%): 350 [M^++2] (4.14), 349 [M^++1] (12.86), 348 [M^+] (24.95), 173 (100.00), 77 $[C_6H_5]^+$ (13.56). Anal. Calcd. for $C_{19}H_{12}N_2O_3S$ (348.38): C, 65.51; H, 3.47; N, 8.04; S, 9.20. Found: C, 65.11; H, 3.86; N, 7.87; S, 9.52.

2. 2. 12. General Procedure for the Synthesis of *N*-Cyclopentylidene and *N*-Cyclohexylidene-4-phenylthiazol-2-amine (12a,b)

To a solution of 4-phenylthiazol-2-amine (1.76 g, 0.01 mol) in 1,4-dioxane containing a catalytic amount of piperidine (0.50 mL), either cyclopentanone (0.84 g, 0.01 mol) or cyclohexanone (0.98 g, 0.01 mol) was added. The reaction mixture was heated under reflux for two hours then cooled, neutralized by pouring onto an acidified ice/water mixture, and crystallized from 1,4-dioxane.

***N*-Cyclopentylidene-4-phenylthiazol-2-amine (12a)**

Orange crystals, yield 73%. Mp 225–227 °C. IR (ν, cm^{-1}): 2950, 2806 (CH_2), 1586, 1456 (C=C), 1519 (C=N). ^{1}H NMR (DMSO-d_6) δ 1.56–1.67 (m, 4H, $2CH_2$), 2.41–2.51 (m, 4H, $2CH_2$), 7.33–7.53 (m, 5H, C_6H_5), 8.44 (s, 1H, thiazole H-5). MS *m/z* (%): 243 [M^++1] (0.45), 242 [M^+] (0.70), 84 (100.00). Anal. Calcd. for $C_{14}H_{14}N_2S$ (242.34): C, 69.39; H, 5.82; N, 11.56; S, 13.23. Found: C, 69.22; H, 5.42; N, 11.17; S, 13.52.

***N*-Cyclohexylidene-4-phenylthiazol-2-amine (12b)**

Shiny paige crystals, yield 71%. Mp 208–210 °C. IR (ν, cm^{-1}): 2950, 2806 (CH_2), 1628, 1455 (C=C), 1586 (C=N). ^{1}H NMR (DMSO-d_6) δ 1.52–1.71 (m, 6H, $3CH_2$), 2.49–2.51 (m, 4H, $2CH_2$), 7.10–7.80 (m, 5H, C_6H_5), 8.39 (s, 1H, thiazole, H-5). MS *m/z* (%): 258 [M^++2] (0.05), 257 [M^++1] (0.12), 256 [M^+] (0.27), 255 [M^+–1] (0.29), 254 [M^+–2] (0.07), 84 (100.00), 77 $[C_6H_5]^+$ (1.46). Anal. Calcd. for $C_{15}H_{16}N_2S$ (256.37): C, 70.27; H, 6.29; N, 10.93; S, 12.51. Found: C, 69.88; H, 5.93; N, 10.90; S, 12.11.

2. 2. 13. Synthesis of 4-Phenyl-*N*-(1-phenylethylidene)thiazol-2-amine (13)[53]

To a solution of 4-phenylthiazol-2-amine (1.76 g, 0.01 mol) in ethanol (20 mL) containing a catalytic amount of triethylamine (0.5 mL), acetophenone (1.20 g, 0.01 mol) was added. The reaction mixture was heated under reflux for three hours then poured into a beaker containing an acidified ice/water mixture. The formed solid product was collected by filtration and crystallized from ethanol.

Yellow crystals, yield 69%. Mp 190–192 °C. IR (ν, cm^{-1}): 3070 (CH aromatic), 2800 (CH_3), 1598, 1481 (C=C), 1523 (C=N). ^{1}H NMR (DMSO-d_6) δ 1.30 (s, 3H, CH_3), 7.01–7.80 (m, 10H, $2C_6H_5$), 7.81 (s, 1H, thiazole, H-5). ^{13}C NMR (DMSO-d_6) δ 38.7, 101.5, 125.5 (2), 127.0, 127.1 (2), 128.4 (2), 128.6 (2), 131.0, 134.9, 143.0, 149.8, 165.0, 168.2. MS *m/z* (%): 279 [M^++1] (0.46), 278 [M^+] (0.78), 277 [M^+–1] (0.81), 276 [M^+–2] (0.67), 176 (100.00), 77 $[C_6H_5]^+$ (36.83). Anal. Calcd. for $C_{17}H_{14}N_2S$ (278.37): C, 73.35; H, 5.07; N, 10.06; S, 11.52. Found: C, 73.66; H, 5.39; N, 10.46; S, 11.90.

2. 2. 14. General Procedure for the Synthesis of Thiazolo[3,2-*a*]pyrimidine-6-carbonitrile Derivatives 14a–f

To a solution of 4-phenylthiazol-2-amine (1.76 g, 0.01 mol) in ethanol (20 mL) containing a catalytic amount of triethylamine (0.50 mL), each of either benzaldehyde (1.06 g, 0.01 mol), *para*-methoxybenzaldehyde (1.08 g, 0.01 mol) or *para*-chlorobenzaldehyde (1.12 g, 0.01 mol) and either malononitrile (0.66 g, 0.01 mol) or ethyl cyanoacetate (1.13 g, 0.01 mol) were added. The reaction mixture was heated under reflux for six hours and then poured onto an acidified ice/water mixture. The formed solid product was collected by filtration and crystallized from ethanol.

5-Amino-3,7-diphenyl-8a*H*-thiazolo[3,2-*a*]pyrimidine-6-carbonitrile (14a)

Off white crystals, yield 75%. Mp 225–227 °C. IR (ν, cm^{-1}): 3419 (NH_2), 3030 (CH aromatic), 2221 (CN), 1585, 1448 (C=C), 1520 (C=N). ^{1}H NMR (DMSO-d_6) δ 7.59, 7.60 (2s, 2H, thiazole H-2, pyrimidine H-8a), 7.62–7.98 (m, 10H, $2C_6H_5$), 8.53 (s, 2H, NH_2). ^{13}C NMR (DMSO-d_6) δ 40.3, 81.6, 113.2, 114.2, 127.5, 128.0 (2), 129.6 (2), 129.5 (2), 130.5 (2), 131.3 (2), 134.4, 156.0, 161.5, 162.0. MS *m/z* (%): 331 [M^++1] (32.57), 64 (100.00). Anal. Calcd. for $C_{19}H_{14}N_4S$ (330.41): C, 69.07; H, 4.27; N, 16.96; S, 9.70. Found: C, 69.39; H, 4.30; N, 16.62; S, 9.31.

5-Amino-7-(4-methoxyphenyl)-3-phenyl-8a*H*-thiazolo[3,2-*a*]pyrimidine-6-carbonitrile (14b)

Yellow needles crystals, yield 78%. Mp 130–132 °C. IR (ν, cm^{-1}): 3406–3283 (NH_2), 3114–3025 (CH aromatic), 2978, 2846 (CH_3), 2216 (CN), 1606, 1506 (C=C), 1564 (C=N). ^{1}H NMR (DMSO-d_6) δ 3.87 (s, 3H, CH_3), 6.92, 6.94 (2s, 2H, thiazole H-2, pyrimidine H-8a), 7.11–8.01 (m, 9H, C_6H_4, C_6H_5), 8.38 (s, 2H, NH_2). MS *m/z* (%): 361 [M^++1] (0.57), 360 [M^+] (0.45), 358 [M^+–2] (0.45), 134 (100.00), 77 $[C_6H_5]^+$ (58.08). Anal. Calcd. for $C_{20}H_{16}N_4OS$ (360.43): C, 66.65; H, 4.47; N, 15.54; S, 8.90. Found: C, 66.81; H, 4.87; N, 15.39; S, 9.22.

5-Amino-7-(4-chlorophenyl)-3-phenyl-8a*H*-thiazolo[3,2-*a*]pyrimidine-6-carbonitrile (14c)

Yellow needles crystals, yield 78%. Mp 228–230 °C. IR (ν, cm^{-1}): 3240 (NH_2), 3092 (CH aromatic), 2223 (CN), 1631, 1483 (C=C), 1581 (C=N). ^{1}H NMR (DMSO-d_6) δ 7.21, 7.22 (2s, 2H, thiazole H-2, pyrimidine H-8a), 7.27–7.98 (m, 9H, C_6H_4, C_6H_5), 8.52 (s, 2H, NH_2). Anal. Calcd. for $C_{19}H_{13}ClN_4S$ (364.85): C, 62.55; H, 3.59; N, 15.36; S, 8.79. Found: C, 62.22; H, 3.21; N, 14.96; S, 9.12.

5-Hydroxy-3,7-diphenyl-8a*H*-thiazolo[3,2-*a*]pyrimidine-6-carbonitrile (14d)

Brownish orange crystals, yield 86%. Mp 140–142 °C. IR (ν, cm^{-1}): 3429–3125 (OH), 3064 (CH aromatic), 2220 (CN), 1604, 1488 (C=C), 1566 (C=N). ^{1}H NMR (DMSO-d_6) δ 6.03, 7.28 (2s, 2H, thiazole H-2, pyrimidine H-8a), 7.33–8.06 (m, 10H, $2C_6H_5$), 8.40 (s, 1H, OH). Anal. Calcd. for $C_{19}H_{13}N_3OS$ (331.39): C, 68.86; H, 3.95; N, 12.68; S, 9.68. Found: C, 68.46; H, 4.35; N, 12.69; S, 10.07.

5-Hydroxy-7-(4-methoxyphenyl)-3-phenyl-8a*H*-thiazolo[3,2-*a*]pyrimidine-6-carbonitrile (14e)

Shiny paige crystals, yield 84%. Mp 309–311 °C. IR (ν, cm^{-1}): 3247–3118 (OH), 3050 (CH aromatic), 2838 (CH_3), 2200 (CN), 1625, 1443 (C=C), 1532 (C=N). ^{1}H NMR (DMSO-d_6) δ 3.87 (s, 3H, CH_3), 6.93, 6.96 (2s, 2H, thiazole H-2, pyrimidine H-8a), 7.17–7.37 (m, 9H, C_6H_4, C_6H_5), 9.90 (s, 1H, OH). ^{13}C NMR (DMSO-d_6) δ 40.3, 55.1, 72.0, 102.0, 114.3 (2), 115.0, 121.9, 127.9, 128.5 (2), 128.7 (2), 131.3 (2), 132.0, 133.9, 158.5, 166.0, 167.1. MS *m/z* (%): 363 [M^++2] (1.23), 362 [M^++1] (0.14), 361 [M^+] (0.09), 134 (100.00), 77 $[C_6H_5]^+$ (26.84). Anal. Calcd. for $C_{20}H_{15}N_3O_2S$ (361.42): C, 66.46; H, 4.18; N, 11.63; S, 8.87. Found: C, 66.27; H, 4.58; N, 11.27; S, 8.47.

7-(4-Chlorophenyl)-5-hydroxy-3-phenyl-8a*H*-thiazolo[3,2-*a*]pyrimidine-6-carbonitrile (14f)

Off white crystals, yield 83%. Mp 290–292 °C. IR (ν, cm^{-1}): 3438–3181 (OH), 3080 (CH aromatic), 2200 (CN), 1631, 1483 (C=C), 1535 (C=N). ^{1}H NMR (DMSO-d_6) δ 7.19, 7.21 (2s, 2H, thiazole H-2, pyrimidine H-8a), 7.22–7.95 (m, 9H, C_6H_4, C_6H_5), 10.01 (s, 1H, OH). Anal. Calcd. for $C_{19}H_{12}ClN_3OS$ (365.84): C, 62.38; H, 3.31; N, 11.49; S, 8.76. Found: C, 62.78; H, 3.71; N, 11.12; S, 8.41.

2. 2. 15. Synthesis of *N*'-(4-Methoxyphenyl)-*N*-(4-phenylthiazol-2-yl)formimidamide (15)

To a solution of 4-phenylthiazol-2-amine (1.76 g, 0.01 mol) in 1,4-dioxane (20 mL) containing triethylamine (0.50 ml), triethyl orthoformate (1.48 g, 0.01) and *para*-anisidine (1.23 g, 0.01) were added. The reaction mixture was heated under reflux for three hours then poured into a beaker containing ice/water mixture. The formed solid product was collected by filtration and crystallized from 1,4-dioxane.

Pale yellow crystals, yield 92%. Mp 208–210 °C. IR (ν, cm^{-1}): 3361–3121 (NH), 3074–3008 (CH aromatic), 2950, 2836 (CH, CH_3), 1606, 1462 (C=C), 1549 (C=N). ^{1}H NMR (DMSO-d_6) δ 3.79 (s, 3H, CH_3), 6.87 (s, 1H, CH), 6.90 (s, 1H, thiazole, H-5), 7.05–7.47 (m, 9H, C_6H_4, C_6H_5), 11.47 (s, 1H, NH). ^{13}C NMR (DMSO-d_6) δ 55.5, 114.5, 114.6, 121.3, 122.1, 126.5 (2), 129.8 (2), 130.3, 131.0, 139.0, 151.2, 152.1, 157.8, 159.0, 166.0. Anal. Calcd. for $C_{17}H_{15}N_3OS$ (309.39): C, 66.00; H, 4.89; N, 13.58; S, 10.36. Found: C, 66.37; H, 5.28; N, 13.18; S, 10.59.

2. 2. 16. General Procedure for the Synthesis of Thiazolo[3,2-*a*]pyrimidine Derivatives 16a,b

To a solution of 4-phenylthiazol-2-amine (1.76 g, 0.01 mol) in ethanol (30 mL) containing a catalytic amount of triethylamine (0.50 mL) and triethyl orthoformate (1.48 g, 0.01 mol), either malononitrile (0.66 g, 0.01 mol) or ethyl cyanoacetate (1.13 g, 0.01 mol) was added. The reaction mixture, in each case, was heated under reflux for five hours then poured into a beaker containing an acidified ice/water mixture. The formed solid product, in each case, was collected by filtration and crystallized from ethanol.

5-Imino-3-phenyl-5*H*-thiazolo[3,2-*a*]pyrimidine-6-carbonitrile (16a)

Yellow crystals, yield 85%. Mp 190–192 °C. IR (ν, cm^{-1}): 3434–3112 (NH), 3050 (CH aromatic), 2210 (CN),

1598, 1479 (C=C), 1523 (C=N); ^{1}H NMR (DMSO-d_6) δ 6.98 (s, 1H, thiazole H-5), 7.02 (s, 1H, pyrimidine H-7), 7.22–7.81 (m, 5H, C_6H_5), 8.60 (s, 1H, NH). ^{13}C NMR (DMSO-d_6) δ 98.0, 101.4, 115.0, 125.5, 127.1 (2), 128.4 (2), 134.9, 149.8, 156.0, 158.0, 168.2. MS m/z (%): 253 [M^++1] (0.09), 252 [M^+] (0.09), 176 (100.00), 77 [C_6H_5]$^+$ (13.42). Anal. Calcd. for $C_{13}H_8N_4S$ (252.29): C, 61.89; H, 3.20; N, 22.21; S, 12.71. Found: C, 61.49; H, 3.59; N, 21.81; S, 12.31.

5-Oxo-3-phenyl-5*H*-thiazolo[3,2-*a*]pyrimidine-6-carbonitrile (16b)

Pale yellow crystals, yield 84%. Mp 170–172 °C. IR (ν, cm^{-1}): 3113 (CH aromatic), 2200 (CN), 1689 (C=O), 1597, 1482 (C=C), 1519 (C=N). ^{1}H NMR (DMSO-d_6) δ 6.99 (s, 1H, thiazole H-5), 7.01 (s, 1H, pyrimidine H-7), 7.23–7.81 (m, 5H, C_6H_5). ^{13}C NMR (DMSO-d_6) δ 98.1, 101.5, 115.0, 125.5, 127.2 (2), 128.5 (2), 134.8, 149.7, 156.1, 158.2, 168.2. Anal. Calcd. for $C_{13}H_7N_3OS$ (253.28): C, 61.65; H, 2.79; N, 16.59; S, 12.66. Found: C, 61.35; H, 3.01; N, 16.30; S, 12.34.

2. 3. Biology

Reagents. Fetal bovine serum (FBS) and L-glutamine were obtained from Gibco Invitrogen Company (Scotland, UK). RPMI-1640 medium was provided from Cambrex (New Jersey, USA). Dimethyl sulfoxide (DMSO), doxorubicin, penicillin, streptomycin and sulforhodamine B (SRB) were obtained from Sigma Chemical Company (Saint Louis, MO, USA).

Samples. Stock solutions of compounds **1**–**16b** were prepared in DMSO and kept at −20 °C. Appropriate dilutions of the compounds were freshly prepared just before the assays. Final concentrations of DMSO did not interfere with the cell growth.

Cell cultures. Three human tumor cell lines, MCF-7 (breast adenocarcinoma), NCI-H460 (non-small cell lung cancer), and SF-268 (CNS cancer) were used. MCF-7 was obtained from the European Collection of Cell Cultures (ECACC, Salisbury, UK) NCI-H460, SF-268, and normal fibroblast cells (WI 38) were kindly provided by the National Cancer Institute (NCI, Cairo, Egypt). They grew as a monolayer and were routinely maintained in RPMI-1640 medium supplemented with 5% heat-inactivated FBS, 2 mM glutamine and antibiotics (penicillin 100 U/mL, streptomycin 100 μg/mL), at 37 °C in a humidified atmosphere containing 5% CO_2. Exponentially growing cells were obtained by plating 1.5×10^5 cells/mL for MCF-7 and SF-268 and 0.75×10^4 cells/mL for NCI-H460, followed by 24 hours of incubation. The effect of the vehicle solvent (DMSO) on the growth of these cell lines was evaluated in all the experiments by exposing untreated control cells to the maximum concentration (0.5%) of DMSO used in each assay.

3. Results and Discussion

3. 1. Chemistry

The 4-phenylthiazol-2-amine was prepared from the reaction of thiourea with ω-bromoacetophenone according to the reported literature.[54] In the present work, we used the title compound in many heterocyclization reactions followed by studying the cytotoxicity of the resulting compounds against different cancer cell lines. Compound 4-phenylthiazol-2-amine reacted with triethyl orthoformate to produce the ethyl *N*-(4-phenylthiazol-2-yl) formimidate **1**. The structure of compound **1** was based on its analytical and spectral data. The ^{1}H NMR spectrum revealed the presence of a triplet at δ 1.91 ppm, a quartet at δ 3.32 ppm for the ethoxy group, a singlet at δ 7.28 ppm for thiazole H-5, and a multiplet at δ 7.32–7.90 ppm for the CH group and phenyl moiety. The mass spectrum showed [M^+] at m/z = 232 in correspondence to the molecular formula $C_{12}H_{12}N_2OS$.

Due to the excellent yield of compound **1**, the current study investigated its reactivity with a variety of chemical reagents. Compound **1** reacted with hydrazine hydrate or phenylhydrazine to give the hydrazide derivatives **2a** or **2b**, respectively. Moreover, it reacted with aniline to give the *N*-phenyl-*N*'-(4-phenylthiazol-2-yl)formimidamide **3**. Also, it reacted with malononitrile in 1,4-dioxane containing a catalytic amount of triethylamine to give the 2-((4-phenylthiazol-2-ylimino)methyl)malononitrile **4** (Scheme 1). Compound **4** was earlier prepared in literature by Covington *et al.* through the two reported patents.[42,43] The analytical and spectral data of compound **4** were consistent with its structure. Thus, in its mass spectrum, the existing [M^++2] ion (m/z = 254), [M^++1] ion (m/z = 253) and [M^+] ions (m/z = 252) confirmed its molecular weight and structure.

The 4-phenylthiazol-2-amine reacted with phenyl isothiocyanate to give the thiourea derivative **5**. Compound **5** was previously reported in the literature[44,45] by Bhargava *et al.*, despite using other reaction conditions involving benzene and heating on a water bath for six hours.[44] In addition, it reacted with chloroacetylchloride to give the 2-chloro-*N*-(4-phenylthiazol-2-yl)acetamide **6**. The structure of compound **6** was established based on its analytical and spectral data. It is worth mentioning that compound **6** was previously synthesized[46–50] using other reaction conditions. However, the current method was the simplest due to the short reaction time and easily available reagents. Moreover, 4-phenylthiazol-2-amine reacted with ethyl cyanoacetate in dimethylformamide solution to give the 2-cyano-*N*-(4-phenylthiazol-2-yl)acetamide **7**. The analytical and spectral data of the latter compound were in agreement with its proposed structure. The ^{1}H NMR spectrum revealed a singlet at δ 4.07 ppm for CH_2 group, a multiplet at δ 7.30–7.90 ppm for benzene ring, a singlet at δ 7.91 ppm for thiazole H-5, and a singlet at δ 12.39 ppm for the presence of NH group.

On the other hand, compound **7** reacted with acetophenone, in the presence of ammonium acetate, to give 6-(1-phenylethylidene)-5*H*-thiazolo[3,2-*a*]pyrimidine derivative **8**. Its structure was proven based on its analytical and spectral data. Compound **7** was capable of Gewald's thiophene synthesis. Its one-pot reaction with elemental sulfur and ethyl cyanoacetate in 1,4-dioxane containing a catalytic amount of triethylamine gave the 5-((4-phenylthiazol-2-yl)carbamoyl)thiophene derivative **9**. The analytical and spectral data of the latter compound were in agreement with its proposed structure. The ^{1}H NMR spectrum revealed a triplet at δ 1.20 ppm for CH_3 group, a quartet at δ 4.05 ppm for CH_2 group, a singlet at δ 7.30 ppm for thiazole CH-5, a multiplet at δ 7.32–7.91 ppm for phenyl moiety, a singlet at δ 8.52 ppm for two NH_2 groups, and a singlet at δ 12.32 ppm due to the presence of NH group.

The appearance of two C=O stretching bands at about 1756 and 1687 cm^{-1} and the presence of NH and two NH_2 bands at a range of 3427–3164 cm^{-1} in the IR spectrum proved the proposed structure. Moreover, the mass spectrum of compound **9** showed a molecular ion peak at m/z = 388 [M$^+$] corresponding to the molecular formula $C_{17}H_{16}N_4O_3S_2$.

Compound **7** reacted with malononitrile in the presence of 1,4-dioxane and a catalytic amount of triethylamine to give the thiazol-2-yl-1,2-dihydropyridine derivative **10**. On the other hand, the reaction of compound **7** with salicylaldehyde in a 1,4-dioxane solution containing a catalytic amount of piperidine gave the 2-oxo-chromene derivative **11**, as outlined in Scheme 2. Compound **11** was previously synthesized by Prashanth *et al.* and Bondock *et al.*, respectively.[51,5]

The 4-phenylthiazol-2-amine reacted with either cyclopentanone or cyclohexanone in 1,4-dioxane containing a catalytic amount of piperidine to give the condensed products **12a** and **12b**, respectively. In addition, it reacted with acetophenone in an ethanol solution containing a catalytic amount of triethylamine to give compound **13**. Compound **13** was reported previously by Xiaodong *et al.*[53] The analytical and spectral data of compounds **12a**, **12b**, and **13** agreed with their respective structures.

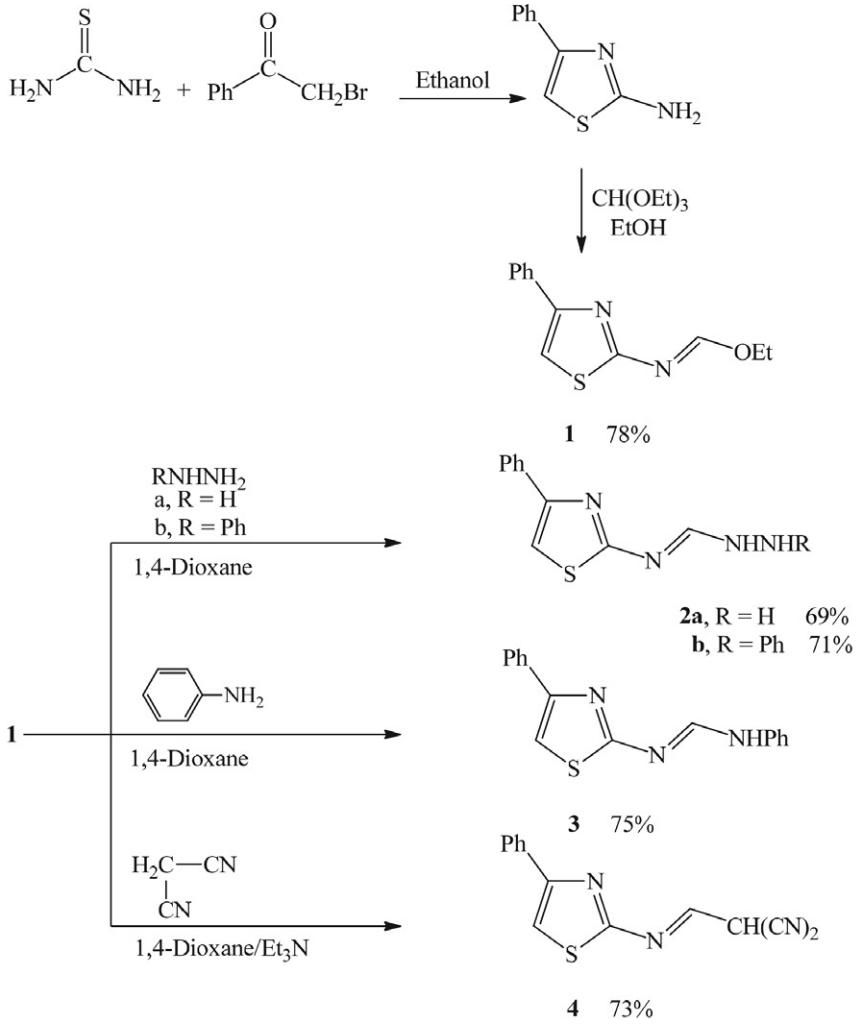

Scheme 1. Synthesis of thiazole derivatives **1**, **2a**,**b**, **3** and **4**.

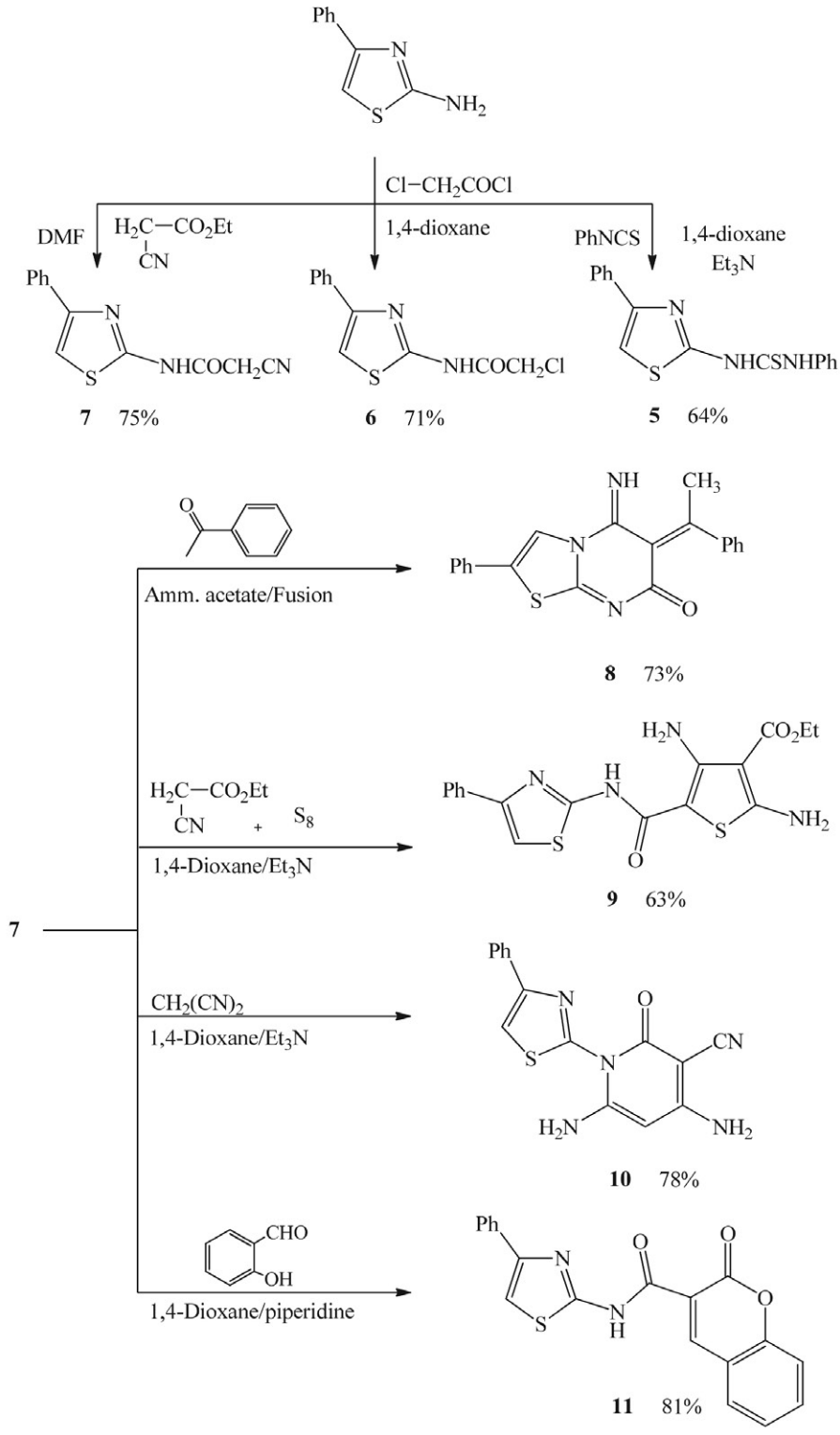

Scheme 2. Synthesis of thiazole derivatives **5**, **6**, **7**, **9**, **11**, thiazolo pyrimidine **8** and thiazol-2-yl pyridine **10** derivatives.

Next, we studied the multi-component reaction starting with compound 4-phenylthiazol-2-amine with the aromatic benzaldehydes and active methylene reagents. Then, the thiazolo[3,2-*a*]pyrimidines **14a**–**f** were synthesized by the reaction of compound 4-phenylthiazol-2-amine with either benzaldehyde, *para*-methoxybenzaldehyde, or *para*-chlorobenzaldehyde and malononitrile or ethyl cyanoacetate in ethanol and triethylamine, respectively (Scheme 3).

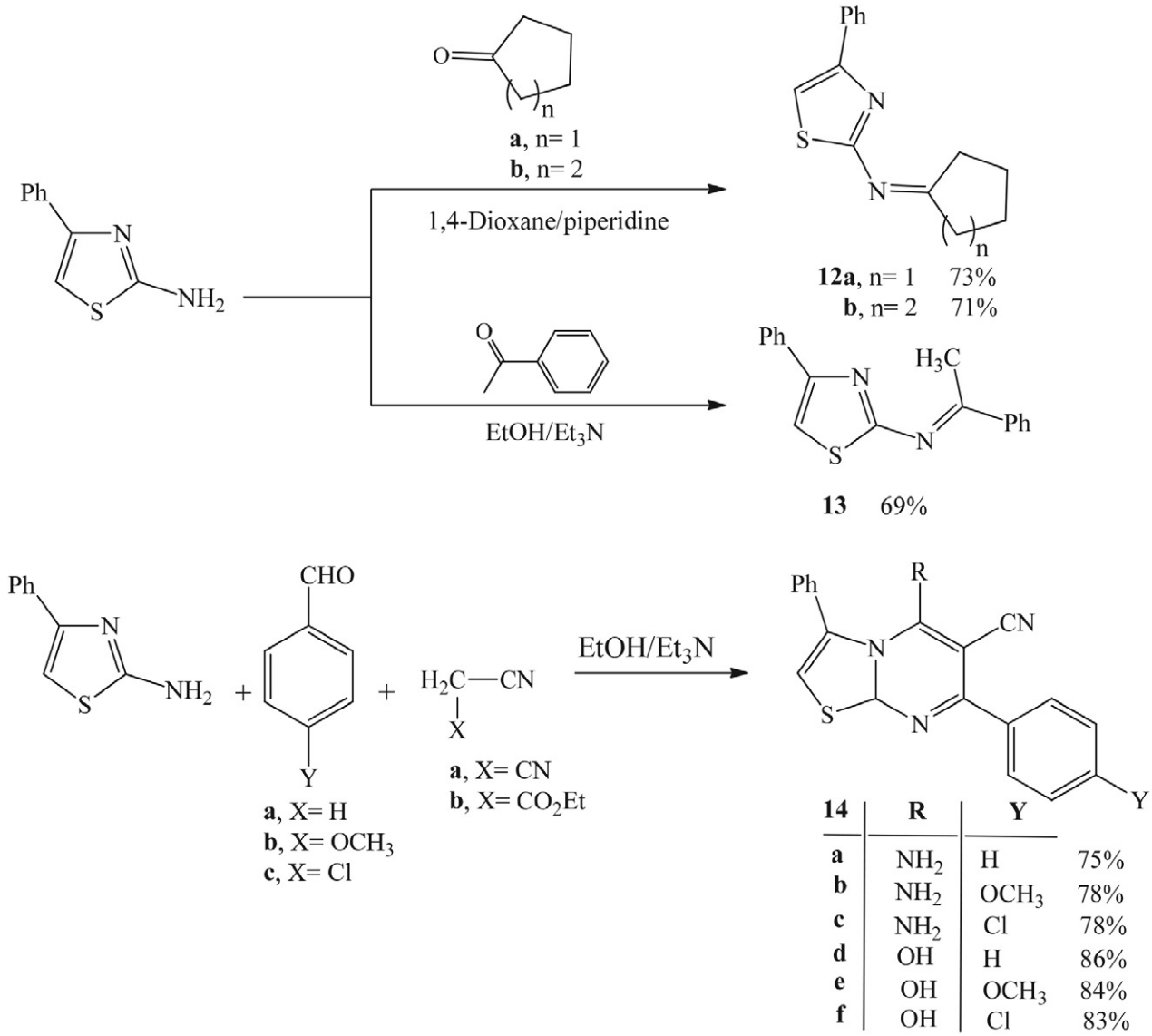

Scheme 3. Synthesis of thiazole derivatives **12a**,**b**, **13** and thiazolo pyrimidine derivatives **14a**–**f**.

The analytical and spectral data of the latter products were consistent with their respective structures. The ^{1}H NMR spectrum of **14a** as an example revealed a singlet at *d* 7.59 ppm for thiazole H-2, a singlet at *d* 7.60 ppm for pyrimidine H-8a, a multiplet at *d* 7.62–7.98 ppm for two phenyl groups and a singlet at *d* 8.53 ppm for NH_2 group.

In Scheme 4, the reaction of the 4-phenylthiazol-2-amine with triethyl orthoformate and *para*-anisidine in 1,4-dioxane gave the *N*'-(4-methoxyphenyl)-*N*-(4-phenylthiazol-2-yl)formimidamide **15**, the structure of which was confirmed based on the analytical and spectral data. Finally, the 4-phenylthiazol-2-amine reacted with either malononitrile or ethyl cyanoacetate and triethyl orthoformate in ethanol and triethylamine to form the thiazolo[3,2-*a*]pyrimidine derivatives **16a** and **16b**, respectively.

3. 2. Biological Activity Evaluations

3. 2. 1. *In Vitro* Anticancer Evaluation of the Synthesized Compounds

The newly synthesized thiazole systems (20 compounds in total) were assessed *in vitro* for their ability to suppress tumor cell growth[55,56] on three human tumor cell lines, namely, MCF-7 (breast adenocarcinoma), NCI-H460 (non-small cell lung cancer), and SF-268 (CNS cancer), and normal fibroblasts cells (WI38) after continuous exposure for 48 hours. In addition, the results were compared to the antiproliferative effects of the reference control doxorubicin.[57] All compounds were dissolved in DMSO at 1 mg/mL immediately before use and diluted just before being added to the cell culture.

The data in Table 1 represent mean values ±S.E.M. of three independent experiments performed in dupli-

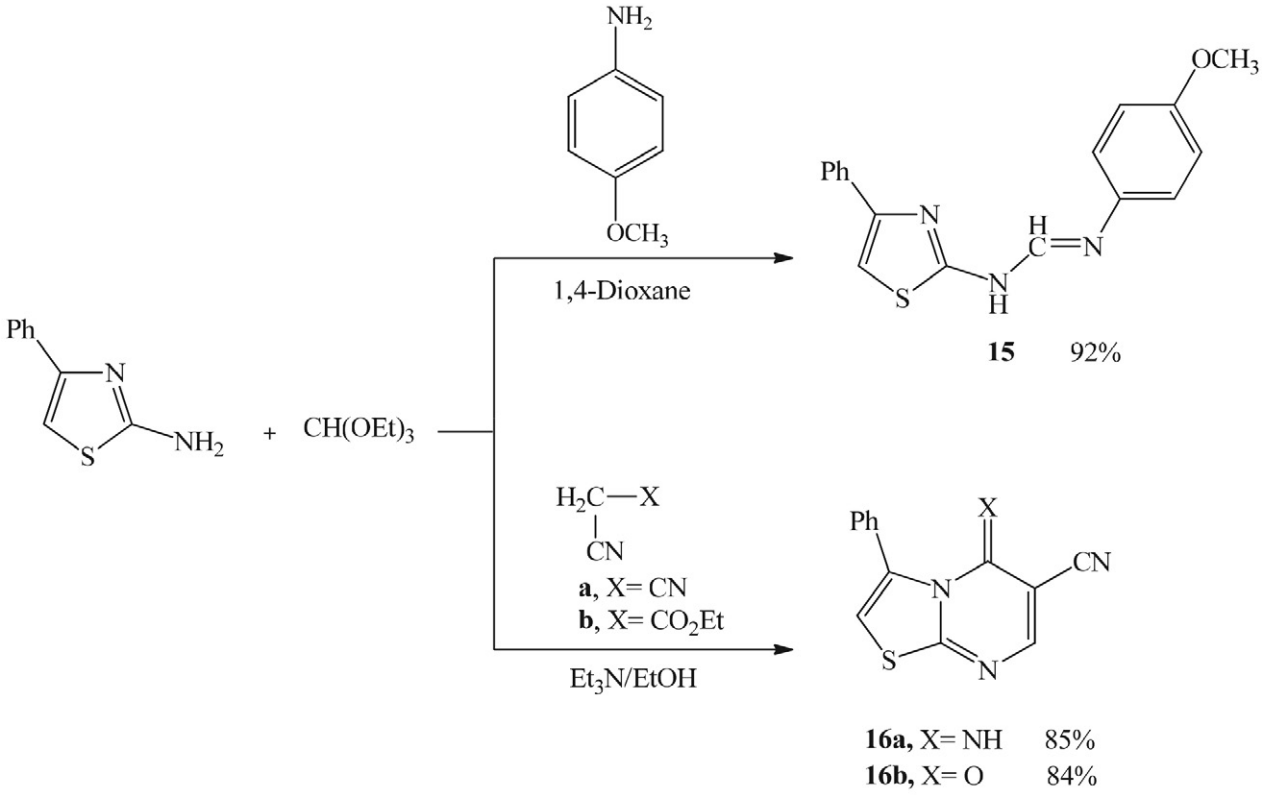

Scheme 4. Synthesis of thiazole derivative **15** and thiazolo pyrimidine derivatives **16a** and **16b**.

Table 1. Effect of the synthesized compounds in IC_{50} (μM) on the growth of three human tumor cell lines and normal human cell line

Compound No.	IC_{50} ± S.E.M. (μM)[(a)]			
	MCF-7	NCI-H460	SF-268	WI-38
2a	22.40 ± 2.12	10.42 ± 3.01	8.63 ± 1.80	>100
2b	1.80 ± 1.00	2.80 ± 0.30	2.80 ± 4.20	56.80 ± 4.0
5	42.60 ± 2.60	26.60 ± 2.60	35.20 ± 12.80	10.50 ± 5.10
6	32.70 ± 6.20	28.50 ± 4.40	40.50 ± 6.90	70.00 ±16.40
7	2.60 ± 0.20	1.00 ± 0.60	0.60 ± 0.08	0.20 ± 0.01
8	0.20 ± 0.008	0.03 ± 0.006	0.05 ± 0.01	>100
9	0.02 ± 0.002	0.01 ± 0.002	0.06 ± 0.008	> 100
10	37.00 ± 7.30	16.70 ± 2.30	38.40 ± 2.60	30.60 ± 6.20
11	12.80 ± 1.40	22.50 ± 0.40	49.80 ± 8.60	30.00 ± 2.30
12a	24.20 ± 2.40	20.60 ± 2.80	16.80 ± 8.50	32.20 ± 4.60
12b	28.40 ± 8.80	20.70 ± 6.20	34.40 ± 2.40	30.60 ± 3.00
13	22.10 ± 10.40	30.80 ± 10.80	26.10 ± 2.80	28.20 ± 0.80
14a	0.01 ± 0.001	0.02 ± 0.006	0.02 ± 0.008	> 100
14b	14.00 ± 1.40	22.80 ± 0.30	22.30 ± 0.80	32.40 ± 0.60
14c	0.60 ± 0.01	0.60 ± 0.06	0.40 ± 0.06	50.40 ± 11.30
14d	33.60 ± 8.50	40.30 ± 12.30	30.40 ± 2.80	62.20 ± 2.00
14e	0.06 ± 0.006	0.06 ± 0.006	0.20 ± 0.08	40.50 ± 5.10
14f	30.20 ± 3.60	38.30 ± 12.50	42.60 ± 5.80	58.70 ± 8.60
15	1.20 ± 0.40	0.80 ± 0.16	1.30 ± 0.06	36.40 ± 1.40
16b	0.80 ± 0.01	0.03 ± 0.007	0.60 ± 0.02	20.20 ± 3.40
***Doxorubicin**	0.0428 ± 0.0082	0.0940 ± 0.0087	0.0940 ± 0.0070	> 100

[(a)] Drug concentration required to inhibit tumor cell proliferation by 50% after continuous exposure for 48 hours; data were expressed as means ±S.E.M. of three independent experiments performed in duplicates.
[*] Doxorubicin was used as a positive control.

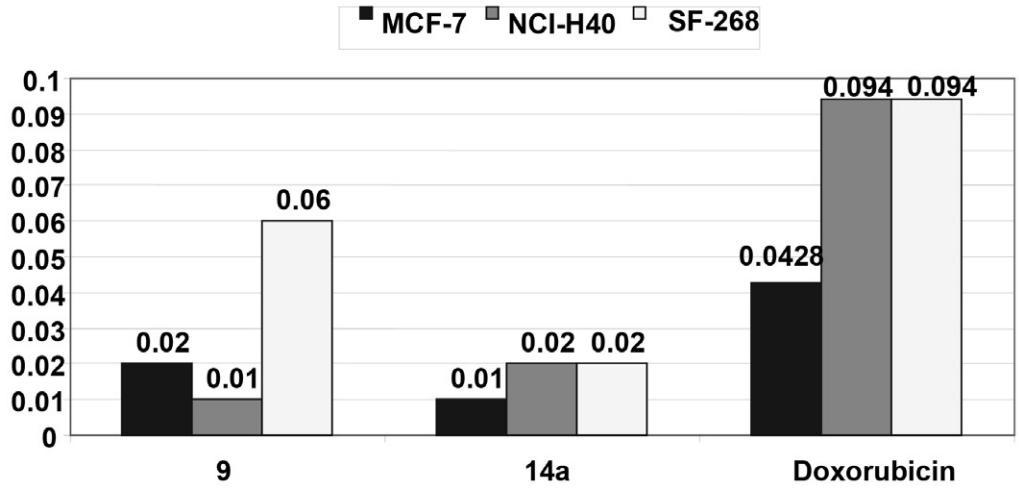

Figure 2. The anticancer evaluation of the most potent synthesized compounds against the three cancer cell lines.

cate. The results indicate that the majority of the compounds demonstrated substantial growth inhibitory effects against the human tumor cells at the concentrations tested.

3. 2. 2. Structure-Activity Relationship

From Table 1 it is clear that compounds **9** and **14a** showed higher effects than the reference doxorubicin for all human cancer cell lines used with IC_{50} values in the μM range (Figure 2). Although few compounds had low cytotoxicity on a specific tumor cell proliferation, they exhibited significant effects toward the others, such as compound **8**, which indicated optimal activity compared to the reference used for two cell lines; non-small cell lung cancer (NCI-H460) and SF-268 (CNS cancer). Also, compounds **14e** and **16b** exhibited a higher effect than the reference doxorubicin on only one cell line (NCI-H460). According to the tested tumor cell, the inhibitory effect of the other compounds towards tumor cell growth varied from high to medium or marginal effects. Moreover, compounds **2b**, **7**, **8**, **14c**, **14e**, **15**, and **16b** exhibited a high effect but not higher than the reference used. For non-small cell lung cancer (NCI-H460), compounds **2b**, **7**, **14c**, **14e**, **15**, and **16b** showed a moderate anticancer effect. Also, for SF-268 (CNS cancer), compounds **2b**, **7**, **14c**, **14e**, **15**, and **16b** showed a high activity but not higher than the doxorubicin. On the other hand, compounds **5**, **6**, **10**, **11**, **12a**, **12b**, **13**, **14b**, **14d**, and **14f** showed a low potent effect. For normal fibroblast cells (WI38), all compounds showed no cytotoxic effect.

Comparing the cytotoxicity of thiazole derivatives **2a** and **2b**, it is clear that the cytotoxicity of **2b** is higher than **2a** due to the presence of the phenyl group responsible for the high potency of **2b**. Moreover, compound **9** showed higher cytotoxicity than doxorubicin due to the presence of the ethoxy group. For some compounds of the thiazolo[3,2-*a*]pyrimidine derivatives **14a**–**f**, the presence of the phenyl group such as in compound **14a** is responsible for the higher cytotoxicity compared to doxorubicin. The compounds **14c** and **14e** revealed higher cytotoxicity due to the presence of chloro and methoxy groups, respectively. In conclusion, it is clear from the results obtained that the presence of the electronegative phenyl, Cl, OCH_3, and OC_2H_5 hydrophobic groups within the thiazole derivatives enhances the cytotoxicity of the tested compounds towards the selected cancer cell lines.

4. Conclusions

The objective of the current study was to synthesize a series of thiazole derivatives starting from 4-phenylthiazol-2-amine through its reaction with different chemical reagents. The anticancer activity of some of the newly synthesized compounds (twenty compounds) was evaluated on three human cancer cell lines and a normal human cell line. The results showed that compounds **9** and **14a** revealed higher effect than the reference doxorubicin when screened *in vitro* against the three human cancer cell lines tested, such as MCF-7 (breast adenocarcinoma), NCI-H460 (non-small cell lung cancer), SF-268 (CNS cancer), and normal fibroblasts human cell line (WI-38).

Acknowledgements

The authors would like to express their gratitude to the Department of Chemistry, Faculty of Science, Cairo University, for conducting this study and providing the necessary facilities.

Conflict of Interest

The authors declare no conflict of interest.

5. References

1. B. Ghasemi, M. Najimi, *Iran. J. Vet. Med.* **2016**, *10*, 47–52. **DOI:**10.22059/IJVM.2016.57050
2. A. M. Khalil, M. A. Berghot, M. A. Gouda, *Eur. J. Med. Chem.* **2009**, *44*, 4434–4440. **DOI:**10.1016/j.ejmech.2009.06.002
3. S. A. Ouf, S. M. Gomha, M. M. Ewies, I. A. A. Sharawy, *J. Heterocycl. Chem.* **2018**, *55*, 258–264. **DOI:**10.1002/jhet.3040
4. M. M. Ghorab, A. I. El-batal, *Boll. Chim. Farm.* **2002**, *141*, 110–117.
5. K. M. Dawood, T. M. A. Eldebss, H. S. A. El-Zahabi, M. H. Yousef, *Eur. J. Med. Chem.* **2015**, *102*, 266–276. **DOI:**10.1016/j.ejmech.2015.08.005
6. N. I. Zelisko, I. L. Demchuk, R. B. Lesyk, *Ukr. Biochem. J.* **2016**, *88*, 105–112. **DOI:**10.15407/ubj88.si01.105
7. O. I. El-Sabbagh, M. M. Baraka, S. M. Ibrahim, C. Pannecouque, G. Andrei, R. Snoeck, J. Balzarini, A. A. Rashad, *Eur. J. Med. Chem.* **2009**, *44*, 3746–3753. **DOI:**10.1016/j.ejmech.2009.03.038
8. R. N. Sharma, F. P. Xavier, K. K. Vasu, S. C. Chaturvedi, S. S. Pancholi, *J. Enzyme Inhib. Med. Chem.* **2009**, *24*, 890–897. **DOI:**10.1080/14756360802519558
9. F. A. Hassa, *Int. J. Appl. Sci. Technol.* **2012**, *2*, 180–187.
10. I. Kayagil, S. Demirayak, *Phosphorus Sulfur Silicon Relat Elem.* **2009**, *184*, 2197–2207. **DOI:**10.1080/10426500802446181
11. J.-H. Park, M. I. El-Gamal, Y. S. Lee, C.-H. Oh, *Eur. J. Med. Chem.* **2011**, *46*, 5769–5777. **DOI:**10.1016/j.ejmech.2011.08.024
12. T. I. de Santana, M. O. Barbosa, P. A. T. M. Gomes, A. C. N. da Cruz, T. G. da Silva, A. C. L. Leite, *Eur. J. Med. Chem.*, **2018**, *144*, 874–886. **DOI:**10.1016/j.ejmech.2017.12.040
13. M. Abdel-Motaal, A. L. Alanzy, M. Asem, *Acta Chim. Slov.* **2020**, *67*, 560–569. **DOI:**10.17344/acsi.2019.5571
14. A. Srinivas, P. Karthik, M. Sunitha, K. V. Reddy, *Acta Chim. Slov.* **2019**, *66*, 700–710. **DOI:**10.17344/acsi.2019.5156
15. M. L. Barreca, J. Balzarini, A. Chimirri, E. De Clercq, L. De Luca, H. D. Höltje, M. Höltje, A. M. Monforte, P. Monforte, C. Pannecouque, A. Rao, M. Zappalà, *J. Med. Chem.* **2002**, *45*, 5410–5413. **DOI:**10.1021/jm020977
16. Y. A. Al-Soud, H. H. Al-Sa'doni, S. O. W. Saber, R. H. M. Al-Shaneek, N. A. Al-Masoudi, R. Loddo, P. La Collac, *Z. Naturforsch.* **2010**, *65b*, 1372–1380. **DOI:**10.1515/znb-2010-1113
17. M. Madni, S. Hameed, M. N. Ahmed, M. N. Tahir, A. Najim, N. A. Al-Masoudi, C. Pannecouque, *Med. Chem. Res.* **2017**, *26*, 2653–2665. **DOI:**10.1007/s00044-017-1963-1
18. V. Jaishree, N. Ramdas, J. Sachin, B. Ramesh, *J. Saudi Chem. Soc.* **2012**, *16*, 371–376. **DOI:**10.1016/j.jscs.2011.02.007
19. M. Djukic, M. Fesatidou, I. Xenikakis, A. Athina Geronikaki, V. T. Angelova, V. Savic, M. Pasic, B. Krilovic, D. Djukic, B. Gobeljic, M. Pavlica, A. Djuric, I. Stanojevic, D. Vojvodic, L. Saso, *Chem-Biol Interact.* **2018**, *286*, 119–131. **DOI:**10.1016/j.cbi.2018.03.013
20. G. Saravanan, V. Alagarsamy, C. R. Prakash, P. D. Kumar, T. P. Selvam, *Asian J. Res. Pharm. Sci.* **2011**, *1*, 134–138.
21. A. H. Abdelazeem, M. T. El-Saadi, A. G. Safi El-Din, H. A. Omar, S. M. El-Moghazy, *Bioorg. Med. Chem.* **2017**, *25*, 665–676. **DOI:**10.1016/j.bmc.2016.11.037
22. P. S. Banerjee, P. K. Sharma, *Med. Chem. Res.* **2012**, *21*, 1491–1508. **DOI:**10.1007/s00044-011-9615-3
23. B. P. Mallikarjuna, B. S. Sastry, G. V. S. Kumar, Y Rajendraprasad, S. M. Chandrashekar, K. Sathisha, *Eur. J. Med. Chem.* **2009**, *44*, 4739–4746. **DOI:**10.1016/j.ejmech.2009.06.008
24. R. Robinson, *J. Chem. Soc. Trans.* **1909**, *95*, 2167–2174. **DOI:**10.1039/CT9099502167
25. S. Gabriel, *Ber. Dtsch. Chem. Ges.* **1910**, *43*, 134–138. **DOI:**10.1002/cber.19100430117
26. S. Gabriel, *Ber. Dtsch. Chem. Ges.* **1910**, *43*, 1283–1287. **DOI:**10.1002/cber.19100430219
27. A. H. Cook, I. Heilbron, A. L. Levy, *J. Chem. Soc.* **1947**, 1594–1598. **DOI:**10.1039/jr9470001594
28. L. F. Frey, K. M. Marcantonio, C.-Y. Chen, D. J. Wallace, J. A. Murry, L. Tan, W. Chen, U. H. Dolling, E. J. J. Grabowski, *Tetrahedron* **2003**, *59*, 6363–6373. **DOI:**10.1016/S0040-4020(03)00878-0
29. W. K. Warburton, *Chem. Rev.* **1957**, *57,* 1011–1020. **DOI:**10.1021/cr50017a004
30. M. Kriek, F. Martins, R. Leonardi, S. A. Fairhurst, D. J. Lowe, P. L. Roach, *J. Biol. Chem.* **2007**, *282*, 17413–17423. **DOI:**10.1074/jbc.M700782200
31. R. M. Mohareb, A. E. M. Abdallah, M. A. Abdelaziz, *Med. Chem. Res.* **2014**, *23*, 564–579. **DOI:**10.1007/s00044-013-0664-7
32. R. M. Mohareb, A. E. M. Abdallah, E. A. Ahmed, *Acta Pharm.* **2017**, *67*, 495–510. **DOI:**10.1515/acph-2017-0040
33. R. M. Mohareb, A. E. M. Abdallah, A. A. Mohamed, *Chem. Pharm. Bull.* **2018**, *66,* 309–318. **DOI:***10.1248/cpb.c17-00922*
34. R. M. Mohareb, E. M. Khalil, A. E. Mayhoub, A. E. M. Abdallah, *J. Heterocycl. Chem.* **2020**, *57*, 1330–1343. **DOI:**10.1002/jhet.3870
35. A. E. M. Abdallah, R. M. Mohareb, E. M. Khalil, M. A. M. A. Elshamy, *Chem. Pharm. Bull.* **2017**, *65,* 469–477. **DOI:**10.1248/cpb.c16-00925
36. A. E. M. Abdallah, G. H. Elgemeie, *Drug. Des. Devel. Ther.* **2018**, *12*, 1785–1798. **DOI:**10.2147/DDDT.S159310
37. A. E. M. Abdallah, R. M. Mohareb, E. A. Ahmed, *J. Heterocycl. Chem.* **2019**, *56*, 3017–3029. **DOI:**10.1002/jhet.3697
38. A. E. M. Abdallah, R. M. Mohareb, *Pigm. Resin Technol.* **2019**, *48*, 89–103. **DOI:**10.1108/PRT-11-2017-0085
39. R. M. Mohareb, Y. R. Milad, A. A. Masoud, *Acta Chim. Slov.* **2021**, *68*, 72–87. **DOI:**10.17344/acsi.2020.6182
40. R. M. Mohareb, R. A. Ibrahim, E. S. Alwan, *Acta Chim. Slov.* **2021**, *68*, 51–64. **DOI:**10.17344/acsi.2020.6090
41. R. M. Mohareb, F. M. Manhi, *A.* Abdelwahab, *Acta Chim. Slov*. **2020**, *67*, 83–95. **DOI:**10.17344/acsi.2019.5224
42. R. R. Covington, D. L. Temple, J. P. Yevich, Pat. Specif. (Aust.) **1985**, AU 541789 B2 19850117.
43. R. R. Covington, D. L. J. Temple, J. P. Yevich, Ger. Offen. **1979**, DE 2918085 A1 19791115.
44. P. N. Bhargava, S. C. Sharma, *Bull. Chem. Soc. Jap*. **1965**, *38*, 905–909. **DOI:**10.1246/bcsj.38.905
45. T. E. Achary, *J. Indian Chem. Soc.* **1975**, *52*, 1204–1206.

46. S. K. Sonwane, S. D. Srivastava, S. K. Srivastava, *Indian J. Chem.* **2008**, *47B*, 633–636.
47. S. K. Sonwane, *Proc. Natl. Acad. Sci., India, Section A: Phys. Sci.* **2008**, *78*, 129–136.
48. M. A. El-Maghraby, *Indian J. Chem*. **1974**, *12*, 1058–1059.
49. O. Tetu, *Bull. Soc. Chim. Fr*. **1966**, *1*, 342–345.
50. B. Dash, *J. Inst. Chem.* (India) **1979**, *51*, 151–155. **DOI:**10.1016/0022-2860(79)80287-2
51. T. Prashanth, B. R. V. Avin, P. Thirusangu; V. L. Ranganatha, B. T. Prabhakar, J. N. N. S.Chandra, S. A. Khanum, *Biomed. Pharmacother*. **2019**, *112*, 108707. **DOI:**10.1016/j.biopha.2019.108707
52. S. Bondock, A. E.-G. Tarhoni, A. A. Fadda, *J. Heterocycl. Chem.* **2014**, *51*, 249–255. **DOI:**10.1002/jhet.1677
53. X. Tang, J. Yang, Z. Zhu, M. Zheng, W. Wu, H. Jiang, *J. Org. Chem.* **2016**, *81*, 11461–11466. **DOI:**10.1021/acs.joc.6b02124
54. S. R. Pattan, A. M. Shamrez, J. S. Pattan, S. S. Purohit, V. V. K. Reddy, B. R. Nataraj, *Indian J. Chem.* **2006**, *45B*, 1929–1932.
55. A. Monks, D. Scudiero, P. Skehan, R. Shoemaker, K. Paull, D. Vistica, C. Hose, J. Langley, P. Cronise, A. Vaigro-Wolff, M. Gray-Goodrich, H. Campbell, J. Mayo, M. Boyd, *J. Natl. Cancer Inst*. **199**1, *83*, 757–766. **DOI:**10.1093/jnci/83.11.757
56. K. D. Paull, R. H. Shoemaker, L. Hodes, A. Monks, D. A. Scudiero, L. Rubinstein, J. Plowman, M. R. Boyd, *J. Natl. Cancer Inst*. **1989**, *81*, 1088–1092. **DOI:**10.1093/jnci/81.14.1088
57. L. H. Li, F.-L.Yu, *Biochem. Mol. Biol. Int.* **1993,** *31*, 879–887.

Povzetek

Načrtovanje in sinteza mnogih novih derivatov tiazola izhaja iz 4-feniltiazol-2-amina, zato smo raziskali reaktivnost te spojine z različnimi kemičnimi reagenti. Strukture novih spojin smo ugotovili na osnovi elementnih analiz in spektroskopskih podatkov. V nadaljevanju smo za dvajset spojin, ki smo jih sintetizirali, ugotovili opazno (v μM območju) protirakavo delovanje na tri različne človeške rakaste celične linije [MCF-7 (adenokarcinom dojke), NCI-H460 (nedrobnocelični pljučni rak) in SF-268 (CNS rak)] ter na celično linijo normalnih človeških fibroblastov (WI-38). Rezultati so pokazali, da sta spojini **9** in **14a** bolj učinkoviti kot pa referenčna spojina doksorubicin.

Scientific paper

Combined Application of MMT K10 Supported Copper Oxide Nanoparticles for Complete Removal of Cr(VI) from Aqueous Solution and their Antibacterial Potential

Mahesh Kumar Gupta,* Praveen Kumar Tandon, Mubashra Afroz and Saumya Agrahari[1]

Department of Chemistry, University of Allahabad, Prayagraj-211002, India

** Corresponding author: E-mail: mahesh27620@gmail.com*

Received: 11-27-2020

Abstract

Montmorillonite K10 (MMT K10) supported copper oxide nanoparticles (CuONPs) were synthesized by incorporating CuONPs onto the surface of MMT K10 by reducing the metal precursor with the help of hydrazine hydrate. Effects of various factors on the efficiency of composite to remove hexavalent chromium were studied to find out the optimum conditions for maximum removal. Under optimum conditions 15 mg of the synthesized nanocomposite was found capable to almost completely remove (99.9%) hexavalent chromium in 30 min from a 10 ppm aqueous chromium solution and that too in a wide range of pH from 2.88 to 5.56. The synthesized MMT K10 supported CuONPs were characterized by UV, SEM-EDX, FTIR and XRD studies. The average particle size of supported CuONPs was found to be 22.9 nm. Antibacterial potential of the prepared composite was also studied for one Gram-positive bacterium *Staphylococcus aureus* (ATCC 25323) and one Gram-negative bacterium *Pseudomonas aeruginosa* (ATCC 27853). The prepared nanocomposite was found to have excellent bactericidal potential and its statistical analysis was performed using *t*-test which indicates both bacterial strains of *Pseudomonas aeruginosa* and *Staphylococcus aureus* show different zone of inhibition for different concentrations.

Keywords: Montmorillonite K10; CuONPs; hydrazine hydrate; hexavalent chromium; bactericidal potential

1. Introduction

Recently water pollution due to heavy metals ions has become a serious concern because metal ions are non-biodegradable, accumulate easily in the environment and even in a low concentration cause adverse health hazards.[1] Presence of chromium in the effluents coming from paint, metal finishing, textile and dyeing, electroplating, and leather tanning industries[2] is of considerable concern due to its highly toxic, carcinogenic and mutagenic nature. It also has adverse effect on plant and animal tissues even at low concentrations.[3–5] Out of many, Cr(III) and Cr(VI) are the most stable oxidation states which are much different in their chemical and toxicological properties. Cr(VI) is more hazardous than Cr(III) species due to its greater water solubility, mobility and bio-accessibility.[6,7] Toxicity of trivalent chromium toward a living cell is 500–1000 times less than hexavalent chromium.[8] Exposure to chromium(VI) causes liver damage, pulmonary congestion, oedema, skin irritation and ulcer.[9]

Out of many techniques proposed for the removal of chromium(VI) from wastewater the extensively used techniques include chemical precipitation, ion exchange, coagulation, reverse osmosis, electrolysis, membrane process, chemical reduction, photocatalytic oxidation, evaporation and biosorption process.[10–15] All these methods have limitations in the sense that they often involve high capital and operational costs, require high energy consumption, and may produce secondary pollutants. Adsorption method has been found to be an attractive technique for the removal of pollutants from wastewater because of its flexibility and simplicity of design, cost effectiveness, eco-friendliness and high efficiency compared to other conventional methods. In addition, adsorption does not generate hazardous substances and avoids the secondary pollution. Due to all these properties adsorption technique has been

extensively applied for the removal of heavy metal ions from wastewater.[16–18]

Metallic nanoparticles have been extensively studied to be used to decontaminate aqueous solutions as compared to conventional adsorbents due to their nanosize which increases the surface area resulting in greater efficiency, faster rate of adsorption and easier separation after adsorption. Metal-based NPs have been found useful in antiviral, antibacterial, antifouling, and antifungal applications also.[19,20] Antibacterial activity of nanoparticles has been widely studied for human pathogenic bacteria *Pseudomonas aeruginosa* and *Staphylococcus aureus*. *Pseudomonas aeruginosa* is a multidrug-resistant pathogen known for its broad spectrum affecting both plants and animals and its infection mainly spreads during hospitalization, similar to ventilator-associated pneumonia and various sepsis syndromes while *Staphylococcus aureus* frequently found in the upper respiratory tract and on the skin. It can adapt to extreme changes in external oxygen concentration, able to grow even in the absence of oxygen and responsible for causing skin infections including abscesses, respiratory infections such as sinusitis, and food poisoning.[21]

The bactericidal property of nanoparticles depends on their size, shape, stability, and concentration added to the growth medium. Bacterial cell size usually lies in micrometer dimension, with pores of nanometer dimension in their outer cellular membranes. Nanoparticles having size less than that of pore size of the bacterial cell membrane, have a unique property of crossing the cell membrane and restrict bacterial growth.[22] Cu and CuO nanoparticles were analyzed as a plausible antibacterial agent for many pathogenic species like *E. coli*, *Bacillus subtilis*, *Vibrio cholera*, *Pseudomonas aeruginosa*, *Syphilis typhus*, and *Staphylococcus aureus*.[23] Addition of silver nanoparticles imparts antimicrobial properties in household products[24,25] and growth of *Escherichia coli* and *Bacillus subtilis* is inhibited by adding copper nanoparticles (CuNPs)[26,27] probably due to interactions with -SH groups leading to protein denaturation.[28] Copper also shows a dual capacity to act as a cofactor and biocatalyst with a critical balance for proper intracellular metal homeostasis and metabolism.[29,30] Metal oxide nanoparticles are 7–50 times less toxic towards mammalian cells compared to ionic forms of respective metals.[9] CuO nanoparticles show excellent antibacterial activity against *Klebsiella pneumoniae, Pseudomonas aeruginosa*, *Salmonella paratyphi* and *Shigella* strains,[31] reduce (99.9%) concentrations of *E. coli* and *S. aureus* after 24 h of incubation.[32] CuO nanoparticles synthesized with a *Streptomyces* species[33] and naturally obtained gum karaya[23] showed excellent reduction of *E. coli, S. aureus, and Aspergillus niger*. Polyaniline coated Cu_2O nanoparticles[34] and have been found to be effective against Gram-positive and Gram-negative bacteria.[22]

Difference in the outermost protective covering of Gram-positive and Gram-negative bacteria may also be a reason for their changed response towards various bactericidal agents. Vast majority of bacteria follow the color differentiation by giving different staining intensity by the Gram technique and this leads to classify bacteria in two major groups, Gram-negative and Gram-positive bacteria. In Gram staining the decolorizing step with alcohol washes the primary stain (crystal violet) from the cells and the secondary stain colors the bacteria red. In contrast Gram-positive bacteria are covered with strong and thick cell walls which do not allow the crystal violet to be removed and thus remain purple.[35] There are many distinguishing features between the Gram-positive and Gram-negative bacteria. Characteristic feature for both classes is that their cytoplasmic membrane is surrounded by a cell wall. Periplasm contains a wide variety of ions and proteins that are needed for numerous functions involving cellular (electron) transport, substrate hydrolysis, degradation and detoxification.

In Gram-negative bacteria the periplasm occupies the space between the plasma membrane and the outer membrane. Existing above the plasma membrane and the outer membrane the periplasm is an integral compartment of the gram-negative cell wall.[36] Outer membrane, peptidoglycan layer, and periplasm along with plasma membrane constitute the gram-negative envelope.[36,37] The presence of the outer membrane in Gram negative bacteria next to the periplasmatic space is the major difference between those bacterial classes as it does not exist in Gram-positive bacteria. This outer membrane is a lipid bilayer, where the inner leaflet is composed of phospholipids and the outer leaflet of lipopolysaccharides.[38] In both families, the cell wall contains peptidoglycan layers that stabilize the cell membranes. The cell wall of Gram-positive bacteria is made of many peptidoglycan layers of about 40–80 nm that is much thicker than the single layered 7–8 nm thick cell wall of Gram-negative bacteria.[39] Therefore, the periplasmic space between the inner and outer membrane in Gram-negative bacteria is much larger than the narrow periplasm of Gram-positive bacteria. Also specific for Gram-positive bacteria is the occurrence of teichoic acid in the cell wall that can be linked via a glycolipid anchor with the plasma membrane. Gram-positive bacteria have larger fraction of negatively charged phosphatidylglycerol whereas Gram-negative bacteria contain larger proportions on zwitterionic phosphatidylethanolamine in addition to phosphatidylglycerol. Presence of different charges on the surface may influence the bactericidal potential also. Peptidoglycan, due to its rigidity determines the strength and cellular shape of bacteria and accounts for around 90% of dry weight in Gram-positive and 10% in Gram-negative bacteria.

To obtain better capacity to remove chromium(-VI) from the contaminated water copper oxide nanoparticles, synthesized with the help of hydrazine hydrate, were supported on MMT K10. Montmorillonite K10 was selected as a supporting material due to its unique properties of

cation exchange and swelling ability in addition to its low cost and eco-friendly nature. It was also observed that copper oxide nanoparticles supported on MMT K10 showed excellent capacity to remove chromium(VI) from the contaminated water compared to the unsupported ones. The interlayer space of montmorillonite provides a very good platform to accommodate the nanoparticulates. Prepared copper oxide nanoparticles were characterized with the help of SEM-EDX, XRD and FTIR spectroscopy. Antibacterial nature of the nanocomposite for one Gram-positive bacterium *Staphylococcus aureus* (ATCC 25323) and one Gram-negative bacterium *Pseudomonas aeruginosa* (ATCC 27853) was also studied. Statistical analysis of two-tailed *t*-test was also performed to show bacteria have different zone of inhibition at different concentrations.

2. Experimental

2. 1. Materials and Methods

To get the solutions of desired strengths the stock solutions of $K_2Cr_2O_7$ and $CuSO_4.5H_2O$ (Merck) were diluted with double distilled water. Montmorillonite K10 (Sigma-Aldrich) was of the highest purity. All other chemicals like hydrazine hydrate, 1,5-diphenylcarbazide (LobaChemie), H_2SO_4, HCl and NaOH (Merck), Luria bertani broth, miller (SRL) and agar-agar (Fisher Scientific) were of Analytical grade or chemically pure substances which were used without further purification.

2. 2. Preparation of Clay-Supported Copper Oxide Nanocomposites (CuONC)

500 mg montmorillonite K10 was added to 10 mL (0.10 M) copper sulphate solution and after heating the solution to 60 °C for 20 min, hydrazine hydrate (0.5 mL) solution was added drop-wise over 5 min with constant stirring. Change in the colour of solution from blue-brown to black[40] indicates the formation of copper nanoparticles which in the presence of dissolved oxygen in water get oxidized to copper oxide nanoparticles. It is important to mention here that addition of 0.5 mL hydrazine hydrate to 10 mL copper sulphate solution of the mentioned strength is necessary for getting the best results. Deviation of this ratio decreases the removal efficiency of the composite. It was observed that increase in the amount of hydrazine hydrate results in the appearance of precipitate in the solution while if the lesser amount is added then proper colour change is not observed. Stirring was continued for an additional 60 min. UV-Vis spectrum of the solution showed two peaks, one of the peak is situated at 243 nm while the other one at 630 nm. The peak situated at 243 nm is due to the Cu_2O shell layer of the Cu-Cu_2O (Copper core-copper oxide shell nanoparticles) while that of peak around 630 nm correspond to the conversion of upper shell layers of the Cu_2O into more thermodynamically stable CuO layers. Appearance of the peaks in solution (Figure 1) confirmed[41,42] the formation of MMT K10 supported CuONPs.

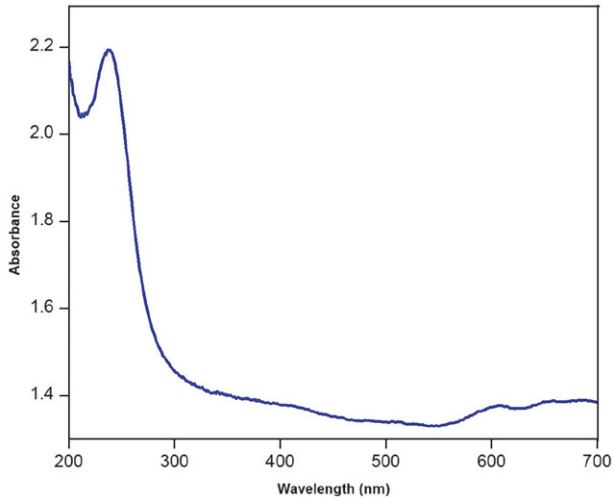

Figure 1: UV-Visible spectra of CuONPs

2. 3. Instrumentation and Measurement of Chromium

The amount of Cr(VI) remaining in the filtrate was measured with a double beam spectrophotometer (Systronics 2203). Standard solutions of NaOH and HCl were used to maintain the desired pH of the solution which was measured along with temperature with a digital pH meter (μ-pH System 361, Systronics). IR spectra were recorded on a spectrum 2 Perkin Elmer spectrophotometer version 10.4.00 FTIR spectrophotometer. SEM analysis was carried out using a JEOL (JSM 6490 LV) scanning electron microscope equipped with EDAX after coating the samples with platinum to investigate the morphological changes in MMT K10 before and after being loaded with CuONPs. Powder X-ray diffraction (PXRD) analysis was carried out using Rigaku Smart lab 3KW to obtain structural information. The surface areas of samples under varying conditions were calculated using a WT Classic Brunaur, Emmett and Teller (BET) surface area analyzer, WAKO, New Delhi India. Luria-Bertani (LB) agar solution was autoclaved with Vertical Autoclave (Metrex), all plating and inoculations were done inside a Vertical Laminar Air Flow (Impact Icon Instruments Company) and inoculated plates were incubated inside BOD Incubator (Metrex Scientific Instruments).

2. 4. Analysis of Remaining Cr(VI) By 1,5-Diphenylcarbazide (DPC) Method

In solution phase Cr(VI) strongly complexes with 1,5-diphenyl carbazide to give a dark pink chromium-diphenyl carbazide complex which absorbs strongly at 540

nm.[43] Stock solution of diphenyl carbazide was prepared by dissolving 250 mg of 1,5-diphenyl carbazide in 50 mL acetone and the solution was kept at 5 °C in freezer. In a typical procedure the calculated concentration of Cr(VI) solution mixed with 0.8 ml of H_2SO_4 (6N) and 1 mL DPC was diluted up to mark in a 25 mL flask. Solution was left for 10 min to develop the colour of Cr-DPC complex, intensity of which depends on the concentration of Cr(VI) in solution. Thus the remaining concentration of Cr(VI) is determined directly with the help of a standard calibration graph plotted between concentration vs. absorbance.

$$\% \text{ removal of contaminant} = \frac{C_i - C_f}{C_i} \times 100$$

where C_i and C_f are initial and final concentrations of contaminant

Stock solution of $K_2Cr_2O_7$ was diluted with double distilled water to get the solutions of desired concentrations. Calculated amount of MMT K10 supported CuNPs (MMT-CuNPs) was added to the stirred solution of Cr(VI). Stirring was continued for a fixed time and then the solution was filtered. Remaining Cr(VI) in the solution was measured with DPC method. To find out the optimum conditions effects of duration of treatment, amount of CuONC, pH, and initial Cr(VI) concentration were studied by changing the variables one by one keeping other factors constant. In all the cases, 10.0 mL of 0.1 M $CuSO_4$ $5H_2O$ and 0.5 mL of hydrazine hydrates were mixed. All experiments were conducted at room temperature.

2. 5. Antibacterial Activity

Gradual increase of resistance in microorganisms against drugs has increased the interest for the synthesis and utilization of novel antimicrobial metal nanoparticles.[44] Using disc diffusion method antibacterial activity of synthesized CuONPs against *Staphylococcus aureus* (ATCC 25323) and *Pseudomonas aeruginosa* (ATCC 27853) bacteria was studied. In all cases, 10.0 mL of 0.1 M $CuSO_4 \cdot 5H_2O$ solution and 0.5 mL of hydrazine hydrates were mixed for the synthesis of CuONPs. Different molar concentrations of 40 mg/mL, 60 mg/mL, 80 mg/mL, and 100 mg/mL of CuONPs were used to determine the zone of inhibition of aforementioned bacterial strains. Control experiments were carried out in the presence of DMSO solvent. Experiments were performed after sterilizing all the equipment and Luria Bertani agar solution in an autoclave at 121 °C for at least 15 minutes under the pressure of 15 psi. For preparation of Luria Bertani agar solution, 2.5 gm of Luria Bertani Broth, Miller and 2 gm of agar-agar were mixed in 100 ml of distilled water thoroughly and then autoclaved. In brief, 20 ml of Luria-Bertani agar solution (pH 7.2 at 60 °C) was poured onto the petriplates and then put to solidification for 20 minutes. The wells were made by using 5 mm gauge which were punched out in petriplates. With the help of micropipette, different concentrations of CuONPs samples i.e., 40 mg/mL, 60 mg/mL, 80 mg/mL, 100 mg/mL were poured into the wells on all petriplates. The petriplates were incubated at 37 °C for 24 h. The size of zone of inhibition was measured by ruler.

3. Results and Discussion

3. 1. Factors Affecting the Removal of Hexavalent Chromium

In order to find out the optimum conditions for maximum removal of Cr(VI) various factors affecting the removal were changed one by one keeping other conditions constant. Result of the change of time of treatment on the removal efficiency is given in Table 1(entries 2–6) and Figure **2A**. Constancy in the efficiency of removal of contaminant at later stages may be due to the relative sizes of contaminant and pores if the size of contaminant is small then stirring for longer duration may not be able to expel the particles from the pores. This may be due to the attainment of the saturation point on achieving almost complete removal. pH of the chromium solution was maintained with the help of standard solutions of sulphuric acid and sodium hydroxide. Removal efficiency of the composite remains constant from pH 2.56 to 5.6 but later on the removal efficiency decreases (Table 1, entries 7 to 10 and 5; Figure **2B**). Probably after a particular pH surface of MMT K10 becomes negatively charged and electrostatic repulsion between the negatively charged surface and the contaminants decreases the efficiency of the composite to remove the contaminants. Effect of increase in the concentration of Cr(VI) sample on the removal efficiency shown in Figure **2C** (Table 1, entries 11 to 14 and 5) may be because of the reason that further increase in the concentration of contaminants beyond the capacity of a particular amount of composite having fixed active sites will not affect the removal and the excess ions of the contaminant will remain in the solution thus decreasing the percentage of removal. It was observed that increase in the amount of nanocomposite increases the removal efficiency till almost complete removal of chromium is obtained (Table 1, 15 to 18 and 5; Figure **2D**). Effect of change of the amount of HH on the removal efficiency (Table 1, entries 19 to 22 and 4; Figure **2E**) may be considered in conjunction with the effect of change of pH of the medium. Initial increase in the amount of HH increases the number of nanoparticles formed which increase the removal efficiency till a maximum is obtained for a fixed amount of copper sulphate. Addition of further HH increases pH of the medium and results of change of pH of the medium clearly show that increase in pH above the optimum value has a negative effect on the efficiency of removal. To determine the effect of loading of CuONC on the solid support, ratio of the amounts of copper sulphate and hydrazine hydrate

Table 1: Effect of various factors on the removal of Cr(VI) from contaminated water (In all the cases 25.0 mL Cr(VI) solution was taken)

S. No.	Time (min)	pH	Conc (ppm)	Amount of nano-composite	Volume of H.H	Reaction volume [$CuSO_4$ $5H_2O$+ H.H] (mL)	Amount of MMT K 10 (mg)	% removal
1.	30	5.56	10	–	–	–	15	11.0
2.	05	5.56	10	15	0.5	10 + 0.5	500	73.3
3.	10	5.56	10	15	0.5	10 + 0.5	500	85.0
4.	20	5.56	10	15	0.5	10 + 0.5	500	98.0
5.	30	5.56	10	15	0.5	10 + 0.5	500	99.9
6.	40	5.56	10	15	0.5	10 + 0.5	500	99.8
7.	30	2.58	10	15	0.5	10 + 0.5	500	99.8
8.	30	4.58	10	15	0.5	10 + 0.5	500	99.8
9.	30	7.59	10	15	0.5	10 + 0.5	500	93.0
10.	30	10.52	10	15	0.5	10 + 0.5	500	11.0
11.	30	5.56	02	15	0.5	10 + 0.5	500	99.5
12.	30	5.56	05	15	0.5	10 + 0.5	500	99.5
13.	30	5.56	15	15	0.5	10 + 0.5	500	92.0
14.	30	5.56	20	15	0.5	10 + 0.5	500	89.0
15.	30	5.56	10	05	0.5	10 + 0.5	500	32.5
16.	30	5.56	10	10	0.5	10 + 0.5	500	77.9
17.	30	5.56	10	12	0.5	10 + 0.5	500	91.8
18.	30	5.56	10	18	0.5	10 + 0.5	500	99.8
19.	30	5.56	10	15	0.2	10 + 0.5	500	80.0
20.	30	5.56	10	15	0.3	10 + 0.5	500	86.0
21.	30	5.56	10	15	0.4	10 + 0.5	500	93.5
22.	30	5.56	10	15	0.6	10 + 0.5	500	99.1
23.	30	5.56	10	15	0.5	4.0 + 0.2	500	38.3
24.	30	5.56	10	15	0.5	6.0 + 0.3	500	51.3
25.	30	5.56	10	15	0.5	8.0 + 0.4	500	80.6
26.	30	5.56	10	15	0.5	12 + 0.6	500	98.1

was varied (Table 1, entries 23 to 26 and 5; Figure **2F**). It was observed that use of 10.0 mL of copper sulphate mixed with 0.5 mL of hydrazine hydrate with addition of 500.0 mg of MMT K10 gave the best results. It may be mentioned that proper colour change was not observed if the ratio of HH and copper sulphate was decreased from 1:20, while formation of suspended particles takes place if the ratio is increased. Proper formation of CuONPs takes place only when 0.5 mL of HH was used to reduce 10 mL (0.1 M) solution of copper sulphate. Maximum yield of 99.9 % for Cr(VI) was obtained only when 1:20 ratio is maintained. Coming to the control experiment negligible (11%) removal of chromium(VI) was observed (Table 1, entry 1) when the experiment was performed only by adding MMT K10 in the contaminated water. This indicates that the clay mineral mainly helps in preventing the agglomeration of CuONPs prepared during the process and has no role in the removal of Cr(VI) from the contaminated water.

3. 2. Powder X-Ray Diffraction Pattern Study

Powder X-ray diffraction patterns of pure MMT K10 and MMT K10 supported CuO nanoparticles are shown in Figure 3. Peaks at 2θ = 20.95 and 26.60 obtained in pure MMT K10 are due to quartz impurity.[45] In MMT K10 supported CuO nanoparticle peaks at 32.70, 35.48, 53.8, 61.8 are due to crystalline CuO which correspond well with the (110), (110), (020) and (–113) planes of the monoclinic copper(II) oxide phase (tenorite, ICSD #01-089-2529).[46] The average size of MMTK10 supported CuO nanoparticles was found to be 22.9 nm which was calculated by using the Debye-Scherrer equation.

$$D = \frac{0.9 \times \lambda}{\beta \times Cos\,\theta}$$

Where D shows crystallite size, λ- wavelength and β- peak width (FWHM).

3. 3. Scanning Electron Microscopy-Energy Dispersive X-ray Analysis

SEM analysis of pure MMT K10 (Figure **4A**) shows asymmetrical particles while EDX spectrum (Figure **4B**) shows Si, O, Al and Mg as the main constituent in decreasing order of concentration.[47] SEM and EDX given in Figure **4C** and **4D** clearly shows that the irregular shape of CuONPs particles are accommodated on MMT K10 surface. The study also confirmed that the synthesized nanoparticles are supported on the surface of the MMT K10 by integration of metal in interlayer present on MMT K10 and are stabilized by the electronic alterations and Vander

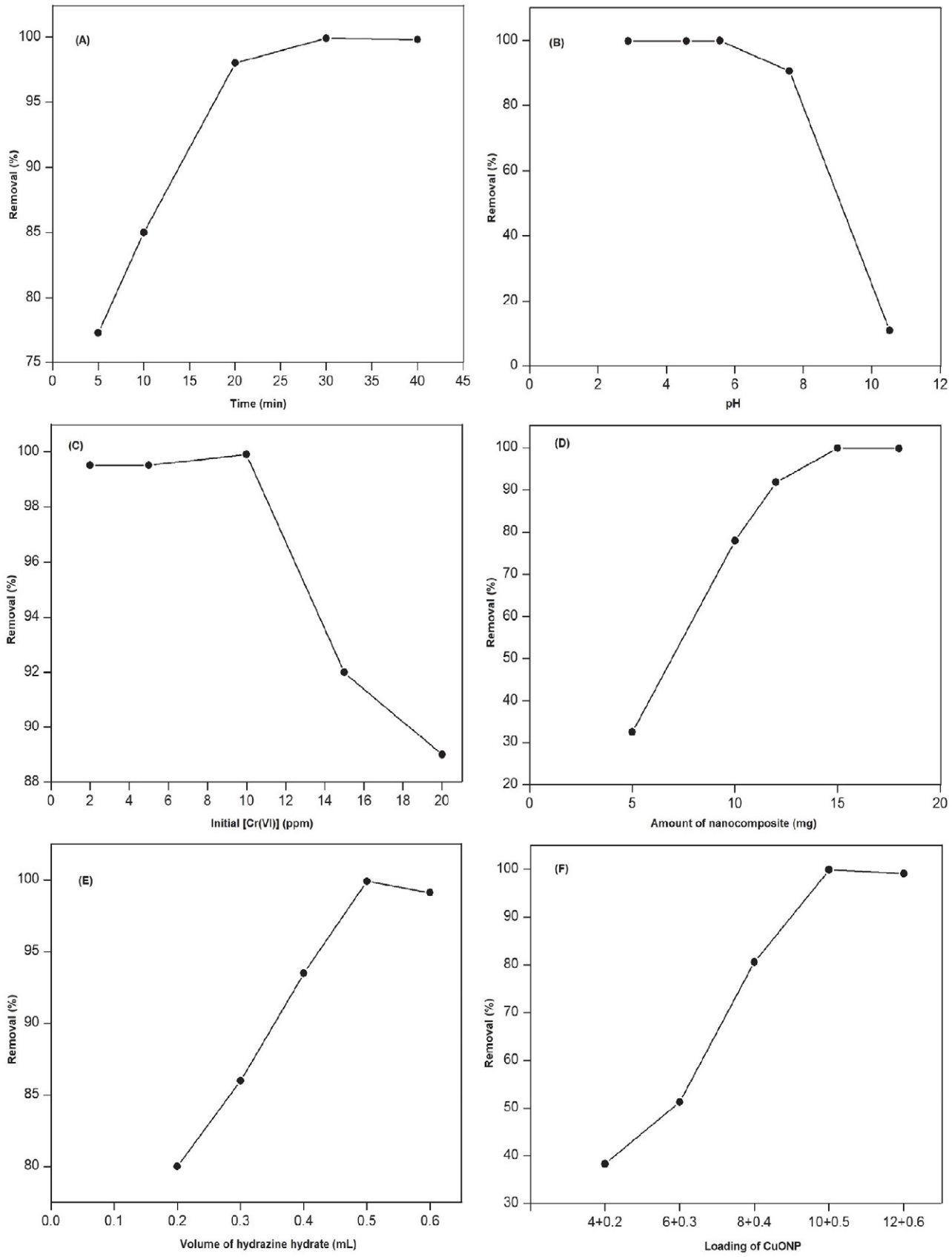

Figure 2: Effect of various factors on the removal of Cr(VI) (A) Duration of experiment, (B) pH (C) Initial Cr(VI) concentration (D) Amount of nano-composite (E) Volume of hydrazine hydrate (F) Loading of CuONP on the support

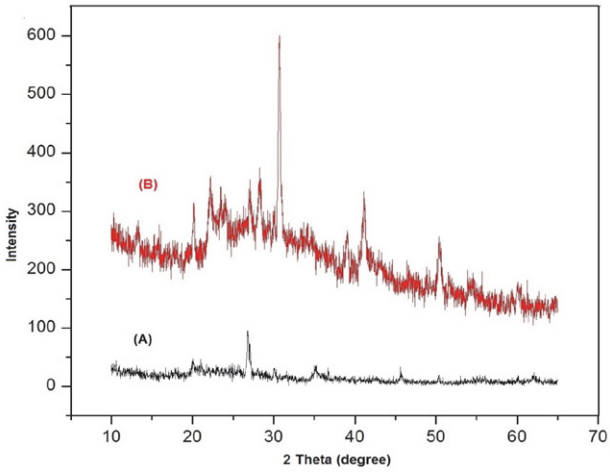

Figure 3: PXRD pattern of (A) pure MMT K10, (B) MMT K10 supported copper oxide nanoparticles

Waals interactions. The EDX study for elemental composition confirmed the presence of the constituent elements O, Si, Mg, Al, and Cu in reduction method. Removal of Cr(VI) was confirmed by taking SEM-EDX of the composite after the treatment of contaminated samples (Figure **4E** and **4F**). The SEM image shows many aggregates of nanoparticles with the adsorbent particles which resulted in a rough surface and porous structure. In EDX study appearance of the extra peak for chromium along with peaks corresponding to O, Si, Al, Cu confirmed the removal of chromium.

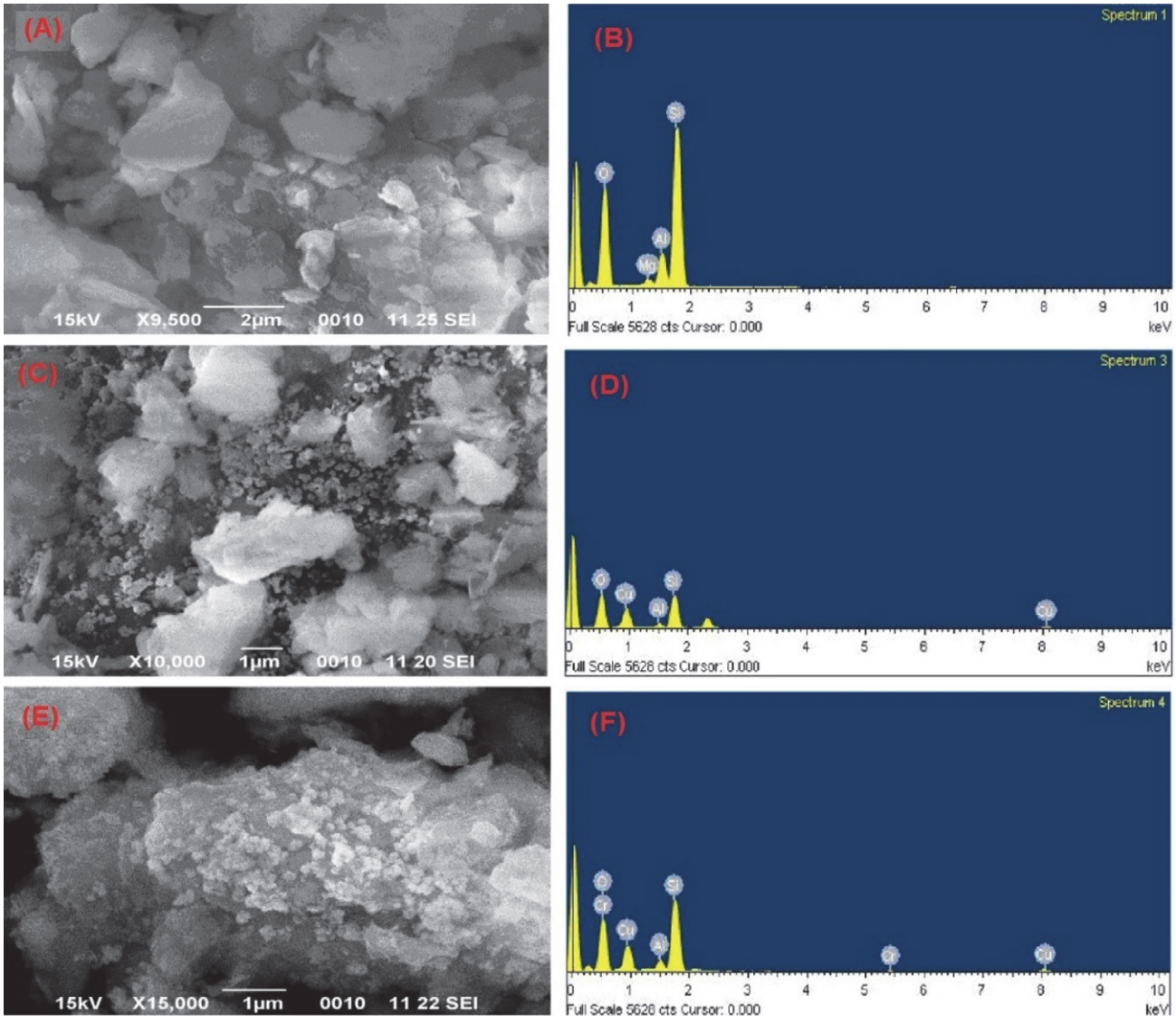

Figure 4: (A) SEM image of pure MMT K10 (B) EDX image of pure MMT K10 (C) SEM image of MMT K10 supported CuONPs (D) EDX image of MMT K10 supported CuONPs (E) SEM image of MMT K10 supported CuONPs after removal of Cr(VI) (F) EDX image of MMT K10 supported CuONPs after removal of Cr(VI)

3. 4. Fourier Transform Infrared Spectroscopy

In FTIR spectra of MMT K10 (Figure **5A**) peaks obtained at 455.60 cm^{-1}, 526.79 cm^{-1} are attributed to Si-O bending and peak at 796.15 cm^{-1} is due to Si-O deformation. Peaks at 1031.90 cm^{-1} and 1210.10 cm^{-1} can be attributed to Si-O stretching. Peak at 920 cm^{-1} is due to (Al, Mg)-OH vibration mode. Peak at 3622.20 cm^{-1} corresponds to O-H stretching at 1367.0 cm^{-1} due to atmospheric CO_2. FTIR spectra of CuONPs supported on MMT K10 (Figure **5B**) shows peak similar to those as obtained in pure MMT K10 with slight shifting in the wave number and intensity. New peak at 613.49 cm^{-1} is observed which is attributed to Cu-O stretching the FTIR spectra confirms loading of CuONPs on the surface of MMT K10.[48–52] FTIR spectra of CuONPs after the removal of chromium (Figure **5C**) shows disappearance of peak at 613.49 cm^{-1} (due to involvement of Cu-O in adsorption of chromium) along with the shifting and decrease in intensity of other peaks compared to MMT K10 supported CuONPs confirms the adsorption of chromium by CuONPs from the solution.

3. 5. Antibacterial Activity of MMT-CuONC Against Gram –ve and Gram +ve Bacteria

The prepared nanoparticles show excellent antibacterial activity against two bacterial strains, one Gram-positive bacterium *Staphylococcus aureus* (ATCC 25323) and one Gram-negative bacterium *Pseudomonas aeruginosa* (ATCC 27853). In all cases, 10.0 mL of 0.1 M $CuSO_4 \cdot 5H_2O$ solution and 0.5 mL of hydrazine hydrates were mixed for the synthesis of CuONPs. It may be mentioned that if the size of nanoparticles is less than that of pore size of the cell membrane of bacteria then they can cross the cell membrane without any hindrance. Control experiments were performed only with MMT K10. It was found that MMT K10 of same concentration shows no capability for antibacterial activity which is clear from Figure 6(A) and 7(A).

The antibacterial activity of CuONPs shows better results against *Pseudomonas aeruginosa* where a maximum zone of inhibition was observed at 39 mm at 100 mg/mL [Figure 6 (B)] in comparison to *Staphylococcus aureus* where a maximum zone of inhibition of 37 mm, at 100 mg/mL [Figure 7 (B)] was observed.

Different molar concentrations of MMT-CuONC are very important in antibacterial activity. Maximum zone of inhibition was observed with different molar concentration of CuONC against *Pseudomonas aeruginosa* while less inhibitory action of CuONC was observed for *Staphylococcus aureus*. On increasing the concentration of CuONC, better inhibitory action can be seen against both Gram-positive *Staphylococcus aureus* and Gram-negative *Pseudomonas aeruginosa* bacteria. Table 2 confirm the results.

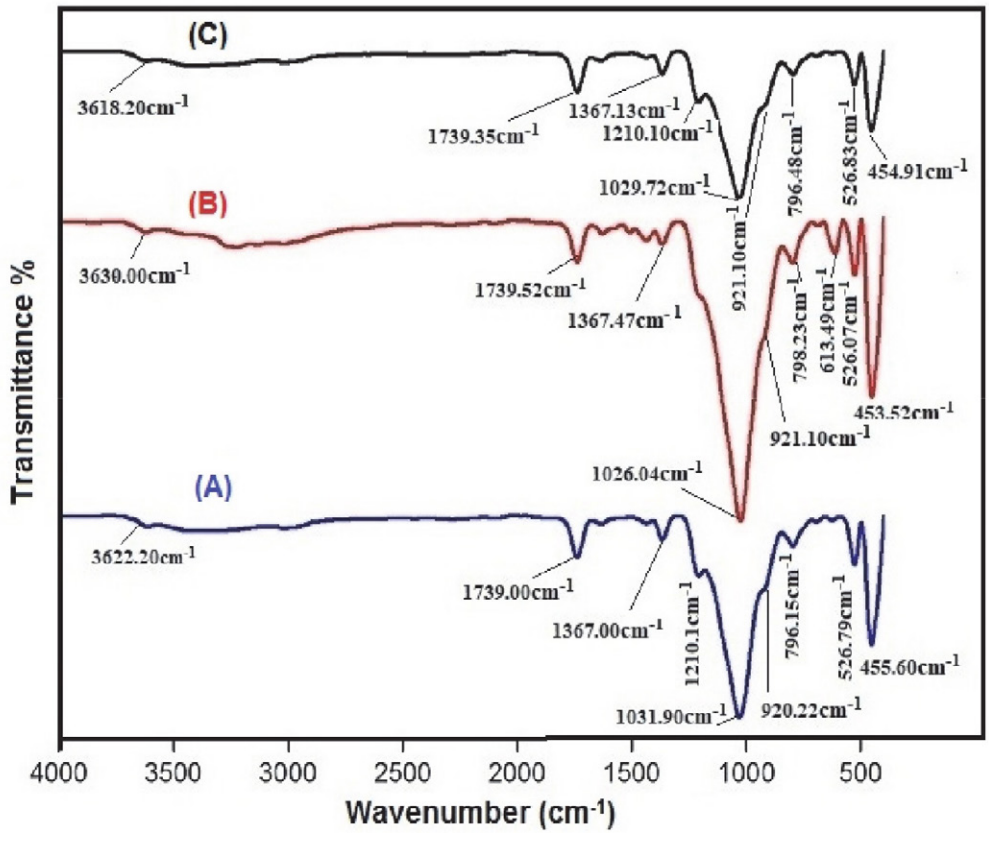

Figure 5: FTIR spectra of (A) MMT K10, (B) loading of CuO nanoparticles, (C) removal of hexavalent chromium

Table 2: Maximum zone of inhibition of different concentration of MMT-CuONC against Gram -ve and Gram +ve bacteria

Microorganisms			CuONPs concentrations (mg/mL)	Maximum Zone of Inhibition (In mm)
Species of Bacteria	**Category of Bacteria**	**Strain**		
Pseudomonas aeruginosa	Gram -ve	ATCC 27853	40	32
			60	34
			80	36
			100	**39**
Staphylococcus aureus	Gram +ve	ATCC 25323	40	18
			60	21
			80	35
			100	**37**

Statistical measurements of zone of inhibition of two bacteria *Pseudomonas aeruginosa* and *Staphylococcus aureus* having standard deviations 35.25 ± 2.98 and 27.75 ± 9.63 was investigated by a two-tail *t*-test of alpha = 0.05 and 6 degree of freedom (df), with a null hypothesis that no differences in the diameters of zone of inhibition for different concentrations of both bacteria where the calculated value of *t* greater than the critical value for *t*, leads to acceptance of the null hypothesis. As mentioned in Table 3, the calculated value of $t = 1.48643622$ which is less than that of the critical value of $t = 2.446911851$ leading to rejection of null hypothesis implying that Gram –ve bacterium *Pseudomonas aeruginosa* and Gram +ve bacterium *Staphylococcus aureus* has different zones of inhibition at different concentrations of CuONC.

Table 3: Statistical measurements of the diameter of zone of inhibition of four samples of *Pseudomonas aeruginosa* and *Staphylococcus aureus* by implying two-tail *t*-test.

***t*-test**	***Pseudomonas aeruginosa***	***Staphylococcus aureus***
Mean	35.25	27.75
Variance	8.916666667	92.91666667
Observations	4	4
Pooled Variance	50.91666667	
Hypothesized Mean Difference	0	
df	6	
t Stat	**1.48643622**	
P(T<=t) one-tail	0.093858141	
t Critical one-tail	1.943180281	
P(T<=t) two-tail	0.187716282	
t Critical two-tail	**2.446911851**	

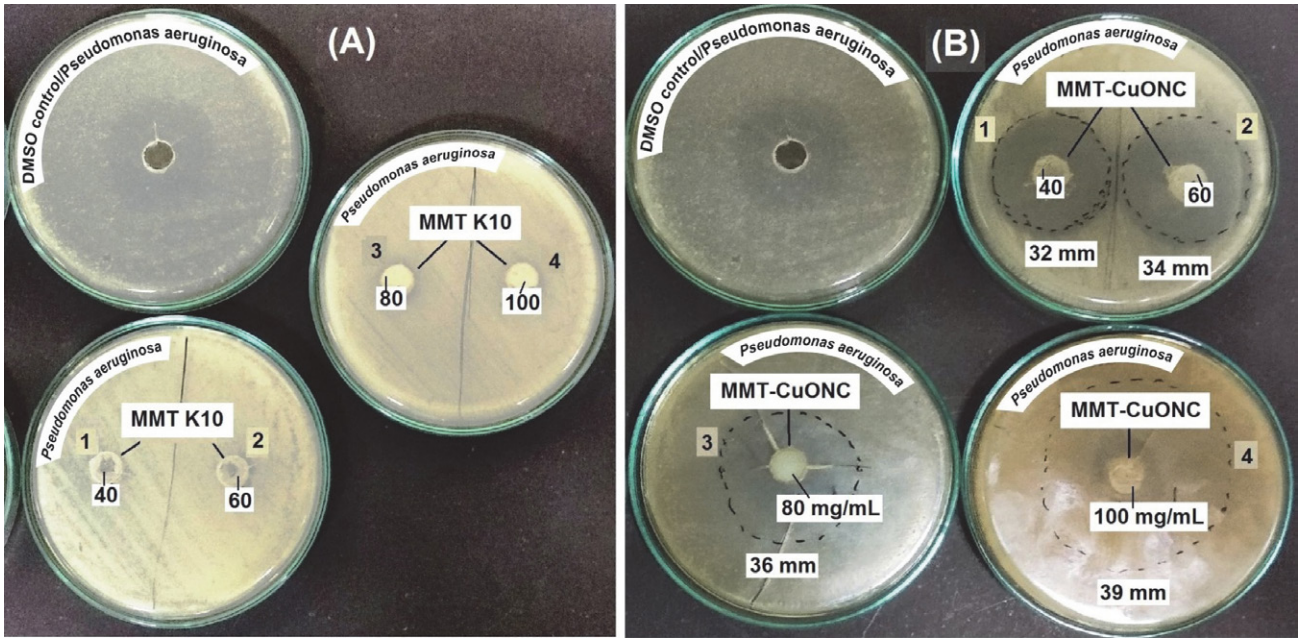

Figure 6: Zone of inhibition of MMT K10 (A) and synthesized MMT supported copper oxide nanoparticles (B) against *Pseudomonas aeruginosa* (Gram negative) at different concentrations (40, 60, 80, 100 mg/mL)

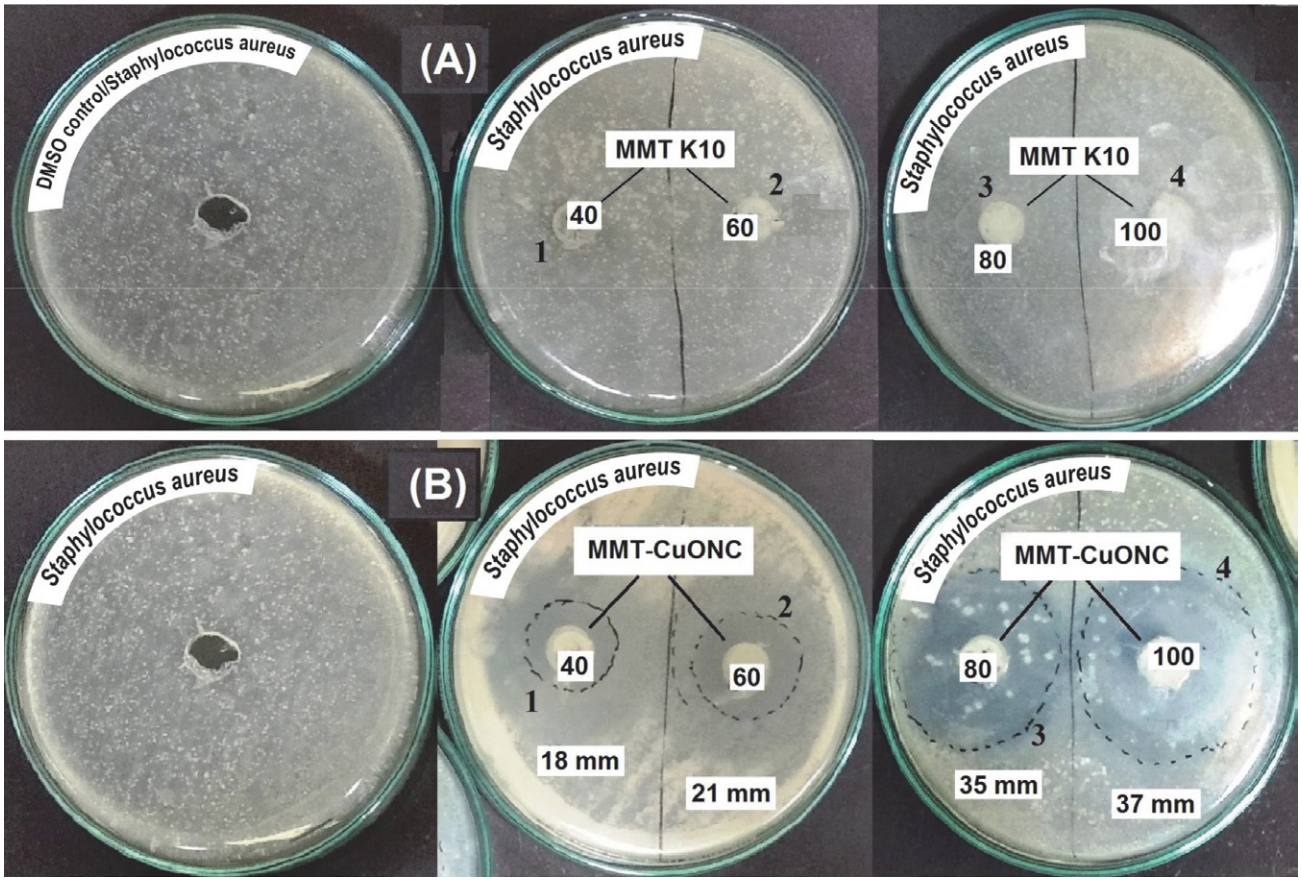

Figure 7: Zone of inhibition of MMT K10 (A) and synthesized MMT supported copper oxide nanoparticles (B) against *Staphylococcus aureus* (Gram positive) at different concentrations (40, 60, 80, 100 mg/mL)

4. Conclusions

In the present study CuONPs, having an average size of 22.9 nm, supported on MMT K10 were synthesized and the prepared nanocomposite was used to remove chromium(VI) from the contaminated water. Antibacterial efficiency of the prepared nanocomposite was also studied against two bacterial strains. It was observed that MMT K10 apart from acting as a stabilizing agent increases the efficiency of CuONC also. Most important observation which to the best of our knowledge has not been reported till now that the synthesized CuONC was able to almost completely (99.9%) remove chromium(VI) from the contaminated water in a very wide pH range of 2.58 to 5.56 and that too within 30 min. Maximum removal of Cr(VI) (99.9%) was obtained at pH 5.56. The nanocomposite showed good antibacterial activity against two bacterial strains, *Staphylococcus aureus* and *Pseudomonas aeruginosa*. 39 mm and 37 mm zones of inhibition at 100 mg/mL were observed in case of *P. aeruginosa* and *S. aureus* respectively. Thus, the prepared nanocomposite has good potential for killing the reported bacterial strains. Moreover, the statistical analysis of two-tail *t*-test also shows that both bacteria have different zone of inhibition for different concentrations of CuONC.

Acknowledgement

Authors thank MNNIT, Prayagraj for XRD, MNIT, BBAU, Lucknow for SEM-EDX and MNIT, Jaipur for FTIR facilities. Author thank U.G.C; New Delhi for the financial support to carry out this work.

5. References

1. J. V. M, R. R, M. Thomas, J. T. Varkey,*Mater. Today Proc.***2019,** *9,* 27–31. **DOI:**10.1016/j.matpr.2019.02.032
2. S. Avudainayagam, M. Megharaj, G. Owens, R. S. Kookana, D. Chittleborough, R. Naidu, *Rev. Environ. Contam. Toxicol.* **2003,** *178,* 53–91. **DOI:**10.1007/0-387-21728-2_3
3. G. López-Téllez, C. E. Barrera-Díaz, P. Balderas-Hernández, G. Roa-Morales, B. Bilyeu, *Chem. Eng. J.* **2011,** *173,* 480–485. **DOI:**10.1016/j.cej.2011.08.018
4. M. Costa, C. B. Klein, *Crit. Rev. Toxicol.***2006,** *36,*155–163. **DOI:**10.1080/10408440500534032
5. Z. Cheng, A. L. K. Tan, Y. Tao, D. Shan, K. E. Ting, X. J. Yin, *Int. J. Photoenergy.***2012,** 1–5. **DOI:***10.1155/2012/608298*
6. E. Sahinkaya, A. Kilic, *Water Res.* **2014,** *50,* 278–286. **DOI:**10.1016/j.watres.2013.12.005
7. J. H. Chen, K. C. Hsu, Y. M. Chang, *Ind. Eng. Chem. Res.*

2013, *52,* 11685–11694. **DOI:**10.1021/ie401233r
8. M. Costa, *Toxicol. Appl. Pharmacol.* **2003,** *188,* 1–5.
9. H. Ma, J. Zhou, L. Hua, F. Cheng, L. Zhou, X. Qiao, *J. Clean. Prod .***2016**. **DOI:**10.1016/j.jclepro.2016.10.193.
10. L. Ben Tahar, M. H. Oueslati, M. J. A. Abualreish, *J. Colloid Interface Sci.* **2018,** *512,* 115–126. **DOI:**10.1016/j.jcis.2017.10.044
11. M. A. Barakat, *Arab. J. Chem.* **2011,** *4,* 361–377. **DOI:**10.1016/j.arabjc.2010.07.019
12. A. S. Dharnaik, P. K. Ghosh, *Environ. Technol.* **2014,** *35,* 2272–2279. **DOI:**10.1080/09593330.2014.902108
13. A. Mnif, I. Bejaoui, M. Mouelhi, B. Hamrouni, *Int. J. Anal. Chem.* **2017,** 1–10. **DOI:**10.1155/2017/7415708
14. A. K. Golder, A. K. Chanda, A. N. Samanta, S. Ray, *Sep. Sci. Technol.* **2007,** *42,*2177–2193. **DOI:**10.1080/01496390701446464
15. Ihsanullah, A. Abbas, A. M. Al-Amer, T. Laoui, M. J. Al-Marri, M. S. Nasser, M. Khraisheh, M. A. Atieh, *Sep. Purif. Technol.* **2016,** *157,* 141–161. **DOI:**10.1016/j.seppur.2015.11.039
16. B. Biškup, B. Subotić, *Sep. Sci. Technol.* **2005,** *39,* 925–940. **DOI:**10.1081/SS-120028454
17. A. B. Moradi, H. M. Conesa, B. H. Robinson, E. Lehmann, A. Kaestner, R. Schulin, *Environ. Pollut.* **2009,** *157,* 2189–2196. **DOI:**10.1016/j.envpol.2009.04.015
18. K. Zare, V. K. Gupta, O. Moradi, A. S. H. Makhlouf, M. Sillanpää, M. N. Nadagouda, H. Sadegh, R. Shahryari-ghoshekandi, A. Pal, Z. Wang, I. Tyagi, M. Kazemi, *J. Nanostructure Chem.* **2015,** *5,* 227–236. **DOI:**10.1007/s40097-015-0158-x
19. S. L. Percival, P. G. Bowler, J. Dolman, *Int. Wound J.* **2007,** *4,* 186–191. **DOI:**10.1111/j.1742-481X.2007.00296.x
20. N. Cioffi, L. Torsi, N. Ditaranto, G. Tantillo, L. Ghibelli, L. Sabbatini, T. Bleve-Zacheo, M. D'Alessio, P. G. Zambonin, E. Traversa, *Chem. Mater.* **2005,** *17,* 5255–5262. **DOI:**10.1021/cm0505244
21. M. Masalha, I. Borovok, R. Schreiber, Y. Aharonowitz, G. Cohen, *J. Bacterio.* **2001,** *183,* 7260–7272. **DOI:**10.1128/JB.183.24.7260-7272.2001
22. V. V. T. Padil, M. Černík, *Int. J. Nanomedicine*, **2013,** *8,* 889–898.
23. A. Azam, A. S. Ahmed, M. Oves, M. S. Khan, S. S. Habib, A. Memic, *Int. J. Nanomedicine,* **2012,** *7,* 6003–6009. **DOI:**10.2147/IJN.S35347
24. D. K. Jena, P. K. Sahoo, *J. App. Pol. Sci.* **2018,** 45968.
25. J. Jain, S. Arora, J. M. Rajwade, P. Omray, S. Khandelwal, K. M. Paknikar, *Mol. Pharm.* **2009,** *6,*1388–1401. **DOI:**10.1021/mp900056g
26. S. Maurya, A. K. Bhardwaj, K. K. Gupta, S. Agarwal, A. Kushwaha, V. Chaturvedi, R. K. Pathak, R. Gopal, K. N. Uttam, A. K. Singh, V. Verma, M. P. Singh, *Cell. Mol. Biol.* **2016,** *62,* 1000131.
27. N. Cioffi, N. Ditaranto, L. Torsi, R. A. Picca, E. De Giglio, L. Sabbatini, L. Novello, G. Tantillo, T. Bleve-Zacheo, P. G. Zambonin, *Anal. Bioanal. Chem.* **2005,** *382,*1912–1918. **DOI:**10.1007/s00216-005-3334-x
28. K. Y. Yoon, J. Hoon Byeon, J. H. Park, J. Hwang, *Sci. Total Environ.* **2007,** *373,*572–575. **DOI:**10.1016/j.scitotenv.2006.11.007
29. K. H. Thompson, C. Orvig, *Science,* **2003**, *300,* 936–939. **DOI:**10.1126/science.1083004
30. M. L. Schilsky, *Pediatr. Transplant,* **2002,** *6,*15–19. **DOI:**10.1034/j.1399-3046.2002.1r069.x
31. O. Mahapatra, M. Bhagat, C. Gopalakrishnan, K. D. Arunachalam, *J. Exp. Nanosci.* **2008,** *3,* 185–193. **DOI:**10.1080/17458080802395460
32. A. Esteban-Cubillo, C. Pecharromán, E. Aguilar, J. Santarén, J. S. Moya,*J. Mater. Sci.* **2006,** *41,*5208–5212. **DOI:**10.1007/s10853-006-0432-x
33. R. Usha, E. Prabu, M. Palaniswamy, C. K. Venil, R. Rajendran, *Glob. J. Biotechnol. Biochem.* **2010,** *5,* 153–160.
34. K. Gopalakrishnan, C. Ramesh, V. Ragunathan, M. Thamilselvan, *Dig. J. Nanomater. Biostructures,* **2012,** *7,* 833–839.
35. M. R. J. Salton, *J. Gen. Microbiol.* **1963**, 30, 223–235. **DOI:**10.1099/00221287-30-2-223
36. T. J. Beveridge, Int. Rev. Cytol, **1981,** *72*, 229–317. **DOI:**10.1016/S0074-7696(08)61198-5
37. T. J. Beveridge, L. L. *Microbiol. Rev.* **1991,** *55*, 684–705. **DOI:**10.1128/mr.55.4.684-705.1991
38. H. Nikaido, T. Nakae, *Adv. Microb. Physiol,***1979**, *20*, 163–250. **DOI:**10.1016/S0065-2911(08)60208-8
39. W. Vollmer, J.V. Holtje, *J. Bacteriol.* **2004**, *186 (18)*, 5978–5987. **DOI:**10.1128/JB.186.18.5978-5987.2004
40. S. Chandra, A. Kumar, P. K. Tomar, *J. Saudi Chem. Soc.* **2014,** *18,* 149–153. **DOI:**10.1016/j.jscs.2011.06.009
41. R. Sivaraj, P. K. S. M. Rahman, P. Rajiv, S. Narendhran, R. Venckatesh, *Spectrochim. Acta – Part A Mol. Biomol. Spectrosc.***2014,** *129,* 255–258. **DOI:**10.1016/j.saa.2014.03.027
42. R. K. Swarnkar, S. C. Singh, R. Gopal, International Conference on Optics and Photonics, **2009,** 1–3.
43. Method 7196A, Chromium hexavalent (colorimetric), http://www3.epa.gov/ epawaste/hazard/testmethods/sw846/pdfs/7196a.pdf. 7196 A1–7196 A6.
44. E. Alzahrani, R. A. Ahmed, *Int. J. Electrochem. Sci.***2016,** *11,* 4712–4723. **DOI:**10.20964/2016.06.83
45. F. W. Harun, E. A. Almadni, E. S. Ali, *Lect. Notes Eng. Comput. Sci.* **2017,** *2,* 606–610.
46. G. M. Raghavendra, J. Jung, D. Kim, J. Seo, *Carbohydr. Polym.* **2017,** *172,* 78–84. **DOI:**10.1016/j.carbpol.2017.04.070
47. I. Muthuvel, B. Krishnakumar, M. Swaminathan,*Indian J. Chem. – Sect. A Inorganic, Phys. Theor. Anal. Chem.* **2012,** *51,* 800–806.
48. P. K. Tandon, R. C. Shukla, S. B. Singh,*Ind. Eng. Chem. Res.* **2013,** *52,*10052–10058. **DOI:**10.1021/ie400702k
49. K. Shameli, M. Mansor Bin Ahmad, Z. Mohsen, W. Z. Yunis, N. A. Ibrahim, A. Rustaiyan, *Int. J. Nanomedicine,* **2011,** *6,* 581–590. **DOI:**10.2147/IJN.S17112
50. A. Azam, A. S. Ahmed, M. Oves, M. Khan, A. Memic, *Int. J. Nanomedicine,* **2012,** *7,*3527–3535.
51. Y. K. Abdel-Monem, S. M. Emam, H. M. Y. Okda, *J. Mater. Sci. Mater. Electron.* **2017,** *28,* 2923–2934. **DOI:**10.1007/s10854-016-5877-3
52. V. K. Gupta, R. Chandra, I. Tyagi, M. Verma,*J. Colloid Nad Inteface Sci.* **2016**, 478, 54–62. **DOI:**10.1016/j.jcis.2016.05.064

Povzetek

Nanodelce bakrovega oksida (CuONPs) na montmorilonitni K10 (MMT K10) osnovi smo pripravili z vključevanjem CuONPs na površino MMT K10 preko redukcije kovinskega prekurzorja s pomočjo hidrazin hidrata. Preučili smo vpliv različnih dejavnikov na učinkovitost odstranjevanje šestvalentnega kroma s pomočjo pripravljenega kompozita. Pod optimalnimi pogoji smo lahko s 15 mg pripravljenega kompozita v 30 min skoraj popolnoma (99.9 %) odstranili šestvalentni krom iz vodne raztopine, ki je vsebovala 10 ppm kroma, v širokem pH območju med 2.88 in 5.56. Sintetiziran MMT K10 – CuONPs kompozit smo okarakterizirali z UV, SEM-EDX, FTIR in XRD. Povprečna velikost kompozitnih delcev je bila 22.9 nm. Antibakterijski potencial pripravljenega kompozita smo preverili z gram-pozitivno bakterijo *Staphylococcus aureus* (ATCC 25323) in gram-negativno bakterijo *Pseudomonas aeruginosa* (ATCC 27853). Ugotovili smo, da pripravljeni kompozit izkazuje močno baktericidno delovanje saj je statistična analiza z uporabo *t*-testa pokazala za oba bakterijska seva različne cone inhibicije pri različnih koncentracijah.

Scientific paper

Variability of Omega-3/6 Fatty Acid Obtained Through Extraction-Transesterification Processes from *Phaeodactylum tricornutum*

Mari Carmen Ruiz-Domínguez,[1,*] Constanza Toledo,[1] Daniel Órdenes,[1, 2] Carlos Vílchez,[3] Paula Ardiles,[1] Jenifer Palma[1] and Pedro Cerezal[1]

[1] *Laboratorio de Microencapsulación de Compuestos Bioactivos, (LAMICBA), Departamento de Ciencias de los Alimentos y Nutrición, Facultad de Ciencias de la Salud, Universidad de Antofagasta, 1240000 Antofagasta, Chile*

[2] *Departamento de Tecnología Médica, Facultad de Ciencias de la Salud, Universidad de Antofagasta, 1240000 Antofagasta, Chile*

[3] *Algal Biotechnology Group, CIDERTA and Faculty of Sciences, University of Huelva, 21007 Huelva, Spain*

** Corresponding author: E-mail: maria.ruiz@uantof.cl*

Received: 12-22-2020

Abstract

The effect of direct transesterification methods on the omega-3/6 composition of extracts from *Phaeodactylum tricornutum* was studied. The aim of this work was to identify an extraction method which allowed to obtain the most suitable profile of fatty acids in terms of its potential benefits to health, particularly if further used in the food industry. Seven methods using acids, alkalis, and heterogeneous-catalysts, (namely methods from 1 to 7, abbreviated as M1-M7) were performed to determine α-linolenic (ALA), linoleic (LA), docosahexaenoic (DHA) and eicosapentaenoic (EPA) acids. The composition of fatty acids was in all cases characterized by the major abundance of palmitic (23.95–34.08%), palmitoleic (30.94–35.56%), oleic acids (3.00–7.41%), and EPA (0.5–6.45%). Unsaturated fatty acids extraction yield was higher with a two-step transesterification process (M6, 63.65%). The total fatty acid methyl ester content (FAME) obtained with acid-transesterification (M1) reached about 21% wt, and 60% w/w total lipids. ALA higher relative content (ALA/LA ratio) was obtained when a lipid pre-extraction step was performed prior to acid-catalysis (M4). The transesterification method based on alkali-catalyst (M3, KOH catalyst) led to obtain higher DHA relative contents (DHA/EPA ratio up to 0.11), although its FAME content was 3.75-fold lower than that obtained with acid-transesterification (M1). Overall, this study shows that direct transesterification with alkali-catalyst (M3) improves the determination of PUFA content from the diatom through a more efficient transesterification-based extraction process, and thus allow to assess the value of the biomass more accurately for application in the food industry.

Keywords: diatom; lipids; fatty acids; DHA/EPA; ALA/LA; PUFA

1. Introduction

Microalgae cultivation has gained much interest these days because of the need for renewable resources with the ability to synthesize valuable products such as pigments, carbohydrates, and fatty acids, among other compounds.[1,2] *Phaeodactylum tricornutum,* in particular, is a model pennate diatom used for physiological studies and biotechnological food and nutritional applications.[3,4] This diatom is known for its rapid growth and antioxidant capacity owing to fucoxanthin (carotenoid) and/or long-chain polyunsaturated fatty acids (PUFAs).[5–7] *P. tricornutum* is one of the few microalgae species that can produce high levels of eicosapentaenoic acid (EPA; C20:5n-3), along with low levels of docosahexaenoic acid (DHA; C22:6n-3) and arachidonic acid (ARA; 20:4n-6).[8] This ability is relevant to the biotechnological industry since PUFAs have beneficial human health effects.

DHA and EPA are essential nutrients that play an important role in infant growth and development, along with adult cardiovascular health.[9, 10] Accordingly, several reports demonstrate that consuming a diet rich in ome-

ga-3 polyunsaturated fatty acids such as DHA and EPA is useful for lowering blood triacylglycerol (TAG) levels in people with hypertriglyceridemia. In addition, intake of PUFA-rich oils have been found to play relevant roles in mitigation of inflammation, disease activity, and oxidative stress biomarkers, through increased levels of antioxidant enzymes[13]. This can be of importance to develop novel foods and nutraceuticals that help prevent or attenuate chronic inflammatory disease[13], and can also be relevant to mind, cardiovascular[11,12], inflammatory[13] and immune[10] health care, and even cancer prevention[14].

Because of its importance, a DHA/EPA ratio is outlined based on the ideal design of diet for fish larvae in aquaculture production, although the optimum ratio varies depending on species.[15] However, there are growing concerns about the role of essential fatty acids in the regulation of animal metabolism.[16–18] An overview of recommended daily dietary intake of DHA and EPA in humans ranges from 0.5 g/day for infants to 1 g/day for adults and patients with coronary heart diseases.[19,20]

Omega-3 fatty acids are synthesized from their precursors, α-linolenic (C18:3n-3; ALA) and linoleic acid (C18:2n-6; LA), which are also present in *P. tricornutum*. ALA and LA are considered essential fatty acids in humans because they cannot be synthesized and must be obtained from the diet. [21] Briefly, Fig.1S (can be seen in the supplementary material section which was adapted from Guo*, et al.*[22] and Arao and Yamada[23]) shows the omega-3/6 synthesis pathway where a sequence of desaturation (DES) and elongation (ELO) steps catalyzed by desaturase and elongase enzymes, respectively (Δ-5 and Δ-6) along with fatty acyl-CoA synthetase lead to the formation of longer chain fatty acids.[24,25] Consumption of food with the optimal omega-3/6 ratio is crucial in maintaining the overall health of the human population.[26] According to previous reports, high LA intake can induce production of proinflammatory cytokines triggered by the release of arachidonic acid (ARA)-derived products.[27–29] Thus, LA intake must be balanced with that intake of other PUFA (optimal omega-3/6 ratio), based on their daily needs. At the same time, the conversion of ALA to EPA/DHA can compete with the biosynthesis of EPA and DHA from LA, due to the competitive inhibition of enzymes (Δ-5 DES and Δ-6 DES, see Fig. 1S).[30]

These facts make *P. tricornutum* species the ideal candidate for possible biotechnological evaluations, particularly involving PUFA production.[5,6,31]

Transesterification reaction between glycerides (microalgal oils) and alcohol (methanol or ethanol) in the presence of a catalyst results in the production of fatty acid methyl esters (FAMEs) or fatty acid ethyl esters (FAEEs), respectively with glycerol as the by-product.[32, 33] The catalyst can be an alkali, acid, or even an enzyme (heterogeneous catalyst) and its selection could in turn, produce variability in the fatty acid profile obtained through transesterification.[34–36] Consequently, getting the profiles of extracted unsaturated fatty acids and DHA/EPA ratios to be adequate for specific applications, namely food, depends not only on the growth conditions of specific microalgal strains but also on the chemical factors determining the extraction process.[31,37,38] In this regard, the selection of a suitable transesterification method becomes crucial to obtain a targeted fatty acid profile for food applications.

Based on this, we hypothesized that temperature and catalyst chemical nature of the transesterification process should have an impact on the extraction yield, which might result in improved, selective extraction of specific fatty acids in relation to others. This can be of relevance to production of PUFA-enriched foods that are based on addition of microalgal fatty acids. Thus, this study aims to determine the most effective transesterification reaction among seven independent methods using different catalyst forms (alkali or acid), in order to improve the analytical determination of unsaturated fatty acids (omega-3). Special attention is given to ALA, LA, DHA and EPA from *P. tricornutum* as these fatty acids are of high value for food applications.

2. Experimental

2. 1. Material

Phaeodactylum tricornutum was provided by the microalgal collection department in "Laboratorio Microalgas y Compuestos Bioactivos" (Universidad de Antofagasta, Chile) and cultured under controlled conditions. Local seawater, sterilized and filtered through 1 μm pore size filters was used to prepare the culture medium, which was supplemented with f/2 salts, silicates, and vitamins as described by Guillard and Ryther[39] The biomass was harvested at the end of the exponential growth phase and then lyophilized in the freeze-drying system (Labconco Freezone 2.5 L Benchtop Freeze Dry System, USA) for this study. Sulfuric acid (H_2SO_4), potassium hydroxide (KOH), and potassium carbonate (K_2CO_3) were used as acid or alkali catalysts (analytical grade reagents). Methanol (MeOH), chloroform ($CHCl_3$), and *n*-hexane of chromatographic quality were used as extraction solvents (Sigma-Aldrich). Mixed FAME standard solutions (FAME Mix C4-C24, Supelco Analytical) and an internal standard (Nu-Check Pre, Inc., Elysian, MN, USA) were used for fatty acid identification.

2. 2. Lipid Analysis

Lipids were extracted as described by Axelsson and Gentili[40] using 20 mg of freeze-dried samples of from *P. tricornutum* with chloroform: methanol (2:1, v/v) as the solvent. The extracted lipids were quantified gravimetrically in triplicate (n = 3).

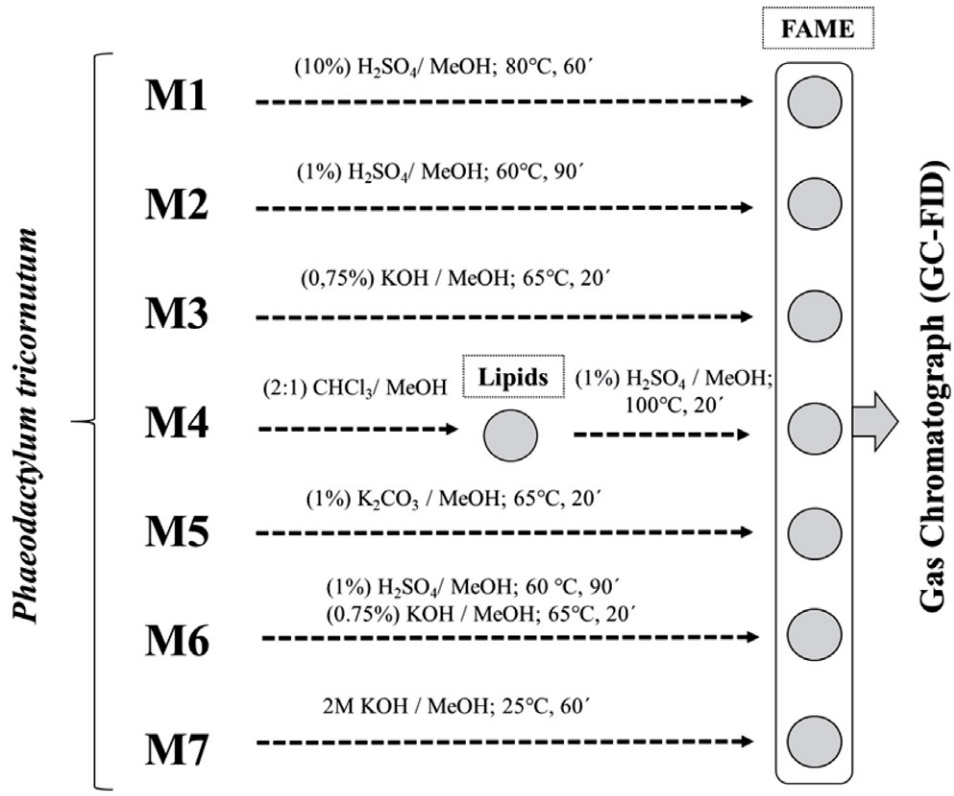

Fig. 1 Experimental design using *P. tricornutum* to obtain FAME. M1–M7 are the abbreviations of seven independent transesterification methods used in the study, as described in Material and Methods section ($p < 0.05$; n = 3).

2. 3. Transesterification Methods

The extraction of fatty acid methyl esters (FAMEs) was carried out through seven independent methods (using alkaline or acid catalysts), as shown in Fig. 1.

M1 was performed according to Lamers, *et al.*[41] M2 and M3 included independent acid and alkali transesterification reactions, respectively, and were as described by Rahman, *et al.*[42] M4 and M5 followed the method of Sung and Han[43], where in M4 was performed by pre-extraction of lipids followed by acid transesterification, and M5 was performed on the biomass directly using an alkaline heterogeneous catalyst such as K_2CO_3. M6 was performed using a two-step transesterification reaction, where the first step was the acid process, and the second step was the alkaline process, according to Rahman, *et al.*[42] Finally, M7 was carried out according to ISO-5508[44] In general, the reaction mixture was prepared by adding 10–50 mg freeze-dried biomass of *P. tricornutum* (with biomass: solvent ratio of 1:30) and 10 ppm of the internal standard with continuous agitation. Then, the flasks were washed with 3 mL hexane and Milli-Q water until the solution turns neutral, and the mixture was separated into two layers by centrifugation (360 *g*, 10 min). The upper oil layer (FAMEs diluted in hexane) was separated and washed with Milli-Q water to analyze and quantify using gas chromatography (Shimadzu 2010 GC-FID, Tokyo, Japan).

2. 4. Fatty Acid Analysis by Gas Chromatography (GC-FID)

A Shimadzu 2010-gas chromatography system equipped with a flame ionization detector (FID) and a split/splitless injector was used to analyze FAME composition. FID is one of the most commonly used detectors in gas chromatography and it works by passing the previously volatilized organic sample through a flame generated from pure hydrogen and compressed air. Then, these ions are detected by a biased electrode located close to the flame. In all cases, samples (1 μL) were injected into a capillary column RESTEK (30 m, 0.32 mm i.d., 0.25 μm film thickness). The injector temperature was maintained at 250 °C in split mode with a split ratio of 1:20, and nitrogen was used as the carrier gas at a constant flow rate of 1.25 mL/min. The oven temperature was programmed initially at 80 °C for 5 min, increased to 165 °C at 4 °C/min for 2 min, and then increased again to 180 °C at 2 °C/min for 5 min. It was heated at a rate of 2 °C/min to 200 °C for 2 min followed by 4 °C/min to 230 °C for 2 min and was finally maintained at that temperature for 2 min reaching 250 °C at 2 °C/min. The detector temperature was maintained at 280 °C. Individual FAMEs were identified by comparing their retention times with those of mixed FAME standards (FAME Mix C4-C24, Supelco Analytical) and quantified by comparing their peak area with those of mixed

FAME standards and an internal standard (tripentadecanoin ~10 ppm/sample, Nu-Check Pre, Inc., Elysian, MN, USA). Finally, FAME content was calculated as a percentage in relation to freeze-dried biomass (% wt.) and total lipids (% w/w) of *P. tricornutum*.

2. 5. Statistical Analysis

To investigate the statistical differences between fatty acid profiles, ALA/LA, and DHA/EPA ratios of *P. tricornutum,* the means of different methods were obtained in triplicate (n = 3). Then, Analysis of Variance (ANOVA) followed by Duncan's Multiple Range Test (MRT) was applied as a post hoc test to measure the specific differences between means values. Analyses were performed with Statgraphics Centurion XVIII (Stat Point Technologies, Inc., Warrenton, VA, USA) software.

3. Results and Discussion

3. 1. Fatty Acid Profile

The effect of each of the seven different transesterification methods on the *P. tricornutum* FA profile is shown in Table 1 and expressed as the percentage of relative abundance of total fatty acids (Insert Table 1 near here). Firstly, M6 (two-step transesterification process), the only method where both acid and alkaline catalysts were used in each one of the steps, produced the highest unsaturated fatty acid content in the diatom extracts, when compared to the other transesterification methods (51.08% MUFAs and 14.42% PUFAs, monounsaturated and polyunsaturated fatty acids). M6 especially stood out in oleic (5.05%), linoleic (LA, 4.01%), α-linolenic (ALA, 2.07%) and eicosapentaenoic (EPA) acid content (6.45% of total fatty acids, FA). Secondly, the acid transesterification methods such as M1 and M2 gave rise to similar FA profiles in *P. tricornutum*, with higher EPA content in extracts obtained by M1 and higher docosahexaenoic (DHA) content in those obtained by M2 (6.05% and 0.32% FA, respectively). Both ALA (omega-3) and LA (omega-6) fatty acids are essential for humans and must be obtained through their daily diet[21]; microalgae are valuable natural sources of these essential fatty acids.[20,45,46] However, the presence of ALA was minimum in both M1 and M2 acid transesterification methods (n.d., (not detected) equal to area $\leq 10^{-3}$) when compared to LA (from 2.92 to 4.42% FA). It is important to remark that the main difference between M1 and M2 methods was the percentage of acid catalyst used. Catalyst concentration is an important factor directly influencing the yield of FAMEs.[47] Macías-Sánchez*, et al.*[48] studied the potential of *Nannochloropsis gaditana* as a source of biodiesel by direct transesterification method utilizing three different catalyst concentrations, including, 2.5, 5, and 10.5% of acetyl chloride and obtained maximum yields with 5% catalyst.

Table 1. Fatty acid profile of *P. tricornutum* obtained by seven independent transesterification methods. Each value means the ratio between the integration area of a given fatty acid peak with respect to the integration area of all peaks obtained by GC-FID, in percentage ($p < 0.05$; n = 3; SD ≤ 5%).

Fatty acids (FA)	Transesterification methods						
	M1	**M2**	**M3**	**M4**	**M5**	**M6**	**M7**
C16:0, Palmitic	34.08 ±1.60 ^{e}	23.95 ±0.95 ^{a}	32.71 ±1.50 ^{d}	30.22 ±1.34 ^{c}	32.59 ±1.23 ^{d}	27.57 ±1.20 ^{b}	33.91 ±1.52 ^{e}
C16:1, Palmitoleic	34.81 ±1.56 ^{c}	33.08 ±1.02 ^{b}	35.56 ±1.59 ^{d}	32.80 ±1.60 ^{b}	33.00 ±1.30 ^{b}	36.24 ±1.65 ^{e}	30.94 ±1.23 ^{a}
C18:0, Stearic	0.62 ±0.07 ^{ab}	0.71 ±0.02 ^{b}	0.79 ±0.02 ^{c}	3.45 ±0.12 ^{f}	1.75 ±0.07 ^{d}	0.53 ±0.01 ^{a}	3.08 ±0.08 ^{e}
C18:1, Oleic	3.20 ±0.12 ^{a}	4.20 ±0.18 ^{b}	4.72 ±0.12 ^{c}	n.d.	5.64 ±0.19 ^{d}	5.05 ±0.20 ^{d}	7.41 ±0.25 ^{e}
C18:2-n6, LA	4.42 ±0.13 ^{d}	2.92 ±0.12 ^{a}	3.34 ±0.13 ^{b}	n.d.	3.44 ±0.11 ^{c}	4.01 ±0.15 ^{d}	3.46 ±0.11 ^{bc}
C18:3-n3, ALA	n.d.	n.d.	0.25 ±0.01 ^{a}	2.19 ±0.08 ^{c}	0.72 ±0.03 ^{b}	2.07 ±0.08 ^{c}	n.d.
C20:5-n3, EPA	6.05 ±0.25 ^{f}	4.51 ±0.21 ^{c}	4.72 ±0.22 ^{d}	0.50 ±0.01 ^{a}	2.86 ±0.07 ^{b}	6.45 ±0.28 ^{g}	4.77 ±0.21 ^{e}
C22:6-n3, DHA	0.14 ±0.01 ^{b}	0.32 ±0.01 ^{c}	0.52 ±0.02 ^{e}	0.01 ±0.00 ^{a}	0.01 ±0.00 ^{a}	0.36 ±0.01 ^{d}	0.01 ±0.00 ^{a}
Others	16.68 ±0.70 ^{c}	30.31 ±1.47 ^{d}	17.39 ±0.76 ^{b}	30.85 ±1.24 ^{d}	20.01 ±0.54 ^{c}	17.71 ±0.69 ^{b}	16.43 ±0.75 ^{a}
% SFA	36.35	36.41	34.86	35.78	36.48	34.49	39.42
% MUFA	38.50	38.32	42.02	36.66	40.81	51.08	40.04
% PUFA	25.15	25.27	23.12	27.55	22.70	14.42	20.53
% Omega-3	6.19	4.83	5.49	2.7	3.59	8.88	4.78
ALA/LA ratio	$\leq 10^{-3}$	$\leq 10^{-3}$	$7.5 \cdot 10^{-2}$	$\geq 10^{+3}$	$2.1 \cdot 10^{-1}$	$5.2 \cdot 10^{-1}$	$\leq 10^{-3}$
DHA/EPA ratio	0.02 $\pm 10^{-3}$ ^{b}	0.07 $\pm 8 \cdot 10^{-3}$ ^{d}	0.11 $\pm 2 \cdot 10^{-3}$ ^{e}	0.03 $\pm 4 \cdot 10^{-3}$ ^{b}	0.004 $\pm 5 \cdot 10^{-4}$ ^{a}	0.06 $\pm 3 \cdot 10^{-3}$ ^{c}	0.003 $\pm 4 \cdot 10^{-4}$ ^{a}

Note: All values were SD ≤ 5%.

Abbreviators: Methylation (M), Fatty acids (FA), Linoleic (LA), Linolenic (ALA), Eicosapentaenoic (EPA), Docosahexaenoic (DHA), Saturated Fatty acids (SFA), Monounsaturated Fatty acids (MUFA), Polyunsaturated fatty acids (PUFA), non-detected (n.d.; area $\leq 10^{-3}$), Omega-3: main n-3 fatty acids present in *P. tricornutum*. They were obtained taking into account all fatty acids integrated (included others profile). Different superscript letters from "a" to "g" indicate statistically significant differences ($p < 0.05$). All results are the average of three independent experiments (n = 3) and are presented as mean ±standard deviation.

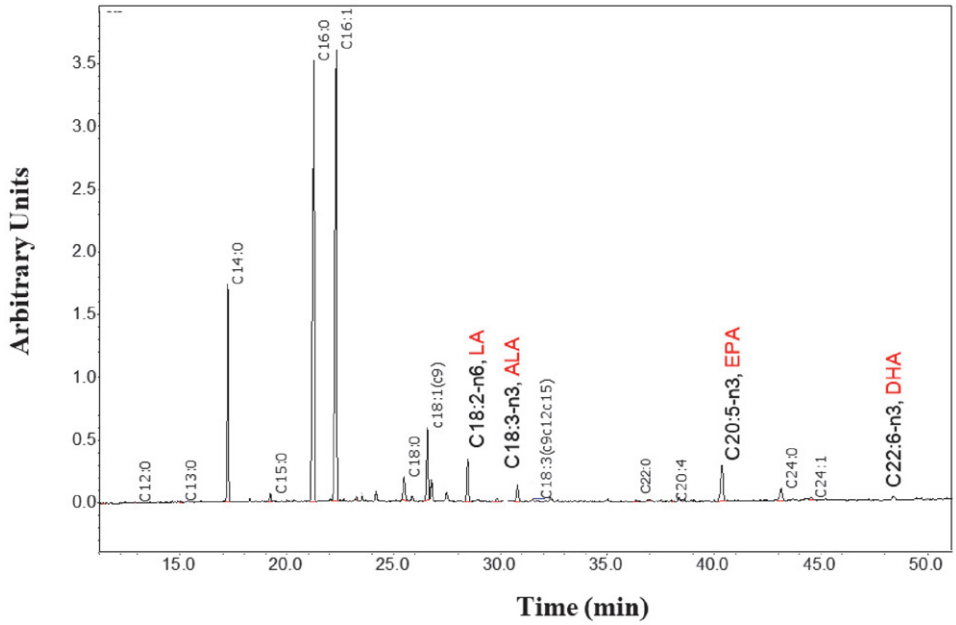

Fig. 2. Representative chromatogram of fatty acids profile present in *P. tricornutum.* Note: the method used was M5 (alkali method).

The alkali-based transesterification with methanol was also tested. The procedures of M3 and M7 were performed with different KOH concentrations and temperatures, while M5 was performed with K_2CO_3. In all cases, the PUFA profiles of *P. tricornutum* were similar with higher EPA content being obtained in the M3 and M7 methods (4.72 and 4.77 FA, respectively). Moreover, M7 had the highest percentage of oleic acid (7.41% FA), and M3 had the highest yield of DHA (0.52% FA). Omega 3-fatty acids content is also presented in Table 1. The values shown in the Table are the results of the addition of the three omega-3 fatty acids identified in *P. tricornutum* extracts: ALA, EPA and DHA. The highest omega 3-fatty acids content in the extracts was obtained with methods M6 and M1 (8.88 and 6.19% FA, respectively). The heterogeneous catalysts (for instance, method M6, two-step transesterification) has been described as one of the most promising tools due to its ability to catalyze both free fatty acids and triglycerides in transesterification reactions at the same time[49]. In particular, M6 led to a fatty acid composition which could benefit the design of functional foods with positive health effects in humans.

All transesterification methods extracted a similar proportion of palmitic (C16:0, from 23.95 to 34.08% FA) and palmitoleic acids (C16:1, values from 30.94 to 36.24% FA) present in *P. tricornutum.* Particularly, palmitoleic acid was the most abundant component in the fatty acids profile of this strain, as described in previous reports.[4,7] Different studies have demonstrated that this monounsaturated fatty acid increases the insulin sensitivity in the liver and muscle of diabetic rats improving hyperglycemia and hypertriglyceridemia problems.[50,51]. Arsić, *et al.*[52] even demonstrated that elite athletes might contribute to positive effect in their physical performance through higher percentages of palmitoleic acid and arachidonic acid in plasma and in erythrocytes.

On the other hand, M5 had a more diversified fatty acid composition, as can be seen from the chromatogram in Fig. 2. Finally, M4 (pre-extraction of lipids followed by acid transesterification) led to less abundant PUFA content for all extracts, and only oleic acid and ALA content (3.45% and 2.19% FA, respectively) could be highlighted.

According to reports, the best transesterification methods for microalgal oils involve sodium hydroxide or potassium hydroxide as the alkaline catalysts.[49,53] The most commonly used acid catalysts include sulfuric acid, hydrochloric acid, or sulfuric acid derivatives. Heterogeneous catalysts are also known as metal oxides or carbonates and result in methoxide formation.[54–56] Studies report that alkali-catalyzed transesterification is faster than acid-catalyzed transesterification, and it is also less corrosive and cost-effective from an industrial point of view.[55,57,58] However, it is known that the alkali catalyst can react with free fatty acids present in the microalgal oils provoking soap formation. Moreover, it can also inhibit the efficiency of separation of glycerol from methyl esters, thus lowering the transesterification yield.[59] In general, our results showed improved levels of PUFAs and omega-3, especially EPA, in *P. tricornutum* under acid and two-step transesterification reactions (M1 and M6, respectively).

Fig. 3 shows the FAME content of *P. tricornutum,* which was calculated relative to biomass (% wt) and total lipids (% w/w) in the seven transesterification methods. Average total lipid content of about 35% was reached in all extracts of *P. tricornutum*.

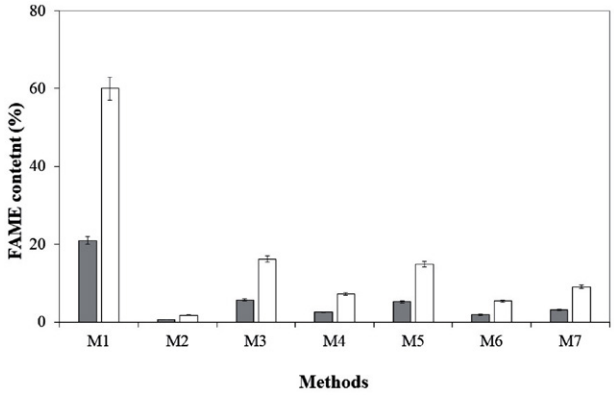

Fig. 3. Total FAME fraction in total lipids (% w/w total lipids, open bars) or in the biomass (% wt, solid bars) of *P. tricornutum* from seven independent transesterification methods ($p < 0.05$; $n = 3$). Note. wt: percentage in relation to freeze-dried biomass.

Accordingly, method M1 yielded the highest content of FAMEs in *P. tricornutum,* with ~21% wt. and ~60% w/w of the total biomass and total lipids, respectively. Below M1 yield, the alkali methods M3 and M5 gave rise to FAME contents of 5.65% wt and 16.20% w/w of the total lipids and 5.22% wt. and 14.90% w/w of the total lipids, respectively. The acid method M2 resulted in the lowest FAME content (0.62% wt. and 1.76% w/w of the total lipids).

Conversely, these results differ from several other reports that describe that alkaline catalysis has higher conversion levels of triglycerides to their corresponding methyl esters with shorter reaction times.[60,61] The results in this paper show improved FAME content for acid transesterification when compared to previous reports. Typically, acid-catalyzed transesterification is more tolerant toward free fatty acids or water presence and catalyzes both esterification and transesterification reactions at the same time.[62,63] Nevertheless, the results obtained with methods M1 and M2 show significant variations with different proportions of H_2SO_4 being used as the only difference between both processes. The difference in yield obtained is probably because a high concentration of the catalyst is always required in acid transesterification to achieve high FAME yields.[64,65]

3. 2. ALA/LA ratio in *Phaeodactylum Tricornutum*

The significance of the α-linolenic to the linoleic acid ratio (ALA/LA ratio) in the diatom extracts is worth analyzing and discussing. According to the data shown in Table 1, the presence of ALA in the extracts obtained by employing the M1, M2, and M7 transesterification methods was negligible (not detected, n.d. area $\leq 10^{-3}$). Conversely, an abundance of LA ranging from 2.92% to 4.92% of the total fatty acid content was found in the extracts. Thus, the methods M1, M2, and M7 lead to very low ALA/LA ratios. On the contrary, the methods M3, M4, M5, and M6 present ALA/LA ratios that differ widely from those previously commented. Mainly, the ratio fluctuates from 7.5 for method M3 to a very high value for method M4 (LA not determined).

Interestingly, M4, consisting of a lipid pre-extraction step followed by acid catalysis, is highly selective for α-linolenic extraction concerning LA. The differential selectivity of the method used for ALA and LA acids enables the production of *P. tricornutum* extracts enriched in either one of these fatty acids. However, as discussed above, the method produces selective extraction of ALA, which is suitable to stimulate the biochemical synthesis of EPA and DHA in humans, while limiting the presence of LA in the extracts, thereby preventing the organisms from having reduced n-3 long-chain PUFA levels.

The above-commented selectivity may directly influence the food applications of the diatom extracts. Linolenic acid tends to occur at much lower levels in the diet and the tissues of the body when compared to linoleic acid.[66] As seen in Fig. 1S (can be seen in supplementary material), ALA can undergo successive desaturation and elongation reactions to biosynthesize the polyunsaturated fatty acids EPA and DHA while LA competes with ALA (18:3n-3) for such endogenous conversion to EPA and DHA.[30,66] In addition, LA also inhibits the incorporation of DHA and EPA into tissues leading to low levels of n-3 long-chain PUFAs[67], which is of crucial importance during pregnancy and infancy. Accordingly, the use of transesterification methods to produce ALA-enriched, LA free extracts can be of value for producing food-grade supplements aimed at balancing the biochemical needs for ALA in humans.

3. 3. DHA/EPA Ratio in *Phaeodactylum Tricornutum*

The DHA/EPA ratio in *P. tricornutum* was also examined using seven independent transesterification methods. Anew, Table 1 shows the results of the application of Duncan's MRT. Our data revealed that the M3 method (using the alkali catalyst KOH (0.75% w/v)) was the best transesterification method with a DHA/EPA ratio of ~0.11 in *P. tricornutum* and was significantly different from the rest. It was followed by M2 (acid process) and M6 (two-step transesterification) methods with the DHA/EPA ratio ranging between 0.07–0.05. Although M2 had an improved DHA/EPA ratio, it was not consistent with regard to FAME content (Fig. 3). Qiao, *et al.*[3] calculated the DHA/EPA ratio in *P. tricornutum* under different culture conditions and obtained lower values than our results with a range between ~0.03–0.06. It was found that temperature was the factor that improved the ratio. This ratio is relevant in the aquaculture field because its proportion plays a significant role in considering sources for preparing feed formulation for the fast-growing stages of fish.[68]

It is also necessary to obtain microalgae culture with a moderate DHA/EPA ratio because they are the initial food for larvae and are required for improving their growth, nonspecific immunity and disease resistance.[16,69] DHA is an essential structural component of the neural tissues, such as the brain and eyes, and is also a significant component of polar lipids.[70] At the same time, EPA is more relevant as a precursor for the synthesis of bioactive compounds that help the effects of DHA, such as the hormone eicosanoids.[71] In fact, these eicosanoids formed from EPA have also been shown to act as a potent regulator of oxidative damage triggered by injury and inflammation in humans, demonstrating beneficial effects against rheumatoid arthritis as a chronic disease[13] or promoting immune function.[72]

Therefore, this ratio is also relevant in human health for controlling hypertriglyceridemia among other anomalies. For this application, the food supplement should yield a DHA/EPA ratio of 0.7:1.[73] Also, specific aquaculture reports show that the dietary requirement of DHA/EPA ratios in marine fish should range from 0.5 to 2.0, according to Council[74] These results clearly demonstrate the variation of the DHA/EPA ratio obtained with different transesterification methods. These results may be useful for the production of aquaculture feed or supplements rich in PUFAs and DHA/EPA ratios.

4. Conclusions

In this work an extraction process leading to obtain a valuable composition of microalgal fatty acids -namely PUFA- for being potentially used in food applications was selected out of several transesterification methods. *P. tricornutum* diatom was used as reference biomass. Our results show the influence the transesterification methods can have on the fatty acid composition and content of microalgal extracts. The transesterification methods assayed with *P. tricornutum* showed fatty acid profiles that are all rich in MUFA and PUFA (mainly omega-3). Specifically, the two-step transesterification method (M6, with acid and alkaline process) improved the selective composition of unsaturated fatty acids (51.08% MUFAs and 14.42% PUFAs) and omega-3 content (8.88% FA) in the diatom extracts. Increased relative contents of ALA (ALA/LA) and DHA (DHA/EPA ratios) in *P. tricornutum* extracts, was found by following the alkaline M3 process when compared to others. The acid transesterification (M1) method was found to enhance the fatty acid content with ~21% wt and ~60% w/w of the total biomass and total lipids, respectively. Thereupon, we proved that the careful selection of the transesterification method is a key tool for producing selectively PUFA-enriched microalgal extracts. The fatty acids ALA, LA, EPA and DHA can be taken as reference components for selecting a suitable method as they are of great relevance to human food and feed industries, among others. According to the obtained results, we suggest that the most recommendable transesterification-based extraction method should be selected as a function of either (or both) highest total PUFA content or/and high relative content of a targeted PUFA, according to the further specific application.

Acknowledgments

Our research group "LAMICBA" thanks "Laboratorio Microalgas y Compuestos Bioactivos Microalgas" at University of Antofagasta, Chile for providing microalgal samples. In addition, this research was financed by several projects belonging to national public resources ANID (National Agency for Research and Development of Chile, previously CONICYT) and the University of Antofagasta. They are codified as PAI-79160037, FONDECYT-11170017, and Undergraduate Thesis Scholarship Fund-649/19, respectively.

Conflict of Interests Statement

The authors declare that there is no conflict of interests.

5. References

1. P. Spolaore, C. Joannis-Cassan, E. Duran,A. Isambert, *J. Biosci. Bioeng.* **2006**, *101*, 87–96. **DOI:**10.1263/jbb.101.87
2. K. H. M. Cardozo, T. Guaratini, M. P. Barros, V. R. Falcao, A. P. Tonon, N. P. Lopes, S. Campos, M. A. Torres, A. O. Souza, P. Colepicolo,E. Pinto, *Comp. Biochem. Physiol. C-Toxicol. Pharmacol.* **2007**, *146*, 60–78. **DOI:**10.1016/j.cbpc.2006.05.007
3. H. Qiao, C. Cong, C. Sun, B. Li, J. Wang,L. Zhang, *Aquaculture*, **2016**, *452*, 311–317. **DOI:**10.1016/j.aquaculture.2015.11.011
4. Y.-H. Yang, L. Du, M. Hosokawa, K. Miyashita, Y. Kokubun, H. Arai,H. Taroda, *J. Oleo Sci.*, **2017**, ess16205.
5. Z.-K. Yang, Y.-F. Niu, Y.-H. Ma, J. Xue, M.-H. Zhang, W.-D. Yang, J.-S. Liu, S.-H. Lu, Y. Guan,H.-Y. Li, *Biotechnol. Biofuels* **2013**, *6*, 67. **DOI:**10.1186/1754-6834-6-67
6. Y. Chisti, *Biotechnol. Adv.* **2007**, *25*, 294–306. **DOI:**10.1016/j.biotechadv.2007.02.001
7. J. Lupette,C. Benning, *Biochimie*, **2020**, *178*, 15–25. **DOI:**10.1016/j.biochi.2020.04.022
8. M. Hamilton, S. Powers, J. Napier,O. Sayanova, *Mar. Drugs*, **2016**, *14*, 53. **DOI:**10.3390/md14030053
9. K. Gharami, M. Das,S. Das, *Neurochem. Int.* **2015**, *89*, 51–62. **DOI:**10.1016/j.neuint.2015.08.014
10. P. C. Calder, *Mol. Nutr. Food Res.* **2012**, *56*, 1073–1080. **DOI:**10.1002/mnfr.201100710
11. K. C. Maki, A. L. Lawless, K. M. Kelley, M. R. Dicklin, A. L. Schild,T. M. Rains, *Prostaglandins Leukot. Essent. Fatty Acids.* **2011**, *85*, 143–148. **DOI:**10.1016/j.plefa.2011.06.005

12. D. Mozaffarian,J. H. Wu, *J. Am. Coll. Cardiol.* **2011**, *58*, 2047–2067. **DOI:**10.1016/j.jacc.2011.06.063
13. D. Vasiljevic, M. Veselinovic, M. Jovanovic, N. Jeremic, A. Arsic, V. Vucic, A. Lucic-Tomic, S. Zivanovic, D. Djuric,V. Jakovljevic, *Clin. Rheumatol.* **2016**, *35*, 1909–1915. **DOI:**10.1007/s10067-016-3168-2
14. C. E. Roynette, P. C. Calder, Y. M. Dupertuis,C. Pichard, *Clin. Nutr.* **2004**, *23*, 139–151. **DOI:**10.1016/j.clnu.2003.07.005
15. L. Luo, L. Ai, X. Liang, W. Xing, H. Yu, Y. Zheng, X. Wu, X. Liang,M. Xue, *Aquac. Nutr.* **2019**, *25*, 239–248. **DOI:**10.1111/anu.12848
16. R. Zuo, Q. Ai, K. Mai, W. Xu, J. Wang, H. Xu, Z. Liufu,Y. Zhang, *Aquaculture*, **2012**, *334–337*, 101–109. **DOI:**10.1016/j.aquaculture.2011.12.045
17. J. Ma, J. Wang, D. Zhang, T. Hao, J. Sun, Y. Sun,L. Zhang, *Aquaculture*, **2014**, *433*, 105–114. **DOI:**10.1016/j.aquaculture.2014.05.042
18. B. M. Codabaccus, C. G. Carter, A. R. Bridle,P. D. Nichols, *Aquaculture*, **2012**, *356*, 135–140. **DOI:**10.1016/j.aquaculture.2012.05.024
19. P. M. Kris-Etherton, W. S. Harris,L. J. Appel, *Circulation*, **2002**, *106*, 2747–2757. **DOI:**10.1161/01.CIR.0000038493.65177.94
20. O. P. Ward,A. Singh, *Process Biochem.*, **2005**, *40*, 3627–3652. **DOI:**10.1016/j.procbio.2005.02.020
21. D. Ristić-Medić, V. Vučić, M. Takić, I. Karadžić,M. Glibetić, *J. Serb. Chem. Soc.* **2013**, *78*, 1269–1289. **DOI:**10.2298/JSC130402040R
22. M. Guo, G. Chen, J. Chen,M. Zheng, *J. Ocean Univ.* **2019**, *18*, 1199–1206. **DOI:**10.1007/s11802-019-3946-y
23. T. Arao,M. Yamada, *Phytochemistry*, **1994**, *35*, 1177–1181. **DOI:**10.1016/S0031-9422(00)94817-9
24. G. Barceló-Coblijn,E. J. Murphy, *Prog. Lipid Res.* **2009**, *48*, 355–374. **DOI:**10.1016/j.plipres.2009.07.002
25. P. C. Calder, *J. Nutr.* **2012**, *142*, 592S–599S. **DOI:**10.3945/jn.111.155259
26. H. Chaves, R. B. Singh, S. Khan, A. Wilczynska,T. Takahashi, in *The Role of Functional Food Security in Global Health*, eds. R. B. Singh, R. R. Watson,T. Takahashi, Academic Press, 2019, p.^pp. Page.
27. A. P. Simopoulos, *Asia Pac. J. Clin. Nutr.* **2008**, *17*, 131–134.
28. P. C. Calder, *Biochimie*, **2009**, *91*, 791–795. **DOI:**10.1016/j.biochi.2009.01.008
29. J. Marchix, B. Choque, M. Kouba, A. Fautrel, D. Catheline,P. Legrand, *The Journal of Nutritional Biochemistry*, **2015**, *26*, 1434–1441. **DOI:**10.1016/j.jnutbio.2015.07.010
30. A. A. Welch, S. Shakya-Shrestha, M. A. Lentjes, N. J. Wareham,K.-T. Khaw, *Am. J. Clin. Nutr.* **2010**, *92*, 1040–1051. **DOI:**10.3945/ajcn.2010.29457
31. Q. Hu, M. Sommerfeld, E. Jarvis, M. Ghirardi, M. Posewitz, M. Seibert,A. Darzins, *Plant J.* **2008**, *54*, 621–639. **DOI:**10.1111/j.1365-313X.2008.03492.x
32. G. Antolín, F. V. Tinaut, Y. Briceño, V. Castaño, C. Pérez,A. I. Ramírez, *Bioresour Technol*, **2002**, *83*, 111–114. **DOI:**10.1016/S0960-8524(01)00200-0
33. W. Parawira, *Crit. Rev. Biotechnol.* **2009**, *29*, 82–93. **DOI:**10.1080/07388550902823674
34. S.-J. Kim, S.-M. Jung, Y.-C. Park,K. Park, *Biotechnol. Bioprocess Eng.* **2007**, *12*, 441. **DOI:**10.1007/BF02931068
35. M. Oda, M. Kaieda, S. Hama, H. Yamaji, A. Kondo, E. Izumoto,H. Fukuda, *Biochem. Eng. J.* **2005**, *23*, 45–51. **DOI:**10.1016/j.bej.2004.10.009
36. Y. Zhang, M. A. Dubé, D. D. McLean,M. Kates, *Bioresour Technol*, **2003**, *90*, 229–240. **DOI:**10.1016/S0960-8524(03)00150-0
37. A. C. Guedes,F. X. Malcata, *Aquaculture*, **2012**, *10*, 59–78.
38. C. Paliwal, M. Mitra, K. Bhayani, S. V. V. Bharadwaj, T. Ghosh, S. Dubey,S. Mishra, *Bioresour. Technol.* **2017**, *244*, 1216–1226. **DOI:**10.1016/j.biortech.2017.05.058
39. R. R. Guillard,J. H. Ryther, *Can. J. Microbiol.* **1962**, *8*, 229–239. **DOI:**10.1139/m62-029
40. M. Axelsson,F. Gentili, *Plos One*, **2014**, *9*, 6. **DOI:**10.1371/journal.pone.0089643
41. P. P. Lamers, C. C. van de Laak, P. S. Kaasenbrood, J. Lorier, M. Janssen, R. C. De Vos, R. J. Bino,R. H. Wijffels, *Biotechnol. Bioeng.* **2010**, *106*, 638–648. **DOI:**10.1002/bit.22725
42. M. Rahman, M. Aziz, R. A. Al-khulaidi, N. Sakib,M. Islam, *J. Radiat. Res. Appl. Sci.* **2017**, *10*, 140–147. **DOI:**10.1016/j.jrras.2017.02.004
43. M. Sung, J.-I. Han, *Bioresour. Technol.* **2016**, *205*, 250–253. **DOI:**10.1016/j.biortech.2015.12.089
44. ISO-5508. Animal and Vegetable Fats and Oils-Analysis by Gas Chromatography of Methyl esters of Fatty Acids; ISO 5508: 1990; International Organization for Standardization: Geneve, Switzerland, 1990.
45. S. Gebreyowhans, J. Lu, S. Zhang, X. Pang,J. Lv, *Int. Dairy J.* **2019**, *97*, 158–166. **DOI:**10.1016/j.idairyj.2019.05.011
46. C. Cardoso, H. Pereira, J. Franca, J. Matos, I. Monteiro, P. Pousao-Ferreira, A. Gomes, L. Barreira, J. Varela, N. Neng, J. M. Nogueira, C. Afonso,N. M. Bandarra, *Aquac. Int.*, **2020**, *28*, 711–727. **DOI:**10.1007/s10499-019-00489-w
47. E. K. Sitepu, K. Heimann, C. L. Raston,W. Zhang, *Renew. Sust. Energ. Rev.* **2020**, *123*, 109762. **DOI:**10.1016/j.rser.2020.109762
48. M. D. Macías-Sánchez, A. Robles-Medina, E. Hita-Peña, M. J. Jiménez-Callejón, L. Estéban-Cerdán, P. A. González-Moreno, E. Molina-Grima, *Fuel*, **2015**, *150*, 14–20. **DOI:**10.1016/j.fuel.2015.01.106
49. M. O. Faruque, S. A. Razzak,M. M. Hossain, *Catalysts*, **2020**, *10*, 1025. **DOI:**10.3390/catal10091025
50. M. Passos, H. Alves, C. Momesso, F. Faria, G. Murata, M. Cury-Boaventura, E. Hatanaka, S. Massao-Hirabara,R. Gorjão, *Lipids Health Dis.* **2016**, *15*, 1–11. **DOI:**10.1186/s12944-016-0385-2
51. H. Cao, K. Gerhold, J. R. Mayers, M. M. Wiest, S. M. Watkins,G. S. Hotamisligil, *Cell*, **2008**, *134*, 933–944. **DOI:**10.1016/j.cell.2008.07.048
52. A. Arsić, V. Vučić, J. Tepšić, S. Mazić, M. Djelić,M. Glibetić, *Appl. Physiol. Nutr. Metab.* **2012**, *37*, 40–47. **DOI:**10.1139/h11-125
53. G. Huang, F. Chen, D. Wei, X. Zhang,G. Chen, *Appl. energy*, **2010**, *87*, 38–46. **DOI:**10.1016/j.apenergy.2009.06.016
54. A. Demirbas, *Energy Conv. Manag.* **2008**, *49*, 125–130.

DOI:10.1016/j.enconman.2007.05.002
55. J. M. Marchetti, V. U. Miguel,A. F. Errazu, *Renew. Sust. Energ. Rev.* **2007**, *11*, 1300–1311. **DOI:**10.1016/j.rser.2005.08.006
56. E. Ehimen, Z. Sun,C. Carrington, *Fuel*, **2010**, *89*, 677–684. **DOI:**10.1016/j.fuel.2009.10.011
57. F. Ma,M. A. Hanna, *Bioresour Technol*, **1999**, *70*, 1–15.
58. A. Demİrbaş, *Energy Conv. Manag.* **2003**, *44*, 2093–2109. **DOI:**10.1016/S0196-8904(02)00234-0
59. I. Atadashi, M. Aroua, A. A. Aziz,N. Sulaiman, *J. Membr. Sci.* **2012**, *421*, 154–164. **DOI:**10.1016/j.memsci.2012.07.006
60. K. Pramanik, *Renew. Energy.* **2003**, *28*, 239–248. **DOI:**10.1016/S0960-1481(02)00027-7
61. U. Schuchardt, R. Sercheli,R. M. Vargas, *J. Braz. Chem. Soc.* **1998**, *9*, 199–210. **DOI:**10.1590/S0103-50531998000300002
62. D. A. G. Aranda, R. T. P. Santos, N. C. O. Tapanes, A. L. D. Ramos,O. A. C. Antunes, *Catal. Lett.* **2008**, *122*, 20–25. **DOI:**10.1007/s10562-007-9318-z
63. I. M. Atadashi, M. K. Aroua, A. R. Abdul Aziz,N. M. N. Sulaiman, *Renew. Sust. Energ. Rev.* **2012**, *16*, 3456–3470. **DOI:**10.1016/j.rser.2012.03.004
64. H. I. El-Shimi, N. K. Attia, S. T. El-Sheltawy,G. I. El-Diwani, *J. Sustain. Bio. Systems.* **2013**, *3*, 224–233. **DOI:**10.4236/jsbs.2013.33031
65. S. Velasquez-Orta, J. Lee,A. Harvey, *Biochem. Eng. J.* **2013**, *76*, 83–89. **DOI:**10.1016/j.bej.2013.04.003
66. T. Brody, *Nutr. biochem.* Elsevier, 1998.
67. R. A. Gibson, B. Muhlhausler,M. Makrides, *Matern. Child Nutr.* **2011**, *7*, 17–26. **DOI:**10.1111/j.1740-8709.2011.00299.x
68. M. Zhang, C. Y. Chen, C. H. You, B. J. Chen, S. Q. Wang,Y. Y. Li, *Aquaculture*, **2019**, *505*, 488–495. **DOI:**10.1016/j.aquaculture.2019.01.061
69. E. Henrotte, R. S. N. M. Mandiki, A. T. Prudencio, M. Vandecan, C. Mélard,P. Kestemont, *Aquac. Res.* **2010**, *41*, e53–e61. **DOI:**10.1111/j.1365-2109.2009.02455.x
70. S. R. Wassall,W. Stillwell, *Chem. Phys. Lipids.* **2008**, *153*, 57–63. **DOI:**10.1016/j.chemphyslip.2008.02.010
71. L. F. C. Castro, D. R. Tocher,O. Monroig, *Prog. Lipid Res.* **2016**, *62*, 25–40. **DOI:**10.1016/j.plipres.2016.01.001
72. P. Calder,R. Grimble, *Eur. J. Clin. Nutr.* **2002**, *56*, S14–S19. **DOI:**10.1038/sj.ejcn.1601478
73. K. C. Maki, K. Yurko-Mauro, M. R. Dicklin, A. L. Schild,J. G. Geohas, *Prostaglandins Leukot. Essent. Fatty Acids*, **2014**, *91*, 141–148. **DOI:**10.1016/j.plefa.2014.07.012
74. N. R. Council, *Nutrient Requirements of Fish and Shrimp,* The National Academies Press, Washington, DC, 2011.

Povzetek

Proučevali smo učinek neposrednih postopkov transesterifikacije na sestavo omega-3/6 ekstraktov iz *Phaeodactylum tricornutum*. Cilj tega dela je bil določiti metodo ekstrakcije, ki omogoča pridobitev najprimernejšega profila maščobnih kislin glede na njihove potencialne koristi za zdravje, še posebej za nadaljnjo uporabo v živilski industriji. Za določitev α-linolenske (ALA), linolne (LA), dokozaheksaenojske (DHA) in eikozapentaenojske kisline (EPA) je bilo uporabljenih sedem metod z uporabo kislin, baz in heterogenih katalizatorjev (metode od 1 do 7, skrajšano M1-M7). Za sestavo maščobnih kislin je bila v vseh primerih značilna največja prisotnost palmitinske (23.95–34.08 %), palmitoleinske (30.94–35.56 %), oleinske kisline (3.00–7.41 %) in EPA (0.5–6.45 %). Izkoristek ekstrakcije nenasičenih maščobnih kislin je bil višji z dvostopenjskim postopkom transesterifikacije (M6, 63.65 %). Skupna vsebnost metilnih estrov maščobnih kislin (FAME), dobljena s kislinsko transesterifikacijo (M1), je dosegla približno 21 % celokupne mase in 60 % vseh lipidov. Višjo relativno vsebnost ALA (razmerje ALA/LA) smo dobili, če smo pred kislinsko katalizo izvedli stopnjo predhodne ekstrakcije lipidov (M4). Metoda transesterifikacije na osnovi alkalnega katalizatorja (katalizator KOH, M3) je privedla do višjih relativnih vsebnosti DHA (razmerje DHA/EPA do 0.11), čeprav je bila pri tem vsebnost FAME 3.75-krat manjša od tiste, pridobljene s kislinsko transesterifikacijo (M1). Na splošno ta študija kaže, da neposredna transesterifikacija z alkalnim katalizatorjem (M3) izboljša določanje vsebnosti PUFA iz diatomej z učinkovitejšim postopkom ekstrakcije, ki temelji na transesterifikaciji, in tako omogoča natančnejšo oceno vrednosti biomase za uporabo v prehrambeni industriji.

DOI: 10.17344/acsi.2021.6656 *Acta Chim. Slov.* **2021,** *68,* 638–644

Scientific paper

Syntheses, Crystal Structures, and Antibacterial Activity of New Tetranuclear Zinc(II) Complexes with Schiff Base Ligands

Heng-Yu Qian

Key Laboratory of Surface & Interface Science of Henan, School of Material & Chemical Engineering, Zhengzhou University of Light Industry, Zhengzhou, 450002 P.R. China

** Corresponding author: E-mail: hengyu_qian@126.com*

Received: 01-08-2021

Abstract

Two new tetranuclear zinc(II) complexes, $[Zn_4(L^1)_2(\mu_2\text{-}\eta^1\text{:}\eta^1\text{-}CH_3COO)_4(\mu_{1,1}\text{-}N_3)_2]$ (**1**) and $[Zn_4(L^2)_4(CH_3CH_2OH)(H_2O)]$ (**2**), where L^1 and L^2 are the deprotonated forms of 4-fluoro-2-((pyridin-2-ylmethylimino)methyl)phenol (HL^1) and 4-fluoro-2-((2-(hydroxymethyl)phenylimino)methyl)phenol (H_2L^2), have been synthesized and characterized by elemental analysis, IR and UV-vis spectroscopy, and single crystal X-ray diffraction. X-ray crystal structural study indicated that the distances between the adjacent Zn atoms are 3.160(1)–3.353(1) Å in **1** and 3.005(1)–3.168(1) Å in **2**. All zinc atoms in **1** are pentacoordinated in trigonal bipyramidal geometry, and those in **2** are in square pyramidal and octahedral geometry. The complexes and the Schiff bases were assayed for antibacterial activities against three Gram-positive bacterial strains (*B. subtilis*, *S. aureus*, and *St. faecalis*) and three Gram-negative bacterial strains (*E. coli*, *P. aeruginosa*, and *E. cloacae*) by MTT method.

Keywords: Tridentate Schiff base; crystal structure; zinc complex; tetranuclear structure; antibacterial property

1. Introduction

Zinc is an important element for biological processes of human beings.[1] However, the mechanism of action of zinc in physiology and pathology are poorly understood. Zinc is also an essential cofactor in six classes of enzymes as well as in several families of regulatory proteins.[2] Its importance in DNA synthesis, control of gene expression, and induction of cell apoptosis is becoming better understood.[3] Schiff bases derived from substituted salicylaldehyde with various organic amines are important ligands in coordination chemistry,[4] and show various biological properties such as antitumor,[5] antibacterial,[6] anti-fungi,[7] and enzyme inhibition.[8] It was reported that the compounds containing one or more halo-atoms on the aromatic ring have improved biological properties, especially for the antibacterial activities.[9] Rai *et al.* reported a series of fluoro, chloro, bromo and iodo-substituted compounds, and found that they have significant antimicrobial activities.[10] Acetate, azide anions and the phenolate group of Schiff base ligands usually act as flexible bridging ligands, which bind different metal atoms to form interesting polymeric structures.[11] In the present work, two new tetranuclear zinc(II) complexes, $[Zn_4(L^1)_2(\mu_2\text{-}\eta^1\text{:}\eta^1\text{-}CH_3COO)_4(\mu_{1,1}\text{-}N_3)_2]$ (**1**) and $[Zn_4(L^2)_4(CH_3CH_2OH)(H_2O)]$ (**2**), where L^1 and L^2 are the deprotonated forms of 4-fluoro-2-((pyridin-2-ylmethylimino)methyl)phenol (HL^1; Scheme 1, left) and 4-fluoro-2-((2-(hydroxymethyl)phenylimino)methyl)phenol (H_2L^2; Scheme 1, right), is reported.

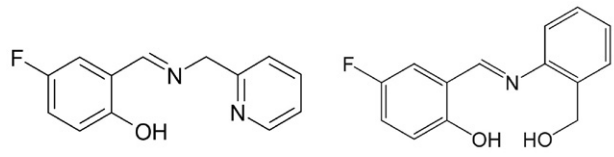

Scheme 1. The Schiff base ligands.

2. Experimental

2. 1. Material and Measurements

All chemical reagents and solvents were of analytical grade and were obtained from Sigma-Aldrich. Elemental analyses were performed on a Perkin-Elmer 2400 II elemental analyzer. Infrared spectra were recorded on a Per-

kin-Elmer RX I FT-IR spectrophotometer with KBr discs. Electronic spectra were obtained with Lambda 35 spectrophotometer.

2. 2. Synthesis of the Schiff Bases

The Schiff bases HL^1 and H_2L^2 were synthesized by refluxing hot ethanolic solution (30 mL) of 5-fluorosalicylaldehyde (0.002 mol, 0.280 g) with 2-aminomethylpyridine (0.002 mol, 0.216 g) and 2-aminophenylmethanol, respectively, for 1 h. The precipitate formed during reflux was filtered, washed with cold EtOH, and recrystallized from hot EtOH.

HL^1: Yield 77%. Anal. Calcd. for $C_{13}H_{11}FN_2O$: C 67.82, H 4.82, N 12.17. Found: C 67.71, H 4.93, N 12.26. IR data (KBr, cm^{-1}): 3327, 1622, 1585, 1571, 1513, 1473, 1438, 1389, 1346, 1285, 1220, 1205, 1153, 1140, 1112, 1034, 960, 877, 830, 797, 762, 723, 710, 633, 620. UV-Vis data in ethanol [λ_{max} (nm), ε (L mol^{-1} cm^{-1})]: 250, 14570; 280, 17530; 300, 18150; 380, 7637.

H_2L^2: Yield 83%. Anal. Calcd. for $C_{14}H_{12}FNO_2$: C 68.56, H 4.93, N 5.71. Found: C 68.67, H 5.02, N 5.63. IR data (KBr, cm^{-1}): 3341, 3243, 1626, 1570, 1485, 1447, 1387, 1355, 1321, 1257, 1201, 1141, 1103, 1034, 955, 870, 795, 767, 716, 667, 626, 575, 535, 466. UV-Vis data in ethanol [λ_{max} (nm), ε (L mol^{-1} cm^{-1})]: 230, 19310; 265, 14220; 347, 13150.

2. 3. Synthesis of the Zn(II) Complex 1

An ethanolic solution (20 mL) of HL^1 (0.20 mmol, 0.046 g) was mixed with an ethanolic solution (30 mL) of $Zn(CH_3COO)_2{\cdot}2H_2O$ (0.50 mmol, 0.11 g) and an aqueous solution (1 mL) of sodium azide (0.20 mmol, 0.013 g), and refluxed in a water bath for 1 h. The separated complex was filtered, washed thoroughly with water, ethanol, ether, and finally dried in a vacuum over fused $CaCl_2$. Yield 56%. Anal. Calcd. for $C_{34}H_{32}F_2N_{10}O_{10}Zn_4$: C 39.26, H 3.10, N 13.46. Found: C 39.05, H 3.18, N 13.33. IR data (KBr, cm^{-1}): 2080, 1640, 1598, 1480, 1437, 1395, 1289, 1213, 1154, 1044, 874, 815, 769, 667, 617, 561, 490, 456. UV-Vis data in ethanol [λ_{max} (nm), ε (L mol^{-1} cm^{-1})]: 232, 19150; 250, 18110; 280, 12560; 370, 5570.

A small amount of the complex was recrystallized from ethanol, affording colorless single crystals suitable for X-ray analysis.

2. 4. Synthesis of the Zn(II) Complex 2

An ethanolic solution (20 mL) of H_2L^2 (0.20 mmol, 0.049 g) was mixed with an ethanolic solution (30 mL) of $Zn(CH_3COO)_2{\cdot}2H_2O$ (0.50 mmol, 110 mg) and refluxed in a water bath for 1 h. The separated complex was filtered, washed thoroughly with water, ethanol, ether, and finally dried in a vacuum over fused $CaCl_2$. Yield 43%. Anal. Calcd. for $C_{58}H_{48}F_4N_4O_{10}Zn_4$: C 53.64, H 3.73, N 4.31. Found: C 53.45, H 3.91, N 4.25. IR data (KBr, cm^{-1}): 3641, 1609, 1536, 1460, 1382, 1306, 1241, 1198, 1139, 1026, 979, 874, 816, 752, 673, 624, 564, 513, 443. UV-Vis data in ethanol [λ_{max} (nm), ε (L mol^{-1} cm^{-1})]: 238, 17270; 281, 11450; 399, 8760.

A small amount of the complex was recrystallized from ethanol, affording colorless single crystals suitable for X-ray analysis.

2. 5. Single Crystal X-Ray Diffraction

X-ray data for the complexes were collected on a Bruker APEX II diffractometer equipped with graphite-monochromated Mo *Kα* radiation (λ = 0.71073 Å). A preliminary orientation matrix and cell parameters were determined from three sets of ω scans at different starting angles. Data frames were obtained at scan intervals of 0.5° with an exposure time of 10 s $frame^{-1}$. The reflection data were corrected for Lorentz and polarization factors. Absorption corrections were carried out using SADABS. The structures of the complexes were solved by direct method and refined by full-matrix least-squares analysis using anisotropic thermal parameters for non-H atoms with the SHELXTL.[12] All H atoms were calculated at idealized positions and refined with the riding models. Crystallographic data for the complexes are summarized in Table 1.

Table 1. Crystal and refinement data for the complexes

Parameter	1	2
Empirical formula	$C_{34}H_{32}F_2N_{10}O_{10}Zn_4$	$C_{58}H_{48}F_4N_4O_{10}Zn_4$
Formula weight	1040.2	1298.5
Crystal size (mm)	0.20 × 0.20 × 0.15	0.16 × 0.15 × 0.15
Temperature (°C)	298(2)	298(2)
Wavelength (Å)	0.71073	0.71073
Crystal system	triclinic	triclinic
Space group	$P\bar{1}$	$P\bar{1}$
a (Å)	8.4606(9)	14.0120(11)
b (Å)	10.8780(11)	14.1500(10)
c (Å)	11.0332(11)	15.1470(10)
α (°)	84.734(2)	101.189(1)
β (°)	86.041(2)	103.022(1)
g (°)	88.243(2)	93.211(1)
V ($Å^3$)	1008.43(18)	2854.7(4)
Z	1	2
D_{calc} (g cm^{-3})	1.713	1.511
μ (Mo Kα) (mm^{-1})	2.427	1.734
F(000)	524	1320
Number of measured reflections	9913	15426
Number of observations ($I > 2\sigma(I)$)	3748	9251
Unique reflections	3175	5361
Parameters	273	722
Number of restraints	0	0
R_1, wR_2 ($I > 2\sigma(I)$)[a]	0.0273, 0.0641	0.0640, 0.1841
R_1, wR_2 (all data)[a]	0.0360, 0.0687	0.1182, 0.2252
Goodness of fit of F^2	1.034	1.013

[a] $R_1 = \Sigma||Fo| - |Fc||/å|Fo|$, $wR_2 = [\Sigma w(Fo^2 - Fc^2)^2/\Sigma w(Fo^2)^2]^{1/2}$.

2. 5. Antibacterial Activity

Antibacterial activity of the Schiff base ligands and the complexes was tested against *B. subtilis*, *S. aureus*, *S. faecalis*, *P. aeruginosa*, *E. coli*, and *E. cloacae* using MTT medium. The minimum inhibitory concentrations (MICs) of the compounds were determined by a colorimetric method using MTT dye.[13] A stock solution of the compounds (50 μg mL^{-1}) in DMSO was prepared and quantities of the compounds were incorporated in specified quantity of sterilized liquid medium. A specified quantity of the medium containing the compounds was poured into micro-titration plates. Suspension of the microorganism was prepared to contain approximately 10^5 cfu mL^{-1} and applied to micro-titration plates with serially diluted compounds in DMSO to be tested, and incubated at 37 °C for 24 h for bacteria. After the MICs were visually determined on each micro-titration plate, 50 µL of phosphate buffered saline (PBS 0.01 mol L^{-1}, pH 7.4: $Na_2HPO_4{\cdot}12H_2O$ 2.9 g, KH_2PO_4 0.2 g, NaCl 8.0 g, KCl 0.2 g, distilled water 1000 mL) containing 2 mg mL^{-1} of MTT was added to each well. Incubation was continued at room temperature for 4–5 h. The content of each well was removed, and 100 µL of isopropanol containing 5% 1 mol L^{-1} HCl was added to extract the dye. After 12 h of incubation at room temperature, the optical density (OD) was measured with a microplate reader at 570 nm.

3. Results and Discussion

3. 1. Synthesis of the complexes

Complex **1** was prepared by the reaction of 4-fluoro-2-[(pyridin-2-ylmethylimino)methyl]phenol, zinc acetate and sodium azide in methanol, and complex **2** was prepared by the reaction of 4-fluoro-2-((2-(hydroxymethyl)phenylimino)methyl)phenol and zinc acetate in methanol. When compared with the zinc complexes with similar Schiff base ligands but different zinc salts,[14] we found that the acetate and azide ligands are interesting bridging groups, which are readily participate in the construction of polynuclear complexes.

3. 2. Crystal Structure Description of Complex 1

The molecular structure of complex **1** is shown in Fig. 1. Selected bond lengths and angles are listed in Table 2. The complex is a phenolate oxygen, nitrate, and end-on azide co-bridged tetranuclear zinc(II) species, with a crystallographic inversion center symmetry. The inversion center is located at the midpoint of the Zn2 and Zn2A atoms (symmetry code for A: $-x$, $1 - y$, $1 - z$). Zn2 forms distances of 3.160(1) and 3.353(1) Å, respectively, with Zn1 and Zn2A. All the zinc atoms are penta-coordinated in trigonal bipyramidal geometry. For the outer zinc atoms, Zn1 and Zn1A, the equatorial plane is defined by the imino nitrogen (N1) of the Schiff base ligand, and two acetate oxygen (O3, O5), and the axial positions are defined by the phenolate oxygen (O1) and pyridine nitrogen (N2) of the Schiff base ligand. For the inner zinc atoms, Zn2 and Zn2A, the equatorial plane is defined by the phenolate oxygen (O1), one acetate oxygen (O4), and one azide nitrogen (N3A), and the axial positions are defined by one acetate oxygen (O2) and one azide nitrogen (N3). The trigonal bipyramidal coordination is distorted, which can be observed from the bond angles related to the zinc atoms. The bond angles of the equatorial planes range from 112.70(8) to 125.55(8)° for Zn1 and from 108.97(7) to 131.25(9)° for Zn2. In addition, the perpendicular angles are 166.31(7)° for Zn1 and 169.41(7)° for Zn2. The coordinate bond lengths are also deviate from the ideal values of trigonal bipyramidal geometry, but they are within normal values as compared to other Schiff base zinc(II) complexes.[15] Zn1 and Zn2 atoms deviate from the best coordination planes defined by the equatorial donor atoms by 0.120(1) Å and 0.155(1) Å, respectively.

The question arises as to whether the coordination polyhedra around the five-coordinated zinc atoms can be described as distorted square pyramid or distorted trigonal bipyramid. Further information can be obtained by determining the structural index τ which represents the relative amount of trigonality (square pyramid, $\tau = 0$; trigonal bipyramid, $\tau = 1$); $\tau = (\beta - \alpha)/60°$, α and β being the two largest angles around the central atom.[16] The values of τ are 0.68 for Zn1 and 0.636 for Zn2. Therefore, the coordination geometries of the zinc atoms in the complex are best described as severely distorted trigonal bipyramids, instead of square pyramids.

In the crystal structure of the complex, the tetranuclear zinc complex molecules are linked through C8–H8A···O3 hydrogen bonds (Table 3), to form 1D chains along the *b* axis (Fig. 2).

3. 3. Crystal Structure Description of Complex 2

The molecular structure of complex **2** is shown in Fig. 3. Selected bond lengths and angles are listed in Table 2. The complex is a hydroxyl oxygen bridged tetranuclear zinc(II) species. The distances among the Zn atoms are in the range 3.005(1)–3.168(1) Å. The Zn1 and Zn2 atoms are penta-coordinated in square pyramidal geometry, as evidenced by the τ values of 0.38 for Zn1 and 0.40 for Zn2. The basal planes are defined by the phenolate oxygen (O5 for Zn1, O3 for Zn2), imino nitrogen (N3 for Zn1, N2 for Zn2) and hydroxyl oxygen (O6 for Zn1, O4 for Zn2) of one Schiff base ligand, and the hydroxyl oxygen (O8 for Zn1, O2 for Zn2) of another Schiff base ligand. The apical positions are occupied by the hydroxyl oxygen (O4 for Zn1, O8 for Zn2). The Zn1 and Zn2 atoms deviate from the basal planes by 0.415(2) and 0.353(2) Å, respectively. The square pyramidal coordination is distorted, which can

Table 2. Selected bond lengths (Å) and angles (°) for the complexes

1			
Zn1–O1	2.0484(16)	Zn1–N1	2.055(2)
Zn1–O3	1.9866(17)	Zn1–N2	2.1321(19)
Zn1–O5	1.9915(18)	Zn2–O1	1.9864(17)
Zn2–O4	1.9707(19)	Zn2–N3A	1.986(2)
Zn2–O2	2.0707(19)	Zn2–N3	2.290(2)
O3–Zn1–O5	112.70(8)	O3–Zn1–O1	95.44(7)
O5–Zn1–O1	97.75(7)	O3–Zn1–N1	125.55(8)
O5–Zn1–N1	120.69(8)	O1–Zn1–N1	87.67(7)
O3–Zn1–N2	91.47(7)	O5–Zn1–N2	90.43(7)
O1–Zn1–N2	166.31(7)	N1–Zn1–N2	78.70(8)
O4–Zn2–O1	108.97(7)	O4–Zn2–N3A	117.91(9)
O1–Zn2–N3A	131.25(9)	O4–Zn2–O2	99.14(8)
O1–Zn2–O2	92.32(7)	N3A–Zn2–O2	92.81(8)
O4–Zn2–N3	88.25(9)	O1–Zn2–N3	92.42(8)
N3–Zn2–N3A	76.96(9)	O2–Zn2–N3	169.41(7)
2			
Zn1–O5	1.942(6)	Zn1–O4	2.021(5)
Zn1–N3	2.054(8)	Zn1–O6	2.061(5)
Zn1–O8	2.156(5)	Zn2–O3	1.987(6)
Zn2–O8	2.003(5)	Zn2–N2	2.021(7)
Zn2–O2	2.069(5)	Zn2–O4	2.118(5)
Zn3–O7	1.968(5)	Zn3–O8	2.086(5)
Zn3–N4	2.094(7)	Zn3–O2	2.112(5)
Zn3–O6	2.133(5)	Zn3–O9	2.255(6)
Zn4–O1	1.943(6)	Zn4–O2	2.083(5)
Zn4–N1	2.119(6)	Zn4–O6	2.119(5)
Zn4–O4	2.173(5)	Zn4–O10	2.265(6)
O5–Zn1–N3	92.2(3)	O5–Zn1–O6	167.0(2)
N3–Zn1–O6	89.9(3)	O5–Zn1–O8	91.4(2)
N3–Zn1–O8	144.4(3)	O6–Zn1–O8	79.58(19)
O4–Zn1–O8	84.1(2)	O4–Zn1–O6	84.6(2)
O5–Zn1–O4	103.8(2)	O4–Zn1–N3	129.1(3)
O3–Zn2–O8	101.2(2)	O8–Zn2–N2	123.4(2)
O8–Zn2–O2	87.20(19)	O8–Zn2–O4	85.5(2)
O3–Zn2–N2	91.0(3)	O3–Zn2–O2	93.6(2)
N2–Zn2–O2	147.5(2)	O3–Zn2–O4	170.9(2)
N2–Zn2–O4	90.5(3)	O2–Zn2–O4	80.4(2)
O7–Zn3–O8	176.1(2)	O7–Zn3–N4	89.2(3)
O8–Zn3–N4	91.2(2)	O7–Zn3–O2	95.8(2)
O8–Zn3–O2	83.95(19)	N4–Zn3–O2	174.9(2)
O7–Zn3–O6	96.5(2)	O8–Zn3–O6	79.6(2)
N4–Zn3–O6	99.7(3)	O2–Zn3–O6	81.1(2)
O7–Zn3–O9	95.2(3)	O8–Zn3–O9	88.7(2)
N4–Zn3–O9	91.2(3)	O2–Zn3–O9	87.1(2)
O6–Zn3–O9	164.1(2)	O1–Zn4–O2	177.2(2)
O1–Zn4–N1	88.9(3)	O2–Zn4–N1	88.5(2)
O1–Zn4–O6	100.5(2)	O2–Zn4–O6	82.1(2)
N1–Zn4–O6	170.6(3)	O1–Zn4–O4	100.4(2)
O2–Zn4–O4	78.8(2)	N1–Zn4–O4	99.5(2)
O6–Zn4–O4	79.61(19)	O1–Zn4–O10	95.9(3)
O2–Zn4–O10	85.4(2)	N1–Zn4–O10	92.7(2)
O6–Zn4–O10	85.7(2)	O4–Zn4–O10	159.8(2)

Symmetry code for A: –*x*, 1 – *y*, 1 – *z*.

be observed from the bond angles related to the zinc atoms. The *cis* and *trans* bond angles of the basal planes range from 79.58(19) to 92.2(3)° and 84.1(2) to 129.1(3)° for Zn1, and from 80.4(2) to 93.6(2)° and 85.2(2) to 123.4(2)° for Zn2.

The Zn3 and Zn4 atoms are hexacoordinated in octahedral geometry. The equatorial planes are defined by the phenolate oxygen (O7 for Zn3, O1 for Zn4), imino nitrogen (N4 for Zn1, N1 for Zn4) and hydroxyl oxygen (O8 for Zn1, O2 for Zn4) of one Schiff base ligand, and the hydroxyl oxygen (O2 for Zn1, O6 for Zn4) of another Schiff base ligand. The axial positions are occupied by the hydroxyl oxygen (O6 for Zn1, O4 for Zn4) and the water oxygen (O9) for Zn3 or ethanol oxygen (O10) for Zn4. The Zn3 and Zn4 atoms deviate from the basal planes by 0.021(2) and 0.003(2) Å, respectively. The octahedral coordination is distorted, which can be observed from the bond angles related to the zinc atoms. The *cis* and *trans* bond angles of the equatorial planes range from 93.95(19) to 95.8(2)° and 174.9(2) to 176.1(2)° for Zn3, and from 82.1(2) to 100.5(2)° and 170.6(3) to 177.2(2)° for Zn4. In addition, the perpendicular angles are 164.1(2)° for Zn3 and 159.8(2)° for Zn4. The coordinate bond lengths are within normal values as compared to other Schiff base zinc(II) complexes.[15]

In the crystal structure of the complex, the tetranuclear zinc complex molecules are linked through C–H···F hydrogen bonds (Table 3), to form a 3D network (Fig. 4).

Table 3. Hydrogen bond distances (Å) and bond angles (°) for the complexes

D*–H···*A	***d*(*D*–H)**	***d*(H···*A*)**	***d*(*D*···*A*)**	**Angle (*D*–H···*A*)**
1				
O8–H8A···O3^{i}	0.97	2.54	3.381(2)	145(3)
2				
C21–H21···F1^{ii}	0.93	2.55	3.419(5)	156(6)
C38–H38···F4^{iii}	0.93	2.55	3.186(5)	126(6)
C47–H47···F2^{iv}	0.93	2.47	3313(5)	150(6)

Symmetry codes: i: –*x*, 2 – *y*, –*z*; ii: –*x*, 1 – *y*, –*z*; iii: –1 + *x*, *y*, *z*; iv: 1 – *x*, 1 – *y*, –*z*.

3. 3. IR and UV-Vis Spectra

In the IR spectra of complex **1**, the strong absorption at 2082 cm^{-1} is due to the vibration of the azide ligand. The intense absorption at 1622 cm^{-1} for HL^{1}, 1626 cm^{-1} for H_2L^2, 1598 cm^{-1} for **1** and 1609 cm^{-1} for **2** is assigned to the azomethine groups, ν(C=N).[17] The bands undergoe negative shift of 17 cm^{-1} for **1** and 13 cm^{-1} for **2** when compared to the free Schiff bases, which can be attributed to donation of the azomethine nitrogen atom lone pair to the Zn atoms. This conclusion is further supported by the presence of weak bands at low wave numbers, which can

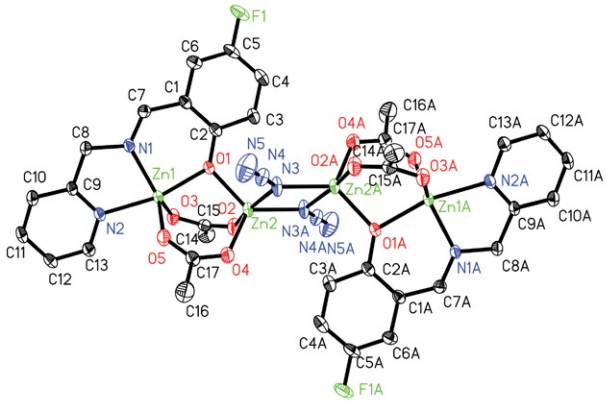

Fig. 1. ORTEP diagram of complex **1** with 30% thermal ellipsoids for all non-hydrogen atoms. Hydrogen atoms are omitted for clarity. Atoms with the suffix A are related to the operate position –*x*, 1 – *y*, 1 – *z*.

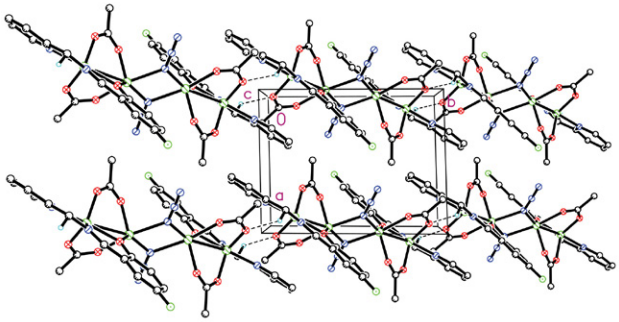

Fig. 2. Hydrogen bond (dashed lines) linked 1D chains of complex **1**, viewed along the *c* axis.

be assigned to ν(Zn-N) and ν(Zn-O). The phenolic ν(C-O) appears as a medium band at 1213 cm^{-1} for **1** and 1241 cm^{-1} for **2**.

3. 4. Antibacterial Activity

The complexes and the free Schiff bases were screened for antibacterial property against three Gram-positive bacterial strains (*B. subtilis*, *S. aureus*, and *St. faecalis*) and three Gram-negative bacterial strains (*E. coli*, *P. aeruginosa*,

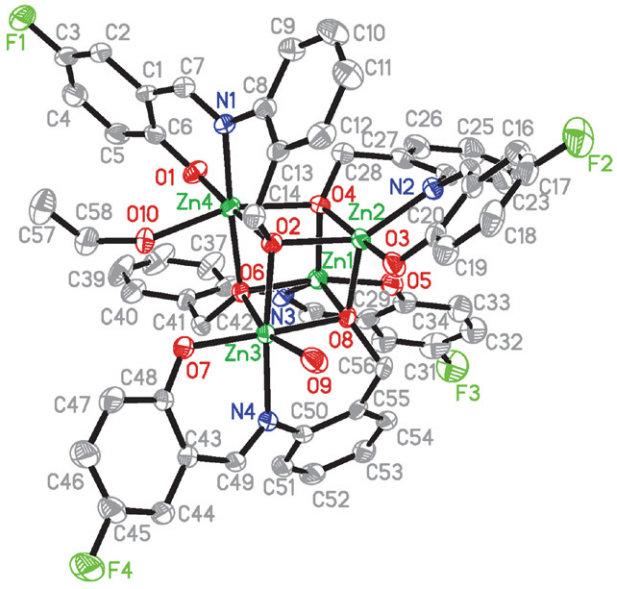

Fig. 3. ORTEP diagram of complex **2** with 30% thermal ellipsoids for all non-hydrogen atoms. Hydrogen atoms are omitted for clarity.

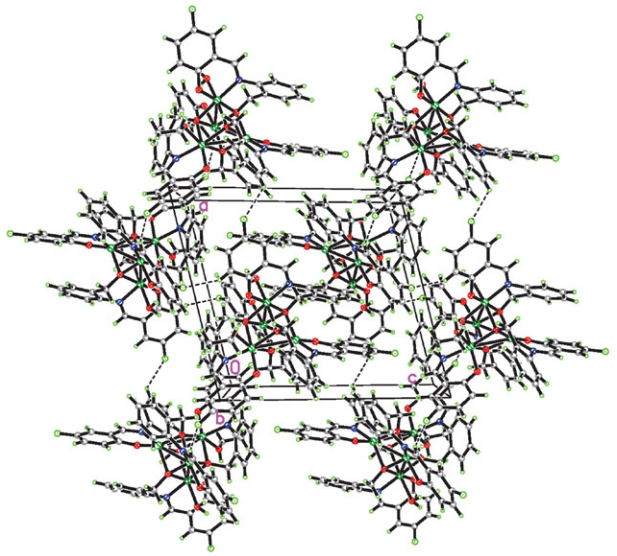

Fig. 4. Hydrogen bond (dashed lines) linked 3D network of complex **2**, viewed along the *b* axis.

Table 4. MICs (μg mL^{-1}) of the compounds and related materials

Tested material	Gram positive			Gram negative		
	B. subtilis	*S. aureus*	*St. faecalis*	*P. aeruginosa*	*E. coli*	*E. cloacae*
1	0.39	6.25	3.12	25	0.78	> 50
2	0.78	3.12	6.25	25	3.12	> 50
HL^1	1.56	12.5	12.5	> 50	3.12	> 50
H_2L^2	3.12	6.25	12.5	> 50	6.25	> 50
NaN_3	25	> 50	> 50	> 50	25	> 50
Penicillin	1.56	1.56	1.56	6.25	6.25	3.12
Kanamycin	0.39	1.56	3.12	3.12	3.12	1.56

and *E. cloacae*) by MTT method. The MICs of the compounds against the bacteria are presented in Table 4. Penicillin and Kanamycin were tested as reference drugs. The complexes show strong activities against the Gram positive bacteria *B. subtilis*, *S. aureus*, *St. faecalis*, and the Gram negative bacteria *E. coli*, medium activity against the Gram negative bacteria *P. aeruginosa*, and no activity against *E. cloacae*. The free Schiff bases show strong activity against the Gram positive bacteria *B. subtilis* and the Gram negative bacteria *E. coli*, medium activity against *S. aureus* and *St. faecalis*, and no activity against *P. aeruginosa* and *E. cloacae*. In general, the antibacterial activities of the complexes are better than the free Schiff bases. The two complexes have higher activity than the vanadium complexes we reported previously,[18] and the zinc, manganese, cobalt and cadmium complexes with hydrazone ligands.[19]

4. Conclusion

Two new tetranuclear zinc(II) complexes with fluoro-containing Schiff base ligands have been prepared and structurally characterized. The Zn atoms are in trigonal bipyramidal, square pyramidal and octahedral coordination. The complexes show strong activities against the Gram positive bacteria *B. subtilis*, *S. aureus*, *St. faecalis*, and the Gram negative bacteria *E. coli*, and medium activity against the Gram negative bacteria *P. aeruginosa*. The antibacterial assay of the free Schiff bases and the complexes indicate that they are potential antibacterial agents for *B. subtilis* and *E. coli*.

5. Supplementary Material

CCDC 967151 (**1**) and 2063585 (**2**) contain the supplementary crystallographic data for this paper. These data can be obtained free of charge at http://www.ccdc.cam.ac.uk/const/retrieving.html or from the Cambridge Crystallographic Data Centre (CCDC), 12 Union Road, Cambridge CB2 1EZ, UK; fax: +44(0)1223-336033 or e-mail: deposit@ccdc.cam.ac.uk.

Acknowledgments

Project supported by the Henan Province Universities and Colleges Funded Scheme (21A530010).

6. References

1. (a) A. Lupo, E. Cesaro, G. Montano, D. Zurlo, P. Izzo, P. Costanzo, *Curr. Genomics* **2013**, *14*, 268; **DOI:**10.2174/1389202911314999002
(b) L. P. Huang, S. Tepaamorndech, *Mol. Aspects Med.* **2013**, *34*, 548; **DOI:**10.1016/j.mam.2012.05.008
(c) S. Tabassum, A. Asim, F. Arjmand, M. Afzal, V. Bagchi, *Eur. J. Med. Chem.* **2012**, *58*, 308. **DOI:**10.1016/j.ejmech.2012.09.051
2. E. Roscioli, R. Hamon, S. Lester, C. Murgia, J. Grant, P. Zalewski, *Biometals* **2013**, *26*, 205. **DOI:**10.1007/s10534-013-9618-2
3. K. L. Cooper, B. S. King, M. M. Sandoval, K. J. Liu, L. G. Hudson, *Toxicol. Appl. Pharm.* **2013**, *269*, 81. **DOI:**10.1016/j.taap.2013.03.008
4. (a) Z. You, H. Yu, Z. Li, W. Zhai, Y. Jiang, A. Li, S. Guo, K. Li, C. Lv, C. Zhang, *Inorg. Chim. Acta* **2018**, *480*, 120; **DOI:**10.1016/j.ica.2018.05.020
(b) Y.-T. Li, J.-W. Dong, Y. Lu, Y.-T. Gu, C.-N. Shang, F.-Y. Liu, Y. Xin, C.-L. Jing, Z.-L. You, *Chinese J. Inorg. Chem.* **2018**, *34*, 1192;
(c) J. Wang, D. Qu, J.-X. Lei, Z.-L. You, *J. Coord. Chem.* **2017**, *70*, 544. **DOI:**10.1080/00958972.2016.1262538
5. (a) V. C. D. Silveira, J. S. Luz, C. C. Oliveira, I. Graziani, M. R. Ciriolo, A. M. da Costa Ferreira, *J. Inorg. Biochem.* **2008**, *102*, 1090; **DOI:**10.1016/j.jinorgbio.2007.12.033
(b) C. Liang, J. Xia, D. Lei, X. Li, Q. Yao, J. Gao, *Eur. J. Med. Chem.* **2014**, *74*, 742. **DOI:**10.1016/j.ejmech.2013.04.040
6. (a) R. M. Ramadan, A. K. Abu Al-Nasr, A. F. Noureldeen, *Spectrochim. Acta A Mol Bio.* **2014**, *132*, 417; **DOI:**10.1016/j.saa.2014.04.151
(b) J. R. Anacona, N. Noriega, J. Camus, *Spectrochim. Acta A Mol Bio.* **2015**, *137*, 16. **DOI:**10.1016/j.saa.2014.07.091
7. (a) G. Saravanan, T. P. Selvam, V. Alagarsamy, S. Kunjiappan, S. D. Joshi, M. Indhumathy, P. D. Kumar, *Drug Res.* **2018**, *68*, 250; **DOI:**10.1055/s-0043-120198
(b) M. Patil, R. Hunoor, K. Gudasi, *Eur. J. Med. Chem.* **2010**, *45*, 2981. **DOI:**10.1016/j.ejmech.2010.03.025
8. (a) M. Durgun, H. Trukmen, M. Ceruso, C. T. Supuran, *Bioorg. Med. Chem. Lett.* **2015**, *25*, 2377; **DOI:**10.1016/j.bmcl.2015.04.007
(b) D. H. Shi, Z. L. You, *Russ. J. Coord. Chem.* **2010**, *36*, 535. **DOI:**10.1134/S1070328410070109
9. (a) M. Gopalakrishnan, J. Thanusu, V. Kanagarajan, R. Govindaraju, *J. Enzym. Inhib. Med. Chem.* **2009**, *24*, 52;
(b) L. Shi, H.-M. Ge, S.-H. Tan, H.-Q. Li, Y.-C. Song, H.-L. Zhu, R.-X. Tan, *Eur. J. Med. Chem.* **2007**, *42*, 558. **DOI:**10.1016/j.ejmech.2006.11.010
10. (a) N. P. Rai, V. K. Narayanaswamy, T. Govender, B. K. Manuprasad, S. Shashikanth, P. N. Arunachalam, *Eur. J. Med. Chem.* **2010**, *45*, 2677;
(b) N. P. Rai, V. K. Narayanaswamy, S. Shashikanth, P. N. Arunachalam, *Eur. J. Med. Chem.* **2009**, *44*, 4522.
11. (a) M. Fleck, M. Layek, R. Saha, D. Bandyopadhyay, *Transition Met. Chem.* **2013**, *38*, 715; **DOI:**10.1007/s11243-013-9741-5
(b) A. Cingolani, S. Galli, N. Masciocchi, L. Pandolfo, C. Pettinari, A. Sironi, *Dalton Trans.* **2006**, *20*, 2479; **DOI:**10.1039/b515630k
(c) F.-S. Guo, J.-D. Leng, J.-L. Liu, Z.-S. Meng, M.-L. Tong, *Inorg. Chem.* **2012**, *51*, 405; **DOI:**10.1021/ic2018314
(d) S. Mukherjee, P. S. Mukherjee, *Dalton Trans.* **2013**, *42*,

4019; **DOI:**10.1039/c2dt32802j
(e) R. Biswas, S. Mukherjee, P. Kar, A. Ghosh, *Inorg. Chem.* **2012**, *51*, 8150. **DOI:**10.1021/ic300547w
12. G.M. Sheldrick, *Acta Crystallogr.* **2008**, *A64*, 112. **DOI:**10.1107/S0108767307043930
13. J. Meletiadis, J. Meis, J. W. Mouton, J. P. Donnelly, P. E. Verweij, *J. Clin. Microbiol.* **2000**, *38*, 2949.
14. (a) A. Erxleben, *Inorg. Chem.* **2001**, *40*, 208; **DOI:**10.1021/ic000600z
(b) H.-R. Wen, Y. Wang, J.-L. Chen, Y.-Z. Tang, J.-S. Liao, C.-M. Liu, *Inorg. Chem. Commun.* **2012**, *20*, 303; **DOI:**10.1016/j.inoche.2012.03.036
(c) H. S. Jena, V. Manivannan, *Inorg. Chim. Acta* **2013**, *394*, 210. **DOI:**10.1016/j.ica.2012.06.041
15. (a) J. Gao, Y.-G. Liu, Y.-Q. Zhou, L. M. Boxer, F. R. Woolley, R. A. Zingaro, *ChemBioChem* **2007**, *8*, 332; **DOI:**10.1002/cbic.200600299
(b) S. Majumder, L. Mandal, S. Mohanta, *Inorg. Chem.* **2012**, *51*, 8739. **DOI:**10.1021/ic300412u
16. A. W. Addison, T. N. Rao, J. Reedijk, J. van Rijn, G. C. Verschoor, *J. Chem. Soc. Dalton Trans.* **1984**, *7*, 1349. **DOI:**10.1039/DT9840001349
17. Y.-M. Zhou, X.-R. Ye, F.-B. Xin, X.-Q. Xin, *Transition Met. Chem.* **1999**, *24*, 118. **DOI:**10.1023/A:1006989707001
18. H.-Y. Qian, *Acta Chim. Slov.* **2019**, *66*, 995.
19. (a) L.-W. Xue, H.-J. Zhang, P.-P. Wang, *Acta Chim. Slov.* **2019**, *66*, 190; **DOI:**10.17344/acsi.2018.4773
(b) L.-H. Wang, X.-Y. Qiu, S.-J. Liu, *Acta Chim. Slov.* **2019**, *66*, 675; **DOI:**10.17344/acsi.2019.5117
(c) Y.-L. Sang, X.-S. Lin, W.-D. Sun, *Acta Chim. Slov.* **2020**, *67*, 581. **DOI:**10.17344/acsi.2019.5595

Povzetek

Sintetizirali smo dva nova štirijedrna cinkova(II) kompleksa, $[Zn_4(L^1)_2(\mu_2\text{-}\eta^1\text{:}\eta^1\text{-}CH_3COO)_4(\mu_{1,1}\text{-}N_3)_2]$ (**1**) in $[Zn_4(L^2)_4(CH_3CH_2OH)(H_2O)]$ (**2**), kjer sta L^1 in L^2 deprotonirani obliki 4-fluoro-2-((piridin-2-ilmetilimino)metil)fenola (HL^1) in 4-fluoro-2-((2-(hidroksimetil)fenilimino)metil)fenol (H_2L^2) ter ju okarakterizirali z elementno analizo, IR in UV-vis spektroskopijo ter rentgensko monokristalno analizo. Rentgenska strukturna analiza razkriva, da so razdalje med sosednjimi cinkovimi atomi 3.160(1)–3.353(1) Å v **1** in 3.005(1)–3.168(1) Å v **2**. Vsi cinkovi atomi v **1** so pentakoordinirani z trigonalno bipiramidalno geometrijo in v **2** s kvadratno piramidalno in oktaedrično geometrijo. Kompleksoma in Schiffovima bazama smo določili antibakterijsko aktivnost proti trem Gram-pozitivnim bakterijskim sevom (*B. subtilis*, *S. aureus*, in *St. faecalis*) in trem Gram-negativnim sevom (*E. coli*, *P. aeruginosa*, and *E. cloacae*) z MTT metodo.

Scientific paper

The Role of Heuristics in the Reasoning Process of Pre-Service Science Teachers on the "Chemical Structure – Acidity/Basicity Relationship" Topic

Gülen Önal Karakoyun[1,*] and Erol Asiltürk[2]

[1] *Van Yuzuncu Yil University, Muradiye Vocational High School, Chemistry and Chemical Business Technologies Department, Chemical Technology Program, Van, Turkey*

[2] *Firat University, Faculty of Education, Science Education Department, Elazig, Turkey*

* *Corresponding author: E-mail: gulenonal@yyu.edu.tr*
Tel.: +905442930447

Received: 01-09-2021

Abstract

The purpose of this research is to examine the effects of 10 heuristics proposed by Talanquer on the reasoning processes of science teacher candidates on the "chemical structure – acidity-basicity relationship" topic. In this phenomenographic research, interviews were conducted with 30 prospective teachers enrolled in the Science Education Program, Education Faculty, Firat University in the spring semester of the 2018–2019 academic year. In the first stage of the two-stage interview, the participants were asked to rank some chemical compounds according to their increasing acidity strength, while in the second stage, they were asked to rank some chemical compounds according to their increasing basicity strength. In the interviews, participants were also asked to explain in detail the reasons for their ranking. From the answers given by the participants to the questions, six different answer patterns were obtained for acidity strength, while five different answer patterns were obtained for basicity strength. It was determined that all ten heuristics affect the reasoning of the participants, and because of the effects of heuristics, students generally use shortcut strategies instead of scientific reasoning. In addition, this study revealed that although it was not included in the model proposed by Talanquer, periodic trends heuristic also affected the reasoning of the participants on the "chemical structure – acidity/basicity relationship".

Keywords: Chemistry education, science education, heuristic, reasoning, acid-base

1. Introduction

Acid-base chemistry contains acid-base theories, auto-ionization of water, acid-base strengths, acid-base equilibriums, hydrolysis of salts, buffer solutions, acid-base reactions and acid-base titrations topics. Acid-base chemistry, which is highly related to daily life, occupy an important place in both science and chemistry curricula. Due to this importance, there are many studies in the literature on subjects such as the level of understanding of acid-base chemistry by students, the misconceptions regarding acid-base chemistry, and the effects of different teaching methods and activities on students' understanding of acid-base chemistry. In the literature these studies, it is reported that students' reasoning, judgment and decision-making processes about acid-base chemistry are generally imperfect.[1–3]

Negative situations such as imperfect reasoning, judgment and decision-making processes of the students has been encountered not only in the field of chemistry[4,5] but also in almost all disciplines.[6,7] Some scientists in different fields such as cognitive psychology, developmental psychology, and science/chemistry education, willing to investigate the reasons for individuals' imperfect reasoning, judgment and decision-making, have concentrated their research on cognitive constraints that guide individuals' reasoning. As a result of these studies, it was revealed that some mental structures that facilitate the decision making of individuals also contain various cognitive factors that restrict scientific reasoning.[8–12] Some of these cognitive elements include implicit assumptions,[13] core knowledge,[14] basic hypotheses and ontological beliefs,[15] intuitive rules,[16] primitive phenomenologies,[17] inductive constraints,[18] conceptual sources[19] and heuristics.[20]

The heuristics that restrict scientific reasoning are related to the Type 1 processes included in the "dual process" theory, which was developed to explain the individuals' judgment and decision-making processes.[21–23] According to this theory, two distinct processes called Type 1 and Type 2 are effective in the reasoning of individuals. Type 1 processes are automatic and very fast processes that do not care about the use of working memory.[21,24,25] No special effort is required to trigger Type 1 processes that progress independently of cognitive ability.[21,26] Type 1 processes are autonomous and are related to the intuitive reasoning of individuals.[26] Learned strategies and naturally occurring reasoning play an important role in type 1 processes.[11] Type 2 processes that require special cognitive effort and conscious intervention are slow processes that progress sequentially. Type 2 processes in which working memory is actively used are related to the effective, analytical and scientific thinking of individuals.[21,24,25,27] The Type 1 processes in the dual-process theory described in detail above, are short-path reasoning strategies and are called heuristics.[21,28,29] In conditions where knowledge or motivation is lacking or when time is limited, heuristics play an extremely active role.[21,30,31] As they evaluate fewer factors and use fewer cues in reasoning and judgment processes, heuristics enable decision-making in a short time without cognitive effort.[32] However, heuristics are also responsible for various cognitive biases observed in reasoning processes.[11,21]

Science/chemistry educators, who examine the judgment, reasoning and decision-making processes of students related to chemistry subjects, have started to benefit from the dual process theory and especially the heuristics, which is frequently mentioned in this theory, since the 2010s. There have been studies in the literature investigating students' intuitive reasoning and heuristic uses in chemistry subjects for a recent time. Chemistry topics in which students' intuitive reasoning and heuristic uses are examined in detail include "bond theories and molecular structures", "chemical problem solving", "addition reactions", "elimination reactions", "chemical reactivity", "acidity strength of molecules", "structure-property relationships of molecules", "classification of chemical substances" and "interpretation of IR and NMR spectra".[12,21,27,29,33–36] In addition to these important studies mentioned above, Talanquer explained the frequently used heuristics in the field of chemistry according to the cognitive processes they used, and collected these heuristics under 10 headings.[11] Since the model of Talanquer can be used as a standard or reference in studies to be carried out on heuristics in the field of chemistry, it has a great importance. Many confusions can be avoided, such as naming heuristics that work with the same mechanism with different names by using this model as a standard in chemistry issues. The model of ten heuristics has been met with great interest in the scientific world, and recently some scientists have started to use this model as a reference or standard. For example, two different research groups investigating the heuristics used by students on the hydrogen bonding topic used the ten heuristic models proposed by Talanquer in their studies.[7,37] Talanquer described and explained each of the ten heuristics that can be effective in the reasoning process of students in chemistry subjects, in his theoretical work, with examples specific to the field of chemistry. These ten heuristics are:[11]

- *Associative activation*: Using mental structures present in memory to fill in the blanks.
- *Fluency*: Using of easily accessible cues in the process of solving the problem.
- *Attribute substitution*: evaluation of other easily accessible attributes instead of the target attribute / Substitution the original question with a simpler question.
- *One reason decision making*: Simplifying reasoning by using a single clue or factor in the process of problem solving.
- *Surface similarity*: The assumption that chemical compounds that are similar to each other in structural representation have similar properties and behavior.
- *Recognition*: More value to recognized objects / less value to unrecognized.
- *Generalization*: Generalization of learned models or rules
- *Rigidity*: Reasoning in an inflexible or non-creative way.
- *Overconfidence*: Exceeding true accuracy due to self-confidence in decision-making processes.
- *Affect:* A positive or negative emotion towards an event, an object, or anything that affects learning.

The purpose of this research is to examine the effects of ten heuristics proposed by Talanquer on the reasoning processes of science teacher candidates on the "chemical structure – acidity/basicity relationship" topic. Therefore, the research problem of this study can be expressed as follows: What is the role of the ten heuristics proposed by Talanquer in the reasoning processes of the science teacher candidates about the "chemical structure – acidity/basicity relationship"? The research questions of this study are as follows:

- Which heuristics affect the reasoning of the students in the process of performing a task in which the compounds are ranked according to their acidity or basicity strengths?
- How to explain the working mechanisms of these heuristics that effected the reasoning of the students in a way specific to the field of chemistry?

2. Method

2. 1. Participants

This study was carried out at Firat University, a state university, during the spring semester in 2018–2019 aca-

demic year. Thirty pre-service science teachers at 2nd, 3rd and 4th grades in Science Teaching Program of Education Faculty voluntarily participated in the research. Sixteen of the participants were male and fourteen of them were female. While determining the students to participate in the study, the achievements of the students in General Chemistry I and General Chemistry II were taken into consideration. Participants were composed of students, 1/3 of whom failed these courses, 1/3 of whom were moderately successful, and 1/3 of whom were highly successful. Instead of using the real name of participants, codes have been given such as S1, S2, S3, S4 and so on...

2. 2. Instruments and Design

In this study, the phenomenographic research method, one of the qualitative research methods, was used to investigate the roles of heuristics in the reasoning processes of the participants on the subject of "chemical structure-acidity/basicity relationship". Phenomenography is a method used in educational research to reveal what different individuals understand or perceive from the same concept.[38,39] The interviews are generally used in phenomenographic research to obtain detailed information on the subject. Therefore, in the present study, interviews were conducted with the participants to accurately determine the reasoning of the participants about "ranking chemical compounds according to their increasing acidity/basicity strength" and to determine the heuristics used by the participants in this process.

In the first stage of the interviews, which were completed in two stages, the participants were asked to rank HCl, H_2S and HI compounds according to their increasing acidity strength, while in the second stage they were asked to rank KOH, $Mg(OH)_2$ and $Ca(OH)_2$ compounds according to their increasing basicity strength. In the interviews, participants were also asked to explain in detail the reasons for their rankings. Maeyer and Talanquer previously used these questions in a different study.[40] After these questions were asked to the students during the interviews, the participants were given 2 minutes to answer each question. It has been stated in the literature that intuitive judgment and decision-making will have a greater effect in cases where the time is limited.[21,22,29] For this reason, the time was limited. Then, in each of the interviews, participants were asked to explain in detail the reasons for their answers. There was no time limit for the participants to explain in detail the reasons for their answers. To determine whether rigidity, overconfidence and affect heuristics took part in the students' answering questions, some additional questions were asked to the participants, both before the relevant chemistry questions were asked to the participants and after the participants answered the questions. The procedures detailed below were used to determine whether rigidity, overconfidence and affect heuristics were effective in the participants' reasoning processes.

Rigidity: In this study, a method was followed to investigate the effects of rigidity heuristics: before asking the relevant chemistry questions to the participants, the following question was asked: "Do you have a constant judgment/bias about the ranking of compounds according to their increasing acidity/basicity strength? For example, do you have any approaches such as "I have judgments/reasoning regarding the order of compounds according to their increasing acidity/basicity strength, which I will not change regardless of the question, I always solve problems regarding the order of compounds according to their increasing acidity/basicity strength using my current judgments/reasoning"? The answers given by the participants to this question were carefully examined. Besides, during the interviews, special attention was paid to whether the participants actually solved the questions using the strategies they were used to before, and whether they were flexible in solving the questions.

Overconfidence: Before asking/showing the relevant chemistry questions to the participants, the following question was asked: "If you are faced with a question about ranking compounds according to their increasing acidity/basicity strength, what level of confidence do you have that you can answer the question correctly. How would you score your confidence level between 1 and 10 points (1 is the lowest, 10 is the highest)"? Immediately after the relevant chemistry questions were asked/shown to the participants, the following question was asked to the participants before the students started solving the question; "What level of confidence do you have that you can answer this question correctly?" Finally, after solving the relevant chemistry question, the following question was asked to the participants: "What level of confidence do you have in yourself that you answered this question correctly? In cases where 8, 9 or 10 points were given as an answer to these three questions, it has been coded as overconfidence heuristic. Students who gave such answers generally made the following statements: "I am confident; I definitely solved / will solve the question correctly".

Affect: Before asking/showing the relevant chemistry questions to the participants, the following question was asked: "How do you feel when talking about the ranking of compounds according to their increasing acidity/basicity strength? Have you experienced any positive or negative effects on this chemistry topic during your education? If there is such an event, is it still effective"? "Besides, after the mentioned chemistry questions were asked/shown to the participants, the following question was asked: You saw the question, what do you feel?" Affect heuristic was coded in cases where it was determined that the participant had negative or positive emotions due to experiences.

2. 3. Data Analysis

The interviews that were recorded with audio and visuals later were transcribed into written documents.

Thus, interview transcripts were produced for each student. With the analysis of the data obtained from the interview transcripts, heuristic reasoning was detected and coded. While coding, other similar studies on students' heuristic reasoning in chemistry were also used.[7,21,22,40]

In order to ensure the inter-rater reliability, eight interview transcripts related to acidity strength and eight interview transcripts related to basicity strength (approximately 25% of total interview transcripts) were selected and the selected interviews were first evaluated and encoded separately by both the researcher and the consultant. The results of both evaluators were compared with each other. The encodings were revised so that there was over 90% agreement between the evaluators. After this compliance was achieved, all remaining interview transcripts were evaluated and coded by the researcher. Ten heuristics proposed by Talanquer were used to create a coding scheme for heuristics. Except for rigidity, overconfidence and affective heuristics, encodings for the other heuristics were made by associating the specific expressions found in the explanations made by students to solve the questions with the heuristics. Specific student expressions that form the basis of coding were presented in the results and discussion section.

3. Results and Discussion

From the answers given by the participants to the questions, six different answer patterns were obtained for acidity strength, while five different response patterns were obtained for basicity strength. These different answer patterns, the numbers and percentages of the students who gave these answers are presented in Table 1.

Table 1. Answer patterns

Answer patterns	n	%
(Acidity Strength, HCl, H2S and HI Compounds)		
$HCl < HI < H_2S$	2	6.66
$HI < HCl < H_2S$	3	10.00
$HI < H_2S < HCl$	6	20.00
$H_2S < HI < HCl$	12	40.00
$HCl < H_2S < HI$	1	3.33
$H_2S < HCl < HI$ (Correct Answer)	6	20.00
(Basicity Strength, KOH, $Mg(OH)_2$ and $Ca(OH)_2$ Compounds)		
$KOH < Mg(OH)_2 < Ca(OH)_2$	8	26.26
$Mg(OH)_2 < Ca(OH)_2 < KOH$ (Correct Answer)	9	30.00
$KOH < Mg(OH)_2 = Ca(OH)_2$	3	10.00
$KOH < Ca(OH)_2 < Mg(OH)_2$	6	20.00
$Ca(OH)_2 < Mg(OH)_2 < KOH$	4	13.33

Two important factors affect the acidity strength of an acid that can be represented as E-H. These factors are the electronegativity and radius of the E atom. As the electronegativity of the E atom increases, it will be easier to separate the hydrogen as a proton (H^+). Therefore, acidity strength will increase. As the radius of the E atom increases, the E–H bond will become weaker. Therefore, hydrogen will be easily released in the form of proton (H^+), that is, the acidity strength will increase. In the periodic table, the radius decreases from left to right, while electronegativity increases. In the periodic table from left to right, the effect of electronegativity is more dominant than the effect of the radius in terms of the effect on the acidity strength. As a result, the acidity strength of the acids shown in the form of E–H increases from left to right in the periodic table. In the periodic table, the radius increases from top to bottom in a group, while electronegativity decreases. In the periodic table, from top to bottom, the effect of the radius is dominant over the effect of electronegativity in terms of the effect on the acidity strength. As a result, from top to bottom in the periodic table, the acidity strength of the acids shown in the form of E–H increases. Due to all these explanations mentioned, the correct answer to the question about acidity strength is $H_2S < HCl < HI$. Two important factors affecting the basicity of a base (where B stands for metal atom) that can be represented as a B–OH. These factors are the charge and radius of the metal atom (B). As the charge of the metal atom shown as B increases, the Coulomb attraction force between the metal atom and the OH group will increase and the separation of the hydroxyl ion will be difficult. Therefore, the basicity strength will decrease. As the radius of the B atom increases, the B–OH bond will become weaker. Therefore, hydroxyl (OH^-) will be easily released, that is, the strength of basicity will increase. The charge of B atom increases from left to right in the periodic table, however, the radius decreases. In the periodic table from left to right, the effect of the charge is more dominant than the effect of the radius in terms of the effect on the basicity strength. As a result, due to the reasons mentioned above, the basicity strength decreases from left to right in the periodic table for bases that can be represented as B–OH. In the periodic table, the charges of metals do not change from top to bottom in a group, and their atomic radii increase. As the radius of the B atom increases, the B–OH bond will become weaker and thus the OH group will be separated more easily. In other words, the basicity of metal hydroxides will increase from top to bottom in the same group in the periodic table. Because of all the explanations mentioned, the correct answer to the question about acidity strength is $Mg(OH)_2 < Ca(OH)_2 < KOH$.

Participants are expected to solve questions with the reasoning explained in detail above. However, in this study, it was determined that the rates of students who gave correct answers to the questions about acidity and basicity strengths were 20.00% and 30.00% respectively. Because scientific reasoning requires a great deal of cognitive

effort, the majority of students may have answered the questions by relying on heuristic strategies that require less cognitive effort. Since the aim of this study was to examine the heuristic use of the students, the answers given by the students to the questions asked were examined in terms of heuristic use. For this purpose, specific expressions in each student's interview transcript were associated with 10 heuristics and encoded. Specific student expressions related to the solution of the problem related to acidity strength are given in Table 2. The periodic trends heuristic in Table 2 is

Table 2. Student Expressions Related to Heuristics (Acidity strength, HCl, H_2S and HI)

Heuristic Code	Summary of student statements
Associative activation	As the hydrogen number increases, acidity increases. Elements that are close to each other in the periodic table show similar chemical properties. Statements in which the "more electronegative, the stronger acid " approach is adopted. As the hydrogen number increases, acidity decreases. Acidity changes from left to right and from top to bottom in the periodic table. Statements in which "the larger the radius, the stronger acid" approach is adopted. The higher the molecular weight, the more acid.
Fluency	Using the hydrogen number in the molecule as an easily accessible clue/Using the number 2 in the H_2S compound as an easily obtainable clue.
Attribute Substitution	Replacing the original question with questions: Which compound has more hydrogen? What is the order of compounds regarding their molecular weight? What are the positions of the S, Cl and I atoms relative to each other in the periodic table? Which of the S and I atoms is closer to the Cl atom in the periodic table? What is the order of S, Cl and I atoms regarding their electronegativities? How are the S, Cl and I atoms ordered regarding their radii?
One-Reason Decision Making	Decision-making by evaluating only electronegativity. Decision-making by evaluating only radii. Decision-making based on whether to recognize one compound only. Decision-making by evaluating only the places of the atoms in the periodic table. Decision-making by evaluating only the weights of compounds.
Surface similarity	HI looks like HCl. HCl looks like HI. H_2S looks like H_2O.
Recognition	I know/recognize HCl (from the lab or from the class). I know/recognize HI (from lab or class). I do not know / have never heard of H_2S before.
Generalization	Generally, all properties increase / decrease in the periodic table from top to bottom, so acidity also increases / decreases from top to bottom. Generally, all properties increase / decrease in the periodic table from left to right, so the acidity also increases / decreases from left to right. Elements that are close to each other in the periodic table generally show similar chemical properties. Atoms with high electronegativity generally have high all other properties. Atoms with large radii generally have high all other properties.
Rigidity	I will decide the acidity strength based on the number of hydrogen in the compounds. I will decide according to the place of the atoms in compounds in the periodic table. I will decide based on the electronegativity of the atoms in compounds. I will decide according to the radii of the atoms in compounds.
Overconfidence	I definitely solved / will solve the problem correctly. My confidence level is 8-10.
Affect	I like / dislike the subject of relative acidity strength of compounds, positive / negative emotion.
Periodic Trends	Acidity increases / decreases from left to right in the periodic table. Acidity increases / decreases from top to bottom in the periodic table.

Periodic Trends: Periodic Trends heuristic is not included in the ten heuristics proposed by Talanquer. However, this heuristic was added to the list since it was determined that the participants in this study also used this heuristic.

not included in the ten heuristics proposed by Talanquer. However, since it was found in this study that the participants also used this heuristic, this heuristic was also taken into consideration and added to the table.

To facilitate comparisons and interpretations, the number and percentages of the participants who used the related heuristics at least once in the process of solving the question about acidity strength are given in Table 3. The percentages given in Table 3 express the ratio of the number of participants who used the relevant heuristics at least once to the total number of participants (N = 30, total number of participants).

Table 3. Number and percentages of participants using relevant heuristic at least once (acidity strengths, HCl, H_2S and HI)

Heuristics	n	% (N = 30)
Associative activation	20	66.66
Fluency	8	26.66
Attribute substitution	20	66.66
One reason decision making	9	30.00
Surface similarity	9	30.00
Recognition	20	66.66
Generalization	10	33.33
Rigidity	5	16.66
Overconfidence	4	13.33
Affect	5	16.66
Periodic trends	8	26.66

Specific student expressions related to the solution of the problem related to basicity strength are given in Table 4.

The number and percentages of the participants who used the related heuristics at least once in the process of solving the question about the basicity strength are given in Table 5. The percentages given in Table 5 express the ratio of the number of participants who have used the relevant heuristics at least once to the total number of participants (N = 30, total number of participants).

Table 5. Number and percentages of participants using relevant heuristic at least once (relative basicity strengths of compounds KOH, $Mg(OH)_2$ and $Ca(OH)_2$)

Heuristics	n	% (N = 30)
Associative activation	25	83.33
Fluency	11	36.66
Attribute substitution	25	83.33
One reason decision making	15	50.00
Surface similarity	3	10.00
Recognition	11	36.66
Generalization	14	46.66
Rigidity	5	16.66
Overconfidence	6	20.00
Affect	5	16.66
Periodic trends	12	40.00

In the process of solving a problem, individuals' evaluation of other and easily accessible attributes instead of the target attribute is a result of the effect of the attribute substitution heuristic.[11] Similarly, individual's unconscious replacement of the question asked to himself/herself by another simple question and focusing on the solution of this simple problem is a result of the attribute substitution heuristic. The electronegativities and radii of Cl, S and I atoms must be consciously evaluated in order to solve the problem related to the acidity strength by using scientific reasoning. Evaluating the electronegativities and radii of the Cl, S and I atoms is the implied target attribute of the question mentioned. However, in this study, when the reasoning of the participants about the solution of the problem related to acidity strength was examined, it was revealed that heuristics affected the participants' interpretation of the question, and thus, there were differences between the target attribute and the comments expressed by the students. In the process of solving the problem related to acidity strength, it was found that, due to the effect of attribute substitution heuristic, twenty of the participants evaluated other attributes instead of the intended target attribute or unconsciously evaluated the intended target attribute. Thus, after reading the question, they replaced the original question with another simple question. The mentioned students focused on the answer to another simple question. Instead of the original question, the different questions that mentioned students focused on in the process of solving the problem related to acidity strength are collectively given in Table 2. Due to the effect of attribute substitution heuristic in the process of solving the problem related the basicity strength, it was determined that twenty-five of the participants evaluated other attributes instead of the intended target attribute or unconsciously evaluated the intended target attribute. Thus, they replaced the original question with another simple question after reading the question. Instead of the charge and radius of the metal atom, these participants evaluated other attributes or unconsciously evaluated the radius, and focused on the answer to another simple question. The questions students focused on in the process of solving the problem related to basicity strength instead of the original question are collectively given in Table 4.

It is reported in the literature that more than one heuristics are effective in the decision-making processes of individuals and that these effective heuristics promote and trigger each other.[11,22] Similar to this situation stated in the literature, in this study, it was concluded that more than one heuristics were effective at the same time. The reasoning of the S14 coded student during the process of solving the question about acidity strength can be given as an example in which more than one heuristics are effective at the same time. From the statements of the S14 coded student, it is understood that fluency, associative activation, attribute substitution and recognition heuristics are effective in the student's problem-solving process. For a person

Table 4. Student Expressions Related to Heuristics (Basicity strength, KOH, $Mg(OH)_2$ and $Ca(OH)_2$)

Heuristic Code	Summary of student statements
Associative activation	The more the number of hydroxyl groups, the higher basicity. Statements in which "the more electronegative, the stronger base" approach is adopted. Basicity changes from left to right and from top to bottom in the periodic table. Statements in which the "larger radius, the stronger base" approach is adopted. A compound with a large molecular weight is more basic.
Fluency	Using the number of hydroxyl groups in the compound as an easily accessible clue / using the number 2 in the compounds $MgOH)_2$ and $Ca(OH)_2$ as an easily accessible clue.
Attribute substitution	Replacing the original question with questions: Which compound has more hydroxyl groups? What is the order of compounds regarding their molecular weight? How are the positions of K, Mg and Ca atoms relative to each other in the periodic table? What is the order of K, Mg and Ca atoms regarding their electronegativities? What is the order of the K, Mg and Ca atoms regarding their radii?
One reason decision making	Decision-making by evaluating only electronegativity. Decision-making by evaluating only radii. Decision-making based on whether to recognize one compound only. Decision-making by evaluating only the places of the atoms in the periodic table. Decision-making by evaluating only the weights of compounds.
Surface similarity	$Mg(OH)_2$ looks like $Ca(OH)_2$.
Recognition	I know/recognize KOH I know/recognize $Ca(OH)_2$ I do not know/recognize $Mg(OH)_2$. I have never heard it before.
Generalization	Generally, all properties increase/decrease in the periodic table from top to bottom, so basicity also increases/decreases from top to bottom. Generally, all properties increase/decrease in the periodic table from left to right, so the basicity also increases/decreases from left to right. Elements that are close to each other in the periodic table generally show similar chemical properties. Atoms with high electronegativity generally have high all other properties. Atoms with large radii generally have high all other properties.
Rigidity	I will decide the basicity strength based on the number of hydroxyl in the compounds. I will decide according to the place of the atoms in compounds in the periodic table. I will decide based on the electronegativity of the atoms in compounds. I will decide according to the radii of the atoms in compounds.
Overconfidence	I definitely solved/will solve the problem correctly My confidence level is 8–10.
Affect	I like/dislike the subject of relative basicity strength of compounds, positive/negative emotion.
Periodic trends	Basicity increases / decreases from left to right in the periodic table. Basicity increases / decreases from top to bottom in the periodic table.

Periodic Trends: Periodic Trends heuristics is not included in the ten heuristics proposed by Talanquer. However, this heuristic was added to the list since it was determined that the participants in this study also used this heuristic.

who is new to any field, it is easier to examine explicitly given properties than implicitly given properties. People tend to use easily accessible information when making judgments and decisions. Individuals' use of easily accessible cues to solve the problem is associated with the fluency heuristic.[11] Therefore, the S14 coded student's use of the number 2 in H_2S (the number of hydrogen atoms in the compound) as an easily accessible clue is associated with the fluency heuristic. Associative activation heuristic shows its effect by unconsciously using the existent mental constructions in that person's memory when faced with a new problem. With the effect of associative activation heuristic, individuals generally use straight or inverse proportion approaches, which can be expressed as "More A-More B" or "More A-Less B".[11] S14 coded student's relationship between acidity and hydrogen and adopting an approach such as "more hydrogen – more acid" is related to associative activation heuristic. In this process, the student fo-

cused on a simpler question such as "Which compound has more hydrogen" instead of the original question. This situation is associated with attribute substitution heuristic. Recognized objects or events have a strong influence on the decisions people make. In cases where individuals recognize one of more than one object and do not recognize the others, they give higher value to the object they recognize. HCl is a chemical compound that students often hear its name. The name of the compound HCl is frequently mentioned in lectures. In addition, this compound is frequently used in many experiments in laboratories. The fact that the S14 coded student gave more value to HCl, which he knew before, and therefore said that HCl is a stronger acid than HI, shows that the recognition heuristic is effective in the reasoning process of this participant.

The fact that some of the participants used the number 2 (the number of hydroxyl groups in the compounds) as an easily accessible clue in $Mg(OH)_2$ and $Ca(OH)_2$ compounds in the process of solving the problem related to the basicity strength is also related to the fluency heuristic. In the process of solving the problem related to the basicity strength, the fact that some of the participants adopt the flat proportion approach expressed as "more hydroxyl – more basic" is related to the associative activation heuristic. In the question about basicity strength, KOH is a chemical compound that students often hear its name. With the effect of recognition heuristic, some of the students evaluated KOH as the compound with the highest basic strength. Some of the students stated that the $Ca(OH)_2$ compound is named as slaked lime in daily life and they have heard its name many times before and therefore they know this compound. With the effect of recognition heuristics, some of the students evaluated $Ca(OH)_2$ as the compound with the highest basic strength. The students' thinking of KOH or $Ca(OH)_2$ as the compound with the highest basicity strength among the compounds in the question with such approaches shows that the recognition heuristic is effective.

The assumption that chemical compounds resembling each other in structural representation are members of the same category and that such compounds have similar properties and behavior is a result of the effect of the surface similarity heuristic. The reasoning of the S3 coded student during the process of solving the question about the basicity strength can be given as an example reasoning process in which the surface similarity heuristic is effective. The S3 coded student's evaluation of $Mg(OH)_2$ and $Ca(OH)_2$ compounds as having the same basicity strength because they are very similar to each other shows that the surface similarity heuristic is effective in this process. In the process of solving the problem related to the acidity strength, some of the participants used one of the approaches such as "HI looks like HCl", "HCl looks like HI" or "H_2S looks like H_2O". These students think that similar compounds will have the same properties. For example, the S9 coded student's "H_2S looks like H_2O. H_2O is neutral. Since it is similar to H_2O, it is likely that H_2S is also neutral or very weak acid" shows that the surface similarity heuristic is effective in this process.

Individuals' extra generalization of previously learned patterns or rules, using the knowledge they have gained from a few previous experiences, without considering all variables, is considered an effect of the generalization heuristic. In this study, it was determined that the generalization heuristic was effective in the decision-making processes of some of the participants in the process of solving the problem related to both acidity and basicity strength. Regarding the acidity and basicity strengths, the participants' expressions determined by this study and revealing that the generalization heuristic is effective were given in Table 2 and Table 4, respectively. In all processes in which generalization heuristic was effective, associative activation heuristic was also effective. These two heuristics triggered and supported each other. The reasoning of the S4 coded student in the process of solving the first question can be given as an exemplary reasoning process in which generalization and associative activation heuristics are effective at the same time. The approach of the student coded S4 that "all other properties of atoms with high electronegativity are generally also high" shows that the generalization heuristic is effective in this process. In this process, the student decided by using the approach that "Probably, the acidity of the compounds formed by the bonding of high electronegativity atoms to hydrogen will also be high". Such an approach shows that the student is relying on a straight-proportion logic expressed as "the more A – the more B". The student's decision with such an approach shows that the associative activation heuristic is also effective in this process.

Individuals generally facilitate reasoning by using a single clue or factor to give a logical answer. In doing so, they use the first feature that comes to mind. S4 coded student made a decision based on only one reason. The S4 coded student only evaluated electronegativity during the decision-making process regarding the question. For this reason, the one-reason decision-making heuristic was also effective in the decision-making process of the S4 coded student. The attributes evaluated by the participants who made a decision based on only one reason in the process of solving the problems regarding acidity and basicity strength were given in Table 2 and Table 4, respectively.

Three of the students stated that they generally hate verbal chemistry subjects, they mainly consider themselves closer to numerical logic, that there are more subjects that require chemical and mathematical processing in chemistry lessons, they do not like to deal with abstract concepts and the relationships between these concepts. As a result, they stated that they did not like and were not interested in the ranking of compounds according to their acidity/basicity strength, as it was the subject of verbal chemistry. Affective heuristic was coded based on these expressions of the mentioned students. Two of the partici-

pants stated that they had a special interest in the periodic table and that they liked topics of the periodic table and the changing properties throughout the periodic table. These students also stated that they knew whether all properties such as atomic radius, ionization energy, electron affinity, acidity and basicity increased or decreased from left to right or from top to bottom in the periodic table. These students also stated that even if they do not know exactly the factors that affect the change of these characteristics, it is sufficient for them to know whether they increase or decrease in the periodic table from top to bottom or from left to right. Based on these expressions of mentioned students, affective heuristics were also coded for these students.

In this study, the procedure described in detail under the title of method was followed to investigate the effects of rigidity heuristics. In order to investigate the effects of rigidity heuristics, the answers given to the questions by the participants were carefully examined. In addition, during the interviews, special attention was paid to whether the participants actually solved the question using the strategies they were used to before, and whether they were flexible in solving the question. As a result of these operations, it was concluded that the rigidity heuristic had an effect on the problem-solving process of five students. The mentioned students stated that regardless of the question/s about the relative acidity/basicity strength of the compounds, they have the approach they believe and rely on to solve the question/s and that they will solve the question/s according to these approaches. The reasoning of the students in the process of solving the questions was examined carefully and it was determined whether these students were flexible in the process of solving the questions. The strategies that the participants declared that they would use in the process of solving the questions about acidity and basicity strengths are presented in Table 2 and Table 4, respectively.

In this study, the procedure described in detail in the method section was followed to investigate the effects of overconfidence heuristic. In order to investigate the effects of overconfidence heuristic, the answers given by the participants to the questions (three questions) were carefully examined. The overconfidence heuristic was coded when 8, 9 or 10 was given as an answer to these three questions. Students who gave this kind of answer usually made the following kinds of statements: "I am confident in myself; I have definitely solved the question correctly". As a result of the procedures performed by following the procedure described in detail above, it was determined that overconfidence heuristic was effective in reasoning about the acidity strength of the four participants and also in reasoning about basicity of the six participants.

Periodic trends heuristic is not included in the ten heuristics proposed by Talanquer. However, since it was determined in this study that the participants also used this heuristic, this heuristic was also taken into consideration. The periodic trends heuristic is also called arbitrary heuristic by some researchers. It is a result of the effect of periodic trends heuristics to make the evaluations such as only the feature increases or the feature decreases without knowing why the features changing from left to right and from top to bottom in the periodic table. It was determined that the periodic trends heuristic was effective in the reasoning processes related to the acidity strength of the eight students. In addition, it was determined that the periodic trends heuristic was effective in the reasoning processes related to the basicity strength of the twelve students. Associative activation, attribute substitution, and generalization heuristics also played an active role in many of the reasoning in which periodic trends heuristic exhibited. These four heuristics triggered and supported each other.

The misconceptions about acid-base strength, which are widely stated in the literature, are: The acidity of a compound increases with the increase in the number of hydrogen in the compound.[2,41] The basicity of a compound increases with the increase in the number of hydroxyls in the compound.[42,43] pH is a measure of acid strength.[2] The pH value of the solution is inversely proportional to the strength of the acid; the lower the pH value of the solution, the higher the acidic power of the solution.[3] For compounds shown as HX, the more electronegativity of the halogen atom (X), the higher the acidity.[3] Concentration indicates the acid-base strength.[44,45] The Kb value reflects the concentration of the basic solution.[1] Diprotic acid is stronger than monoprotic acid.[46] All acids are strong acids.[44,45] In this study, the main purpose of which was to examine the heuristic uses of the students, in-depth interviews with the participants regarding the acidity and the basicity strength of the compounds allowed to observe some misconceptions held by the students. The misconceptions determined in this study are as follows: "As the number of hydrogen in compounds increases, the acidity strength of the compounds increases". "As the number of hydrogen in the compounds increases, the acidity strength of the compounds decreases". " As the number of hydroxyls in the compounds increases, the basic strength of the compounds increases". "For hydrogen halides shown as HX, the acidity strength decreases from top to bottom in the periodic table". "For hydrogen halides shown in the form of HX, as the electronegativity of the halogen atom (X) increases, the acidity strength increases". "As the molecular weights of the compounds increase, the acidity strength increases". "As the molecular weights of the compounds increase, the basicity strength increases". "As the electronegativity of the atom to which the hydroxyl group is attached increases, the basicity strength increases". The misconceptions determined in the present study and the misconceptions determined in the different studies in the literature are generally similar. However, different from the misconceptions found in the literature, in this study, it was determined that the students correlated the acidity or basicity strengths with the molecular weights of the compounds.

The fact that the participants used heuristics frequently caused the rate of students who gave correct answers to the questions to be low. In many studies in the literature on students' reasoning in chemistry subjects, similar to the results of the present study, the accuracy rates of participant answers were generally low. For example, in two different studies on students 'understanding of hydrogen bonding, the accuracy rate of participants' answers was found to be 27.00% and 16.66%.[7,37] The accuracy rate of the participants' answers was found to be 36.00% in a study on "chemical bond theories and molecular structures", and 31.00% in a study on addition reactions.[33,21]

There is only one study in the literature that examines the heuristic reasoning of the students in the process of performing a task where it is desired to rank HCl, H_2S and HI compounds according to their increasing acidity strength and KOH, $Mg(OH)_2$ and $Ca(OH)_2$ compounds according to their increasing basicity strength.[40] In the mentioned study, it was determined that the heuristics of "recognition", "one reason decision making", "arbitrary/periodic trends" and "representativeness" were effective in the reasoning processes of the participants, and explanations and comments were made based on these four heuristics. In the present study, the reasoning of the participants was examined based on 10 heuristics. In order to present the results of the current research visually, the frequencies of the participants' use of the heuristics are given as a graphical representation in Figure 1.

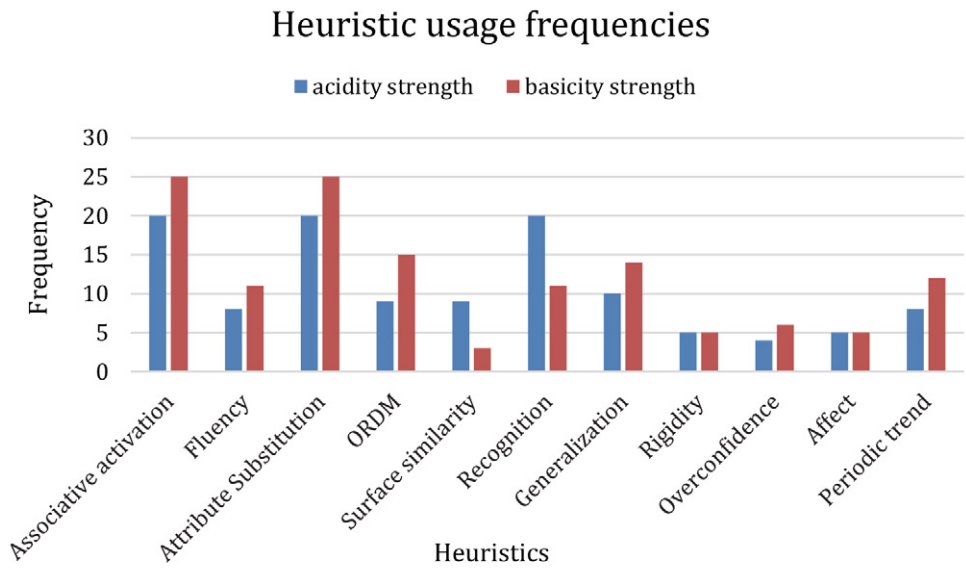

Figure 1. Graphical presentation of heuristic usage frequencies

In the study conducted by Maeyer and Talanquer[40] on the ranking of HCl, H_2S and HI compounds according to their increasing acidity strength and KOH, $Mg(OH)_2$ and $Ca(OH)_2$ compounds according to their increasing basicity strength, the accuracy rate of student answers to both questions was determined as 20.60%. In the mentioned study, it was also stated that the percentage of participants using one-reason decision-making, recognition and periodic trends heuristics were 50.00%, 79.40% and 11.80% respectively for the question related to acidity strength and 67.60%, 35.30% and 41.20% respectively for the question related to basicity strength. In the current study, in which the students were asked to solve the same questions, the accuracy rate of the student answers for the question about acidity strength was found to be 20.00%, and 30.00% for the question about the basicity strength. In the current study, it was also determined that the percentage of participants using one-reason decision-making, recognition and periodic trends heuristics were 30.0%, 66.66% and 26.66% respectively for the question related to acidity strength and 50.00%, 36.66% and 40.00% respectively for the question related to basicity strength. The accuracy rates of student answers determined by the present study are similar to the rates determined in the study conducted by Maeyer and Talanquer.[40] The usage percentages of one-reason decision making, recognition and periodic tendency heuristics determined in the study conducted by Maeyer and Talanquer[40] and the usage percentages determined by this study are generally different. On the other hand, in the solution processes of the questions about the acidity/ basicity strength, the explanations and determinations made in the present study about the action mechanisms of these three heuristics and the explanations and determinations made by Maeyer and Talanquer[40] are similar.

This study revealed that when faced with questions about "chemical structure – acidity/basicity relationship", pre-service science teachers rely heavily on intuitive reasoning rather than analytical thinking in decision-making processes, and students frequently use heuristics. These

heuristics reduced the cognitive effort in students and caused students to produce incorrect answers. Except for two studies on students' understanding of hydrogen bonding, the ten heuristic models proposed by Talanquer were not used in all other studies examining the effects of heuristics on chemistry subjects. With the current research carried out to fill this gap in the literature, the effects of all 10 heuristics proposed and defined by Talanquer on students' reasoning processes on the "chemical structure – acidity/basicity relationship" were examined in detail.

4. Conclusions

In the process of ranking compounds according to their increasing acidity/basicity strength, the roles of all ten heuristics proposed by Talanquer were examined for the first time in this study. This study, in which the subject of "chemical structure – acidity/basicity relationship" was evaluated and examined in the context of a cognitive psychology theory, will make an important contribution to the literature in this sense. The fact that the students used heuristics frequently in the process of answering the questions shows that most of the students preferred shortcut strategies instead of scientific/chemical reasoning. The heuristics identified in this study are typical examples of cognitive constraints that restrict students' scientific reasoning under conditions where time and knowledge are limited. These heuristic strategies have allowed students to reduce cognitive effort and produce answers in the absence of necessary information, but these cognitive constraints often misled students and caused them to give incorrect answers. Knowing how students think about the "chemical structure – acidity/basicity relationship" and the role of heuristics in this topic can help chemistry educators to develop strategies that encourage meaningful learning about the "chemical structure – acidity/basicity relationship". In order to develop measurement tools that will evaluate student learning validly and reliably, it is useful to examine students' general and field-specific reasoning strategies in detail. Therefore, this study may contribute to the development of measurement tools in the field of chemistry. For example, this study revealed that particular attention should be paid to chemical molecules or compounds involved in chemistry questions to be asked. In the chemistry-related questions in this study, an important effect of fluency heuristics was found, as there are clues that participants can easily obtain in the structural representation of the compounds. In addition, the fact that the compounds that the students knew before, such as HCl or KOH, were also included in the questions caused the recognition heuristic to be used by most of the participants. Knowing these and similar situations and results will be useful for instructors who will prepare questions to evaluate students.

As heuristic reasoning is unconscious, automatic, fast, and cognitively economic, students frequently use it. Developing analytical reasoning skills instead of heuristic reasoning are a very time-consuming and difficult process, as students often have the habit of using heuristics for the reasons mentioned above. We believe that it would be beneficial to give more importance to the education of students in judgment and decision-making strategies in order to contribute to students' decision making with scientific reasoning instead of heuristic reasoning.

The reason why heuristic strategies are frequently used may be that the shortcut problem solving strategies taught to students throughout their education have reduced students' tendency to use scientific reasoning skills. Thus, students may have acquired the habit of solving problems using shortcut strategies. One of the most common types of reasoning is intuitive reasoning. Therefore, the task of educators is not to prevent an intuitive judgment, but to investigate how intuitive judgment affects students' understanding and interpretation, and to create successful reasoning and thinking methods specific to the field after carefully analyzing the data obtained from these studies. While a subject is being taught to students in chemistry lessons, it can be very useful to explain the wrong reasoning ways that can be encountered due to frequently used shortcut strategies about that topic. It is often recommended that students be asked to solve different and new types of chemistry questions in order to gain the habit of solving questions using chemical processes instead of shortcut reasoning strategies that are unrelated to scientific reasoning.

In this study, data were collected from a limited number of student enrolled in the Science Teaching Program of Firat University. As a necessity of the interview method, the fact that a small number of participants were interviewed is a limitation of this study. For this reason, we recommend that similar studies be carried out in different institutions. The participants who were interviewed within the scope of this study were determined on a voluntary basis and no reward was given to these participants for their time and effort. Another limitation of this study is the possibility that this situation negatively affects the students' motivation to spend time and their cognitive efforts to answer the questions. More studies are also needed on how Type 2 processes can be activated more to correct biases caused by Type 1 processes in different chemistry issues. In addition, it is beneficial to investigate the effects of various teaching strategies that will be planned to eliminate the negative effects of heuristics that affect chemistry subjects.

Acknowledgements

The authors would like to thank the prospective teachers enrolled in the Science Education Program, Education Faculty throughout Firat University who participated in this research for being willing to share their experience. Gülen Önal Karakoyun and Erol Asiltürk contributed equally to this work. This study was prepared from the

relevant parts of Gülen Önal Karakoyun's PhD thesis. ORCID numbers of authors: Gülen Önal Karakoyun; https://orcid.org/0000-0002-7675-0006; Erol Asiltürk; https://orcid.org/0000-0001-8126-7812.

Conflicts of Interest

The authors declare no conflict of interest.

5. References

1. R. Artdej, T. Ratanaroutaia, R. K. Collb, T.Thongpanchange, *Res. Sci. Technol. Educ.* **2010**, *28*, 167–183. **DOI:**10.1080/02635141003748382
2. G. Demircioğlu, A. Ayas, H. Demircioğlu, *Chem. Educ. Res. Pract.* **2005,** *6,* 36–51. **DOI:**10.1039/B4RP90003K
3. A. Mutlu, B. C. Sesen, J. *Balt. Sci. Educ*. **2016**, *15*, 79–96.
4. M. Slapničar, V. Tompa, S. A. Glažar, I. Devetak, J. Pavlin, *Acta Chim. Slov.* **2020**, *67*, 904–915. **DOI:**10.17344/acsi.2020.5908
5. R. Kozma, E. Chin, J. Russell, N. Marx, J. Learn. Sci. **2000**, 9,105–143. **DOI:**10.1207/s15327809jls0902_1
6. K. S. Taber, *Chem. Educ. Res. Pract.* **2001,** *2,* 123–158. **DOI:**10.1039/B1RP90014E
7. K. Miller, T. Kim, *Biochem. Mol. Biol. Educ.* **2017***, 45*, 411–416. **DOI:**10.1002/bmb.21061
8. G. Hatano, K. Inagaki, *Int. J. Behav. Dev.* **2000**, 24, 267 – 275. **DOI:**10.1080/01650250050118240
9. F. C. Keil, *Cogn. Sci.* **1990**, *14*, 135–168. **DOI:**10.1207/s15516709cog1401_7
10. H. M. Wellman, S. Gelman, In: D. Kuhn, R. Siegler (Eds.): Cognition, perception and language. Handbook of child psychology, Wiley, New York, **1998**, pp. 523–573.
11. V. Talanquer, *J. Chem. Educ.* **2014***, 91,* 1091–1097. **DOI:**10.1021/ed4008765
12. J. Maeyer, V. Talanquer, *J. Res. Sci. Teach.* **2013***, 50,* 748–767. **DOI:**10.1002/tea.21092
13. S. Vosniadou, *Learning and Instruction*, **1994**, *4*, 45–69. **DOI:**10.1016/0959-4752(94)90018-3
14. E. S. Spelke, K. D. Kinzler, *Dev. Sci.* **2007**, *10*, 89–96. **DOI:**10.1111/j.1467-7687.2007.00569.x
15. M. T. H. Chi, In S. Vosniadou (Ed.), International Handbook of Research on Conceptual Change, Routledge, New York, **2008**, pp. 61–82.
16. R. Stavy, D. Tirosh, How students (mis-)understand science and mathematics: Intuitive rules. Columbia University, Teachers College Press, New York, **2000.**
17. A. A. diSessa, *Cognition and Instruction*, **1993**, *10*, 165–255. **DOI:**10.1080/07370008.1985.9649012
18. A. Perfors, J. B. Tenenbaum, T.L. Griffiths, F. Xu, *Cognition*, **2011**, *120*, 302–321. **DOI:**10.1016/j.cognition.2010.11.015
19. E. F. Redish, In E. F. Redish, M. Vicentini, (Eds.): Proceedings of the international school of physics, "Enrico Fermi" course CLVI, IOS Press, Amsterdam, **2004**
20. G. Gigerenzer, W. Gaissmaier, *Annu. Rev. Psychol.* **2011**, *62*, 451–482. **DOI:**10.1146/annurev-psych-120709-145346
21. M. Ugras, *J. Baltic Sci. Educ.* **2018***, 17*, 343–356. **DOI:**10.33225/jbse/18.17.356
22. N. Graulich, *J. Chem. Educ.* **2014***, 92,* 205–211. **DOI:**10.1021/ed500641n
23. S. A. Sloman, *Psychol.Bull.* **1996**, *119*, 3–22. **DOI:**10.1037/0033-2909.119.1.3
24. J. S. B. T. Evans, Psychon. Bull. Rev. **2006**, *13*, 378–395. **DOI:**10.3758/BF03193858
25. J. S. B. T. Evans, *Annu. Rev. Psychol.* **2008***, 59*, 255–278. **DOI:**10.1146/annurev.psych.59.103006.093629
26. K. E. Stanovich, R. F. West, *Behav. Brain Sci.* **2000***, 23*, 645–726. **DOI:**10.1017/S0140525X00003435
27. J. R. Maeyer, *Common-se nse chemistry: the use of assumptions and heuristics in problem solving.* Ph. D. Thesis. Arizona: University of Arizona. **2013.**
28. D. Kahneman, S. Frederick, Representativeness Revisited: Attribute Substitution in Intuitive Judgment. Cambridge University Press, Cambridge, **2002.** **DOI:**10.1017/CBO9780511808098.004
29. L. K. McClary, V. Talanquer, *Int. J. Sci. Educ.* **2011***, 33,* 1433–1454. **DOI:**10.1080/09500693.2010.528463
30. A. K. Shah, D. M. Oppenheimer, *Psychol. Bull.* **2008**, *134*, 207–222. **DOI:**10.1037/0033-2909.134.2.207
31. H. A. Simon, *Annu. Rev. Psychol.* **1990**, *41*, 1–19. **DOI:**10.1146/annurev.ps.41.020190.000245
32. P. M. Todd, G. Gigerenzer, *Behav. Brain Sci.***2000***, 23*, 727–741. **DOI:**10.1017/S0140525X00003447
33. N. Graulich, H. Hopf, P. R. Schreiner, *Chem. Eur. J.* **2011***, 17,* 30–40. **DOI:**10.1002/chem.201002370
34. N. Graulich, H. Hopf, P. R. Schreiner, *Chem. Asian J.* **2011***, 6,* 3180–3188. **DOI:**10.1002/asia.201100110
35. M. M. Cooper, L. M. Corley, S. M. Underwood, *J. Res. Sci. Teach.* **2013***, 50*, 699–721. **DOI:**10.1002/tea.21093
36. M. C. Connor, S. A. Finkenstaedt-Quinn, G. V. Shultz, *Chem. Educ. Res. Pract.* **2019***, 20*, 522–541. **DOI:**10.1039/C9RP00033J
37. G. O. Karakoyun, E. Asiltürk, *J. Sci Learning*, **2020**, *4*, 50–60. **DOI:**10.17509/jsl.v4i1.23737
38. N. Didis, O. Ozcan, A. Abak, *Hacettepe University J. Educ.* **2008**, 34, 86–94.
39. M. Wihlborg, *High. Educ. Res. Dev*. **2004**, 23, 433–453. **DOI:**10.1080/0729436042000276459
40. J. Maeyer, V. Talanquer, *Sci. Educ.* **2010***, 94,* 963–984. **DOI:**10.1002/sce.20397
41. Muntholib, J. Mayangsari, Y.N. Pratiwi, M. Muchson, R. Joharmawan, Yahmin, S. Rahayu, First International Conference on Science, Mathematics, and Education, (ICoMSE 2017): Advances in Social Science, Education and Humanities Research, Malang, Indonesia, 2017, Indonesia, **2018**, pp. 251–268.
42. H. Pan, L. Henriques *Sch. Sci. Math.* **2015**, *115*, 237–243. **DOI:**10.1111/ssm.12124
43. I. Cetingul, O. Geban, *Hacettepe University J. Educ.* **2011**, *41*, 112–123.

44. B. Ross, *High School Students' Concepts of Acids and Bases*, Master Thesis. Kingston, Ontario, Canada: Queen's University, **1989**.
45. B. Ross, H. Munby, *Int. J. Sci. Educ.* **1991**, *13*, 11–23. **DOI:**10.1080/0950069910130102
46. K. Y. Hoe, R. Subramaniam, *Chem. Educ. Res. Pract.* **2016**, 17, 263–282. **DOI:**10.1039/C5RP00146C

Povzetek

Namen te raziskave je proučiti učinke desetih hevristik, ki jih je predlagal Talanquer, na postopke sklepanja kandidatov za učitelje naravoslovja na temo »kemijska struktura – razmerje kislost/bazičnost«. V tej fenomenografski raziskavi so bili v spomladanskem semestru študijskega leta 2018–2019 opravljeni razgovori s 30 bodočimi učitelji, ki so bili vpisani v program za izobraževanje na področju naravoslovja, Fakulteta za izobraževanje Univerze Firat. V prvi fazi dvostopenjskega intervjuja so bili udeleženci pozvani, naj nekatere kemijske spojine razvrstijo glede na njihovo naraščajočo kislostjo, v drugi fazi pa nekatere kemijske spojine glede na njihovo naraščajočo bazičnost. V intervjujih so bili udeleženci pozvani tudi, da podrobno pojasnijo razloge za uvrstitev. Od odgovorov, ki so jih na vprašanja dali udeleženci, so dobili šest različnih vzorcev odgovorov glede jakosti kislin ter pet različnih vzorcev odgovorov glede jakosti baz. Ugotovljeno je bilo, da vseh deset hevristik vpliva na razmišljanje udeležencev, zaradi učinkov hevristike pa študentje na splošno namesto znanstvenega argumentiranja uporabljajo bližnjice. Poleg tega je ta študija razkrila, da čeprav ni bila vključena v model, ki ga je predlagal Talanquer, hevristični periodični trendi vplivajo tudi na razmišljanje udeležencev o »razmerju kemijska struktura – kislost/bazičnost«.

DOI: 10.17344/acsi.2021.6679 *Acta Chim. Slov.* **2021,** *68,* 658–666

Scientific paper

Optimization of Extraction Conditions of Bioactive Compounds by Ultrasonic-Assisted Extraction from Artichoke Wastes

Izzet Turker and Hilal Isleroglu*

Tokat Gaziosmanpasa University, Faculty of Engineering and Architecture, Food Engineering Dept., 60150, Tokat, Turkey

** Corresponding author: E-mail: hilal.isleroglu@gop.edu.tr*
Phone: +903562521616 (2888); Fax: +903562521729

Received: 01-16-2021

Abstract

In this study, bioactive compounds were extracted by ultrasonic-assisted extraction and classical extraction processes using distilled water as solvent from artichoke leaves which are considered as agricultural wastes. Antioxidant capacity, total phenolic and total flavonoid content values of the obtained bioactive extracts were determined, and extraction yields and times were evaluated to compare the extraction processes. Also, the optimum extraction conditions of ultrasonic-assisted extraction (extraction time and ultrasonic power) which provide the highest extraction yield were determined using D-optimal design by 'desirability' function approach. According to the results, bioactive extracts having high antioxidant capacity were obtained at shorter times and higher extraction yields were achieved by ultrasonic-assisted extraction process than classical extraction. The highest extraction yield was estimated as 98.46% with an application of 20.05 minutes of extraction time and 65.02% of ultrasonic amplitude for the ultrasonic-assisted extraction process.

Keywords: Artichoke, ultrasonic-assisted extraction, extraction yield, optimization, bioactive compounds

1. Introduction

One of the most important problems in the food industry is the management of waste produced during food processing. Especially in recent years, the increase in the world population and food consumption cause the formation of a large amount of waste products. The fruit and vegetable processing industry are currently concerned with the utilization of wastes (leaves, roots and water released after washing). Waste products obtained as a result of industrial processing of agricultural products may have rich natural antioxidant content. In general, this antioxidative effect is related with the chemical differentiations of phenolic compounds of these waste materials contain.[1] It is known that some plants have antimicrobial and antioxidant properties, and the production of extracts with antimicrobial and antioxidant properties from byproducts and wastes obtained during the production and processing of these plants are becoming increasingly important today. It is generally thought that the hydroxyl groups possessed by these extracts containing phenolic compounds are responsible for the antioxidant and antimicrobial properties.[1–2] One of the products that has gained popularity in Turkey in recent years is artichoke (*Cynara scolymus* L.). Because of its rich content, artichoke and parts of the artichoke plant attract the attention of the food industry and health-oriented consumers.[3] It is known that artichoke wastes constitute 60–80% of the total plant. In the food industry, artichoke wastes are used in the production of herbal food supplements and dietary fiber. In addition, it is thought that artichoke leaves can be used as a natural additive with antioxidant and antimicrobial effects due to their high phenolic content.[4] In literature, the liver-protective properties, anticarcinogenic effects and cholesterol-lowering effects of artichokes were presented.[5] It has also been reported that artichoke is a good source of antioxidants due to the significant amount of caffeic acid it contains. It is known that caffeic acid derivatives are the main phenolic substances found in the heart of artichokes. In addition, flavonoids such as apigenin and luteolin are found in artichoke and the leaves of artichokes as other phenolic compounds having antioxidant activity.[6–7]

Compounds with antioxidant properties have an important effect in delaying the oxidation of substrates. The strong effects of powerful but synthetic antioxidant substances such as BHT [2,6-bis (1,1-dimethylethyl) -4-methylphenol] used in the food industry and their negative effects on human health have been determined by some studies.[8–9] The fact that consumers consider the components harmful to health and avoid the consumption of products having such synthetic additives accelerated the search of the food industry for natural and cheap additives suitable for use in foods. It is thought that extracts that can be an alternative to synthetic antioxidant substances can be obtained from a product such as artichoke which produces a high rate of waste and can be grown in terms of climate in Turkey. Being cheap and having high antioxidant activity, artichoke wastes may create an important potential in Turkey.[10]

The extraction process is based on the principle of obtaining the target components from the material with the highest efficiency and with the least damage to the target component. Conventional extraction methods used for the extraction of bioactive materials can be listed as classical extraction (directly treating the material with the solvent and mixing), decoction extraction, solvent extraction (liquid-liquid extraction) and steam distillation.[11] High pressure process, high hydrostatic pressure extraction and pulsed electric field processes can also be considered as conventional extraction methods.[12–14] These methods are frequently used for extraction of bioactive materials from plant materials and waste products. However, excessive solvent consumption and long extraction time are the main challenges of conventional extraction methods.[15] Solvents such as chloroform, chlorobenzene, acetone, ethanol, methanol and acetonitrile are generally used in these techniques. However, the toxic properties of the solvents and their residue in the target components made it necessary to develop environmentally friendly extraction techniques. In order to shorten the extraction time, increase the extraction yield and reduce the solvent usage novel extraction techniques are taking interest in the food industry. Moreover, it is vital to determine the suitable extraction method of the bioactive compounds from plants in terms of extraction yield.[16]

Most of the industrial applications have tended towards green technologies. Hence, the techniques for the extraction of polyphenols from food wastes should also be innovative and environmentally friendly. Microwave extraction, supercritical fluid extraction and ultrasonic-assisted extraction (UAE) are the most frequently used green extraction techniques recently. UAE has green impacts on the extraction process of bioactive compounds in terms of yield and short processing times when compared with classical extraction (CE) methods and has frequently been the subject of the literature due to its ease of use, portability and lower cost compared to other innovative techniques.[17–19] UAE has a lot of advantages when compared with conventional extraction techniques such as higher extraction yield, short extraction time, lower extraction temperature and reduced usage of the solvent. Moreover, less number of structural and molecular changes of the material occur by the usage of UAE.[20,21] UAE is a developing extraction technology which can be suitable for scaling up. Patist et al.[22] reported that ultrasonic applications in the food industry may be profitable when input and output costs were considered. Industrial scale UAE devices are being produced by companies such as REUS (France) and Hielscher (Germany).[11] Nevertheless, in literature, the studies involving the application of large-scale UAE devices are very rare. Because, while some process parameters can be the same when scale up is done such as solvent type and solvent material ratio and temperature, other process parameters like power and frequency of the ultrasonic device may differ due to the nonlinear nature of the process. However, in order to avoid this challenge, multi-mode devices which can ensure more intense cavitation have been designed by researchers[11,23] and these studies can be very useful in the future for UAE process of the bioactive materials.

UAE is successfully applied for different kind of food products and industrial wastes in order to obtain bioactive materials.[11,21,24] In the UAE, the parameters affecting the process are mainly ultrasonic power, ultrasonic intensity or amplitude, duty cycle (the ratio of pulse duration and cycle time), solvent type, solvent to solid ratio, extraction time and extraction temperature.[21] In general, low power and high frequency ultrasound have been applied at UAE processes for food materials and wastes.[25] Even though having substantial advantages over traditional extraction techniques, the success of UAE is mostly dependent to the optimization process. Optimization of the UAE process can ensure increased extraction rate and can prevent solvent wastage.[24]

The study was aimed to show the effect of a green technology on the extraction of bioactive compounds from an agricultural waste and to make a comparison between the CE and UAE. Antioxidant capacity, total phenolic and total flavonoid contents of the obtained bioactive extracts from artichoke leaves at the different process conditions were determined. The process parameters which are extraction time (ET) and ultrasonic amplitude (UA) were investigated using D-optimal design by desirability function approach. Antioxidant capacity, total phenolic and total flavonoid contents of the obtained extracts at the different process conditions were determined. Also, CE was compared with UAE process in terms of extraction time and extraction yield.

2. Experimental

2. 1. Material

In the study, the leaves of the artichoke (*Cynara scolymus* L.) hearts were used which were grown in Tokat/Turkey. The bracts were dried by sun drying method until

their moisture content were below 10%. After drying, dry leaves were powdered by a rotary blender (Sinbo SHB 3020, Turkey). Following to the sieving process using a sieve having 630 μm pore diameters, the samples under the sieve were collected. Ready-to-use powdered samples were stored at –18 °C until analysis.

2. 2. Classical Extraction Processes

Powdered samples were mixed with distilled water using a magnetic stirrer for a period of 120–1440 minutes. The ratio (w v^{-1}) of the sample and the distilled water was applied as 3 g powder sample in 50 mL distilled water. Analyzes were carried out for the samples mixed for different durations (Table 1).

2. 3. Ultrasonic-Assisted Extraction Processes

For UAE process, distilled water was used as solvent and the ratio of powder sample to distilled water was 3 g 50 mL^{-1} as it was done in CE process. UAE process was carried out using a laboratory scale sonicator (Q Sonica Q 500, 500 W, 20 kHz, ABD) having a 13 mm diameter probe. In order to prevent overheating of probe and samples, the α value was determined as 0.8. α value was calculated as $\alpha = t_{open}/(t_{open}+t_{closed})$. Here, t_{closed} indicates the time (s) that sonication is active, and indicates the time (s) that sonication is passive.[26] The optimum condition which ensured the highest extraction yield was determined using D-Optimal design. Independent process variables were selected as ET (min) (X_1) and UA (%) (X_2) and the limits of the process variables were applied in the range of 20–60 minutes and 30–80%, respectively. Moreover, the extraction temperature was kept constant at ~ 25 °C using a constructed ice bath apparatus to prevent the samples from overheating during extraction process.

2. 4. Soxhlet Extraction

To determine all of the phenolic compounds from powdered artichoke leaves, Soxhlet extraction method was used. Three grams of sample was weighed into a Soxhlet cartridge and extraction was carried out in a Soxhlet device using 200 mL of ethanol for 24 hours. The ethanol which contained the bioactive extract was evaporated using a rotary evaporator and after that concentrated extract was recovered using 50 mL ethanol (same as the ratio used for the extraction processes, 3 g sample in 50 mL solvent).[27]

2. 5. Determination of the Extraction Yield

The antioxidant capacity values of bioactive extracts obtained by UAE processes were compared to the antioxidant capacity value which was obtained by Soxhlet extraction, and extraction yields (%) were calculated for different conditions (Equation 1). Extraction yield was used as a response for the optimization.[27]

2. 6. Analysis

To make the samples usable for the analysis after extraction, firstly the obtained suspensions were centrifuged at 9000 rpm for 5 minutes (Hettich EBA 21, Germany). After that, the supernatant phase was filtered using a coarse filter paper, and the filtrate was collected.

2. 6. 1. Determination of Antioxidant Capacity

1.95 mL of DPPH solution at a concentration of 0.1 mM was mixed with 50 μL of extract. The absorbance values of the samples which were kept in dark for 30 minutes were determined at 515 nm wavelength (PG Instruments T80, United Kingdom). The antioxidant capacities of the samples were expressed in mM trolox 100 g dry $sample^{-1}$.[28] By application of Soxhlet extraction to the artichoke leaves, the antioxidant capacity value was calculated as 318.69 ± 2.89 mM trolox 100 g dry $sample^{-1}$.

2. 6. 2. Determination of Total Phenolic Content

Total phenolic contents of the samples were determined using Folin-Ciocalteau method. Total phenolic content was expressed in gallic acid equivalent (mg gallic acid 100 g dry $sample^{-1}$) after reading the absorbances of the samples at 725 nm wavelength.[15] As a result of Soxhlet extraction, the total phenolic content of artichoke leaves powder was calculated as 1639.33 ± 18.86 mg gallic acid 100 g dry $sample^{-1}$.

2. 6. 3. Determination of Total Flavonoid Content

The total flavonoid content of the samples was determined spectrophotometrically using aluminum chloride method. The absorbance values of the samples were read at 510 nm and the total flavonoid content was calculated in terms of mg quercetin in 100 g dry sample.[29] Total flavonoid content of the artichoke leaves powder was calculated as 1522.27 ± 10.29 mg quercetin 100 g dry $sample^{-1}$ by Soxhlet extraction.

2. 7. Statistical Analysis

One-sample t-test, comparison of the analysis results of the samples and determination of the Pearson coefficients were carried out using SPSS 22.0 (IBM, USA) package program. The regression analysis which was used to

$$\text{Extraction yield (\%)} = \frac{\text{Antioxidant capacity of the extracts obtained by CE or UAE}}{\text{Antioxidant capacity of the extracts obtained by Soxhlet extraction}} \times 100 \quad (1)$$

determine the effects of the independent process variables on the extraction yield, response surface graph and optimization study was done using Design Expert 7.0 (Stat-Ease Inc., USA) package program. For the UAE process, effects of the process variables on the extraction yield were investigated and the process was optimized according to the 'desirability' function approach to ensure the maximum extraction yield. According to the mathematical model, significant terms in the model for extraction yield were determined by variance analysis.

3. Results and Discussion

TThe results obtained by the CE process are given in Table 1. Extraction yields, antioxidant capacity values, total phenolic and total flavonoid contents of the samples mixed with magnetic stirrer for different periods were determined. It was determined that as the ET increased, the extraction yield increased up to the 22nd hour and there was no increase for the extraction yield at the 24th hour ($p < 0.05$) (Table 1). When the results for all analyzes were examined, it was found that there was an approximately 4-fold difference between the 2nd hour and 24th hour of ET. It is thought that the reason why the values obtained by Soxhlet extraction cannot be reached in the CE process is that the process takes place at room temperature and the magnetic stirring process cannot be effective enough to reveal some of the antioxidant compounds from the cells. In addition, since only pure water is used as solvent in the CE process and the mechanical effect is insufficient, the extraction yield could not reach the values higher than 79%. In the study, it is seen that the extraction yield increased with the increase in total phenolic and total flavonoid contents (Table 1). It was determined that there is a positive correlation between extraction yield-total phenolic content and extraction yield-total flavonoid content and the correlation coefficients were calculated as 0.998 and 0.997, respectively ($p < 0.05$).

The extraction yields, antioxidant capacity values, total phenolic and total flavonoid contents obtained according to the D-Optimal design applied for the UAE process are shown in Table 2. Similar to the CE process, there is a positive correlation between extraction yield-total phenolic content and extraction yield-total flavonoid content of bioactive extracts, and the correlation coefficients were determined as 0.996 and 0.986, respectively ($p < 0.05$). Same results were obtained in literature by several researchers. Lou et al.[30] reported that there was a positive correlation between antioxidant activity and total phenolic content of the kumquat extracts. Likewise, Chlopicka et al.[31] revealed that DPPH and total phenolic compounds of breads showed significant and positive correlation. Ibrahimi and Hajdari[32] studied the flavonoid content and antioxidant activity of honey and they reported that the flavonoid content and antioxidant activity values were highly correlated (Pearson correlation coefficient of 0.881).

According to the design, the extraction yield of 37% even at the lowest ET and UA value shows the positive effect of the ultrasonication process. While the extraction yield obtained in the CE process in 2 hours was 17%, in the UAE process, two times higher extraction yield was obtained at the lowest UA value (30%) and in six times shorter ET. UAE process showed better results at shorter ET when compared with CE. This phenomenon was explained with the effect of cavitation bubbles created by ultrasound on the tissue of the sample and made it easier to release phenolic compounds present in the cells by breaking down the cell walls.[33] In a recent study, Stumpf et al.[34] optimized the extraction procedure for determination of phenolic ac-

Table 1. Extraction yield, antioxidant capacity, total phenolic and total flavonoid contents for CE processes

ET (min)	Extraction yield (%)	Antioxidant Capacity (mM trolox 100 g dry sample^{-1})	Total Phenolic Content (mg gallic acid 100 g dry sample^{-1})	Total Flavonoid Content (mg quercetin 100 g dry sample^{-1})
120	16.77 ± 2.98^{k}	53.43 ± 9.48^{k}	307.30 ± 3.14^{k}	360.92 ± 14.41^{j}
240	23.26 ± 0.91^{j}	74.13 ± 2.89^{j}	443.52 ± 3.59^{j}	426.41 ± 16.47^{i}
360	28.79 ± 0.32^{i}	91.76 ± 1.03^{i}	534.97 ± 7.18^{i}	518.10 ± 2.06^{h}
480	39.95 ± 0.58^{h}	127.33 ± 1.86^{h}	678.49 ± 5.39^{h}	668.00 ± 24.70^{g}
600	44.75 ± 0.26^{g}	142.63 ± 0.82^{g}	807.41 ± 2.69^{g}	800.43 ± 18.52^{f}
720	50.93 ± 0.58^{f}	162.31 ± 1.86^{f}	880.12 ± 2.25^{f}	929.96 ± 12.35^{e}
840	61.31 ± 0.78^{e}	195.39 ± 2.47^{e}	1063.65 ± 4.94^{e}	1014.36 ± 4.12^{d}
960	67.48 ± 0.84^{d}	215.07 ± 2.68^{d}	1124.62 ± 2.25^{d}	1126.43 ± 14.41^{c}
1080	73.06 ± 0.45^{c}	232.85 ± 1.44^{c}	1179.86 ± 1.35^{c}	1178.82 ± 10.29^{b}
1200	75.81 ± 0.06^{b}	241.59 ± 0.21^{b}	1250.36 ± 3.14^{b}	1257.40 ± 6.17^{a}
1320	78.14 ± 0.39^{a}	249.03 ± 1.24^{a}	1271.31 ± 2.25^{a}	1263.23 ± 10.29^{a}
1440	78.46 ± 0.45^{a}	250.05 ± 1.44^{a}	1278.93 ± 2.25^{a}	1264.68 ± 16.47^{a}

ET: Extraction time (min)
(a-k) Means with uncommon superscripts within a column are significantly different ($p < 0.05$).

ids and flavonoids in artichoke leaves. They reported that UAE proved to be more effective than the standard protocol of European Pharmacopoeia (Ph. Eur.) and UAE method can be recommended to be as the standard protocol in the long term. Similarly, Carrera et al.[35] used UAE and CE processes to extract phenolic compounds from grapes and compared the methods in terms of total phenolic content of samples. In the UAE process, it was reported that 8 mg g^{-1} grape of phenolic compounds were extracted in 6 minutes of application, and 6.4 mg g^{-1} grape of phenolic compounds were extracted in 60 minutes in the CE process. Considering the simplicity and high efficiency of the method, it has been demonstrated that UAE is more effective than CE. When our data are examined, it is seen that the extraction yield increases as the ET increases at low UA values. On the other hand, it was determined that the extraction yield decreases with the increase of the ET, especially at 68% and 80% UA values. Very high amplitude values may cause agitation of the solvent rather than cavitation and it is important to optimize amplitude value in UAE processes.[11] Moreover, this can be explained by the fact that high-level sonication partially degrades the antioxidant-effective components as the ET increases.[36]

The total phenolic and total flavonoid contents of the obtained extracts by UAE process are shown in Table 2. At the optimum point which was determined as 20.05 minutes of ET and 65.02% of UA, the total phenolic content was determined as 1601.79 ± 12.11 mg gallic acid 100 g dry sample^{-1} and the total flavonoid content was 1515.57 ± 4.51 mg quercetin 100 g dry sample^{-1}. In a study, total phenolic content of artichoke leaves was determined as 4.39 ± 0.81 mg gallic acid 100 g dry sample^{-1} in 4 hours at 40 °C by using 80% ethanol with CE method.[5] Another study of Gouveia and Castilho[37], in which they used UAE of 35 kHz and 200 W for 60 min at room temperature, revealed the total phenolic content of methanolic extract of artichoke leaves as 233.6 mg gallic acid 100 g dry sample^{-1}. On the other hand, in a different study in which the CE process was used, the total phenolic content of artichoke leaves was determined as 1836 mg gallic acid 100 g dry sample^{-1}.[29] In a recent study, Rudić et al.[38] valorized the artichoke leaves dust, which were obtained after industrial processing of tea blends by using microwave assisted extraction of polyphenols. They reported that the total flavonoid content at the optimum point was 7975 ± 112 mg quercetin 100 g dry sample^{-1}. Antioxidant capacity, total phenolic and total flavonoid content of the artichoke plant can vary depending on the artichoke species and its different organs. Kollia et al.[33] studied the antioxidant activity of different artichoke species using UAE and CE and they revealed that cardoon's head extract of the cardoon and globe artichoke had the highest antioxidant activity when compared with the leaves and stems of these different species. On the other hand, Wang et al.[39] analyzed the antioxidative phenolic compounds present in the *C. scolymus* L and it was observed that the leaves had the highest total phenolic compounds when compared with artichoke hearts. Likewise, Falleh et al.[40] pointed that leaves of the

Table 2. Extraction yield, antioxidant capacity, total phenolic and total flavonoid contents for UAE processes

ET (min) (X_1)	UA (%) (X_2)	Extraction yield (%)	Antioxidant Capacity (mM trolox 100 g dry sample^{-1})	Total Phenolic Content (mg gallic acid 100 g dry sample^{-1})	Total Flavonoid Content (mg quercetin 100 g dry sample^{-1})
20	30	36.58	126.60 ± 2.89^{k}	599.74 ± 2.69^{kl}	774.24 ± 14.41^{f}
20	30	37.01	121.20 ± 0.62^{l}	606.73 ± 7.63^{k}	702.92 ± 4.12^{g}
20	30	35.81	123.97 ± 1.24^{kl}	587.04 ± 6.29^{l}	628.70 ± 14.42^{h}
40	30	40.65	140.15 ± 1.44^{j}	666.42 ± 4.94^{j}	678.18 ± 6.17^{gh}
60	30	46.58	144.67 ± 0.82^{i}	763.59 ± 7.18^{h}	804.80 ± 37.05^{f}
60	30	45.03	139.13 ± 1.24^{j}	738.19 ± 3.59^{i}	775.69 ± 57.63^{f}
40	43	67.54	221.04 ± 1.65^{f}	1107.15 ± 4.94^{f}	1107.51 ± 12.35^{e}
20	55	86.02	267.83 ± 1.44^{e}	1410.07 ± 4.49^{c}	1363.64 ± 16.47^{c}
40	55	91.59	302.95 ± 1.24^{bc}	1501.52 ± 2.68^{b}	1436.41 ± 16.44^{b}
40	55	91.90	305.72 ± 0.62^{b}	1506.60 ± 2.69^{b}	1449.51 ± 30.87^{b}
40	55	91.32	293.48 ± 1.86^{d}	1497.07 ± 4.95^{b}	1368.01 ± 6.17^{c}
60	55	91.63	301.49 ± 1.24^{c}	1502.15 ± 2.22^{b}	1430.59 ± 32.93^{b}
30	68	96.28	312.57 ± 0.82^{a}	1578.36 ± 2.25^{a}	1515.00 ± 8.23^{a}
50	68	80.94	264.91 ± 1.44^{e}	1326.88 ± 3.14^{e}	1325.81 ± 28.81^{cd}
20	80	95.78	309.51 ± 1.03^{a}	1570.10 ± 0.90^{a}	1372.38 ± 28.88^{c}
20	80	83.30	267.10 ± 1.24^{e}	1365.62 ± 1.80^{d}	1372.38 ± 4.12^{c}
40	80	81.48	265.49 ± 2.27^{e}	1335.77 ± 1.35^{e}	1296.70 ± 16.47^{d}
60	80	64.98	200.35 ± 2.89^{h}	1065.24 ± 4.94^{g}	1066.76 ± 16.74^{e}
60	80	65.95	203.84 ± 2.06^{g}	1081.11 ± 7.18^{g}	1087.13 ± 37.05^{e}

ET: Extraction time, UA: Ultrasonic amplitude
(a-k) Means with uncommon superscripts within a column are significantly different ($p < 0.05$).

globe artichoke (*C. cardunculus* L.) had two times higher TPC (1479 mg gallic acid 100 g dry sample^{-1}) than that of artichoke heart flowers (696 mg gallic acid 100 g dry sample^{-1}). Sihem et al.[41] revealed that TPC values and antioxidant activity of Tunisian globe artichoke leaves were higher than the bracts and floral stems. These differences can be explained with the origin of the artichoke, cultivation conditions, climate and the harvesting time. According to the results obtained in our study and the results found in the literature, it is seen that the total phenolic and total flavonoid contents of the artichoke leaves are affected by factors such as genetic diversity and harvest time.[5] Garcia-Castello et al.[42] extracted flavonoids from grapefruit solid wastes by UAE and they reported that total phenolic content and antioxidant capacity of the UAE extracts were 50% and 66% higher than that of CE at lower extraction times, respectively. They found optimum process conditions as 25°C extraction temperature, 40% ethanol concentration and 55 minutes of extraction time which yielded total phenolic content of 80.0 mg gallic acid g dry weight^{-1} and antioxidant capacity of 38.3 mmol trolox g dry weight^{-1}. They also reported that UAE extracts obtained using only distilled water had 75.3 mg gallic acid g dry weight^{-1} and 31.9 mmol trolox g dry weight^{-1}, which were similar to the values found at the optimum process conditions. Usage of the distilled water as the solvent in the UAE can ensure economic and environmental process, which was presented in our study as well.

For UAE, the effect of process variables on extraction yield is given by ANOVA table (Table 3). The quadratic model created for the extraction yield is statistically significant at the 99% level ($p < 0.01$) and the lack of fit is statistically insignificant at the 95% confidence level ($p > 0.05$) (Table 3). According to the results, the process variable that has the most significant effect on the model is the UA value. In addition to the linear and quadratic effect of the UA, it was determined that the linear effect of the ET and the ET-UA interaction had a significant effect on the model ($p < 0.05$) (Table 3). Ghafoor et al.[43] optimized the UAE of polyphenols from grapeseed and it was reported that antioxidant capacity of the extracts was significantly affected by linear and quadratic terms of ET. On the other hand, the quadratic effect of the ET does not have a statistically significant effect on the model ($p > 0.05$) (Table 3). In addition to lack of fit values, to understand what extent the obtained model for the extraction process by UAE meets the experimental data R^2, adjusted R^2 (adj-R^2), adequate precision, predicted residual error sum of squares (PRESS) and coefficient of variation C.V. (%) were determined (Table 3). According to the results, the obtained model was suitable to predict extraction yield values ($R^2 > 0.95$). On the other hand, as new terms that can be added to the model always tend to increase the R^2 value, it is recommended to use adj-R^2 values in the expression of model fit.[44] Results showed that R^2 and adj-R^2 values for the model were very close to each other (< 1.6%) (Table 3), and this reveals that the model does not contain statistically insignificant terms.

The second-order polynomial model in terms of coded factors obtained for the extraction process using UAE and used for the optimization study is given by Equation (2). In addition, the 3D response surface graph including isohips curves showing the effect of the ET and UA on the extraction yield and the relationship between the

Table 3. ANOVA table representing the effect of linear, quadratic and interaction terms on extraction yield for UAE model and statistical parameters

Source	DF	Sum of Squares	F Value	p – Value
Model	5	9198.99	60.11	< 0.0001
X_1	1	158.90	5.19	0.0402
X_2	1	3726.18	121.74	< 0.0001
X_1X_2	1	597.20	19.51	0.0007
X_1^2	1	26.27	0.86	0.3711
X_2^2	1	2531.55	82.71	< 0.0001
Residual	13	397.90		
Lack of Fit	6	297.69	3.47	0.0644
Pure Error	7	100.22		
Total	18	9596.90		
Parameter	**Value**			
R^2	0.9585			
adj- R^2	0.9426			
Adequate Precision	19.113			
PRESS	972.67			
C.V. (%)	7.77			

X_1: Extraction time (min), X_2: Ultrasonic amplitude (%), DF: Degrees of freedom, Adj- R^2: Adjusted R^2, PRESS: Predicted residual error sum of squares, C.V. (%): Coefficient of variation

experimental extraction yields and the extraction yields estimated from the model are shown in Figure 1. When Figure 1(a) is examined, linear isohips curves show the interaction between ET and UA. Moreover, the greater the slope for the UA indicates that the UA has the most significant effect for the model. It has been visually demonstrated that the extraction yield decreases due to the increasing ET, especially at high UA values, and the effect of ET is lower at low UA values (Figure 1a). In Figure 1(b), the experimental extraction yields (x axis) and the extraction yields estimated from the model (y axis) were plotted and a linear equation of was obtained. The linear equation showed that predicted and experimental values of extraction yield are very close to each other proving that the model is appropriate.

$$\text{Extraction yield (\%)} = +91.85 - 3.75X_1 + 17.99X_2 - 8.18X_1X_2 - 29.44X_2^2 \quad (2)$$

was determined by the single sample t-test and it was seen that there was no statistical difference between the two values ($p > 0.05$).

4. Conclusions

In this study, bioactive extracts having antioxidant properties were obtained from artichoke leaves which can be categorized as agricultural waste using only distilled water as solvent. The UAE and CE were used as extraction processes and they were compared in terms of extraction yield and time. Results showed that bioactive extracts with high antioxidant capacity were obtained at short times and at the room temperature by UAE application. Also, by UAE process, higher extraction yield and shorter extraction time were ensured when compared with CE. Thus, the study presents that utilization of a waste product which is

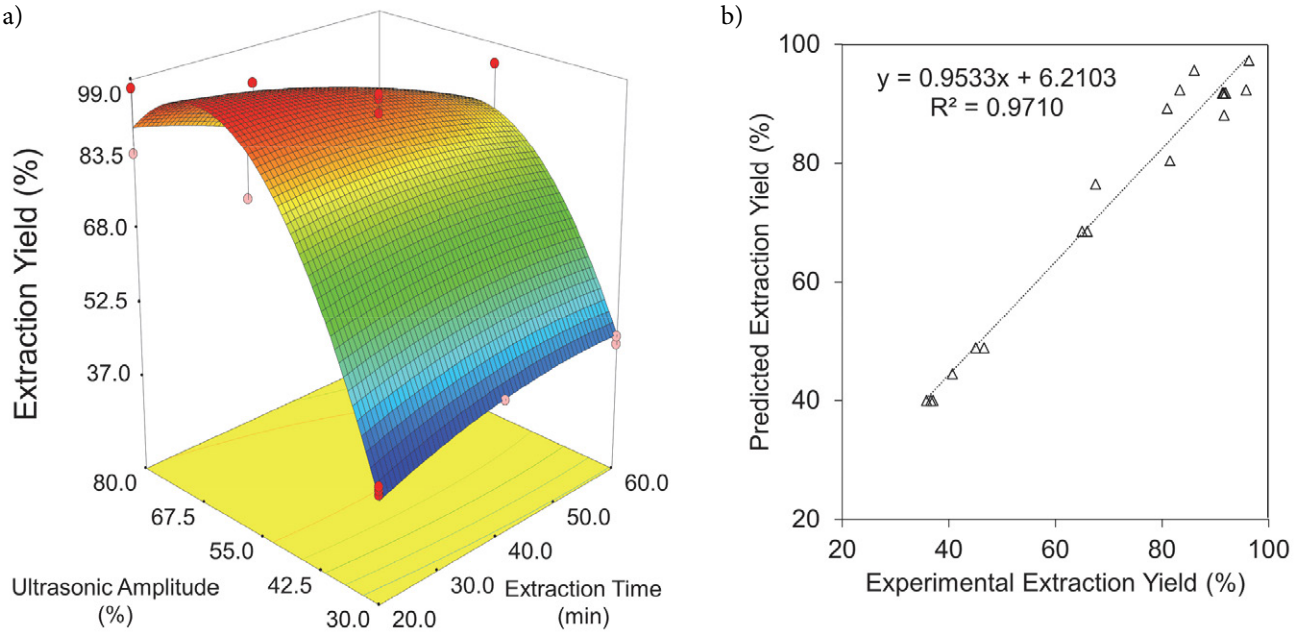

Figure 1. (a) Effect of process parameters on extraction yield and (b) relationship between experimental and predicted extraction yields.

Numerical optimization study was carried out for UAE process to determine the optimum point. 19 solutions with values close to each other were calculated by program and the solution which had the highest 'desirability' value was chosen as the optimum point. The extraction yield was calculated as 98.46% at the optimum point which was having 20.05 minutes of ET and 65.02% of UA. The average experimental extraction yield at the optimum point was determined as 98.77 ± 0.12% according to the optimum point verification trials performed in triplicate. Whether there was a statistically significant difference between the estimated and experimental extraction yields

a natural antioxidant source can be done by a novel and green extraction technique. Even though ultrasonic systems have high capital cost, in the long term, UAE process can be advantageous for obtaining bioactive extracts from artichoke leaves due to short extraction and high extraction yield.

Acknowledgements

This study was financially supported by Tokat Gaziosmanpasa University Scientific Research Projects Committee (Project No: 2019/108).

5. References

1. M. T. Bakić, S. Pedisić, Z. Zorić, V. Dragović-Uzelac, A. N. Grassino, *Acta Chim. Slov.* **2019**, *66(2)*, 367–377. **DOI**: 10.17344/acsi.2018.4866
2. S. J. Kim, A. R. Cho, J. Han. *Food Control* **2013**, *29(1)*, 112–120. **DOI**: 10.1016/j.foodcont.2012.05.060
3. D. Hygreeva, M. C. Pandey, K. Radhakrishna, *Meat Sci.* **2014**, *98(1)*, 47–57, 2014. **DOI**: 10.1016/j.meatsci.2014.04.006
4. V. Lattanzio, P. A. Kroon, V. Linsalata, A. Cardinali, *J. Funct. Foods* **2009**, *1(2)*, 131–144. **DOI**: 10.1016/j.jff.2009.01.002
5. H. Ergezer, H. İ. Kaya, Ö. Şimşek Ö, *Czech J. Food Sci.* **2018**, *36(2)*, 154–162. **DOI**: 10.17221/179/2017-CJFS
6. R. Gebhardt, M. Fausel, *Toxicol. In Vitro*, **1997**, *11(5)*, 669–672. **DOI**: 10.1016/S0887-2333(97)00078-7
7. V. Lattanzio, A. Cardinali, D. Di Venere, V. Linsalata, S. Palmieri, *Food Chem.* **1994**, *50(1)*, 1–7. **DOI**: 10.1021/jf202800n.
8. R. Llorach, J. C. Espin, F. A. Tomas-Barberan, F. Ferreres, *J. Agric. Food Chem.* **2002**, *50(12)*, 3458–3464. **DOI**: 10.1021/jf0200570.
9. A. A. M. Botterweck, H. Verhagen, R. A. Goldbohm, J. Kleinjans, P. A. Van den Brandt, *Food Chem. Toxicol.* **2000**, *38(7)*, 599–605. **DOI**: 10.1016/S0278-6915(00)00042-9
10. J. E. N. Dolatabadi, S. Kashanian, *Food Res. Int.* **2010**, *43(5)*, 1223–1230. **DOI**: 10.1016/j.foodres.2010.03.026
11. C. Wen, J. Zhang, H. Zhang, C. S. Dzah, M. Zandile, Y. Duan, M. Haile, X. Luo, *Ultrason. Sonochem.* **2018**, *48*, 538–549. **DOI:** 10.1016/j.ultsonch.2018.07.018
12. M. Corrales, A.F. García, P. Butz, B. Tauscher, *J. Food Eng.* **2009**, *90(4)*, 415–421. **DOI**: 10.1016/j.jfoodeng.2008.07.003
13. X. Jun, *J. Food Eng.* **2009**, *94(1)*, 105–109. **DOI**: 10.1016/j.jfoodeng.2009.03.003
14. F. J. Barba, O. Parniakov, S.A. Pereira, A. Wiktor, N. Grimi, N. Boussetta, J.A. Saraiva, J. Raso, O. Martin-Belloso, D. Witrowa-Rajchert, N. Lebovka, E. Vorobiev, *Food Res. Int.* **2015**, *77(4)*, 773–798. **DOI**: 10.1016/j.foodres.2015.09.015
15. T. Claus, S. A. Maruyama, S. V. Palombini, P. F. Montanher, E. G. Bonafé, O. D. O. S. Junior, M. Matsushita, J. V. Visentainer, *LWT-Food Sci. Technol.* **2015**, *61(2)*, 346–351. **DOI**: 10.1016/j.lwt.2014.12.050
16. S. Akyıl, I. İlter, M. Koç, Z. Demirel, A. Erdoğan, M. Conk-Dalay, F. Kaymak-Ertekin, *Acta Chim. Slov.* **2020**, *67(4)*, 1250–1261. **DOI**: 10.17344/acsi.2020.6157
17. S. Oancea, D. Ghincevici, O. Ketney, *Acta Chim. Slov.* **2014**, *62(1)*, 242–248. **DOI**: 10.17344/acsi.2014.895
18. T. Xia, S. Shi, X. Wan, *J. Food Eng.* **2006**, *74(4)*, 557–560. **DOI**: 10.1016/j.jfoodeng.2005.03.043
19. B. K. Tiwari, *Trends Anal. Chem.* **2015**, *71*, 100–109. **DOI**: 10.1016/j.trac.2015.04.013
20. M. Vinatoru, T. Mason, I. Calinescu, *TrAC, Trends Anal. Chem.* **2017**, *97*, 159–178. **DOI**: 10.1016/j.trac.2017.09.002
21. K. Kumar, S. Srivastav, V. S. Sharanagat, *Ultrason. Sonochem.* **2020**, *70*, 105325. **DOI**: 10.1016/j.ultsonch.2020.105325
22. A. Patist, D. Bates, *Innov. Food Sci. Emerg. Technol.* **2008**, *9(2)*, 147–154. **DOI**: 10.1016/j.ifset.2007.07.004
23. M. A. Rostagno, J. M. Prado (Eds.), Natural Product Extraction: Principles and Applications, Royal Society of Chemistry Publishing, Cambridge, UK, **2013**, 398 p.
24. C. D. Dzah, Y. Duan, H. Zhang, C. Wen, J. Zhang, G. Chen, H. Ma, *Food Biosci.* **2020**, *35*, 100547. **DOI**: 10.1016/j.fbio.2020.100547
25. P. Juliano, F. Bainczyk, P. Swiergon, M. I. M. Supriyatna, C. Guillaume, L. Ravetti, P. Canamasas, G. Cravotto, X. Q. Xu, *Ultrason. Sonochem.* **2017**, *38*, 104–114. **DOI**: 10.1016/j.ultsonch.2017.02.038
26. C. H. Chan, T. Y. See, R. Yusoff, G. C. Ngoh, K. W. Kow, *Food Chem.* **2017**, *221*, 1382–1387. **DOI**: 10.1016/j.foodchem.2016.11.016
27. T. Y. See, S. I. Tee, T. N. Ang, C. H. Chan, R. Yusoff, G. C. Ngoh, *Int. J. Food Eng.* **2016**, *12(7)*, 711–717. **DOI**: 10.1515/ijfe-2016-0094
28. W. Brand-Williams, M. E. Cuvelier, C. Berset, *LWT- Food Sci. Technol.* **1995**, 28, 25–30. **DOI**: 10.1016/S0023-6438(95)80008-5.
29. A. A. Gaafar, Z. A. Salama, *J. Biol. Agric. Healthcare* **2013**, *3(12)*, 1–6.
30. S. N. Lou, Y. C. Lai, Y. S. Hsu, C. T. Ho, *Food Chem.* **2016**, *197(A)*, 1–6. **DOI**: 10.1016/j.foodchem.2015.10.096
31. J. Chlopicka, P. Pasko, S. Gorinstein, A. Jedryas, P. Zagrodzki, *LWT- Food Sci. Technol.* **2012**, *46(2)*, 548–555. **DOI**: 10.1016/j.lwt.2011.11.009
32. H. Ibrahimi, A. Hajdari, *J.Agric. Res.* **2020**, *59*(4), 452–457. **DOI**: 10.1080/00218839.2020.1714194
33. E. Kollia, P. Markaki, P. Zoumpoulakis, C. Proestos, *Nat. Prod. Res.* **2017**, *31(10)*, 1163–1167. **DOI**: 10.1080/14786419.2016.1219864
34. B. Stumpf, M. Künne, L. Ma, M. Xu, F. Yan, H. P. Piepho, B. Honermeier, J. *Pharmaceut. Biomed.* **2020**, *177*, 112879. **DOI**: 10.1016/j.jpba.2019.112879
35. C. Carrera, A. Ruiz-Rodríguez, M. Palma, C. G. Barroso, *Anal. Chim. Acta* **2012**, *732*, 100–104. **DOI**: 10.1016/j.aca.2011.11.032
36. H. Feng, G. V. Barbosa-Cánovas, J. Weiss. Ultrasound Technologies for Food and Bioprocessing, Vol. 1. Springer, **2011**, New York, the USA.
37. S. C. Gouveia, P. Castilho, *Food Res. Int.* **2012**, *48(2)*, 712–724. **DOI**: 10.1016/j.foodres.2012.05.029
38. S. Rudić, S. Dimitrijević-Branković, S. Dimitrijević, M. Milić, *Sep. Purif. Technol.* **2021**, *256*, 117714. **DOI**: 10.1016/j.seppur.2020.117714
39. M. Wang, J. E. Simon, I. F. Aviles, K. He, Q. Y. Zheng, Y. Tadmor, *J. Agric. Food Chem.* **2003**, *51*(3), 601–608. **DOI**: 10.1021/jf020792b
40. H. Falleh, R. Ksouri, K. Chaieb, N. Karray-Bouraoui, N. Trabelsi, M. Boulaaba, C. Abdelly, *C. R. Biol.* **2008,** *331(5)*, 372–379. **DOI**: 10.1016/j.crvi.2008.02.008
41. D. Sihem, D. Samia, P. Gaetano, L. Sara, M. Giovanni, C. Hassiba, G. Laura, H. A. Noureddine, *Sci. Hortic.-Amsterdam* **2015**, *190*, 128–136. **DOI**: 10.1016/j.scienta.2015.04.014
42. E. M. Garcia-Castello, A. D. Rodriguez-Lopez, L. Mayor, R. Ballesteros, C. Conidi, A. Cassano, *LWT-Food Sci. Technol.* **2015**, *64(2)*, 1114–1122. **DOI**: 10.1016/j.lwt.2015.07.024

43. K. Ghafoor, Y. H. Choi, J. Y. Jeon, I. H. Jo, *J. Agric. Food Chem.* **2009**, *57(11)*, 4988–4994. **DOI**: 10.1021/jf9001439
44. R. H. Myers, D. C. Montgomery. Response Surface Methodology, Process and Product Optimization Using Designed Experiments. 2nd ed, John Wiley and Sons, **1995**, New York, USA, 700 p.

Povzetek

V raziskavi smo primerjali učinkovitost uporabe ultrazvočne in klasične ekstrakcije z destilirano vodo za izolacijo bioaktivnih komponent iz artičokovih listov, ki predstavljajo kmetijski odpadek. Določevali smo antioksidacijsko sposobnost in vsebnost celokupnih fenolov ter flavonoidov ekstrahiranih bioaktivnih komponent in primerjali učinkovitost ter trajanje ekstrakcije. Z uporabo D-optimalnega načrtovanja eksperimentov in kriterija »zaželjene« funkcije smo določili pogoje maksimalnega izkoristka ultrazvočne ekstrakcije (čas in moč ultrazvoka). Eksperimenti so pokazali, da lahko z ultrazvočno ekstrakcijo dosežemo višje izkoristke bioaktivnih komponent z visoko antioksidativno sposobnostjo v krajšem času kot pri klasični ekstrakciji. Najvišji izkoristek 98.46 % smo dosegli z 20.05 minutno ekstrakcijo in 65.02 % amplitudo ultrazvoka.

Scientific paper

In vitro and *In silico* Evaluation of Structurally Diverse Benzyl-pyrrolidine-3-ol Analogues as Apoptotic Agents via Caspase Activation

Tahira Naqvi, [¥,1] Asif Amin,[2] Shujat Ali,[3] Mohsin Y. Lone,[4] Nadeem Bashir,[1,3] Shafi U. Khan,[5] Thet T. Htar[5] and Masood Ahmad Rizvi[*,3]

[1] *Higher Education Department, Government of J&K, India.*
[¥] *Current address Government College for Women M.A Road Srinagar.*

[2] *Department of Biotechnology, University of Kashmir, J&K, India*

[3] *Department of Chemistry, University of Kashmir, Srinagar, J&K, India*

[4] *Department of Chemistry, Indian Institute of Technology, Gandhinagar, Gujarat, India*

[5] *School of Pharmacy, Monash University Jalan Lagoon Selatan, Bandar 47500, Malaysia*

** Corresponding author: E-mail: masoodku2@gmail.com*

Received: 02-13-2021

Abstract

The activation of caspases is central to apoptotic process in living systems. Defects in apoptosis have been implicated with carcinogenesis. Need to develop smart agents capable of inducing apoptosis in tumor cells is obvious. With this motive, diversity oriented synthesis of 1-benzylpyrrolidin-3-ol analogues was envisaged. The multi component Ugi reaction synthesized library of electronically diverse analogues was explored for cytotoxic propensity towards a panel of human cancer cell lines at 10 μM. The lead compounds exhibit a selective cytotoxicity towards HL-60 cells as compared to cell lines derived from solid tumors. Besides, their milder cytotoxic effect on non-cancerous cell lines reaffirm their selective action towards cancer cells only.The lead molecules were tested for their ability to target caspase-3, as a vital protease triggering apoptosis. The lead compounds were observed to induce apoptosis in HL-60 cells around 10 μM concentration. The lead compounds exhibited various non-covalent supra type interactions with caspase-3 key residues around the active site. The binding ability of lead compounds with caspase-3 was studied via molecular docking and molecular dynamic (MD) simulations. MD simulations indicated the stability of compound-caspase-3 complex throughout the 50 ns simulation run. The stability and bio-availability of the lead compounds under physiological conditions was assessed by their interaction with Bovine Serum Albumin (BSA) as model protein. BSA interactions of lead compounds were studied by various bio-physical methods and further substantiated with *in silico* MD simulations.

Keywords: Benzyl-pyrrolidine-3-ol; caspase-3; molecular dynamic simulations; bioavailability, UGI reaction; Biophysical methods.

1. Introduction

Apoptosis or programmed cell death is a unique homeostatic process which eliminates the virus infected cells, cells with damaged DNA and cancerous cells.[1] While as a series of genetic changes transform normal cell into malignant ones, evasion or resistance to apoptosis is considered as an essential factor in this malignant transformation.[2] Apoptosis is a securely regulated process mediated by the family of proteases known as caspases, which cause the proteolytic cleavage of key cellular proteins inducing morphological and biochemical changes associated with apoptosis.[3] Since caspases are considered as pivotal cell death effector molecules, most signaling pathways activated by anticancer drugs ultimately result in activation of caspases. Therefore caspases represent attractive targets for the development of apoptotic agents that can selectively guide the cancer cell towards apoptosis and induce their con-

trolled cell death. Towards this endeavor of potentiating chemotherapeutics, we employed both *in vitro* and bioinformatics based approach to facilitate the development of putative proapoptotic agents from Benzylpyrrolidin-3-ol derivatives. A structure activity relationship (SAR) based drug designing strategy relying on the structural diversity and ability to interact with a defined bio-target was investigated. A library of structurally diverse, 1-benzylpyrrolidin-3-ol analogues was synthesized by multi component Ugi reaction[4,5] and assessed for its ability to induce apoptosis in a panel of human cancer cell lines. Benzylpyrrolidin-3-ol, is a privileged structural motif present in wide range of naturally occurring bioactive compounds and a common intermediate in synthesis of many pharmacoactive molecules.[6] Pharmaceuticals such as anti-hypertensive barnidipine,[7] quinolinone antibiotic clinafloxacin B,[8] muscarinic receptor antagonists darifenacine C,[8] carbapenem antibiotic RS-533,[9] anticoagulant DX- 9065a[10] and naturally occurring detoxification agent detoxin A1-D[11] have 3-substituted pyrrolidine moiety in the pharmacophoric unit Scheme 1.

displayed a range of cytotoxicity towards studied panel of cancer cell lines: HL-60 (human leukemia), A549 (human lung adenocarcinoma), NCI H322 (human brochioalveolar carcinoma), A431 (human epidermoid carcinoma), and T98G (human Glioblastoma), with **5j** and **5p** observed as lead cytotoxic compounds. The lead compounds **5j** and **5p** exhibit a selective cytotoxicity towards HL-60, cells as compared to cell lines derived from solid tumors. Besides, their milder cytotoxic effect on non-cancerous cell lines reaffirm their selective action towards cancer cells only. Computational methods are very unique for mechanistic investigation and prediction,[25–28] as such Molecular docking was employed to explore possible modes of the interaction along with prominent supra interactions between the lead compounds and caspase-3 target. To investigate the binding stability of lead compounds with caspase-3, 50 ns molecular dynamic (MD) simulation was also carried out. From the pharmaceutical perspectives of bioavailability, and drug stability, the interaction of lead compounds **5j** and **5p** was explored with the Bovine serum albumin (BSA) as modular transport protein. The interaction of **5j**

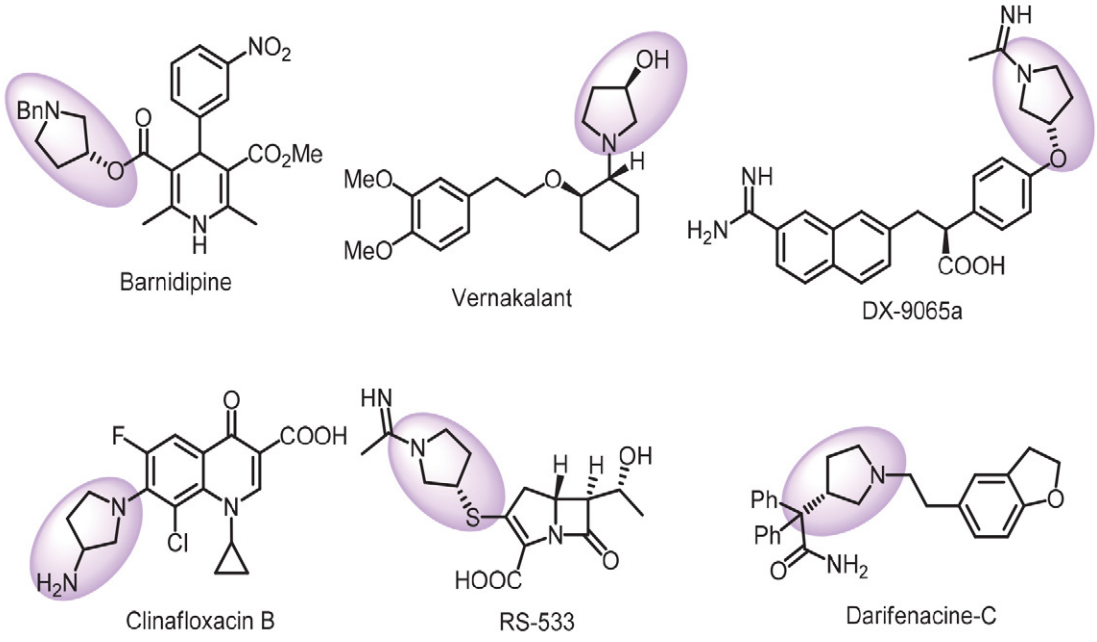

Scheme 1. Bioactive molecules containing 3-substituted pyrrolidine moiety.

Thus, keeping in view importance of 1-benzylpyrrolidin-3-ol moiety in medicinal chemistry and in continuation of our research interests in designing synthetic methodologies and chemical biology,[12–24] we envisaged diversity-oriented synthesis of 1-benzylpyrrolidin-3-ol analogues via Ugi multi component reaction (Ugi-4CR). As an initial screening step, the synthesized library of the compounds **(5a-p)** was screened for ability to induce cytotoxicity towards a panel of human cancer cell lines. In the synthesized library, compounds at 10 μM concentration and **5p** with BSA was quantified by *in vitro* biophysical methods and was further explored using molecular dynamic (MD) simulations.

2. Experimental

2. 1. Materials and Methods

In an initial attempt, equimolar amounts of substrates were used under standard U-4CR conditions in

methanol at room temperature, but no product formation took place. However, when attempted at higher temperatures (80 °C), reaction afforded the Ugi product **(5a)** in 90% yield.

General procedure for Ugi-4 component reaction (5a-p): ***1-(2-aminobenzyl)pyrrolidin-3-ol-(2-aminobenzyl) pyrrolidin-3-ol*** (0.096 g, 0.5 mmol), *p*-nitro benzaldehyde (0.0755 g, 0.5 mmol), benzoic acid (0.061 gm, 0.5 mmol) and *tert*-butyl isocyanide (169 µL, 1.5 mmol) were dissolved in MeOH (5 mL) and refluxed at 80 °C. Reaction mixture was refluxed until 1-(2-aminobenzyl) pyrrolidin-3-ol completely disappeared on TLC. This followed concentrating reaction mixture over vacum evaporator. Ethylacetate was added to reaction system and extracted with saturated aqueous $NaHCO_3$ followed by brine solution. The organic layer was dried with Na_2SO_4 and residue was purified by column chromatography (CH_3OH:CH_2Cl_2 1:20) to give compound **5a** in 78% yield. Characterization was done by ^1H NMR and High-resolution electrospray ionisation mass spectrometry by comparing to accurate mass measurements and molecular formula.

Cell culture

Cell lines including HL-60 (human leukemia), A549 (human lung adenocarcinoma), NCI H322 (human brochioalveolar carcinoma), A431 (human epidermoid carcinoma), and T98G (human Glioblastoma) used in the study were obtained from National Centre for Cell Science (NCCS), Pune, India. Proper authentication of each cell line was carried out using standard procedures at the repository. HL-60 was maintained in RPMI-1640 while as the rest of cell lines were cultured using DMEM supplemented with 10% fetal bovine serum and 100 U/ml penicillin and 100 mg/ml streptomycin. Cells were cultured under standard culture conditions of 5% CO_2 and 37 °C temperature.

Cell proliferation assay

The *in vitro* cytotoxicity of the synthesized compounds against chosen human cancer cell lines was determined by using SRB (sulphorhodamine B) assay. Cells were seeded at a density of 8×10^3 to15×10^3 cells per 100µL in a well of 96 well tissue culture plates and incubated at 37 °C under 5% CO_2 and 95% relative humidity for 24 h.The test compounds(**5a-5p**) (100µL in each well) were added at different concentrations and again incubated for 48h in CO_2 incubator. Cells were fixed with 50% w/v trichloroacetic acid by gently layering on the top of the wells. Subsequently, plates were incubated for 1h at 4 °C. Thereafter, the plates were washed with distilled water three times and air dried. Cell growth was measured by adding SRB dye (0.4% w/v in 1% acetic acid, 100µL/well). The unbound dye was washed with 1% acetic acid 3 times and air dried. The dye was dissolved in tris-buffer (100µL/well, 0.01M, pH 10.4) and plates were kept on mechanical shaker for 10 min. The optical density (OD) was recorded at 540 nm with microplate reader (BioTek Synergy HT) . IC_{50} was determined by using Prism, version 5.04, from Graph Pad Software (La Jolla, CA). The assay was repeated three independent times

***In vitro* Proliferation Assay**

HL-60 cells were seeded in 96 well microtiter plates at a density of 15×10^3cells/well and treated with varying concentration of the test compounds(**5a-5p**) for 48h. 20 µL of 2.5mg L^{-1} of MTT dye was added to each well and incubated for 4 h before termination. Excess media was then blotted off and MTT purple formazan crystals were dissolved in 150 µL of DMSO. Optical density was measured at 570nm with microplate reader (BioTek Synergy HT). IC_{50} was determined by using Prism, version 5.04, from GraphPad Software (La Jolla, CA). The assay was repeated three independent times

Fluorescence microscopy

HL-60 cells were stained with DNA specific fluorescent nuclear dye 4'-6-diamidino-2-phenylindole (DAPI) to determine the nuclear morphological changes and analyzed under fluorescent microscope. Cells were treated with varying concentrations(5,10,15 µM) of **5j** and **5p**. After 24h incubation, cells were washed and resuspended in PBS. Smears of cells were made on glass slides, air dried, fixed in methanol for 20 min at –20 °C, again air dried and stained in dark for 20 min with DAPI (1 µg mL^{-1}), then mounted using glycerol-PBS mixture (90:10) and analyzed under fluorescence microscope (Olympus) using UV filter at 40 Xmagnification. The experiment was repeated three independent times.

Cell cycle analysis

For cell cycle phase distribution analysis, HL-60 cells (5×10^5) were seeded in a 6 well tissue culture plate and there after the cells were treated with different concentrations (5,10,15 µM) of **5j** and **5p** compounds for 24 h, washed with PBS and fixed in ice cold 70% ethanol at –20 °C, overnight. Cells were then centrifuged and washed with PBS followed by the addition of RNase (100 µg/mL) at 37 °C for 45 min and stained with propidium iodide (PI) to determine the cell cycle phase distribution. DNA fluorescence was measured using flow cytometer FACS Aria (Becton Dickinson, USA) and resulting DNA distributions were analyzed for the proportions of cells in apoptosis, G1-phase, S- phase, and G2-M phases of the cell cycle.

Mitochondrial membrane potential

Mitochondrial membrane potential was measured using Rhodamine-123{RH-123} staining and analyzed by flow cytometer. HL-60 cells (5×10^5) were treated with different concentrations(5,10,15 µM) of **5j** and **5p** for 24h. Before termination of experiment, cells were treated with RH-123 (200nM) for 1 hr, centrifuged and washed with

PBS. Cells were re suspended in PBS and fluorescence intensity was analyzed by BD-FACS Aria flow cytometer with an excitation wavelength of 488 nm and emission wavelength of 525 nm in FITC channel. The experiment was repeated three independent times.

Preparation of protein lysates, estimation and western blot analysis

After treatment with different concentrations (5,10,15 μM) of **5j** and **5p**, HL- 60 cells (3×10^6) were harvested, washed with PBS and resuspended in lysis buffer containing RIPA and *protease* and phosphatase inhibitor cocktail. Cells were incubated for 45 min on ice with periodic vortexing and centrifuged at 14000 x g for 15min. Supernatant was collected and stored at –20 °C. The protein concentration was determined with Quanti Pro BCA assay kit according to manufacturer's protocol using Bovine Serum Albumin (BSA) as standard. An equal concentration of protein was subjected to 10% SDS-PAGE and transferred to polyvinylidene difluoride membrane at 4 °C. The membrane was blocked with 3% BSA inTBS-Tween 20 and probed with primary PARP-1 (1:3000), Abcam, rabbit polyclonal, β-actin (1:5000), Sigma Aldrich, rabbit polyclonal and horseradish peroxidase linked respective secondary antibodies (1:5000), Thermo Scientific Ltd.The signals were detected by using western chemiluminescent HRP substrate and exposed to X-ray film for analysis.

BSA binding experiments of 5j and 5p

Spectrophotometric measurements were carried on Shimadzu 1650 UV-visible spectrophotometer with thermostatic control. Fluorescence spectra were recorded using 1.0 cm quartz cells over Shimadzu 184 Spectrofluorimeter –5000(Japan) equipped with a xenon flash lamp and a thermostat bath. The absorption measurements of fixed BSA concentration (50 μM)was recorded in the range of 200–350 nm in presence of increasing concentration of lead compounds **5j** and **5p** (10–50 μL of 1mM). In fluorescence quenching experiments, BSA concentration was fixed at 50 μM to which10–50 μL of 1mMconcentration of **5j** and **5p** was added. Fluorescence spectra were recorded at three different temperatures (298,303 and 308 K) in TrisHCl buffer solution (pH = 7.4) in the range of 300–500 nm upon excitation at wavelength of λ 296 nm in each case.

***In Silico* studies:**

Molecular docking

The lead molecules **5j** and **5p** were docked into the condensation site of Caspase-3 (PDB ID:3DEI) by using CDOCKER utilities within the Discovery Studio Client 18.1.0. Initially, a receptor description file was prepared and the binding cavity was defined around the co-crystallized ligand isoquinoline-1,3,4-trione derivative (RXB). Re-docking of the RXB was furnished to validate the applicability of the docking protocol. Among the generated receptor-ligand conformations of **5j** and **5p,** the one with lowest CDOCKER energies were analysed for the interactions accountable for biological activity.

Molecular dynamics (MD) simulations

MD simulations were performed to study the stability of lead compounds **5j** and **5p** in complex with the caspase-3 (PDB ID:3DEI) and BSA (PDB ID:4OR0) proteins. As the caspase-3 is active in dimer form (A and C chain), therefore, both the chains along with lead compounds were chosen for simulation whereas, due to identical nature of both the chains of BSA, only chain-A complexed with **5j** and **5p** was considered for the simulation overall a set of four-ligand complexes viz **5j**-caspase-3, **5p**-caspase-3, **5j**BSA and **5p**-BSA were simulated for the duration of 50ns. (For more details see supporting information)

3. Results and Discussion

3. 1. Synthesis of Benzyl-pyrrolidine-3-ol Analogues

Diversity targeted synthesis of sixteen (**5a-p**) 1-benzyl-pyrrolidine-3-ol derivatives was attempted using Ugi four component reaction (Figure S1). In diversity oriented synthesis, the primary amine functionality of 1-(2-aminobenzyl) pyrrolidin-3-ol **(1)** and tert-butyl isocyanide **(4)** were fixed components while as different aldehydes and acid molecules were varying components of Ugi reaction for synthesized analogs. For reaction optimization, 1-(2-Aminobenzyl) pyrrolidin-3-ol **(1),** p-nitro benzaldehyde **(2a)**, benzoic acid **(3)** and tert-butyl isocyanide were selected as model substrates. After optimizing Ugi reaction conditions with model substrates. The optimized reaction was then subjected to different aromatic aldehydes and acid molecules as substrates. The diversity oriented synthesis was attempted using a set of aromatic aldehydes to give the corresponding products in good yields. Furthermore, the optimized protocol was used for synthesis of a follow-up library with 1-(2-aminobenzyl) pyrrolidin-3-ol (1)**,** p-trifluromethoxy benzaldehyde (**2b**) and tert-butyl isocyanide (4), and a set of aromatic and aliphatic acids as substrates resulting in good yields of corresponding Ugi adducts. In addition, the reaction conditions were observed to be well tolerable to amino acids and mono protected diacids. From substrate scope investigation, reaction behavior was observed to be largely insensitive (except for reaction times and % yields) to electronic and steric differences in substrate variants to produce corresponding products (**5a-p**) in good yields (Figure 1). The reagents used in the synthesis are color coded in Figure 1 and their chemical structures are summarized in Table S1 (see supporting information)

3. 2. Lead molecules from Benzyl-pyrrolidine-3-ol Analogues Exhibit Favorable Interactions with Caspase-3

Prior to *in silico studies*, all the compounds(**5a-p**) in the synthesized library were screened for their ability to induce cytotoxicity against a panel of human cancer cell lines including HL-60 (human leukemia), A549 (human lung adenocarcinoma), NCI H322 (human brochioalveolar carcinoma), A431 (human epidermoid carcinoma), and T98G (human Glioblastoma). It was observed that the compounds **5j** and **5p** induce significant inhibition of cell growth in selected human cancer cell lines Figure 2. (Table S2 and Figure S2) The lead compounds **5j** and **5p** exhibit a selective cytotoxicity towards HL-60, cells as compared to cell lines derived from solid tumors(IC_{50} values of the

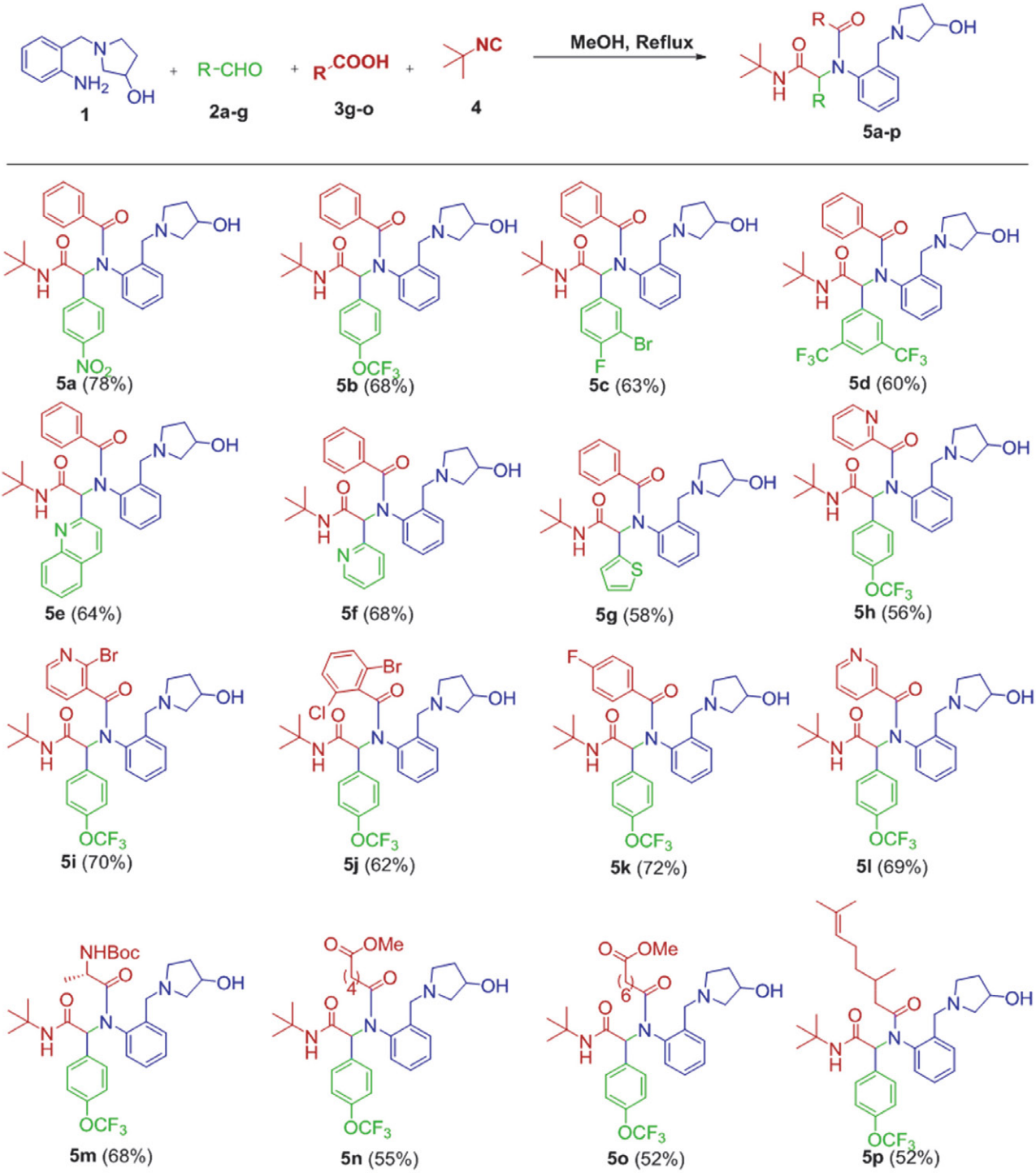

Figure 1. Diversity oriented synthesis of 1-benzyl-pyrrolidine-3-ol analogues using UGI reaction protocol.

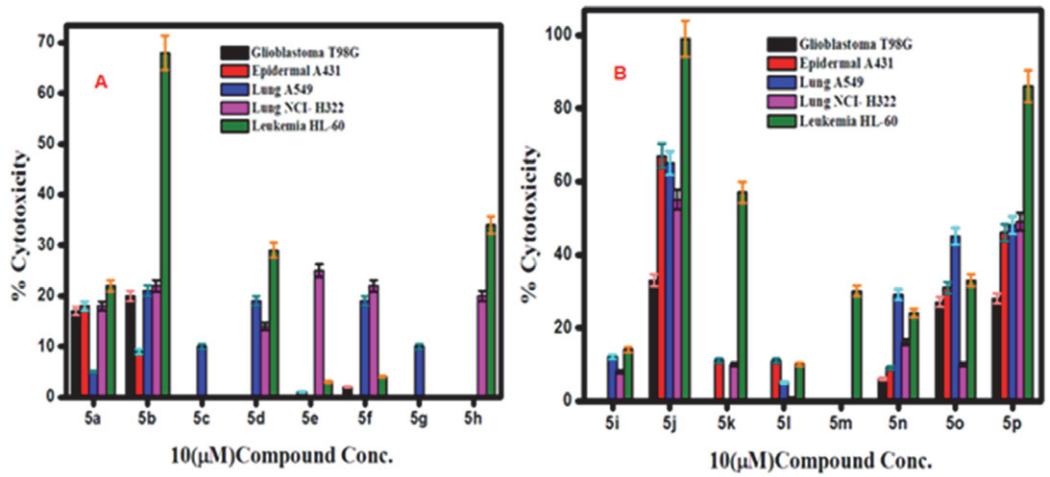

Figure 2. % Cytotoxicity of 1-benzyl-pyrrolidine-3-ol analogues towards a panel of human cancer cells with lead compounds **5j** and **5p**.

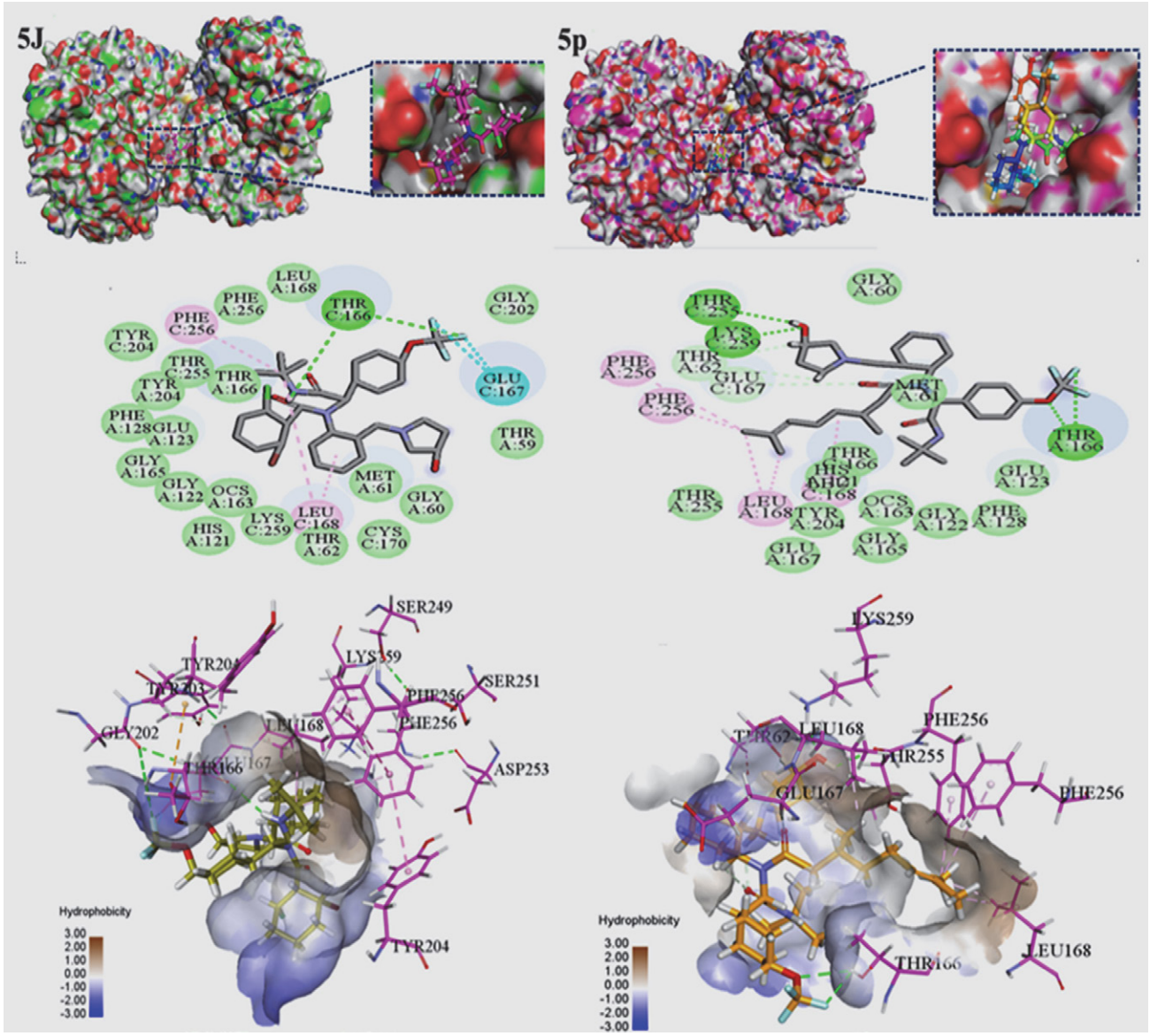

Figure 3: Surface, 2D and 3D representations of the lead molecules **5j** and **5p** around the active site of caspase-3.

compounds **5j** and **5p** towards selected cancer cell lines Table S3). Besides, their milder cytotoxic effects on non-cancerous cell lines reaffirm their selective action towards cancer cells. Thus lead compounds were subjected to detailed investigations as apoptotic agents via *in vitro* and *in silico* studies.

Caspases are crucial mediators of cell death pathway activated by apoptosis-inducing stimuli. Among them, caspase-3 is a frequently activated apoptotic protease, catalyzing specific cleavage of many key cellular proteins thereby it is a putative target for cytotoxic drug designing.[29–33] To explore the possible modes of interaction between lead molecules and caspase-3, *in silico* studies were attempted. The detailed molecular docking and dynamic simulation studies were attempted on these lead compounds after validating the protocol by re-docking of the co-crystal ligand RXB into the active site of the caspase-3 protein. A good agreement of RMSD (less than 2Å) between the re-docked and bound conformation of RXB affirms the usefulness of optimized protocol for subsequent studies. Thus, **5j** and **5p** were docked into the active site of the reference crystal structure 3DEI. From the generated docked poses, most stable pose (lowest CDOCKER interaction energies) from each compound was selected to analyze the binding interaction with the target protein.

It is evident from the 2D interaction plots (Figure 3) that amino acids from chain A and chain C were involved in forming various supra interactions with compounds **5j** and **5p.** Analysis of binding interaction between target protein and compound **5j** and **5p** revealed that H-bond formed with amino acid residue THR166 was common for both compounds. While in case of **5j** amino acid residue of Glu167 was involved in forming two carbon-halogen bonds with compound. Additionally compound **5p** was forming H-bonds with amino acid residue of Thr255 and Lys259 as shown in Figure 3B. Moreover hydrophobic interactions were also formed by His121(A), Met 61(A), Phe128(A) and Glu167(C) with compound **5j** while in case of compound **5p**, hydrophobic interaction were formed by Leu168(A), Phe256(C), Phe256(A) and Leu168(C) (Figure 3C). In addition to H-bond and hydrophobic bond, in case of compound **5p,** three carbon hydrogen bonds were also formed by amino acid residue of Thr162 (A) and Glu167 (C).

To explore the binding stability of lead compounds **5j** and **5p** with caspase-3, 50ns molecular dynamic simulations were performed. Various parameters viz. protein RMSD and RMSF, ligand RMSD and RMSF and the number of contacts established during the simulation were computed. The large-scale movements of **5j** and **5p** caspase-3 complexes were found to be similar with an average fluctuation near to 3.0 Å (Figure 4A). These results connote that binding of **5j** and **5p** at the active site have not perturbed the stability of protein backbone during the simulation. In addition, the structural integrity of protein chains and residual mobility of the ligands (**5j** and **5p**) were characterized by calculating protein-RMSF. A similar kind of fluctuation pattern was noticed for both the ligands and is depicted in Figure 4B. Owing to the inherent flexibility of loops and terminals, the residues in the window of 100–200 and 350–400 residue indexes, have shown the protein-RMSF up to 4.2 Å. However, the protein-RMSF for most of the residues stays below 1.8 Å. These fewer fluctuations can be attributed to the secondary structure elements viz. alpha helices and beta strands and were observed throughout the simulation run. To check the stability of **5j** and **5p** within the binding pocket, ligand-RMSD and ligand-RMSF were computed (Figure 4B). It is clear from the ligand RMSD plots that the compounds **5j** and **5p** have shown an average deviation within the window size of 1.0–1.5 Å and 0.8–1.6 Å respectively. These insignificant deviations observed throughout the simulation run affirm their stability within the binding pocket. Moreover, the atomic fluctuation of the ligand atoms were depicted from ligand-RMSF plots (Figure 4B). The ligand atoms pertaining to the polar groups displayed high fluctuations compared to the atoms concealed deep into the pocket. Besides RMSD and RMSF of the protein and ligand, the genesis of protein -ligand contacts plays an essential role in the complex binding. As can be seen from Figure 4C, that an average of 4–10 contacts were noticed for both **5j** and **5p** within the protein during the simulation run of 50 ns. Overall, an acceptable range of all the essential parameters were observed for the both **5j** and **5p** caspase-3 complexes, which confirms their stability within the active site. Binding of **5j** and **5p** to the active site of caspase-3 might alters its conformation and activate the dynamically important regions in the active site that promote its activity which gets manifested as the heightened apoptosis when HL-60 cells are treated with such compounds. Furthermore binding of these compounds to the active site of caspase-3 might enhance its activity through the sequestration of inhibitory zinc ions in a way reminiscent of small molecule mediated activation of procaspases.[34,35] Thus caspase-3 binding ability of **5j** and **5p** predicts their propensity as apoptotic agents for controlled cancer cell death.

3. 3. Lead molecules from Benzyl-pyrrolidine-3-ol Analogues Induce Apoptosis *In vitro*

Prompted by the *in silico* inputs of **5j** and**5p** binding to caspase-3, we investigated whether these induce apoptosis under *in vitro* conditions. For experimental studies, HL-60 cell line was selected as being the most impacted cell line for cytotoxicity by **5j** and **5p**. The effect of lead compounds **5j** and **5p** on caspase-3 activity was initially evaluated using enzyme kinetics assay. The fluorimetric assay involves hydrolysis of acetyl-Asp-Glu-Val-Asp-7-amido-4-methylcoumarin (Ac-DEVD-AMC) substrate by caspase-3, producing 7-amino-4-methylcoumarin (AMC) as fluorescent moiety. HL-60 cells were seeded in 96-well plate at 1×10^5 cells/well, and treated with **5j** and **5p** (10

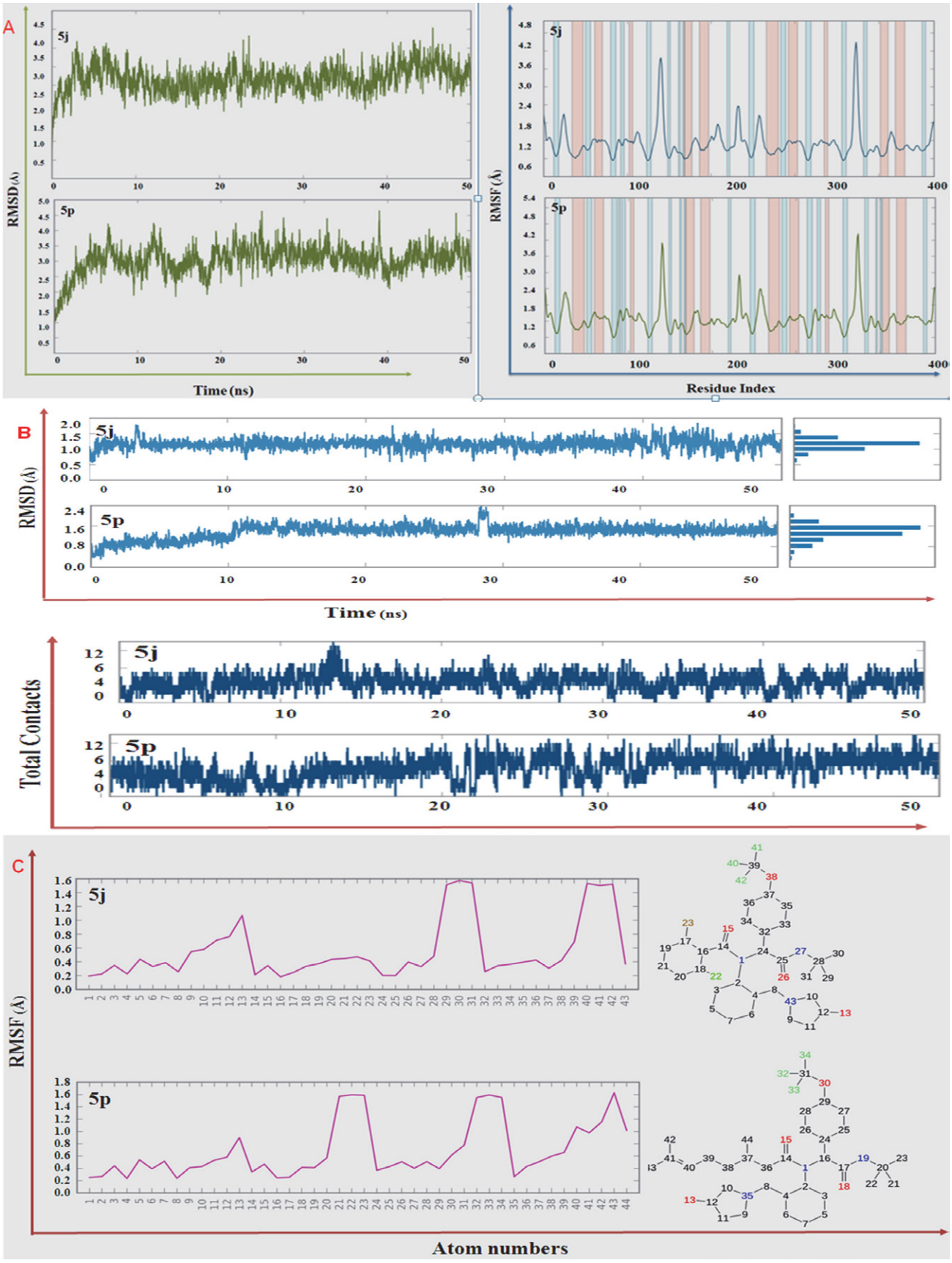

Figure 4: Graphical representation of the (A) Protein (B) Ligand-RMSD and RMSF plots with respect to time and total number of contacts formed between 5j, 5p and the protein respectively, and (C) with respect of atom numbers during the simulation run of 50 ns.

μM) for 48h. Then, cells were lysed in lysis buffer (1X). Cell lysate were microcentrifuge for 10 min at 4 °C. After centrifugation, supernatant was transferred to the tube and diluted. Finally, 200 μL of substrate solution and 25 μL of lysate solution was added to assay plates and plates were incubated at 37 °C in the dark. Relative fluorescent units (RFUs) were acquired at time intervals of 0, 1, 2, 4 and 6 hr duration. During the assay, activated caspase-3 and 7 induced by **5j** and **5p** cleaved the fluorogenic substrate between DEVD and AMC, resulted in highly fluorescent AMC measured at excitation of 380 nm and emission between 420–460 nm. Therefore, the amount of AMC produced was proportional to the number of apoptotic cells in the treated sample Figure 5.

After visualizing caspase activity of **5j** and **5p** from enzyme kinetic assay Figure 5, we attempted to decipher apoptosis via caspase-3 activation as a mechanism of their cytotoxicity using different biological assays Treatment of HL-60 cells with **5j** and **5p** at 5, 10 and 15 μM concentra-

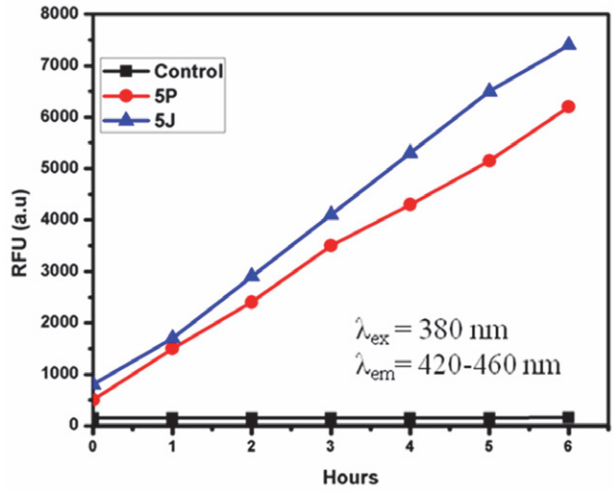

Figure 5: HL-**60** cells were seeded in a 6-well plate at a density of 1 × 10^5 cells/well, treated with **5J** and **5P** at various concentrations (0–30 μM) for 48hr and then lysed with Lysis Buffer. Cell lysates were added to the assay plate carrying the substrate solution, at 37 °C in dark. Relative fluorescent units (RFUs) were obtained at different time intervals.

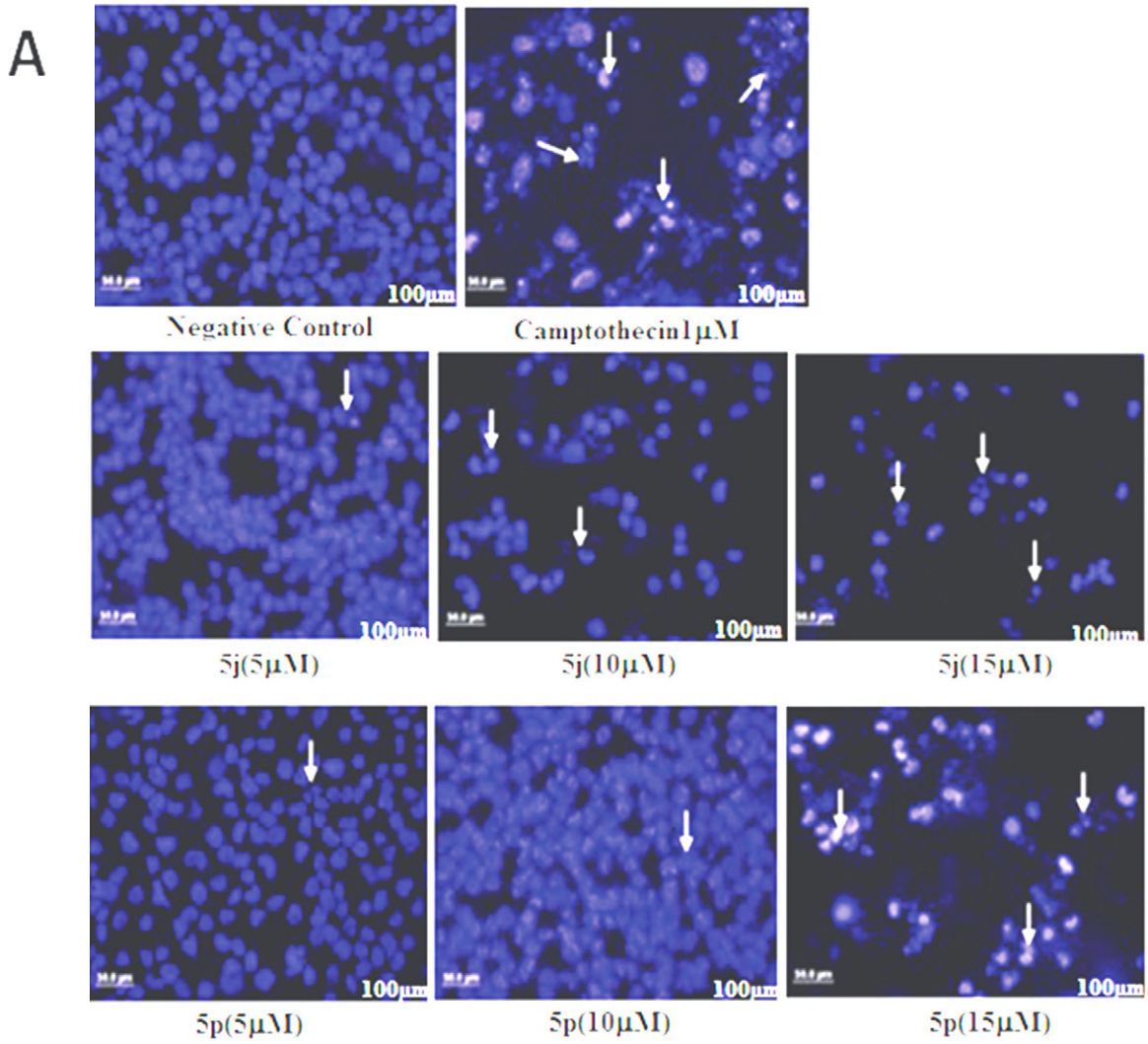

Figure 6A. 5j and **5p** induce apoptosis in HL-60 cells. **(A)** Cells were treated with test compounds **5j** and **5p** at 5, 10 and 15 μM for 24h, stained with DAPI and observed under fluorescence micropscope. The arrow in each case showed appearance of apoptotic bodies.

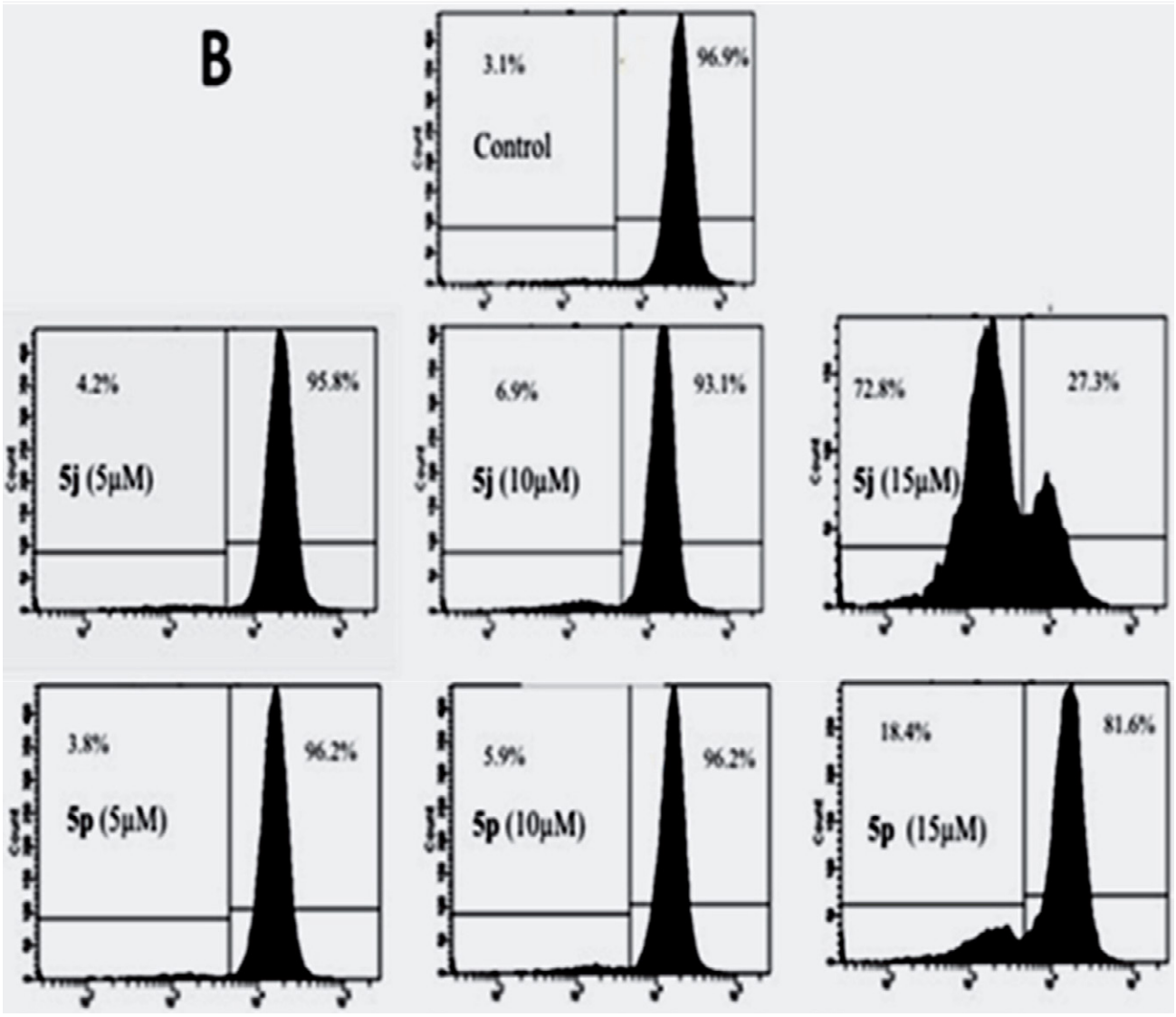

Figure 6B. (B) HL-60 cells were incubated with (5, 10 and 15 μM) of compounds **5j** and **5p** for 24 h followed by staining with Rhodamine-123 (200 nM) for 1 h and analyzed by flow cytometer. Data was analyzed by Cell Quest Pro software from BD Biosciences. Both the assays were repeated three independent times.

tions induced typical apoptotic response under microscopic analysis.Untreated cells were spherical in shape while as the treated cells showed membrane blebbing, shrinkage and condensation of nuclear material, reminiscent of the apoptosis induced by treatment with camptothecin, a known apoptotic inducer used as control drug. These results suggest that **5j** and **5p** induce apoptotic type cellular morphology in HL-60 cells in a dose dependent manner (Figure. 6A). These findings were further corroborated by loss in mitochondrial membrane potential in HL-60 cells induced by **5j** and **5p.** The loss of mitochondrial trans-membrane potential ($\Delta\Psi m$) is a precursory event that triggers mitochondrial matrix remodeling leading to cytochrome *c* release. In turn the release of cytochrome *c* from mitochondrial intermembrane space induces assembly of the apoptosome that is required for activating downstream caspases.[36,37] To measure the mitochondrial membrane potential, the kinetics of Rhodamine-123 fluorescence quenching was evaluated using flow cytometry. The results indicated that at 5, 10 and 15 μM concentrations both **5j** and **5p** led to the dose dependent loss of mitochondrial membrane potential, with **5j** showing a pronounced effect at 15 μM concentration (Figure 6B).

In the cell cycle analysis studies, it was also observed that treatment of HL-60 cells with **5j** and **5p** exhibited a dose dependent increase in hypo diploid sub-G1 fraction, an indication of apoptotic population. In **5j** treated cells, sub-G1 population increased with increasing concentration from 1.4%, 5% to 44.7% at 5, 10 and 15 μM respectively, whereas untreated control showed 1.4% sub-G1 DNA fraction. **5p** displayed a similar trend with 1.7%, 2.6% and

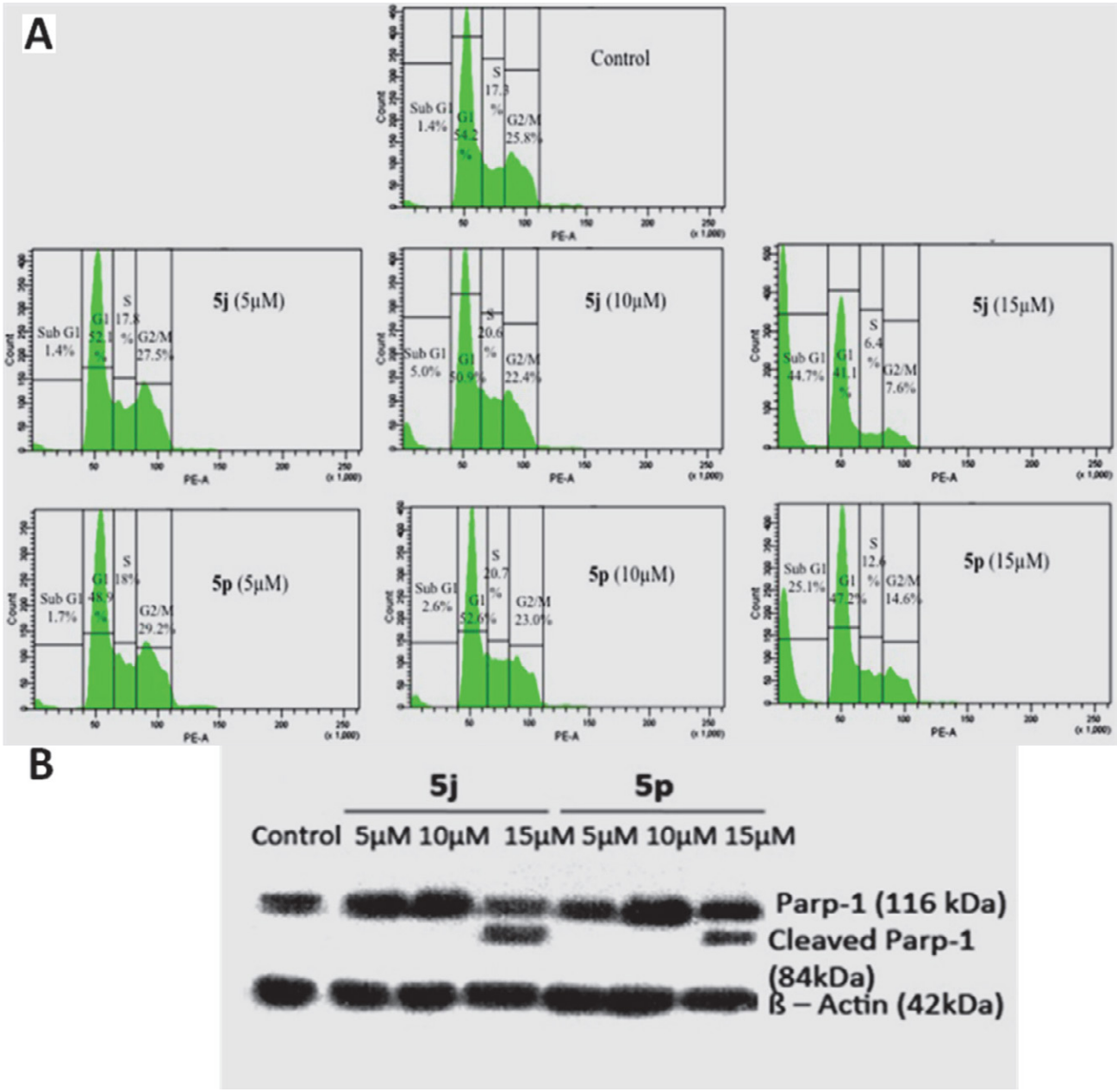

Figure 7. 5j and **5p** arrest cell cycle in sub-G1 phase and induce cleavage of PARP-1. Cells were treated with 5, 10 and 15 μM concentration of **5j** and **5P** and (A) cell cycle phase distribution analysis was carried by out Flow cytometry (B) representative blot indicating the cleavage status of PARP-1 in treated HL-60 cells.

25.1% sub-G1 population at 5, 10 and 15 μM respectively (Figure 7A).

The confirmation of apoptosis by **5j** and **5p** was carried out through cleavage study of poly (ADP ribose) polymerase-1 (PARP-1) by using western blott.[38] The western blot analysis of PARP-1 in HL-60 cancer cell line was performed following 24h treatment with 5, 10 and 15 μM concentrations of **5j** and **5p**. Densitometry of the protein was carried out and normalized with β-actin for analysis. From results it was observed that both **5j** and **5p** induce cleavage of PARP-1, thus contributing towards activation of apoptotic pathways (Figure 7B)

3. 4. Lead Molecules of Benzyl-pyrrolidine-3-ol Analogues Stably Interact with Bovine Serum Albumin

Serum albumins are abundant plasma proteins for transportation and stabilization of drug molecules within biological system. [39]Bovine Serum Albumin (BSA) is a close similitude of Human Serum Albumin (HSA) and has been extensively studied as model carrier protein. From the pharmaceutical perspectives of bioavailability, and drug stability under physiological conditions, we investigated interaction of **5j** and **5p** with BSA through molecular

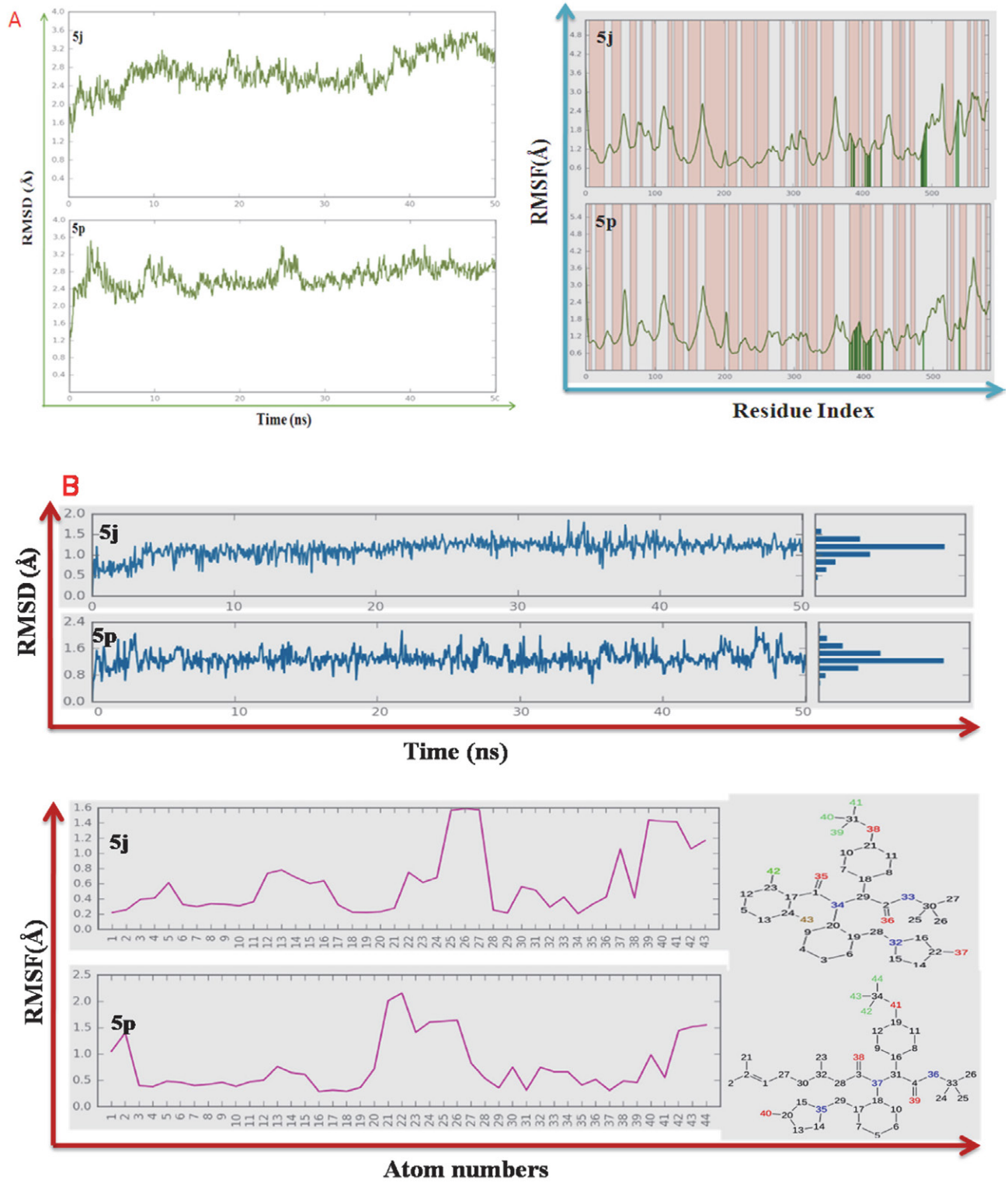

Figure 8: Graphical representation of the (A) Protein (B) Ligand-RMSD and RMSF plots with respect to time and atom number respectively between **5j** and **5p** and BSA during the 50 ns simulation.

dynamic simulations and further substantiated with various biophysical methods.[40]For an insight in the interaction of **5j** and **5p** with BSA carrier protein, MD simulations were performed on their best docked pose. The essential descriptors: RMSD, RMSF and number of contacts formed throughout the simulation were calculated for both **5j** and **5p** with BSA. The ligand-RMSD and ligand-RMSF were determined to assign the stability of **5j**

and **5p** within the binding pocket of BSA (Figure 8A). It is evident from the ligand RMSD plots that the compound **5j** and **5p** have shown an average deviation within the window size of 0.5–1.3Å and 0.8–1.5Å respectively. These small deviations endorse stability of ligands within the binding pocket. In addition, the ligand-RMSF plots were exploited to depict the atomic fluctuation of the ligand atoms. It was noticed that the polar group atoms of the lead molecules displayed elevated fluctuations as compared to the atoms buried deep within the binding pocket. The protein RMSD plots of **5j** and **5p** BSA complexes show fluctuations upto 3.6Å during the simulations (Figure 8B). These results indicate that binding of the **5j** and **5p** have induced minor conformational changes in the protein backbone. Owing to the inherent flexibility of loops and terminals, the undulation in protein-RMSF upto 3.5Å was noticed for the residues 250–300 and above 500 for **5j** whereas, upto 4.0Å for the residues 500 and above for **5p**. The protein-RMSF for most of the residues of **5j**-BSA and **5p**-BSA complexes stays below 1.8Å and 1.5Å respectively. These fewer fluctuations can be attributed to the secondary structure elements viz. alpha helices and beta strands and were observed throughout the 50 ns simulation run.

The formation of protein-ligand contact plays an important role in the complex binding, the different kinds of contacts established during the 50 ns simulation run were investigated and are highlighted in protein-ligand interaction diagram (Figure 8B) Compared to **5j**, more number of contacts were noticed for **5p,** which can be attributed to its extended chemical structure. Taken together, the essential parameters observed for both **5j** and **5p** BSA complexes are well within the acceptable limit which indicates their stability inside the binding pocket of BSA. Thus, **5j** and **5p** can be considered as effective BSA binders and therefore can be predicted to have good stability and mobility towards their biotargets under physiological conditions.

The *in silico* predictions of **5j** and **5p** as BSA binding compounds were verified by absorption and fluorescence quenching experiments. The absorption spectrum of pure BSA shows a peak at 280nm which undergoes a hypochro-

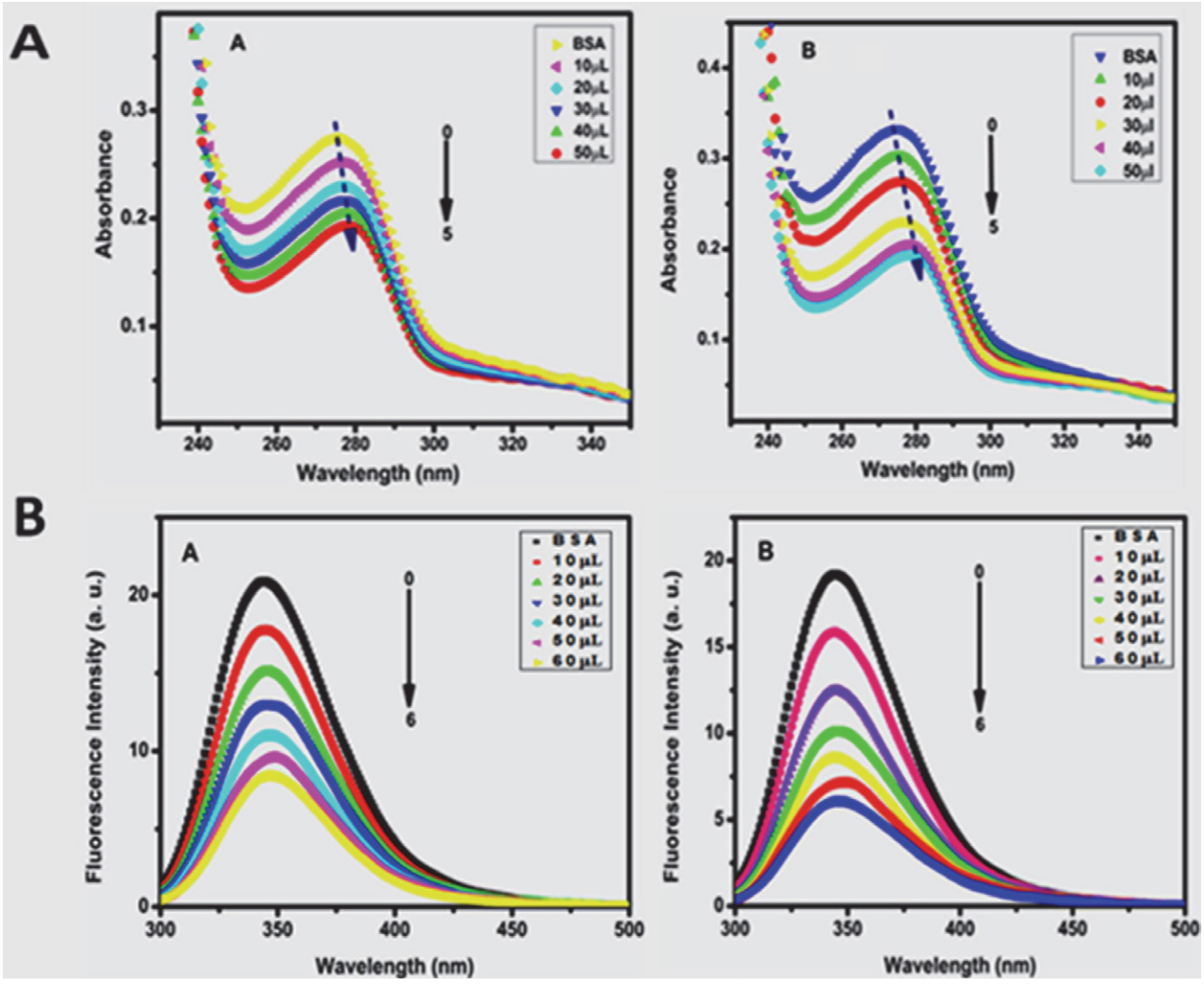

Figure 9: Changes in (A) absorption spectra and (B) emission spectra of BSA on addition of 10–50 μL of 1mM of **5j** and **5p**.

mic effect with a slight bathochromic shift on sequential addition of **5j** and **5p** respectively (Figure 9A). These results suggest that both **5j** and **5p** interact with BSA and also possibly induce some structural changes in modular carrier protein. BSA shows a strong emission peak at λem 350 nm when excited at λex 280 nm, attributed to the Trp residue. Changes in the emission maximum of BSA in presence of added drug are a mark of protein drug interaction. The effect of increasing concentrations of **5j** and **5p** on the fluorescence emission spectra of BSA is shown in (Figure 9B) The BSA emission undergoes a dose dependant hypochromic effect (intrinsic fluorescence quenching) upon sequential addition of **5j** and **5p** indicating that both **5j** and **5p** interact with BSA with relatively more, quenching in case of **5p** compared to **5j.**

Stern-Volmer analysis was used to analyze the fluorescence quenching data of BSA with **5j** and **5p** equations 1-2.

$$F^0/F = 1 + KSV[Q] = 1 + Kq\tau^0[Q] \quad (1)$$

$$\& \quad Kq = KSV/\tau^0 \quad (2)$$

where F^0 and F are the fluorescence intensities of BSA in the absence and presence of quencher; [Q] represents quencher concentration, KSV is the Stern-Volmer quenching constant, Kq is the quenching rateconstant and τ^0 is the average lifetime of molecule in the absence of drug and its value is 10^{-8} sec.[24] The calculated Stern-volmer constants (KSV) for **5j** and **5p** are $5.1 \times 10^4\ M^{-1}$ and $6.71 \times 10^4\ M^{-1}$ respectively indicating that quenching of BSA by **5p** is more compared to **5j**. Figure 10 depicts Stern-Volmer plots of **5j** and **5p** at three different temperatures with the corresponding KSV values shown in Table S4. On increasing the temperature from 298K to 308K, KSV values decrease from $5.1 \times 10^4\ M^{-1}$ to $2.14 \times 10^4\ M^{-1}$ in case of **5j** and $6.71 \times 10^4\ M^{-1}$ to $3.91 \times 10^4\ M^{-1}$ in case of **5p**. The calculated value of Kq for both **5j** and **5p** was found to be greater than the maximum scatter collision quenching constant, i.e. 2×10^{10} L $mol^{-1}s^{-1}$. Thus, observed changes in absorption spectra, temperature trend of KSV value and calculated quenching rate constants more than maximum scatter collision quenching suggest static quenching as plausible mechanism of BSA by **5j** and **5p.** [41]

4. Conclusion

Synthesis and investigation of apoptotic propensity of structurally diverse benzylpyrrolidin-3-ol analogues using in-*silico* and *in-vitro* methods is presented. The compounds **5j** and **5p** were identified as lead cytotoxic molecules from Ugi four component reaction synthesized library of sixteen compounds **(5a-p).** The lead compounds **5j** and **5p** exhibited proportionally higher cytotoxicity towards HL-60, as compared to cell lines derived from solid tumors. Besides, their milder cytotoxic effects on non-cancerous cell lines indicate selective action towards cancer cells. The docking and molecular dynamic simulation (MDS) of the lead molecules with caspase-3 as a major mediator of apoptosis predicted apoptosis as potential cytotoxicity mechanism. Various covalent and non-covalent interactions were shown to be involved between compounds **(5a-p)** and amino acids present around active site of caspase-3. The MDS results of **5j** and **5p** complexes with caspase-3 indicate that their binding to caspase-3 is very stable and does not affect the overall architecture of protein. However their binding brings some aberrant action which propels apoptosis. The *in silico* prediction was confirmed by *in vitro* apoptotic markers: loss of mitochondrial

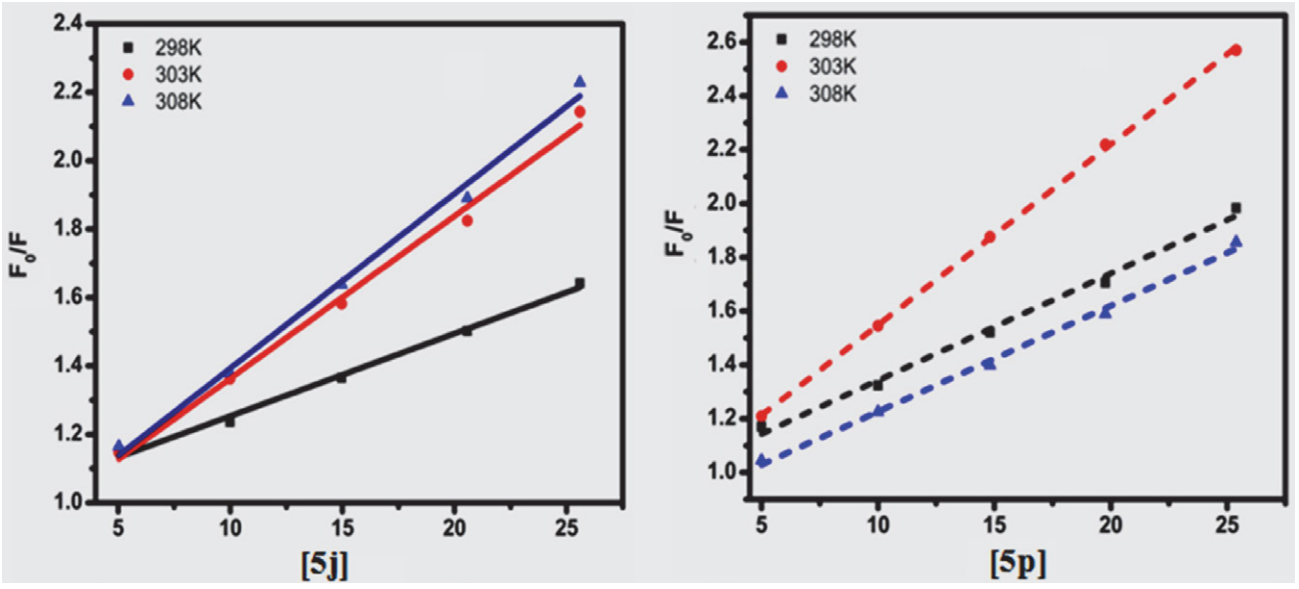

Figure 10: Stern-Volmer plots for binding of **5j** and **5p**with BSA at three temperatures.

membrane potential, cell cycle analysis emergence of apoptotic bodies under fluorescence microscopy. Besides, cleavage of PARP-1 confirmed that both **5j** and **5p** induce apoptotic cell death in a dose dependant manner. From the perspective of drug bioavailability, and stability, interaction of lead molecules (**5j** and **5p**) with Bovine Serum Albumin (BSA) as model protein was investigated using *in silico* molecular dynamics (MD) simulations and also substantiated by biophysical methods. Both **5j** and **5p** were observed to bind to BSA with a good binding constant and hence can be considered to be stable and available to their biotargets under physiological conditions.

Supporting Information Summary

Supporting information includes methods and materials used for biological activity studies. Detailed insilico procedure. The tables TS1 to TS3 in supporting file depict cytotoxic selectivity, IC50 and BSA binding data. Apart for experimental details, characterization data (^{1}HNMR, ^{13}CNMR and Mass spectra) of the benzylpyrrolidin-3-ol analogues compounds (**5a-5p**),

5. References

1. D. R Green, S. J Martin, *Curr Opin Immunol.* **1995**, *7*, 694–703. **DOI:**10.1016/0952-7915(95)80079-4
2. D. Hanahan, R. A. Weinberg, *Cell.* **2011**, *144*, 646–674. **DOI:**10.1016/j.cell.2011.02.013
3. M. O. Hengartner, Nature 2000, 407, 770–776. **DOI:**10.1038/35037710
4. A. Domling, I. Ugi, *Angew. Chem. Int. Ed. Engl.* **2000**, *39*, 3168–3210. **DOI:**10.1002/1521-3773(20000915)39:18<3168::AID-ANIE3168>3.0.CO;2-U
5. A. Domling, *Chem. Rev.* **2006**, *106*, 17–89. **DOI:**10.1021/cr0505728
6. K. Tamazawa, H. Arima, T. Kojima, Y. Isomura, M. Okada, S. Fujita, T. Furuya, T. Takenaka, O. Inagaki, M. M Terai, J. Med. Chem. **1986**, 29, 2504–2511. **DOI:**10.1021/jm00162a013
7. C. Palombo, E. Malshi, C. Morizzo, F. Rakebrandt, V. Corretti, F. Santini, A. G. Fraser, M. Kozakova, Clin. Ther. **2009**, 31, 2873–2885. **DOI:**10.1016/j.clinthera.2009.12.011
8. E. Rubinstein, Chemotherapy **2001**, 47, 3–8. **DOI:**10.1159/000057837
9. T. Miyadera, Y. Sugimura, T. Hashimoto, T. Tanaka, K. Iino, T. Shibata, S. Sugawara, *J. Antibiot.* **1983**, *36***,** 1034–1039. **DOI:**10.7164/antibiotics.36.1034
10. T. Nagahara, Y. Yokoyama, K. Inamura, S. Katakura, S. Komoriya, H. Yamaguchi, T. Hara, M. Iwamoto, J. Med. Chem. **1994**, 37, 1200–1207. **DOI:**10.1021/jm00034a018
11. H. Yonehara, H. Seto, S. Aizawa, T. Hidaka, A. Shimazu, N. Otake, *J. Antibiot***. 1968**, *21*, 369–370. **DOI:**10.7164/antibiotics.21.369
12. R. M. Jagtap, M. A. Rizvi, Y. B. Dangat, S. K. Pardeshi , *J. SulfurChem.* **2016**, *37*, 401–425. **DOI:**10.1080/17415993.2016.1156116
13. N. Chalotra, A. Ahmed, M. A. Rizvi, Z. Hussain, Q. N. Ahmed, B. A. Shah, *J. Org. Chem.* **2018**, *83*, 14443–14456. **DOI:**10.1021/acs.joc.8b02193
14. S. Sultan, M. S. Bhat, M. A. Rizvi, B. A. Shah, *J. Org. Chem.* **2019**, *84*, 8948–8958. **DOI:**10.1021/acs.joc.9b00855
15. N. Chalotra, M. A. Rizvi, B. A. Shah, *Org. Lett*, **2019**, *21*, 4793–4797. **DOI:**10.1021/acs.orglett.9b01677
16. J. Kumar, A. Ahmad, M. A. Rizvi, M. A. Ganie, C. Khajuria, B. A. Shah, *Org. Lett*. **2020**, *22*, 4793–4797. **DOI:**10.1021/acs.orglett.0c02055
17. M. A. Rizvi, S. K. Moosvi, T. Jan, S. Bashir, P. Kumar, W. D. Roos, H. C. Swart, *Polymer.* 2019, *163*, 1–12 **DOI:**10.1016/j.polymer.2018.12.044
18. G. Ali, N. A. Dangroo, S. Raheem, T. Naqvi, T. Ara M. A. Rizvi, Acta Chim. Slov. **2020**, *67,* 195–202. **DOI:**10.17344/acsi.2019.5348
19. F. Kouser, V. K. Sharma, M. Rizvi, S. Sultan, N. Chalotra , V. K. Gupta, U. Nandi, B. A. Shah, *TetrahedronLett*. **2018**, *59*, 2161–2166 **DOI:**10.1016/j.tetlet.2018.04.046
20. M. Kumar, A. Kumar, M. A. Rizvi, B. A. Shah, RSC Adv. **2015**, *5*, 55926–55937. **DOI:**10.1039/C5RA05695K
21. M. A. Rizvi, N. Teshima, G. M. Peerzada *Croat. Chem. Acta,* **2013**, *86,* 345–350. **DOI:**10.5562/cca2167
22. A. Kumar, M. A. Rizvi, S. Kumar, S. Bhushan, F. A. Malik, N. Batra, A. Joshi, J. Singh, *Chem. Biol. Interact* . **2014**, *222*, 60–67. **DOI:**10.1016/j.cbi.2014.08.011
23. A. Pandey, M. A. Rizvi, B. A, Shah, S. Bani, *Cytokine* **2016**, *79*, 103–113. **DOI:**10.1016/j.cyto.2016.01.004
24. M. Kumar, A. Kumar, M. Rizvi, M. Mane, K. Vanka, S. C. Taneja, B. A. Shah, Eur. J. Org. Chem. **2014**, *2014*, 5247–5255. **DOI:**10.1002/ejoc.201402551
25. M. A. Rizvi, M. Mane, M. A. Khuroo, G. M. Peerzada, *Monatsh Chem*, **2017**, *148*, 655–668. **DOI:**10.1007/s00706-016-1813-8
26. Y. Dangat, M. A. Rizvi, P. Pandey, K. Vanka, *J. Organomet. Chem.,* **2015**, *801*, 30–41. **DOI:**10.1016/j.jorganchem.2015.10.015
27. M. V. Mane, M. A. Rizvi, K. Vanka, *J. Org. Chem.* **2015**, *80,* 2081–2091. **DOI:**10.1021/jo5023052
28. A. Kumawat, S. Raheem, F. Ali, T. A. Dar, S. Chakrabarty, M. A. Rizvi, *J. Phys. Chem. B* **2021**, *125*, 6, 1531–1541. **DOI:**10.1021/acs.jpcb.0c08111
29. M. Zhou, X. Liu, Z. Li, Q. Huang, F. Li, C. Y. Li, Int. *J. Cancer.* **2018**, *143*, 921–930. **DOI:**10.1002/ijc.31374
30. X. Feng, Y. Yu, S. He, J. Cheng, Y. Gong, Z Zhang, X. Yang, B. Xu, X. Liu, CY. Li, L. Tian, Q. Huang, *Cancer Lett*. **2017**, *385*, 12–20. **DOI:**10.1016/j.canlet.2016.10.042
31. M. Mukai, T. Kusama, Y. Hamanaka, T. Koga, H. Endo, M. Tatsuta, M. Inoue, *CancerRes*. **2005**, *65*, 9121–9125. **DOI:**10.1158/0008-5472.CAN-04-4344
32. K. Lauber, E. Bohn, S. M. Krober, Y. J. Xiao, S. G. Blumenthal, R. K. Lindemann, P. Marini, C. Wiedig, A. Zobywalski, S. Baksh, Y. Xu, I. B. Autenrieth, K. S. Osthoff, C. Belka, G. Stuhler, S. Wesselborg, *Cell.* **2003**, *113*, 717–730. **DOI:**10.1016/S0092-8674(03)00422-7
33. L. Flanagan, M. Meyer, J. Fay, S. Curry, O. Bacon, H. Duess-

mann, K. John, KC. Boland, DA. McNamara, E. W. Kay, H. Bantel, H. Schulze Bergkamen, J. H. M. Prehn., *Cell Death Dis*. **2016**, *7*: e2087. **DOI:**10.1038/cddis.2016.7
34. Q. P. Peterson, D. R. Goode, D. C. West, K. N. Ramsey, J. J. Lee, P. J. Hergenrother, *J. Mol. Biol.,* **2009**, *388*, 144–158. **DOI:**10.1016/j.jmb.2009.03.003
35. Q. P. Peterson, D. C. Hsu, D. R. Goode, C. J. Novotny, R. K. Totten, P. J. Hergenrother, *J. Med. Chem.* **2009**, *52,* 5721–5731. **DOI:**10.1021/jm900722z
36. M. O. Hengartner, *Nature*, **2000**. *407*, 770–776. **DOI:**10.1038/35037710
37. C. Adrain, S. J. Martin, *Trends Biochem. Sci.,* **2001**, *26*, 390–397. **DOI:**10.1016/S0968-0004(01)01844-8
38. C. Soldani, A. I. Scovassi, *Apoptosis,* **2002** *7*, 321–328. **DOI:**10.1023/A:1016119328968
39. F. Mirzaee, L. Hosseinzadeh, M. R. Ashrafi-Kooshk, S Esmaeili, S Ghobadi, M. H. Farzaei, M. R Zad-Bari, R Khodarahmi, *Protein Pept. lett.* **2019**, *26*, 132–47. **DOI:**10.2174/0929866525666181114152242
40. M. A. Rizvi, Z. Hussain, F. Ali, A. Amin, S. H. Mir, G. Rydzek, R. M. Jagtap, S. K. Pardeshi, R. A. Qadri, K. Ariga, *Phys. Chem. Chem. Phys.,* **2020**, *22*, 7942–7951 **DOI:**10.1039/D0CP00253D
41. M. A. Rizvi, M. Zaki, M. Afzal, M. Mane, M. Kumar, B. A. Shah, S. Srivastav, S. Srikrishna, G. M. Peerzada, S. Tabassum, *Eur. J. Med. Chem*. **2015**, *90*, 876–888. **DOI:**10.1016/j.ejmech.2014.12.014

Povzetek

Aktivacija kaspaz je osrednjega pomena za apoptozni proces v živih sistemih. Napake v apoptozi so povezane s karcinogenezo. Potreba po razvoju pametnih učinkovin, ki bi lahko povzročila apoptozo v tumorskih celicah, je očitna. S tem namenom je bila predvidena sinteza raznolikih analogov 1-benzilpirolidin-3-ola. Pripravljena je bila večkomponentna, z Ugi reakcijami sintetizirana knjižnica analogov in raziskana njihova citotoksičnost na naboru človeških rakavih celičnih linij pri koncentraciji 10 μM. Spojini vodnici kažeta selektivno citotoksičnost za celice HL-60 v primerjavi s celičnimi linijami, pridobljenimi iz trdnih tumorjev. Poleg tega njihov blažji citotoksični učinek na nerakave celične linije dodatno potrjuje njihovo selektivnost za rakave celice. Spojini vodnici sta bili testirani za njihovo sposobnost ciljanja kaspaze-3 kot glavne proteaze, ki sproži apoptozo. Opaženo je bilo, da spojini vodnici inducirata apoptozo v celicah HL-60 pri koncentraciji 10 μM. Spojini vodnici sta izkazovali različne nekovalentne interakcije supra tipa s ključnimi preostanki kaspaze-3 v okolici aktivnega mesta. Sposobnost vezave spojin vodnic s kaspazo-3 so preučevali z molekularnim sidranjem in simulacijami molekularne dinamike (MD). Simulacije MD so pokazale stabilnost kompleksa s kaspazo-3 v celotnem simulacijskem ciklu 50 ns. Stabilnost in biološko uporabnost spojin vodnic v fizioloških pogojih je bila ocenjena z njihovo interakcijo z govejim serumskim albuminom (BSA) kot modelnim proteinom. Interakcije BSA s spojinami vodnicami so bile preučene z različnimi biofizikalnimi metodami in nadalje potrjene z računalniškimi simulacijami MD.

Scientific paper

Genetic Variability in Slovenian Cohort of Patients with Oculocutaneous Albinism

Tinka Hovnik,[1,2,*] Maruša Debeljak,[1] Manca Tekavčič Pompe,[2,3] Sara Bertok,[4] Tadej Battelino,[2,4] Branka Stirn Kranjc[2,3] and Katarina Trebušak Podkrajšek[1,2]

[1] *University Medical Centre Ljubljana, University Children's Hospital, Clinical Institute for Special Laboratory Diagnostics, Vrazov trg 1, SI-1000 Ljubljana, Slovenia*

[2] *University of Ljubljana, Faculty of Medicine, Vrazov trg 2, SI-1000 Ljubljana, Slovenia*

[3] *University Medical Centre Ljubljana, Eye Hospital, Grablovičeva 46, SI-1000 Ljubljana, Slovenia*

[4] *University Medical Centre Ljubljana, University Children's Hospital, Department of Pediatric Endocrinology, Diabetes and Metabolic Diseases, Bohoričeva 20, SI-1000 Ljubljana, Slovenia*

** Corresponding author: E-mail: tinka.hovnik@kclj.si*

Received: 04-23-2021

Abstract

Oculocutaneous albinism (OCA) is an inherited disorder affecting the visual system and skin pigmentation. Our aim was to evaluate genetic and clinical heterogeneity in a cohort of Slovenian paediatric patients with clinically suspected OCA using advanced molecular-genetics approach. In as much as 20 out of 25 patients, genetic variants explaining their clinical phenotype were identified. The great majority of patients (15/25) had genetic variants in *TYR* gene associated with OCA type 1, followed by variants in *TYRP1*, *SLC45A2* and *HPS1* genes causative for OCA3, OCA4 and Hermansky-Pudlak syndrome type 1, respectively. We concluded that OCA phenotype could not predict genotype and vice versa. Nevertheless, the diagnostic yield after targeted next generation sequencing (NGS) was 80% and proved to be affective in our paediatric cohort of patients with various degree of OCA. Even in 16 patients with normal complexion the diagnostic yield was 62,5%. Interestingly, we have identified a patient of white European ancestry with OCA3, which is an extremely rare report, and one patient with OCA due to the Hermansky-Pudlak syndrome type 1.

Keywords: Oculocutaneous albinism, Hermansky-Pudlak syndrome type 1, next generation sequencing, genetic variant

1. Introduction

Albinism is a rare inherited disorder affecting visual system and skin pigmentation, and has a global incidence of approximately 1 in 17.000.[1,2] The most handicapping manifestations are ocular abnormalities, namely reduced visual acuity with nystagmus, strabismus, photophobia, foveal hypoplasia and misrouting of optic nerve fibres at the chiasm.[3,4] Albinism is clinically classified in three groups. In ocular albinism (OA, OMIM # 300500) pigmentation is impaired only in the eyes, while in oculocutaneous albinism (OCA) also pigmentation of the skin and/or hair is impaired. In syndromic forms, such as syndrome Hermansky-Pudlak and Chediak-Higashi syndrome, additional manifestations are present.[5]

OCA is associated with defective biosynthesis or transport of melanin.[6] Each of the several OCA types is related to the individual genetic defect. OCA1 is caused by disease causing variants in *TYR* gene (OMIM* 606933)[7] encoding enzyme tyrosinase catalysing the first two steps in melanin biosynthesis.[8] In OCA1A subtype, enzyme activity is completely abolished and patients have no pigment and severe ocular symptoms. In OCA1B subtype, residual tyrosinase activity is present and consequently patients may develop some pigment after infancy.[9] Among patients with mild OCA1B, two relatively common *TYR* variants, namely NM_000372.4:c.575C>A (p.Ser192Tyr) and NM_000372.4: c.1205G>A (p.Arg402Gln) located in cis and were reported as a prevalent cause when inherited in trans with pathogenic *TYR* variant.[10–14]

OCA2 is the commonest type and represents about 30% of OCA worldwide.[15] It is caused by disease causing variants in *OCA2* gene (OMIM* 611409) encoding inte-

gral melanosomal transmembrane protein.[16] Patients have various amounts of cutaneous pigment. OCA3 is more common in Africa but is extremely rare in white European or Asiatic populations.[17] It is caused by disease causing variants in *TYRP1* gene (OMIM* 115501) encoding tyrosinase-related protein 1 involved in melanin biosynthesis pathway. OCA4 is caused by disease causing variants in *SLC45A2* gene (OMIM* 606202)[18] encoding melanosomal MATP protein, that might affects tyrosinase activity through the regulation of the melanosomal pH.[19] In 2013, three additional rare OCA types, namely OCA5, OCA6 and OCA7, and their associated genes, were added to the consensus list of albinism types.[2] Recently, additional gene was reported in relation to the oculocutaneous albinism, namely dopachrome tautomerase gene (*DCT*) shown to be associated with autosomal recessive form.[20]

Clinical evaluation of a child with suspected albinism should consist of full clinical examination with special emphasis on nystagmus evaluation, iris transillumination defects detection, foveal hypoplasia gradation and retinal pigment epithelium evaluation.[21] The diagnostic tools of great importance are optical coherence tomography (OCT) for foveal hypoplasia gradation[22] and visual evoked potentials (VEP) which can demonstrate misrouting of optic nerve fibers in the chiasm.[23] Despite significant technological advances in genetic testing, a substantial fraction of individuals with OCA remains genetically unexplained. Missing heritability after common four gene testing was reported to be between 10 and 25% in complete OCA and up to 50% in partial OCA[24] and was still as high as 28% in panel based NGS approach.[12] Nevertheless, next generation sequencing (NGS) based genetic testing presents a possibility for an early definitive diagnosis and management of the disease, especially since OCA types are often difficult to differentiate clinically. Our aim was to evaluate genetic and clinical heterogeneity in a cohort of Slovenian paediatric patients with clinically suspected OCA using combined molecular-genetic approach.

2. Methods

2. 1. Patients

Paediatric individuals with clinical signs of OCA were examined at the outpatient clinic of the Eye Hospital at the University Medical Centre Ljubljana. Clinical ophthalmological examination with visual acuity for distance and near, colour vision, perimetry, ocular motility, biomicroscopy, fundus examination andelectrophysiology was performed. Main albinism signs in the studied group of children were: ocular hypopigmentation with iris translucency or fundus hypopigmentation, foveal hypoplasia, misrouting, nystagmus, skin and hair hypopigmentation. Best corrected monocular and binocular visual acuity was tested using Teller Acuity Cards, Cambridge Acuity Crowding Cards, Lea Symbols Cards; verbal optotypes for distance and near visual acuity were tested with HOTV optotype and Jaeger tables. Colour vision was assessed at first or follow-up examinations with non-verbal and verbal Ishihara plates. Visual evoked potentials (VEPs) to flash and onset stimulation were recorded in all children[25] at presentation and follow-up, and macular OCT (spectral domain optical coherence tomography) in some cooperative children. OCT images, were obtained in mydriasis with OCT Topcon 3D OCT-1000 (Topcon Medical Systems, Tokyo, Japan) and/or Spectralis HRA + OCT (Heidelberg Engineering, Germany). The retinal thickness and total macular volume were determined using the OCT apparatus software.

All participants or parents of minors gave their written informed consent prior to the study (approved by the Republic of Slovenia National Medical Ethics Committee nr. 132/03/15) and the study followed the statement of the Republic of Slovenia National Medical Ethics Committee nr. 0120–489/2018/7 and principles of the Declaration of Helsinki.

2. 2. Genetic Testing

Genetic testing was performed at the Clinical Institute for Special Laboratory Diagnostics of the University Children's Hospital at the University Medical Centre Ljubljana. Genomic DNA was isolated from peripheral blood samples with FlexiGene DNA Kit 250 (Qiagen, Hilden, Germany). In male patients, ocular albinism due to *GPR143* gene variants was previously excluded.[26] To evaluate the genetic aetiology of ocular albinism, we performed targeted NGS with TruSightOne Sequencing Panel on the MiSeq platform desktop sequencer coupled with MiSeq Reagent kit v3 (all Illumina, USA). Following on-board primary analysis, we performed secondary data analysis with Variant Studio 2.3 software (Illumina, USA). Rare variants with minor allele frequency less than 5% in genes reported to be related to syndromic and non-syndromic OCA (*AP3B1, BLOC1S3, BLOC1S6, C10ORF11, GPR143, HPS1, HPS3, HPS4, HPS5, HPS6, LYST, MC1R, MITF, MLPH, MYO5A, OCA2, RAB27A, SLC24A5, SLC45A2, TYR, TYRP1)* were further evaluated. Possibly causative variants were confirmed by targeted Sanger sequencing using custom oligonucleotides, BigDye Terminator v3.1 sequencing kit, and ABI Genetic Analyser 3500 (both Applied Biosystems, USA).

The pathogenicity of the variants was evaluated as recommended by the American College of Medical Genetics (ACMG)[27], while novel variants were evaluated with ensemble *in silico* prediction tools CADD,[28] REVEL,[29] VEST4[30] and SpliceAI,[31] while their frequency in general population was assessed using GnomAd database.[32] Additionally, we evaluated large deletions and duplications of the *OCA2* and *TYR* genes with multiplex ligation-dependent probe amplification (MLPA). The probe mix SALSA MLPA P325 OCA2 (MRC-Holland, The Netherlands)

was used according to the manufacturer's instructions. We included three normal control samples to normalize for the allele dosage. We separated amplification products with capillary electrophoresis on ABI Genetic Analyser 3500 (Applied Biosystems, USA) and analysed raw data with GeneMapper® Software Version 4 (Life Technologies, USA). Peak patterns were evaluated using Coffalyser v8 software (MRC-Holland, The Netherlands).

3. Results

3. 1. Clinical Characteristics

Altogether, 25 paediatric individuals, median age 12 years (age range 5–19), 16 male/9 female from 24 unrelated families with clinical signs of OCA were included in the study; patients 12* and 13* were brothers. Among them, 16 had normal complexion in regard to the family members. Their clinical characteristics were summarised in the Table 1. All patients had horizontal and/or rotary nystagmus. Patients had no clear deficit of near and colour vision, their corrected vision for distance was within limits of mild amblyopia. The patients' best corrected visual acuity for distance was 0.2–0.6 Snellen equivalent (0.7–0.2 log MAR). Perimetry revealed no evident lesions of the visual pathways. Electrophysiological evaluation (VEP) showed contralateral asymmetry in all studied children, but not being apparent in the control (Figure 1). Retinal pigmentation was normal or with rare retinal pigment epithelial pigmentation at the posterior pole or retinal vessels, and

Table 1: Clinical finding in children with suspected OCA. M-male, F-female. ***Iris translucency***: – not present; 1/3 one third; 2/3 two thirds; 3/3 total. ***Foveal pit*** : ± underdeveloped; + minimal foveal depression; ++ absent; +++ no foveal depression, choroidal vessels seen at the posterior pole and foveal area. ***Retinal pigmentepithelial pigmentation***: – changes not evident; ± rare, abnormal periphery; rare +, choroidal vessels seen at the posterior pole, but not in the foveal area; rare ++, choroidal vessels seen also in the foveal area. ***Refraction:*** HA – hypermetropic astigmatism, low (≤ 2.50 D, Dcyl); medium (> 2.5 D, Dcyl); high myopia (–10 and –11 D). ***Photophobia:*** + minimal outside; ++ in light condition outside, inside; +++ in normal light, * siblings.

Proband	Gender	Skin pigmentation in the context of the family	Iris translucency	Foveal pit	Retinal pigment epithelial pigmentation	Refraction	Photophobia	Classification according to the genetic defect
1	M	unremarkable	1/3	+	–	Low HA	–	OCA1
2	F	unremarkable	1/3	±	–	Low HA	–	
3	M	unremarkable	1/2	+	–	Low HA	–	
4	M	unremarkable	1/3	+	Rare +	Medium HA	+	
5	F	unremarkable	1/3	+	Rare +	Low HA	–	
6	F	unremarkable	1/3	+	Rare +	Low HA	–	
7	M	fair	2/3	++	Rare +	Medium HA	++	Highly likely OCA1
8	F	unremarkable	–	+	Rare +	Low HA	–	
9	F	unremarkable	–	–	Rare +	Low HA	–	
10	M	unremarkable	1/3	+	Rare +	Low HA	–	
11	M	fair	1/3	+	–	Medium HA	–	
12*	M	fair	–	+	Rare +	Low HA	–	
13*	M	fair	1/3	+	Rare +	Low HA	–	
14	F	unremarkable	1/3	+	Rare +	Medium HA	–	
15	M	fair	–	++	Rare +	Medium HA	–	
16	F	unremarkable	1/3	+	Rare +	Medium HA	+	OCA3
17	M	fair	–	+	Rare +	Medium HA	–	
18	M	fair	2/3	++	Rare +	Medium HA	–	OCA4
19	M	fair	3/3	+	Rare +	Medium HA	+	
20	F	fair	1/3	+++	Rare ++	Low HA	+	Hermansky-Pudlak syndrome type 1
21	M	unremarkable	1/3	+	Rare ±	Low HA	++	?
22	M	unremarkable	–	–	Rare +	Medium HA	–	
23	M	unremarkable	1/3	+++	Rare +	High myopia	–	
24	F	unremarkable	1/3	±	Rare ±	Low HA.	+	
25	M	unremarkable	1/3	+	–	Low HA	–	

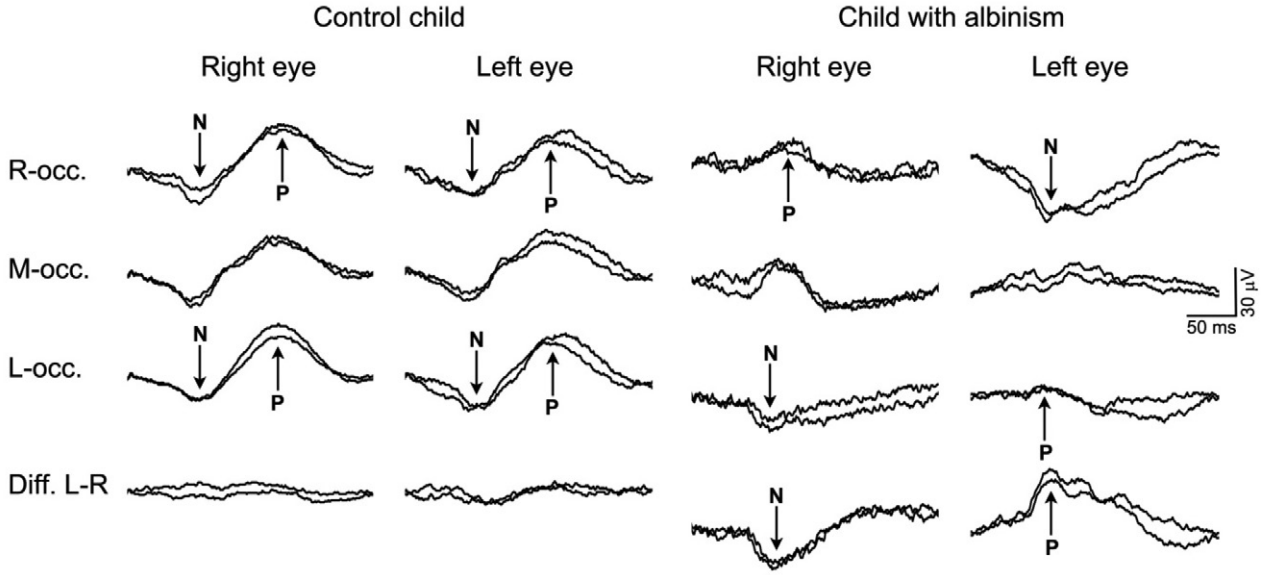

Figure 1: Flash VEP from a control child and child with albinism. In a control child there is a symmetrical distribution of the P and N waves over the lateral two electrodes (R-occ.: right occipital electrode, L-occ.: left occipital electrode) and no deflections of polarity on the differential channel (Dif. L-R), representing the difference in potentials between the left and right electrodes (subtraction of the right from the left occipital signal). In a child with albinism, there is a marked asymmetry over the lateral two electrodes, with the waves of opposite were compared between the eyes (albino crossed asymmetry). From the right eye a positive (P) wave is seen over the right electrode and a negative (N) wave is above the left electrode, while from the left eye the distribution of P and N waves is exactly the opposite. This asymmetry is even more clearly seen on a differential channel, where predominance on the negative wave is seen on the right eye, and a positive one on the left eye.

evident macular hypoplasia, but normal optic discs. Complexion, hair and lashes pigmentation did not differ among individual participants. None of the children had really dark or red complexion or hair, iris pigmentation was blue to green, none of the included children had brown iris.

At the time of the first referral to the genetic testing, no additional signs or symptoms were reported. However, at the time when the genetic results were issued in 2018 and results led to the diagnosis of the Hermansky-Pudlak syndrome type 1, patient 20 she was already referred to the gastroenterological assessment by her paediatrician because of the chronic abdominal pain and occasional diarrhoea. Fulminant Crohn's disease with perianal fistulas was diagnosed and treated with infliximab (Remicade). According to the clinical practice, she was also referred to the paediatric haematology department where prolonged bleeding due to thrombocytopathy was recognised.

3. 2. Genetic Testing

Genetic characteristics of the cohort were summarised in Table 2. Patients 1 to 6 had pathogenic variants on both alleles of the *TYR* gene causative for OCA1. Additionally, probands 7 to 15 had variants on both alleles of the *TYR* gene highly suspected to be causative for at least mild form of OCA1. Patients 16 and 17 had pathogenic variants on both alleles of the *TYRP1* gene causative for OCA3. Patients 18 and 19 had pathogenic variants on both alleles of the *SLC45A2* gene causative for OCA4, while patient 20 had pathogenic variants on both alleles of the *HPS1* gene causative for Hermansky-Pudlak syndrome type 1. Patients 21 to 25 carried monoallelic variants that could not fully explain the clinical presentations. Parental analysis confirmed the segregation of the detected pathological variants.

Among the genetic variants detected in the cohort, three variants, namely *TYR* NM_000372.4: c.1430G>A, p.Trp477Ter; *SLC45A2* NM_016180.4: c.302G>A, p.Arg101His; *TYRP1* NM_000550.2: c.913+1G>A were not previously reported in patients with OCA and were predicted to be deleterious. Their general population data and *in silico* prediction scores are summarised in the Table 3. *SLC45A2* missense variant NM_016180.4: c.302G>A; p.Arg101His was detected in homozygous state in patient 19. Nonsense variant *TYR* NM_000372.4: c.1430G>A; p.Trp477Ter introducing premature termination codon was detected in patients 3 and 10 in compound heterozygous state with another monoallelic variant in *TYR* gene. Intronic *TYRP1* variant located in consensus splice donor site (*TYRP1*, NM_000550.2: c.913+1G>A) was detected in patient 21 in heterozygous state, while variant on the other *TYRP1* allele has not been detected.

Diagnostic yield after the targeted NGS sequencing was 80% (20/25). MLPA analysis did not reveal large deletions or duplications in analysed regions of *OCA2* or *TYR* genes, as detected height ratios of the fluorescent peaks were in the normal height ratio range between 0.7–1.3.

Table 2: Genetic variants detected in OCA patients (novel variants are in bold; M: male; F: female; homo: homozygous variant; hetero: heterozygous variant; PA-paternal allele, MA-maternal allele, ? segregation analysis was inconclusive; * siblings.).

Proband	Variant		ACMG classification [27]	HGMD Professional 2021.1[31]	ClinVar[33]
1/M	*TYR* NM_000372.4: c.1A>G (NP_000363.1: p.Met1?)	Homo	Likely path.	OCA1, CM981972	Pathogenic
	TYR NM_000372.4: c.1205G>A (NP_000363.1: p.Arg402Gln)	Homo	Benign	OCA1, CM971555	Conflic. int. path
2/F	*TYR* NM_000372.4: c.650G>A (NP_000363.1: p.Arg217Gln)	Homo	Path.	OCA1, CM930714	Likely path.
	TYR NM_000372.4: c.1205G>A (NP_000363.1: p.Arg402Gln)	Homo	Benign	OCA1, CM971555	Conflic. int. path
3/M	*TYR* NM_000372.4: c.650G>A (NP_000363.1p.Arg217Gln)	Het,MA	Path.	OCA1, CM930714	Likely path.
	***TYR* NM_000372.4: c.1430G>A (NP_000363.1p.Trp477Ter)**	Het,PA	Likely path.	Not reported	Not reported
4/M	TYR NM_000372.4: c.265T>C (NP_000363.1: p.Cys89Arg)	Het MA	Path.	OCA1, CM910381	Pathogenic
	TYR NM_000372.4: c.1352A>G (NP_000363.1: p.Tyr451Cys	Het PA	Likely path.	OCA1, CM117403	Likely path.
	TYR NM_000372.4: c.1217C>T (NP_000363.1: p.Pro406Leu	Het MA	Likely path.	OCA1,CM910385	Likely path.
5/F	TYR NM_000372.4: c.265T>C; (NP_000363.1: p.Cys89Arg)	Het	Path.	OCA1, CM910381	Pathogenic
	TYR NM_000372.4: c.325G>A (NP_000363.1: p.Gly109Arg)	Het	Likely path.	OCA1, CM13052	Likely path.
	TYR NM_000372.4: c.1352A>G (NP_000363.1: p.Tyr451Cys)	Het	Likely path.	OCA, CM117403	Likely path.
6 /F	*TYR* NM_000372.4: c.1A>G (NP_000363.1: p.Met1?)	Het PA	Likely path.	OCA1, CM981972	Pathogenic
	TYR NM_000372.4: c.1217C>T (NP_000363.1: p.Pro406Leu)	Het MA	Likely path.	OCA1, CM910385	Likely path.
	TYR NM_000372.4: c.1205G>A (NP_000363.1: p.Arg402Gln)	Het PA	Benign	OCA1, CM971555	Conflic. int. Path
	TYR NM_000372.4: c.575C>A (NP_000363.1: p.Ser192Tyr)	Het MA	Benign		Benign
7/M	*TYR* NM_000372.4: c.265T>C (NP_000363.1: p.Cys89Arg)	Het MA	Path.	OCA1, CM910381	Path
	TYR NM_000372.4: c.1352A>G (NP_000363.1: p.Tyr451Cys)	Het MA	Likely path.	OCA, CM117403	Likely path.
	TYR NM_000372.4: c.1205G>A (NP_000363.1: p.Arg402Gln)	Het PA	Benign	OCA1, CM971555	Conflic. int. path.
	TYR NM_000372.4: c.575C>A (NP_000363.1: p.Ser192Tyr)	Het (?)	Benign		Benign
8/F	*TYR* NM_000372.4: c.1063G>C (NP_000363.1: p. Ala355Pro)	Het PA	Path.	OCA1, CM971550	Pathogenic
	TYR NM_000372.4: c.1217C>T (NP_000363.1: p.Pro406Leu)	Het PA	Likely path	OCA1, CM910385	Likely path.
	TYR NM_000372.4: c.1205G>A (NP_000363.1: p.Arg402Gln)	Het MA	Benign	OCA1, CM971555	Conflic. int. path.
	TYR NM_000372.4: c.575C>A (NP_000363.1: p.Ser192Tyr)	Het MA	Benign		Benign
9/F	TYR NM_000372.4: c.265T>C; (NP_000363.1: p.Cys89Arg)	Het PA	Path.	OCA1, CM910381	Pathogenic
	TYR NM_000372.4: c.1352A>G (NP_000363.1: p.Tyr451Cys)	Het PA	Likely path.	OCA, CM117403	Likely path.
	TYR NM_000372.4: c.1205G>A (NP_000363.1: p.Arg402Gln)	Het MA	Benign	OCA1, CM971555	Conflic. int. path
10 /M	***TYR* NM_000372.4: c.1430G>A (NP_000363.1p.Trp477Ter)**	Het PA	Likely path.	Not reported	Not reported
	TYR NM_000372.4: c.1205G>A (NP_000363.1: p.Arg402Gln)	Het MA	Benign.	OCA1, CM971555	Conflic. int. Path
	TYR NM_000372.4: c.575C>A (NP_000363.1: p.Ser192Tyr)	Het (?)	Benign		Benign
11/M	*TYR* NM_000372.4: c.650G>A (NP_000363.1: p.Arg217Gln)	Het	Path.	CM930714	Likely path.
	TYR NM_000372.4: c.1205G>A (NP_000363.1: p.Arg402Gln)	Homo	Benign	CM041478	Conflic. int. path
12*/M	*TYR* NM_000372.4: c.650G>A (NP_000363.1: p.Arg217Gln)	Het	Path.	OCA1, CM930714	Likely path.
	TYR NM_000372.4: c.1205G>A (NP_000363.1: p.Arg402Gln)	Homo	Benign	OCA1, CM971555	Conflic. int. Path
	TYR NM_000372.4: c.575C>A (NP_000363.1: p.Ser192Tyr)	Het	Benign		Benign
13*/M	*TYR* NM_000372.4: c.650G>A (NP_000363.1: p.Arg217Gln)	Het	Path.	OCA1, CM930714	Likely path.
	TYR NM_000372.4: c.1205G>A (NP_000363.1: p.Arg402Gln	Homo	Benign	OCA1, CM971555	Conflic. int. Path
	TYR NM_000372.4: c.575C>A (NP_000363.1: p.Ser192Tyr)	Het	Benign		Benign

Proband	Variant		ACMG classification [27]	HGMD Professional 2021.1[31]	ClinVar[33]
14/F	TYR NM_000372.4: c1217C>T (NP_000363.1: p.Pro406Leu)	Het PA	Likely path	OCA1, CM910385	Likely path.
	TYR NM_000372.4: c.1205G>A (NP_000363.1: p.Arg402Gln)	Het MA	Benign	OCA1, CM971555	Conflic. int. Path
	TYR NM_000372.4: c.575C>A (NP_000363.1: p.Ser192Tyr)	Homo	Benign		Benign
15/M	TYR NM_000372.4: c.1217C>T (NP_000363.1: p.Pro406Leu)	Het	Likely path	OCA1, CM910385	Likely path.
	TYR NM_000372.4: c.1205G>A (NP_000363.1: p.Arg402Gln)	Het	Benign	OCA1, CM971555	Conflic. int. Path
	TYR NM_000372.4: c.575C>A (NP_000363.1: p.Ser192Tyr)	Homo	Benign		Benign
16/F	*TYRP1*, NM_000550.2: c.670C>T (NP_000541.1:p.His224Tyr)	Homo	Likely path.	Not reported	Likely path.
17 /M	*TYRP1* NM_000550.2: c.70G>A (NP_000541.1: p.Ala24Thr	Het	Benign	OCA3: CM135782	Conflic. int. path
	TYRP1 NM_000550.2: c.418G>T (NP_000541.1: p.Glu140Ter)	Het	Pathogenic	OCA3: CM172531	Not reported
18/M	*SLC45A2* NM_016180.4: c.606G>C (NP_057264.3:p.Trp202Cys)	Homo	Likely path.	OCA4: CM040231	Conflic. int. Path/ Likely path.
19/M	***SLC45A2* NM_016180.4: c.302G>A (NP_057264.3:p. Arg101His)**	Homo	Likely path.	Not reported	Not reported
	TYR NM_000372.4: c. 589G>A (NP_000363.1:p.Asp197Asn)	Het	VUS	Not reported	Not reported
20/F	*OCA2* NM_000275.2: c.1025A>G (p.Tyr342Cys)	Het	Likely path.	OCA, CM091279	Likely path./ VUS
	HPS1, NM_000195.3: c.972dupC (NP_000186.2:p.Met325HisfsTer128)	Het	Pathogenic	Hermansky-Pudlak, CI962292	Likely path
	HPS1, NM_000195.3: c 1189delC (NP_000186.2:p.Gln397SerfsTer2)	Het	Pathogenic	Hermansky-Pudlak, CD982692	Likely path
21/M	***TYRP1*, NM_000550.2: c.913+1G>A**	Het	Likely path.	Not reported	Not reported
22/M	*TYR* NM_000372.4: c.1205G>A (NP_000363.1p.Arg402Gln)	Het	Benign	OCA1, CM971555	Conflic. int. path
	TYR NM_000372.4: c.575C>A (NP_000363.1: p.Ser192Tyr)	Homo	Benign		Benign
23/M	*TYR* NM_000372.4: c.1205G>A (NP_000363.1p.Arg402Gln)	Het	Benign	OCA1, CM971555	Conflic. int. path
24/F	*TYR* NM_000372.4: c.575C>A (NP_000363.1: p.Ser192Tyr)	Het	Benign		Benign
25/M	*TYR* NM_000372.4: c.575C>A (NP_000363.1: p.Ser192Tyr)	Homo	Benign		Benign

Table 3: General population frequencies and *in silico* prediction scores of the novel genetic variants detected in OCA patients (REVEL[29], VEST4[30] and SpliceAI[31] values O-1, and CADD[28] Phred values: variants with higher scores are predicted to be more likely pathogenic; nd: not detected)

Variant	Position and MAF (gnomAD[32])	*In silico* prediction tools and scores
***TYR* NM_000372.4: c.1430G>A (NP_000363.1p.Trp477Ter)**	nd	CADD: 39 VEST4:0,88
***SLC45A2* NM_016180.4: c.302G>A (NP_057264.3:p. Arg101His)**	chr5:33984282: rs763531791 MAF: A = 0,0024% (6/251,262 alleles)	CADD: 36,6 REVEL:0.829 VEST4: 0.65
***TYRP1*, NM_000550.2: c.913+1G>A**	chr9:12698656: rs748926400 MAF: A = 0,0016% (4/250,176 alleles)	CADD: 34 SpliceAI: 0.85

4. Discussion

OCA shows considerable clinical heterogeneity.[2] Consequently, individual types of albinism might be difficult to differentiate clinically in children, especially in those with light complexion, where there might be an overlap with other related disorders. Even though OCA is a genetically heterogeneous disorder, NGS based genetic testing enables timely definitive etiological diagnosis and consequently appropriate management of the disease. This is of notable importance in cases with mild or partial clinical manifestations.[10]

Among 25 paediatric patients of Slovenian descent with clinically suspected OCA, as much as 16 had normal complexion in regard to the other family members, and some of them had only mild albinism-related features (Table 1). In as much as 20 out of 25 patients (80%) in the entire cohort, genetic variants explaining their clinical phenotype were identified (Table 2). This is in accordance with other recent reports, where molecular diagnosis was achieved in 92% of patients with mild partial albinism[10] and 72,3% of patients with albinism.[12] Great majority of patients in our cohort (60% – 15/25) had *TYR* disease causing variants. This is surprisingly high when compared to the large cohort of 990 tested patients in France, where the number was 41,8%[12]. High frequency of *TYR* disease causing variants can partly be explained with the fact that ocular albinism due to *GPR143* variants was previously excluded from our group of patients.[26] For instance in above mentioned large cohort *GPR143* variants were responsible for 7% of the cases.[12] Among our remaining patients, 4% (1/25) had only monoallelic disease causing variants that cannot fully explain the clinical presentation, while in 16% (4/25) no disease causing variant was detected in analysed genes. This is comparable with the large reported cohort, where 12% of patients had monoallelic variants and 15,5% had no detected disease causing variants.[12] Surprisingly, we did not identify variants in *OCA2* gene that would be a probable cause of albinism in our cohort. We identify only one *OCA2* variant in heterozygous state in a patient 20 carrying *HPS1* disease causing variants. NGS results in this study were confirming the results of our earlier testing approach using selective gene Sanger sequencing. This is in concordance with a previously reported group of patients with partial OCA, where OCA2 disease causing variants were identified only in heterozygous state together with the heterozygous variant in *TYR* gene.[10]

The novel *TYR* NM_000372.4: c.1430G>A (NP_000363.1 p.Trp477Ter) variant was detected in patients 3 and 10 in compound heterozygous state with another *TYR* variant. This variant is introducing premature termination codon and was predicted to be pathogenic. Both patients harbouring this variant had mild signs of OCA with normal complexion, mild to medium iris transillumination, foveal depression still present, but smaller, normal or rare retinal pigment epithelium, and no photophobia. The mild phenotypic characteristics in patient 10 are likely associated with hypomorfic variant present on the other *TYR* gene allele as it was previously reported.[14]

SLC45A2 variant NM_016180.4: c.302G>A (NP_057264.3: p.Arg101His) was detected in homozygous state in patient 19. It has so far not been reported in OCA and was predicted to be pathogenic. A different amino acid change, namely p.Arg101Cys, on the same position as here reported variant, was previously reported in a patient with OCA4, but his clinical characteristics were not described in more details (HGMD acc. nr. CM083847). Variants in *SLC45A2* gene are associated with OCA4. This is a rare OCA type, reported in approximately 3% of European patients,[34–36] but is more common in Japan.[37] OCA4 is clinically variable and overlapping with other OCA types.[5] Patient 19 had mild clinical phenotype with fair complexion, minimal foveal depression, rare retinal pigment epithelium, choroidal vessels seen at the posterior pole, but not in the foveal area, medium hypermetropic astigmatism, and minimal photophobia. His clinical presentation did not differ significantly from other patients, nevertheless, he was the only patients in this group with complete iris transillumination.

Variants in *TYRP1* gene are associated with OCA3, an extremely rare type in Caucasian patients, reported only in individual patients[17] and in 2,1% of patients in a cohort of mainly but not exclusively French origin.[12] Patient 16 had homozygous *TYRP1* variant NM_000550.2:c.670C>T (NP_000541.1:p.His224Tyr) that was previously reported in ClinVar database in a patient with ocular albinism (Allele ID: 360904) but was so far not reported in Human Gene Mutation Database. He had normal complexion, mild iris transillumination, choroidal vessels seen at the posterior pole, but not in the foveal area, medium hypermetropic astigmatism, and minimal photophobia. His clinical presentation did not differ significantly from other patients and was not concordant with the reported Caucasian patients, who had light-yellow skin, yellow-gold hair with orange highlights and fair eyelashes, divergent strabismus, and no photophobia.[17]

Among the variants that were classified as highly susceptive for OCA was also the *TYR* gene harbouring two allelic variants, namely NM_000372.4:c.575C>A (p.Ser192Tyr) and NM_000372.4: c.1205G>A (p.Arg402Gln). Those variants individually are frequently reported in general population and consequently regarded as benign. Nevertheless, when these are located *in cis* they are much rarer and when inherited *in trans* with pathogenic *TYR* variant, they were repeatedly reported to be causative for mild or partial form of OCA.[10–13] This complex *TYR* allele was present in several patients in our cohort, while in six patients (subjects 8, 10, 12, 13, 14, 15) it was inherited in *trans* with other *TYR* variant. Therefore, those patients we classified as likely OCA1. They all had normal or fair complexion, rare retinal pigment epithelium, low or medium hypermetropic astigmatism, and no photophobia – con-

cordant with mild OCA. Among them, two were brothers (subject 12 and 13) with very similar clinical presentation. They only differed in iris transillumination that was present in mild form only in the younger brother (subject 13). Similarly as in our cohort, this complex allele was the most common disease causing allele in a previously reported group of patients with partial OCA.[10]

Patient 20 was compound heterozygote for two known disease causing variants in *HPS1* gene associated with Hermansky-Pudlak syndrome type 1. Additionally, she was a heterozygous carrier of know disease causing variant in *OCA2* gene associated with OCA2. In our cohort, she had the most severe retinal pigment epithelium phenotype with choroidal vessels seen also in the foveal area. She had fair complexion, mild iris transillumination, no foveal depression, low hypermetropic astigmatism, and photophobia. She was referred to genetic testing due to her albinism-related symptoms and the genetic testing results led to the diagnosis of the Hermansky-Pudlak syndrome type 1 in 2018 when she was 11 years old. Later on, fulminant Crohn's disease with perianal fistulas and prolonged bleeding due to thrombocytopathy were recognised, both known manifestations of Hermansky-Pudlak syndrome.[38,39] The diagnostic pathway that led to the diagnosis of Hermansky-Pudlak syndrome in this patient confirms the importance of genetic testing in children with albinism. As previously suggested, early identification of the genetic aetiology of albinism can reveal serious syndromic causes of albinism that need appropriate clinical management including clinical evaluation of possible extraocular manifestations.[40]

In our cohort of patients, phenotype could not predict genotype or vice versa, and there were no specific clinical signs correlating with the molecular diagnosis. Nevertheless, these children seem to be of lighter complexion with greater foveal hypoplasia and rare retinal pigment epithelium. Iris transillumination did not correlate with photophobia or other clinical signs, but it was present to a certain extent in all subjects. Furthermore, all subjects had low to medium hypermetropic astigmatism, with one who was highly myopic.

In conclusion, NGS based genetic testing had a high diagnostic yield of 80% in our paediatric cohort of patients with various degrees of OCA and previously excluded OA due to disease causing variants in *GPR143* gene. Interestingly, we have identified a patient of white European ancestry with OCA3, which is an extremely rare report, and one patient with OCA due to the Hermansky-Pudlak syndrome type 1.

Acknowledgements

The authors thank Assist. Prof. Jelka Brecelj, PhD, and Assist. Prof. Maja Šuštar, PhD, for electrophysiological assessment and assistance, as well as Mrs. Barbara Klemenc for technical assistance with OCTs and fundus imaging.

This work was supported by the Slovenian Research Agency (grants P3-0343, P1-0170).

Declaration of interest:

There is no conflict of interest declared.

5. References

1. Marçon CR, Maia M. Albinism: epidemiology, genetics, cutaneous characterization, psychosocial factors. *An Bras Dermatol*. **2019;** *94(5),* 503–520. **DOI:**10.1016/j.abd.2019.09.023
2. Montoliu L, Grønskov K, Wei AH, et al. Increasing the complexity: New genes and new types of albinism. *Pigment Cell Melanoma Res*. **2014;** *27(1),* 11–18. **DOI:**10.1111/pcmr.12167
3. Käsmann-Kellner B, Seitz B. Phänotyp des visuellen systems bei okulokutanem und okulärem albinismus. *Ophthalmologe*. **2007;** *104(8),* 648–661. **DOI:**10.1007/s00347-007-1571-4
4. Kruijt CC, de Wit GC, Bergen AA, Florijn RJ, Schalij-Delfos NE, van Genderen MM. The Phenotypic Spectrum of Albinism. *Ophthalmology*. **2018**, *125(12),* 1953–1960. **DOI:**10.1016/j.ophtha.2018.08.003
5. Summers CG. Albinism: Classification, clinical characteristics, and recent findings. *Optom Vis Sci*. **2009;** *86(6),* 659–662. **DOI:**10.1097/OPX.0b013e3181a5254c
6. Summers CG, King RA. Ophthalmic Features of Minimal Pigment Oculocutaneous Albinism. *Ophthalmology*. **1994;** *101(5),* 906–914. **DOI:**10.1016/S0161-6420(13)31250-0
7. Spritz R, Strunk K, LB G, RA K. The New England Journal of Medicine Downloaded from nejm.org on April 1, 2015. For personal use only. No other uses without permission. Copyright © 1990 Massachusetts Medical Society. All rights reserved. *New Englnd J Med*. **1990;** *322(24),* 1724–1728. **DOI:**10.1056/NEJM199006143222407
8. Lerner AB, Fitzpatrick TB. Biochemistry of melanin formation. *Physiol Rev*. **1950;** *30(1),* 91–126. **DOI:**10.1152/physrev.1950.30.1.91
9. King RA, Pietsch J, Fryer JP, et al. Tyrosinase gene mutations in oculocutaneous albinism 1 (OCA1): Definition of the phenotype. *Hum Genet*. **2003;** *113(6),* 502–513. **DOI:**10.1007/s00439-003-0998-1
10. Campbell P, Ellingford JM, Parry NRA, et al. Clinical and genetic variability in children with partial albinism. *Sci Rep*. **2019;** *9(1),* 16576. **DOI:**10.1038/s41598-019-51768-8
11. Norman CS, O'Gorman L, Gibson J, et al. Identification of a functionally significant tri-allelic genotype in the Tyrosinase gene (TYR) causing hypomorphic oculocutaneous albinism (OCA1B). *Sci Rep*. **2017;** *7(1),* 4415. **DOI:**10.1038/s41598-017-04401-5
12. Lasseaux E, Plaisant C, Michaud V, et al. Molecular characterization of a series of 990 index patients with albinism. *Pigment Cell Melanoma Res*. **2018;** *31(4),* 466–474. **DOI:**10.1111/pcmr.12688
13. Jagirdar K, Smit DJ, Ainger SA, et al. Molecular analysis of

common polymorphisms within the human Tyrosinase locus and genetic association with pigmentation traits. *Pigment Cell Melanoma Res*. **2014;** *27(4),* 552–564. **DOI:**10.1111/pcmr.12253

14. Monfermé S, Lasseaux E, Duncombe-Poulet C, et al. Mild form of oculocutaneous albinism type 1: Phenotypic analysis of compound heterozygous patients with the R402Q variant of the TYR gene. *Br J Ophthalmol*. **2019;** *103(9),* 1239–1247. **DOI:**10.1136/bjophthalmol-2018-312729
15. Rooryck C, Morice-Picard F, Lasseaux E, et al. High resolution mapping of OCA2 intragenic rearrangements and identification of a founder effect associated with a deletion in Polish albino patients. *Hum Genet*. **2011;** *129(2),* 199–208. **DOI:**10.1007/s00439-010-0913-5
16. Rosemblat S, Durham-Pierre D, Gardner JM, Nakatsu Y, Brilliant MH, Orlow SJ. Identification of a melanosomal membrane protein encoded by the pink-eyed dilution (type II oculocutaneous albinism) gene. *Proc Natl Acad Sci U S A*. **1994;** *91(25),* 12071–12075. **DOI:**10.1073/pnas.91.25.12071
17. Rooryck C, Roudaut C, Robine E, Müsebeck J, Arveiler B. Oculocutaneous albinism with TYRP1 gene mutations in a Caucasian patient. *Pigment Cell Res*. **2006;** *19(3),* 239–242. **DOI:**10.1111/j.1600-0749.2006.00298.x
18. Newton JM, Cohen-Barak O, Hagiwara N, et al. Mutations in the human orthologue of the mouse underwhite gene (uw) underlie a new form of oculocutaneous albinism, OCA4. *Am J Hum Genet*. **2001;** *69(5),* 981–8. **DOI:**10.1086/324340
19. Bin BH, Bhin J, Yang SH, et al. Membrane-associated transporter protein (MATP) regulates melanosomal pH and influences tyrosinase activity. *PLoS One*. **2015;** *10(6),* e0129273. **DOI:**10.1371/journal.pone.0129273
20. Pennamen P, Tingaud-Sequeira A, Gazova I, et al. Dopachrome tautomerase variants in patients with oculocutaneous albinism. *Genet Med*. **2021;** *23(3),* 479–487. **DOI:**10.1038/s41436-020-00997-8
21. Gargiulo A, Testa F, Rossi S, et al. Molecular and clinical characterization of albinism in a large cohort of Italian patients. *Investig Ophthalmol Vis Sci*. **2011.** **DOI:**10.1167/iovs.10-6091
22. Thomas MG, Kumar A, Mohammad S, et al. Structural grading of foveal hypoplasia using spectral-domain optical coherence tomography: A predictor of visual acuity? *Ophthalmology*. **2011**. **DOI:**10.1016/j.ophtha.2011.01.028
23. Brecelj J. Visual electrophysiology in the clinical evaluation of optic neuritis, chiasmal tumours, achiasmia, and ocular albinism: an overview. *Doc Ophthalmol*. **2014;** *129(2),* 71–84. **DOI:**10.1007/s10633-014-9448-8
24. Simeonov DR, Wang X, Wang C, et al. DNA Variations in Oculocutaneous Albinism: An Updated Mutation List and Current Outstanding Issues in Molecular Diagnostics. *Hum Mutat*. **2013;** *34(6),* 827–835. **DOI:**10.1002/humu.22315
25. Brecelj J, Sustar M, Pečarič-Meglič N, Škrbec M, Stirn-Kranjc B. VEP characteristics in children with achiasmia, in comparison to albino and healthy children. *Doc Ophthalmol.* **2012;** *124(2),* 109–123. **DOI:**10.1007/s10633-012-9315-4
26. Trebušak Podkrajšek K, Stirn Kranjc B, Hovnik T, Kovač J, Battelino T. GPR143 gene mutation analysis in pediatric patients with albinism. *Ophthalmic Genet*. **2012;** *33(3),* 167–170. **DOI:**10.3109/13816810.2011.559651
27. Richards S, Aziz N, Bale S, et al. Standards and guidelines for the interpretation of sequence variants: A joint consensus recommendation of the American College of Medical Genetics and Genomics and the Association for Molecular Pathology. *Genet Med*. **2015;** *17(5),* 405–424. **DOI:**10.1038/gim.2015.30
28. Combined Annotation Dependent Depletion. http://cadd.gs.washington.edu/.
29. Ioannidis NM, Rothstein JH, Pejaver V, et al. REVEL: An Ensemble Method for Predicting the Pathogenicity of Rare Missense Variants. *Am J Hum Genet*. **2016;** *99(4)* 877–885. **DOI:**10.1016/j.ajhg.2016.08.016
30. Douville C, Masica DL, Stenson PD, et al. Assessing the Pathogenicity of Insertion and Deletion Variants with the Variant Effect Scoring Tool (VEST-Indel). *Hum Mutat*. **2016;** *37(1)* 28–35. **DOI:**10.1002/humu.22911
31. Jaganathan K, Kyriazopoulou Panagiotopoulou S, McRae JF, et al. Predicting Splicing from Primary Sequence with Deep Learning. *Cell*. **2019;** *176(3),* 535–548.e24. **DOI:**10.1016/j.cell.2018.12.015
32. The Genome Aggregation Database. http://gnomad.broadinstitute.org//.
33. Landrum MJ, Chitipiralla S, Brown GR, et al. ClinVar: Improvements to accessing data. *Nucleic Acids Res*. **2020;** *48(D1),* D835–D844. **DOI:**10.1093/nar/gkz972
34. Mauri L, Barone L, Al Oum M, et al. SLC45A2 mutation frequency in Oculocutaneous Albinism Italian patients doesn't differ from other European studies. *Gene*. **2014;** *533(1),* 398–402. **DOI:**10.1016/j.gene.2013.09.053
35. Grønskov K, Ek J, Sand A, et al. Birth prevalence and mutation spectrum in Danish patients with autosomal recessive albinism. *Investig Ophthalmol Vis Sci*. **2009;** *50(3),* 1058–1064. **DOI:**10.1167/iovs.08-2639
36. Rundshagen U, Zühlke C, Opitz S, Schwinger E, Käsmann-Kellner B. Mutations in the MATP Gene in Five German Patients Affected by Oculocutaneous Albinism Type 4. *Hum Mutat*. **2004;** *23(2),* 106–110. **DOI:**10.1002/humu.10311
37. Inagaki K, Suzuki T, Shimizu H, et al. Oculocutaneous Albinism Type 4 Is One of the Most Common Types of Albinism in Japan. *Am J Hum Genet*. **2004;** *74(3),* 466–471. **DOI:**10.1086/382195
38. De Jesus Rojas W, Young LR. Hermansky-Pudlak Syndrome. *Semin Respir Crit Care Med*. **2020;** *41(2),* 238–246. **DOI:**10.1055/s-0040-1708088 8
39. El-Chemaly S, Young LR. Hermansky-Pudlak Syndrome. *Clin Chest Med*. **2016;** *37(3),* 505–511. **DOI:**10.1016/j.ccm.2016.04.012
40. Lenassi E, Clayton-Smith J, Douzgou S, et al. Clinical utility of genetic testing in 201 preschool children with inherited eye disorders. *Genet Med*. **2020;** *22(4),* 745–751. **DOI:**10.1038/s41436-019-0722-8

Povzetek

Okulokutani albinizem (OCA) je dedna motnja, ki vpliva na vidni sistem in pigmentacijo kože. Naš cilj je bil z uporabo naprednega molekularno-genetskega pristopa oceniti genetsko in klinično heterogenost v kohorti slovenskih pediatričnih pacientov s klinično domnevanim OCA. Pri 20 od 25 pacientov so bile ugotovljene genetske različice, ki pojasnjujejo njihov klinični fenotip. Velika večina pacientov (15/25) je imela genetske različice gena *TYR*, povezanega z OCA tipa 1, sledile so mu različice genov *TYRP1, SLC45A2* in *HPS1*, ki so vzrok za OCA3, OCA4 in Hermansky-Pudlakov sindrom tipa 1. Ugotovili smo, da fenotip OCA ne more napovedati genotipa in obratno. Kljub temu je bil diagnostični izkoristek po ciljanem sekvenciranju naslednje generacije (NGS) 80 % in se je izkazal za učinkovitega v naši pediatrični kohorti pacientov z različno stopnjo OCA. Tudi pri 16 pacientih z normalno poltjo je bil diagnostični izkoristek 62,5 %. Zanimivo je, da smo identificirali pacienta belega evropskega porekla z OCA3, kar je izjemno redko poročano, in enega pacienta z OCA zaradi Hermansky-Pudlakovega sindroma tipa 1.

Scientific paper

Anion Induced Synthesis, Structural Characterization and Antibacterial Activity of Zinc(II) Complexes Derived from 5-Bromo-2-((2-(diethylamino)ethylimino)methyl) phenol

Huan-Yu Liu,* Xiang Gan, Jin-Yan Ding, Zhi-Tao Li and Qiao Chen

[1] *School of Chemistry and Chemical Engineering, Guangdong Pharmaceutical University, Zhongshan 528458, P.R. China*

[2] *Guangdong Cosmetics Engineering and Technology Research Center, Zhongshan 528458, P.R. China*

[3] *Guangdong Provincial Key Laboratory of Pharmaceutical Bioactive Substances, Guangdong Pharmaceutical University, Guangzhou 510006, P.R. China*

* *Corresponding author: E-mail: liuhuanyu03@163.com*

Received: 02-01-2021

Abstract

By changing the anions of zinc salts, three different zinc(II) complexes, $[Zn_2(HL)_2(NCS)_4]\cdot 2CH_3OH$ (**1**), $[Zn_2L(\mu_2\text{-}\eta^1\text{:}\eta^1\text{-}CH_3COO)_2(NCS)]$ (**2**) and $[Zn(HL)I_2]\cdot CH_3OH$ (**3**), where L = 5-bromo-2-((2-(diethylamino)ethylimino)methyl)phenolate, HL = 5-bromo-2-((2-(diethylammonio)ethylimino)methyl)phenolate, have been synthesized and characterized by IR and UV-Vis spectroscopy, as well as single-crystal X-ray diffraction. X-ray analysis indicates that the Zn atoms in the complexes are in trigonal bipyramidal, square pyramidal and tetrahedral coordination. The anions of the zinc salts lead to the formation of different structures of the complexes. Antibacterial activity of the complexes against *Staphylococcus aureus*, *Escherichia coli*, *Klebsielle pneumoniae* and *Candida albicans* strains was studied.

Keywords: Schiff base; Zinc complex; Self-assembly; Crystal structure; Antibacterial activity

1. Introduction

Schiff base compounds play important role in the pharmaceutical industry as antibacterial, antiradical, antifungal, anticancer and antiviral agents.[1] Salen type Schiff bases are privileged ligands in coordination chemistry that can form versatile structures of complexes with various metals.[2] Among the large number of Schiff base complexes, those with zinc atoms have received particular attention due to their remarkable biological activities.[3] Zinc is the second most abundant trace metal in the human body and can be considered as non-toxic to humans. It is essential for the structures, regulation and catalytic action of over 300 enzymes.[4] The structures of Schiff base complexes are sensitive. A number of zinc complexes have shown antimicrobial activities,[5] and therefore zinc complexes deserve further attention in this regard. In this paper, three new zinc(II) complexes, $[Zn_2(HL)_2(NCS)_4]\cdot 2CH_3OH$ (**1**), $[Zn_2L(\mu_2\text{-}\eta^1\text{:}\eta^1\text{-}CH_3COO)_2(NCS)]$ (**2**) and $[Zn(HL)I_2]\cdot CH_3OH$ (**3**), where L = 5-bromo-2-((2-(diethylamino) ethylimino)methyl)phenolate, HL = 5-bromo-2-((2-(diethylammonio)ethylimino)methyl)phenolate, have been synthesized, characterized, and assayed for the antibacterial effects.

2. Experimental

2. 1. General Methods and Materials

Zinc nitrate, zinc acetate, zinc iodide, ammonium thiocyanate, 4-bromosalicylaldehyde and *N,N*-diethylethane-1,2-diamine were obtained from Sigma-Aldrich. All other reagents were of analytical reagent grade. Elemental analyses (C, H, N) were performed with a PE-2400 II apparatus. Infrared spectra were recorded on KBr pellets with a Nicolet Nexus 670 FT-IR spectrometer in the 400–4000 cm^{-1} range. UV-Vis spectra were obtained on a Lambda 900 spectrometer. Molar conductance was measured with a Shanghai DDS-11A conductometer. X-ray dif-

fraction was carried out on a Bruker SMART 1000 CCD diffractometer.

2. 2. Synthesis of $[Zn_2(HL)_2(NCS)_4]\cdot 2CH_3OH$ (1)

4-Bromosalicylaldehyde (1.0 mmol, 0.20 g) and *N,N*-diethylethane-1,2-diamine (1.0 mmol, 0.12 g) were dissolved in methanol and refluxed for 10 min. After cooling to room temperature, zinc nitrate hexahydrate (2.0 mmol, 0.38 g) was added to the solution, and stirred for 10 min. Then, ammonium thiocyanate (2.0 mmol, 0.15 g) was added and stirred for another 10 min and filtered. The filtrate was allowed to evaporate slowly for 3 days at room temperature and colorless crystals were obtained. The crystals were isolated by filtration, washed with methanol and dried in air. Yield: 0.23 g (45%). Anal. Calcd. for $C_{32}H_{46}Br_2N_8O_4S_4Zn_2$ (%): C, 37.47; H, 4.52; N, 10.93. Found (%): C, 37.33; H, 4.63; N, 11.12. IR data (KBr, ν_{max}/cm^{-1}): 3616 (OH), 3381 (NH), 2095, 2070 (NCS), 1634 (C=N), 1578, 1530, 1474, 1455, 1391, 1273, 1192, 1133, 1085, 1023, 961, 919, 857, 793, 598, 583, 523, 477, 455. UV-Vis data (MeOH; λ_{max}, nm): 227, 247, 266, 322, 365.

2. 3. Synthesis of $[Zn_2L(\mu_2\text{-}\eta^1{:}\eta^1\text{-}CH_3COO)_2(NCS)]$ (2)

4-Bromosalicylaldehyde (1.0 mmol, 0.20 g) and *N,N*-diethylethane-1,2-diamine (1.0 mmol, 0.12 g) were dissolved in methanol and refluxed for 10 min. After cooling to room temperature, zinc acetate dihydrate (2.0 mmol, 0.22 g) was added to the solution, and stirred for 10 min. Then, ammonium thiocyanate (2.0 mmol, 0.15 g) was added and stirred for another 10 min and filtered. The filtrate was allowed to evaporate slowly for 5 days at room temperature and colorless crystals were obtained. The crystals were isolated by filtration, washed with methanol and dried in air. Yield: 0.34 g (56%). Anal. Calcd. for $C_{18}H_{24}BrN_3O_5SZn_2$ (%): C, 35.73; H, 4.00; N, 6.94. Found (%): C, 35.87; H, 4.12; N, 6.85. IR data (KBr, ν_{max}/cm^{-1}): 2083 (NCS), 1648 (C=N), 1592, 1538, 1477, 1443, 1394, 1345, 1277, 1205, 1173, 1076, 1042, 936, 910, 851, 795, 736, 668, 617, 600, 543, 460. UV-Vis data (MeOH; λ_{max}, nm): 240, 275, 343.

2. 4. Synthesis of $[Zn(HL)I_2]\cdot CH_3OH$ (3)

4-Bromosalicylaldehyde (1.0 mmol, 0.20 g) and *N,N*-diethylethane-1,2-diamine (1.0 mmol, 0.12 g) were dissolved in methanol and refluxed for 10 min. After cooling to room temperature, zinc iodide (2.0 mmol, 0.32 g) was added to the solution, and stirred for 10 min. Then, ammonium thiocyanate (2.0 mmol, 0.15 g) was added and stirred for another 10 min and filtered. The filtrate was allowed to evaporate slowly for 6 days at room temperature and colorless crystals were obtained. The crystals were isolated by filtration, washed with methanol and dried in air. Yield: 0.41 g (64%). Anal. Calcd. for $C_{13}H_{21}BrI_2N_2O_2Zn$ (%): C, 24.53; H, 3.33; N, 4.40. Found (%): C, 24.66; H, 3.24; N, 4.47. IR data (KBr, ν_{max}/cm^{-1}): 3528 (OH), 3286

Table 1. Crystallographic and refinement data for the complexes

	1	2	3
Molecular formula	$C_{32}H_{46}Br_2N_8O_4S_4Zn_2$	$C_{18}H_{24}BrN_3O_5SZn_2$	$C_{13}H_{21}BrI_2N_2O_2Zn$
Formula weight	1025.57	605.11	636.40
T, K	298(2)	298(2)	298(2)
Crystal system	Monoclinic	Monoclinic	Monoclinic
Space group	$P2_1/n$	$P2_1/c$	$P2_1/n$
a, Å	8.9614(19)	15.6123(13)	8.1733(11)
b, Å	22.7484(17)	8.3289(12)	14.3725(13)
c, Å	10.5794(13)	18.4164(15)	17.1426(13)
β, °	97.195(2)	93.024(1)	92.850(1)
V, Å^3	2139.7(5)	2391.4(4)	2011.3(4)
Z	2	4	4
ρ_{calcd}, g cm^{-3}	1.592	1.681	2.102
μ(MoK_α , mm^{-1})	3.228	3.796	6.282
F(000)	1040	1216	1200
Measured reflections	11876	13619	10379
Unique reflections	3945	4451	3737
Observed reflections ($I \geq 2\sigma(I)$)	2467	2659	2501
Parameters	238	326	198
Restraints	0	90	3
Goodness of fit on F^2	0.996	1.006	0.998
R_1, wR_2 ($I \geq 2\sigma(I)^*$	0.0628, 0.1840	0.0380, 0.0909	0.0502, 0.1209
R_1, wR_2 (all data)*	0.1109, 0.2397	0.0802, 0.1090	0.0809, 0.1392

* $R_1 = \Sigma||F_o| - |F_c||/\Sigma|F_o|$, $wR_2 = \{\Sigma[w(F_o^2 - F_c^2)^2]/\Sigma[w(F_o^2)^2]\}^{1/2}$

(NH), 1626 (C=N), 1580, 1515, 1462, 1429, 1401, 1287, 1233, 1180, 1133, 1066, 1053, 923, 870, 803, 779, 683, 602, 570, 527, 498, 462. UV-Vis data (MeOH; λ_{max}, nm): 218, 245, 267, 366.

2. 5. X-ray Crystallography

The program SAINT was used for integration of the diffraction profiles.[6] Structures were solved by direct methods using the SHELXS program of the SHELXTL package and refined by full-matrix least-squares methods with SHELXL (semi-empirical absorption corrections were applied using the SADABS program).[7] The positions of the non-hydrogen atoms were located in difference Fourier syntheses and least-squares refinement cycles, and finally refined anisotropically. The C8-C9-N2-C10-C11-C12-C13 moiety of complex **2** is disordered over two sites, with occupancies of 0.52(1) and 0.48(1). The water hydrogen atoms of complex **3** were located from the electronic density map and refined isotropically, with O–H and H···H distances restrained to 0.85(1) and 1.37(2) Å, respectively. The remaining hydrogen atoms of the complexes were placed theoretically onto the specific atoms and refined isotropically as riding atoms. Crystallographic data and experimental details for structural analyses are summarized in Table 1. Selected bond lengths and angles for the complexes are listed in Table 2.

Table 2. Selected bond distances (Å) and angles (°) for the complexes

		1	
Zn1–O1	1.965(5)	Zn1–N1	2.123(6)
Zn1–N3	1.971(7)	Zn1–N4	1.994(7)
Zn1–O1A	2.224(5)		
O1–Zn1–N3	118.5(3)	O1–Zn1–N4	123.9(3)
N3–Zn1–N4	116.1(3)	O1–Zn1–N1	90.1(2)
N3–Zn1–N1	97.0(3)	N4–Zn1–N1	95.2(3)
O1–Zn1–O1A	77.4(2)	N3–Zn1–O1A	90.0(2)
N4–Zn1–O1A	91.0(2)	N1–Zn1–O1A	167.48(19)
		2	
Zn1–O1	2.110(3)	Zn1–O2	1.987(3)
Zn1–N1	1.997(5)	Zn1–N2	2.220(4)
Zn2–N3	1.926(5)	Zn1–O4	1.981(4)
Zn2–O1	1.959(3)	Zn2–O3	1.961(3)
Zn2–O5	1.945(3)		
O4–Zn1–O2	107.45(15)	O4–Zn1–N1	143.47(16)
O2–Zn1–N1	109.05(16)	O4–Zn1–O1	90.47(13)
O2–Zn1–O1	96.39(13)	N1–Zn1–O1	86.86(15)
O4–Zn1–N2	94.51(16)	O2–Zn1–N2	94.36(15)
N1–Zn1–N2	81.48(18)	O1–Zn1–N2	166.22(16)
N3–Zn2–O5	111.59(17)	N3–Zn2–O1	119.37(16)
O5–Zn2–O1	101.44(14)	N3–Zn2–O3	107.47(16)
O5–Zn2–O3	110.21(14)	O1–Zn2–O3	106.46(13)
		3	
Zn1–I1	2.5498(10)	Zn1–I2	2.5906(10)
Zn1–O1	1.955(5)	Zn1–N1	2.033(5)
O1–Zn1–N1	94.6(2)	O1–Zn1–I1	111.47(16)
N1–Zn1–I1	115.92(17)	O1–Zn1–I2	111.73(17)
N1–Zn1–I2	106.76(17)	I1–Zn1–I2	114.61(3)

Symmetry operation for A: 1 – *x*, 1 – *y*, – *z*.

2. 6. Antibacterial Assay

The complexes and ligands were tested for their *in vitro* antibacterial activity against *Staphylococcus aureus*, *Escherichia coli*, *Klebsielle pneumoniae* and *Candida albicans* strains using the paper disc diffusion method (for the qualitative determination) and the serial dilutions in liquid broth method (for determination of MIC).[8] Suspensions in sterile peptone water from 24 h cultures of microorganisms were adjusted to 0.5 McFarland. Muller–Hinton Petri dishes of 90 mm were inoculated using these suspensions. Paper disks (6 mm in diameter) containing 10 μL of the substance to be tested (at a concentration of 2048 μg/mL in DMSO) were placed in a circular pattern in each inoculated plate. Incubation of the plates was done at 37 °C for 18–24 h. Reading of the results was done by measuring the diameters of the inhibition zones generated by the tested substances. Tetracycline and fluconazole were used as a reference substance.

Determination of MIC was done using the serial dilutions in liquid broth method. The materials used were 96-well plates, suspensions of microorganism (0.5 McFarland), Muller–Hinton broth (Merck) and stock solutions of each substance to be tested (2048 μg/mL in DMSO). The following concentrations of the substances to be tested were obtained in the 96-well plates: 1024, 512, 256, 128, 64, 32, 16, 8.0, 4.0 and 2.0 μg/mL. After incubation at 37 °C for 18–24 h, the MIC for each tested substance was determined by macroscopic observation of microbial growth. It corresponds to the well with the lowest concentration of the tested substance where microbial growth was clearly inhibited.

3. Results and Discussion

3. 1. Synthesis and Characterization

The Schiff base ligand was prepared by the condensation reaction of 4-bromosalicylaldehyde and *N,N*-diethylethane-1,2-diamine in methanol, which was used to prepare the complexes directly. The three complexes were facile synthesized by reaction of the freshly synthesized Schiff base ligand, ammonium thiocyanate and different zinc salts, *viz.* zinc nitrate for **1**, zinc acetate for **2**, and zinc iodide for **3** (Scheme 1). The anions of the zinc salts lead to the formation of different structures of the complexes. The thiocyanate ligand was incorporated in the preparation of the complexes, and it coordinated to complexes **1** and **2**, while absent in complex **3**. All the complexes are soluble in methanol, ethanol, acetonitrile,

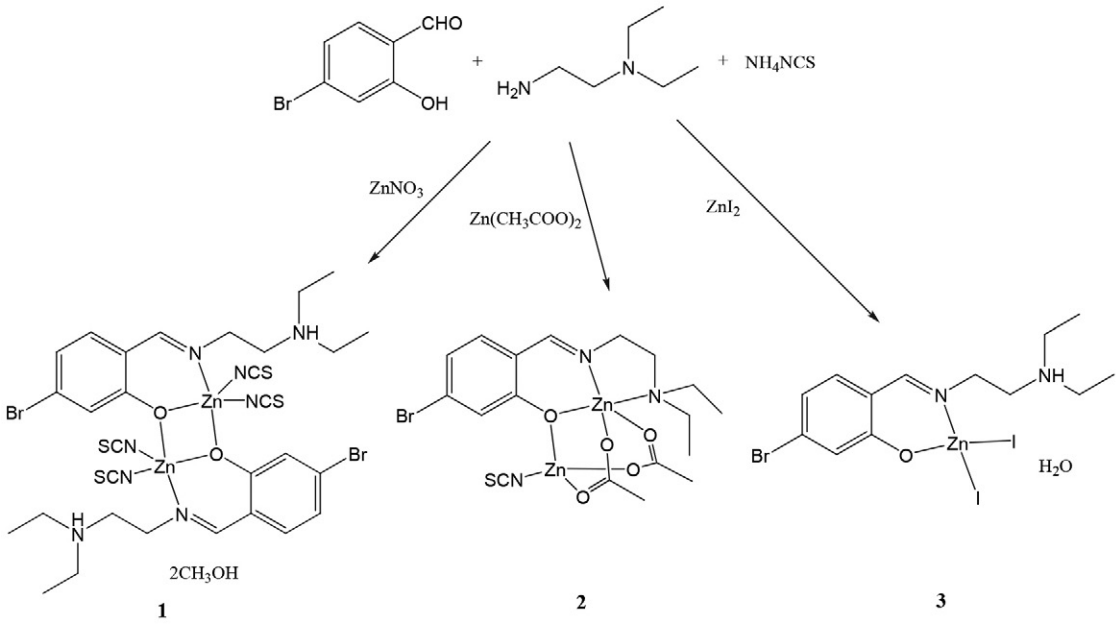

Scheme 1. The synthesis of the complexes

DMF and DMSO, and stable in air at room temperature. Elemental analyses of the complexes are in accordance with the molecular structures proposed by the X-ray analysis. The molar conductivity values in methanol in 20–35 Ω^{-1} cm^2 mol^{-1} range indicated that they are non-electrolytes.[9]

3. 2. Structure Description of Complex 1

The molecular structure of complex **1** is shown in Figure 1. The complex bears crystallographic inversion center symmetry. The inversion center is located at the midpoint of the two Zn atoms, which are bridged by two phenolate O atoms, and has a separation of 3.273(1) Å. Besides, there are two methanol molecules which are connected to the dinuclear zinc complex molecule *via* N2–H2A···O2 hydrogen bonds. Each Zn atom is coordinated in a trigonal bipyramidal geometry, as evidenced by the τ value of 0.73.[10] The basal plane is defined by the phenolate oxygen (O1) and two thiocyanate nitrogen (N3 and N4), and the two axial positions are occupied by the imino nitrogen (N1) and the symmetry related phenolate oxygen (O1A). The Zn-O/N bonds are comparable to those observed in similar zinc complexes with Schiff base ligands.[11] The bond angles in the basal plane vary from 116.1(3) to 123.9(3)°, which are close to the ideal value of 120°. The axial bond N1-Zn1-O1A form an angle of 167.5(2)°, which deviates larger from the ideal value of 180°. The Schiff bases act as bidentate ligands and adopt zwitterionic form, with the amino nitrogen protonated. The four thiocyanate ligands coordinate to the Zn atoms with terminal coordination mode.

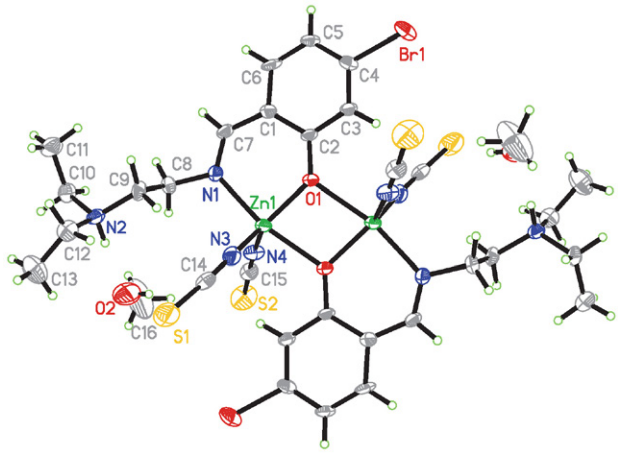

Figure 1. A perspective view of complex **1** with the atom labeling scheme. Thermal ellipsoids are drawn at the 30% probability level.

3. 3. Structure Description of Complex 2

The molecular structure of complex **2** is shown in Figure 2. The two Zn atoms are bridged by one phenolate O atom, and two acetate ligands, with a distance of 3.131(1) Å. The Zn1 atom is coordinated in a square pyramidal geometry, as evidenced by the τ value of 0.38.[10] The basal plane is defined by the phenolate oxygen (O1), imino nitrogen (N1) and amino nitrogen (N2) of the Schiff base ligand, and one acetate oxygen (O4). The apical position is occupied by the acetate oxygen (O2). The *cis* and *trans* angles in the basal plane are in the ranges of 81.5(2)–94.5(2)° and 143.5(2)–166.2(2)°, respectively. The bond angles between the apical and basal donor atoms are 94.4(2)–109.0(2)°. Thus, the square pyramidal coordina-

tion is severely distorted. The Zn1 atom deviates from the least-squares plane defined by the four basal donor atoms by 0.412(2) Å. The Zn2 atom is coordinated by the phenolate oxygen (O1) of the Schiff base ligand, the thiocyanate nitrogen (N3) and two acetate oxygens (O3 and O5), forming a tetrahedral geometry. The bond angles are in the range of 101.4(2)–119.4(2)°. The Zn–O/N bonds are comparable to those observed in similar zinc complexes with Schiff bases.[12] The Schiff base acts as a tridentate ligand. The thiocyanate ligand coordinates to the Zn atom with terminal coordination mode.

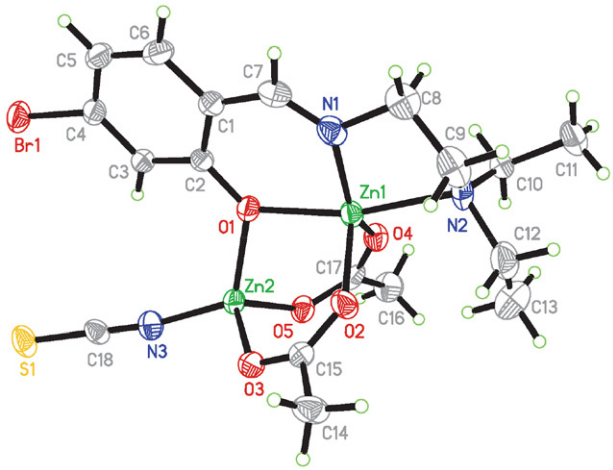

Figure 2. A perspective view of complex **2** with the atom labeling scheme. Thermal ellipsoids are drawn at the 30% probability level. Only the major component of the disordered group is shown.

3. 4. Structure Description of Complex 3

The molecular structure of complex **3** is shown in Figure 3. The water molecule is linked to the zinc complex molecule *via* O2–H2A···O1 hydrogen bond. The Zn atom is coordinated by the phenolate oxygen (O1) and imino nitrogen (N1) of the Schiff base ligand, and two I atoms (I1 and I2), forming a tetrahedral geometry. The bond angles are in the range of 94.6(2)–115.9(2)°. The Zn–O/N bonds

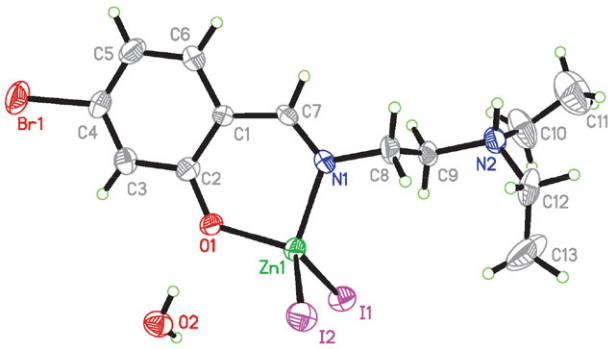

Figure 3. A perspective view of complex **3** with the atom labeling scheme. Thermal ellipsoids are drawn at the 30% probability level.

are comparable to those observed in similar zinc complexes with Schiff bases.[13] The Schiff base acts as a bidentate ligand and adopts zwitterionic form, with the amino nitrogen protonated.

3. 5. Infrared and UV-Vis Spectra

Infrared spectra provide valuable information regarding the functional group attached to the zinc center. Complex **1** contains non-coordinating methanol molecules, and complex **2** contains non-coordinating water molecule, which are clear from the well-defined bands at 3616 cm^{-1} for **1** and 3528 cm^{-1} for **2**. The weak and sharp bands at 3381 cm^{-1} for **1** and 3286 cm^{-1} for **3** can be attributed to the N–H vibrations. The intense absorptions at 2070-2095 cm^{-1} for **1** and **2** arise from the thiocyanate ligands.[14] The bands at 1270–1290 cm^{-1} may be assigned to the Ar–O stretching vibrations. The typical absorptions at 1626–1648 cm^{-1} are caused by the vibrations of the azomethine groups of the Schiff base ligands.[15] The spectrum of complex **2** displays the characteristic bands of acetate ligands at 1592 cm^{-1} for $\nu_{as}(CO_2)$ and 1394 cm^{-1} for $\nu_s(CO_2)$.[16] The bands in the region 400–600 cm^{-1} may be attributed to Zn–O and Zn–N vibrations.

The electronic spectra of these complexes were recorded in methanol solution. The bands at 245–275 nm are attributed to $\pi \rightarrow \pi^*$ transitions of the Schiff base ligands.[17] The charge-transfer bands are observed at 320–370 nm.[18]

3. 6. Antibacterial Activity

The three complexes were screened for antibacterial activities. The results are listed in Table 3. Complexes **1** and **3** have similar activities against the four bacteria. They show strong activity against *Staphylococcus aureus*, medium activity against *Escherichia coli*, and weak activities against *Klebsielle pneumonia* and *Candida albicans*. Complex **2** has strong activity against *Staphylococcus aureus*, medium activity against *Klebsielle pneumonia*, and weak activities against *Escherichia coli* and *Candida albicans*. In general, complexes **1** and **3** have stronger activities against *Staphylococcus aureus*, *Escherichia coli* and *Candida albicans* than complex **2**. While for *Klebsielle pneumonia*, complex **2** has stronger activity than the other two. All the complexes have better activities on *Staphylococcus aureus* and *Escherichia coli* than the zinc complexes with the ligands 4-methoxybenzoic acid (1-pyridin-2-ylmethylidene) hydrazide and benzoic acid (1-pyridin-2-ylethylidene)hydrazide,[19] the oxovanadium complexes derived from *N*'-(3-bromo-2-hydroxybenzylidene)picolinohydrazide and 2-chloro-*N*'-(2-hydroxy-3-methoxybenzylidene)benzohydrazide,[20] the cobalt, zinc and cadmium complexes derived from 2-hydroxy-*N*'-(pyridin-2-ylmethylene)benzohydrazide,[21] and the nickel complex with the ligand *N,N*'-bis(5-chloro-2-hydroxybenzylidene)-1,3-propanediamine.[22] Complexes **1** and **3** have better activities on

Table 3. Antibacterial activity as MIC values (μg/mL)

Compound	*Staphylococcus aureus*	*Escherichia coli*	*Klebsielle pneumoniae*	Candida albicans
1	0.50	4.0	16	32
2	2.0	8.0	4.0	64
3	0.50	2.0	8.0	32
Tetracycline	0.25	2.0	1.0	–
Fluconazol	–	–	–	2.0

Staphylococcus aureus and *Escherichia coli* than the copper complexes with the ligands 2-((2-(dimethylamino) ethylimino)methyl-4,6-difluorophenolate and 2,4-difluoro-6-((3-morpholinopropylimino)methyl)phenolate,[23] and similar activities with the copper complex derived from 2-hydroxy-5-methylbenzaldehyde oxime.[24]

Notably, complexes **1** and **3** have similar activity against *Staphylococcus aureus*, and complex **3** has similar activity against *Escherichia coli* when compared with Tetracycline. The chelation of the Schiff base ligand may reduce the polarity of the metal ion because of partial sharing of its positive charge with the donor group and possible electron delocalization over the whole chelate ring. The coordination may facilitate the ability of a complex to cross the lipid layer of the bacterial cell membrane and in this way may be affected the mechanisms of growth and development of microorganisms.[25]

4. Conclusion

Three new zinc complexes derived from the Schiff base ligand 5-bromo-2-((2-(diethylamino)ethylimino) methyl)phenol have been synthesized and characterized. Single crystal structures of the complexes indicate that two of them are dinuclear zinc complexes, and the third one is mononuclear zinc complex. The anions of the zinc salts result in the variation of the final structures. The complexes have interesting antibacterial activities against *Staphylococcus aureus*, *Escherichia coli*, *Klebsielle pneumoniae* and *Candida albicans* strains.

Supplementary Data

CCDC 2059026 (**1**), 2059027 (**2**) and 2059029 (**3**) contain the supplementary crystallographic data for this paper. These data can be obtained free of charge *via* http://www.ccdc.cam.ac.uk/conts/retrieving.html, or from the Cambridge Crystallographic Data Centre, 12 Union Road, Cambridge CB2 1EZ, UK; fax: (+44) 1223-336-033; or e-mail: deposit@ccdc.cam.ac.uk.

Acknowledgments

We acknowledge the special funds of Key Disciplines Construction from Guangdong and Zhongshan cooperating, and Guangdong Pharmaceutical University Cosmetics Talent Practice Teaching Base.

6. References

1. (a) Y. Chen, P. Li, S. J. Su, M. Chen, J. He, L. W. Liu, M. He, H. Wang, W. Xue, *RSC Advances* **2019**, *9*, 23045–23052; **DOI:**10.1039/C9RA05139B (b) A. Jarrahpour, J. Sheikh, I. El Mounsi, H. Juneja, T. Ben Hadda, *Med. Chem. Res.* **2013**, *22*, 1203–1211; **DOI:**10.1007/s00044-012-0127-6 (c) M. Das, S. Mukherjee, B. Koley, I. Choudhuri, N. Bhattacharyya, P. Roy, B. C. Samanta, M. Barai, T. Maity, *New J. Chem.* **2020**, *44*, 18347–18361; **DOI:**10.1039/D0NJ03844J (d) T. F. F. Magalhaes, C. M. da Silva, L. B. F. dos Santos, D. A. Santos, L. M. Silva, B. B. Fuchs, E. Mylonakis, C. V. B. Martins, M. A. de Resende-Stoianoff, A. de Fatima, *Lett. Appl. Microbiol.* **2020**, *71*, 490–497; **DOI:**10.1111/lam.13356 (e) N. Turan, A. Savci, K. Buldurun, Y. Alan, R. Adiguzel, *Lett. Org. Chem.* **2016**, *13*, 343–351; **DOI:**10.2174/1570178613666160422161855 (f) S. Pasa, M. Tuneg, M. Boga, *Pharm. Chem. J.* **2019**, *53*, 302–311; **DOI:**10.1007/s11094-019-01997-y (g) N. Caliskan, A. Usta, F. S. Beris, N. Baltas, E. Celik, *Lett. Org. Chem.* **2020**, *17*, 631–638. **DOI:**10.2174/1570178617666200108111211
2. (a) G. Consiglio, I. P. Oliveri, S. Cacciola, G. Maccarrone, S. Failla, S. Di Bella, *Dalton Trans.* **2020**, *49*, 5121–5133; **DOI:**10.1039/D0DT00494D (b) K. Ghosh, S. Banerjee, S. Chattopadhyay, *CrystEngComm* **2019**, *21*, 6026–6037; **DOI:**10.1039/C9CE00922A (c) D. Majumdar, S. Dey, D. Das, D. K. Singh, S. Das, K. Bankura, D. Mishra, *J. Mol. Struct.* **2019**, *1185*, 112–120; **DOI:**10.1016/j.molstruc.2019.02.092 (d) S. Roy, A. Dey, M. G. B. Drew, P. P. Ray, S. Chattopadhyay, *New J. Chem.* **2019**, *43*, 5020–5031; **DOI:**10.1039/C8NJ05616A (e) B. Agrahari, S. Layek, R. Ganguly, D. D. Pathak, *New J. Chem.* **2018**, *42*, 13754–13762; **DOI:**10.1039/C8NJ01718B (f) K. Ghosh, K. Harms, A. Bauza, A. Frontera, S. Chattopadhyay, *Dalton Trans.* **2018**, *47*, 331–347. **DOI:**10.1039/C7DT03929H
3. (a) M. Das, S. Mukherjee, B. Koley, I. Choudhuri, N. Bhattacharyya, P. Roy, B. C. Samanta, M. Barai, T. Maity, *New J. Chem.* **2020**, *44*, 18347–18361; **DOI:**10.1039/D0NJ03844J (b) S. Dasgupta, S. Karim, S. Banerjee, M. Saha, K. D. Saha, D. Das, *Dalton Trans.* **2020**, *49*, 1232–1240; **DOI:**10.1039/C9DT04636D (c) M. Azam, S. M. Wabaidur, M. J. Alam, A. Trzesowska-Kruszynska, R. Kruszynski, M. Alam, S. I. Al-Resayes, S. Dwivedi, M. R. Khan, M. S. Islam, N. T. M. Lbaqami, *Inorg. Chim. Acta* **2019**, *487*, 97–106; **DOI:**10.1016/j.

ica.2018.12.009 (d) T. Basak, M. G. B. Drew, S. Chattopadhyay, *Inorg. Chem. Commun.* **2018**, *98*, 92–98. **DOI:**10.1016/j.inoche.2018.10.004
4. E. Ispir, M. Kurtoglu, S. Toroglu, Synth. React. Inorg. Met.-Org. Nano-Met. Chem. 2006, 36, 627–631. **DOI:**10.1080/15533170600910553
5. (a) N. Turan, A. Savci, K. Buldurun, Y. Alan, R. Adiguzel, *Lett. Org. Chem.* **2016**, *13*, 343–351; **DOI:**10.2174/1570178613666160422161855 (b) S. A. Hosseini-Yazdi, A. Mirzaahmadi, A. A. Khandar, V. Eigner, M. Dusek, M. Mahdavi, S. Soltani, F. Lotfipour, J. White, *Polyhedron* **2017**, *124*, 156–165; **DOI:**10.1016/j.poly.2016.12.004 (c) M. Orojloo, P. Zolgharnein, M. Solimannejad, S. Amani, *Inorg. Chim. Acta* **2017**, *467*, 227–237; **DOI:**10.1016/j.ica.2017.08.016 (d) D. Majumdar, J. K. Biswas, M. Mondal, M. S. S. Babu, R. K. Metre, S. Das, K. Bankura, D. Mishra, *J. Mol. Struct.* **2018**, *1155*, 745–757. **DOI:**10.1016/j.molstruc.2017.11.052
6. Bruker AXS, SAINT Software Reference Manual, Madison, WI, 1998.
7. (a) G. M. Sheldrick, SADABS, Siemens Area Detector Absorption Corrected Software, University of Göttingen: Göttingen, Germany, 1996; (b) G. M. Sheldrick, *Acta Crystallogr.* **2015**, *C71*, 3–8.
8. T. Rosu, E. Pahontu, S. Pasculescu, R. Georgescu, N. Stanica, A. Curaj, A. Popescu, M. Leabu, *Eur. J. Med. Chem.* **2010**, *45*, 1627–1634. **DOI:**10.1016/j.ejmech.2009.12.015
9. W. J. Geary, *Coord. Chem. Rev.* **1971**, *7*, 81–122. **DOI:**10.1016/S0010-8545(00)80009-0
10. A. W. Addison, T. N. Rao, J. Reedijk, J. van Rijn, G. C. Verschoor, *J. Chem. Soc. Dalton Trans.* **1984**, *7*, 1349–1356. **DOI:**10.1039/DT9840001349
11. (a) A. A. Hoser, W. Schilf, A. S. Chelmieniecka, B. Kolodziej, B. Kamienski, E. Grech, K. Wozniak, *Polyhedron* **2012**, *31*, 241–248; **DOI:**10.1016/j.poly.2011.09.020 (b) H. Adams, L. R. Cummings, D. E. Fenton, P. E. McHugh, *Inorg. Chem. Commun.* **2003**, *6*, 19–22. **DOI:**10.1016/S1387-7003(02)00676-7
12. (a) P. Maiti, A. Khan, T. Chattopadhyay, S. Das, K. Manna, D. Bose, S. Dey, E. Zangrando, D. Das, *J. Coord. Chem.* **2011**, *64*, 3817–3831; **DOI:**10.1080/00958972.2011.631534 (b) J. Reglinski, S. Morris, D. E. Stevenson, *Polyhedron* **2002**, *21*, 2175–2182. **DOI:**10.1016/S0277-5387(02)01172-5
13. C. Arici, M. Aksu, *Anal. Sci.* **2002**, *18*, 727–728. **DOI:**10.2116/analsci.18.727
14. S. Basak, S. Sen, S. Banerjee, S. Mitra, G. Rosair, M. T. G. Rodriguez, *Polyhedron* **2007**, *26*, 5104–5112. **DOI:**10.1016/j.poly.2007.07.025
15. A. Jayamani, M. Sethupathi, S. O. Ojwach, N. Sengottuvelan, *Inorg. Chem. Commun.* **2017**, *84*, 144–149. **DOI:**10.1016/j.inoche.2017.08.013
16. B.-H. Ye, X.-Y. Li, I. D. Williams, X.-M. Chen, *Inorg. Chem.* **2002**, *41*, 6426–6431. **DOI:**10.1021/ic025806+
17. L. Pogany, J. Moncol, M. Gal, I. Salitros, R. Boca, *Inorg. Chim. Acta* **2017**, *462*, 23–29. **DOI:**10.1016/j.ica.2017.03.001
18. B. Sarkar, M. G. B. Drew, M. Estrader, C. Diaz, A. Ghosh, *Polyhedron* **2008**, *27*, 2625–2633. **DOI:**10.1016/j.poly.2008.05.004
19. Y.-L. Sang, X.-S. Lin, W.-D. Sun, *Acta Chim. Slov.* **2020**, *67*, 581–585. **DOI:**10.17344/acsi.2019.5595
20. H.-Y. Qian, *Acta Chim. Slov.* **2019**, *66*, 995–1001. **DOI:**10.4149/neo_2019_190112N36
21. L.-H. Wang, X.-Y. Qiu, S.-J. Liu, *Acta Chim. Slov.* **2019**, *66*, 675–680. **DOI:**10.17344/acsi.2019.5117
22. C.-L. Zhang, X.-Y. Qiu, S.-J. Liu, *Acta Chim. Slov.* **2019**, *66*, 484–489. **DOI:**10.17344/acsi.2019.5019
23. S.-F. Yu, X.-Y. Qiu, S.-J. Liu, *Acta Chim. Slov.* **2020**, *67*, 1301–1308. **DOI:**10.17344/acsi.2020.6321
24. Y.-L. Sang, X.-S. Liu, *Acta Chim. Slov.* **2019**, *66*, 168–172.
25. M. Tumer, D. Ekinci, F. Tumer, A. Bulut, *Spectrochim. Acta A Mol. Biomol. Spectrosc.* **2007**, *67*, 916–929. **DOI:**10.1016/j.saa.2006.09.009

Povzetek

Sintetizirali smo tri različne cinkove(II) komplekse z uporabo različnih cinkovih soli: $[Zn_2(HL)_2(NCS)_4]\cdot 2CH_3OH$ (**1**), $[Zn_2L(\mu_2\text{-}\eta^1\text{:}\eta^1\text{-}CH_3COO)_2(NCS)]$ (**2**) in $[Zn(HL)I_2]\cdot CH_3OH$ (**3**), kjer je L = 5-bromo-2-((2-(dietilamino)etilimino) metil)fenolat, HL = 5-bromo-2-((2-(dietilammonio)etilimino)metil)fenolat, ter jih okarakterizirali z IR in UV-Vis spektroskopijo kakor tudi z monokristalno rentgensko difrakcijo. Rentgenska strukturna analiza je razkrila, da imajo cinkovi atomi trigonalno bipiramidalno, kvadratno piramidalno in tetraedrično koordinacijo. Anioni v cinkovih soleh vodijo do nastanka različnih struktur. Določili smo tudi antibakterijsko aktivnost spojin na *Staphylococcus aureus*, *Escherichia coli*, *Klebsielle pneumoniae* in *Candida albicans*.

DOI: 10.17344/acsi.2021.6721 *Acta Chim. Slov.* **2021,** *68,* 700–708

Scientific paper

Synthesis, Characterization and Crystal Structures of Zinc(II) and Cobalt(III) Complexes Derived from Tridentate NNO- and NON- Schiff Bases with Antibacterial Activities

Heng-Yu Qian

Key Laboratory of Surface & Interface Science of Henan, School of Material & Chemical Engineering, Zhengzhou University of Light Industry, Zhengzhou, 450002 P.R. China

** Corresponding author: E-mail: hengyu_qian@126.com*

Received: 02-02-2021

Abstract

Two new polynuclear zinc complexes $[Zn_2Br_2(L^1)_2]$ (**1**) and $[Zn(\mu_{1,5}\text{-dca})L^2]_n$ (**2**), and two new mononuclear cobalt(III) complexes $[CoL^1N_3(Brsal)]$ (**3**) and $[CoL^2(HL^2)]$ (**4**), where L^1 = 5-bromo-2-(((2-dimethylamino)ethyl)imino)methyl) phenolate, L^2 = 5-bromo-2-(((2-hydroxyethyl)imino)methyl)phenolate, dca = dicyanoamide, Brsal = 5-bromo-2-formyl-phenolate, have been synthesized and characterized. The complexes were characterized by elemental analyses, IR, UV-Vis spectra, molar conductivity, and single crystal X-ray diffraction. X-ray analysis indicates that the Zn atoms in complex **1** are in distorted square pyramidal coordination, the Zn atoms in complex **2** are in distorted trigonal bipyramidal coordination, and the Co atoms in complexes **3** and **4** are in octahedral coordination. The molecules of the complexes are stacked through π···π interactions and hydrogen bonds. The complexes were assayed for antibacterial activities against three Gram-positive bacterial strains (*B. subtilis*, *S. aureus*, and *St. faecalis*) and three Gram-negative bacterial strains (*E. coli*, *P. aeruginosa*, and *E. cloacae*) by MTT method.

Keywords: Schiff base; zinc complex; cobalt complex; X-ray diffraction; antibacterial activity

1. Introduction

Schiff bases are an important class of organic compounds and a great number of Schiff base compounds have been prepared due to their facile synthesis. These compounds have received considerable attention in pharmaceutical fields because of their excellent biological activities.[1] Moreover, Schiff bases are a kind of significant ligands in coordination chemistry, which can form versatile structures with interesting biological, magnetic, catalytic and photoluminescent properties.[2] In recent years, much efforts have been paid on zinc and cobalt complexes with Schiff base ligands due to their indispensable application in biological area such as antimicrobial agents.[3] We have reported some manganese and zinc complexes with antibacterial activities.[4] In continuation of our work on the exploration of new antibacterial agents, we report herein the synthesis, characterization including single crystal X-ray structures of two new zinc(II) and two new cobalt(III) complexes, $[Zn_2Br_2(L^1)_2]$ (**1**), $[Zn(\mu_{1,5}\text{-dca})L^2]_n$ (**2**), $[CoL^1N_3(Brsal)]$ (**3**) and $[CoL^2(HL^2)]$ (**4**), where L^1 = 5-bromo-2-(((2-dimethylamino)ethyl)imino)methyl)phenolate, L^2 = 5-bromo-2-(((2-hydroxyethyl)imino)methyl)phenolate, dca = dicyanoamide, Brsal = 5-bromo-2-formylphenolate. The antibacterial activity against three Gram-positive bacterial strains (*B. subtilis*, *S. aureus*, and *St. faecalis*) and three Gram-negative bacterial strains (*E. coli*, *P. aeruginosa*, and *E. cloacae*) by MTT method was studied.

2. Experimental

2. 1. Materials and Physical Methods

4-Bromosalicylaldehyde, *N,N*-dimethylethane-1,2-diamine and 2-aminoethanol were purchased from Sigma-Aldrich. All other reagents and solvents were purchased from commercial sources and used as received. FT-IR spectra were recorded as KBr pellets on Bruker Tensor-27. Elemental (C, H, and N) analyses were performed on a Perkin-Elmer 2400 II analyzer. Electronic

spectra were obtained with Lambda 35 spectrophotometer. Single crystal X-ray diffraction was carried out with a Bruker Apex II CCD diffractometer. Molar conductivity of the complexes in methanol was measured with a DDS-11A molar conductivity meter.

Caution! Azide complexes of metal ions are potentially explosive. Only a small amount of material should be prepared, and they should be handled with caution.

2. 2. Synthesis of Complex 1

4-Bromosalicylaldehyde (0.20 g, 1.0 mmol) and *N,N*-dimethylethane-1,2-diamine (0.088 g, 1.0 mmol) were dissolved in methanol (30 mL), to the mixture was added zinc bromide (0.23 g, 1.0 mmol). A colorless solution was formed immediately. After 20 min stirring, the solution was filtered and the filtrate was kept for slow evaporation. The diffraction quality colorless single crystals that deposited over a period of a few days were collected by filtration and washed with methanol. The yield was 0.25 g (60%). Anal. Calcd. for $C_{22}H_{28}Br_4N_4O_2Zn_2$ (%): C, 31.80; H, 3.40; N, 6.74. Found (%): C, 31.95; H, 3.51; N, 6.68. IR data (KBr, cm^{-1}): 1647, 1585, 1523, 1512, 1478, 1427, 1388, 1323, 1289, 1178, 1131, 1081, 1062, 951, 920, 863, 850, 823, 811, 778, 726, 692, 667, 612, 565, 518, 490, 461. UV-Vis data in methanol [λ_{max} (nm), ε ($L{\cdot}mol^{-1}{\cdot}cm^{-1}$)]: 225, 7250; 270, 6350; 330, 2610.

2. 3. Synthesis of Complex 2

4-Bromosalicylaldehyde (0.20 g, 1.0 mmol) and 2-aminoethanol (0.061 g, 1.0 mmol) were dissolved in methanol (30 mL), to the mixture was added zinc nitrate hexahydrate (0.30 g, 1.0 mmol) and sodium dicyanoamide (0.089 g, 1.0 mmol). A colorless solution was formed immediately. After 20 min stirring, the solution was filtered and the filtrate was kept for slow evaporation. The diffraction quality colorless single crystals that deposited over a period of a few days were collected by filtration and washed with methanol. The yield was 0.12 g (32%). Anal. Calcd. for $C_{11}H_9BrN_4O_2Zn$ (%): C, 35.28; H, 2.42; N, 14.96. Found (%): C, 35.09; H, 2.53; N, 15.11. IR data (KBr, cm^{-1}): 3635, 2341, 2275, 2195, 1643, 1584, 1529, 1466, 1428, 1402, 1377, 1343, 1292, 1250, 1195, 1131, 1067, 941, 906, 851, 779, 673, 610, 528, 504, 457. UV-Vis data in methanol [λ_{max} (nm), ε ($L{\cdot}mol^{-1}{\cdot}cm^{-1}$)]: 245, 6830; 275, 4260; 360, 1572.

2. 4. Synthesis of Complex 3

4-Bromosalicylaldehyde (0.20 g, 1.0 mmol) and *N,N*-dimethylethane-1,2-diamine (0.088 g, 1.0 mmol) were dissolved in methanol (30 mL), to the mixture was added cobalt chloride hexahydrate (0.24 g, 1.0 mmol), sodium azide (0.065 g, 1.0 mmol) and additional 4-bromosalicylaldehyde (0.20 g, 1.0 mmol). A brown solution was formed immediately. After 20 min stirring, the solution was filtered and the filtrate was kept for slow evaporation. The diffraction quality colorless single crystals that deposited over a period of a few days were collected by filtration and washed with methanol. The yield was 0.23 g (40%). Anal. Calcd. for $C_{18}H_{18}Br_2CoN_5O_3$ (%): C, 37.85; H, 3.18; N, 12.26. Found (%): C, 37.72; H, 3.25; N, 12.33. IR data (KBr, cm^{-1}): 2027, 1647, 1618, 1589, 1521, 1497, 1454, 1430, 1387, 1295, 1185, 1133, 1059, 1022, 995, 922, 854, 778, 729, 692, 613, 570, 515, 493, 466. UV-Vis data in methanol [λ_{max} (nm), ε ($L{\cdot}mol^{-1}{\cdot}cm^{-1}$)]: 225, 7030; 260, 9150; 325, 3120.

2. 5. Synthesis of Complex 4

4-Bromosalicylaldehyde (0.20 g, 1.0 mmol) and 2-aminoethanol (0.061 g, 1.0 mmol) were dissolved in methanol (30 mL), to the mixture was added cobalt nitrate hexahydrate (0.29 g, 1.0 mmol). A brown solution was formed immediately. After 20 min stirring, the solution was filtered and the filtrate was kept for slow evaporation. The diffraction quality colorless single crystals that deposited over a period of a few days were collected by filtration and washed with methanol. The yield was 0.15 g (28%). Anal. Calcd. for $C_{18}H_{17}Br_2CoN_2O_4$ (%): C, 39.74; H, 3.15; N, 5.15. Found (%): C, 39.83; H, 3.10; N, 5.24. IR data (KBr, cm^{-1}): 3427, 1647, 1586, 1523, 1464, 1425, 1383, 1328, 1289, 1246, 1200, 1131, 1103, 1058, 938, 907, 847, 783, 730, 675, 657, 606, 576, 550, 499, 470, 443. UV-Vis data in methanol [λ_{max} (nm), ε ($L{\cdot}mol^{-1}{\cdot}cm^{-1}$)]: 245, 8160; 275, 3920; 360, 2335.

2. 6. X-Ray Structure Determination

Intensity data of the complexes were collected at 298(2) K on a Bruker Apex II CCD diffractometer using graphite-monochromated MoK_a radiation (λ = 0.71073 Å). For data processing and absorption correction the packages SAINT and SADABS were used.[5] Structures of the complexes were solved by direct and Fourier methods and refined by full-matrix least-squares based on F^2 using SHELXL.[6] The non-hydrogen atoms were refined anisotropically. The H atoms of the hydroxyl groups of complexes **2** and **4** were located from difference Fourier maps and refined with O–H distances restrained to 0.85(1) Å. The remaining hydrogen atoms have been placed at geometrical positions with fixed thermal parameters. Crystallographic data of the complexes are summarized in Tables 1a and 1b. Selected bond lengths and angles are listed in Table 2.

2. 7. Antibacterial Activity

Antibacterial activity of the complexes was tested against *B. subtilis*, *S. aureus*, *S. faecalis*, *P. aeruginosa*, *E. coli*, and *E. cloacae* using MTT medium. The minimum inhibitory concentrations (MICs) of the compounds were determined by a colorimetric method using MTT dye.[7] A stock solution of the compounds (50 μg mL^{-1}) in DMSO was prepared and quantities of the compounds were incorporated in specified quantity of sterilized liquid medium.

Table 1a. Crystallographic data and refinement details for the zinc complexes

	1	2
Molecular formula	$C_{22}H_{28}Br_4N_4O_2Zn_2$	$C_{11}H_9BrN_4O_2Zn$
Molecular weight	830.86	374.50
Crystal color, habit	Colorless, block	Colorless, block
Crystal size, mm	0.26 × 0.23 × 0.23	0.27 × 0.26 × 0.23
Crystal system	Triclinic	Monoclinic
Space group	*P*-1	$P2_1/c$
Unit cell dimensions:		
a, Å	7.3961(12)	7.5248(13)
b, Å	11.4754(13)	15.8344(10)
c, Å	17.3227(15)	11.5157(12)
α, °	82.449(1)	90
β, °	82.053(1)	97.377(1)
γ, °	88.895(1)	90
V, Å^3	1443.5(3)	1360.7(3)
Z	2	4
ρ_{calcd}, g cm^{-3}	1.912	1.828
μ, mm^{-1}	7.223	4.743
θ Range collected, °	1.20–25.50	2.20–25.49
T_{min} and T_{max}	0.2553 and 0.2874	0.3608 and 0.4084
Reflections collected/ unique	6833/5179	7112/2519
Observed reflections ($I \geq 2s(I)$)	3685	2032
Data/restraints/ parameters	5179/0/311	2519/1/176
GOOF on F^2	1.018	1.205
R_1, wR_2 ($I \geq 2s(I)$)	0.0417, 0.0888	0.0613, 0.1727
R_1, wR_2 (all data)	0.0722, 0.1013	0.0741, 0.1788

Table 1b. Crystallographic data and refinement details for the cobalt complexes

	3	4
Molecular formula	$C_{18}H_{18}Br_2CoN_5O_3$	$C_{18}H_{17}Br_2CoN_2O_4$
Molecular weight	571.12	544.09
Crystal color, habit	Brown, block	Brown, block
Crystal size, mm	0.17 × 0.15 × 0.15	0.15 × 0.08 × 0.08
Crystal system	Monoclinic	Monoclinic
Space group	$P2_1/n$	$P2_1/c$
Unit cell dimensions:		
a, Å	6.5842(17)	16.2848(13)
b, Å	13.6064(13)	25.8585(13)
c, Å	23.301(2)	21.4256(13)
α, °	90	90
β, °	92.048(2)	94.958(2)
γ, °	90	90
V, Å^3	2086.1(6)	8988.6(10)
Z	4	16
ρ_{calcd}, g cm^{-3}	1.818	1.608
μ, mm^{-1}	4.683	4.343
θ Range collected, °	1.73–25.50	1.84–25.50
T_{min} and T_{max}	0.5032 and 0.5401	0.5620 and 0.7226
Reflections collected/ unique	10831/3868	47610/16621
Observed reflections ($I \geq 2s(I)$)	2344	7217
Data/restraints/ parameters	3868/0/264	16621/11/973
GOOF on F^2	1.050	0.979
R_1, wR_2 ($I \geq 2s(I)$)	0.0540, 0.1252	0.0795, 0.2014
R_1, wR_2 (all data)	0.1069, 0.1481	0.1878, 0.2636

A specified quantity of the medium containing the compounds was poured into micro-titration plates. Suspension of the microorganism was prepared to contain approximately 10^5 cfu mL^{-1} and applied to micro-titration plates with serially diluted compounds in DMSO to be tested, and incubated at 37°C for 24 h for bacteria. After the MICs were visually determined on each micro-titration plate, 50 μL of phosphate buffered saline (PBS 0.01 mol L^{-1}, pH 7.4: $Na_2HPO_4 \cdot 12H_2O$ 2.9 g, KH_2PO_4 0.2 g, NaCl 8.0 g, KCl 0.2 g, distilled water 1000 mL) containing 2 mg mL^{-1} of MTT was added to each well. Incubation was continued at room temperature for 4–5 h. The content of each well was removed, and 100 μL of isopropanol containing 5% 1 mol L^{-1} HCl was added to extract the dye. After 12 h of incubation at room temperature, the optical density (OD) was measured with a microplate reader at 570 nm.

3. Results and Discussion

3. 1. Chemistry

Reaction of the newly formed Schiff base HL[1] with zinc bromide affords the dinuclear zinc complex **1**, with cobalt chloride and sodium azide affords the mononuclear cobalt complex **3**. Similarly, reaction of the newly formed Schiff base HL[2] with zinc nitrate and sodium dicyanoamide affords the polynuclear zinc complex **2**, with cobalt nitrate affords the mononuclear cobalt complex **4**. The poor conductivity of the complexes (20–45 Ω^{-1} cm^2 mol^{-1}) indicated that the ligands are coordinated to the metal centers and are not dissociated in solution.[8]

3. 2. Infrared and Electronic Spectra

In the infrared spectra, the weak absorptions at 3635 cm^{-1} for **2** and 3427 cm^{-1} for **4** are assigned to the hydroxyl groups of the Schiff base ligands. The characteristic imine stretching of the complexes is observed at 1643–1647 cm^{-1} as strong signal.[9] In the spectrum of **2**, appearance of intense bands at 2341, 2275 and 2195 cm^{-1} indicates the presence of dicyanoamide ligand.[10] In the spectrum of **3**, appearance of intense band at 2027 cm^{-1} indicates the presence of azide ligand.[11] The Schiff base ligands coordination is substantiated by the phenolic C–O stretching bands at 1170–1200 cm^{-1} in the four complexes.[12] Coordination of the Schiff bases is further confirmed by the appearance of weak bands in the low wave numbers 400–600 cm^{-1}, corresponding to ν(M–N) and ν(M–O).[13]

Table 2. Selected bond distances (Å) and angles (°) for the complexes

1			
Zn1–Br3	2.3869(10)	Zn2–Br4	2.3923(9)
Zn1–O1	1.995(3)	Zn1–O2	2.121(4)
Zn1–N3	2.089(5)	Zn1–N4	2.198(5)
Zn2–N1	2.089(4)	Zn2–N2	2.189(5)
Zn2–O1	2.106(3)	Zn2–O2	2.016(3)
O1–Zn1–N3	135.37(18)	O1–Zn1–O2	75.09(13)
N3–Zn1–O2	82.28(17)	O1–Zn1–N4	100.58(17)
N3–Zn1–N4	80.5(2)	O2–Zn1–N4	149.77(19)
O1–Zn1–Br3	111.83(12)	N3–Zn1–Br3	111.38(14)
O2–Zn1–Br3	107.00(11)	N4–Zn1–Br3	102.37(15)
O2–Zn2–N1	132.01(16)	O2–Zn2–O1	75.01(13)
N1–Zn2–O1	82.47(15)	O2–Zn2–N2	99.64(17)
N1–Zn2–N2	81.05(17)	O1–Zn2–N2	151.69(17)
O2–Zn2–Br4	116.62(11)	N1–Zn2–Br4	110.05(12)
O1–Zn2–Br4	105.80(11)	N2–Zn2–Br4	101.41(14)
2			
Zn1–O1	2.000(6)	Zn1–O2	2.231(7)
Zn1–N1	2.007(6)	Zn1–N2	1.988(8)
Zn1–N4A	2.017(7)		
N2–Zn1–O1	98.7(3)	N2–Zn1–N1	128.6(3)
O1–Zn1–N1	91.1(2)	N2–Zn1–N4A	108.2(3)
O1–Zn1–N4A	97.6(3)	N1–Zn1–N4A	120.3(3)
N2–Zn1–O2	86.7(3)	O1–Zn1–O2	167.5(2)
N1–Zn1–O2	76.8(3)	N4A–Zn1–O2	91.3(3)
3			
Co1–O1	1.890(4)	Co1–O2	1.926(4)
Co1–O3	1.943(5)	Co1–N1	1.871(5)
Co1–N2	2.036(5)	Co1–N3	1.973(5)
N1–Co1–O1	95.0(2)	N1–Co1–O2	86.99(19)
O1–Co1–O2	87.43(18)	N1–Co1–O3	178.2(2)
O1–Co1–O3	86.52(19)	O2–Co1–O3	94.05(18)
N1–Co1–N3	89.6(2)	O1–Co1–N3	90.0(2)
O2–Co1–N3	175.5(2)	O3–Co1–N3	89.5(2)
N1–Co1–N2	86.3(2)	O1–Co1–N2	178.2(2)
O2–Co1–N2	91.4(2)	O3–Co1–N2	92.3(2)
N3–Co1–N2	91.3(2)		

4			
Co1–O1	1.880(7)	Co1–O2	1.912(7)
Co1–O3	1.893(7)	Co1–O4	1.908(7)
Co1–N1	1.888(9)	Co1–N2	1.910(8)
Co2–O5	1.892(7)	Co2–O6	1.912(7)
Co2–O7	1.891(6)	Co2–O8	1.926(6)
Co2–N3	1.909(8)	Co2–N4	1.872(8)
Co3–O9	1.881(7)	Co3–O10	1.912(7)
Co3–O11	1.861(7)	Co3–O12	1.941(6)
Co3–N5	1.920(8)	Co3–N6	1.909(7)
Co4–O13	1.884(7)	Co4–O14	1.912(8)
Co4–O15	1.882(8)	Co4–O16	1.910(6)
Co4–N7	1.904(9)	Co4–N8	1.883(9)
O1–Co1–N1	95.0(3)	O1–Co1–O3	89.5(3)
N1–Co1–O3	89.7(3)	O1–Co1–O4	91.3(3)
N1–Co1–O4	89.1(4)	O3–Co1–O4	178.6(3)
O1–Co1–N2	89.2(3)	N1–Co1–N2	174.1(4)
O3–Co1–N2	94.5(3)	O4–Co1–N2	86.8(3)
O1–Co1–O2	178.7(3)	N1–Co1–O2	84.8(4)
O3–Co1–O2	91.8(3)	O4–Co1–O2	87.4(3)
N2–Co1–O2	90.9(3)	N4–Co2–O7	94.4(3)
N4–Co2–O5	91.0(3)	O7–Co2–O5	89.5(3)
N4–Co2–N3	174.6(4)	O7–Co2–N3	87.1(3)
O5–Co2–N3	94.2(3)	N4–Co2–O6	88.7(3)
O7–Co2–O6	91.9(3)	O5–Co2–O6	178.6(3)
N3–Co2–O6	86.0(3)	N4–Co2–O8	85.7(3)
O7–Co2–O8	176.8(3)	O5–Co2–O8	87.3(3)
N3–Co2–O8	93.0(3)	O6–Co2–O8	91.2(3)
O11–Co3–O9	90.7(3)	O11–Co3–N6	95.2(3)
O9–Co3–N6	87.4(3)	O11–Co3–O10	90.5(3)
O9–Co3–O10	178.7(3)	N6–Co3–O10	92.5(3)
O11–Co3–N5	89.2(3)	O9–Co3–N5	95.1(3)
N6–Co3–N5	174.9(3)	O10–Co3–N5	84.9(3)
O11–Co3–O12	178.6(3)	O9–Co3–O12	89.7(3)
N6–Co3–O12	86.2(3)	O10–Co3–O12	89.0(3)
N5–Co3–O12	89.4(3)	O15–Co4–N8	94.5(4)
O15–Co4–O13	89.9(4)	N8–Co4–O13	90.0(4)
O15–Co4–N7	87.8(4)	N8–Co4–N7	174.7(4)
O13–Co4–N7	94.7(4)	O15–Co4–O16	178.2(4)
N8–Co4–O16	86.0(4)	O13–Co4–O16	88.3(3)
N7–Co4–O16	91.8(3)	O15–Co4–O14	90.4(4)
N8–Co4–O14	90.1(4)	O13–Co4–O14	179.7(3)
N7–Co4–O14	85.2(4)	O16–Co4–O14	91.4(3)

Symmetry code for A: –1 + *x*, *y*, *z*.

The electronic spectra of the complexes exhibit typical bands centered at 320–360 nm which can be assigned to ligand to metal charge transfer.[14] The bands at 220–250 nm and 260–280 nm are attributed to the π–π^* and n–π^* transitions.[15]

3. 3. Structure Description of Complex 1

Molecular structure of complex **1** is shown in Fig. 1. The two [ZnL^1] units are linked by two phenolate O atoms. The Zn atoms are coordinated in distorted square pyramidal geometry as evidenced by the τ values of 0.24 for Zn1 and 0.33 for Zn2.[16] The basal planes of the square pyramidal coordination are defined by the imino N, amino N and phenolate O atoms of the Schiff base ligands. The apical positions of the square pyramidal coordination are occupied by the Br ligands. The Zn1 and Zn2 atoms deviate from the corresponding basal planes by 0.645(2) and 0.659(2) Å, respectively. The square pyramidal coordination is distorted from ideal model, as evidenced by the bond angles. The *cis* and *trans* angles in the basal plane are in the ranges of 75.09(13)–100.58(17)° and 135.37(18)–

149.77(19)° for Zn1, and 75.01(13)–99.64(17)° and 132.01(16)–151.69(17)° for Zn2, respectively. The bond angles among the apical and basal donor atoms are in the ranges of 102.37(15)–111.83(12)° for Zn1 and 101.41(14)–116.62(11)° for Zn2. The distortion is mainly caused by the strain created by the four- and five-membered chelate rings Zn1-O1-Zn2-O2, Zn1-N3-C19-C20-N4 and Zn2-N1-C8-C9-N2. The Zn-O, Zn-N and Zn-Br bond lengths are comparable to those observed in bromide coordinated Schiff base zinc complexes.[17]

As shown in Fig. 2, the complex molecules are linked through C–H···Br hydrogen bonds (Table 3), to form a three dimensional network. In addition, there are π···π interactions among the molecules (Cg1···Cg1[a] 4.423(4) Å, Cg2···Cg2[b] 4.446(4) Å, symmetry codes: a) 1 – *x*, – *y*, 1 – *z*; b) 2 – *x*, 1 – *y*, – *z*; Cg1 and Cg2 are the centroids of C1–C2–C3–C4–C5–C6 and C12–C13–C14–C15–C16–C17, respectively).

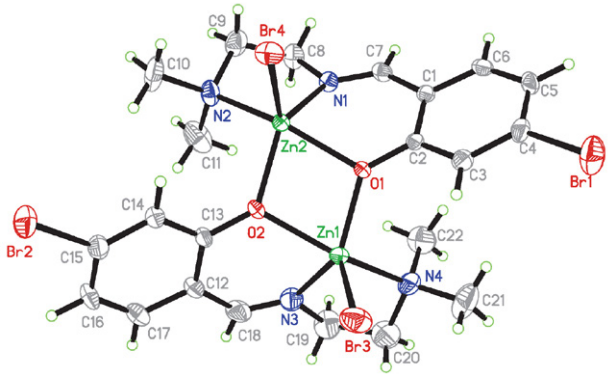

Fig. 1. Molecular structure of complex **1**.

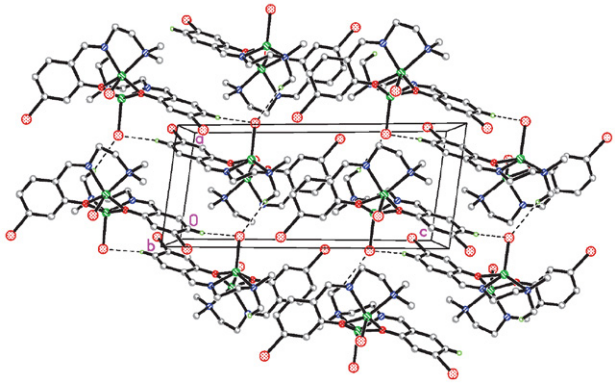

Fig. 2. Molecular packing structure of complex **1**.

3. 4. Structure Description of Complex 2

Molecular structure of complex **2** is shown in Fig. 3. The [ZnL^2] units are linked by $\mu_{1,5}$-dca ligands, to form zigzag chain structure. The Zn atom is coordinated in distorted trigonal bipyramidal geometry as evidenced by the τ value of 0.65.[16] The basal plane of the trigonal bipyramidal coordination is defined by the imino N atom of the Schiff base ligand and two terminal N atoms from two dca ligands. The axial positions of the trigonal bipyramidal coordination are occupied by the phenolate O and hydroxyl O atoms of the Schiff base ligand. The Zn atom deviates from the basal plane by 0.195(2) Å. The trigonal bipyramidal geometry is distorted from ideal model, as evidenced by the bond angles. The angles in the basal plane are in the range of 108.2(3)–128.6(3)°. The bond angles among the axial and basal donor atoms are in the range of 76.8(3)–98.7(3)°. And, the two axial donor atoms form an angle of 167.5(2)° with the Zn atom. The distortion is mainly caused by the strain created by the five-membered chelate ring Zn1-N1-C8-C9-O2. The Zn-O and Zn-N bond lengths are comparable to those observed in dca coordinated Schiff base zinc complexes.[18]

As shown in Fig. 4, the [CuL^2] units are bridged by $\mu_{1,5}$-dca ligands, to form zigzag chain along the *a* axis. The chains are further linked through O–H···O hydrogen bonds (Table 3) along the *c* axis to form two dimensional sheets parallel to the *ac* plane. In addition, there are π···π interactions among the molecules (Cg3···Cg3[c] 4.256(5) Å, Cg3···Cg4[c] 3.900(5) Å, Cg3···Cg4[d] 4.245(5) Å, Cg4···Cg4[c] 4.972(5) Å, Cg4···Cg4[d] 4.096(5) Å, symmetry codes: c) 1 – *x*, – *y*, – *z*; d) 2 – *x*, – *y*, – *z*; Cg3 and Cg4 are the centroids of Zn1–O1–C2–C1–C7–N1 and C1–C2–C3–C4–C5–C6, respectively).

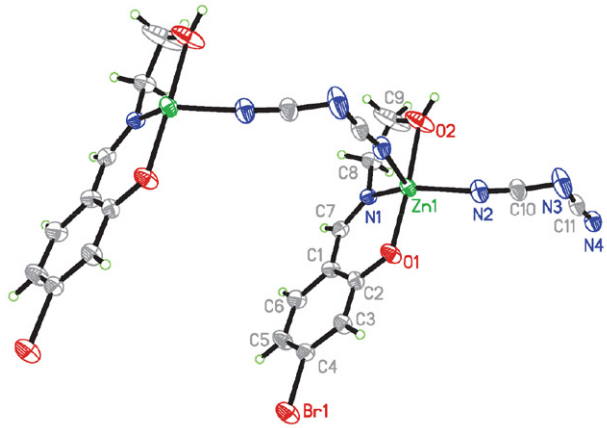

Fig. 3. Molecular structure of complex **2**.

3. 5. Structure Description of Complex 3

Molecular structure of complex **3** is shown in Fig. 5. The Co atom is coordinated by one Schiff base ligand, one 5-bromo-2-formylphenolate ligand and one azide ligand, forming octahedral coordination. The equatorial plane of the octahedral coordination is defined by the phenolate O, imino N and amino N atoms of the Schiff base ligand, and the carbonyl O atom of the 5-bromo-2-formylphenolate ligand. The axial positions of the octahedral coordination are occupied by the phenolate O atom of the 5-bro-

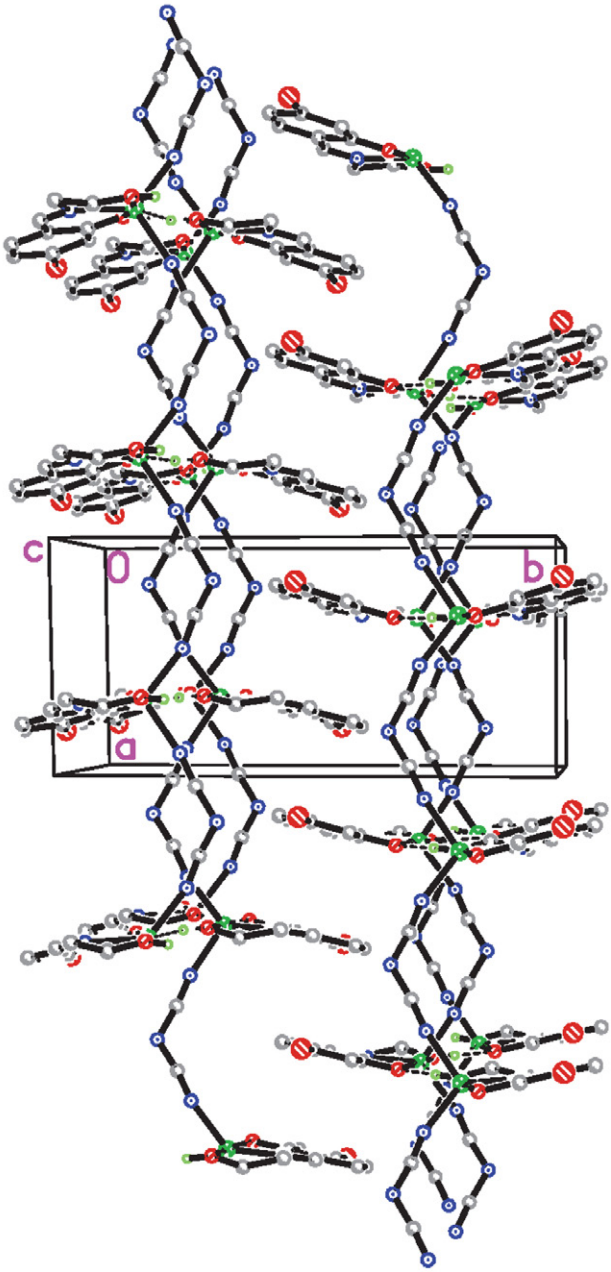

Fig. 4. Molecular packing structure of complex **2**.

mo-2-formylphenolate ligand, and the azide N atom. The Co atom deviates from the equatorial plane by 0.003(2) Å. The octahedral geometry is distorted from ideal model, as evidenced by the bond angles. The *cis* and *trans* angles in the equatorial plane are in the ranges of 86.3(2)–95.0(2) ° and 178.2(2)°, respectively. The bond angles among the axial and equatorial donor atoms are in the range of 87.0(2)–94.0(2)°. And, the two axial donor atoms form an angle of 175.5(2)° with the Co atom. The distortion is mainly caused by the strain created by the five-membered chelate ring Co1-N1-C8-C9-N2. The Co-O and Co-N bond lengths are comparable to those observed in azide coordinated Schiff base cobalt complexes.[19]

As shown in Fig. 6, the molecules are linked through C–H···N hydrogen bonds (Table 3), to form one dimensional chains along the *b* axis. The chains are further linked by weak Br···N interactions along the *c* axis to form a two dimensional sheets parallel to the *bc* plane.

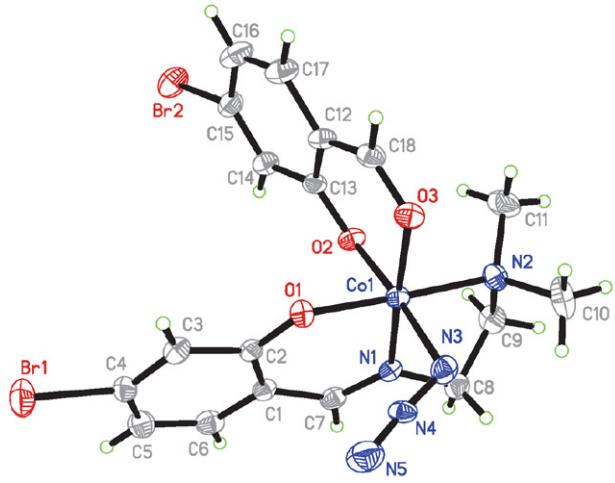

Fig. 5. Molecular structure of complex **3**.

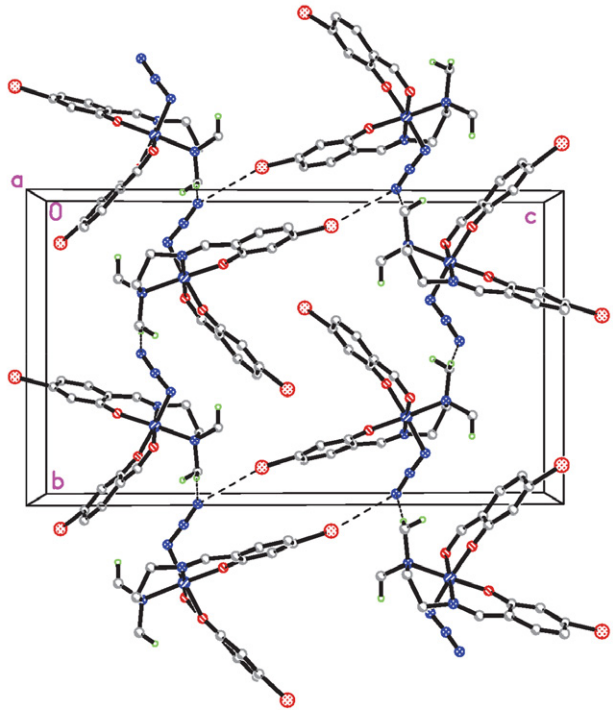

Fig. 6. Molecular packing structure of complex **3**.

3. 6. Structure Description of Complex 4

Molecular structure of complex **4** is shown in Fig. 7. The asymmetric unit of the compound contains four [$CoL^2(HL^2)$] units, which are linked together by O–H···O hydrogen bonds (Table 3). The Co atom in each unit is coordinated by one monoanionic and one dianionic Schiff

base ligands, forming octahedral coordination. The equatorial plane of the octahedral coordination is defined by the phenolate O, imino N and the deprotonated hydroxyl O atom of the the dianionic Schiff base ligand, and the imino N atom of the monoanionic Schiff base ligand. The axial positions of the octahedral coordination are occupied by the phenolate O and hydroxyl O atoms of the monoanionic Schiff base ligand. The Co atoms deviate from the corresponding equatorial planes by 0.040(2) Å for Co1, 0.017(2) Å for Co2, 0.024(2) Å for Co3 and Co4. The octahedral geometry is distorted from ideal model, as evidenced by the bond angles. The *cis* and *trans* angles in the equatorial planes are in the ranges of 86.8(3)–94.5(3)° and 174.1(4)–178.6(3)° for Co1, 85.7(3)–94.4(3)° and 174.6(4)–176.8(3)° for Co2, 86.2(3)–95.2(3)° and 174.9(3)–178.6(3)° for Co3, and 86.0(4)–94.5(4)° and 174.7(4)–178.2(4)° for Co4, respectively. The bond angles among the axial and equatorial donor atoms are in the ranges of 84.8(4)–95.0(3)° for Co1, 86.0(3)–94.2(3)° for Co2, 84.9(3)–95.1(3)° for Co3, and 85.2(4)–94.7(4)° for Co4. And, the two axial donor atoms form angles of 178.7(3)° with Co1 and Co3 atoms, 178.6(3)° with Co2 atom, and 179.7(3)° with Co4 atom. The distortion is mainly caused by the strain created by the five-membered chelate rings Co1-N1-C8-C9-O2, Co1-N2-C17-C18-O4, Co2-N3-C26-C27-O6, Co2-N4-C35-C36-O8, Co3-N5-C44-C45-O10, Co3-N6-C53-C54-O12, Co4-N6-C65-C64-O16, and Co4-N7-C62-C63-O14. The Co-O and Co-N bond lengths are comparable to those observed in Schiff base cobalt complexes.[20]

As shown in Fig. 8, the molecules are linked through O–H···O hydrogen bonds (Table 3), to form one dimensional chains along the *a* axis. The chains are further linked by C–H···Br hydrogen bonds, to form two dimensional sheets parallel to the *bc* plane. In addition, there are π···π interactions among the molecules (Cg5···Cg6[e] 4.619(5) Å, Cg7···Cg5[f] 4.881(5) Å, symmetry codes: e) –1 + *x*, *y*, *z*; f) 1 + *x*, *y*, *z*; Cg5, Cg6 and Cg7 are the centroids of Co3–O11–C47–C46–C52–N6, Co4–O13–C56–C55–C61–N7 and C55–C56–C57–C58–C59–C60, respectively).

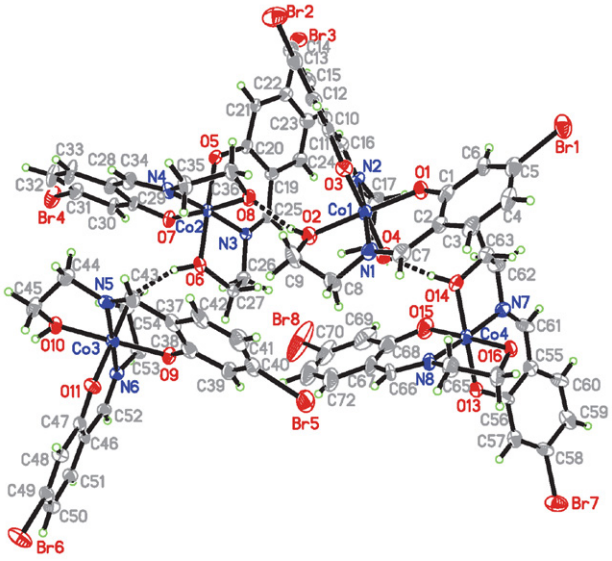

Fig. 7. Molecular structure of complex **4**.

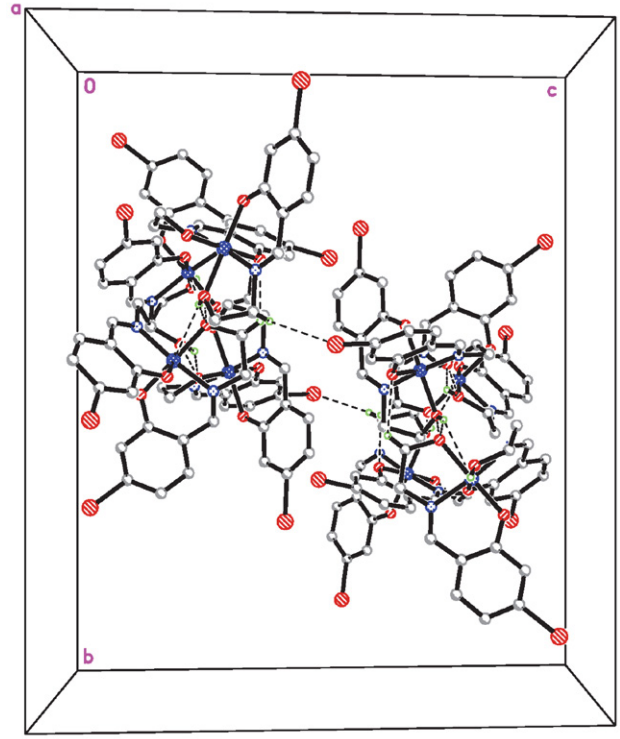

Fig. 8. Molecular packing structure of complex **4**.

Table 3. Hydrogen bond distances (Å) and bond angles (°) for the complexes

D–H···*A*	*d*(*D*–H)	*d*(H···*A*)	*d*(*D*···*A*)	Angle (*D*–H···*A*)
		1		
C16–H16···Br3^{i}	0.93	2.88	3.700(3)	148(5)
C21–H21C···Br3	0.96	2.92	3.590(3)	127(5)
C22–H22A···Br3^{ii}	0.96	2.90	3.815(3)	161(5)
		2		
O2–H2···O1^{iii}	0.85(1)	1.82(4)	2.647(9)	164(14)
		3		
C10–H10C···N3	0.96	2.41	2.801(4)	104(5)
C11–H11A···O2	0.96	2.39	2.970(4)	118(5)
C11–H11C···N5^{iv}	0.96	2.61	3.565(4)	171(5)
		4		
O10–H10···O16^{v}	0.85(1)	1.61(2)	2.445(9)	169(4)
O14–H14···O4^{vi}	0.85(1)	1.65(5)	2.45(1)	156(13)
O6–H6···O12^{vii}	0.85(1)	1.66(6)	2.436(9)	150(11)
O2–H2···O8	0.85(1)	1.69(7)	2.419(9)	143(11)
C18–H18B···O15^{vi}	0.97	2.56(7)	3.300(9)	133(11)
C54–H54A···O7^{vii}	0.97	2.56(7)	3.252(9)	129(11)
C62–H62B···Br4^{viii}	0.97	2.84(7)	3.756(9)	158(11)

Symmetry codes for i): 2 – *x*, 1 – *y*, – *z*; ii): –1 + *x*, *y*, *z*; iii): *x*, 3/2 – *y*, –1/2 + *z*; iv): 1/2 – *x*, 1/2 + *y*, 1/2 – *z*; v): –1 + *x*, *y*, *z*; vi): 1 – *x*, 1/2 + *y*, 1/2 – *z*; vii): 1 – *x*, –1/2 + *y*, 1/2 – *z*; viii): *x*, 1/2 – *y*, 1/2 + *z*.

3. 7. Antibacterial Activities

The two complexes and the free Schiff base were screened for antibacterial activities against three Gram-positive bacterial strains (*B. subtilis*, *S. aureus*, and *St. faecalis*) and three Gram-negative bacterial strains (*E. coli*, *P. aeruginosa*, and *E. cloacae*) by MTT method. The MICs of the compounds against the bacteria are presented in Table 4. Penicillin and Kanamycin were tested as reference drugs. Complex **1** show strong activities against *B. subtilis*, *S. aureus* and *St. faecalis*, moderate activity against *P. aeruginosa*, and weak activities against *E. coli* and *E. cloacae*. Complex **2** show strong activities against *B. subtilis*, *S. aureus* and *St. faecalis*, and weak activities against *P. aeruginosa*, *E. coli* and *E. cloacae*. Complexes **3** and **4** show moderate or weak activities against the bacteria except for *E. coli*. Obviously, the two zinc complexes have better activities than the two cobalt complexes. Interestingly, complexes **1** and **2** are excellent agents for *B. subtilis* and *St. faecalis*, which even comparable to the effects of Penicillin and Kanamycin.

Table 4. MICs (μg mL^{-1}) of the compounds and related materials

Tested material	Gram positive			Gram negative		
	B. subtilis	*S. aureus*	*St. faecalis*	*P. aeruginosa*	*E. coli*	*E. cloacae*
1	0.78	3.12	0.39	6.25	25	12.5
2	1.56	3.12	1.56	12.5	25	25
3	6.25	6.25	25	25	> 50	6.25
4	6.25	12.5	25	25	> 50	25
Penicillin	1.56	1.56	1.56	6.25	6.25	3.12
Kanamycin	0.39	1.56	3.12	3.12	3.12	1.56

4. Conclusion

In summary, two new polynuclear zinc(II) complexes and two new mononuclear cobalt(III) complexes with tridentate Schiff base ligands have been synthesized. Single crystal structures of the complexes were confirmed by X-ray diffraction method and described. The antibacterial assay of the complexes indicates that the zinc complexes are prospective antibacterial agents for *B. subtilis* and *St. faecalis*.

5. Supplementary Materials

X-ray crystallographic data for the complexes have been deposited with the Cambridge Crystallographic Data Centre (The Director, CCDC, 12 Union Road, Cambridge, CB2 1 EZ, UK; e-mail: deposit@ccdc.cam.ac.uk; http://www.ccdc.cam.ac.uk; fax: +44-(0)1223–336033) and are available free of charge on request, quoting the deposition numbers CCDC 2060468 for **1**, 2060469 for **2**, 2060470 for **3** and 2060472 for **4**.

Acknowledgments

This project was supported by the Henan Province Universities and Colleges Funded Scheme (21A530010).

6. References

1. (a) N. Caliskan, A. Usta, F. S. Beris, N. Baltas, E. Celik, *Lett. Org. Chem.* **2020**, *17*, 631–638; **DOI:**10.2174/1570178617666200108111211
(b) M. Durgun, C. Turkes, M. Isik, Y. Demir, A. Sakli, A. Kuru, A. Guzel, S. Beydemir, S. Akocak, S. M. Osman, Z. AlOthman, C. T. Supuran, *J. Enzym. Inhib. Med. Chem.* **2020**, *35*, 950–962; **DOI:**10.1080/14756366.2020.1746784
(c) N. Q. Haj, M. O. Mohammed, L. E. Mohammood, *ACS Omega* **2020**, *5*, 13948–13954; **DOI:**10.1021/acsomega.0c01342
(d) S. Omidi, A. Kakanejadifard, *RSC Advances* **2020**, *10*, 30186–30202; **DOI:**10.1039/D0RA05720G
(d) A. M. Bhagare, J. S. Aher, M. R. Gaware, D. D. Lokhande, A. V. Kardel, A. D. Bholay, A. C. Dhayagude, *Bioorg. Chem.* **2020**, *103*, 104129; **DOI:**10.1016/j.bioorg.2020.104129
(e) R. Cordeiro, M. Kachroo, *Bioorg. Med. Chem. Lett.* **2020**, *30*, 127655. **DOI:**10.1016/j.bmcl.2020.127655
2. (a) N. Ganji, S. Daravath, A. Rambabu, K. Venkateswarlu, D. S. Shankar, Shivaraj, *Inorg. Chem. Commun.* **2020**, *121*, 108247; **DOI:**10.1016/j.inoche.2020.108247
(b) A. Mandal, A. Sarkar, A. Adhikary, D. Samanta, D. Das, *Dalton Trans.* **2020**, *49*, 15461–15472; **DOI:**10.1039/D0DT02784G
(c) T. A. Bazhenova, L. V. Zorina, S. V. Simonov, V. S. Mironov, O. V. Maximova, L. Spillecke, C. Koo, R. Klingeler, Y. V. Manakin, A. N. Vasiliev, *Dalton Trans.* **2020**, *49*, 15287–15298; **DOI:**10.1039/D0DT03092A
(d) A. Frei, A. P. King, G. J. Lowe, A. K. Cain, F. L. Short, H. Dinh, A. G. Elliott, J. Zuegg, J. J. Wilson, M. A. T. Blaskovich, *Chem. Eur. J.* **2020**, **DOI:**10.1002/chem.202003545;
(e) S. Lahkar, R. Borah, N. Deori, S. Brahma, *Polyhedron* **2020**, *192*, 114848; **DOI:**10.1016/j.poly.2020.114848
(f) A. Neshat, F. Osanlou, M. Kakavand, P. Mastrorilli, E. Schingaro, E. Mesto, S. Todisco, *Polyhedron* **2021**, *193*, 114873. **DOI:**10.1016/j.poly.2020.114873
3. (a) G. Kalaiarasi, S. Dharani, S. R. J. Rajkumar, M. Ranjani, V. M. Lynch, R. Prabhakaran, *Inorg. Chim. Acta* **2021**, *515*,

120060; **DOI:**10.1016/j.ica.2020.120060
(b) C. E. Satheesh, P. R. Kumar, P. A. Suchetan, H. Rajanaika, S. Foro, *Inorg. Chim. Acta* **2021**, *515*, 120017;
(c) N. Turan, A. Savci, K. Buldurun, Y. Alan, R. Adiguzel, *Lett. Org. Chem.* **2016**, *13*, 343–351;
DOI:10.2174/1570178613666160422161855
(d) S. A. Hosseini-Yazdi, A. Mirzaahmadi, A. A. Khandar, V. Eigner, M. Dusek, M. Mahdavi, S. Soltani, F. Lotfipour, J. White, *Polyhedron* **2017**, *124*, 156–165;
DOI:10.1016/j.poly.2016.12.004
(e) M. Orojloo, P. Zolgharnein, M. Solimannejad, S. Amani, *Inorg. Chim. Acta* **2017**, *467*, 227–237;
DOI:10.1016/j.ica.2017.08.016
(f) K. Singh, Y. Kumar, P. Puri, C. Sharma, K. R. Aneja, *Bioinorg. Chem. Appl.* **2011**, 901716.

4. (a) H.-Y. Qian, N. Sun, *Transition Met. Chem.* **2019**, *44*, 501–506; **DOI:**10.1007/s11243-018-00296-x
(b) H.-Y. Qian, Z.-L. You, *Synth. React. Inorg. Met.-Org. Nano-Met. Chem.* **2009**, *39*, 193–198;
(c) H.-Y. Qian, Z.-L. You, J. Chem. Crystallogr. **2011**, 41, 1593–1597; **DOI:**10.1007/s10870-011-0145-0
(d) H.-Y. Qian, *Russ. J. Coord. Chem.* **2018**, *44*, 32–38. **DOI:**10.1134/S1070328418010074
5. G. M. Sheldrick, *SAINT (version 6.02), SADABS (version 2.03)*, Madison (WI, USA): Bruker AXS Inc., **2002**.
6. G. M. Sheldrick, *SHELXL-97, A Program for Crystal Structure Solution*, Göttingen (Germany): University of Göttingen, **1997**.
7. J. Meletiadis, J. Meis, J. W. Mouton, J. P. Donnelly, P. E. Verweij, *J. Clin. Microbiol.* **2000**, *38*, 2949–2954.
DOI:10.1128/JCM.38.8.2949-2954.2000
8. W. J. Geary, *Coord. Chem. Rev.* **1971**, *7*, 81–122.
DOI:10.1016/S0010-8545(00)80009-0
9. G. Kastas, C. A. Kastas, A. Tabak, *Spectrochim. Acta A* **2019**, *222*, 117198. **DOI:**10.1016/j.saa.2019.117198
10. (a) A. Ray, G. Pilet, C. J. Gomez-Garcia, S. Mitra, *Polyhedron* **2009**, *28*, 511–520; **DOI:**10.1016/j.poly.2008.11.054
(b) K. Bhar, S. Chattopadhyay, S. Khan, R. K. Kumar, T. K. Maji, J. Ribas, B. K. Ghosh, *Inorg. Chim. Acta* **2011**, *370*, 492–498. **DOI:**10.1016/j.ica.2011.02.055
11. (a) S. Chattopadhyay, M. S. Ray, M. G. B. Drew, A. Figuerola, C. Diaz, A. Ghosh, *Polyhedron* **2006**, *25*, 2241–2253;
DOI:10.1016/j.poly.2006.01.024
(b) S. Basak, S. Sen, S. Banerjee, S. Mitra, G. Rosair, M. T. Garland Rodriguez, *Polyhedron* **2007**, *26*, 5104–5112.
DOI:10.1016/j.poly.2007.07.025
12. S. Daravath, A. Rambabu, N. Vamsikrishna, N. Ganji, S. Raj, *J. Coord. Chem.* **2019**, *72*, 1973–1993.
DOI:10.1080/00958972.2019.1634263
13. A. A. El-Sherif, A. Fetoh, Y. K. Abdulhamed, G. M. Abu El-Reash, *Inorg. Chim. Acta* **2018**, *480*, 1–15.
DOI:10.1016/j.ica.2018.04.038
14. S. Shit, P. Talukder, J. Chakraborty, G. Pilet, M. S. El Fallah, J. Ribas, S. Mitra, *Polyhedron* **2007**, *26*, 1357–1363.
DOI:10.1016/j.poly.2006.11.013
15. A. Jayamani, M. Sethupathi, S. O. Ojwach, N. Sengottuvelan, *Inorg. Chem. Commun.* **2017**, *84*, 144–149.
DOI:10.1016/j.inoche.2017.08.013
16. A. W. Addison, T. N. Rao, J. Reedijk, J. van Rijn, G. C. Verschoor, *J. Chem. Soc., Dalton Trans.* **1984**, *7*, 1349–1356.
DOI:10.1039/DT9840001349
17. (a) P. Kundu, P. Chakraborty, J. Adhikary, T. Chattopadhyay, R. C. Fischer, F. A. Mautner, D. Das, *Polyhedron* **2015**, *85*, 320–328; **DOI:**10.1016/j.poly.2014.08.011
(b) P. Chakraborty, A. Guha, S. Das, E. Zangrando, D. Das, *Polyhedron* **2013**, *49*, 12–18. **DOI:**10.1016/j.poly.2012.09.017
18. (a) P. Chakraborty, J. Adhikary, S. Samanta, D. Escudero, A. C. Castro, M. Swart, S. Ghosh, A. Bauza, A. Frontera, E. Zangrando, D. Das, *Cryst. Growth Des.* **2014**, *14*, 4111–4123;
DOI:10.1021/cg500717n
(b) G. Marinescu, A. M. Madalan, S. Shova, M. Andruh, *J. Coord. Chem.* **2012**, *65*, 1539–1547;
DOI:10.1080/00958972.2012.675435
(c) M. Karmakar, A. Frontera, S. Chattopadhyay, *CrystEngComm* **2020**, *22*, 6876–6885. **DOI:**10.1039/D0CE01105C
19. (a) N. Mondal, D. K. Dey, S. Mitra, K. M. A. Malik, *Polyhedron* **2000**, *19*, 2707–2711; **DOI:**10.1016/S0277-5387(00)00584-2
(b) S. Shit, D. Saha, D. Saha, T. N. G. Row, *Inorg. Chim. Acta* **2014**, *415*, 103–110. **DOI:**10.1016/j.ica.2014.02.036
20. (a) A. Lalehzari, J. Desper, C. J. Levy, Inorg. Chem. **2008**, 47, 1120–1126; **DOI:**10.1021/ic702015u
(b) F. Chen, M. S. Askari, X. Ottenwaelder, *Inorg. Chim. Acta* **2013**, *407*, 25–30. **DOI:**10.1016/j.ica.2013.07.017

Povzetek

Sintetizirali in karakterizirali smo nov večjedrni cinkov kompleks, $[Zn(\mu_{1,5}\text{-dca})L^1]_n$ (**1**) in dva nova enojedrna kobaltova kompleksa $CoL^2N_3(Brsal)]$ (**2**) ter $[CoL^1(HL^1)]$ (**3**), kjer je L^1 = 5-bromo-2-(((2-hidroksietil)imino)metil)fenolat, L^2 = 5-bromo-2-(((2-dimetilamino)etil)imino)metil)fenolat, dca = dicianoamid, Brsal = 5-bromo-2-formilfenolat. Spojine smo analizirali z elementno analizo, IR, UV-VIS spektroskopijo, meritvami molarne prevodnosti in monokristalno rentgensko analizo. Strukturna analiza kaže, da se cinkov atom v spojini **1** nahaja v popačeni trigonalno bipiramidalni koordinaciji, medtem ko so atomi kobalta v spojinah **2** in **3** oktaedrično koordinirani. Molekule so medsebojno povezane z vodikovimi vezmi in π···π interakcijami. Testirali smo antibakterijsko učinkovitost kompleksov na treh grampozitivnih (*B. subtilis*, *S. aureus* in *St. faecalis*) in treh gramnegativnih rodovih bakterij (*E. coli*, *P. aeruginosa* in *E. cloacae*) z metodo MTT.

Scientific paper

Mineral Composition of Herbaceous Species *Seseli rigidum* and *Seseli pallasii*: a Chemometric Approach

Marija D. Ilić,[1,*] Violeta D. Mitić,[2] Snežana B. Tošić,[2] Aleksandra N. Pavlović,[2] Marija S. Marković,[3] Gordana S. Stojanović[2] and Vesna P. Stankov Jovanović[2]

[1] *Laboratory Sector, Laboratory for Analytical Chemistry, Veterinary Specialized Institute "Niš", DimitrijaTucovića 175, Niš, 18106, Serbia*

[2] *University of Niš, Faculty of Science and Mathematics, Department of Chemistry, Višegradska 33, Niš, 18000, Serbia*

[3] *University of Niš, Faculty of Science and Mathematics, Department of Biology and Ecology, Višegradska 33, Niš, 18000, Serbia*

** Corresponding author: E-mail: marija.fertico@gmail.com*
Tel.: 00381 62 365 228

Received: 05-09-2021

Abstract

Nutrients play an essential role in many metabolic processes whose deficiency or excess can be harmful to the plant itself and through the food chain to both animals and humans. Medicinal plants used in the food and pharmaceutical industries can be contaminated with increased concentrations of heavy metals. The plant species *Seseli rigidum* and *Seseli pallasii* from the Balkan Peninsula are used in traditional medicine and spices in the diet, so it was necessary to determine the mineral composition to ensure their safe application. In this work, the mineral composition was determined in medicinal species of the genus *Seseli* using inductively coupled plasma with optical emission spectrometry (ICP-OES). Two multivariate statistic methods –principal component analysis (PCA) and hierarchical cluster analysis (HCA) were applied to distinguish samples regarding their mineral composition. The mineral composition of both studied species is following the literature data. The results obtained using multivariate statistics methods agree and distinguish certain parts of the tested plants based on the highest content of micro, macro, or trace elements.

Keywords: *Sesli rigidum*, *Seseli pallasii*, mineral composition, ICP-OES, multivariate statistics

1. Introduction

Almost all metals present in nature can be found in plants. They affect the life processes, anatomical and morphological structure, chemical composition, yield, and prevalence of certain plant species. According to plants' presence, elements can be divided into macro elements, microelements, and trace elements.[1] Macroelements are structural components of tissues; they have specific functions in the cells and basal metabolism and water and acidic-alkaline balance.[2] Microelements are needed in much smaller quantities, less than 100 mg per day, making up less than 0.01% of body mass. Microelements are Zn, Fe, Si, Mn, Cu, Cr, fluorides, and iodides. Elements primarily present in low quantities (e.g., Pb, Cd, V) in plants, pose a significant threat to human health when consumed, causing adverse effects and hence, they are categorized as toxic to humans. Therefore, the determination of their content and action mechanism has become an area of particular interest and priority in different areas. This classification does not reflect their importance in plant metabolism; only their role is different. Unlike macro elements, microelements act catalytically at low concentrations and are strictly specific.[3,4]

Medicinal plants of the genus Seseli have long been used in traditional medicine in the form of infusion and tinctures.[5,6] They contain many compounds (essential oils, secondary metabolites) that can preserve good health due to their potential antioxidant, antimicrobial, hepatoprotective, anticancer, and anti-inflammatory activity.[7] If medicinal plants are applied for pharmacological and veterinary purposes and in humans' and animals' diets, the increased content of individual heavy metals in plants can reduce their therapeutic activity or even be toxic to humans. Therefore, their use is limited. Consequently, the concentration of heavy metals in plants is strictly limited and defined by international standards.[8]

Regarding the preceding comments, the primary purpose of this research was to evaluate the contents of elements (Al, B, Ba, Ca, Cd, Cr, Cu, Fe, K, Mg, Mn, Na, Ni, Pb, V, and Zn) in selected medicinal plants (*Seseli rigidum* Waldst. & Kit. and *Seseli pallasii* Basser*)*, using inductively coupled plasma optical emission spectrometry (ICP-OES).

2. Experimental

2. 1. Reagents

Analytical grade nitric acid (HNO_3) and 70% perchloric acid ($HClO_4$) supplied from Fischer scientific were used as reagents for the wet digestion of samples. Ultra-scientific (USA) ICP multi-element standard solutions of about 20.00 ± 0.10 mg L^{-1} were used as a stock solution for calibration. The containers used for sample storage were cleaned to avoid contamination of the samples with traces of any metal. Containers were treated with 5% nitric acid and washed with ultra-pure water 18 MΩ cm (MicroMed highpurity watersystem, TKA Wasseraufbereitungs systeme GmbH).

2. 2 Instrumentation

All analyses were carried out on aniCAP 6000 inductively coupled plasma optical emission spectrometer (ThermoScientific, Cambridge, United Kingdom), which uses an Echelle optical design and a Charge Injection Device (CID) solid-state-detector. The optimum instrumental conditions are listed in Table 1.

Table 1. Operational parameters for ICP-OES measurements

Parameters	Values
Flush pump rate	100 rpm
Analysispump rate	50 rpm
RF power	1150 W
Nebuliser gas	0.7 l/min
Coolant gas flow	12 l/min
Auxiliary gas flow	0.5 l/min
Plasma view	dual-mode

2. 3. The Selection of Analytical Lines

Before the analysis, spectral lines were selected, spectral interferences and matrix effect in both axial and radial view modes were checked for a total of 44 lines recommended by the ICP OES spectrometer library, which corresponded to 16 identified elements. The analytical lines were selected according to the ratio of the slope of the calibration curve and slope of the standard addition method line ($Slope_{cal}/Slope_{sam}$).

2. 4. Validation

Based on the calibration curve of each metal, the selected wavelengths of the analyte lines, coefficient of determination, the limit of detection, and limit of quantification are shown in Table 2. The instrument was calibrated at a four-point calibration curve. The linearity of each element was tested, ranging from 0 ppm to 5 ppm. The calibration curve linearity for each element was evaluated by the coefficient of determination (R^2). Samples were analyzed in triplicate.

The detection (LOD) and quantification (LOQ) limits were calculated with three and ten times of the blank's standard deviation of the regression line (3σ and 10σ criterion), divided with a slope of the calibration curve.[9]

The spyking method was appled for the recovery test. To each plant sample, 2 ml of element standard solution (containing 62.5 mg L^{-1} of Al, B, Ba, Ca, Fe, Mg, Na and 6.25 mg L^{-1} of B, Cd, Cr, Cu, Mn, Ni, Pb, V, Zn). The samples were prepared as is described in the section Sample preparation. All experiments were done in triplicate.

2. 5 Plant Material

Seseli rigidum Waldst. & Kit. was collected on rocky terrain on the Vidlič Mountain in southeast Serbia in July (the flowering stage) and in September (fruit phase) 2013, while *Seseli pallasii* Basser was collected in (fruit phase) August 2013 in the area of Kravlje, Serbia. Voucher specimen *S. rigidum* (No 16447) was deposited in the Herbarium of Botanical Garden "Jevremovac", Faculty of Biology, University of Belgrade, while voucher specimen of *S. pallasii* was deposited in Herbarium of Department of Biology and Ecology, Faculty of Science and Mathematics (HMN), University of Niš (No 7211).

2. 6 Sample Preparation

Before the analysis, root and aerial vegetative parts (leaf, flower, and fruit) were separated, dried at room temperature. The dried samples were powdered in a stainless steel mill, obtaining fine particles that passed through a 2 mm mesh and kept in polypropylene pouches for analysis. The wet digestion method of the dried samples was adopted to enable the measurement of the metal concentrations. The metal content in the plant material was determined after the acidic treatment. First, a volume of 10 mL concentrated HNO_3 was added to the sample (1 g), heated up in the open glass to a small volume (until red vapors originating from NO_2 are removed). Digestion was continued with 4 mL 70% $HClO_4$ and again evaporated to a low volume. Finally, the solutions were transferred to standard vessels and diluted to a volume of 25 mL.[3,4]

2. 7 Data Analysis

Chemometrics is an interdisciplinary scientific field, which includes multiparametric statistical analysis, math-

Table 2. Analyte line selected with the ratio $Slope_{cal}/Slope_{sam}$, regression coefficient (R^2), LOD, LOQ of the calibration for each metal determination, and Recovery values for spiked samples. Plasma view mode: axial.

Element	λ (nm)	$Slope_{cal}/Slope_{sam}$	R^2	LOD (μg/g)	LOQ (μg/g)	Recovery (%)
Al	396.152	0.976	0.99951	0.0850	0.2802	83.3
B	208.959	0.987	0.99943	0.0014	0.0051	84.3
Ba	455.403	0.965	0.99901	0.0272	0.0776	86.3
Ca	317.933	0.945	0.99992	0.0752	0.2503	94.8
Cd	228.802	1.056	0.99999	0.0226	0.0756	101.2
Cr	267.716	0.905	0.99991	0.0610	0.2034	113.7
Cu	224.700	1.019	0.99993	0.0532	0.1775	111.2
Fe	259.940	1.011	0.99984	0.0248	0.0502	122.2
K	766.490	0.984	0.99995	0.0215	0.0846	97.7
Mg	202.583	0.991	0.99993	0.0584	0.1954	116.5
Mn	257.610	0.982	0.99995	0.0422	0.1408	97.8
Na	589.592	1.011	0.99997	0.0920	0.3530	112.3
Ni	231.604	0.983	0.9998	0.0240	0.0678	106.5
Pb	220.353	0.958	0.99998	0.0309	0.1030	115.9
V	311.071	0.899	0.99904	0.0208	0.5213	97.5
Zn	202.548	0.981	0.99997	0.0350	0.1168	109.7

ematical modeling, computer methods, and analytical chemistry. Using mathematical, informational, and statistical methods, it is possible to efficiently and quickly classify compounds and samples into one of the categories.[10,11]

To establish valid mathematical relations, it is necessary to convert all information into numerical ones and then model a mathematical pattern using the basic set of input data obtained experimentally (normalization).

Principal Component Analysis (PCA) is a technique of forming new variables representing combinations of source variables, which allows the extraction of important information and data from the original data sets. By applying PCA, the number of initial data is reduced, and as a result, new so-called variables are obtained- main components (Principal Components, PC).[12]

There are different criteria for determining the required number of components. The Kaiser criterion is most commonly used, according to which all components whose eigenvalue is less than 1 are rejected.[13] The number of principal components used for further calculations should explain at least 80% of the total data variance.

HCA is a clustering method that explores the organization of samples in groups and among groups depicting a hierarchy. The result of HCA is usually presented in a dendrogram- plot which shows the organization of samples and their relationships in a tree form. There are two main approaches to resolve the grouping problem in HCA, agglomerative or divisive.

In the first one, each sample is initially considered a cluster, and subsequently, pairs of clusters are merged. In a divisive approach algorithm start with one cluster including all samples, recursive splits are performed. Clustering is achieved using an appropriate metric of samples' distance (Euclidean distance) and linkage criterion among groups. Complete, single, and average, and Ward's linkage is the more common variants of linkage criteria. Based on the optimal value of a target function, Ward's method is a common choice[12].

All statistical calculations were made using a statistical software package STATISTICA 8.0 (StatSoft, Tulsa, Oklahoma, USA). The datasets were normalized and PCA and HCA were applied to analyze the obtained results.

The following designations were used for the listed parts of plants *S. rigidum* and *S. pallasii* in dendrograms and diagrams: *S.r* L- *S. rigidum* Leaf, *S.r* Fl- *S. rigidum* Flower, *S.r* Fr- *S. rigidum* Fruit, *S.r* R- *S. rigidum* Root, *S.p* L- *S. pallasii* Leaf, *S.p* Fl- *S. pallasii* Flower, *S.p* Fr- *S. pallasii* Fruit and *S.p* R- *S. pallasii* Root

3. Results

Contents of all analyzed metals (Al, B, Ba, Co, Cu, Fe, Mn, V, Zn, Na, Mg, Ca, K, Cd, Cr, Ni, and Pb in ppm) in leaf, flower, fruit, and root of the plant species *S. rigidum* and *S. pallasii* are shown in Figure 1.

3. 1. Microelements (Al, B, Ba, V, Co, Fe, Cu, Mn, and Zn)

The concentration of aluminum in *S. rigidum* ranges from 4.24 to 19.98 ppm and in *S. pallasii* from 2.75–21.18 ppm.

The lowest concentration of boron was determined in the root of *S. rigidum* (8.16 ppm), while the highest (13.09 ppm) was determined in the fruit. The concentration of boron in *S. pallasii* ranged from 6.58–22.02 ppm. The highest barium concentration was determined in the root of *S. rigidum* (4.85 ppm), and the smallest in the fruit, 0.96 ppm. The barium concentration in *S. pallasii* ranges from 0.47

ppm in the root to 2.21 ppm in the leaf. The highest concentrations of cobalt, copper and iron were determined in the root (5.55, 10.98, and 9.52 ppm, respectively). The lowest concentration was found in the leaf of *S. rigidum* (1.64; 3.99 and 2.30 ppm, respectively). Cobalt was determined at the highest level in *S. pallasii* root (7.14 ppm), while the amount in other parts of the plant is ranged from 2.65 ppm in the leaf to 4.03 ppm in the fruit. The highest amount of iron was determined in the root of *S. pallasii* at 8.83 ppm, while the lowest concentration in the leaf is 2.17 ppm. The most considerable amount of copper was determined in the reproductive parts of *S. pallasii*- the flower (7.64 ppm) and the fruit (6.60 ppm), while in the root and the leaf were significantly lower (3.34 and 1.83 ppm). The highest concentration of manganese was recorded in the leaf of *S. rigidum* and *S. pallasii* (8.25 and 8.23 ppm), while in the root of S. *rigidum* was significantly lower (2.73 ppm). Vanadium was present in approximately the same concentration in all parts of the investigated plants. In *S. rigidum*, the highest content was determined in the root (1.58 ppm), the lowest in the fruit (1.49 ppm), while in *S. pallasii*, it ranges from 1.52 ppm in the leaf up to 1.68 ppm in the root. Zinc content was ranged from 17.80–35.25 ppm in *S. pallasii* and similarly in *S. rigidum* ranging from 10.3–37.2 ppm.

3. 2 Macroelements (Na, Mg, Ca, and K)

The highest amount of calcium was determined in the leaf of *S. rigidum* (942.68 ppm), while a double lower quantity was determined in the root (467.78 ppm). The root of *S. rigidum*, compared with the other plant's parts, contained deficient potassium and magnesium (775.39 and 958.90 ppm). In comparison, a significantly higher amount of potassium is determined in the fruit (2949 ppm). The highest concentration of magnesium was determined in the leaf (2284.74 ppm). The sodium content is significantly lower compared to other macroelements determined. An enormous amount of sodium was determined in the fruit and root (85.47 and 81.09 ppm), while the leaf and flower contain almost the same concentration of this element (52.51 and 53.16 ppm). The highest potassium content was determined in the fruit of *S. pallasii* (2279.26 ppm) and the lowest in the root 677.86 ppm. The highest sodium concentration was 172.30 ppm in the root and the smallest in the fruit (32.15 ppm). The lowest concentration of magnesium was determined in the root of *S. pallasii*, while in the flower of this plant, the amount of three times higher concentration was determined (15975.98 ppm). The highest concentration of calcium was determined in flower at 1189.86 ppm, while the root contains 460.41 ppm.

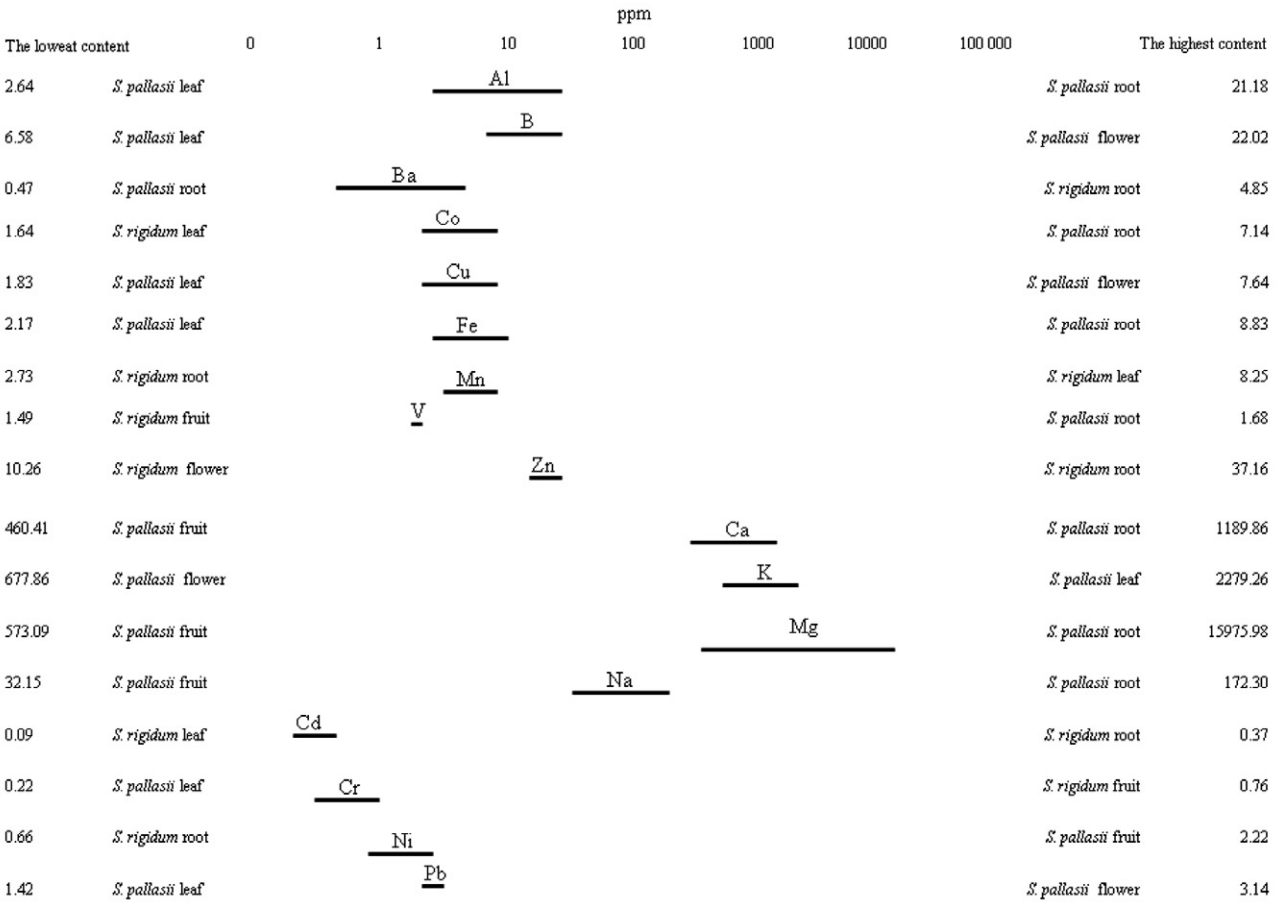

Figure1. Contents of Al, B, Ba, Co, Cu, Fe, Mn, V, Zn, Na, Mg, Ca, K, Cd, Cr, Ni, and Pb in leaf, flower, fruit, and root of the plant species *S. rigidum* and *S. pallasii*

3. 3 Heavy Metals (Cd, Cr, Ni, and Pb)

The highest concentration of cadmium was determined at the root of *S. rigidum* (0.37 ppm), while in other parts; the concentration of this heavy metal was significantly lower. The cadmium content in the fruit of *S. pallasii* (0.23 ppm) is almost two and a half times higher than in the fruit of *S. rigidum* (0.10 ppm). The highest lead content is in the root (3.11 ppm) and the lowest in the flower of *S. rigidum* (1.87 ppm). The highest lead concentration was in flower (3.14 ppm), while it is the lowest in *S. pallasii* leaf (1.42 ppm). The highest chromium concentration was determined in the fruit (0.76 ppm) and the smallest in the leaf (0.40 ppm). The highest chromium concentration was determined in the *S. pallasii* flower (0.82 ppm), while in other parts of the plant, it was significantly lower. The content of nickel in the observed plant species is similar, although a certain amount of Ni in the fruit of *S. rigidum* (1.36 ppm) is almost twice as large as the fruit of *S. pallasii*, while the content of Ni in the root of both plant species is almost the same.

4. Discussion

The extent of aluminum concentration in analyzed plants of the genus Seseli is slightly lower than in medicinal plants from Serbia's territory.[14,15] The obtained results show that boron is mobile in the plant and accumulates mainly in the reproductive parts (fruit). The obtained boron concentrations are following 26 herbaceous species boron content from Serbia,[14] ranged from 5.1–118.7 ppm. The barium content in the plants of the genus Seseli is in the lower concentration range than in the previous research of herbs from Serbia, Turkey, Spain,[16] Africa, and Asia, as well as in the leaf of *Mentha piperitae* from Poland.[14,16–19] Cobalt, copper, and iron are critical biogenic elements responsible for plant growth. Cobalt concentrations in the studied plants are above average concentrations (0.05–0.50 ppm) but still out of critical concentrations (30–40 ppm).[7] The distribution of copper in vegetative parts of *S. pallasii* is contrary to the corresponding parts of *S. rigidum*. Average copper concentrations in the plant material are from 3–15 ppm, while the toxic concentration is 20 ppm.[7] Based on the obtained results for *S. pallasii* and *S. rigidum*, it is evident that the content of the copper is in average concentrations, which is in line with previous studies of medicinal plants.[16,17, 19–21] The typical iron concentration in plants varies from 50–250 ppm, while concentrations above 500 ppm are toxic.[7] Iron in the analyzed plant species is within a range of average concentrations. In species of the genus Seseli, lower iron content was registered compared to many medicinal and aromatic plants and green and black tea.[14,17,20–24] The concentration of zinc in both plant species' roots is approximately the same, while in the above-ground parts, it is lower (especially in the flower *S. rigidum*). Compared with the other observed metals in *S. pallasii*, zinc was present in higher concentrations. The flower of *S. pallasii* contained the highest concentrations of almost all determined elements compared to other plant parts.[25–26]

Simultaneously, in *S. rigidum*, the situation is reversed: the highest concentrations of the specified metals are recorded in the root.

Dudić et al. 2007 determined the content of Mg, Ca, Fe, Cr, and Ni in the root, stem, and leaf of *S. rigidum* from different regions, with serpentine (silicate) limestone substrate.[27] The total content of magnesium was 14150 and 11280 ppm (silicate and limestone), while calcium concentrations were 13500 and 21110 ppm (silicates and limestone). Such a large amount of Ca and Mg was explained because the plant *S. rigidum* is tolerant to high concentrations of these metals in the substrate. The plant's mineral composition depends on the leaves' and roots' morphological structure. However, in many cases, the substrate's structure and composition make the results of different studies incomparable since plants are harvested from different geographical areas.

Ca and Mg concentrations determined in *S. pallasii* and *S. rigidum* ranged in approximately the same range of concentrations. However, in both plant species, the smallest amount of Ca and Mg were determined in the root, while the highest concentration of these metals is determined in the above-ground parts and the flower. In all previous studies, the concentration of calcium was significantly higher than in the species of the genus Seseli,[18,28] while the concentrations of Mg are comparable with these from the present study.[18,21,28]

In addition to adverse impacts on plants, heavy metals pose a threat to human health due to their persistence in nature. Lead and cadmium are trace elements that are not essential, but they can accumulate in biological systems and become potential contaminants through the food chain. They are toxic for humans, even at low doses. Excessive concentrations of heavy metals inhibit physiological processes such as respiration, photosynthesis, transpiration rates, cell elongation, N-metabolism, mineral nutrition, and biomass decrease and, consequently, can cause plant death.[29] Accordingly, it is necessary to monitor their even low concentrations in potential sources and, therefore, medicinal herbs. Comparing the obtained results for the heavy metal content (Cd and Pb) in *S. rigidum* and *S. pallasii* to the prescribed WHO values [30], the plants grew in an unpolluted environment are with no increased content of these heavy metals. A certain amount of cadmium and lead in *S. pallasii* is comparable with these metals' content from the unpolluted environment from Serbia's territory.[20]

Chromium, present in traces, is a necessary metal for a healthy metabolism, and its defiance can cause various disorders both in the plant itself and in consumers. The known fact is that chromium enhances insulin activity. Chromium is relatively evenly distributed in all parts of *S. rigidum*. The concentration of Cr in *S. rigidum* and *S. pallasii* is within the average concentration of this element.[7]

However, it is higher than chromium content in medicinal plants traditionally used in Serbia's alternative medicine.[7]

The amounts of nickel in traces can be helpful in the human organism, especially for enzyme activation, but it can be toxic at higher concentrations. Also, exposure to higher concentrations of nickel causes oxidative stress. The obtained results for both plant species show that the content of nickel is in average concentrations and comparable to the results of analyzed herbs' infusions.[7,15]

4. 1. Statistical Comparison of the Mineral Composition of S. rigidum and S. pallasii

The multivariate analysis applied to the mineral composition of plants *S. rigidum* and *S. pallasii* includes analysis of the main components (PCA) and hierarchical cluster analysis (HCA).

By PCA analysis, the original variables are converted into new correlation variables, which are called the main components, wherein the first major component explains 81.91% of the total variability of the mineral composition of *S. rigidum* and *S. pallasii*. The second principal component explains 11.36%, while the third component covers 5.33% of the total variability.

PCA analysis of *S.p* R and *S.r* R variables are isolated concerning other variables, whose clustering is primarily due to aluminum and zinc content. In contrast, *S.r* Fr is grouped based on the boron content.

The data treated using PCA analysis were subjected to hierarchical cluster analysis (HCA).

Application of HCA analysis to the results of microelements content in the leaf, flower, fruit, and root of the plant species *S. rigidum* and *S. pallasii* concerning the content of microelements (Al, B, Ba, V, Co, Fe, Cu, Mn, and Zn) in parts (leaf, flower, fruit, and root) of the studied plants are shown in Figure 2.

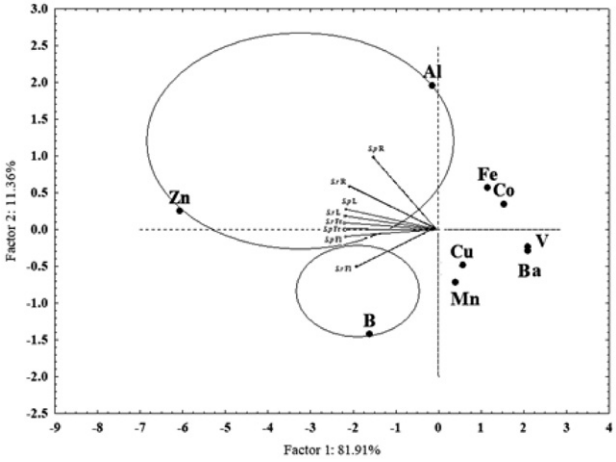

Figure 2. PCA diagram of the variables of the content of microelements (Al, B, Ba, V, Co, Fe, Cu, Mn, and Zn) in the leaf, flower, fruit, and root of plant species *S. rigidum* and *S. pallasii*

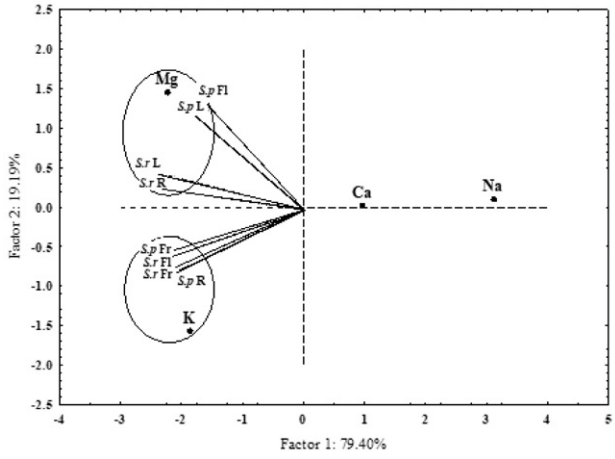

Figure 4. PCA diagram of variables of the macroelements content (Na, Mg, Ca, and K) in the leaf, flower, fruit, and root of plant species *S. rigidum* and *S. pallasii*

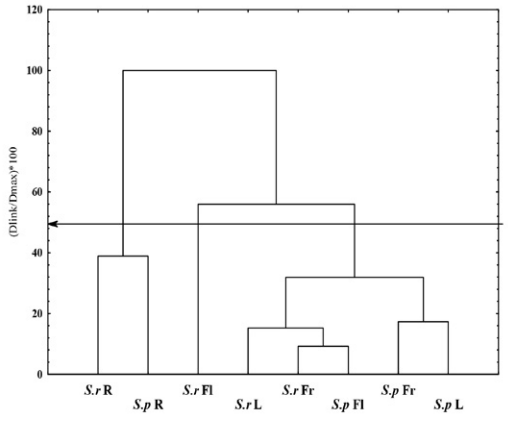

Figure 3. Dendrogram of the microelements content (Al, B, Ba, V, Co, Fe, Cu, Mn, and Zn) in the leaf, flower, fruit, and root of plant species *S. rigidum* and *S. pallasii*

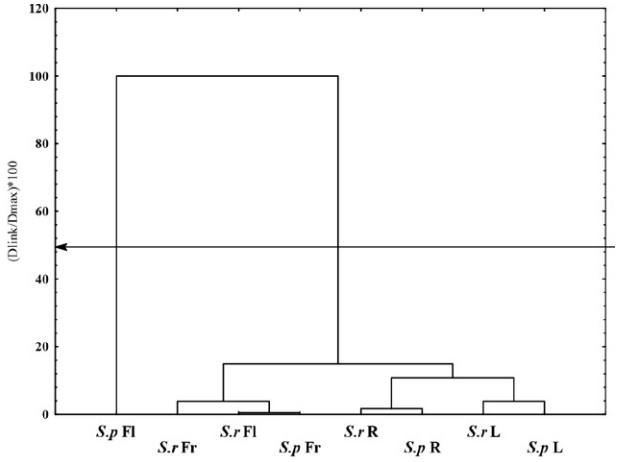

Figure 5. Dendrogram of macroelements content (Mg, Ca, Na and K) in the leaf, flower, fruit, and root of plant species *S. rigidum* and *S. pallasii*

Two statistically significant clusters were obtained based on the cluster analysis of individual parts of plants *S. rigidum* and *S. pallasii* (Figure 3).

Species are grouped because they have significantly higher wrinkle content than the roots of *S. rigidum* and *S. pallasii*; accordingly, the other cluster can be called a worm cluster.

The cluster analysis separates the underground parts of studied herbs from the above-ground parts based on microelements' content, confirming that the microelements are present in higher concentrations in the root than in the above-ground parts.

The first major component explains 79.40% of the variance among variables, while the eigenvalue is 6.35. The second major component explains 19.19% of the total variance. Together, these two components explain 98.58% variances. PCA results are illustrated in Figure 4.

Data subjects of PCA analysis were subject to hierarchical cluster analysis (HCA).

Figure 5 shows a dendrogram of macroelements content (Mg, Ca, Na, and K) in parts of the plants (leaf, flower, fruit, and root) *S. rigidum* and *S. pallasii*.

After cluster analysis, two clusters were obtained. *S.p* Fl is singled out separately and represents the first cluster, which is in accordance with the highest magnesium content, so the first cluster can be called a magnesium cluster. Within the second cluster, there are two subclasses. The first subclass consists of two sub-clusters, one consisting of *S.p* L and *S.r* L (Euclid's distance= 938), and the other *S.p* R and *S.r* R (Euclid's distance = 407). In the second subcluster, the plants' reproductive parts were isolated, respectively *S.p* Fr and *S.r* Fl (Euclid's distance= 109), most similar in content macroelements. The first subcluster is characterized by the vegetative parts of plants *S. pallasii* and *S. rigidum* that have increased magnesium and potassium content and higher calcium content than the reproductive parts of plants isolated in another subclause characterized by higher potassium content. In general, this cluster can be called potassium clusters.

PCA results are illustrated in Figure 6.

If HCA analysis is applied to the matrix of data used for PCA analysis, the obtained results can be presented with a dendrogram (Figure 7).

The HCA test results for the composition of the heavy metal content (Cd, Cr, Ni, and Pb) in the leaf, flower, fruit, and root of the plant species *S. rigidum* and *S. pallasii* are shown in Figure 7.

Based on cluster analysis, three statistically significant clusters were obtained. Within the first cluster, two sub-clusters were singled out. Within the first subclass, the *S.p* L is grouped, while in the second variant, *S.p* R, *S.p* L, *S.r* Fl, and *S.r* F. Variants *S.r* L and *S.r* Fl are most similar in heavy metals' content (Euclid's distance= 0.17). In *S. rigidum*' fruit, the highest chromium amount was determined concerning other variables within the first cluster. In the second cluster, *S.p* Fl and *S.r* R (Euclid's distance= 0.60) were isolated, grouped based on the most abundant lead content and the same cadmium, chromium, and nickel content. In the third cluster, *S.p* Fr is distinguished because of the higher content of nickel and lead compared to other examined parts of plants *S. rigidum* and *S. pallasii*.

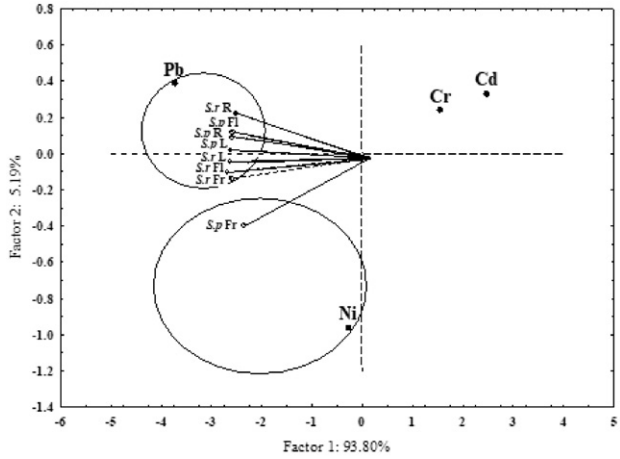

Figure 6. PCA Diagram of heavy metal content (Cd, Cr, Ni, and Pb) content variables in leaf, flower, fruit, and root of plant species *S. rigidum* and *S. pallasii*

The results obtained with PCA and HCA analysis are in excellent agreement. In the PCA analysis, *S.r* R was distinguished because it has the most abundant lead content, while on the opposite side of the diagram was *S.p* Fr because it has a high nickel content (which distinguishes it from other parts of plants), but also significantly lower chromium and cadmium content which was diagonally in the PCA diagram. In the cluster analysis of *S.r* R and *S.p* Fl, a flower of *S. pallasii* was found in the same subcluster due to the highest lead content, while *S.p* Fr was distinguished as a separate cluster due to the higher nickel content than in other examined parts of plants *S. rigidum* and *S. pallasii*.

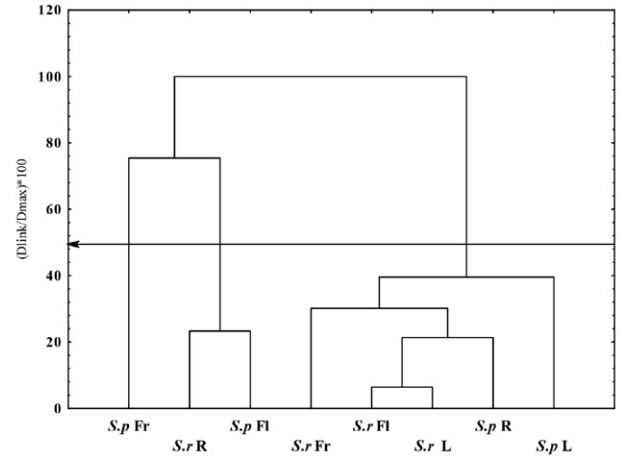

Figure 7. Dendrogram of heavy metals content (Cd, Cr, Ni, and Pb) in the leaf, flower, fruit, and root of plant species *S. rigidum* and *S. pallasii*

5. Conclusion

The flower of *S. pallasii,* compared to the other parts of that plant, contains the highest concentrations of almost all of the specified metals, while in the case of *S. rigidum*, the situation of the different- highest concentrations of the specified metals is recorded at the root. The results obtained for both plant species show that metals' content is within ranges previously reported for the plants from the same area and in the acceptable amounts prescribed by WHO for human consumption.

Both multivariate statistics methods agree and distinguish certain parts of the investigated plants based on the highest content of micro-, macroelement, or heavy metals.

6. References

1. K. O. Soetan, C. O. Olaiya, O. E. Oyewole, *Afr. J. Food Sci*. **2010**, *4*, 200–222. https://academicjournals.org/article/article1380713863_Soetan%20et%20al.pdf
2. B. Imelouane, M. Tahri, M. Elbastrioui, F. Aouinti, A. Elbachiri, *J. Mater. Environ. Sci.* **2011**, *2*, 104–111. http://www.jmaterenvironsci.com/Document/vol2/13-JMES-52-2010-Emelouane.pdf
3. M. Tuzen, *Microchem. J*. **2003**, *74*, 289–297. **DOI:**10.1016/S0026-265X(03)00035-3
4. M. Hoenig, *Talanta.* **2001**, *54*, 1021–1038. **DOI:**10.1016/S0039-9140(01)00329-0
5. J. Matejić, A. Džamić, T. Mihajilov-Krstev, V. Ranđelović, Z. Krivošej, P. Marin, *Cent. Eur. J. Biol.* **2012**, *7*, 1116–1122. **DOI:**10.2478/s11535-012-0094-4
6. K. Skalicka-Wozniaka, R. Losb, K. Glowniaka, A. Malm, *Nat. Prod. Commun*. **2010**. *5*, 1427–1430. **DOI:**10.1177/1934578X1000500916
7. A. Stanojković-Sebić, R. Pivić, D. Josić, Z. Dinić, A. Stanojković, *Tarim. Bilim. Derg.* **2015**, *21*, 317–325. **DOI:**10.1501/Tarimbil_0000001334
8. WHO, Library Cataloguing in Publication Data: Quality control methods for medicinal plant materials, World Health Organization Geneva, England, **1998**.
9. S. Chandran, S. P. Singh, *Pharmazie* **2007**, *62*, 4–14. **DOI**: 10.1691/ph2007.1.5064
10. S. Wold, *Chemometr. Intell. Lab*. **1995**, *30*, 109–115. **DOI:**10.1016/0169-7439(95)00042-9
11. P. J. Gemperline, Practical Guide to Chemometrics, Taylor & Francis Group, London, **2006** **DOI:**10.1201/9781420018301
12. D. Granato, J. S. Santos, G. B. Escher, B. L. Ferreira, R. M. Maggio, *Trends Food Sci. Tech.* **2018**, *72*, 83–90. **DOI:**10.1016/j.tifs.2017.12.006
13. H. F. Kaiser. *Educ. Psychol. Meas.* **1960**, *20*, 141–151. **DOI:**10.1177/001316446002000116
14. S. Ražić; A. Onjia; S. Đogo; L. Slavković; A. Popović, *Talanta*. **2005**, *67*, 233–239. **DOI:**10.1016/j.talanta.2005.03.023
15. Ž. A. Mihaljev, M. M. Živkov-Baloš, Ž. N. Ćupić, S. M. Jakšić, *Acta. Pol. Pharm*. **2014**, *71*, 385–391. **DOI:**10.2298/HEMIND130424029M
16. P. L. Fernandez-Caceres, M. J. Martın, F. Pablos, A. G. Gonzalez, *J. Agr. Food. Chem*. **2001**, *49*, 4775–4779. **DOI:**10.1021/jf0106143
17. E. Altintig, H. Altundag, M. Tuzen, *B. Chem. Soc. Ethiopia.* **2014**, *28*, 9–16. **DOI:**10.4314/bcse.v28i1.2
18. A. Moreda-Pineiroa, A. Fisherb, S. J. Hill, *J. Food Compos. Anal*. **2003**, *16*, 195–211. **DOI:**10.1016/S0889-1575(02)00163-1
19. A. Lozak, K. Soltyk, P. Ostapczuk, Z. Fijalek, *Sci. Total Environ*. **2002**, *289*, 33–40. **DOI:**10.1016/S0048-9697(01)01015-4
20. S. Ražić, V. Kuntić, *Int. J. Food Prop*. **2013**, *16*, 1–8. **DOI:**10.1080/10942912.2010.526273
21. S. Basgel, S. B. Erdemoglu, *Sci. Total. Environ*. **2006**, *359*, 82–89. **DOI:**10.1016/j.scitotenv.2005.04.016
22. M. R. Gomez, S. Cerutti, L. L. Sombra, M. F. Silva, L. D. Martinez, *Food Chem. Toxicol*. **2007**, *45*, 1060–1064. **DOI:**10.1016/j.fct.2006.12.013
23. S. Tokalioglu, *Food Chem*. **2012**, *134*, 2504–2508. **DOI:**10.1016/j.foodchem.2012.04.093
24. A. G. Brudzinka-Kosior, A. Samecka-Cymerman, K. Kolon, L. Mroz, A. J. Kempers, *Ecotox. Environ. Safe*. **2012**, *80*, 349–354. **DOI:**10.1016/j.ecoenv.2012.04.005
25. M. Ilić, V. Stankov-Jovanović, V. Mitić, M. Dimitrijević, J. Cvetković, S.Tošić *Safe. Eng.* **2016**, *6*, 1–5, **DOI:**10.7562/SE2016.6.01.01
26. M. Ilić, V. Mitić, M. Marković, S. Ćirić, S. Tošić, G.Stojanović, V. Stankov Jovanović, "XXIII SAVETOVANJE O BIOTEHNOLOGIJI", Zbornik radova, Čačak, Srbija, **2018**, 293–298.
27. B. Dudić, T. Rakić, J. Šininžarar-Sekukulić, V. Atanackovitć, B. Stevanović, *Arch. Biol. Sci.* **2007**, *59*, 341–349. **DOI:**10.2298/ABS0704341D
28. S. Nookabkaew, N. Rangkadilok, J. Satayavivad, *J. Agr. Food Chem*. **2006**, *54*, 6939–6944. **DOI:**10.1021/jf060571w
29. P. Zornoza, S. Vázquez, E. Esteban, M. Fernández-Pascual, R. Carpena, *Plant Physiol. Bioch*. **2002**, *40*, 1003–1009. **DOI:**10.1016/S0981-9428(02)01464-X
30. A. Szymczycha-Madeja, M. Welna, P. Pohl, *Microchem. J*. **2015**, *121*, 122–129. **DOI:**10.1016/j.microc.2015.02.009

Povzetek

Hranila igrajo bistveno vlogo v številnih metabolnih procesih, katerih pomanjkanje ali presežek lahko škoduje rastlini sami in prek prehranjevalne verige tudi živalim in ljudem. Zdravilne rastline, ki se uporabljajo v živilski in farmacevtski industriji, so lahko onesnažene z večjimi koncentracijami težkih kovin. Rastlinski vrsti *Seseli rigidum* in *Seseli pallasii* z Balkanskega polotoka se uporabljata v tradicionalni medicini in kot začimbi v prehrani, zato je potrebno določiti mineralno sestavo, da se zagotovi njuna varna uporaba. V tem delu smo mineralno sestavo določili pri zdravilnih vrstah rodu *Seseli* z uporabo induktivno sklopljene plazme z optično emisijsko spektrometrijo (ICP-OES). Za ločevanje vzorcev glede na njihovo mineralno sestavo sta bili uporabljeni dve multivariatni statistični metodi - analiza glavnih komponent (PCA) in hierarhična skupinska analiza (HCA). Mineralna sestava obeh preučevanih vrst sledi literaturnim podatkom. Rezultati, pridobljeni z uporabo multivariatnih statističnih metod, se ujemajo in omogočajo diskriminacijo nekaterih delov preizkušenih rastlin na podlagi največje vsebnosti mikroelementov, makroelementov ali elementov v sledovih.

DOI: 10.17344/acsi.2021.6756 *Acta Chim. Slov.* **2021,** *68,* 718–727

Scientific paper

Substituent Effects in 3,3' Bipyrazole Derivatives. X-ray Crystal Structures, Molecular Properties and DFT Analysis

Ibrahim Bouabdallah,[1] Tarik Harit,[1,*] Mahmoud Rahal,[2] Fouad Malek,[1] Monique Tillard[3] and Driss Eddike[1]

[1] *Laboratory of Applied Chemistry and Environment, Faculty of Sciences, Mohammed First University Bd Mohamed VI, BP: 717, Oujda 60000, Morocco.*

[2] *Laboratoire de Chimie Physique, Faculté des Sciences, Université Chouaib Doukkali, BP 20, 24000, El Jadida, Morocco*

[3] *ICGM, Univ Montpellier, CNRS, ENSCM, Montpellier, France*

** Corresponding author: E-mail: tarikharit@gmail.com; t.harit@ump.ac.ma. Tel.: +212 536 500 601, Fax: +212 536 500 603*

Received: 02-17-2021

Abstract

The single crystal X-ray structure of new 1,1'-bis(2-nitrophenyl)-5,5'-diisopropyl-3,3'-bipyrazole, **1**, is triclinic P $\bar{1}$, a = 7.7113(8), b = 12.3926(14), c = 12.9886(12) Å, α = 92.008(8), β = 102.251(8), γ = 99.655(9)°. The structural arrangement is compared to that of 5,5'-diisopropyl-3,3'-bipyrazole, **5**, whose single crystal structure is found tetragonal $I4_1/a$, a = b = 11.684(1), c = 19.158(1) Å. The comparison is also extended to the structures previously determined for 1,1'-bis(2-nitrophenyl)-5,5'-propyl-3,3'-bipyrazole, **2,** 1,1'-bis(4-nitrophenyl)-5,5'-diisopropyl-3,3'-bipyrazole, **3,** and 1,1'-bis(benzyl)-5,5'-diisopropyl-3,3'-bipyrazole, **4**. Density Functional Theory (DFT) calculations are used to investigate the molecular geometries and to determine the global reactivity parameters. The geometry of isolated molecules and the molecular arrangements in the solid state are analyzed according to the nature of the groups connected to the bipyrazole core.

Keywords: Crystal structure; bipyrazole; DFT; substituent; reactivity indices.

1. Introduction

The C,C-linked bipyrazole derivatives have taken much interest in several fields.[1] Indeed, they have proven to be useful as potential anti-inflammatory,[2] cytotoxic,[3] antifungal,[4] extracting[5] and inhibitor corrosion[6] agents. These compounds also found applications in the synthesis of polymer materials.[7] Some authors have reported that bipyrazole compounds are active components and in particular, they are able to capture active oxygen and free radicals *in-vivo*.[8] Then, bipyrazoles are used as agents for preventing or treating various diseases induced by active oxygen.[8] Moreover, they have found a more unexpected application in the rocket industry as novel oxygen-rich energetic materials.[9]

It has been reported that the position and the nature of substituents on the pyrazole ring considerably affect their biological activities as well as their catalytic and complexing properties.[3-5,10,11] However, and to the best of our knowledge, no study has attempted to describe their effects on the geometry of molecules and the structure of compounds.

This paper presents the single crystal structures of 1,1'-di(2-nitrophenyl)-5,5'-diisopropyl-3,3'-bipyrazole, **1,** and 5,5'-diisopropyl-3,3'-bipyrazole, **5,** analyzed comparatively with those of similar bipyrazole compounds. An analysis of the molecular geometry and the arrangement of molecules in crystals is carried out for five compounds differing by the nature of their R1 and R2 substituents. The molecules' geometry has been optimized using DFT calculations enabling an evaluation of the reactivity through quantum chemical reactivity descriptors.

2. Experimental and Computational Details

2. 1. Synthesis of 1 and 5

The C,C-linked bipyrazole derivatives **1–5** were generally synthesized according to the literature method,[12,13] as represented in Scheme 1.

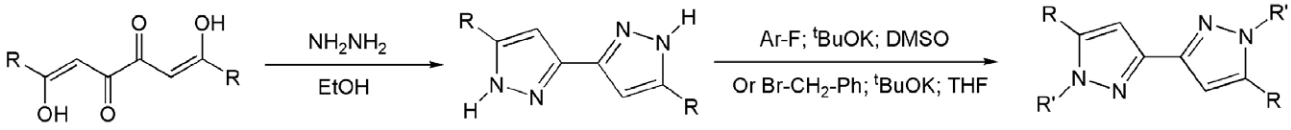

Scheme 1. General synthetic pathway to C,C-linked bipyazoles **1**-**5**

The compound **1** ($C_{24}H_{24}N_6O_4$, M_r = 460.49) was collected as a solid by filtration and oven-dried in vacuum. Yellow single crystals were obtained by recrystallization in ethanol. Compound **5** recrystallized from ethanol, has been synthesized by the condensation of hydrazine with 3,8-dihydroxy-2,9-dimethyl deca-3,7-diene-5,6-dione. The homogeneity of these compounds in their crystallized form was checked by spectroscopic methods (IR, NMR...) and found similar to those reported in our previous works.[12,13]

2. 2. Data Collection and Refinement

A stereomicroscope equipped with a polarizing filter was used to select single crystals suitable for X-ray diffraction study. Experiments were carried out on Xcalibur CCD (Oxford Diffraction) four-circle diffractometer, using the Mo Kα radiation and the CrysAlis software.[14] A yellow platelet of **1** of dimensions 0.06 × 0.15 × 0.21 mm was chosen to record the diffracted intensities at room temperature within the complete sphere. It displayed the triclinic P $\bar{1}$ symmetry with lattice parameters a = 7.713(3), b = 12.371(6), c = 12.986(5) Å, α = 92.07(3), β = 102.36(4), γ = 99.54(4)°. A colorless square bipyramid of **5** with dimensions 0.17 × 0.20 × 0.30 mm was used for data collection at –100 °C. It displayed the tetragonal $I4_1/a$ symmetry with lattice parameters a = 11.685(1), c = 19.158(1) Å. The data sets, including symmetry equivalent and redundant reflections, were merged as unique reflection data sets for uses in structure solution with the program SHELXS97[15] and full-matrix least-squares refinements on F^2 with the program SHELXL97.[16] The atomic positions and anisotropic displacement parameters were refined for all non-hydrogen atoms. The H atoms were treated as riding, following the HFIX/AFIX instructions, they were given an isotropic displacement parameter equal to –1.2 times (–1.5 for terminal –CH_3) the Ueq of the parent C atom. The main crystallographic data for **1** and **5** are reported in **Table 1,** comparatively with those of the other bipyrazole derivatives **2**-**4**. The corresponding CIF files are available at the Cambridge crystallographic data center[17] and can be obtained free of charge with the CCDC numbers 1879242 (**1**) and 1877532 (**5**).

2. 3. Computational Details

Geometries were optimized without any symmetry constraints at the DFT (density functional theory) level. Calculations were performed using the tools implemented in the program Gaussian03W[18] with B3LYP functional and 6-31G(d,p) and 6-311++G(d,p) basis sets. The quantum mechanical code Dmol^3 was also used in full geometry optimization tasks by minimization of the total energy with B3LYP hybrid functional, effective core potentials and double numerical plus polarization DNP basis sets.[19,20] The GaussView 5.0.8[21] and Materials studio[22] interfaces were used to develop and visualize the molecular structures and their calculated properties.

3. Results and Discussion

The information that will be presented and discussed below concerns five molecules of bipyrazole derivatives, based on a 3,3'-bipyrazole core substituted at the 1,1' and 5,5' positions by different chemical R groups (**Fig. 1**).

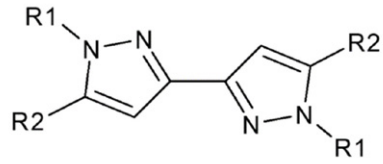

1 : R1 = o-$NO_2C_6H_4$ – R2 = –$CH(CH_3)_2$
2 : R1 = o-$NO_2C_6H_4$ – R2 = –$CH_2CH_2CH_3$
3 : R1 = p-$NO_2C_6H_4$ – R2 = –$CH(CH_3)_2$
4 : R1 = –$CH_2C_6H_4$ R2 = –$CH(CH_3)_2$
5 : R1 = –H R2 = –$CH(CH_3)_2$

Fig. 1. Molecular structure of compounds considered in this work

All these molecules are centrosymmetric and their comparison deserves to be conducted to understand how the different functional groups act on their geometry, on their packing in solid state and thus on their chemical properties. The crystal structures of several compounds, the molecular geometries and the indices of global reactivity will be analyzed comparatively to evaluate these substituents effects. All the molecules considered in this work are formed with a 3,3'-bipyrazole core and bear R1 substit-

uent, hydrogen, nitro-phenyl or benzyl, attached to the N atom of the pyrazole ring at the 1,1' positions and R2 substituent, either linear propyl or isopropyl group, attached to the neighboring C atom at the 5,5' positions.

3. 1. Crystal Structure of 1

The structure displays the triclinic symmetry and is described in the $P\bar{1}$ space group which is the most common for organic crystals. The unit cell of dimensions a = 7.7113(8), b = 12.3926(14), c = 12.9886(12) Å, α = 92.008(8), β = 102.251(8), γ = 99.655(9)° contains two molecules of 1,1›-(2-nitrophenyl)-5,5›-isopropyl bipyrazole (**Fig. 2**) in which phenyl rings are connected to the nitrogen atom of the 3,3'-bipyrazole core while the isopropyl group is attached to the neighboring carbon atom.

The calculated density of 1.282 g.cm^{-3} is in line with the expectations for such a compound. The two molecules in the lattice of **1** are chemically equivalent but, as can be seen with the atom labels indicated in **Fig. 2**, they are crystallographically independent. Each molecule is placed on an inversion center located in the middle of the C1C1 and C21C21 bonds. The crystal structure of **1** brings a proof that the isolated regio-isomer adopts the form 1,1'-bis(2-nitrophenyl)-5,5'-diisopropyl-3,3'-bipyrazole which well agrees with the results of our previous works.[12,13,23,24]

3. 2. Crystal Structure of 5

The structure of 5,5'-di-isopropyl-1,1'H-3,3'-bipyrazole was solved from low-temperature diffraction data. Nevertheless, some disorder was observed at the isopropyl groups that deviate from the mean plane of the molecule and has been considered in the structural refinements. The compound **5** crystallizes with the tetragonal $I4_1/a$ symmetry and lattice parameters a = b = 11.684(1), c = 19.158(1) Å. The unit cell contains 8 molecules, which leads to a calculated density of 1.109 g · cm^{-3}. The eight molecules are symmetry-related and placed on inversion centers lying at the middle of the C1C1 bond as shown in **Fig. 3.**

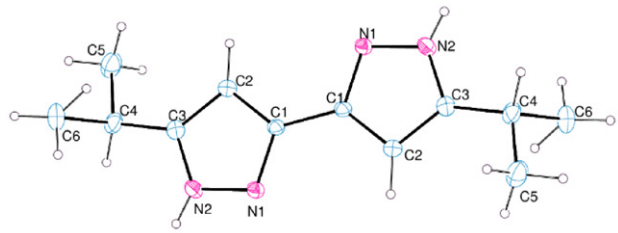

Fig. 3. The molecular unit of **5** with its inversion center in the middle of the C1C1 bond.

The knowledge of this crystal structure was decisive to provide proof of the predominance of the tautomer that the theory predicts with the best stability, i.e. the tautomer having the H positions at N2 atoms.[25]

3. 3. Effect of the Substituents on the Molecular Arrangement in the Solid State

The structure of compounds and the crystal morphologies are often strongly related whereas the arrange-

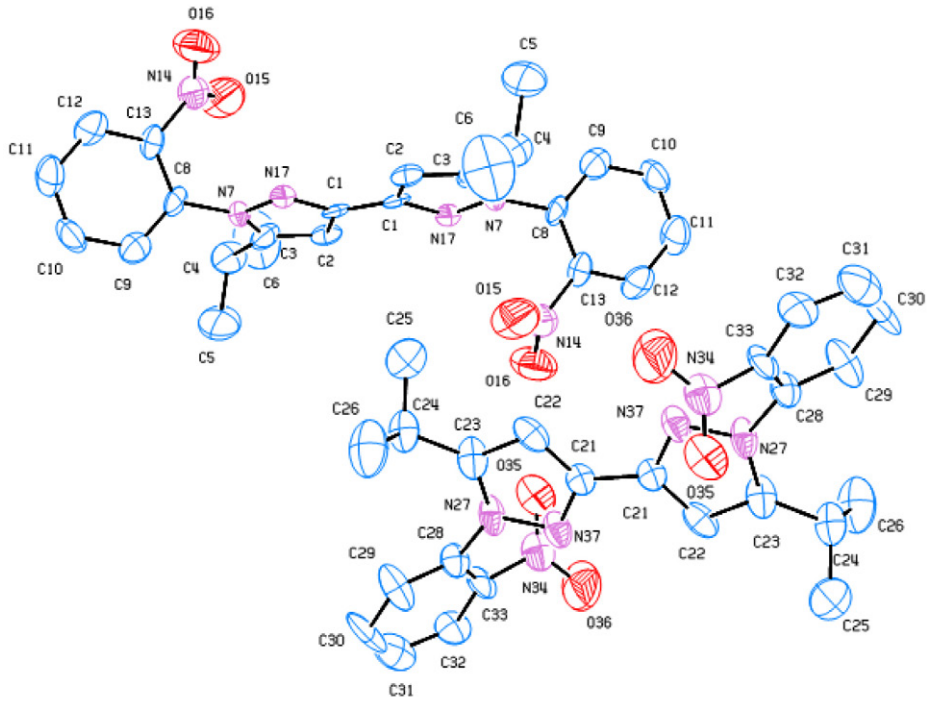

Fig. 2. Representation of the independent molecules of **1**. The H atoms are omitted for clarity.

ment of atoms or molecules in the crystal may condition the solid state properties of a compound such as color, solubility, density, stability, reactivity… Good knowledge of the molecular stacking gives advantages in understanding the specific chemical behaviors. Also, having some control over the crystal structures could be a way to modify the properties of a system in the desired direction. Comparison of the crystal structures of bipyrazole derivatives having the same 3,3'-bipyrazole core is a useful source of information on the relationships which may exist between the arrangement of molecules and the presence or the nature of chemical groups R1 and R2.

As it could be seen in **Fig. 4**, the molecules are packed in different ways in the various solid compounds. Nevertheless, some resemblance can be found for compounds **1** and **5** with overlapping of the molecular cores along the a-axis direction.

This could have given rise to π-stacking interactions in these compounds if the molecules had been close enough. In the isomeric compounds **1** and **2**, the molecules only differ by their R2 substituent, either iso- or linear propyl group, yet their molecular packing in the crystal does not show obvious similarities. It is the same between isomeric compounds **1** and **3**, with molecules bearing the same groups R1 and R2 but differing by the fixation of the nitrophenyl group, either in the ortho or para position. Curiously, a certain analogy could be found in the alignment of the molecules that form zig-zag images in the projections along the c-axis in the **2** and **3** isomers (varying both by the nature of R1 and R2 substituents) but also in projection along the a-axis in compound **4.** Even if the three molecules characterizing these compounds have the same isopropyl R2 substituent (like also compound **5**), they are however differentiated by their R1 substituent changing from o-$NO_2C_6H_4$ in **2** to p-$NO_2C_6H_4$ in **3** and to -$CH_2C_6H_5$ in **4** (it is -H in **5**). Under these conditions, it is extremely difficult to draw conclusions and establish a simple relationship between the geometry of the molecule, the nature and the size of the substituents and a type of molecular packing in the solid state material.

3. 4. Effect of the Substituents on the Crystal Parameters

The crystal structures of the compounds **1** and **5** are compared with other solid state structures we previously determined for the bipyrazole derivatives **2-4.**[13,23,24] The main data about these structures are collected in **Table 1.** It is obvious that changing the nature of the R1 and R2 moieties attached to the 3,3'-bipyrazole core of the molecule has great consequences on the crystallographic parameters of the solid compounds. Except in bipyrazole **2**, all the molecules contain an isopropyl group at the R2 position. The crystal symmetry of the solid compounds roughly decreases with the size of the R1 group attached to the nitrogen, from tetragonal in **5** to orthorhombic in **2**, monoclinic in **4** and finally triclinic in **1**. The three isomers **1**, **2** and **3** have rather unlike structures in which both the molecular packing and the symmetry are modified. Note that it is the isomer **2**, with a propyl linear chain at R2 position which displays the highest calculated density. Its unit cell is also twice as large as those of **1** and **3** but contains twice as many molecules.

From **2** to **1**, the replacement of the linear propyl by an isopropyl R2 fragment leads to a less symmetrical arrangement of the molecules ($P\bar{1}$ instead of P222) and a decrease in the density for the crystal. Conversely, the crystal symmetry evolves from $P\bar{1}$ to $P2_1/c$ and the density

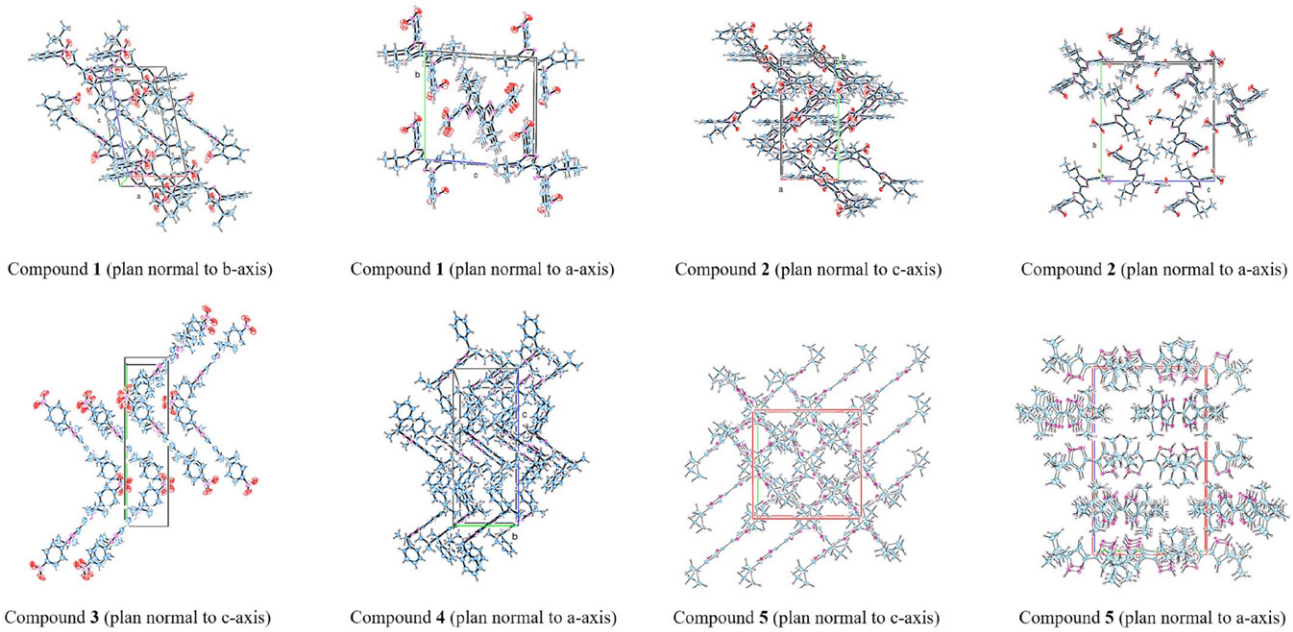

Fig. 4. Arrangement of molecules (projections) in the crystal structures for compounds **1**-**5**

Table 1. The main experimental crystal parameters of 3,3'-bipyrazole compounds **1-5**

Compound	$C_{24}H_{24}N_6O_4$ **1**	$C_{24}H_{24}N_6O_4$ **2**	$C_{24}H_{24}N_6O_4$ **3**	$C_{26}H_{30}N_4$ **4**	$C_{12}H_{18}N_4$ **5**
R1	o-$NO_2C_6H_4$–	o-$NO_2C_6H_4$–	p-$NO_2C_6H_4$–	–$CH_2C_6H_5$R2	–H
R2	–$CH(CH_3)_2$	–$CH_2CH_2CH_3$	–$CH(CH_3)_2$	–$CH(CH_3)_2$	–$CH(CH_3)_2$
M	460.47	460.47	460.47	398.53	218.29
Z	2	4	2	4	8
D (g.cm^{-3})	1.282	1.354	1.327	1.189	1.109
F(000)	484	968	484	856	944
Crystal system	Triclinic	Orthorhombic	Monoclinic	Monoclinic	Tetragonal
Space group	P	P222	$P2_1/c$	$P2_1/c$	$I4_1/a$
a (Å)	7.7113(8)	7.720(1)	6.1760(11)	9.6539(16)	11.6845(13)
b (Å)	12.3926(14)	16.200(2)	23.036(4)	9.7888(17)	11.6845(13)
c (Å)	12.9886(12)	18.058(2)	8.1040(14)	23.562(4)	19.1580(12)
α (°)	92.008(8)	90	90	90	90
β (°)	102.251(8)	90	91.190(15)	90	90
γ (°)	99.655(9)	90	90	90	90
V (Å^3)	1192.57(31)	2258.5(5)	1152.7(4)	2226.6(6)	2615.6(6)

*Z represents the number of chemical formula units contained in a unit cell

increases when the R1 nitro-phenyl group fixation changes from ortho in **1** to para in **3**. The bipyrazole compounds **3** and **4** adopt the same crystal symmetry $P2_1/c$, yet the nature of the group R1, either nitro-phenyl or benzyl, has consequences on the molecular geometry and it influences the molecular packing that is quite different in the two compounds. The density in **4** is lower than in **3** which leads to less compact stacks for the two molecules which do not contain heteroelement since **5**, with the smallest molecules, has also the lowest density.

3. 5. Effect of the Substituents on the Geometry of the Molecules

The geometry of the molecules encountered in the five 3,3'-bipyrazole compounds under study can be characterized using some specific parameters. The selected geometrical parameters such as bond distances, bond angles and torsion angles are schematically represented in **Fig. 5**.

Their experimental values taken from the X-ray single crystal structures are given in **Table 2** with the values measured after geometry optimization without any constraint of isolated molecules. A comparison of these quantities is a way to evaluate both the packing constraints in the solid and the effects of the nature of R1 and R2 moieties. First of all, it is interesting to note the good correlation between the experimental and theoretical values in each series of parameters selected to describe the geometry of the molecules. Whether in calculations with 6-31G(d,p), 6-311++G(d,p) in Gaussian03W or with DNP and effective core potentials in Dmol^3, the geometry optimizations lead to very similar results and the correlation coefficients R^2 are mostly higher than 0.985. However, lower values (0.786–0.801) were found for the bond angles in compound **5** which attest to the distortion of the molecule in the crystal. With hydrogen as R1 group, the molecule of **5** is rather small and subjected to greater constraints when it is arranged in the solid state. This is mainly due to the proximity of other molecules with which it is involved in intermolecular interactions. In other cases, the high correlation coefficients confirm a very slight distortion of the bipyrazole core. The main reason is the larger size of the R substituents that hold away the molecules from each other and thus protect the bipyrazole core from deformations by shifting the intermolecular interactions to the molecule periphery.

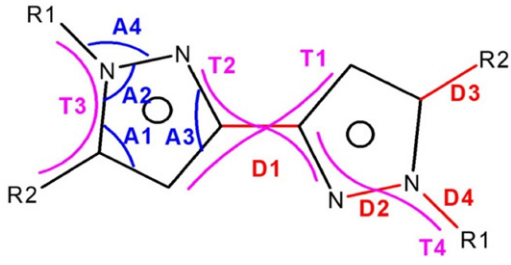

Fig. 5. The parameters selected to describe the geometry of bipyrazole molecules.

The resonance effects and ring properties have been discussed for pyrazole compounds[26] and a comparison of the geometrical parameters between pyrazoles and bipyrazoles compounds could also have provided interesting information. This would deserve to be investigated in a future work which could also include effects of neighbouring molecules, as for example fluorinated phenols that may provide infinite supramolecular motifs.[27]

3. 5. 1. Bond Distances

Between the C,C-linked pyrazole rings, the calculated bond distance D1 is always shorter than the experimental distance for the five bipyrazole compounds. Such a

Table 2. Experimental and DFT (G03W and Dmol^3) calculated values for selected geometrical parameters (Å, °) in compounds **1-5**

	1			**2**				**3**				**4**				**5**			
R1		o-$NO_2C_6H_4$–			o-$NO_2C_6H_4$–			p-$NO_2C_6H_4$–				$-CH_2C_6H_5$				–H			
R2		–$CH(CH_3)_2$			–$CH_2CH_2CH_3$			–$CH(CH_3)_2$				–$CH(CH_3)_2$				–$CH(CH_3)_2$			
Method	dmol^3	G03W	G03W	Exp.	dmol^3	G03W	G03W	Exp.	dmol^3	G03W	G03W	Exp.	dmol^3	G03W	G03W	Exp.	dmol^3	G03W	G03W	Exp.
	B3LYP	6-31G	6-311+G		B3LYP	6-31G	6-311+G		B3LYP	6-31G	6-311+G		B3LYP	6-31G	6-311+G		B3LYP	6-31	G6-311+G	
D1	1.454	1.459	1.458	1.469	1.457	1.458	1.458	1.468	1.454	1.458	1.458	1.461	1.454	1.460	1.460	1.473	1.457	1.460	1.459	1.468
D2	1.360	1.363	1.361	1.369–1.367.	1.358	1.362	1.360	1.366–1.363.	1.362	1.364	1.362	1.367	1.355	1.357	1.355	1.375	1.349	1.352	1.350	1.323
D3	1.502	1.508	1.507	1.479–1.501.	1.498	1.501	1.499	1.482–1.493.	1.505	1.510	1.509	1.497	1.502	1.509	1.507	1.497	1.491	1.496	1.495	1.493
D4	1.418	1.418	1.415	1.422–1.431.	1.414	1.414	1.414	1.424–1.426.	1.413	1.415	1.416	1.423	1.463	1.456	1.457	1.440	1.005	1.079	1.008	1.043
R^2	0.984	0.983	0.984		0.988	0.985	0.987		0.995	0.994	0.996		0.949	0.972	0.972		0.995	0.998	0.995	
A1	105.2	105.4	105.4	103.9–105.8.	105.6	105.5	105.5	105.0–105.4.	105.8	105.5	105.6	105.0	105.8	105.8	105.9	106.6	105.4	105.4	105.4	109.2
A2	112.7	112.8	112.6	114.0–112.3.	112.5	112.6	112.5	113.3–112.8.	111.7	112.2	112.0	112.7	112.2	112.6	112.4	111.7	113.6	113.8	113.5	109.4
A3	112.4	111.6	111.4	112.1–112.2.	111.4	111.5	112.5	112.1–111.5.	111.3	111.4	111.3	111.7	111.1	111.2	111.0	112.4	111.2	111.4	111.2	110.1
A4	117.5	118.0	117.9	115.6–118.8.	118.9	118.1	118.1	118.8-118.5.	117.9	117.4	117.7	129.1	117.7	118.0	118.5	117.9	118.9	118.8	118.8	124.2
R^2	0.997	0.992	0.988		0.996	1.000	0.996		0.971	0.950	0.961		0.988	0.984	0.984		0.801	0.786	0.801	
T1	179.4	180.0	180.0	180.0	177.8	180.0	180.0	178.1	178.6	179.9	180.0	180.0	172.1	179.8	179.1	180.0	172.7	180.0	180.0	180.0
T2	179.4	180.0	180.0	180.0	176.5	180.0	180.0	179.1	179.8	180.0	180.0	180.0	174.4	179.8	179.3	180.0	176.6	180.0	180.0	180.0
T3	1.3	6.3	6.3	6.5	3.1	1.6	0.7	5.1	0.7	1.2	1.5	14.6	5.6	3.2	3.5	8.5	1.3	0.2	0.2	0.0
T4	178.7	17894	179.0	176.9	178.2	177.9	178.3	177.9	178.8	178.7	179.0	178.9	175.2	176.8	177.4	175.6	179.5	180.0	180.0	180.0
R^2	1.000	1.000	1.000	1.000	1.000	1.000	1.000	1.000	1.000	1.000	1.000	1.000	0.999	1.000	1.000	1.000	0.999	1.000	1.000	1.000

bond lengthening in the crystal is an effect of intermolecular interactions that reduce the electron delocalization on this part of the molecule.

The D2 parameter designates the N-N bond within the pyrazole ring. It has been reported that its length varies over a wide range, from 1.234 to 1.385 Å,[28] with the nature of the substituents bound to the N atoms (here, these are the groups R1). The shortest N-N experimental bond length of 1.323 Å is found in compound **5**. The values of 1.369 Å (N7-N17) and 1.367 Å (N27-N37) measured in bipyrazole **1** structure are close to those measured in the isomers **2** (1.363 Å and 1.366 Å) and **3** (1.369 Å). The longer D2 bond of 1.375 Å in **4** indicates a certain reduction in aromaticity compared to compounds **1**, **2**, **3** in which both D1 and D2 bonds have a more pronounced π character explaining their shortening.

The experimental D3 bond lengths from the isopropyl R2 group to pyrazole ring, of 1.501 Å (C3-C4) and 1.479 Å (C23-C24) in bipyrazole **1** are found slightly shorter than the methyl-phenyl bond of 1.52 Å in toluene.[29] Nevertheless, they do not deviate too much from the D3 distances to isopropyl in **3** (1.493 Å), to propyl in **2** (1.482, 1.493 Å) and from the slightly higher D3 distance of 1.497 Å to benzyl measured in **4.**

The D4 links between the group R1 and the N atom of the pyrazole ring have very close length in the three isomers, 1.422-1.431 Å in **1**, 1.424-1.426 Å in **2** and 1.423 Å in **3** but they are significantly elongated to 1.440 Å in **4** and even more to 1.493 Å in **5**. This reinforces the affirmation made above that the methylene group placed between the pyrazolic and phenyl rings in compound **4** breaks the electron delocalization, which leads to a more covalent and longer D4 bond. When the nitrogen atom is directly bonded to the phenyl ring as in compounds **1**–**3**, the electron delocalization can extend to the phenyl ring and the D4 distance is then shortened.

Besides, according to the literature reports, the C=N bond (adjacent to N-N) in pyrazole compounds ranges from 1.313 to 1.320 Å,[28] which is slightly shorter than the experimental bonds of 1.328 and 1.329 Å in compound **1** and 1.333 Å in compound **5** but also than the calculated bonds ranging from 1.332 to 1.336 in compounds **1**–**5**. It can also be noted that the N-O bond lengths ranging from 1.190 to 1.214 Å in compound **1** are slightly shorter than those from 1.201 to 1.227 Å in isomers **2** and **3**.

In summary, the groups R1 and R2 act differently on the geometry of the molecules. The group R1 does not have a very marked effect while the nature of the group R2 greatly influences the bond lengths and the geometry of the bipyrazole core in these C,C-linked pyrazole compounds.

3. 5. 2. Bond Angles

The careful examination of experimental angles may provide additional information. The internal C-C-N pyrazolic A1 angle is very close in compounds **2** and **3** (105.5 and 105.7°), it is 103.9 and 105.8° in the two independent molecules of **1**. Instead, it is more obtuse in **4** (106.6°) and in **5** (109.2°) which have not R1 nitrophenyl substituents.

Also, the N-N-C angle, A2, centered on the nitrogen atom outwardly bonded to R1, displays close values in isomers 1 and 2 only differing by their R2 substituent, which leads to claim that the R2 substituent has a very weak influence. Besides, replacing in **1** of the o-nitrophenyl R1 group either by a p-nitrophenyl (**3**) or by a benzyl (**4**) only causes a small reduction by about 1° of this angle.

On the other hand, the angles A3 or N-C-C centered on the C atom involved in pyrazole rings interconnections measured at 112.1–112.2° in the structure of **1** remain in the order of the A3 angles in other three bipyrazole compounds **1**-**5**. The A3 angle appears to be independent on the substituents linked to the 3,3'-bipyrazole core.

Finally, values of the C-N-N external pyrazolic A4 angle, 115.6° and 118.8° in the two crystallographically independent molecules of bipyrazole **1**, are quite similar to A4 angles of 118.8 and 118.5° in compound **2**. They lie between the slightly weaker angles of 117.9° in **4** and the markedly higher angles of 124.2 and 129.1° in bipyrazole **5** and **3**, respectively. Of course, only one A4 value is given for the centrosymmetric compounds **3**, **4** and **5** where the molecules are symmetry-related.

3. 5. 3. Torsion Angles

Looking first at the torsion angles inside the R1 groups (not reported here) between the nitro groups and the benzyl ring to which they are attached, a difference between isomers **1** and **2** can be noticed. These isomers differing only by the nature of their fragments (linear or branched), these angular values reflect both the steric repulsions between the propyl and nitro groups and the effects of intermolecular interactions. Both their experimental values of 50.3–56.1° in **1**, 48.5–48.9° in **2** and their calculated values of ~38 and 32° in the geometry-optimized isolated molecules give a measure of the amplitude of these effects. This angle of ~1.5° in the optimized molecule of **4** is in agreement with an electronic delocalization on the whole R1 para nitrophenyl fragment. Similar changes occur for the pyrazole-to-benzyl torsion angles of 42.3 and 70.2° in crystal of **1**, 48.3 and 70.7° in crystal of **2** while they are ~60° in the optimized isolated molecules of **1** and **2** (and 48° in **3**).

Let's go back now to the specific parameters selected above. The relative position of the two pyrazole rings is characterized by T1 and T2 torsion angles which remain very close to 180° in all the compounds, proving the negligible effect of the R1 and R2 substituents on the bipyrazole core planarity.

The T4 torsion angles are associated with the relative positions of the R1 (at N atom) group and of the pyrazole ring. The comparison of their values in the crystals of **1**, **2** and **3**, where the phenyl ring is directly connected to the pyrazole, shows that this angle varies in the range 176.7–178.9°. The T4 angle is reduced to 175.6 ° in crystal of **4** where the phenyl ring is linked to pyrazole through a CH_2 group. As stated above, this is linked to the role played by the methylene group with regard to aromaticity.

Finally, as might be expected, the experimental values of T3 angle between R1 and R2 groups indicate that this torsion angle is the most sensitive to the nature of the substituents attached to the pyrazole rings. Switching from a linear to a branched propyl group R2, from **2** to **1,** causes an increase by 1.4° in the T3 angle. By continuing the changes, from **1** to **3,** by fixing the nitro group in the para rather than in the ortho position, the angle T3 is greatly affected and becomes twice as high (14.6 instead of 6.5°). Instead, from **3** to **4**, replacing the paranitrophenyl group with a benzyl group in 4 gives a decrease down to 8.5° of the T3 angle which thus decreases along the series of investigated bipyrazoles in the order **3** > **4** > **1** > **2.**[13,23,24] As in compound **5**, the group R1 is hydrogen and T3 has a zero value, it is not taken into account in this comparison.

3. 6. Effect of Substituents on the Global Reactivity Parameters

The characteristics of the frontier orbitals (HOMO and LUMO) and especially their energy levels are important parameters to understand the behavior of a molecule during a chemical reaction.[29,30] The LUMO will mainly act as an electron acceptor while the HOMO will act as electron donor and the difference in their energy levels represents the stability of the molecule. Measuring the gap ($E_{HOMO} - E_{LUMO}$) is therefore a means of evaluating the reactivity of the molecule[31] and the smaller the gap, the greater the chemical reactivity.[32] The ease of polarization of such a molecule induces an increase in the reactivity by the transfer of electrons to an acceptor.[33] To compare the bipyrazole molecules having different R substituents, the energy gaps calculated for the DFT optimized molecules **1–5** are given in **Table 3** with frontier orbital, total and binding energies. The largest gaps are calculated for the lowest reactive molecules of **4** and **5**. Replacing in **4** the benzyl by nitro phenyl groups (fixed either in ortho or para position) leads to molecules **1** and **3** and increases significantly the reactivity. The energy gap is quite similar for the three isomers **1**, **2** and **3** but shows however a tendency for the isomer **1** to display the lowest values. This indicates a weak sensitivity to the position of the nitro groups attached to the benzyl rings but also to the nature of the alkyl groups linked to the pyrazole rings. Whatever the theory level, the total energy and binding energy are lower for the isomer **3** indicating its better stability.

Table 3. DFT calculated energies (total, binding and frontier orbital) and resulting reactivity indices for molecules **1-5**

	1			**2**			**3**			**4**			**5**		
R1		o-$NO_2C_6H_4$– $-CH(CH_3)_2$			o-$NO_2C_6H_4$– $-CH_2CH_2CH_3$			p-$NO_2C_6H_4$– R2 $-CH(CH_3)_2$			$-CH_2C_6H_5$ $-CH(CH_3)_2$			–H $-CH(CH_3)_2$	
Method	Dmol^3 B3LYP	G03W 6-31G	G03W 6-311++G	Dmol^3 B3LYP	G03W 6-31G	G03W 6-311++G	Dmol^3 B3LYP	G03W 6-31G	G03W 6-311++G	Dmol^3 B3LYP	G03W 6-31G	G03W 6-311++G	Dmol^3 B3LYP	G03W 6-31G	G03W *6-311++G*
Etot Ha	–1650.63467	–1558.22428	–1558.60332	–1650.63495	–1558.22370	–1558.60432	–1650.65967	–1558.24802	–1558.62493	–1302.99776	–1227.88206	–1228.14922	–561.03455	–529.87299	–529.99958
Ebinding Ha	–107.35615		–	–107.35643			–107.38115			–89.82212	–	–	–36.60678	–	–
Ebinding eV/atom	–50.36743	–	–	–50.36756	–	–	–50.37916	–	–	–40.73643	–	–	–45.27827	–	–
HOMO Ha	–0.21776	–0.21114	–0.22490	–0.21867	–0.21206	–0.22513	–0.23451	–0.22729	–0.23964	–0.19235	–0.19867	–0.21090	–0.213422	–0.20445	–0.21923
LUMO Ha	–0.09160	–0.08328	–0.09692	–0.09143	–0.08020	–0.09475	–0.10453	–0.09543	–0.11211	–0.00175	–0.00579	–0.02334	0.004604	0.01197	–0.01216
HOMO ev	–5.93	–5.75	–6.12	–5.95	–5.77	–6.13	–6.38	–6.18	–6.52	–5.23	–5.41	–5.74	–5.81	–5.56	–5.97
LuMO ev	–2.49	–2.27	–2.64	–2.49	–2.18	–2.58	–2.84	–2.60	–3.05	–0.05	–0.16	–0.64	0.13	0.33	–0.33
gap	3.43	3.48	3.48	3.46	3.59	3.55	3.54	3.59	3.47	5.19	5.25	5.10	5.93	5.89	5.63
µM debye	0.00	0.00	0.00	0.77	0.37	0.38	0.00	0.00	0.00	0.01	0.10	0.09	0.01	0.04	0.04
I	5.93	5.75	6.12	5.95	5.77	6.13	6.38	6.18	6.52	5.23	5.41	5.74	5.81	5.56	5.97
A	2.49	2.27	2.64	2.49	2.18	2.58	2.84	2.60	3.05	0.05	0.16	0.64	–0.13	–0.33	0.33
η	1.72	1.74	1.74	1.73	1.79	1.77	1.77	1.79	1.73	2.59	2.62	2.55	2.97	2.94	2.82
µ	–4.21	–4.01	–4.38	–4.22	–3.98	–4.35	–4.61	–4.39	–4.79	–2.64	–2.78	–3.19	–2.84	–2.62	–3.15
χ	4.21	4.01	4.38	4.22	3.98	4.35	4.61	4.39	4.79	2.64	2.78	3.19	2.84	2.62	3.15
σ	0.58	0.57	0.57	0.58	0.56	0.56	0.57	0.56	0.58	0.39	0.38	0.39	0.34	0.34	0.35
ω	5.16	4.61	5.51	5.14	4.41	5.33	6.02	5.37	6.60	1.34	1.47	1.99	1.36	1.16	1.76

The electric dipolar moment μ_M can be calculated for the isolated molecules, it measures the separation of positive and negative electric charges within a system. In such molecules having the same substituents on each of the two pyrazole rings, it is not so surprising that no global polarity was calculated for the molecules after geometry optimization. However, the electric dipole moment calculated for the initial geometry (the one in the crystal) that are given in **Table 3** may have a non-zero value, this is the case for the bipyrazole **2** molecule. The orthorhombic symmetry of the crystal structure is such that the atoms of the molecule are not constrained to conform to an inversion center, which leads to a polarity (0.33 to 0.77D depending on the level of theory) reflecting the intermolecular interactions and packing constraints. Contrarily, in molecules of **1**, **3** and **4** the electrons are more equally distributed. The almost-zero (0.04D) dipolar moment in the molecule of **5** suggests that the angular deformations (see above) result rather from the disorder phenomena of the group R2

A series of theoretical indices based on DFT, otherwise known as global reactivity descriptors, are also often used to measure the relative stabilities of isomers and to evaluate the chemical reactivity of molecules. Their values are defined in literature as depending on the ionization energy (I) and electron affinity (A), also related to the energy of the frontier orbitals according to $I = -E_{HOMO}$ and $A = -E_{LUMO}$.[25] The electronegativity is $\chi = (I+A)/2$, the chemical hardness is $\eta = (I-A)/2$ and softness $\sigma = \eta^{-1}$, the electronic chemical potential $\mu = -(I+A)/2$ and the global electrophilicity index $\omega = \mu^2(2\eta)^{-1}$. These descriptors have been calculated using these relations and their values are reported in **Table 3**.

The deviations in the chemical potential µ (and in the electronegativity χ of opposite sign) associated with changes in the substituting moieties describe the tendency of gaining electrons towards the molecule.[34] According to the µ values calculated (whatever the theoretical level), the molecules are classified in the order **4** ≈ **5** > **2** ≈ **1** > **3**, so that the best acceptor molecules are **4** and **5** while the molecule **3** is that which donates its electrons the most easily. Unlike nitro-phenyl, the benzyl group gives to molecules a greater electron-accepting power. Also, the fixation of the nitro group in position ortho makes the molecule more electron-accepting than its fixation in position para. Based on the molecules examined in this work, the presence of branches on the aliphatic chain in the R2 group decreases the ability of the molecule to accept electrons.

The chemical hardness (η) is the inverse of chemical softness (σ) which estimates the capacity of a group of atoms to receive electrons[35] and is directly

linked to the resistance to deformation or to the polarization of the electronic cloud.[36] The values calculated for η lead to divide the molecules studied in two groups: first the isomers **1**, **2** and **3** with low values of chemical hardness ranging from 1.72 to 1.79 eV and secondly, the compounds **4** and **5** with significantly higher values of chemical hardness, 2.55 to 2.97 eV. This means that the benzyl group induces greater resistance to deformation than nitro phenyl. The results are in agreement with what has been reported on the small variations caused by the nature of the R2 alkyl groups and the position (on the phenyl ring) of the nitro groups.[37]

Finally, the global electrophilicity index (ω) gives a measure of the stabilization energy involved in a process during which a molecule acquires an additional electronic charge from its environment.[38] It is interesting to note that a correlation has been established between the electrophilic index and the toxicity[39] and that the organic compounds with the highest electrophilicity indices would be the most toxic. Moreover, it has been stated that the global electrophilicity index provides information about the electrophilic or nucleophilic nature of a medicinal compound.[39] Thus the classification according to the decreasing values of ω appears in order **3** > **1** > **2** > **4** ≈ **5** for the molecules of bipyrazole derivatives studied, with very lower indices for the last two compounds, particularly for the molecule **4** comprising a benzyl radical as R1 fragment. With high electrophilicity indices, the molecules of the three isomers **1–3** are characterized with a strong electrophile character.

4. Conclusion

The isolated regio-isomer obtained by the N-arylation reaction between 5,5'-diisopropyl-3,3'-bipyrazole and 2-fluoronitrobenzene, adopts the form named 1,1'-bis(2-nitrophenyl)-5,5'-diisopropyl-3,3'-bipyrazole. The nature of the substituents attached to the 3,3'-bipyrazole unit was examined in five bipyrazole derivatives to evaluate their influence both on the molecular structure (geometry of isolated molecule) and on the molecular arrangement in the solid state (crystal structure and molecular interactions). The changes in the crystallographic characteristics (lattice, symmetry…) and in the arrangement of molecules (packing, interactions…) within the crystals are very important. A good correlation is observed between calculated (optimized geometries) and experimental (in the crystal) parameters with regard to the geometric characteristics of the bipyrazole molecules. The global reactivity indices were used to classify the molecules according to their properties and clearly, the molecule with a benzyl substituent stands out from the **3** isomers with a nitrophenyl group.

Disclosure statement

No potential conflict of interest was reported by the author(s)

5. References

1. B. F. Abdel-Wahab, K. M. Dawood, *Arkivoc*, **2012**, *i,* 491–545. **DOI:**10.3998/ark.5550190.0013.112
2. H. M. Faidallah, S. A. Rostom, K.A. Khan, *Arch. Pharmacal Res.* **2015**, *38*, 203–215. **DOI:**10.1007/s12272-014-0392-7
3. I. Bouabdallah, L. A. M'barek, A. Zyad, A. Ramdani, I. Zidane and A. Melhaoui, *Nat. Prod. Res.* **2007**, *21*, 298–302. **DOI:**10.1080/14786410701192801
4. S. Singh, V. Punia, C. Sharma, K. R. Aneja, O. Prakash, R. Pundeer, *J. Heterocycl. Chem.* **2015**, *52*, 1817–1822. **DOI:**10.1002/jhet.1505
5. I. Bouabdallah, I. Zidane, B. Hacht, A. Ramdani, R. Touzani, *J. Mater. Environ. Sci.* **2010**, *1*, 20–24.
6. K. Tebbji, A. Aouinti, A. Attayibat, B. Hammouti, H. Oudda, M. Benkaddour, S. Radi, S. Nahle, *Ind. J. Chem. Tech.* **2011**, *18*, 244–253.
7. Y. Murakami and T. Yamamoto, *Bull. Chem. Soc. Jpn.* **1999**, *72*, 1629–1635. **DOI:**10.1246/bcsj.72.1629
8. O. Heitaro, I. Takashi, S. Kazuhisa, O. Tetsuo, Bipyrazole derivative, and medicine or reagent comprising the same as active component, US Patent No. 6, 121, 305, date of patent 19 September 2000.
9. I. L. Dalinger, K. Y. Suponitsky, T. K. Shkineva, D. B. Lempert, A. B. Sheremetev, *J. Mater. Chem. A*, **2018**, *6*, 14780–14786. **DOI:**10.1039/C8TA05179H
10. H. Beyzaei, Z. Motraghi, R. Aryan, M. M., Zahedi, A. Samzadeh-Kermani, *Acta Chim. Slov.* **2017**, *64(4)*, 911–918. **DOI:**10.17344/acsi.2017.3609
11. E. H. El-Sayed, A. A. Fadda, A. M. El-Saadaney, *Acta Chim. Slov.* **2020**, *67(4)*, 1024–1034. **DOI:**10.17344/acsi.2019.5007
12. I. Bouabdallah, R. Touzani, I. Zidane, A. Ramdani, S. Radi, *Arkivoc*, **2006**, *xiv*, 46–52. **DOI:**10.3998/ark.5550190.0007.a10
13. I. Bouabdallah, A. Ramdani, I. Zidane, R. Touzani, D. Eddike, S. Radi, A. Haidoux, *J. Mar. Chim. Heterocycl.* **2004**, *3*, 39–44.
14. CrysAlis'Red 171 software package, Oxford diffraction Ltd, Abingdon, United Kingdom, 2004.
15. G.M. Sheldrick, SHELXS 97. A program for crystal structures solution, University of Göttingen. Germany 1997.
16. G.M. Sheldrick, SHELXL97. A program for refining crystal structures, University of Göttingen. Germany 1997.
17. The Cambridge Crystallographic Data Center (CCDC) <http://www.ccdc.cam.ac.uk/conts/retrieving.html >.
18. M. J. Frisch, G. W. Trucks, H. B. Schlegel, G. E. Scuseria, M. A. Robb, J. R. Cheeseman, J. A. Montgomery, Jr., T. Vreven, K. N. Kudin, J. C. Burant, J. M. Millam, S. S. Iyengar, J. Tomasi, V. Barone, B. Mennucci, M. Cossi, G. Scalmani, N. Rega, G. A. Petersson, H. Nakatsuji, M. Hada, M. Ehara, K. Toyota, R. Fukuda, J. Hasegawa, M. Ishida, T. Nakajima, Y. Honda, O. Kitao, H. Nakai, M. Klene, X. Li, J. E. Knox, H. P. Hratchian, J. B. Cross, V. Bakken, C. Adamo, J. Jaramillo, R. Gomperts, R. E. Stratmann, O. Yazyev, A. J. Austin, R. Cammi, C. Pomelli, J. W. Ochterski, P. Y. Ayala, K. Morokuma, G. A. Voth, P. Salvador, J. J. Dannenberg, V. G. Zakrzewski, S. Dapprich, A. D. Daniels, M. C. Strain, O. Farkas, D. K. Malick, A. D. Ra-

buck, K. Raghavachari, J. B. Foresman, J. V. Ortiz, Q. Cui, A. G. Baboul, S. Clifford, J. Cioslowski, B. B. Stefanov, G. Liu, A. Liashenko, P. Piskorz, I. Komaromi, R. L. Martin, D. J. Fox, T. Keith, M. A. Al-Laham, C. Y. Peng, A. Nanayakkara, M. Challacombe, P. M. W. Gill, B. Johnson, W. Chen, M. W. Wong, C. Gonzalez, J. A. Pople, Gaussian 03, Revision C.02, Gaussian Inc., Pittsburgh, PA, 2003.
19. B. Delley, *J. Chem. Phys.* **1990**, *92*, 508–517. **DOI:**10.1063/1.458452
20. B. Delley, *Int. J. Quantum Chem.* **1998**, *69*, 423–433. **DOI:**10.1002/(SICI)1097-
21. T. Keith, J. Millam, GaussView, Version 5, Roy Dennington, Semichem Inc., Shawnee Mission, KS, 2009.
22. Materials Studio version 3.1.0; Accelrys, Inc., San Diego, 2004.
23. I. Bouabdallah, A. Ramdani, I. Zidane, D. Eddike, M. Tillard, C. Belin, *Acta Cryst.* **2005**, *E61*, o4243–o4245. **DOI:**10.1107/S1600536805037785
24. I. Bouabdallah, A. Ramdani, I. Zidane, R. Touzani, D. Eddike, A. Haidoux, *J. Mar. Chim. Heterocycl.* **2006**, *5,* 52–57. **DOI:**10.3390/M483
25. I. Bouabdallah, M. Rahal, T. Harit, A. El Hajbi, F. Malek, D. Eddike, M. Tillard, A. Ramdani, *Chem. Phys. Lett.* **2013**, *588*, 208–214. **DOI:**10.1016/j.cplett.2013.10.046
26. P. A. Channar, A. Saeed, M. F. Erben, F. A. Larik, S. Riaz, U. Flörke, M. Arshad, *J. Mol. Struct*. **2019**, *1191*, 152–157. **DOI:**10.1016/j.molstruc.2019.04.085
27. K. V. Domasevitch, *Acta Cryst.* **2008**, *C64*, o326–o329. **DOI:**10.1107/S0108270108013632
28. R. Krishna, D. Velmurugan, R. Murugesan, M. S. Sundaram, R. Raghunathan, *Acta Cryst.* **1999**, *C55*, 1676–1677.
29. L.E. Sutton, Tables of interatomic distances and configurations in molecules and ions, The Chemical Society, London, 1965.
30. M. Ghara, S. Pan, J. Deb, A. Kumar, U. Sarkar, P. K. Chattaraj, *J. Chem. Sci.* **2016**, *10*, 1537–1548. **DOI:**10.1007/s12039-016-1150-9
31. T. B. Hadda, Z. K. Genc, V. H. Masand, N. Nebbache, I. Warad, S. Jodeh, M. Genc, Y. N. Mabkhot, A. Barakat, H. S. Zamora, *Acta Chim. Slov.* **2015**, *62(3)*, 679–688.
32. I. Seghir, N. Nebbache, Y. Meftah, S. E. Hachani, S. Maou, *Acta Chim. Slov.* **2019**, *66(3)*, 629–637. **DOI:**10.17344/acsi.2019.5044
33. D. F. V. Lewis, C. Loannides, D. V. Parke, *Xenobiotica* **1994**, *24*, 401–408. **DOI:**10.3109/00498259409043243
33. M. A. Migahed, E. G. Zaki, M. M. Shaban, *RSC Adv.* **2016**, *6*, 71384–71396. **DOI:**10.1039/C6RA12835A
34. D. Pegu, J. Deb, C. Van Alsenoy, U. Sarkar, *Spectrosc. Lett.* **2017**, *50*, 232–243. **DOI:**10.1080/00387010.2017.1308381
35. P. Senet, P. Chemical, *Chem. Phys. Lett.* **1997**, *275*, 527–532. **DOI:**10.1016/S0009-2614(97)00799-9
36. D. C. Ghosh, J. Jana, *Current Sci.* **1999**, *76*, 570–573. **DOI:**10.1097/00004032-199905000-00018
37. I. Bouabdallah, M. Rahal, T. Harit, A. El-hajbi, F. Malek, *J. Mar. Chim. Heterocycl.* **2017**, *16*, 124–134.
38. S. Vinita, S, Pratibha, K. Ashok, *J. Chil. Chem. Soc.* **2014**, *59*, 2327–2334. **DOI:**10.4067/S0717-97072014000100019
39. R. M. LoPachin, T. Gavin, A. DeCaprio, D. S. Barber, *Chem. Res. Toxicol.* **2012**, *25*, 239–251. **DOI:**10.1021/tx2003257

Povzetek

Kristalna struktura nove spojine 1,1'-bis(2-nitrofenil)-5,5'-diizopropil-3,3'-bipirazola, **1**, je triklinska tipa $P\bar{1}$ s sledečimi parametri: a = 7.7113(8), b = 12.3926(14), c = 12.9886(12) Å, α = 92.008(8), β = 102.251(8), γ = 99.655(9)°. Strukturo smo primerjali s tisto za 5,5'-diizopropil-3,3'-biprazol, **5**, za katerega je bila ugotovljena tetragonalna $I4_1/a$ struktura s parametri: a = b = 11.684(1), c = 19.158(1) Å. Primerjavo smo razširili tudi na poprej določene strukture 1,1'-bis(2-nitrofenil)-5,5'-propil-3,3'-bipirazola, **2,** 1,1'-bis(4-nitrofenil)-5,5'-diizopropzl-3,3'-bipzrazola, **3,** in 1,1'-bis(benzil)-5,5'-diizopropil-3,3'-bipirazola, **4**. Za raziskave molekularnih geometrij in določitve globalnih reaktivnostnih parametrov smo uporabili izračune na osnovi teorije gostotnega funkcionala (DFT). Geometrija izoliranih molekul in ureditev molekul v trdnem stanju smo analizirali glede na naravo skupin, ki so povezne na bipirazolovo jedro.

DOI: 10.17344/acsi.2021.6817 *Acta Chim. Slov.* **2021,** *68,* 728–735

Scientific paper

Quantification of Hydroperoxides by Gas Chromatography with Flame Ionisation Detection

Damjan Jan Pavlica, Črtomir Podlipnik and Matevž Pompe*

Faculty of Chemistry and Chemical Technology, University of Ljubljana, Ljubljana, 1001, Slovenia

** Corresponding author: E-mail: Matevz.Pompe@fkkt.uni-lj.si*

Received: 03-12-2021

Abstract

Hydroperoxides are of great importance in the fields of atmospheric and biological chemistry. However, there are several analytical challenges in their analysis: unknown and usually low UV absorption coefficients, high reactivity, thermal instability, and a lack of available reference standards. To overcome these limitations, we propose a GC-FID approach involving pre-column silylation and quantification via the effective carbon number approach. Four hydroperoxides of α-pinene were synthesized in the liquid phase with singlet oxygen and identified using literature data on isomer yield distribution, MS spectra, estimated boiling temperatures of each isomer (retention time), their thermal stability and derivatisation rate. The developed procedure was used for the determination of hydroperoxides in bottled and autooxidised turpentine. We anticipate that this method could also be applied in atmospheric chemistry, where the reactivity of singlet oxygen could help explain the high formation rates of secondary organic aerosols.

Keywords: hydroperoxides, α-pinene, photooxidation, singlet oxygen, gas chromatography

1 Introduction

Organic hydroperoxides are used industrially as radical initiators, bleaching agents, and disinfectants. They are formed in the process of oxidative ageing, which they simultaneously promote by radical chain reactions. In ethereal solvents, they can be stable at low concentrations but become explosive at higher concentrations. Degradation by peroxidation decomposes all organic matter and is hazardous to health because hydroperoxides are irritating to skin, eyes, and mucous membranes and are potent allergens.[1] In rats, they induce progressive oxidative damage and cell death when inhaled.[2]

Hydroperoxides (HPs) are formed in nature as primary oxidation products of volatile organic compounds, for example, α-pinene, which is emitted from coniferous trees. This compound is the most abundant monoterpene in the air and plays an essential role in the growth of atmospheric particles.[3] It is present in essential oils and thus in various types of cosmetic and cleaning products. It is also the main component of turpentine, which is used as a paint thinner and as an ingredient in paints, polishes, adhesives, topical remedies and household chemicals. It has been found that 3.1% of the German population is allergic to turpentine.[4] The most likely major haptens in turpentine are Δ3-carene hydroperoxide and oxidation products of α- and β-pinene.[5]

Despite the need to monitor and quantify HPs in various matrices, their analysis is complicated due to low UV absorption, thermal instability, catalyzed decomposition, and lack of available reference standards. Quantification is mainly performed by chemical assays, such as the iodometric[6] or triphenylphosphine assay[7] or assays with other reducing agents, followed by an analysis of the reaction products.[8] However, these methods only provide information on the total amount of HPs present, and interference by other compounds cannot be excluded. For the monitoring and quantification of specific HPs, chromatographic and NMR methods can be used.

Some authors reported using gas chromatography (GC) methods without derivatisation, but only for HPs with low molecular masses.[9] HPs with higher molecular masses are partially decomposed at high oven elution temperatures and therefore often derivatised to more thermostable species. Most methods involve silylation[11,12] or reduction of HPs to alcohols with sodium sulfite,[9,13] sodium borohydride,[14] triphenylphosphine[9,14] or trimethyl phosphine.[15] Derivatisation to alcohols can be used if the resulting alcohols were not previously present in the sample. HPs in the gas phase can be analysed directly by chemical ionization mass spectrometry.[16]

High-pressure liquid chromatography (HPLC) for HP quantification is very convenient because separation

occurs at lower temperatures. However, due to lack of chromophores, HPs must be detected by post-column reactions or by MS. Post-column reactions include a method using phosphine (the fluorescent product phosphine oxide is formed)[17] or a chemiluminescence reaction using luminol.[18] The preferred MS ionisation techniques for detecting terpene HPs are electrospray ionisation (ESI)[19,20] and atmospheric pressure chemical ionisation (APCI).[19,21] Post-column reactions are specific for the peroxy functional group, whereas in MS, specific fragment loss of 34 Da (loss of H_2O_2) is observed sporadically.[21] Identification of the peroxy functional group can be confirmed by dual injection, with and without iodometric sample pretreatment, which reduces HP species to alcohols.[20]

Quantification of α-pinene HPs is very demanding because reference standards are nonexistent. Additionally, HPs have limited stability, so reliable quantitative methods are needed to assess purity, such as GC-FID with predicted relative response factors or NMR.[11] Quantitative NMR spectrometry is a universal, non-destructive, absolute detection technique and provides a quantitative reference for other analytical methods. Analytes in the μM concentration range can be detected, with precision and accuracy of around 1%.[22] The authenticity of individual spectra can be assessed by generating various one-dimensional and multidimensional experiments. The major hurdles are sensitivity, spectral overlap, dynamic range, selection of the internal standard, interpretation and processing of the spectra, and the use of expensive equipment and deuterated solvents. Therefore, when performing routine targeted analysis, optimized molecule-specific chromatographic methods are preferred. GC-FID has a dynamic range of 10^7 and the analysis time depends only on the mixture composition and not on the concentration as in NMR. In our case, the separation of isomers took 30 minutes. In the absence of calibration standards, the relative concentrations of the organic peroxides can be estimated from the GC-FID peak intensities by peak area normalization approach, application of the effective carbon number (ECN) concept, or by some other algorithm based on the chemical structure of the analytes.[23]

To date, only two HPs have been synthesised in the reaction of α-pinene with singlet oxygen.[13,14] Electrophilic singlet oxygen ($^1O_2$) reacts with a double bond in the ene addition reactions, where allylic hydrogen is abstracted to give allyl-HPs in which the double bond has migrated. The reaction of singlet oxygen with α-pinene in this manner generates pinocarvyl-hydroperoxide and 4-hydroperoxy-4,6,6-trimethylbicyclo[3.1.1]hept-2-ene (Fig.1.). The $^1O_2$ attack on the double bond occurs on the sterically less congested π face. The two methyl groups on the methylene bridge are distinctively anti-directing; therefore, the HPs resulting from the syn attack are formed only in trace amounts.[14,24] Upon storage in solution, the OOH group can migrate to the other side of the double bond,[25] which has already been observed as the rearrangement of pinocarvyl-hydroperoxide to myrtenyl-hydroperoxide.[9] In this work, we observe for the first time the rearrangement of 4-hydroperoxy-4,6,6-trimethylbicyclo[3.1.1]hept-2-ene (HP2) to verbenyl-hydroperoxide.

In the absence of isolated reference standards, the identification of separate peaks in the GC chromatogram was based on literature data on isomer yield distribution, MS spectra, estimated boiling temperatures of individual isomers (retention time), their thermal stability, and rate of derivatisation. Trimethylsilylation increased the thermostability and allowed us to validate linearity, selectivity and repeatability of the GC-FID method. The concept of the effective carbon number allowed determination without standards of known purity.

2 Experimental Section

2. 1. Chemicals, Synthesis of HPs and Air Exposure Procedure

For the synthesis of the HPs, we have used: α–pinene, >97% purity, Fluka (Buchs, Switzerland), methylene blue, Merck (Darmstadt, Germany) and HPLC grade acetonitrile, ≥99.9% purity, Fischer (Zürich, Switzerland).

HPs of α-pinene were synthesised by a modified photochemical procedure.[13,14] Photooxidation of α-pinene

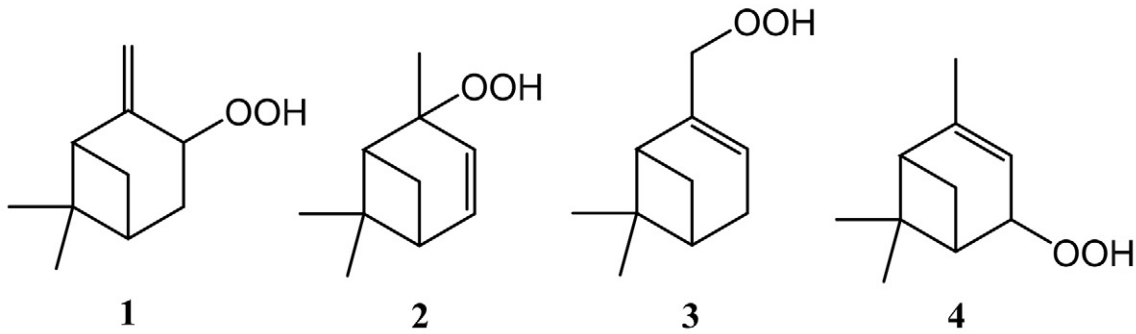

Figure 1. Structures of the hydroperoxides studied: pinocarvyl-hydroperoxide 1, 4-hydroperoxy-4,6,6-trimethylbicyclo[3.1.1]hept-2-ene 2, myrtenyl-hydroperoxide 3 and verbenyl-hydroperoxide 4.

was carried out in a flask at room temperature in acetonitrile using methylene blue as a sensitiser and a 60 W household daylight lamp as a light source. The flask was opened to allow oxygenation and mixed manually every 12 h for 14 days, followed by analysis by GC-MS and GC-FID. The structures of four resulting HPs of α-pinene are shown in Fig. 1.

Derivatisation reagent N-Methyl-N-(trimethylsilyl) trifluoroacetamide (MSTFA) was purchased from Fluka (Buchs, Switzerland), toluene from Sigma-Aldrich (Taufkirchen, Germany), cumene-hydroperoxide, 80% purity from Sigma-Aldrich (Taufkirchen, Germany), tetradecane of >99% purity from Merck (Schuchardt, Germany).

Turpentine was purchased from HGtrade (Ljubljana, Slovenia). A sample of turpentine was exposed to air in an Erlenmeyer flask at room temperature and under a 60-watt household daylight lamp. The neck of the flask was covered with aluminium foil to prevent contamination. The flask was stirred daily. After 20 days, the sample was derivatised, and the specific HPs were determined by GC-FID.

2. 2. Derivatisation Procedure

For the analysis of turpentine oil ≈ 200 mg of sample was weighed into a vial, then ≈ 200 mg internal standard solution (3 mg/g cumene-hydroperoxide in toluene) and ≈ 200 mg MSTFA (250 μL) were precisely weighted. The vial was closed, mixed by hand, and kept at room temperature for 2 h. 1 μL of the resulting solution was injected into the GC-FID.

For calibration, the following procedure was used: A stock solution of cumene-hydroperoxide at 2.5 mg/mL was prepared in acetonitrile and stored at 5 °C, calibration solutions (0.6, 1, 6, 25, 50, 90 μg/mL) were further diluted in acetonitrile. From each calibration solution, an aliquot of 0.4 mL was transferred to a vial, to which 0.4 mL of internal standard tetradecane (40 mg/kg in toluene) and 0.4 mL of the derivatisation reagent MSTFA (50 mg/g in toluene) were added. The vial was closed, mixed by hand, and kept at room temperature for 2 h. 1 μL of the resulting solution was injected into the GC-FID. The derivatised HP solutions were found to be stable in the refrigerator for at least three days.

2. 3. Instrumentation and Analysis

The GC separation was performed on GC Trace 1300, Thermo Scientific (Waltham, USA), equipped with a Rxi–5Sil MS column from Restek (Bellefonte, USA), 30 m x 0.32 mm x 0.25 μm. The carrier gas was helium under a constant flow of 2 mL/min and a split ratio of 50:1. The injector and FID temperatures were 250 and 280 °C, respectively. The oven was held at 60 °C for 0.3 min; then the temperature was raised to 80 °C at a rate of 5 °C/min and held for 3 min, then the temperature was raised to 160 °C at a rate of 5 °C/min and to 275 °C at a rate of 40 °C/min and held for 4 min.

The GC-MS separation was performed on GC Trace 1310 and MS TSQ 9000 from Thermo Scientific (Waltham, USA). A Restek (Bellefonte, USA) 5-MS column with 0.25 μm film thickness (30 m x 0.25 mm i.d.) was used for separation. The temperature programme was translated from GC-FID with the help of EZGC, an online freely available method translator tool from Restek (Bellefonte, USA). The carrier gas was helium under a constant flow of 1.56 mL/min. The injector and transfer line temperatures were 250 and 280 °C, respectively. The oven was held at 60 °C for 0.1 min; then the temperature was raised to 80 °C at a rate of 5.6 °C/min and held for 2.95 min, then the temperature was raised to 160 °C at a rate of 5.1 °C/min and raised to 275 °C at a rate of 38.4 °C/min and held for 4.15 min. The temperature of the ion source was 250 °C.

2. 4. Quantification

Due to the lack of commercially available standards for the HPs, we used the concept of effective carbon number (ECN) to calculate the response factors. The ECN is calculated using the contributions of different molecular structures with the error of predicting about 3% RSD.[26] Since there are no recommendations for calculating the ECN of trimethylsilyl peroxides, we treated these compounds as the corresponding trimethylsilyl oxides with ECN for the H-C-O-TMS group = 3.69. The relative mass response factors of silylated peroxides were calculated using the following equation:

$$f = \frac{M_{rx}}{M_{rr}} \frac{ECN_r}{ECN_x} \quad (1)$$

where r = reference compound (cumene HP); x = uncalibrated compound and M_r = molecular mass.

3 Results and Discussion

3. 1. Qualitative Analysis

Irradiation of α-pinene in acetonitrile solution with methylene blue as sensitizer resulted in four HPs. Initially, pinocarvyl-hydroperoxide and later 4-hydroperoxy-4,6,6-trimethylbicyclo[3.1.1]hept-2-ene were formed. When methylene blue was replaced by rose bengal, no change in the reaction products was observed. Furthermore, the same products were obtained by chemically prepared $^1O_2$ in the reaction between NaOCl and H_2O_2, all confirming the involvement of $^1O_2$ in the product formation. Continuing the synthesis, two more HPs were formed, probably not only by rearrangement reactions[25] but also by radical mechanisms,[15] with H abstraction from α-pinene by peroxyl radicals and $^3O_2$ addition.

A typical chromatogram of the optimised separation of the four isomers is shown in Fig. 2. In the absence of

standards, the assignment of separation order was based on literature data on isomer yield distribution and estimated boiling temperatures (retention time). The identification was later confirmed with MS spectra, thermal stability and rate of derivatisation. The most abundant HP in the reaction of $^1O_2$ with α-pinene is HP1, with an absolute yield of 99%.[14] It is reasonable to assume that the structural variations between the isomers do not affect their FID detector response; if so, the chromatogram's largest peak belongs to pinocarvyl-hydroperoxide (HP1). The remaining three isomers can be compared in order of elution because chromatographic retention time depends on chemical structure (size, shape, charge, and composition). For the isomers, the more branched the chain, the lower the boiling point tends to be. Therefore, the tertiary HP 4-hydroperoxy-4,6,6-trimethylbicyclo[3.1.1]hept-2-ene (HP2) elutes first, and the primary HP myrtenyl-hydroperoxide (HP3) elutes last. The remaining peak belongs to the verbenyl-hydroperoxide (HP4).

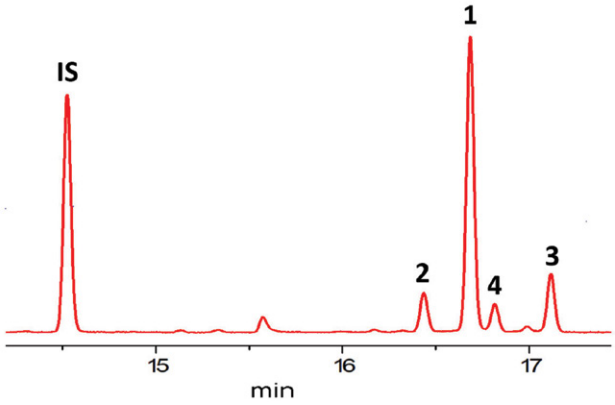

Figure 2. GC-FID chromatogram of four HP isomers obtained by photooxygenation of α-pinene: Cumene-hydroperoxide (**IS**, 14.5 min), 4-hydroperoxy-4,6,6-trimethylbicyclo[3.1.1]hept-2-ene (**2**, 16.4 min), pinocarvyl-hydroperoxide (**1**, 16.7 min), verbenyl-hydroperoxide (**4**, 16.8 min) and myrtenyl-hydroperoxide (**3**, 17.1 min). Retention times are given in parentheses.

3. 2. Derivatisation

Ideally, one would prefer to detect HPs directly, without derivatisation.[9] To test this possibility, different injector temperatures were compared (from 70 °C to 250 °C), and significant decomposition of HPs was observed. Primary HPs are known to be the most thermolabile,[12] and indeed, 20% of HP3 was degraded with temperature. HP1 was the least decomposed at 10%. To test the effect of degradation on the column, the analysis was performed under a fast and slow temperature gradient. The HPs elute at about 130 °C, and at this temperature partial decomposition has already been observed in the injector. However, since the compounds spend most of their retention time dissolved in the liquid stationary phase, this could stabilize them. Therefore, we additionally tested the decomposition on the column with fast and slow temperature gradient. Under a fast temperature gradient, we quantified 3 to 9% more specific HPs, confirming the decomposition in the column. This rules out the possibility of avoiding thermal degradation by cool-on-column injection, so α-pinene HPs require derivatisation for quantitative determination.

Derivatisation to alcohols requires that the resulting alcohol was not previously present in the quantified product mixture or that its concentration was known beforehand. Essential oils of conifers and hence our sample, turpentine, contain some proportion of corresponding alcohols. Alcohols are also formed after the degradation of hydroperoxides. Neuenschwander et al.[15] determined HPs via double injection, with and without reduction. The HP yield was quantified from the increase in alcohol content obtained, and no difference in yields was observed between split injection at 250 °C and cool-on-column injection at 50 °C. Since thermal degradation of HPs was observed in our experiments, they would be underestimated by this reduction method. We opted for silylation with MSTFA, in which the active hydrogens in the HPs are replaced by a TMS group. Silylation has a shortcoming: it cannot be applied to consumer product matrices with high water or alcohol content (e.g. eau de toilette, detergents).

After derivatisation, the positional isomers could be separated chromatographically with even better resolution, while retention times increased by only 1-1.5 min (Fig. 3). A reversal in elution order was observed for compounds HP1 and HP4. This was confirmed by comparing their derivatised/underivatised MS spectra and by comparing their GC-FID peak areas, as FID responses in-

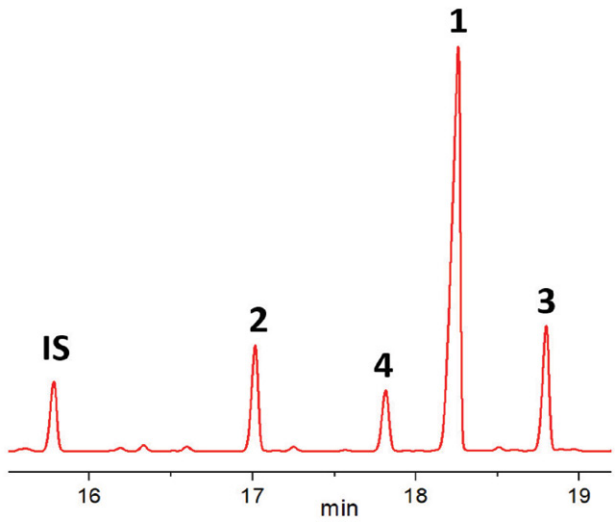

Figure 3. GC-FID chromatogram of TMS derivatives of α-pinene HPs obtained from the reaction of α-pinene with singlet oxygen: Cumene-hydroperoxide (**IS**, 15.8 min), 4-Hydroperoxy-4,6,6-trimethylbicyclo[3.1.1]hept-2-ene (**2**, 17.0 min), verbenyl-hydroperoxide (**4**, 17.8 min), pinocarvyl-hydroperoxide (**1**, 18.3 min) and myrtenyl-hydroperoxide (**3**, 18.8 min). Retention times are given in parentheses.

creased proportionally to the addition of three carbon atoms. The thermal stability of the TMS derivatives of HPs was investigated under different injector temperatures ranging from 70 °C to 270 °C. No adsorption on the column was observed at low temperatures, and no thermal decomposition was observed up to 250 °C. The repeatability of derivatisation at LOD (1 ppm, n=6) showed an RSD of 4.6%; thus, the method allows accurate determination.

Since HPs decompose at higher temperatures, we derivatised HPs at room temperature. The stability of HPs at room temperature was examined for 4 hours to exclude possible decomposition during the derivatisation process. Derivatisation was considered complete when chromatographic peaks for TMS derivatives stopped increasing and no peaks corresponding to unreacted HPs remained in the GC-FID chromatogram. Tertiary hydroperoxides (HP2 and IS) were derivatised in 25 min, primary HP (HP3) in 5 min, after only brief mixing. This difference can be explained by steric hindrance. We opted for a derivatization time of 2 h to give some extra time for samples with high concentrations of HPs.

3. 3. EI Fragmentation

Identification was made by classical mass spectra interpretation and by comparison with an authentic reference standard, 80% cumene-HP. The TMS derivative of cumene-HP and the internal standard tetradecane were the only chromatographic peaks in calibration solutions. Their identity was confirmed by a NIST mass spectra library search. The mass spectrum of the TMS derivative of cumene-HP is characterized by a large fragment peak at $[M\text{-}105]^+$ and a smaller peak at *m/z* 105 (Fig. 4). The ions at *m/z* 135 and *m/z* 151 apparently correspond to $[M\text{-}OSi(CH_3)_3]^+$ and $[M\text{-}Si(CH_3)_3]^+$, respectively. The molecular ion cannot be observed. The second most abundant peak is the tropylium cation, which is characteristic of aromatic compounds.

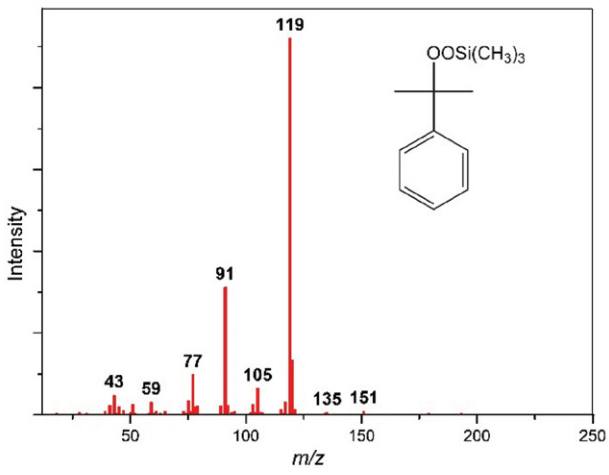

Figure 4. Mass spectra of the TMS derivative of cumene-HP.

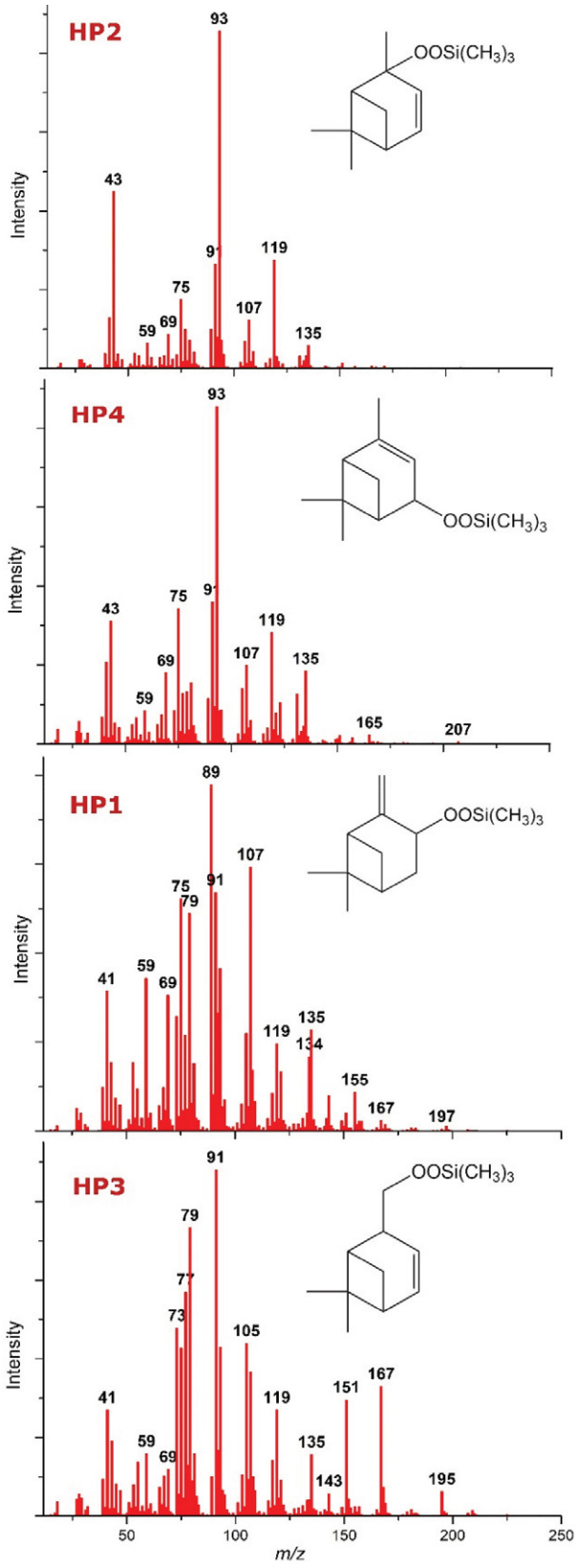

Figure 5. Mass spectra of the TMS derivatives of α-pinene HPs: 4-Hydroperoxy-4,6,6-trimethylbicyclo[3.1.1]hept-2-ene (HP2), verbenyl-hydroperoxide (HP4), pinocarvyl-hydroperoxide (HP1) and myrtenyl-hydroperoxide (HP3).

The tropylium cation is also observed in the mass spectra of α-pinene and its derivatives from the NIST mass spectral library as well as in the mass spectra of our TMS derivatives of α-pinene-HPs (Fig. 5). Again, the molecular ions are not observed and the fragmentation is extensive. The extensive fragmentation into a large number of low-mass ions makes selected-reaction monitoring less profitable, but on the other hand, the spectra are more informative and allow discrimination between the different positional isomers. Comparison of the mass spectra of derivatised and underivatised HPs confirmed the reversal of the elution order for HP1 and HP4 after derivatisation.

Common to all spectra is both a signal at *m/z* 135, due to the loss of the TMS-peroxy radical (-105 Da) and a specific ion series of terpenes with the molecular formula C_nH_{2n-5}: 65, 79, 93, 107, 121, and 135 (Fig. 5). The base peaks are typical hydrocarbon fragments: in the spectra of HP2 and HP4 *m/z* 93 ($C_7H_9^+$) and for HP3 *m/z* 91. The base peak of HP1 is *m/z* 89, corresponding to $[OSi(CH_3)_3]^+$. Other TMS fragments are also observed: *m/z* 73, corresponding to $[Si(CH_3)_3]^+$ and *m/z* 105, corresponding to $[OOSi(CH_3)_3]^+$. This is to be expected since most ionisation occurs at the silicon (ionisation potential 8.1 versus 13.6 eV for oxygen).[10,12]

Even when there are similarities between isomers in their EI spectra, the ions' relative intensities vary considerably. The relative abundance of high-molecular-mass ions decreases in the order primary HP > secondary HPs > tertiary HP (Fig. 5). This trend can be explained by a greater distance of the ionized atoms from the strained bicyclic skeletal structure in primary HP and by fragmentation mechanisms. We propose an H-rearrangement mechanism for the stabilization of *m/z* 151, which would help explain its high abundance in primary HP (Fig. 6).

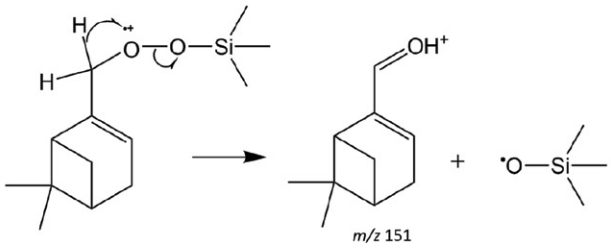

Figure 6. The mechanism for the formation of the fragment *m/z* 151, which is formed in higher amount in myrtenyl-hydroperoxide (HP3).

3. 4. Method Validation

A validation procedure was carried out i.e. linear regression range, precision and limit of quantification/detection were determined. Quantification was based on the peak area for cumene-HP relative to the peak area of the internal standard tetradecane. The linearity of the GC method was evaluated from 0.6 to 90 μg/mL of cumene-HP using five concentration levels, 0.6, 1, 6, 25, 50, 90 μg/mL. The R^2 value was greater than 0.999, LOD was 0.6 μg/mL, and LOQ was 1 μg/mL. The LOD was determined as the concentration giving a signal to noise ratio (S/N ratio) of at least 3, and LOQ as the lowest point of the calibration curve subject to linearity. Injection repeatability was evaluated using six injections of a standard solution, and the percentage of relative standard deviation (%RSD) in the peak area was 0.15%. Sample repeatability was evaluated by preparing six replicates of the same sample (with derivatisation for GC), and the %RSD in the peak area was 4.6%. The validation proved that the developed GC method was suitable for monitoring the α-pinene reaction with singlet oxygen. The selectivity of the method was verified by analysing turpentine samples, and all four HPs could be identified in autooxidised turpentine (Fig. 7).

3. 5. Analysis of Real Samples

To investigate the applicability of the proposed method for the determination of HPs in real samples, turpentine was analysed before and after autoxidation. The sample of turpentine contained 72% α–pinene and 9% β-pinene. During exposure to air, HPs concentrations increased with time (Fig. 7). Turpentine autooxidation also increased the mixture's complexity; new peaks were formed as the hydroperoxides were degraded to secondary oxidation products, e.g. aldehydes, alcohols, epoxides. The concept of the effective carbon number allowed us to quantify the responses without standards of known purity. The calculated value of the relative mass response factor for α-pinene HP with IS cumene-peroxide was 0.987. Due to a poor evaluation of the chemical structure in the ECN calculation, a bias could enter the quantification. In our case, the ECN could be overestimated by about 2% because we used an aromatic internal standard and aliphatic analytes.[27]

HPs in the turpentine sample were confirmed by four points of identification, retention times of HPs and HPs TMS derivatives, and by MS spectra of HPs and HPs TMS derivatives. The method's selectivity was verified by analysing samples of turpentine and screening for peaks that might interfere with α-pinene HPs. HP3 coeluted with a compound with a normalised concentration of 150 ppm (chromatogram A in Fig. 7, the right part of the double peak). With increasing concentration after prolonged autooxidation, the concentration of HP3 increased (chromatogram B in Fig. 7). Therefore, in an oxidised turpentine sample, an overestimation of 2% HP3 is to be expected at a concentration of 7.57 mg HP3/g.

The turpentine sample data show a high presence of HPs. The total mass fraction of HPs in bottled turpentine was 0.1% and increased to 5.1% after 20 days of air exposure. HP2 had the highest yield, which is expected for a radical reaction in which the most stable, tertiary radical is

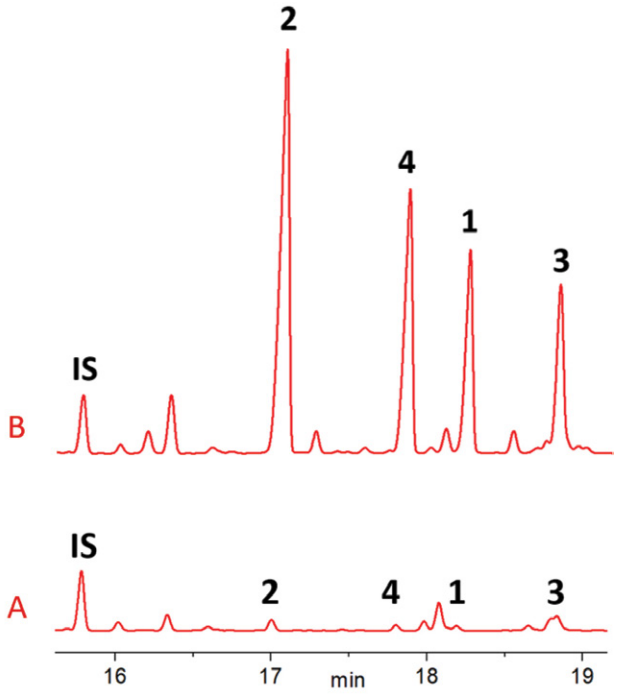

Figure 7. The chromatogram of turpentine before (A) and after 20 days of autooxidation (B).

Table 1. Concentrations of α-pinene hydroperoxides in turpentine before and after 20 days of air-exposure compared to concentrations of hydroperoxides synthesised photochemically with singlet oxygen (data in mg/g).

	HP2	HP4	HP1	HP3	Σ
Turpentine	0.416	0.207	0.186	0.626*	1.44
oxidised turpentine	21.7	12.5	8.84	7.57	50.6
photooxidised α-pinene	3.55	2.14	17.6	4.17	27.4

*double peak

formed. HP2 represents 43% of all radically sensitized HPs, and HP1 represents 64% of all HPs synthesized with singlet oxygen (Table 1). With this difference in yields, it would be possible to assess the importance of singlet oxygen as an atmospheric oxidant based on measurements of the concentrations of individual α-pinene HPs in the air.

4. Conclusions

The manuscript addresses the problem of quantifying reactive unstable organic species for which no standard reference material is available. We present the first GC-FID method for the quantification of all four α-pinene hydroperoxides formed in a reaction with α-pinene. The hydroperoxides were prepared by a simple photochemical synthesis in a laboratory flask. Pre-column silylation improved their stability, and the concept of effective carbon number allowed quantification despite the standards' poor stability. We believe that this new synthesis and analysis approach could be used for other unstable hydroperoxides as well.

The applicability of the proposed method was demonstrated on samples of bottled and oxidised turpentine. Each analysis was performed within 200 min with a quantification limit in the μg/mL range. After 20 days of air exposure, the mass fraction of hydroperoxides in turpentine increased 35-fold to 5.1%. This level is likely capable of causing oxidative damage to the skin and lungs.

For more complex matrices, such as hydroalcoholic products and atmospheric particles, an extraction step could be added. To further improve accuracy, isolation of individual α-pinene HPs and their purity determination by NMR would allow calibration and full validation of our GC-FID method. GC-MS or LC-MS could provide additional selectivity and better robustness, especially if isotope-labelled internal standards were available.

In addition to demonstrated importance of hydroperoxides in the analysis of essential oils, hydroperoxides of α-pinene are also important in atmospheric chemistry, where photoreactions of α-pinene with singlet oxygen could help explain high formation rates of secondary organic aerosols.[3,27] The formation of hydroperoxides with singlet oxygen is, in contrast to the radical formation, independent of the NO_x concentration. As NO_x levels decrease due to emission control measures, photochemical HPs will become even more important for atmospheric chemistry.

Acknowledgements

The study was carried out with financial support from the Slovenian Research Agency (P1-0153) and the World Federation of Scientists. The authors would like to thank Aleksandra Kuljanin and Dr. Ida Kraševec for advice and help during manuscript preparation.

5. References

1. A.-T. Karlberg, M. A. Bergström, A. Börje, K. Luthman, J. L. G. Nilsson, *Chem. Res. Toxicol.* **2008**, *21*, 53-69. **DOI:**10.1021/tx7002239
2. L. A. Morio, K. A. Hooper, J. Brittingham, T.-H. Li, R. E. Gordon, B. J. Turpin, D. L. Laskin, *Toxicol. Appl. Pharmacol.* **2001**, *177*, 188–199. **DOI:**10.1006/taap.2001.9316
3. M. Ehn, J. A. Thornton, E. Kleist, M. Sipilä, H. Junninen, I. Pullinen, M. Springer, F. Rubach, R. Tillmann, B. Lee, F. Lopez-Hilfiker, S. Andres, I.-H. Acir, M. Rissanen, T. Jokinen, S. Schobesberger, J. Kangasluoma, J. Kontkanen, T. Nieminen, T. Kurtén, L. B. Nielsen, S. Jørgensen, H. G. Kjaergaard,

M. Canagaratna, M. D. Maso, T. Berndt, T. Petäjä, A. Wahner, V.-M. Kerminen, M. Kulmala, D. R. Worsnop, J. Wildt, T. F. Mentel, *Nature* **2014**, *506*, 476–479. **DOI:**10.1038/nature13032
4. R. Treudler, G. Richter, J. Geier, A. Schnuch, C. E. Orfanos, B. Tebbe, *Contact Dermatitis* **2000**, *42*, 68–73. **DOI:**10.1034/j.1600-0536.2000.042002068.x
5. S. Hellerström, N. Thyresson, S.-G. Blohm, G. Widmark, *J. Invest. Dermatol.* **1955**, *24*, 217–224. **DOI:**10.1038/jid.1955.35
6. K. S. Docherty, W. Wu, Y. B. Lim, P. J. Ziemann, *Environ. Sci. Technol.* **2005**, *39*, 4049–4059. **DOI:**10.1021/es050228s
7. T. Nakamura, H. Maeda, *Lipids* **1991**, *26*, 765–768. **DOI:**10.1007/BF02535628
8. G. L. Beutner, S. Ayers, T. Chen, S. W. Leung, H. C. Tai, Q. Wang, *Org. Process Res. Dev.* **2020**, *24*, 1321–1327. **DOI:**10.1021/acs.oprd.0c00251
9. W. F. Brill, *J. Chem. Soc. Perkin Trans. 2* **1984**, *0*, 621–627. **DOI:**10.1039/p29840000621
10. J. Polzer, K. Bächmann, *J. Chromatogr. A* **1993**, *653*, 283–291. **DOI:**10.1016/0021-9673(93)83186-V
11. S. Leocata, S. Frank, Y. Wang, M. J. Calandra, A. Chaintreau, *Flavour Fragr. J.* **2016**, *31*, 329–335. **DOI:**10.1002/ffj.3324
12. J. Rudbäck, A. Ramzy, A.-T. Karlberg, U. Nilsson, *J. Sep. Sci.* **2014**, *37*, 982–989. **DOI:**10.1002/jssc.201300843
13. G. O. Schenck, H. Eggert, W. Denk, *Justus Liebigs Ann. Chem.* **1953**, *584*, 177–198. **DOI:**10.1002/jlac.19535840112
14. C. W. Jefford, A. F. Boschung, R. M. Moriarty, C. G. Rimbault, M. H. Laffer, *Helv. Chim. Acta* **1973**, *56*, 2649–2659. **DOI:**10.1002/hlca.19730560748
15. U. Neuenschwander, F. Guignard, I. Hermans, *ChemSusChem* **2010**, *3*, 75–84. **DOI:**10.1002/cssc.200900228
16. F. Bianchi, T. Kurtén, M. Riva, C. Mohr, M. P. Rissanen, P. Roldin, T. Berndt, J. D. Crounse, P. O. Wennberg, T. F. Mentel, J. Wildt, H. Junninen, T. Jokinen, M. Kulmala, D. R. Worsnop, J. A. Thornton, N. Donahue, H. G. Kjaergaard, M. Ehn, *Chem. Rev.* **2019**, *119*, 3472–3509. **DOI:**10.1021/acs.chemrev.8b00395
17. K. Akasaka, H. Ohrui, *J. Chromatogr. A* **2000**, *881*, 159–170. **DOI:**10.1016/S0021-9673(00)00330-7
18. M. J. Calandra, J. Impellizzeri, Y. Wang, *Flavour Fragr. J.* **2015**, *30*, 121–130. **DOI:**10.1002/ffj.3232
19. J. Nilsson, J. Carlberg, P. Abrahamsson, G. Hulthe, B.-A. Persson, A.-T. Karlberg, *Rapid Commun. Mass Spectrom.* **2008**, *22*, 3593–3598. **DOI:**10.1002/rcm.3770
20. R. Zhao, C. M. Kenseth, Y. Huang, N. F. Dalleska, J. H. Seinfeld, *Environ. Sci. Technol.* **2018**, *52*, 2108–2117. **DOI:**10.1021/acs.est.7b04863
21. M.-C. Reinnig, J. Warnke, T. Hoffmann, *Rapid Commun. Mass Spectrom.* **2009**, *23*, 1735–1741. **DOI:**10.1002/rcm.4065
22. S. K. Bharti, R. Roy, *TrAC Trends Anal. Chem.* **2012**, *35*, 5–26. **DOI:**10.1016/j.trac.2012.02.007
23. T. Cachet, H. Brevard, A. Chaintreau, J. Demyttenaere, L. French, K. Gassenmeier, D. Joulain, T. Koenig, H. Leijs, P. Liddle, G. Loesing, M. Marchant, Ph. Merle, K. Saito, C. Schippa, F. Sekiya, T. Smith, *Flavour Fragr. J.* **2016**, *31*, 191–194. **DOI:**10.1002/ffj.3311
24. M. Prein, W. Adam, *Angew. Chem. Int. Ed. Engl.* **1996**, *35*, 477–494. **DOI:**10.1002/anie.199604771
25. I. A. Yaremenko, V. A. Vil', D. V. Demchuk, A. O. Terent'ev, *Beilstein J. Org. Chem.* **2016**, *12*, 1647–1748. **DOI:**10.3762/bjoc.12.162
26. J. T. Scanlon, D. E. Willis, *J. Chromatogr. Sci.* **1985**, *23*, 333–340. **DOI:**10.1093/chromsci/23.8.333
27. M. Kállai, J. Balla, *Chromatographia* **2002**, *56*, 357–360. **DOI:**10.1007/BF02491945
28. A. Manfrin, S. A. Nizkorodov, K. T. Malecha, G. J. Getzinger, K. McNeill, N. Borduas-Dedekind, *Environ. Sci. Technol.* **2019**, **DOI:**10.1021/acs.est.9b01609.
29. Z. Tan, K. Lu, A. Hofzumahaus, H. Fuchs, B. Bohn, F. Holland, Y. Liu, F. Rohrer, M. Shao, K. Sun, Y. Wu, L. Zeng, Y. Zhang, Q. Zou, A. Kiendler-Scharr, A. Wahner, Y. Zhang, *Atmospheric Chem. Phys.* **2019**, *19*, 7129–7150. **DOI:**10.5194/acp-19-7129-2019

Povzetek

Hidroperoksidi so zelo pomembni na področju atmosferske in biološke kemije. Vendar pa pri njihovi analizi obstaja več analitičnih izzivov: neznani in običajno nizki absorpcijski koeficienti, visoka reaktivnost, toplotna nestabilnost in pomanjkanje razpoložljivih referenčnih standardov. Da bi odpravili te omejitve, predlagamo pristop GC-FID, ki vključuje predkolonsko silacijo in kvantifikacijo s pristopom na podlagi efektivnega števila ogljikov (*angl.* Effective Carbon Number). V tekoči fazi smo s singletnim kisikom sintetizirali štiri hidroperokside α-pinena in jih identificirali na podlagi literarnih podatkov o izkoristku posameznega izomera, MS spektrov, ocenjenih temperaturah vrelišča vsakega izomera (retencijski čas), njihovi toplotni stabilnosti in stopnji derivatizacije. Razviti postopek smo uporabili za določanje hidroperoksidov v ustekleničenem in avtooksidiranem terpentinu. Predvidevamo, da bi se ta metoda lahko uporabila tudi v atmosferski kemiji, kjer bi reaktivnost singletnega kisika lahko pomagala razložiti visoke stopnje tvorbe sekundarnih organskih aerosolov.

DOI: 10.17344/acsi.2021.6836 *Acta Chim. Slov.* **2021,** *68,* 736–743

Scientific paper

Understanding of Symmetry: Measuring the Contribution of Virtual and Concrete Models for Students with Different Spatial Abilities

Thayban Thayban,[1] Habiddin Habiddin,[1,2*] Yudhi Utomo[1] and Muarifin Muarifin[3]

[1] *Graduate Program, Department of Chemistry, Faculty of Mathematics and Natural Sciences, Universitas Negeri Malang – Indonesia*

[2] *PUI PT Disruptive Learning Innovation (DLI), Universitas Negeri Malang – Indonesia*

[3] *Faculty of Sport Science, Universitas Negeri Malang – Indonesia*

** Corresponding author: E-mail: Habiddin_wuni@um.ac.id*

Received: 03-18-2021

Abstract

Virtual and concrete models have been of interest in chemistry teaching to improve students' understanding of a three-dimensional representation of chemical concepts such as symmetry. This study aims to determine the effectiveness of using concrete and virtual models on students' understanding of symmetry. Students' understanding was also explored in light of their spatial ability. The study was conducted using a quasi-experimental design with 62 students as participants. Two different instruments, spatial ability and understanding of symmetry tests, were employed for data collection. Data analysis was performed using the Pearson product-moment correlation and two-way variance analysis test. The results showed the virtual model's contribution to improving students' understanding of symmetry is higher than that of the concrete model for both students with high spatial ability (HSA) and low spatial ability (LSA). Also, the better students' spatial ability, the better their understanding of molecular symmetry.

Keywords: Virtual Model, Concrete Model, Molecular Symmetry, Spatial Ability

1. Introduction

Molecular symmetry is an essential topic that is generally provided for university students taking an inorganic chemistry course. Symmetry governing the physical and spectroscopic properties of molecules provides clues regarding electronic and molecular structure as well as the way of reaction carried out.[1] The topic is also essential in other chemistry branches, such as predicting optical activity in organic chemistry.[2] Recognizing and understanding three-dimensional representations is a paramount ability to understand chemical concepts, particularly symmetry. Having good visual-spatial thinking skill is highly required to build a robust understanding of symmetry.[3] Also, students should visualize and predict three dimensions of unfamiliar motion.[4] The sound understanding of symmetry and 3D orientation of chemical compound and reaction contributes to students' success in learning other chemical concepts.[5] It is the building blocks for understanding modern molecular chemistry.[6] Difficulty in understanding symmetry contributes to the barrier to understand other chemical concepts.[7] These statements confirm that a good understanding of symmetry is essential for chemistry students. Visualising a two-dimensional object to a three-dimensional object requires several thinking tasks. Firstly, the interpretation and understanding of different charts must be done correctly before translating them into three-dimensional forms.[8–11] Secondly, converting abstract objects into real objects.[12] However, the results of our preliminary observations showed that the vast majority of students could not predict the shapes of molecules and determine the angle of the molecular shape. These inabilities could be rooted in students' tendency to describe molecular shapes based solely on Lewis structures without considering molecules' position as three-dimensional objects.[13] Also, the explanation of abstract concepts in text-

books is generally only based on two-dimensional visualisations,[14] which distort mental models.

Recent studies[11,15–17] revealed that students still find it challenging to visualise two-dimensional forms implying an insufficient spatial ability. This insufficient ability could be rooted in difficulty identifying the rotation axis position relative to the object based on the visualisation of objects before and after rotation and difficulty visualising an object's appearance after rotation and reflection operations.[18] Students' spatial abilities contributing to students' understanding of chemistry and other science disciplines[19] are categorized into three types covering Spatial Visualization (SV), Spatial Orientation (SO), and Spatial relations (SR).[17,20,21] They define SV as an ability to transform a two-dimensional (2D) object to the three-dimensional (3D) representation; SO as the ability to imagine an object from a different perspective; and SR as an ability to visualize the movement or operation of an object including rotation, inversion and reflection. The contribution of these spatial abilities in improving students' understanding of chemistry has been reported in some pieces of literature. For example, students with high SR ability demonstrated a strong understanding in determining the 2D and 3D rotations of CH_3COOH.[21]

Students' ability to build mental visualization of molecular shapes or spatial ability can be improved by optimizing their *representational competence.*[10,22,23] The term representational competence describes an ability to understand chemical phenomena and translate the phenomena from one representation to other, for example, connecting macroscopic to symbolic and or submicroscopic and *vice versa*, drawing and predicting chemical reactions phenomena.[22,24,25] The contribution of this competence towards students' success in science learning has been of concern in many areas[26,27] including science, technology, engineering, and math (STEM),[28] and physics.[29] This competence has also been considered as an essential factor to be improved in all educational levels.[28]

Representational competence can be improved by applying a virtual model-assisted learning strategy or concrete model.[10,23,30] In particular, plenty of previous studies confirmed that the concrete model had been a powerful tool to promote students' representational competence.[31] Virtual or concrete model-assisted learning provides visio-spatial information better than without using a model.[10] Virtual and concrete model which interact with students' visual sense[32] and haptic and visual sense[10] respectively, facilitate students to recognize the symmetry element and symmetry operation of a molecule. For example, in some molecules such as H_2O and NH_3, the C_n axis is quite clear to be recognized, but some molecules are challenging.[33] Therefore, drawing a molecule in a particular orientation will provide a better way to catch one rotational axis.[33] Surely, the 3D representation such as virtual and concrete model will serve the better view to assist students in recognizing the rotational axis. For example, identifying the C_3 and C_2 axes of the CH_4 molecule will be challenging without having the virtual or concrete model displaying the three-dimensional orientation of the molecule. Research comparing the effectiveness of using virtual and concrete models in chemistry has been carried out.[8,10,34] The results found different outcomes. Fjeld[34] found that the concrete model demonstrated better support to students' achievement than a virtual model.

On the other hand, Abraham et al.[8] and Stull & Hegarty[10] found an insignificant difference between the two models. The difference in cognitive construct when using the two models could be a complementary aspect for each other. Fjeld[34] revealed that the virtual model requires more cognitive tasks than the concrete model. Therefore, combining the two models is reasonable exercises.[10] The works focusing on designing instructional video and other virtual representation to improve the quality of teaching and learning has been carried out[35] including how students interact emotionally to the virtual representation.[36,37]

Several approaches have been applied in teaching symmetry as well as overcoming students' unscientific understanding of the topic including hands-on symmetry project,[38] three-dimensional (3D) models,[39–41] virtual laboratories,[3] common daily objects,[42] and drawing 2D projection.[43] A study focusing on the difference between using concrete and virtual model is limited. Therefore, this study aimed to explore how concrete and virtual media affect the students' understanding of symmetry and how students' spatial ability influences it. The result of this study will provide a vital perspective to be applied in the teaching of symmetry. The virtual model in this study is an online multimedia application provided by the website https://symotter.org/. Meanwhile, the concrete models were created by students representing molecular geometries.

2. Methodology

2. 1. Research Design and Participants

This study employed a quasi-experimental design and involved two classes/groups (with 31 students for each) of third-year students at the Chemistry Department, Universitas Negeri Gorontalo taking chemical bonding. In this university, symmetry is one of the topics discussed in the chemical bonding course. The *convenience sampling technique* was applied because the study was carried out in a natural setting in which the authors were not allowed to randomize the classes. Students experiencing concrete model were named Students with Concrete Model (SCM), and students experiencing virtual models were named Students with Virtual Model (SVM).

2. 2. Procedure

This study was carried out according to the following procedure.

– Preliminary test

Before the treatment, the two groups were given a preliminary test to determine whether they posed an equal academic ability. The test covered the geometry molecule topic, a prerequisite topic, before embarking on the symmetry class. The homogeneity test using *Levene's Test* ($P > 0.05$) showed that the prior academic ability between the two groups was equal.

– Intervention

The intervention in the form of a guided inquiry teaching approach was applied for the two groups. Syntaxes or stages of the inquiry teaching for the two groups were the same and described as follow: orientation, exploration, concept formation, and application. In the orientation stage, the lecturer provides a brief explanation of the topic that will be discussed. In the exploration stage, students explored a task given. For example, in the teaching of *reflection through a plane of symmetry,* students observed the molecular structure of PCl_3 and predicted any possible symmetry operation of the molecule. In the concept formation stage, the lecturer provided several stimulus questions to understand the concept. For example, identify the rotation operation of the PCl_3 molecule, the main axis (if any), etc. Students are encouraged to employ the media (concrete model for SCM and virtual model for the SVM). In the application process, students clarify their answer in class discussion with the guidance of the lecturer. In addition, several exercises to reinforce students' understanding of the topic were also implemented. In this stage, the students have also employed the media to find out all the symmetry operations at the molecules.

As explained above, all the teaching experiences but the media applied in the concept formation stage and application for the two groups were the same. The two groups' symmetry teaching was carried out on the same day with the subsequent time slots to avoid interaction thread between the two groups. The virtual model was applied as symmetry learning media for the SVM class, and the concrete model was applied SCM class. The teaching of molecular symmetry to both groups was carried out in three meetings with 120 minutes for each.

– Post-test

After completing all three meetings, students' understanding of molecular symmetry was measured using a short answer test with 18 questions. The instrument is named Students' Understanding of Molecular Symmetry Test (SUMST).

2. 3. Learning Media and Instrument

2. 3. 1. Virtual Model

The virtual model was applied as the learning media to facilitate students' understanding of symmetry for a virtual class. The virtual models are available on the website of https://symotter.org/. The website (*Symmetry @ Otterbein*) offers three features like the following. (1) *Symmetry Tutorial* provides an interactive point group that can guide the user through all elements and operations of symmetry with interactive displays and animations. (2) *Symmetry Gallery* is a collection of more than hundreds of unique molecules with interactive views of all elements of symmetry and animation of symmetry operations. The molecules are arranged by groups of points, so the user can select samples to show a particular element of symmetry. (3) *Symmetry Challenge* provides a detailed flow chart of the process of determining the point group of each molecule. Figure 1 below depicts a virtual model of molecular symmetry available on the website.

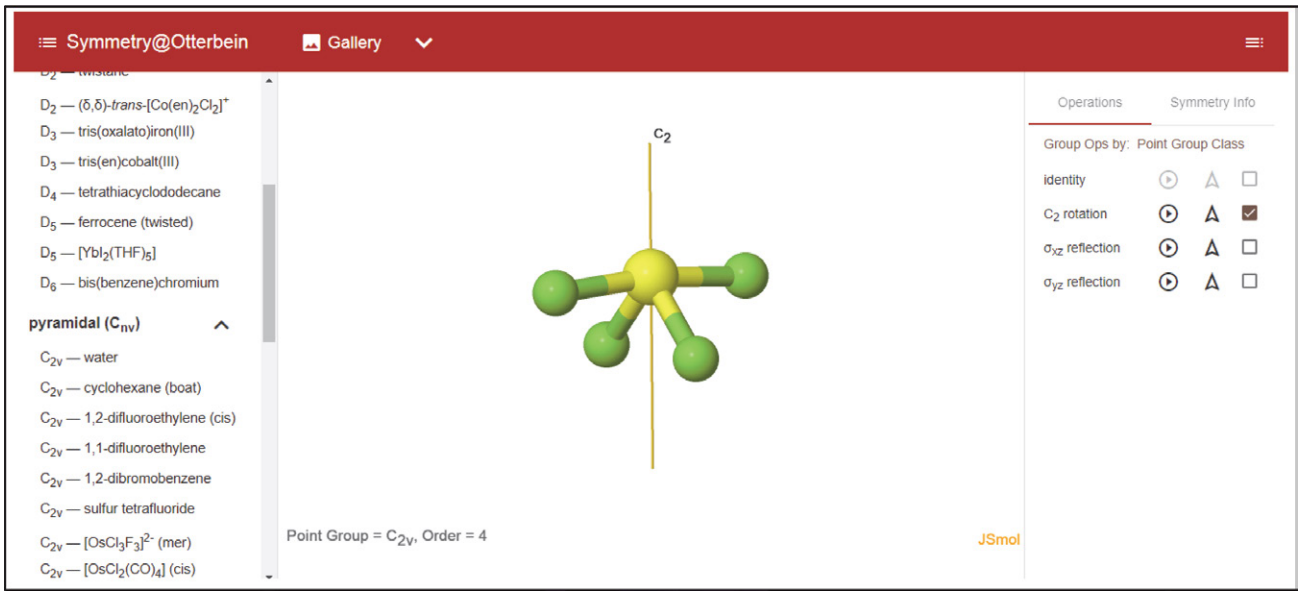

Figure 1. Example of the virtual model presented in the teaching of SVM.

2. 3. 2. Concrete Model

The concrete model was applied as the learning media to facilitate students' understanding of symmetry for concrete class. The concrete models were produced by utilizing daily materials such as pencil eraser and needles. Students were required to create the concrete model to build their understanding of the symmetry operation unconsciously. The molecular shape design was arranged to form an angle following the experimental molecule's angle and affect the symmetry operation.

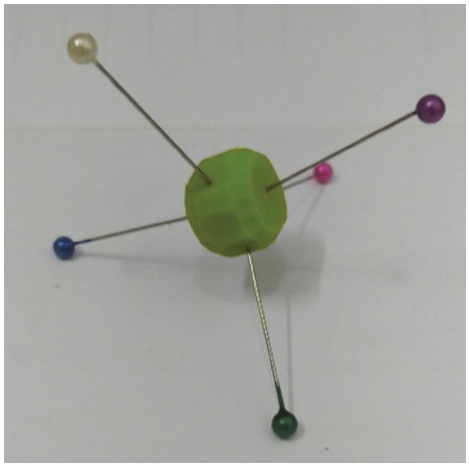

Figure 2. Example of a concrete model produced in the teaching of SCM.

2. 4. Spatial Ability Test

The *Purdue Spatial Visualization Test* (PSVT) developed by Guay[44] was applied to measure students' spatial ability was in a multiple-choice question and 30 items. This instrument has been the most frequent tool to be employed in the study of spatial ability. The example of a question is provided in Figure 3 below. The spatial ability test instrument has high category reliability with a value of 0.95.

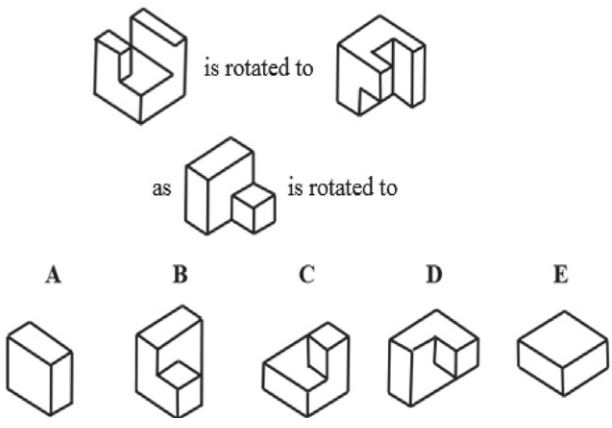

Figure 3. Example of a question in the PSVT.

2. 5. Students' Understanding of Molecular Symmetry Test (SUMST)

Students' understanding of molecular symmetry after teaching using virtual and concrete models was measured using the SUMST. The SUMST was in the form of a short answer question and represented all symmetrical operations that exist in the molecule in depth. The test instrument consisted of 18 items with a Cronbach Alpha coefficient of 0.905, falling in the very high category. The instrument is available on request.

2. 6. Data Analysis

2. 6. 1. *Students' Spatial Ability*

The level of students' spatial ability is categorised based on the PSVT score. Students who obtained scores above the average are included in students with high category spatial abilities (HAS). In contrast, students who obtained scores below the average are included in students with low category spatial abilities (LSA).

2. 6. 2. Students' Spatial Ability and Understanding of Symmetry

The correlation between students' spatial ability and students' understanding of symmetry was measured using *Pearson product-moment correlation*. Before the correlation test performed, the prerequisite tests, including the normality test and the homogeneity test, were applied. The normality test using the *Kolmogorov-Smirnov test* (*One-Sample KS*) obtained $P > 0.05$, which means that the data is normally distributed. The homogeneity test using *Levene's Test* obtained $P > 0.05$, which means the data is homogeneous.

2. 6. 2. The Effectiveness of Virtual and Concrete Models on Students 'Understanding of Symmetry

Two-way analysis of variance (ANOVA) was used to determine (1) the difference in the effectiveness of using virtual and concrete models on students 'understanding of molecular symmetry with different spatial abilities and (2) the interaction between virtual models and concrete models on students' spatial abilities in learning molecular symmetry.

2. 6. 3. Ethics Approval

Ethical approval has been obtained from Universitas Negeri Malang and Universitas Negeri Gorontalo. All the students who participated in this study have been provided with all the information regarding the study. They have agreed to participate voluntarily by filling the consent form.

3. Results and Discussion

3. 1. Student Spatial Ability Level

Students' spatial abilities were classified into three categories, including spatial visualization (SV), spatial relation (SR) and spatial orientation (SO).[17,20,21] All three categories were identified using the related type of spatial questions. Ten questions represented each category. The example portrayed in Figure 3 above is a type of SV question. The description of students' spatial ability level is presented in Table 1.

Table 1. Students' Spatial Ability Test Results

Spatial ability category	Number of Students (%)	
	High	Low
SV	77.4	22.6
SR	58.1	41.9
SO	75.8	24.2

The table described that the number of students with high spatial level ability is always higher than that of each category with low spatial ability. The previous study [45] supports this finding that spatial abilities develop well at the age 11–16.

3. 2. Spatial Abilities, Virtual & Concrete models, and Understanding of Molecular Symmetry

Students' responses to the SUMST instrument representing their understanding of molecular symmetry for virtual and concrete models with high and low spatial ability levels are presented in Table 2.

Table 2. Students' Responses to the SUMST and spatial ability level

Spatial ability level	Students' score to the SUMST	
	SVM class	SCM class
High	X = 66.20 N = 17 SD = 13.83	X = 51.9 N = 19 SD = 18.93
Low	X = 44.34 N = 14 SD = 21.05	X = 36.80 N = 12 SD = 21.5

The Table 2 shows that the virtual model provided a better contribution to the students' understanding of symmetry for high spatial ability (HSA) and low spatial ability (LSA) students. This finding is in accordance with the previous research.[10,30,46] The better performances of SVM students were demonstrated in several aspects. SVM group demonstrated better performance than the SCM group in predicting molecular shape, especially in determining the bond angles. The availability and accuracy of information regarding bond angle a molecular geometry cause students to become accustomed to predict molecular shape including bond angles, making it easier for students to identify molecular symmetry operations. This familiarity leads to better cognitive training and the improvement of cognitive abilities.[47]

Below is the different level of students' responses in predicting the shape of the $PFCl_4$ molecule for the two groups. SVM students understood that the angle of Cl_{eq}–P–Cl_{eq} (*eq= equatorial*) would be distorted and <120° due to the difference in electronegativity between the Cl atom and the F atom, which is in the axial position. Meanwhile, SCM students assumed that the difference in electronegativity would not affect the angle of the molecule (120°) (Figure 4). Such error in determining the bond angle will lead to an incorrect choice in determining the rotation and reflection operations.[48]

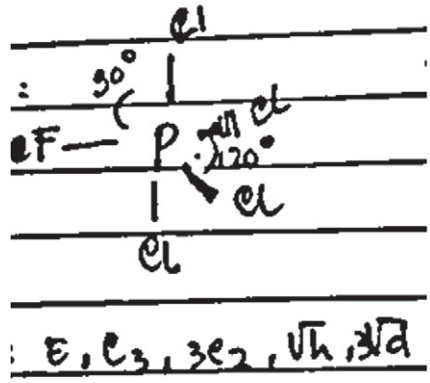

Figure 4. Example of an incorrect answer of SCM students regarding $PFCl_4$ molecule

SVM students also identified the rotation operations through the actual rotation axis than SCM did. The limited possibilities in manipulating the movement of molecular shapes for SVM strengthen students' long-term memory retention. In contrast, the concrete model provides plenty of possibilities for SCM students to do movement manipulations of molecular shape leading to overload memory remembering these movements. The limited possibilities help students remember every detail of three-dimensional objects' movement.[46] The two groups demonstrated the different responses in determining the rotational operations of the SeF_6 molecule. SVM students identified that the SeF_6 molecule exhibit C_4, C_3, and C_2 of axes rotations. Meanwhile, SCM students assumed that the molecule only exhibits C_3 and C_2 axes rotation.

SVM students are also more successful in identifying reflection operations in the mirror plane than SCM students. The virtual model's availability of mirror plane

features (vertical, horizontal, and diagonal mirror planes) supported a better understanding of SVM students when studying the mirror plane's reflection operation. In identifying the reflection operation on the mirror plane of the POF_3 molecule, SVM understood that the molecule has a vertical mirror plane at the F atom's corners. Meanwhile, SCM students assumed that the molecule has a horizontal and diagonal mirror plane.

The difference in students' understanding between SVM and SCM students is also described based on each topic's correct answer (Table 3). SVM students obtained a higher average score than SCM students. This fact emphasizes that the virtual model is adequate for teaching chemistry concepts involving three-dimensional objects,[49] such as molecular geometry and molecular symmetry, particularly for high spatial ability students.

3. 3. The Relationship between Spatial Abilities and Understanding Molecular Symmetry

Table 2 above also shows a contribution of students' spatial ability towards their success in understanding molecular symmetry. In particular, students with a high spatial ability (HSA) demonstrated a better understanding of molecular symmetry than low spatial ability (LSA) students, as uncovered in the previous studies.[3,50] HSA students could use spatial visualization, spatial orientation, and spatial relation, strengthening their understanding of molecular symmetry operations such as rotation, reflection, inversion, and pseudo rotation operations. In determining the reflection operation on the AsH_3 molecule, LSA students believed that the molecule has four mirror planes, including one horizontal mirror plane and three dihedral mirror planes. This error resulted from a low understanding of the spatial visualization aspect, leading to the difficulty of translating the bold visual notation code and dotted line notation in molecular structures.[11]

Table 3. The comparison of Correct Answers between SVM and SCM students

No.	Sub-topic	Correct Answers (%)	
		SVM	SCM
1	Predict molecular shape	68	67
2	Identify the rotation operation via the actual axis of rotation	53	50
3	Identify the major axes	45	41
4	Identify the reflection operation on the mirror plane	33	31
5	Identify any inversion operations through the centre of symmetry	49	45
6	Identify the rotation operation via the pseudo rotation axis	35	35
7	Predict the polarity of molecules based on the symmetry operations they have	33	29
8	Predict the conservation of molecules based on the symmetry operations they have	46	43

The phenomena discussed above provide strong evidence of different students' understanding due to the use of virtual and concrete models in teaching molecular symmetry. Students' interaction with the concrete and virtual model may also affect the understanding of students. The flexible use of the *keyboard* and *mouse* to manipulate the 3D object movement produce a limitless interaction between students and the virtual model as much as the interaction of SCM students with the concrete model. However, the advantage of the virtual model over the concrete model is its better and more representative shape of the molecules. Two-way ANOVA confirmed the difference in students' understanding between the two groups with the F values of 5.049 at the significant level of 0.028. The values imply the difference in students' understanding of molecular symmetry between the SVM and SCM students. The percentage of correct answer between the two groups presented in Table 3 confirms that the virtual model is more effective than the concrete model in increasing student' understanding of molecular symmetry. The test also found that there is no interaction between learning media and spatial skills (F (1.62) = 0.484; P > 0.05).

In term of the ability of *spatial relations*, holding this ability contributed to students' competence in manipulating representative three-dimensional objects in space.[14] LSA students believed that the SO_2F_2 molecule has a C_3

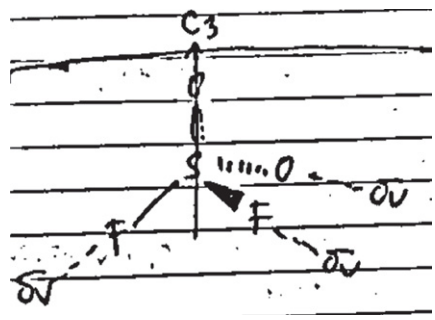

Figure 5. Example of LSA students' error in determining the rotation operation of SO_2F_2 molecule

rotation operation (Figure 5). This error could be the result of an inability to determine the geometry of the molecule.

The different responses between the two groups were also found when determining the rotation operation on the SeF_6 molecule. Robust knowledge in *spatial orientation* will lead students to determine the molecular rotation operations on different axes 36 correctly. SLA students believed that SeF_6 molecules only have the C_4 rotation operation as the main axis due to their inability to imagine the appearance of the SeF_6 molecule from various viewpoints, which allows determining the existence of other rotation operations.

In terms of combining spatial visualization, spatial orientation, and spatial relations abilities, the discrepancy between the two groups' responses was determined by determining the rotation operation via the pseudo axis (*Sn*) of the CCl_4 molecule. LSA students were unable to show a pseudo-axis rotation operation on the CCl_4 molecule. Students' mistakes were shown in several ways. Firstly, they can perform rotation operations correctly but cannot for reflection operations. Secondly, they performed rotation and reflection operations correctly but could not determine the new molecule's position from a different point of view.

The findings above show that students' spatial ability correlates to their understanding of molecular symmetry both for HAS and LAS students. The better students' spatial ability, the better they understand the topic of molecular symmetry. This correlation was also confirmed by the statistical test result using *Person product-moment correlation* with an *r*-value of +0.395.

4. Conclusion

This study confirms that the virtual model provides a better contribution toward students' understanding of molecular symmetry. Also, students' spatial ability affects students' understanding of the topic. Students' understanding of molecular symmetry increase with the increase of their spatial ability. This study implies that employing a virtual model in the teaching of molecular symmetry is a fruitful approach. Improving students' spatial ability is essential to be a solid milestone in learning chemistry concepts involving three-dimensional objects such as molecular geometry and molecular symmetry.

Acknowledgements

We thank Prof. Effendy, PhD, for his tremendous and valuable supports in doing this study.[26]

5. Reference

1. P. Atkins, T. Overton, J. Rourke, M. Weller, F. Armstrong, *Inorganic Chemistry*, Oxford University Press, Oxford, 4th Edn., 2006.
2. S. F. A. Kettle, *J. Chem. Educ.* **2009**, *86*, 634. **DOI:**10.1021/ed086p634
3. K. Achuthan, V. K. Kolil, S. Diwakar, *Educ. Inf. Technol.* **2018**, *23*, 2499–2515. **DOI:**10.1007/s10639-018-9727-1
4. B. K. Niece, *J. Chem. Educ.* **2019**, *96*, 2059–2062. **DOI:**10.1021/acs.jchemed.9b00053
5. S. E. McKay, S. R. Boone, *J. Chem. Educ.* **2001**, *78*, 1487. **DOI:**10.1021/ed078p1487
6. A. Korkmaz, W. S. Harwood, *J. Sci. Educ. Technol.* **2004**, *13*, 243–253. **DOI:**10.1023/B:JOST.0000031263.82327.6e
7. J. D. Dunitz, *Proc. Natl. Acad. Sci.* **1996**, *93*, 14260 LP – 14266. **DOI:**10.1073/pnas.93.25.14260
8. M. Abraham, V. Varghese, H. Tang, *J. Chem. Educ.* **2010**, *87*, 1425–1429. **DOI:**10.1021/ed100497f
9. S. Padalkar, M. Hegarty, *J. Educ. Psychol.* **2015**, *107*, 451–467. **DOI:**10.1037/a0037516
10. A. T. Stull, M. Hegarty, *J. Educ. Psychol.* **2016**, *108*, 509–527. **DOI:**10.1037/edu0000077
11. H. K. Wu, P. Shah, *Sci. Educ.* **2004**, *88*, 465–492. **DOI:**10.1002/sce.10126
12. J. T. Olimpo, B. C. Kumi, R. Wroblewski, B. L. Dixon, *Chem. Educ. Res. Pract.* **2015**, *16*, 143–153. **DOI:**10.1039/C4RP00169A
13. C. Furió, M. L. Calatayud, S. L. Bárcenas, O. M. Padilla, *Sci. Educ.* **2000**, *84*, 545–565.
14. I. Tuvi-Arad, P. Gorsky, *Chem. Educ. Res. Pract.* **2007**, *8*, 61–72. **DOI:**10.1039/B6RP90020H
15. M. Stieff, *Learn. Instr.* **2007**, *17*, 219–234. **DOI:**10.1016/j.learninstruc.2007.01.012
16. M. Stieff, S. Raje, *Spat. Cogn. Comput.* **2010**, *10*, 53–81. **DOI:**10.1080/13875860903453332
17. M. Harle, M. Towns, *J. Chem. Educ.* **2011**, *88*, 351–360. **DOI:**10.1021/ed900003n
18. H. Tuckey, M. Selvaratnam, *Stud. Sci. Educ.* **1993**, *21*, 99–121. **DOI:**10.1080/03057269308560015
19. M. Cole, J. Wilhelm, B. M. Vaught, C. Fish, H. Fish, *Educ. Sci.* **2021**, *11*, 4. **DOI:**10.3390/educsci11010004
20. N. Barnea, in: J. K. Gilbert, C. J. Boulter (Eds.), Developing Models in Science Education, Springer Netherlands, Dordrecht, 2000, pp. 307–323.
21. Y. Rahmawati, H. Dianhar, F. Arifin, *Educ. Sci.* **2021**, *11*, 185. **DOI:**10.3390/educsci11040185
22. Kozma, J. Russell, *J. Res. Sci. Teach.* **1997**, *34*, 949–968. **DOI:**10.1002/(SICI)1098-2736(199711)34:9<949::AID-TEA7>3.0.CO;2-U
23. M. Stieff, R. C. Bateman, D. H. Uttal, in: J. K. Gilbert (Ed.), Visualization in science education, Springer Netherlands, Dordrecht, 2005, pp. 93–120. **DOI:**10.1007/1-4020-3613-2_7
24. R. Kozma, J. Russell, in: J. K. Gilbert (Ed.), Visualization in science education, Springer Netherlands, Dordrecht, 2005, pp. 121–145. **DOI:**10.1007/1-4020-3613-2_8
25. M. Stieff, D. DeSutter, *J. Res. Sci. Teach.* **2021**, *58*, 128–156. **DOI:**10.1002/tea.21650
26. M. M. Cooper, M. Stieff, D. DeSutter, *Top. Cogn. Sci.* **2017**, 9, 902–920. **DOI:**10.1111/tops.12285
27. A. J. Magana, S. Balachandran, *J. Sci. Educ. Technol.* **2017**,

26, 332–346. **DOI:**10.1007/s10956-016-9682-9
28. M. Stieff, S. Scopelitis, M. E. Lira, D. Desutter, *Sci. Educ.* **2016**, *100*, 344–363. **DOI:**10.1002/sce.21203
29. T. S. Volkwyn, J. Airey, B. Gregorcic, C. Linder, *Learn. Res. Pract.* **2020**, 6, 88–107. **DOI:**10.1080/23735082.2020.1750670
30. A. T. Stull, T. Barrett, M. Hegarty, *Comput. Human Behav.* **2013**, *29*, 2546–2556. **DOI:**10.1016/j.chb.2013.06.012
31. H.-Y. Chang, *Sci. Educ.* **2018**, *102*, 1129–1149. **DOI:**10.1002/sce.21457
32. R. A. Ruddle, D. M. Jones, *J. Exp. Psychol. Appl.* **2001**, *7*, 286–296. **DOI:**10.1037/1076-898X.7.4.286
33. W.-K. Li, G.-D. Zhou, T. Mak, *Advanced Structural Inorganic Chemistry*, Oxford University Press, Oxford, 2008.
34. M. Fjeld, J. Fredriksson, M. Ejdestig, F. Duca, K. Bötschi, B. Voegtli, P. Juchli, in: *Proceedings of the SIGCHI Conference on Human Factors in Computing Systems*, Association for Computing Machinery, New York, NY, USA, 2007, pp. 805–808.
35. R. E. Mayer, *J. Appl. Res. Mem. Cogn.* **2021**, **DOI:**10.1016/j.jarmac.2021.03.007
36. A. P. Lawson, R. E. Mayer, N. Adamo-Villani, B. Benes, X. Lei, J. Cheng, *Comput. Human Behav.* **2021**, *114*, 106554. **DOI:**10.1016/j.chb.2020.106554
37. A. P. Lawson, R. E. Mayer, N. Adamo-Villani, B. Benes, X. Lei, J. Cheng, *Int. J. Artif. Intell. Educ.* **2021**, *31*, 134–153. **DOI:**10.1007/s40593-021-00238-2
38. K. Fuchigami, M. Schrandt, G. L. Miessler, *J. Chem. Educ.* **2016**, *93*, 1081–1084. **DOI:**10.1021/acs.jchemed.5b00325
39. A. V Savchenkov, *J. Chem. Educ.* **2020**, *97*, 1682–1687. **DOI:**10.1021/acs.jchemed.0c00192
40. E. B. Flint, *J. Chem. Educ.* **2011**, *88*, 907–909. **DOI:**10.1021/ed100893e
41. V. F. Scalfani, T. P. Vaid, *J. Chem. Educ.* **2014**, *91*, 1174–1180. **DOI:**10.1021/ed400887t
42. P. Jittam, P. Ruenwongsa, B. Panijpan, *Biosci. Educ.* **2008**, *12*, 1–8. **DOI:**10.3108/beej.12.6
43. L. Chen, H. Sun, C. Lai, *J. Chem. Educ.* **2015**, *92*, 1422–1425. **DOI:**10.1021/ed500898p
44. R. Guay, *Purdue Spatial Visualization Test*, Purdue Research Foundation, West Lafayette, Indiana, 1976.
45. H.-D. Barke, T. Engida, *Chem. Educ. Res. Pract.* **2001**, *2*, 227–239. **DOI:**10.1039/B1RP90025K
46. T. J. Barrett, A. T. Stull, T. M. Hsu, M. Hegarty, *Comput. Educ.* **2015**, *81*, 69–81. **DOI:**10.1016/j.compedu.2014.09.009
47. S. M. Jaeggi, J. Karbach, T. Strobach, *J. Cogn. Enhanc.* **2017**, *1*, 353–357. **DOI:**10.1007/s41465-017-0057-9
48. Effendy, *Molekul, Struktur, dan Sifat-sifatnya*, Indonesian Academic Publishing, Malang, 2017.
49. A. T. Stull, M. Gainer, S. Padalkar, M. Hegarty, *J. Chem. Educ.* **2016**, *93*, 994–1001. **DOI:**10.1021/acs.jchemed.6b00194
50. I. Tuvi-Arad, R. Blonder, *Chem. Educ. Res. Pract.* **2010**, *11*, 48–58. **DOI:**10.1039/C001046B

Povzetek

Virtualni in konkretni modeli se uporabljalo pri poučevanje kemijskih vsebin, da bi študentje lažje razumeli tridimenzionalno predstavitev kemijskih konceptov, kot je simetrija. Cilj te študije je ugotoviti učinkovitost uporabe konkretnih in virtualnih modelov pri razumevanju simetrije. Razumevanje študentov smo raziskovali tudi glede na njihove prostorske sposobnosti. Študija je bila izvedena s kvazi-eksperimentalnim načrtom, v katerem je sodelovalo 62 študentov. Za zbiranje podatkov sta bila uporabljena dva različna pristopa in sicer prostorska sposobnost in testi razumevanja simetrije. Analiza podatkov je bila izvedena s pomočjo Pearsonovega korelacijskega koeficienta in ANOVA. Rezultati so pokazali, da je prispevek virtualnega modela k izboljšanju razumevanja simetrije študentov višji kot pri konkretnem modelu tako za študente z visoko prostorsko sposobnostjo (HSA) kakor tudi nizko prostorsko sposobnostjo (LSA). Opazili smo tudi, da imajo boljše razumevanje molekulske simetrije tisti študenti, ki imajo boljšo prostorsko predstavo.

DOI: 10.17344/acsi.2021.6789 *Acta Chim. Slov.* **2021,** *68,* 744–752

Technical paper

Marker Compounds Adsorbed on Dust Particles (PM10) Sampled According to Standard EN 12341 in the Outdoor Air Near the Cement Plant

Ernest Vončina

*National Laboratory of Health, Environment and Food (retired)**

** Corresponding author: E-mail: ernest.voncina@gmail.com, phone +386 51 371 641*

Received: 05-16-2021

Abstract

Compounds adsorbed onto PM10 in the air near the cement plant were determined. Several side reactions that occur in the hot flue gas stream at the same time as the actual main reactions are also possible. This leads to the formation of traces of organic nitrogen compounds. For the GC/MS determination of polar organic compounds silylation as a derivatization method was used. Organic compounds detected are derivatives of sugars, sugar alcohols, and mono-, di- and tri-carboxylic acids. The composition is characteristic for pollution of the urbane atmosphere. Nitrogen organic compounds formed during the urea thermolytic process in hot cement kiln gases represent parabanic acid, 5-hydroxyhydantoin, 4,5-dihydroxyhydantoin, 5-oxoproline, and cyanuric acid. The inorganic part of aerosols detected includes oxyanions of sulfamic acid, sulfate, sulfite, phosphate, and vanadate(V) with ammonium as a cation.

Chemical compositions of particles are crucial to assess the health impacts since the biological responses to aerosols are not always linked with major constituents but rather with toxicologically potent minor components.

Keywords: PM10; cement; SNCR; sulfamic acid; vanadic(V) acid; parabanic acid

1. Introduction

Stationary monitoring networks use the mass concentration of PM2.5 or PM10 as the metric and particles are treated as equally toxic, without regard to their source and chemical composition.[1,2] Airborne particles vary in chemical composition, their solubility and reactivity, mass, size, number, shape and surface area depending upon the source and atmospheric processing. All of these properties have the potential to influence health. The recommended general analytical parameters for the control of cement sector environmental pollutants have been issued and are presented in Table 1. Knowledge of detailed chemical compositions of particles is crucial to assess the health impacts since the biological responses to aerosols are not always linked with major constituents, but rather with toxicologically potent minor components.

The capability of PM to induce disease may be the result of multiple components acting through different physiological mechanisms. It is important to determine which components and sources of PM are most harmful since the identification of regulation targets can better protect human health.

After gravimetric determination of PM10, the chemical composition of the adsorbed organic fraction on PM10 in the air near cement plant was determined.[3] The aim of the study was to find specific marker compounds for cement kiln emissions. Cement plant emission monitoring is obligatory to demonstrate compliance with existing laws, regulation, and agreements. Co- incineration of hazardous wastes should only be performed if the cement kiln operates according to the best available techniques.[4] The suitability of the production site must be assessed to avoid risks associated with a potential release of vapours and odours or the possibility of leaks that might release hazardous waste or other substances of concern into the environment. Requiring control of technical solutions should be in accordance with the best available technology associated emission levels (BAT-AEL). The recent recommended values for the cement sector environmental pollutants have been issued and are presented in Table1.

Small quantities of ammonia can be observed in the flue gas from cement kilns. The ammonia originates from

Table 1. The BAT-AEL are 24-hour average values referred to dry gas in standard conditions (0 °C, 100 kP) and 10 % oxygen.

Environmental pollutants	BAT-AEL (mg/Nm^3)
Total dust	<10–20
NO_x (NO, NO_2, NO_x, expressed as NO_2)	200–450
SO_2	50–400
HCl	10
HF	1
Sb+AS+Pb+Cr+Co+Mn+Ni+V	0.5
Cd+Tl	0.05
Hg	0.05
PCDD and PCDF (dioxins and furans)	0.05–0,1 (I-TEQ ng/Nm^3)
NH_3 (ammonia slip from injection system)	<30–50

the pyrolysis of nitrogenous fuels and raw materials or from reagents used for denitrification of NO_x gases.[5,6] With the combustion of fossil fuels, massive harmful emissions of nitrogen oxides (NO_x), mainly including NO and NO_2, have been discharged into the atmosphere. To reduce the severe NO_x emission techniques, such as selective catalytic reduction (SCR) and selective non-catalytic reduction (SNCR) were developed.[7,8]

Injection of higher values of urea can improve NO_x reduction but may also increase ammonia slip. Reduction chemistry is a relatively simple chemical process. The process begins with an ammonia-based reagent, ammonia or urea, being vaporized within the appropriate temperature range, the gas-phase urea or ammonia then decomposes into free radicals, including NH_3 and NH_2.[9] After a series of reactions, the ammonia radicals come into contact with the NO_x and reduce it to N_2 and H_2O. Since NO_x includes both NO and NO_2, the main overall stoichiometric reactions with urea and ammonia are as follows (1,2):

$$2NO+2NH_3+1/2O_2 \rightarrow 2N_2+3H_2O \quad (1)$$

$$2NO_2+4NH_3+O_2 \rightarrow 3N_2+6H_2O \quad (2)$$

Several side reactions that occur in the hot flue gas stream at the same time as the actual main reactions are also possible. This leads to the formation of traces of organic nitrogen compounds. The aim of the study was to find specific marker compounds for cement kiln emissions, which show the difference according to the composition of the surrounding air in the broader area.

2. Experimental Section

2. 1. Sample Collection and Weather Conditions at the Time of Measurements

Aerosol samples were collected at a distance of approximately 550 m in a south-westerly direction from the central chimney of the clinker furnace. An air sample was taken at the height of 1.5 meters above ground level. Sampling was achieved under the operating conditions of the rotary kiln from 06/07/2015, starting around 2 pm and ending on 09/07/2015 at 2 pm. Three consecutive samples (sample 01, sample 02, sample 03) were taken, each within 24 hours. Sampling sites are illustrated in Figure 1.

Meteorological data were monitored during the measurements at 10 min intervals. In Figure 1, the wind rose diagram shows the general wind direction and the wind direction frequency of blowing between each sampling period. The weather conditions at the time of sampling were different; the first two days (sample 01 and sample 02) the SW wind blew with low speed, while the last day (sample 03) the wind turned in the NE direction and was intensified. Measured wind speed was from 5 to 25 m/s; the air temperature was between 20 to 34 °C and relative humidity 50–95 % during sampling time.

2. 2. Sampling of Particulate Matter PM10

The research included samples of particulate matter PM10 collected according to standard EN 12341:2014 using low-volume air sampler (TCR Tecora Skypost PM, Leckel SEQ 47/50) with a flow rate of 38.3 L/min.

Aerosol samples were collected on quartz filters (Munktell, quartz microfiber discs, 47 mm) during the period from day 06/07/2015 with beginning at 2 pm and finished on 09/07/2015 at 2 pm. Three samples were gathered consecutively; each sample was collected within 24 hours. All experimental devices, including a low-volume air sampler probe and glassware, were pre-extracted with dichloromethane. A reagent blank was analysed before sample analysis in each batch. Quartz filters were combusted before use at 500 °C for six hours. After the gravimetric determination of PM10 particles (Standard EN 12341:2014) the collected samples were placed in a glass vial with a Teflon cap and stored at –20 °C prior to analysis. Samples were extracted three times (3 × 20 mL) using a shaker with orbital movement with a mixture of dichloromethane/methanol (2:1 v/v). On a rotary evaporator, the combined extracts were evaporated to dryness. Dry residues of extracts were dis-

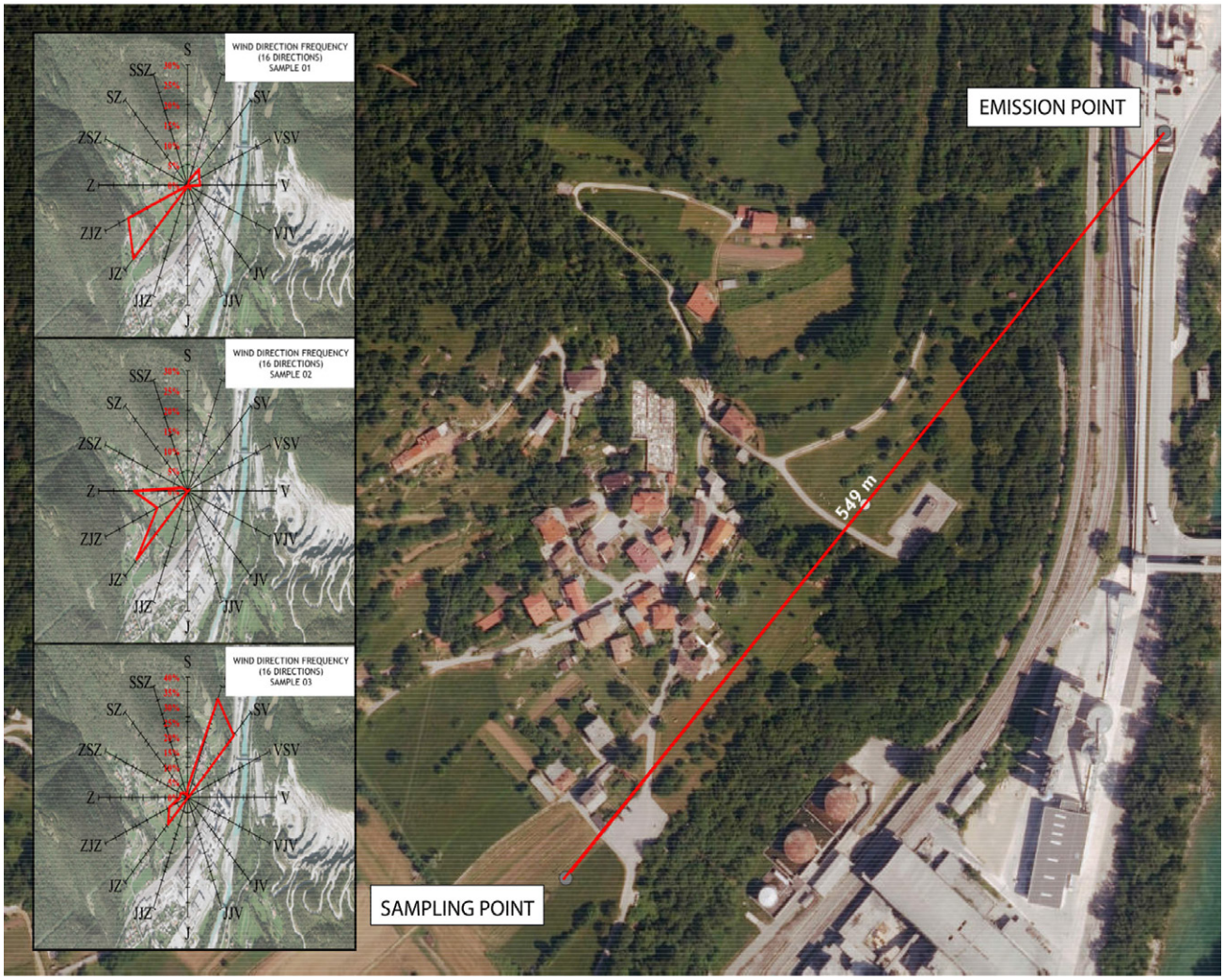

Figure 1. Position of the sampling point, the direction and distance to the emission source. Left: wind roses diagram for sample 01, 02 and 03 from 6. July to 9. July 2015. http://gis.arso.gov.si/atlasokolja/.

solved in pyridine and derivatised with MSTFA (*N*-methyl-*N*-trimethylsilyl trifluoroacetamide) for one hour at 60 °C. Concentrated and derivatized extracts with a final volume of 100 µL were quantitatively transferred into a glass vial and analysed with GC/MS.

2. 3. Instrumental Analysis

Agilent (5973) mass spectrometer connected to a gas chromatograph Agilent (6890) and Agilent autosampler (7683) was used. For the chromatographic separation, an Agilent capillary column DB-UI 8270 D with the dimensions of 30 m and an internal diameter of 0.25 mm and a film thickness of stationary phase 0.25 µm was used. The temperature program was following: 0.75 min at a temperature of 105 °C, 30 °C /min up to 120 °C (0.1 min), 2.7 °C/min to 320 °C (5 min). The carrier gas was helium (He 6.0, Messer Austria) at a constant flow of 0.9 ml/min. The ion source temperature was 250 °C. The injection port and transfer line were kept at 290 °C. The mass spectrometer was operated in electron ionization (+EI) mode at 70 eV and scanned in full scan mode in the range 70–800 Da. Chromatograms were processed by a computer program AMDIS (Automated Mass Spectral Deconvolution and Identification System Software). Detected compounds were identified by comparing their spectra with those reported in the Willey and NIST (W10N14) standard mass spectra database and with data in the literature or by own spectra interpretation. The reported mass spectra showed a good mass spectral match quality, better than 90.

3. Results and Discussion

3. 1. Influences of the Urbane Background Atmosphere

At the time of measurements, weather conditions were different, the first two samples were gathered when SW wind blowing, while the third sample was gathered

when NE wind was blown. When the wind has turned from SW to NE in the direction to sampling point, in the extract of sample 03 a group of nitrogenous organic compounds traces was detected. From the review of detected compounds in all three chromatograms of sample 01, 02 and 03 (Figure 2 and Figure 3) the most intensive polar organic compounds are derivatives of sugars, sugar alcohols and mono-, di- and tri-carboxylic acid. Carboxylic acids are frequently present in atmospheric aerosol samples. These compounds could be oxidation products from

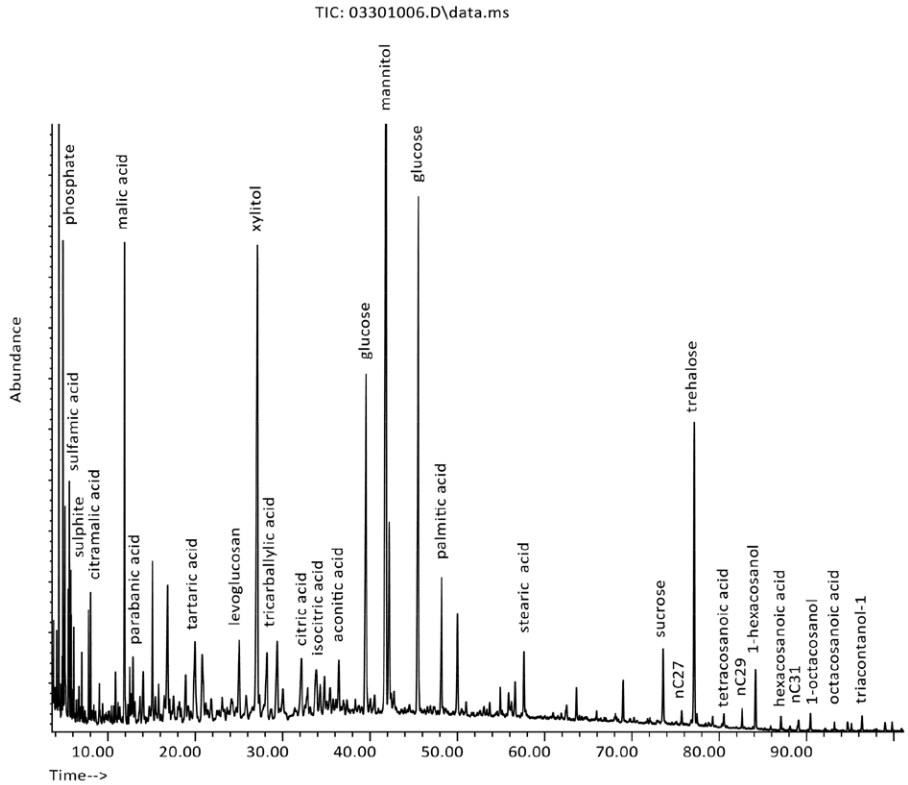

Figure 2. GC/MS total ion chromatograms showing trimethylsilylated derivatives observed in the extract in sample 03.

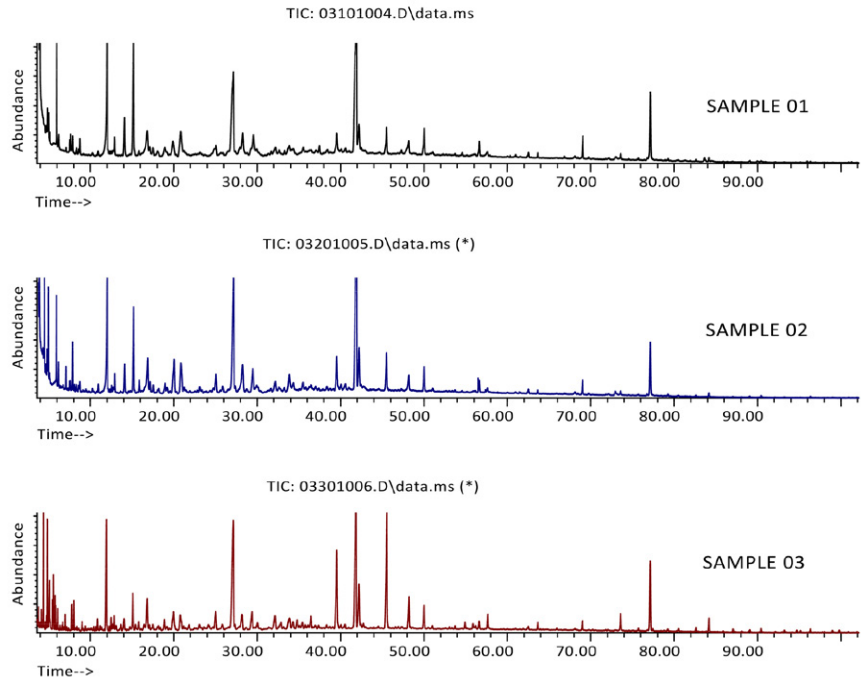

Figure 3. Comparison of the total ion chromatogram (TIC) between samples 01, 02 and 03.

biopolymers or incomplete combustion product, and they could represent secondary organic compounds formed by photochemical reactions.[10,11] The presence of n-alkanes and a fraction of polycyclic aromatic compounds (PAH) is low, at detection limit of the experimental method. It is related to the summer season, when there is no use of fossil fuels for heating and at the same time the photochemical degradation is high. Compounds are characteristic for pollution of the urbane atmosphere and show the impact of different sources such as traffic, various industrial processes, incineration, and energetic production system. Several comprehensive reviews on the topic of the presence, formation, and composition of atmospheric aerosols exist.[12,13,14]

3. 2. Influences of the Cement Plant Emmisions

Ammonia is the most abundant basic gas which participates in acid–base reactions in the condensed phase on atmospheric particle matter. Condensable particulate matter is not directly emitted as a solid or liquid at the stack. Instead, gaseous emissions such as sulfuric acid, sulfamic acid, ammonium sulfate or sulfamate and certain metal vapours condense upon cooling and dilution in the ambient air to form solid or liquid particles following discharge from the stack. The inorganic part of aerosols detected in sample 03 as TMS derivatives include sulfamic acid (Figure 4), sulfite, sulfate, phosphate and to lesser extent vanadate(V) (Figure 5). Ammonia catalyzes the atmospheric oxidation of sulfur dioxide to sulfur trioxide and reacts rapidly with acidic components of the atmosphere. The ammonium salts as components of aerosols are formed.[15] Because the concentration of water is greater than the concentration of ammonia, under normal atmospheric conditions, SO_3 will react predominantly with water, not with ammonia. Under the conditions expected during a massive release of ammonia, the reaction of SO_3 (a strong Lewis acid) with ammonia (a good electron pair donor) sulfamic acid is formed (3).[16]

$$NH_3(g) + SO_3(g) \rightarrow {}^{+}NH_3\text{-}SO_3^{-}(g) \rightarrow \rightarrow H_2N\text{-}SO_3H(s) \quad (3)$$

The vanadium content in soils and waters is primarily determined by the geological parent material. Anthropogenic emissions, mainly from the combustion of fossil fuels or industry processes, may enhance soil vanadium concentrations locally. Vanadium is an essential element that has beneficial effects at low concentration but becomes toxic when present in higher amounts. Vanadium in tetravalent and pentavalent oxidation states, especially as ammonium salt in the environmental samples as are aerosol particles, are water soluble and toxic. Speciation analysis of this element is important for evaluating the potential risk to the environmental and biological systems rather than determining total vanadium contents.[17–21]

Urea pyrolysis reaction (4,5) plays an important role in the urea-based NO_x removal process.

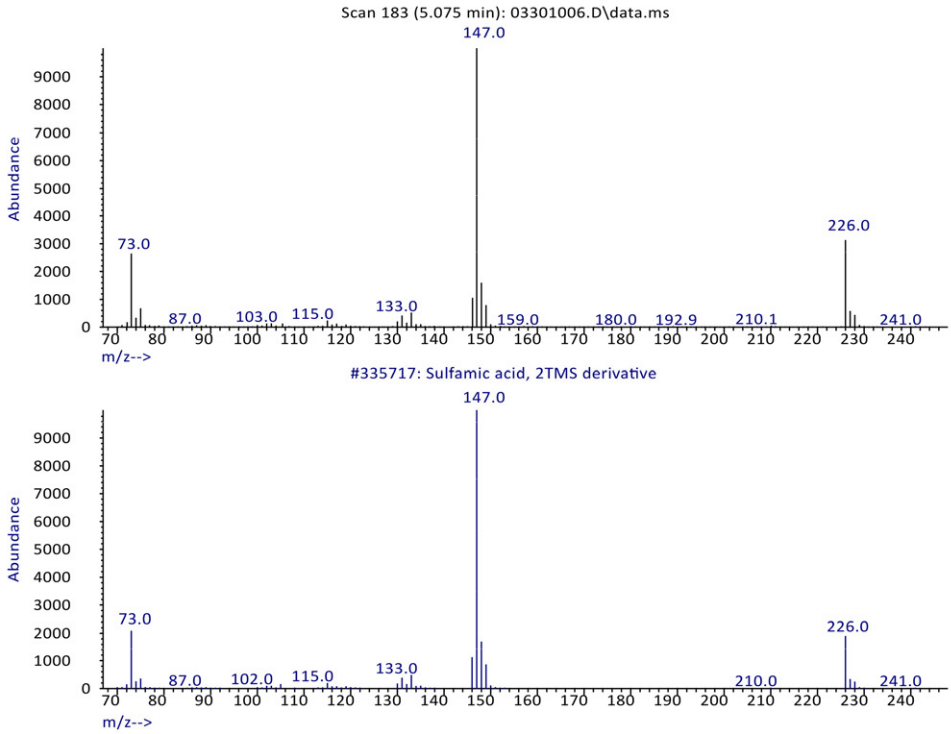

Figure 4. Mass spectrum comparison of sulfamic acid in sample 03 and Willey-NIST library mass spectral data.

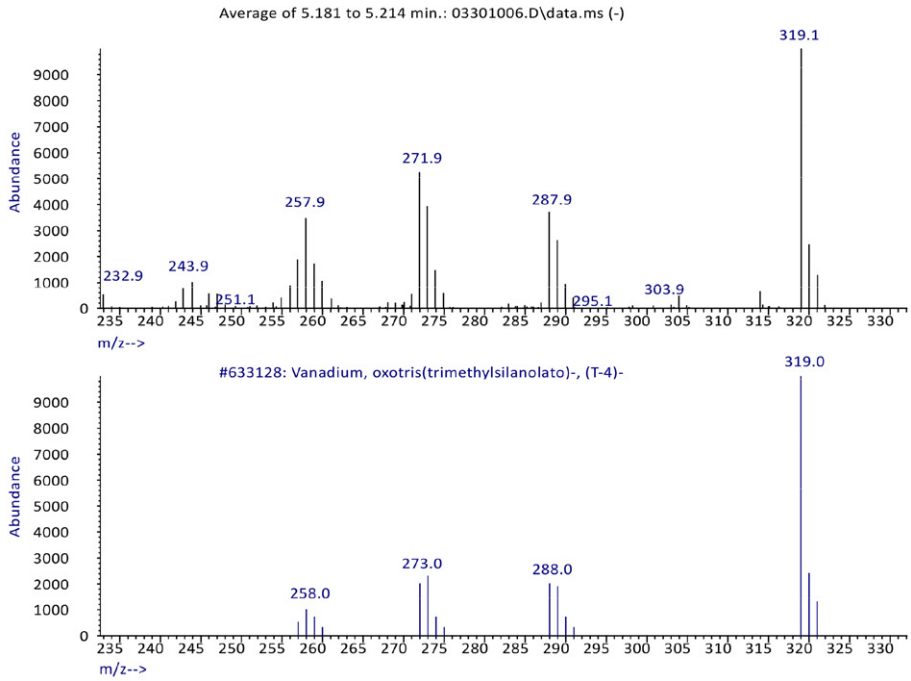

Figure 5. Mass spectrum comparison of vanadic(V) acid 3TMS derivative in sample 03 and Willey-NIST library mass spectral data.

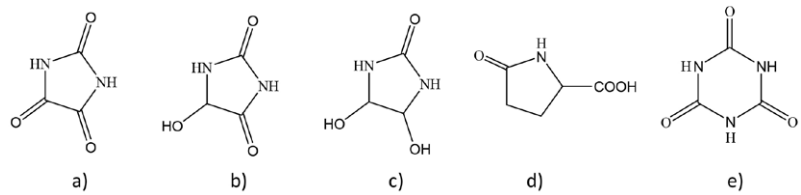

Figure 6. The formation tentatively involves the condensation reaction of urea and glyoxal, hydrated glyoxal or oxalic acid as a reactant. Imidazoline-2,4,5-trione (a) 5-hydroxy-2,4-imidazolidindione (b), 4,5-dihydroxy-2-imidazolidinone (c), 5-oxo-proline (d) and cyanuric acid (e) as a side reaction of urea thermolytic decomposition were also detected.

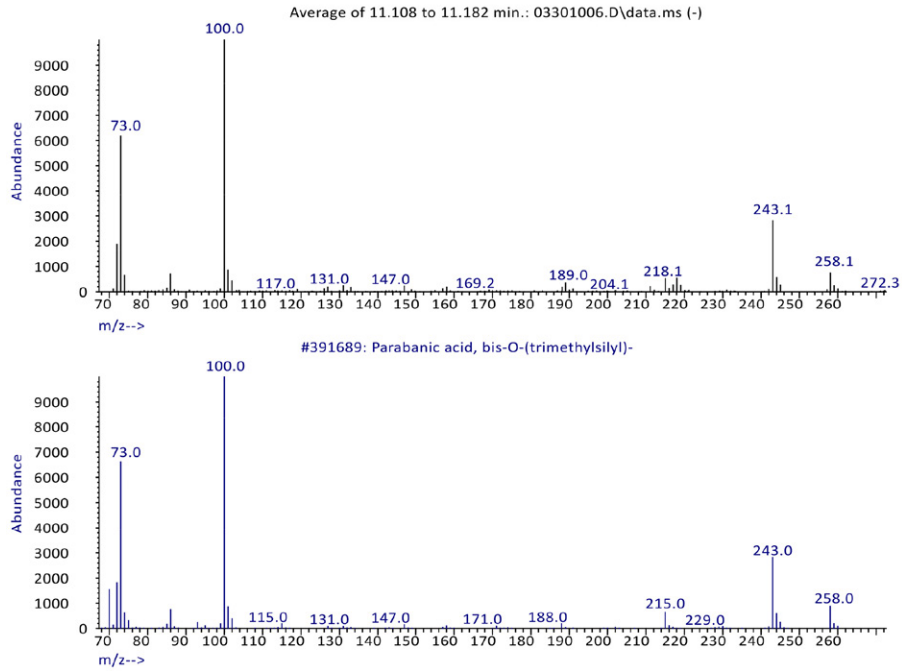

Figure 7. Mass spectrum comparison of imidazolidine-2,4,5-trione 2TMS derivative (parabanic acid 2TMS) in sample 03 and Willey-NIST library mass spectral data.

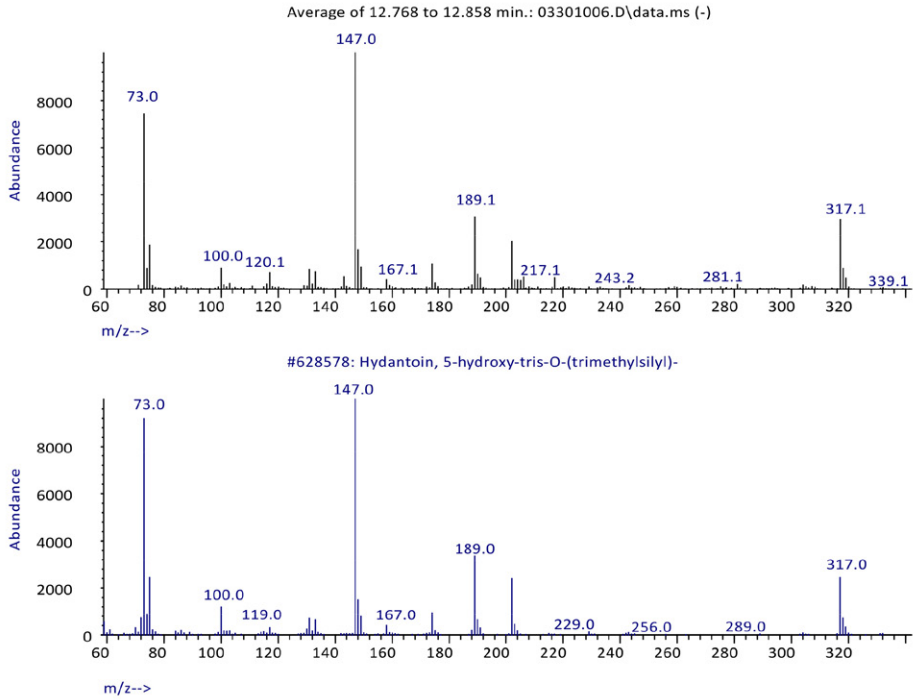

Figure 8. Mass spectrum comparison of 5-hydroxy-hydantoin 3TMS derivative in sample 03 and Willey-NIST library mass spectral data.

$$NH_2CONH_2 \rightarrow NH_3 + HNCO \quad (4)$$

$$HNCO + H_2O \rightarrow NH_3 + CO_2 \quad (5)$$

Overview of recorded mass spectra gives the presence of nitrogen compounds formed during the urea thermolytic process in hot cement kiln gases (Figure 6, 7 and 8).

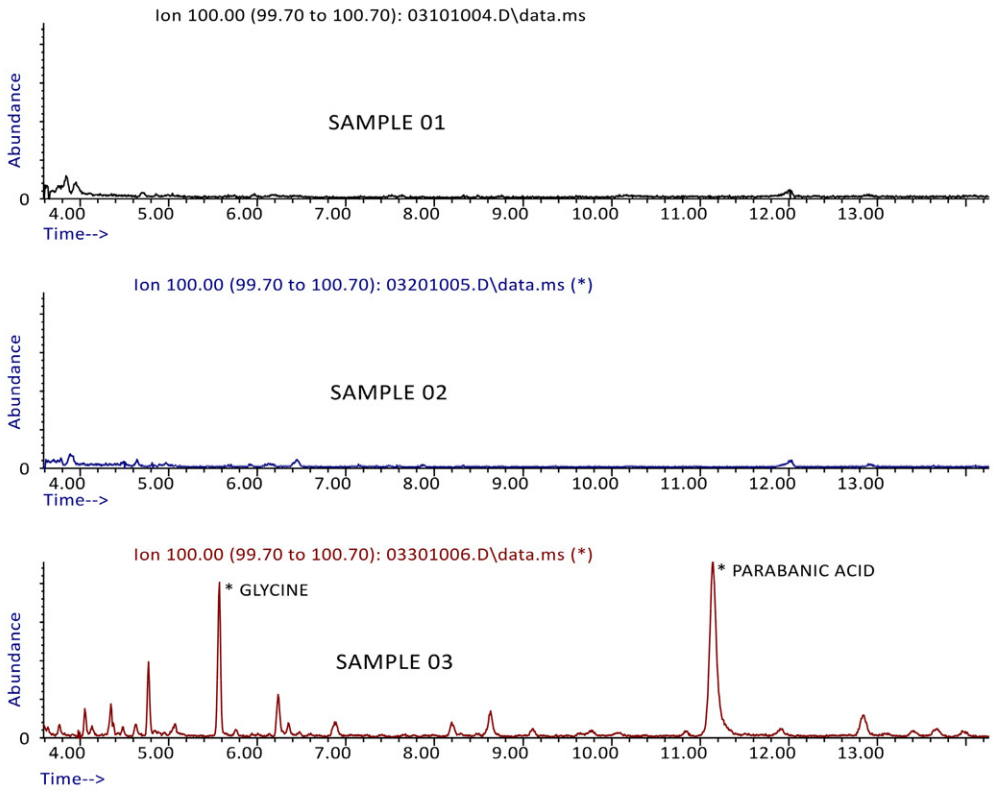

Figure 9. Comparison of ion current of mass fragments *m/z* 100 characteristic for silylated derivatives of glycine and parabanic acid TMS derivative from all three sample extracts.

The number of potential reaction partners in ambient aerosols is high, and the identification of appropriate tracer compounds is necessary to estimate the source of organic compounds. It is expected that imidazolidinone formation from α-dicarbonyl compounds and ammonia or urea in aerosols should be favoured in regions with aerosols exhibiting more alkaline pH values and higher ammonium concentrations which is valid for cement plant emissions.

Three amino acid were detected. The most abundant species are glycine, then β-alanine and in traces γ-aminobutyric acid, both as a nonproteinogenic amino acid, formed as degradation of biomass in raw materials or thermic processes.[22,23] At pyro-processing of raw material in cement plant amino acid decompose thermally, they do not sublimate, nor do they melt. Only three gases are formed, mostly H_2O, NH_3 to a lesser extent, and hardly any CO_2. Cysteine forms H_2S but not CS_2. Thermolytically formed liquid or solid residues are lactams and heterocyclic compounds with 5- or 6-membered non- (or only partially) aromatic rings, containing one or two nitrogen atoms, most of them with peptide bonds present.[24]

Air quality monitoring at fixed sites is a major instrument to check compliance with the limit or target values, which have been set for the protection of human health.[25] Comparison of the ion current of mass fragments m/z 100 characteristic for silylated derivatives of glycine and parabanic acid from all three sample extracts is presented in Figure 9. It shows the inadequacy of the position of the monitoring site with respect to the wind conditions at the time of sampling that might lead to different assessments of air pollution exposure.

Monitoring of NO_x and leak of NH_3 gases with determination of organic nitrogen compounds composition can help to control the SNCR or SCR process in cement kiln and to determine different influences on air pollution. It is suggested that surface-monitoring sites should be established downwind and upwind of cement factories to simultaneously monitor their emissions. Our research suggests that additionally to obligatory cement plant emission monitoring program also further, more detailed investigation of the impact of emissions on the environment is strongly recommended.

4. Conclusions

With the GC/MS analytical approach, the composition of organic compounds adsorbed onto dust particles sampled according to standard EN 12341 in the outdoor air near the cement plant was determined. Recorded mass spectra show the presence of nitrogen compounds formed during urea thermolytic process in hot cement kiln gases. Parabanic acid (imidazoline-2,4,5-trione), 5-hydroxyhydantoin (5-hydroxy-2,4-imidazolidindione), 4,5-dihydroxyhydantoine (4,5-dihydroxy-2-imidazolidinone), 5-oxo-proline and cyanuric acid as a side reaction of urea thermolytic decomposition were detected in sample 03. Amino acid detected were glycine, β-alanine and traces γ-aminobutyric acid. The inorganic part of aerosols detected in sample 03 as TMS derivatives include in descendent order: sulfamic acid > sulfate > sulfite > phosphate and to a lesser extent vanadate(V). Special attention should be devoted to the presence of vanadate(V) oxyanion and sulfamic acid. The particle matter toxicity derives not only from the physical presence of particles on biological tissues but also from the toxic effects of chemical constituents. Knowledge of detailed chemical compositions of particles is crucial to assess the health impacts since the biological responses to aerosols are not always linked with major constituents, but rather with toxicologically potent minor components. This demonstrates the necessity of the identification of organic compounds at trace levels to enable a better understanding of relevant air pollution processes.

5. References

1. Directive 2008/50/EC of the European Parliament and of the Council of 21 May 2008 on ambient air quality and cleaner air for Europe, OJ L 152, **2008**, pp. 1–44.
2. SIST EN 12341:2014, Ambient air – Standard gravimetric measurement method for the determination of the PM10 or PM2,5 mass concentration of suspended particulate matter, https://standards.iteh.ai/catalog/standards/sist/5d138eac-4d44-4419-a069-eb23d01a9b0c/sist-en-12341-2014 (accessed January 3, 2021)
3. A. Miuc, E. Vončina, U. Lešnik, *Acta Chim. Slov.* **2015**, *62,* 834–848. **DOI:**10.17344/acsi.2015.1542
4. Best available techniques (BAT) reference document for the production of cement, lime and magnesium oxide: Industrial emissions directive **2010**/75/EU: (Integrated Pollution Prevention and Control), pp. 1–480. **DOI:**10.2788/12850
5. E. Borrás, L. A. Tortajada-Genaro, F. Sanz, A. Muñoz, *Atmosphere* **2021**, 12, 94, 1–15. **DOI:**10.3390/atmos12010094
6. B. Jiang, D. Xia, *Clean Techn Environ Policy* **2020**, **DOI:**10.1007/s10098-020-01923-x
7. EPA-456/F-99-006R, November **1999** Nitrogen Oxides (NOx), Why and How They Are Controlled, i–48, (technical bulletin), https://www3.epa.gov/ttncatc1/dir1/fnoxdoc.pdf (accessed January 8, 2021)
8. H. C. Kim, C. Bae, M. Bae, O. Kim, B. U. Kim, C. Yoo, J. Park, J. Choi, J.-bum Lee, B. Lefer, A. Stein, S. Kim, *Atmosphere* **2020**, 11, 881, 2–14. **DOI:**10.3390/atmos11080881
9. D. Wang, N. Dong, Y. Niu, S. Hui, *Hindawi Journal of Chemistry* **2019,** 1–11. **DOI:**10.1155/2019/6853638
10. E. Borrás, L. A. Tortajada-Genaro, F. Sanz A. Muñoz , *Atmosphere* **202**1, 12, 2-15, 94, **DOI:**10.3390/atmos12010094
11. P. Sricharoenvech, A. Lai, T. N. Oo , M. M. Oo, J. J. Schauer, K. L. Oo, K. K. Aye, *Int. J. Environ. Res. Public Health* ,**2020**, 17, 4145; **DOI:**10.3390/ijerph17114145

12. D. J. Bryant, W. J. Dixon, J. R. Hopkins, R. E. Dunmore, K. L. Pereira, M. Shaw, F.A. Squires, T. J. Bannan, A. Mehra, S. D. Worrall, A. Bacak, H.Coe, C. J. Percival, L. K. Whalley, D. E. Heard, E. J. Slater, B. Ouyang, T. Cui, J. D. Surratt, D.Liu, Z. Shi, R. Harrison, Y. Sun, W. Xu, A.C. Lewis, *Atmos. Chem. Phys.* **2020**, 20, 7531–7552. **DOI:**10.5194/acp-20-7531-2020
13. T. Schilirò, S. Bonetta, L. Alessandria,V. Gianotti, E.Carraro, G. Gilli, *Environmental Toxicology and Pharmacology* **2015**, 39, 2, 833–844. **DOI:**10.1016/j.etap.2015.02.00
14. R. Zhang, G. Wang, S. Guo, M. L. Zamora, Q. Ying, Y. Lin, W. Wang, M. Hu, Y. Wang, *Chem. Rev.* **2015**, 115, 3803–3855. **DOI:**10.1021/acs.chemrev.5b00067
15. J. J. Renard, S. E. Calidonna, M. V. Henley *Journal of Hazardous Materials B* **2004**,108, 29–60. **DOI:**10.1016/j.jhazmat.2004.01.015
16. H. Li, J. Zhong, H. Vehkamäki, T, Kurtén, W. Wang, M. Ge, S. Zhang, Z. Li, X. Zhang, J.S. Francisco, X. C. Zeng, *J. Am. Chem. Soc.* **2018**, 140, 35, 11020–11028. **DOI:**10.1021/jacs.8b04928
17. M. A. Larsson, Vanadium in Soils - Chemistry and Ecotoxicity, Swedish University of Agricultural Sciences, **2014**, (electronic version), 1–60, https://pub.epsilon.slu.se/11653/1/larsson_ma_141117.pdf (accessed January 8, 2021)
18. X. C. Goso, H. Lagendijk, M. Erwee and G. Khosa *Hydrometallurgy Conference 2016: Sustainable Hydrometallurgical Extraction of Metals Cape Town,* 1–3 August **2016**, 69–79. Indicative Vanadium Deportment in the Processing of Titaniferous Magnetite by the Roast–Leach and Electric Furnace Smelting Processes.
19. X. Hu, Y. Yue, X. Peng, *Environ Sci Pollut. Res.* **2019**, 26:17891–17900. **DOI:**10.1007/s11356-017-0342-2
20. K. H. Jung , D. Torrone, S. Lovinsky-Desir, M. Perzanowski, J. Bautista, J. R. Jezioro1, L. Hoepner, J. Ross, F. P. Perera, S. N. Chillrud, R. L. Miller, *Respiratory Research* **2017**, 18:63, 1–11. **DOI:**10.1186/s12931-017-0550-9
21. F. Dominici, R. D. Peng, K. Ebisu, S. L. Zeger, J. M. Samet, M. L. Bell, *Environ Health Perspect* **2007**, 115, 1701–1703. **DOI:**10.1289/ehp.10737
22. E. Barbaro, R. Zangrando, I. Moret, C. Barbante, P. Cescon, A. Gambaro, *Atmospheric Environment* **2011**, 45, 5050–5057. **DOI:**10.1016/j.atmosenv.2011.01.068
23. I. M. Weiss, C. Muth, R. Drumm, H. O. K. Kirchner, *BMC Biophysics* **2018**, 11:2, 2–15. **DOI:**10.1186/s13628-018-0042-4
24. F. J. Kelly, J. C. Fussell, *Phil.Trans.R.Soc.* **2020**, 378:20190322. **DOI:**10.1098/rsta.2019.0322
25. C. Nagl, W. Spangl, I. Buxbaum, *Sampling points for air quality*, Study for the Committee on the Environment, Public Health and Food Safety, Policy Department for Economic, Scientific and Quality of Life Policies, European Parliament, Luxembourg, **2019**, 1–102, https://www.europarl.europa.eu/RegData/etudes/STUD/2019/631055/IPOL_STU(2019)631055_EN.pdf (accessed January 5, 2021)

Povzetek

Cilj študije je poiskati markerske spojine emisij iz cementnih peči, ki kažejo na razliko glede na sestavo okoliškega zraka na širšem območju. Določili smo sestavo organskih spojin adsorbiranih na prašnih delcih PM10, ki so bili odvzeti v skladu s standardom EN 12341:2014 v vzorcih zraka v bližini cementarne. Možnih je tudi več stranskih reakcij, ki se pojavijo v toku vročih dimnih plinov hkrati z dejanskimi glavnimi reakcijami. To vodi do nastanka sledi organskih dušikovih spojin. Za GC/MS analizo hlapnih in pol hlapnih polarnih spojin smo uporabili silililiranje kot metodo derivatizacije. Glavnino zaznanih spojin predstavljajo spojine silililiranih derivatov sladkorjev, sladkornih alkoholov ter mono-, di- in tri-karboksilnih kislin. Sestava je značilna za onesnaženo urbano ozračje. Med organskimi dušikovimi spojinami, ki nastanejo med termolitskim razpadom sečnine v vročih plinih cementne peči, smo zaznali parabansko kislino, 5-hidroksihidantoin, 4,5-dihidroksihidantoin, 5-oksoprolin in cianurno kislino. Anorganski del aerosolov vključuje sililirane derivate sulfamske kisline, sulfata, sulfita, fosfata in vanadijeve(V) kisline. Podrobna kemijska sestava prašnih delcev PM10 je pomembna za toksikološko oceno vplivov na okolje in zdravje, saj biološki odziv ni vedno povezan s spojinami, ki jih je največ.

DRUŠTVENE VESTI IN DRUGE AKTIVNOSTI
SOCIETY NEWS, ANNOUNCEMENTS, ACTIVITIES

Vsebina

Contents

»Kisanje« severnega Jadrana

Jadran Faganeli,[1,*] Nives Ogrinc,[2] Samo Tamše,[2] Bor Krajnc[2] Valentina Turk,[1] Alenka Malej[1] in Nives Kovač[1]

[1] *Morska biološka postaja, Nacionalni inštitut za biologijo, Fornače 41, 6330 Piran, Slovenija*

[2] *Odsek za znanosti o okolju, Institut Jožef Stefan, Jamova cesta 39, 1000 Ljubljana, Slovenija*

** Corresponding author: E-mail: jadran.faganeli@nib.si, Tel.: +386 5 9232911*

Received: 08-16-2021

Povzetek

Prikazan je kratek pregled dosedanjega znanja o karbonatnem ravnotežju severnega Jadrana, ki je dobro pufran zaradi dotoka karbonata z rekami alpskega in kraškega izvora in s tem omejenemu »kisanju«. V prihodnosti napovedujemo še vedno uravnoteženost s povečanim raztapljanjem CO_2. V plitvih evtrofnih obalnih vodah bo lahko povezan vpliv povečanja atmosferskega CO_2, naraščajoče temperatutre in rečnega vnosa antropogenega CO_2 ter zmanjšane puferske kapacitete povečal »kisanje« morja in pomembno vplival na karbonatne organizme.

Ključne besede: karbonatno ravnotežje; tok CO_2; kisanje morja; severni Jadran

Danes se karbonatno ravnotežje v morju spreminja zaradi raztapljanja naraščajočega CO_2 (v obalnih predelih tudi dušikovih in žveplovih oksidov) v atmosferi (najmanj četrtina) kot posledica človekove dejavnosti.[1] V morskem karbonatnem ravnotežju, ki ga opredeljujejo alkalnost (TA, A_T ali T_A), raztopljeni anorganski ogljik (ang. Dissolved Inorganic Carbon – DIC), parcialni tlak (fugativnost) CO_2 (pCO_2, fCO_2) in pH (dovolj dve spremenljivki, najbolje najtežje merljivi DIC in pCO_2, z uporabo konstant ravnotežij različnih avtorjev v odvisnosti od temperature, tlaka in slanosti), sta hitrejši reakciji fotosinteza in respiracija ter disociacija ogljikove kisline (ionski reakciji) kot pa vzpostavitev ravnotežja med atmosferskim CO_2 in morsko vodo.[2] Posledica je znižanje pH, danes približno 0,1, glede na predindustrijsko dobo. Pojav je znan kot »kisanje morja« (»acidifikacija«). Površinska plast oceana je še vedno prenasičena glede na aragonit (prisoten v koralah in mehkužcih) in kalcit (prisoten v kokolitoforidih in foraminiferah). V estuarijih vodi absorpcija CO_2 do znižanja pH, v odvisnosti od lokalnega pufranja (puferske kapacitete) vode, tudi zaradi evtrofikacije.[3,4]

Tudi Jadransko morje je ponor CO_2 in privzema približno 1–3 mol C m^{-2} $leto^{-1}$.[5] Večji ponor je v zimskem in vetrovnem obdobju in vpliv temperature (»topnostna črpalka«) presega porabo v primarni produkciji (»biološka črpalka«). Ponor CO_2 v Jadranu je primerljiv z Lyonskim zalivom v SZ Sredozemlju (4–5 mol C m^{-2} $leto^{-1}$).[6,7] Primerjava podatkov z dveh zimskih križarjenj v severnem Jadranu leta 1983 in 2008 je pokazala padec pH 0,063[8], kar ustreza letnemu padcu (»kisanju«) pH 0,003, in je primerljivo s Sredozemljem: med 0,003 in 0,004 pH v odprtih in obalnih vodah.[8,9,10] Pri navajanju trendov in primerjav moramo upoštevati, na žalost ne vedno, različne uporabljene analizne metode (potenciometrično ali kolorimetrično določanje pH, merjeni ali izračunani pCO_2) in natančnost meritev v karbonatnem ravnotežju v morju (pH ± 0.002, TA ± 1 µmol/kg, DIC ± 1 µmol/kg, pCO_2 ± 0.5 µbar (± 0.05 Pa)[11], kar večkrat vodi do ocen, ki jih ni mogoče eksperimentalno preveriti in primerjati. Ker je pufranost (izračunani Revellov faktor[2] kot indikator puferske kapacitete približno 10) Jadranskega morja razmeroma visoka, le-to ni izdatno podvrženo »kisanju«.[12] Izmerjena TA (2,6–2,7 mmol l^{-1}) v Jadranskem morju je med najvišjimi v Sredozemlju[12,13,14] zaradi rečnega vnosa (slika 1) karbonata s preperevanjem apnenca in dolomita v Apeninih, Alpah, Krasu in Dinarskem pogorju (slika 2).[15,16] Jadransko morje (319 Gmol $leto^{-1}$) je, takoj za Egejskim morjem z vnosom iz Črnega morja, najpomembnejši rečni vnos alkalnosti v Sredozemlje.[14] Približno 60 % vnosa alkalnosti izvira iz Pada.[17] V severnem Jadranu alkalnost pada z naraščanjem slanosti[18] (slika 3). Vode Jadranskega morja so prenasičene glede na kalcit in aragonit v celem letu.[19] Pri dnu je nasičenost sicer manjša zaradi bentoške respiracije in remineralizacije predvsem v poletnem obdobju gostotne razslojenosti vodnega stolpa.

Slika 1. Severni Jadran z rečnimi pritoki.

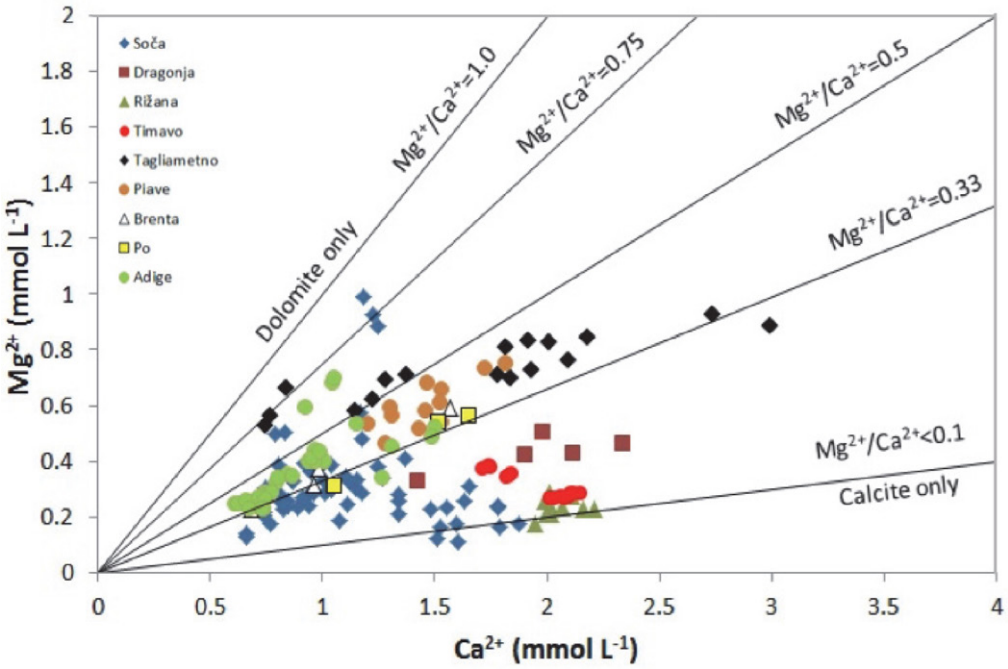

Slika 2. Ca^{2+} in Mg^{2+} v severnojadranskih rekah. Razmerje $Mg^{2+}/Ca^{2+} < 0,1$ kaže raztapljanje čistega kalcita, razmerje $Mg^{2+}/Ca^{2+} = 0,33$ ponazarja vode, ki raztapljajao enake molske deleže kalcita in dolomita, razmerje Mg^{2+}/Ca^{2+} približno 1 pa raztapljanje čistega dolomita.[25]

Tudi Tržaški zaliv deluje na letni ravni kot ponor CO_2 (približno 1,5 mol m^{-2} $leto^{-1}$) in je bolj izrazit pozimi s prevladujočim vplivom temperature in vetra (slika 4).[16,20,21,22] Poleti lahko obstoji šibek nasprotni tok v smeri atmosfere, posebej še v izlivu (estuariju) Soče.[22,23] Reke (predvsem Soča), ki se stekajo v Tržaški zaliv, izpirajo karbonatna področja (Julijske Alpe, Kras) podvržena intenzivnemu preperevanju.[24] Zato sta alkalnost in koncentracija DIC v rečnih vodah in posledično v obalnem morju višje (slika 5). Na osnovi masne bilance in izotopske sestave $^{13}C_{DIC}$ smo ocenili, da reke prispevajo približno do 15% k DIC v površinski plasti morja v

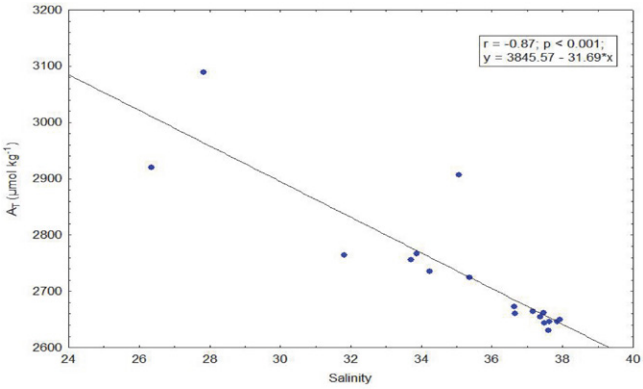

Slika 3. Alkalnost (A_T) v odvisnosti od slanosti v severozahodnem Jadranu pod vplivom izliva reke Pad v obdobju gostotne razslojenosti vodnega stolpa[17]

zalivu.[25] Povečane koncentracije DIC in hranil se nato zmanjšajo zaradi bioprodukcije predvsem v času povečanega zadrževalnega časa vode v zalivu.[22] Vpliv posameznih procesov na alkalnost in DIC je nazorno prikazan v nomogramu (slika 6). Vpliv temperature (»termični«) na (izračunani) pCO_2 ($pCO_{2,NT}$) prevladuje nad biološkim (»netermičnim«) vplivom ($pCO_{2,T}$) (slika 6) v celotnem letnem obdobju v zalivu[16], v severnem Jadranu pa je »termični« vpliv izrazit poleti in biološki vpliv prevladuje v ostalih sezonah.[18] Meritve pH v zalivu kažejo višje vrednosti pozimi in nižje poleti v plasti pri dnu (slika 7). Karbonatno ravnotežje v plasti pri dnu uravnavajo procesi na meji sediment-voda in v pornih vodah površinskega sedimenta. Študij bentoških tokov DIC in njihove izotopske sestave ^{13}C ($d^{13}C_{J\text{-}DIC}$) ter tokov Ca in Mg je pokazal, da prihaja na meji sediment-voda do

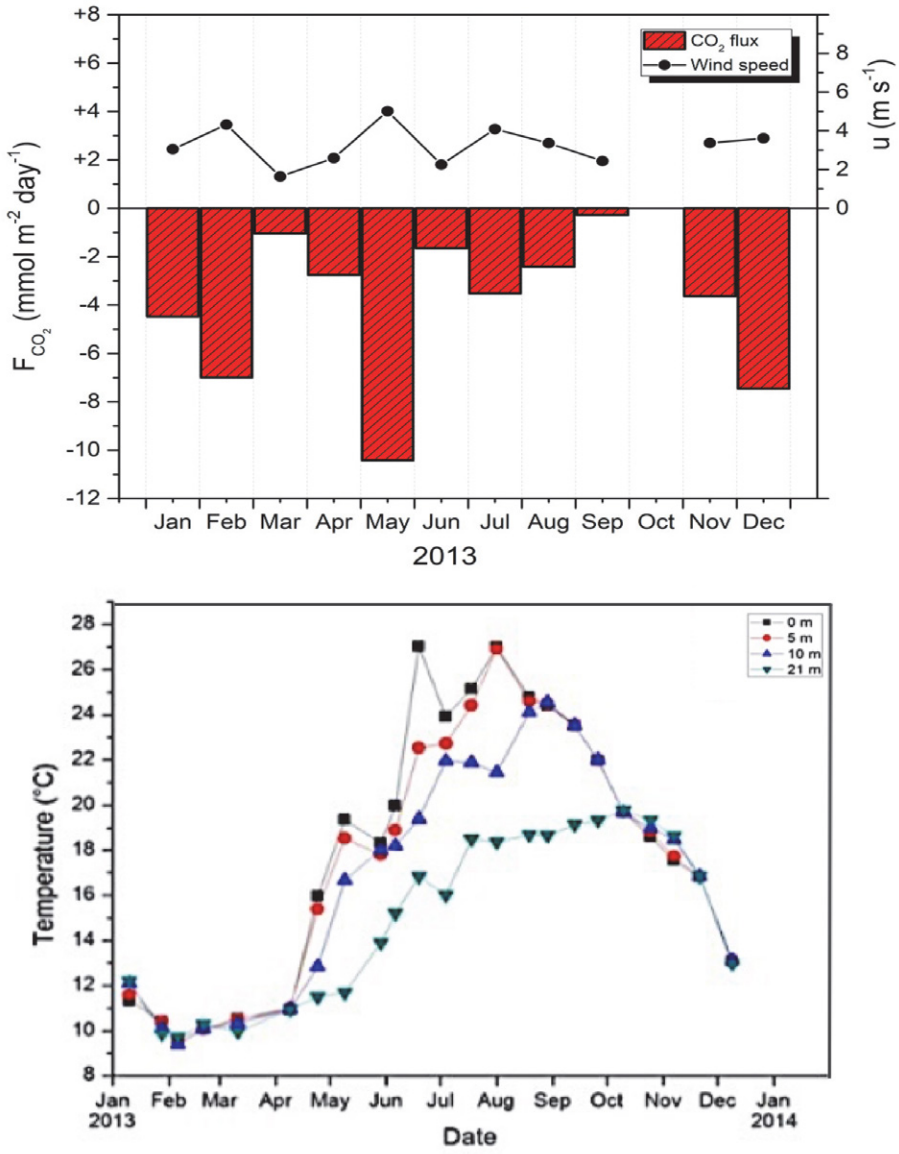

Slika 4. Tok CO_2 med zrakom in vodo (F), povprečna dnevna hitrost vetra 5 m and morsko gladino (u) in temperature morja v Tržaškem zalivu (oceanografska boja »VIDA«). Negativne vrednosti predstavljajo tok CO_2 iz atmosfere v morje.[25]

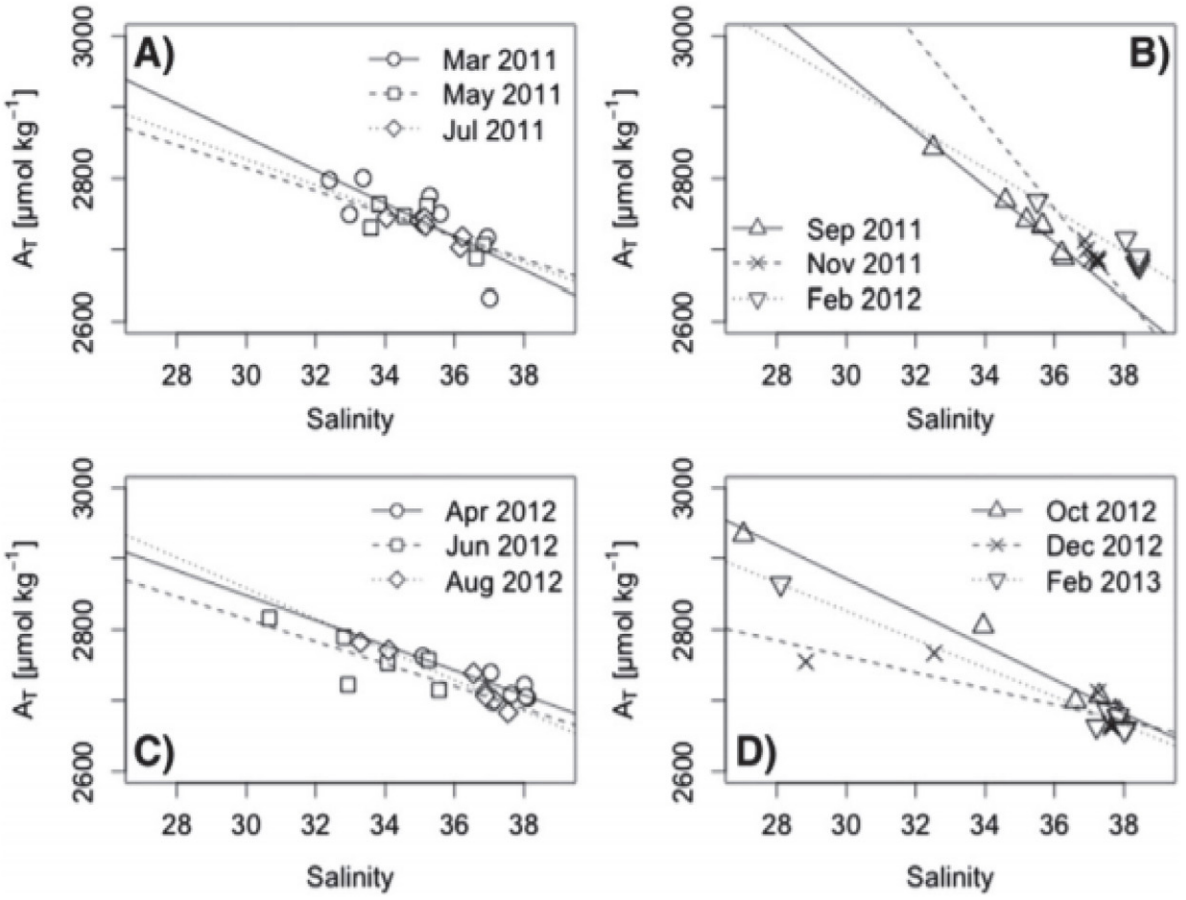

Slika 5. Alkalnost (A_T) in slanost v površinski plasti morja v Tržaškem zalivu[22]

obarjanja karbonatov in obsežnih intenzivnih izmenjav ter adsorpcije Ca in Mg na (in v) glinene minerale.[26] Izotopska sestava $^{13}C_{DIC}$ kaže, da je bentoški tok DIC večinoma organskega izvora in sicer v toplejšem (poletnem) obdobju izvira iz razgradnje razgradljivega organskega C sedimentiranega fitoplanktona in bentoških mikroalg, v hladnejšem (zimskem) obdobju pa iz razgradnje bolj odpornega (tudi kopenskega) sedimentiranega organskega C. V poletnem obdobju gostotne razslojenosti vodnega stolpa prihaja do intenzivne remineralizacije na meji sediment-voda, posebno v anoksičnih razmerah[27], in oksidacije sulfida v H_2SO_4.[28] Takrat poteka omejeno raztapljanje karbonatov, ki prispeva približno 10% k toku DIC (slika 8). Podobne vrednosti (5%) so zasledili tudi ob obali italijanske dežele Emilia-Romagna.[29] Tudi v pornih vodah v površinskem sedimentu izvira nastali DIC s pretežno razgradnjo organske snovi. Delež z izvorom v raztapljanju karbonatov je višji kot na meji sediment-voda in je pomemben v hladnejših obdobjih, ko je razgradnja organske snovi upočasnjena.[30] Zmanjšano raztapljanje (ali povečano obarjanje) ponazarjajo tudi nižje koncentracije Ca in Mg v pornih vodah v anoksičnih razmerah nad sedimentom v primerjavi z oksičnimi razmerami (slika 9). Na pH morske vode vpliva tudi kinetika heterogenih reakcij v sedimentih, saj je reakcija H^+ s karbonati hitrejša kot s silikati. Ker je morje v Tržaškem zalivu prenasičeno glede na kalcit in aragonit (slika 7) in je njegova pufranost visoka, zaliv ni podvržen občutnemu »kisanju«.[16]

V prihodnosti lahko pričakujemo (napovedovanje z modeli) še vedno prenasičenost morja glede na kalcit in aragonit, vendar moramo upoštevati, da organizmi potrebujejo izdatno nasičenje s karbonatnimi minerali. Prognoze (Ocean Carbon Cycle Model Intercomparison Project – OCMIP-3, 1994–2020) kažejo, da bo pufranost morja v severnem Jadranu v prihodnosti verjetno še vedno uravnotežena s povečanim raztapljanjem CO_2. V plitvih evtrofnih obalnih vodah (npr. ob obali dežele Emilia-Romagna, Italija) bo lahko povezan vpliv povečanja atmosferskega CO_2, naraščajoče temperatutre in rečnega vnosa antropogenega CO_2 ter zmanjšane pufranosti povečal »kisanje« morja.[18,25] Pričakujemo lahko pomemben negativen (povečano raztapljanje) vpliv na karbonatne organizme[33], vpliv na mikrobne procese pa zaenkrat ostaja neznanka. Večina študij je pokazala, da sprememba pH vpliva bolj na biogeokemijske procese (kroženje N) kot na mikrobno biodiverziteto.[34,35,36] Morske bakterije vzdržujejo znotrajcelično alkalno homeostazo pH[37], ki je odvisna od pH medija (sinteza znotrajceličnih kislin in baz ali ekspresija genov, ki kodirajo procese protonske čr-

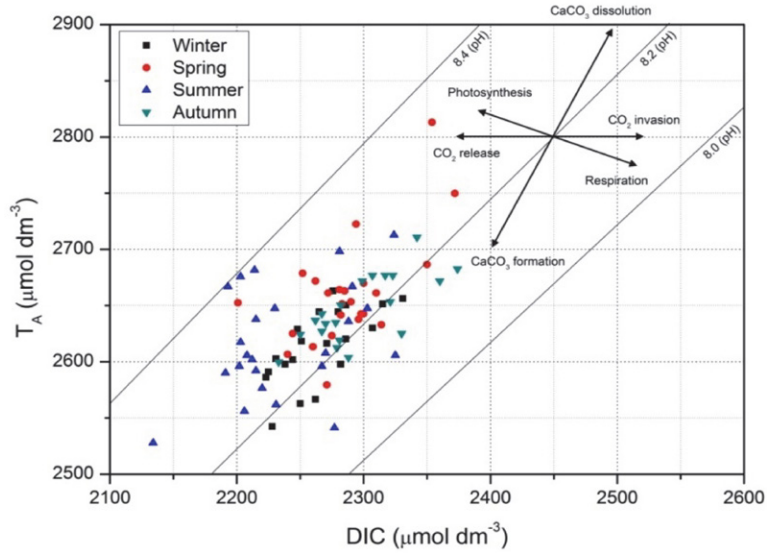

Slika 6. Nomogram med alkalnostjo (T_A) in raztopljenim anorganskim ogljikom (DIC)[32] v Tržaškem zalivu (Oceanografska boja »VIDA«): zima (črno), pomlad (rdeče), poletje (modro) in jesen (zeleno).[17] Premice ponazarjajo konstantni pH kot funkcijo DIC in TA, puščice ponazarjajo vpliv procesov na porazdelitev TA in DIC: fotosinteza, respiracija, raztapljanje karbonata ($CaCO_3$), obarjanje karbonata ($CaCO_3$), raztapljanje atmosferskega CO_2, sproščanje CO_2 v atmosfero

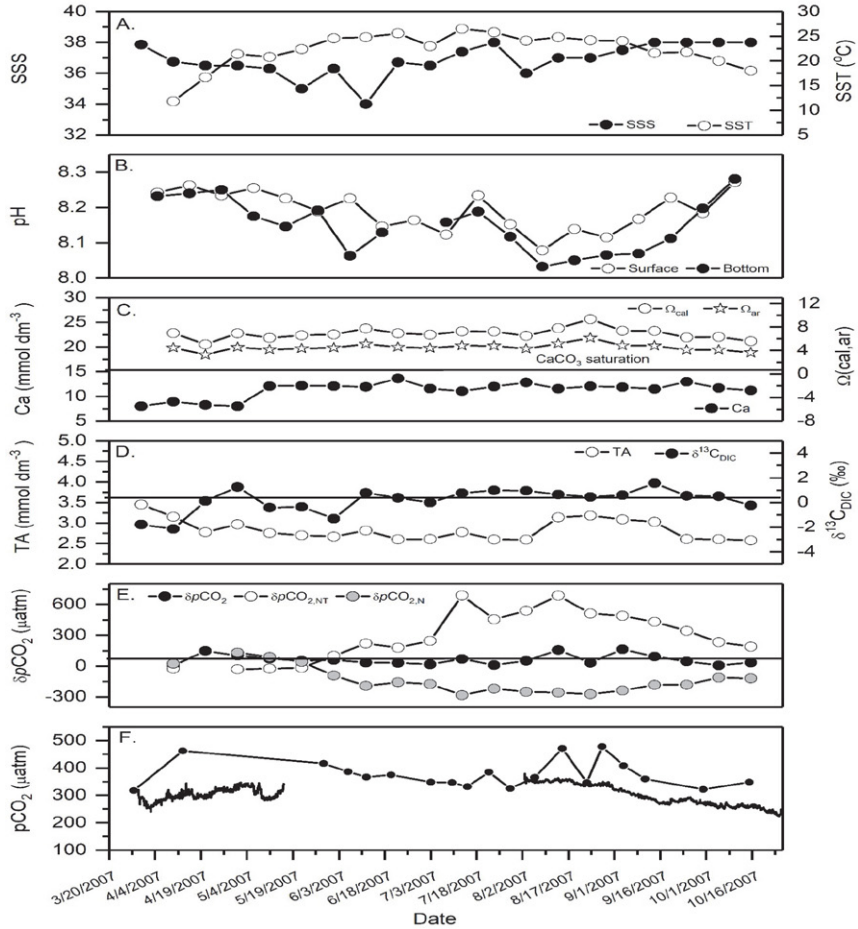

Slika 7. Sezonske spremembe povprečnih dnevnih rečnih pritokov v Tržaškem zalivu (A), alkalnosti (TA) and $\delta^{13}C_{DIC}$ (B), koncentracije Ca in nasičenost glede na kalcit in aragonit (C), slanost in temperatura (D), normalizirane vrednosti pCO_2 glede na slanost in temperaturo (δpCO_2) ter »termični« ($\delta pCO_{2,T}$) in »netermični« ($\delta pCO_{2,NT}$) vplivi na morski $pCO2$ v južnem delu Tržaškega zaliva (E) in pCO_2 (F) • – iz TA in pH,[16] – *in situ* v globini 3 m.[22] Razlike med izračunanimi in merjenimi *in situ* pCO_2 pripisujemo predvsem izbiri disociacijskih konstant ogljikove kisline v morski vodi, vpliv raztopljenih organskih baz (ang. Dissolved Organic Carbon – DOC) pa je majhen.[16]

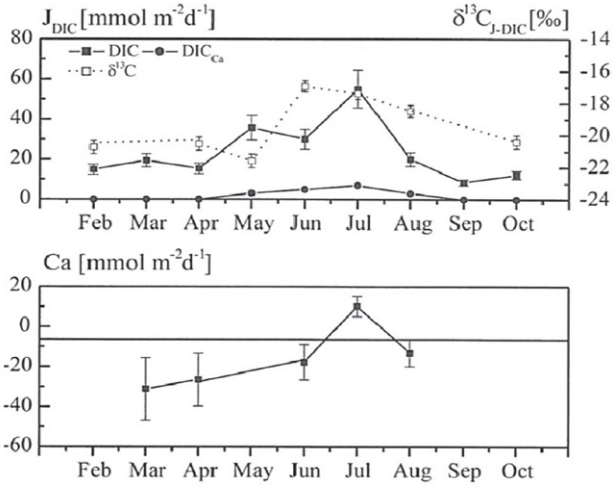

Slika 8. Bentoški tokovi celotnega raztopljenega anorganskega ogljika (J_{DIC}) in kot posledica raztapljanja karbonatov (J_{DICCa}), njihova izotopska sestava ^{13}C (vrednosti $\delta^{13}C_{DIC}$) in bentoški tokovi Ca v Tržaškem zalivu[26]

Zahvala

Prispevek temelji na izsledkih projekta J1-8156, ki ga je podprla Agencija republike Slovenije za raziskovalno delo (ARRS).

Literatura

1. C. L. Sabine, R. A. Feely, N. Gruber, R. M. Key, K. Lee, J. L. Bullister, R. Waninkhof, C. S. Wong, D. W. R. Wallace, B. Tilbrook, F. J. Millero, T.-H. Peng, A. Kozyr, T. Ono, A. F. Rios, *Science* **2004**, *305*, 367–371. **DOI:**10.1126/science.1097403
2. F. J. Millero, Chemical oceanography. CRC Press, Boca Raton, **2006**.
3. A. V. Borges, N. Gypsen, *Limnol. Oceanogr.* **2010**, *55*, 346–353. **DOI:**10.4319/lo.2010.55.1.0346
4. W.-J. Cai W.-J. Huang, G. W. Luther III, D. Pierrot, M. Li, J. Testa, M. Xue, A. Joesoef, R. Mann, J. Brodeur, Y.-Y. Xu, B. Chen, N. Hussain, G. G. Waldbusser, J. Cornwell, W. M. Kemp, *Nature Comm.* **2017**, *8*, 1–12.
5. G. Cossarini, S. Querin, C. Solidoro, *Ecol. Model.* **2015**, *314*, 118–134. **DOI:**10.1016/j.ecolmodel.2015.07.024
6. C. Copin-Montegut, M. Begovic, L. Merlivat, *Mar. Chem.* **2004**, *85*, 169–189. **DOI:**10.1016/j.marchem.2003.10.005
7. F. Touratier, C. Goyet, L. Houpert, X. D. de Madron, D. Le-

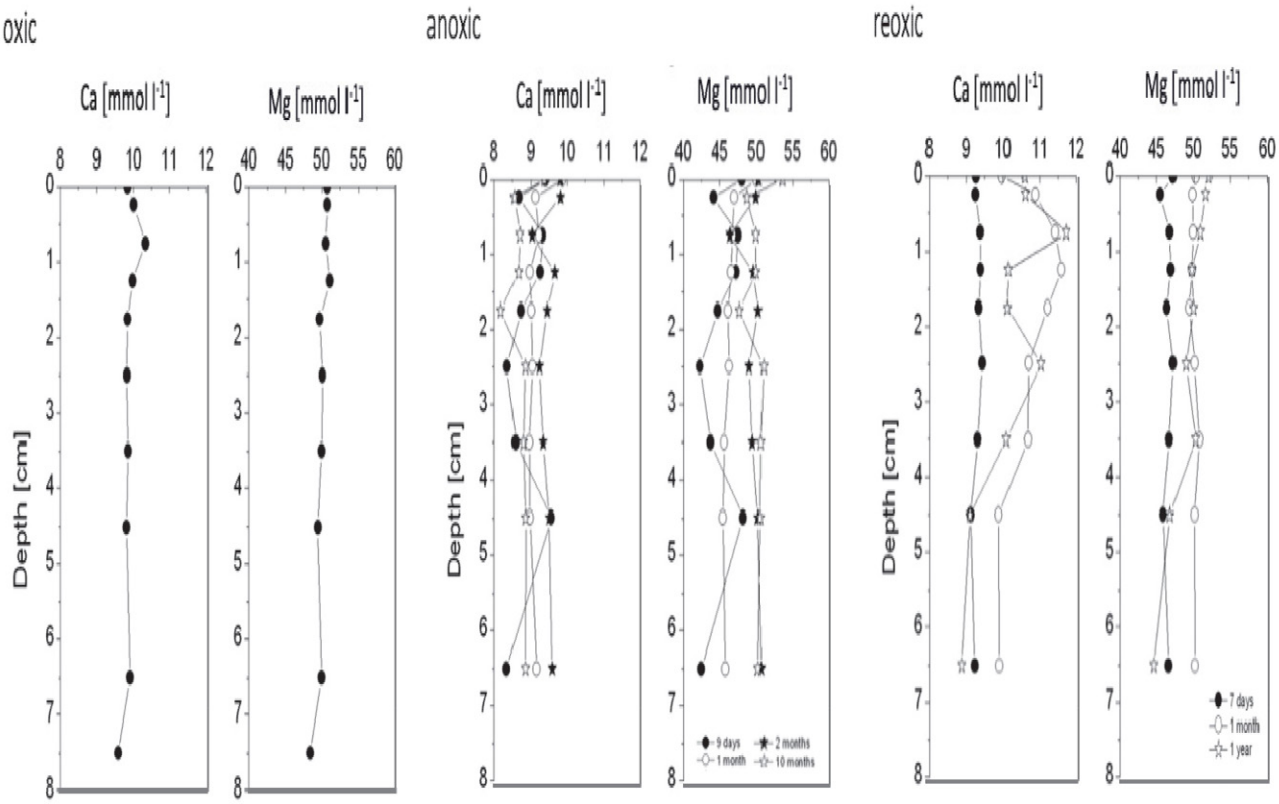

Slika 9. Koncentracije Ca in Mg v pornih vodah sedimenta Tržaškega zaliva z oksično, anoksično in ponovno oksično plastjo vode and sedimentom[31]

palke). Temperatura, slanost in anorganska ter organska hranila vplivajo na številčnost in produktivnost mikrobov in s tem na trofično stanje morja. Negativni vplivi »kisanja« lahko povzročajo spremembe v prehranjevalnih verigah in s tem posledično vplivajo na ribolov in marikulturo.

fevre, M. Stabholz, V. Guglielmi, *Deep-Sea Res. I* **2016**, *113*, 33–48. **DOI:**10.1016/j.dsr.2016.04.003
8. A. Luchetta, C. Cantoni, G. Catalano, *Chem. Ecol.* **2010**, *26*, 1–17. **DOI:**10.1080/02757541003627688
9. A. E. R. Hassoun, E. Gemayel, E. Krassakopoulou, C. Goyet, M. Abboud-Abi Saab, V. Guglielmi, F. Touratier, C. Falco, *Deep-Sea Res. I* **2015**, *164*, 54–73.
10. S. Flecha, F. F. Perez, J. Garcia-Lafuente, S. Sammartino, A. F. Rios, I. E. Huertas, *Scient. Rep.* **2015**, *5*, 16770. **DOI:**10.5465/ambpp.2015.16770abstract
11. A. Dickson, C. Sabine, J. R. Christian, PICES Special Pubbl. 3, **2007**.
12. G. Ingrosso, M. Bensi, V. Cardin, M. Giani, *Deep-Sea Res. I* **2017**, *123*, 118–128. **DOI:**10.1016/j.dsr.2017.04.004
13. A. Schneider, D. W. R. Wallace, A. Kortzinger, *Geophys. Res. Lett.* **2007**, *34*, L15608. **DOI:**10.1029/2006GL028842
14. E. Gemayel, A. E. R. Hassoun, M. A. Benallal, C. Goyet, P. Rivaro, M. Abboud-Abi Saab, E. Krassakopoulou, F. Touratier, P. Ziveri, *Earth Syst. Dyn.* **2015**, *6*, 789–800. **DOI:**10.5194/esd-6-789-2015
15. K. Szramek, J. C. McIntosh, E. L. Williams, T. Kanduč, N. Ogrinc, L. M. Walter, *Geochem. Geophys. Geosyst.* **2007**, *8*, 1–28.
16. S. Tamše, N, Ogrinc, L. M. Walter, D. Turk, J. Faganeli, *Estuar. Coasts* **2014**, *38*, 151–164. **DOI:**10.1007/s12237-014-9812-7
17. M. J. Brush, M. Giani, C. Totti, J. M. Testa, J. Faganeli, N. Ogrinc, W. M. Kemp, S. Fonda Umani, in: T. C. Malone, A. Malej, J. Faganeli (Ed.): Coastal ecosystems in transition: A comparative analysis of the Northern Adriatic and Chesapeake Bay, AGU Wiley, New Jersey, **2021**, pp. 147–175.
18. L. Urbini, M. Ingrosso, T. Djakovac, S. Piacentino, M. Giani, *Front. Mar. Sci.* **2020. DOI:** 10. 3389/fmars-202000679
19. C. Cantoni, A. Luchetta, J. Chiggiato, S. Cozzi, K. Schroeder, L. Langone, *Mar. Geol.* **2016**, *375*, 15–27. **DOI:**10.1016/j.margeo.2015.08.013
20. C. Cantoni, A. Luchetta, M. Celio, S. Cozzi, F. Raicich, G. Catalano, *Estuar. Coast. Shelf Sci.* **201**2, *115*, 51–62. **DOI:**10.1016/j.ecss.2012.07.006
21. D. Turk, V. Malačič, W. R. McGillis, *J. Geophys. Res.* **2010**, *115*, C10043. **DOI:**10.1029/2009JC006034
22. G. Ingrosso, M. Giani, T. Cibic, A. Karuza, M. Kralj, P. Del Negro, *J. Mar. Syst.* **2016**, *155*, 35–49.
23. G. Ingrosso, M. Giani, C. Comici, M. Kralj, S. Piacentino, C. De Vittor, P. Del Negro, *Estuar. Coast. Shelf Sci.* **2016**, *168*, 58–70. **DOI:**10.1016/j.ecss.2015.11.001
24. K. Szramek, L. M. Walter, T. Kanduč, N. Ogrinc, *Aquat. Geochem.* **2011**, *17*, 357–396. **DOI:**10.1007/s10498-011-9125-4
25. S. Tamše, Ph D Thesis, Jozef Stefan International Postgraduate School, Ljubljana, **2014**.
26. N. Ogrinc, J. Faganeli, J. Pezdic, *Org. Geochem.* **2003**, *34*, 681–692. **DOI:**10.1016/S0146-6380(03)00023-8
27. J. Faganeli, N. Ogrinc, *Mar. Freshwat. Res.* **2009**, *60*, 700–711. **DOI:**10.1071/MF08065
28. M. E. Hines, J. Faganeli, R. Planinc, *Biogeochemistry* **1997**, *39*, 65–86. **DOI:**10.1023/A:1005806508707
29. D. E. Hammond, P. Giordani, W. M. Berelson, R. Poletti, *Mar. Chem.* **1999**, *66*, 53–79. **DOI:**10.1016/S0304-4203(99)00024-9
30. N. Ogrinc, J. Faganeli, *Acta Chim. Slov.* **2003**, *50*, 645–662.
31. N. Koron, N. Ogrinc, E. Metzger, B. Riedel, J. Faganeli, *Biogeosciences Discuss.* **2013**, *10*, 11729–11755.
32. R. E. Zeebe, D. Wolf-Gladrow, CO_2 in Seawater: Equilibrium, Kinetics, Isotopes, Elsevier, Amsterdam, **2001**.
33. N. Bednaršek, B. Guilloux, C. Galdies, D. Melaku Canu, R. A. Feeley, R. Guerra, B. Gašparović, I. Godrijan, A. Malej, S. Simoncelli, C. Solidoro, V. Turk, S. Zunino, in: K. Hornidge, M. Hadjimichael (Ed.): Ocean acidification impact on the aquaculture and fisheries as a governance challenge in the Mediterranean Sea. Ocean governance. Pasts, presents, futures, Springer, Berlin, **2021**.
34. D. C. Capone, D. A. Hutchins, *Nature Geosci.* **2013**, *6*, 711–717. **DOI:**10.1038/ngeo1916
35. J. E. Dore, R. Lukas, D. W. Sadler, M. J. Church, D. W. Karl, *Proc. Nat. Acad. Sci. US* **2009,** *106*, 12235–12240. **DOI:**10.1073/pnas.0906044106
36. J. M. Beman, C.-E. Chow, A. L. King, Y. Feng, J. A. Fuhrman, A. Andersson, N. R, Bates, B. N. Popp, D. A. Hutchins, *Proc. Nat. Acad. Sci. US* **2011**, *108*, 208–213. **DOI:**10.1073/pnas.1011053108
37. I. R. Booth, *Microbiol. Rev.* **1986**, *49*, 359–378. **DOI:**10.1128/mr.49.4.359-378.1985

Abstract

The present knowledge of the carbonate system in the northern Adriatic is described in this short overview. Its buffer capacity is rather high, due to riverine input of carbonates dissolved from Alpine and Karstic watersheds, and the waters should have a higher resilience to acidification. In the shallow eutrophic areas, the combined effect of rising atmospheric CO_2, warming and river-induced anthropogenic CO_2 with the associated decrease in buffer capacity could act to acidification process. Significant effect on calcifying organisms is expected in the future.

Acta Chimica Slovenica

Author Guidelines

Submissions

Submission to ACSi is made with the implicit understanding that neither the manuscript nor the essence of its content has been published in whole or in part and that it is not being considered for publication elsewhere. All the listed authors should have agreed on the content and the corresponding (submitting) author is responsible for having ensured that this agreement has been reached. The acceptance of an article is based entirely on its scientific merit, as judged by peer review. There are no page charges for publishing articles in ACSi. The authors are asked to read the Author Guidelines carefully to gain an overview and assess if their manuscript is suitable for ACSi.

Additional information

- Citing spectral and analytical data
- Depositing X-ray data

Submission material

Typical submission consists of:

- full manuscript (PDF file, with title, authors, abstract, keywords, figures and tables embedded, and references)
- supplementary files
  - ***Full manuscript*** (original Word file)
  - ***Statement of novelty*** (Word file)
  - ***List of suggested reviewers*** (Word file)
  - ***ZIP file containing graphics*** (figures, illustrations, images, photographs)
  - ***Graphical abstract*** (single graphics file)
  - ***Proposed cover picture*** (optional, single graphics file)
  - ***Appendices*** (optional, Word files, graphics files)

Incomplete or not properly prepared submissions will be rejected.

Submission process

Before submission, authors should go through the checklist at the bottom of the page and prepare for submission.

Submission process consists of 5 steps.

Step 1: Starting the submission

- Choose one of the journal sections.
- Confirm all the requirements of the ***checklist.***
- Additional plain text comments for the editor can be provided in the relevant text field.

Step 2: Upload submission

- Upload full manuscript in the form of a Word file (with title, authors, abstract, keywords, figures and tables embedded, and references).

Step 3: Enter metadata

- First name, last name, contact email and affiliation for all authors, in relevant order, must be provided. Corresponding author has to be selected. Full postal address and phone number of the corresponding author has to be provided.
- ***Title and abstract*** must be provided in plain text.
- Keywords must be provided (max. 6, separated by semicolons).
- Data about contributors and supporting agencies may be entered.
- ***References*** in plain text must be provided in the relevant text filed.

Step 4: Upload supplementary files

- Original Word file (original of the PDF uploaded in the step 2)
- ***List of suggested reviewers*** with at least five reviewers with two recent references from the field of submitted manuscript must be uploaded as a Word file. At the same time, authors should declare (i) that they have no conflict of interest with suggested reviewers and (ii) that suggested reviewers are experts in the field of the submitted manuscript.
- All ***graphics*** have to be uploaded in a single ZIP file. Graphics should be named Figure 1.jpg, Figure 2.eps, etc.
- ***Graphical abstract image*** must be uploaded separately
- ***Proposed cover picture*** (optional) should be uploaded separately.
- Any additional ***appendices*** (optional) to the paper may be uploaded. Appendices may be published as a supplementary material to the paper, if accepted.
- For each uploaded file the author is asked for additional metadata which may be provided. Depending of the type of the file please provide the relevant title (Statement of novelty, List of suggested reviewers, Figures, Graphical abstract, Proposed cover picture, Appendix).

Step 5: Confirmation

- Final confirmation is required.

Article Types

Feature Articles are contributions that are written on editor's invitation. They should be clear and concise summaries of the most recent activity of the author and his/her research group written with the broad scope of ACSi in mind. They are intended to be general overviews of the authors' subfield of research but should be written in a way that engages and informs scientists in other areas. They should contain the following (see also general directions for article structure in ACSi below): (1) an introduction that acquaints readers with the authors' research field and outlines the important questions to which answers are being sought; (2) interesting, new, and recent contributions of the author(s) to the field; and (3) a summary that presents possible future directions. Manuscripts normally should not exceed 40 pages of one column format (letter size 12, 33 lines per page). Generally, experts in a field who have made important contribution to a specific topic in recent years will be invited by an editor to contribute such an **Invited Feature Article**. Individuals may, however, send a proposal (one-page

maximum) for an Invited Feature Article to the Editor-in-Chief for consideration.

Scientific articles should report significant and innovative achievements in chemistry and related sciences and should exhibit a high level of originality. They should have the following structure:

1. Title (max. 150 characters),
2. Authors and affiliations,
3. Abstract (max. 1000 characters),
4. Keywords (max. 6),
5. Introduction,
6. Experimental,
7. Results and Discussion,
8. Conclusions,
9. Acknowledgements,
10. References.

The sections should be arranged in the sequence generally accepted for publications in the respective fields and should be successively numbered.

Short communications generally follow the same order of sections as Scientific articles, but should be short (max. 2500 words) and report a significant aspect of research work meriting separate publication. Editors may decide that a Scientific paper is categorized as a Short Communication if its length is short.

Technical articles report applications of an already described innovation. Typically, technical articles are not based on new experiments.

Preparation of Submissions

Text of the submitted articles must be prepared with Microsoft Word. Normal style set to single column, 1.5 line spacing, and 12 pt Times New Roman font is recommended. Line numbering (continuous, for the whole document) must be enabled to simplify the reviewing process. For any other format, please consult the editor. Articles should be written in English. Correct spelling and grammar are the sole responsibility of the author(s). Papers should be written in a concise and succinct manner. The authors shall respect the ISO 80000 standard [1], and IUPAC Green Book [2] rules on the names and symbols of quantities and units. The Système International d'Unités (SI) must be used for all dimensional quantities.

Graphics (figures, graphs, illustrations, digital images, photographs) should be inserted in the text where appropriate. The captions should be self-explanatory. Lettering should be readable (suggested 8 point Arial font) with equal size in all figures. Use common programs such as MS Excel or similar to prepare figures (graphs) and ChemDraw to prepare structures in their final size. Width of graphs in the manuscript should be 8 cm. Only in special cases (in case of numerous data, visibility issues) graphs can be 17 cm wide. All graphs in the manuscript should be inserted in relevant places and **aligned left**. The same graphs should be provided separately as images of appropriate resolution (see below) and submitted together in a ZIP file (Graphics ZIP). Please do not submit figures as a Word file. In **graphs**, only the graph area determined by both axes should be in the frame, while a frame around the whole graph should be omitted. The graph area should be white. The legend should be inside the graph area. The style of all graphs should be the same. **Figures and illustrations** should be of sufficient quality for the printed version, i.e. 300 dpi minimum. **Digital images and photographs** should be of high quality (minimum 250 dpi resolution). On submission, figures should be of good enough resolution to be assessed by the referees, ideally as JPEGs. High-resolution figures (in JPEG, TIFF, or EPS format) might be required if the paper is accepted for publication.

Tables should be prepared in the Word file of the paper as usual Word tables. The captions should appear above the table and should be self-explanatory.

References should be numbered and ordered sequentially as they appear in the text, likewise methods, tables, figure captions. When cited in the text, reference numbers should be superscripted, following punctuation marks. It is the sole responsibility of authors to cite articles that have been submitted to a journal or were in print at the time of submission to ACSi. Formatting of references to published work should follow the journal style; please also consult a recent issue:

1. J. W. Smith, A. G. White, *Acta Chim. Slov.* **2008**, *55*, 1055–1059.
2. M. F. Kemmere, T. F. Keurentjes, in: S. P. Nunes, K. V. Peinemann (Ed.): Membrane Technology in the Chemical Industry, Wiley-VCH, Weinheim, Germany, **2008**, pp. 229–255.
3. J. Levec, Arrangement and process for oxidizing an aqueous medium, US Patent Number 5,928,521, date of patent July 27, **1999**.
4. L. A. Bursill, J. M. Thomas, in: R. Sersale, C. Collela, R. Aiello (Eds.), Recent Progress Report and Discussions: 5th International Zeolite Conference, Naples, Italy, 1980, Gianini, Naples, **1981**, pp. 25–30.
5. J. Szegezdi, F. Csizmadia, Prediction of dissociation constant using microconstants, http://www. chemaxon.com/conf/Prediction_of_dissociation _constant_using_microco nstants.pdf, (assessed: March 31, 2008)

Titles of journals should be abbreviated according to Chemical Abstracts Service Source Index (CASSI).

Special Notes

- Complete characterization, **including crystal structure**, should be given when the synthesis of new compounds in crystal form is reported.
- Numerical **data should be reported with the number of significant digits corresponding to the magnitude** of experimental uncertainty.
- **The SI system of units and IUPAC recommendations** for nomenclature, symbols and abbreviations should be followed closely. Additionally, the authors should follow the general guidelines when citing spectral and analytical data, and depositing crystallographic data.
- **Characters** should be correctly represented throughout the manuscript: for example, 1 (one) and l (ell), 0 (zero) and O (oh), x (ex), D7 (times sign), B0 (degree sign). Use Symbol font for all Greek letters and mathematical symbols.
- The rules and recommendations of the **IUBMB** and the **International Union of Pure and Applied Chemistry (IUPAC)** should be used for abbreviation of chemical names, nomenclature of chemical compounds, enzyme nomenclature, isotopic compounds, optically active isomers, and spectroscopic data.

- **A conflict of interest** occurs when an individual (author, reviewer, editor) or its organization is involved in multiple interests, one of which could possibly corrupt the motivation for an act in the other. Financial relationships are the most easily identifiable conflicts of interest, while conflicts can occur also as personal relationships, academic competition, etc. **The Editors** will make effort to ensure that conflicts of interest will not compromise the evaluation process; potential editors and reviewers will be asked to exempt themselves from review process when such conflict of interest exists. When the manuscript is submitted for publication, **the authors** are expected to disclose any relationships that might pose potential conflict of interest with respect to results reported in that manuscript. In the Acknowledgement section the source of funding support should be mentioned. The statement of disclosure must be provided as Comments to Editor during the submission process.
- **Published statement of Informed Consent.** Research described in papers submitted to ACSi must adhere to the principles of the Declaration of Helsinki (***http://www.wma.net/e/policy/b3.htm***). These studies must be approved by an appropriate institutional review board or committee, and informed consent must be obtained from subjects. The Methods section of the paper must include: 1) a statement of protocol approval from an institutional review board or committee and 2), a statement that informed consent was obtained from the human subjects or their representatives.
- **Published Statement of Human and Animal Rights.**When reporting experiments on human subjects, authors should indicate whether the procedures followed were in accordance with the ethical standards of the responsible committee on human experimentation (institutional and national) and with the Helsinki Declaration of 1975, as revised in 2008. If doubt exists whether the research was conducted in accordance with the Helsinki Declaration, the authors must explain the rationale for their approach and demonstrate that the institutional review body explicitly approved the doubtful aspects of the study. When reporting experiments on animals, authors should indicate whether the institutional and national guide for the care and use of laboratory animals was followed.
- To avoid conflict of interest between authors and referees we expect that not more than one referee is from the same country as the corresponding author(s), however, not from the same institution.
- Contributions authored by **Slovenian scientists** are evaluated by non-Slovenian referees.
- Papers describing **microwave-assisted reactions** performed in domestic microwave ovens are not considered for publication in *Acta Chimica Slovenica.*
- *Manuscripts that are **not prepared and submitted** in accord with the instructions for authors are not considered for publication.*

Appendices

Authors are encouraged to make use of supporting information for publication, which is supplementary material (appendices) that is submitted at the same time as the manuscript. It is made available on the Journal's web site and is linked to the article in the Journal's Web edition. The use of supporting information is particularly appropriate for presenting additional graphs, spectra, tables and discussion and is more likely to be of interest to specialists than to general readers. When preparing supporting information, authors should keep in mind that the supporting information files will not be edited by the editorial staff. In addition, the files should be not too large (upper limit 10 MB) and should be provided in common widely known file formats to be accessible to readers without difficulty. All files of supplementary materials are loaded separately during the submission process as supplementary files.

Proposed Cover Picture and Graphical Abstract Image

Graphical content: an ideally full-colour illustration of resolution 300 dpi from the manuscript must be proposed with the submission. Graphical abstract pictures are printed in size 6.5 x 4 cm (hence minimal resolution of 770 x 470 pixels). Cover picture is printed in size 11 x 9.5 cm (hence minimal resolution of 1300 x 1130 pixels)

Authors are encouraged to submit illustrations as candidates for the journal Cover Picture*. The illustration must be related to the subject matter of the paper. Usually both proposed cover picture and graphical abstract are the same, but authors may provide different pictures as well.

* The authors will be asked to contribute to the costs of the cover picture production.

Statement of novelty

Statement of novelty is provided in a Word file and submitted as a supplementary file in step 4 of submission process. Authors should in no more than 100 words emphasize the scientific novelty of the presented research. Do not repeat for this purpose the content of your abstract.

List of suggested reviewers

List of suggested reviewers is a Word file submitted as a supplementary file in step 4 of submission process. Authors should propose the names, full affiliation (department, institution, city and country) and e-mail addresses of five potential referees. Field of expertise and at least two references relevant to the scientific field of the submitted manuscript must be provided for each of the suggested reviewers. The referees should be knowledgeable about the subject but have no close connection with any of the authors. In addition, referees should be from institutions other than (and countries other than) those of any of the authors. Authors declare no conflict of interest with suggested reviewers. Authors declare that suggested reviewers are experts in the field of submitted manuscript.

How to Submit

Users registered in the role of author can start submission by choosing USER HOME link on the top of the page, then choosing the role of the Author and follow the relevant link for starting the submission process.

Prior to submission we strongly recommend that you familiarize yourself with the ACSi style by browsing the journal, particularly if you have not submitted to the ACSi before or recently.

Correspondence

All correspondence with the ACSi editor regarding the paper goes through this web site and emails. Emails are sent and recorded in the web site database. In the correspondence with the editorial office please provide ID number of your manuscript. All emails you receive from the system contain relevant links. **Please do not answer the emails directly but use the embedded links in the emails for carrying out relevant actions.** Alternatively, you can carry out all the actions and correspondence through the online system by logging in and selecting relevant options.

Proofs

Proofs will be dispatched via e-mail and corrections should be returned to the editor by e-mail as quickly as possible, normally within 48 hours of receipt. Typing errors should be corrected; other changes of contents will be treated as new submissions.

Submission Preparation Checklist

As part of the submission process, authors are required to check off their submission's compliance with all of the following items, and submissions may be returned to authors that do not adhere to these guidelines.

1. The submission has not been previously published, nor is it under consideration for publication in any other journal (or an explanation has been provided in Comments to the Editor).
2. All the listed authors have agreed on the content and the corresponding (submitting) author is responsible for having ensured that this agreement has been reached.
3. The submission files are in the correct format: manuscript is created in MS Word but will be **submitted in PDF** (for reviewers) as well as in original MS Word format (as a supplementary file for technical editing); diagrams and graphs are created in Excel and saved in one of the file formats: TIFF, EPS or JPG; illustrations are also saved in one of these formats. The preferred position of graphic files in a document is to embed them close to the place where they are mentioned in the text (See ***Author guidelines*** for details).
4. The manuscript has been examined for spelling and grammar (spell checked).
5. The ***title*** (maximum 150 characters) briefly explains the contents of the manuscript.
6. Full names (first and last) of all authors together with the affiliation address are provided. Name of author(s) denoted as the corresponding author(s), together with their e-mail address, full postal address and telephone/fax numbers are given.
7. The ***abstract*** states the objective and conclusions of the research concisely in no more than 150 words.
8. Keywords (minimum three, maximum six) are provided.
9. ***Statement of novelty*** (maximum 100 words) clearly explaining new findings reported in the manuscript should be prepared as a separate Word file.
10. The text adheres to the stylistic and bibliographic requirements outlined in the ***Author guidelines***.
11. Text in normal style is set to single column, 1.5 line spacing, and 12 pt. Times New Roman font is recommended. All tables, figures and illustrations have appropriate captions and are placed within the text at the appropriate points.
12. Mathematical and chemical equations are provided in separate lines and numbered (Arabic numbers) consecutively in parenthesis at the end of the line. All equation numbers are (if necessary) appropriately included in the text. Corresponding numbers are checked.
13. Tables, Figures, illustrations, are prepared in correct format and resolution (see ***Author guidelines***).
14. The lettering used in the figures and graphs do not vary greatly in size. The recommended lettering size is 8 point Arial.
15. Separate files for each figure and illustration are prepared. The names (numbers) of the separate files are the same as they appear in the text. All the figure files are packed for uploading in a single ZIP file.
16. Authors have read ***special notes*** and have accordingly prepared their manuscript (if necessary).
17. References in the text and in the References are correctly cited. (see ***Author guidelines***). All references mentioned in the Reference list are cited in the text, and vice versa.
18. Permission has been obtained for use of copyrighted material from other sources (including the Web).
19. The names, full affiliation (department, institution, city and country), e-mail addresses and references of five potential referees from institutions other than (and countries other than) those of any of the authors are prepared in the word file. At least two relevant references (important recent papers with high impact factor, head positions of departments, labs, research groups, etc.) for each suggested reviewer must be provided. Authors declare no conflict of interest with suggested reviewers. Authors declare that suggested reviewers are experts in the field of submitted manuscript.
20. Full-colour illustration or graph from the manuscript is proposed for graphical abstract.
21. ***Appendices*** (if appropriate) as supplementary material are prepared and will be submitted at the same time as the manuscript.

Privacy Statement

The names and email addresses entered in this journal site will be used exclusively for the stated purposes of this journal and will not be made available for any other purpose or to any other party.

ISSN: 1580-3155

Koristni naslovi

Slovensko kemijsko društvo
www.chem-soc.si
e-mail: chem.soc@ki.si

Wessex Institute of Technology
www.wessex.ac.uk

SETAC
www.setac.org

European Water Association
http://www.ewa-online.eu/

European Science Foundation
www.esf.org

European Federation of Chemical Engineering
https://efce.info/

International Union of Pure and Applied Chemistry
https://iupac.org/

Novice europske zveze kemijskih društev EuChemS najdete na:

Brussels News Updates
http://www.euchems.eu/newsletters/

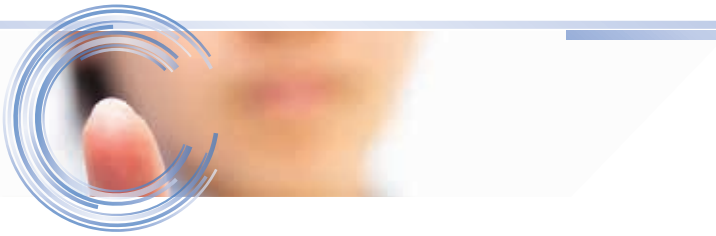

DONAU LAB Ljubljana
Member of LPPgroup

Donau Lab d.o.o., Ljubljana
Tbilisijska 85
SI-1000 Ljubljana
www.donaulab.si
office-si@donaulab.com

Planetarni centrifugalni mikser ARM-310CE

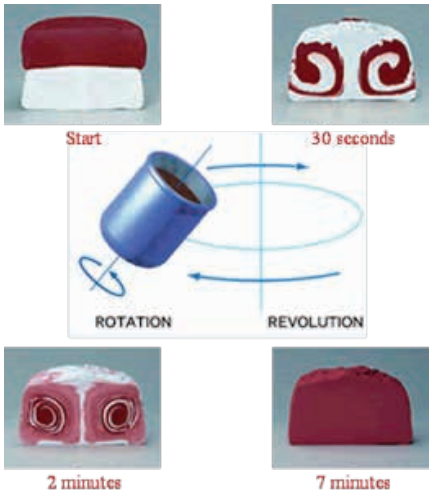

Brezkontaktno mešanje in disperzija

Tudi za zelo viskozne materiale

Širok spekter uporabe

Atraktivna cena

THINKY

Razvoj in inovacije za globalno uspešnost

Znanje, kreativnost zaposlenih in inovacije so ključnega pomena v okolju, kjer nastajajo Heliosovi pametni premazi. Z rešitvami, ki zadostijo široki paleti potreb, kontinuiranim razvojem ter s kakovostnimi produkti Helios predstavlja evropski center za inovacije, know-how in poslovni razvoj skupine Kansai Paint.

Part of KANSAI PAINT

www.helios-group.eu

HELIOS

Designing Excellence

MAGNEZIJ Krka 300

VAŠA PRVA IZBIRA*

*Vir: Prodajni podatki v lekarnah, ePharma Market Slovenija, za leto 2020 – kategorija izdelkov z magnezijem.

BODITE NEUSTAVLJIVI

Magnezij Krka 300 vsebuje **magnezijev citrat** in **vitamin B_2**.

- ✓ Magnezij in vitamin B_2 prispevata k **zmanjševanju utrujenosti** in **izčrpanosti**.
- ✓ Magnezij prispeva tudi k **normalnemu delovanju mišic**.

www.magnezijkrka.si

KRKA

Prehransko dopolnilo ni nadomestilo za uravnoteženo in raznovrstno prehrano. Skrbite tudi za zdrav življenjski slog.

NATIONAL INSTITUTE OF CHEMISTRY 75

Hajdrihova 19,
1000 Ljubljana
Slovenia
www.ki.si

_research EXCELENCE

Basic and applied research in materials, life sciences, biotechnology, chemical engineering, structural and theoretical chemistry, analytical chemistry and environmental protection.

In line with EU research and innovation priorities: nanotechnology, genomics and biotechnology for health, sustainable development, climate change, energy efficiency and food quality and safety.

We expand knowledge and technology transfer to domestic and foreign chemical, automotive and nanobiotechnology industries.

We are aware of the power of youth, so we transfer our knowledge to younger generations and offer many opportunities for cooperation.

contact: mladi@ki.si

Lek d.d.

70 let razvoja kemijske stroke. Čestitamo!

Slovensko kemijsko društvo je ključnega pomena za napredek kemije, kemijske tehnologije in kemijskega inženirstva v Sloveniji.

Kemija je za farmacevtsko industrijo neprecenljiva znanost. Ima ključno vlogo pri odkrivanju, raziskovanju in razvoju novih zdravil, s katerimi bolnikom zagotavljamo kakovostno, varno in učinkovito zdravljenje.

Hvala za desetletja odličnega sodelovanja, osnovanega na izjemni strokovnosti in zavzetosti za razreševanje temeljnih izzivov današnjih in prihodnjih generacij. Verjamemo, da nas bodo skupne vrednote ter želja po nadaljnjem razvoju in bogatitvi slovenske znanstvene stroke še naprej povezovale v uspešnih zgodbah.

Želimo vam še veliko zagona in uspešnosti pri vašem plemenitem poslanstvu.

Smo Novartis.
Soustvarjamo medicino.

top EMPLOYER SLOVENIJA SLOVENIA 2021
CERTIFIED EXCELLENCE IN EMPLOYEE CONDITIONS

NAJUGLEDNEJŠI DELODAJALEC - 2020 - MojeDelo.com universum

NOVARTIS | Reimagining Medicine

Lek farmacevtska družba d.d., Verovškova ulica 57, 1526 Ljubljana, Slovenija, www.lek.si

Acta Chimica Slovenica

Acta Chimica Slovenica

Year 2021, Vol. 68, No. 3

The structure and thermodynamics of water and aqueous solutions is of great importance for all sciences, especially chemistry and biology, and industry. Water exhibits many anomalous properties that affect life at a larger scale. The reason for water's complexity is due to its strong orientation-dependent hydrogen bonding and strong intermolecular associations. Page 505–520.